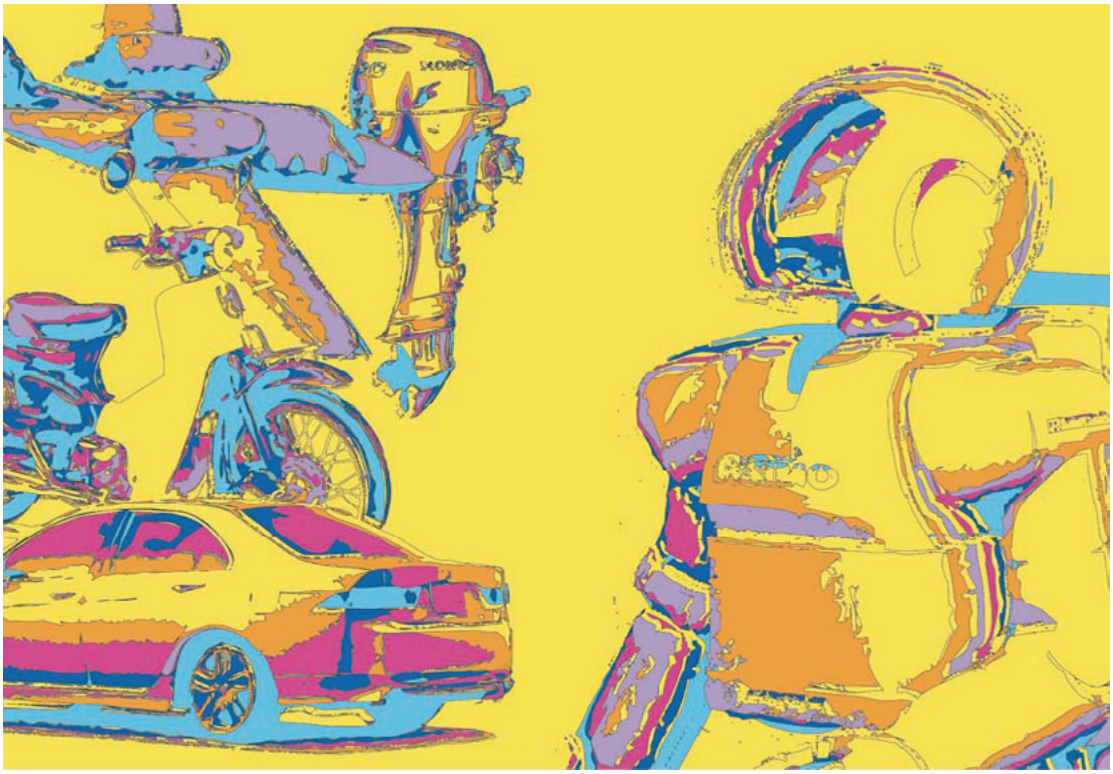
R&D Technical Review



April 2003



Comment on the Cover

Technological sensuality.



Wako R&D Center
Daisuke Toriyama

Development of the Honda FCX Fuel Cell Vehicle

Satoshi KAWASAKI* Masami OGURA*
Tohru ONO* Yozo KAMI*

ABSTRACT

Honda has developed the ultimate clean power fuel cell vehicle, the FCX, to respond to environmental and energy issues. Honda simultaneously marketed the FCX in the U.S. and Japan in December 2002. This vehicle is provided with a compressed pure hydrogen type fuel cell and an Ultra capacitor as a combined power source, and is driven by a high-performance drive motor. Honda's original packaging technologies enable these units to be fitted in a compact body. The FCX has a practical driving range, high maximum speed, and excellent power performance. The vehicle also ensures crash safety from all directions and comfortably seat four adults.

1. Introduction

In order to make a significant response to various environmental and energy issues, including air pollution, global warming, and the depletion of petroleum resources, the ideal is to have an energy source that does not depend on fossil fuels, in addition to having no toxic substances or CO_2 emissions. Prior to the FCX, Honda had been developing and marketing the electric vehicle Honda EV PLUS, and hybrid vehicles. The focus is now on hydrogen, as the next generation of ideal fuels. Honda has been developing a power train that gives high vehicle energy efficiency, based on a fuel cell that makes possible the ultimate environmental performance. Electricity is generated from a chemical reaction between hydrogen and oxygen, with water discharged as the only by-product. The aim has been to actualize a fuel cell vehicle giving advanced passenger vehicle performance, habitability, and safety.

The FCX series began with simultaneous announcements, in September 1999, of the prototypes V1 and V2, followed in 2000 by V3 and by V4 in 2001. In 2002 the FCX was announced, with further research and refinements made through drive tests using in-house test vehicles, collision safety, hydrogen safety, and electrical safety tests. In addition, tests were carried out on public roads – by participation in the CaFCP (California Fuel Cell Partnership) in the US, and by the Japanese Ministry of Land, Infrastructure and Transport's certification program in Japan.

As a result, on December 2, 2002, Honda announced the world's first fuel cell vehicle, with vehicles delivered to both the Japanese Cabinet Office in Japan, and to the city of Los Angeles in the USA on the same day.

2. Development History

A history of the major specifications for the FCX is provided in Table 1 by showing the transition of specifications from V1, V2, V3, and V4 to the current FCX. The FCX-V1 announced in 1999 was a pure hydrogen fuel cell vehicle, with a hydrogen tank of metal hydride. The V2 was a methanol reformer type fuel cell vehicle.

In September 2000, the FCX-V3 was introduced for participation in the CaFCP. Performance of the power plant system was confirmed by adopting a pure hydrogen gas type fuel cell vehicle which stores the hydrogen fuel in high-pressure hydrogen gas tanks. Furthermore, public road testing was implemented in California with V3 vehicles having a fuel cell stack built by either Canada's Ballard Power Systems or Honda's own in-house developed stack. In July of 2001, Japanese certification was obtained, and public road testing began. The testing continued for approximately one year.

In September of 2001, the basic structure and layout were reviewed, and the announcement of the FCX-V4, which became the foundation for the completed FCX vehicle, was made. The results of the major collision testing items were

* Tochigi R&D Center

Table 1 History of major specifications

	FCX V1	FCX V2	FCX V3 / V3 with Honda FC Stack	FCX V4	FCX
Exterior					
Hydrogen supply system	Metal hydride	Methanol reformer	High-pressure hydrogen tank (25MPa)	High-pressure hydrogen tank (35MPa)	High-pressure hydrogen tank (35MPa)
Hydrogen storage volume	—	—	100L	137L	156.6L
Fuel cell stack	PEMFC (Proton-exchange membrane fuel cell)	PEMFC (Proton-exchange membrane fuel cell)	PEMFC (Proton-exchange membrane fuel cell)	PEMFC (Proton-exchange membrane fuel cell)	PEMFC (Proton-exchange membrane fuel cell)
Power assist	Battery	Battery	Ultra capacitor	Ultra capacitor	Ultra capacitor
Maximum motor output	49kW[67PS]	49kW[67PS]	60kW[82PS]	60kW[82PS]	60kW[82PS]
Maximum motor torque	—	—	238N·m[24.3kg·m]	238N·m[24.3kg·m]	272N·m[27.7kg·m]
Maximum speed	—	—	130 km/h	140 km/h	150km/h
Range (With LA4 mode)	—	—	180 km	315 km	355 km
Passenger	2	2	4	4	4
Cargo space volume	—	—	—	98 L	102 L

favorable, and it was possible to establish the layout of the major structural elements for the vehicle. V4 also received Japanese certification, and while repeating public road testing, it formed the basis for the production vehicle, the FCX. With these series of modifications, the FCX was manufactured in 2002.

3. Overview of the Vehicle

3.1. Vehicle Appearance

Figure 1 is a photograph of the FCX, and Fig. 2 shows the interior design. The exterior design is based on the body of Honda's electric vehicle, the EV PLUS[(1), (2)]. The design, with the fuel cell power unit fitted in the bottom half of the body, gives a feeling of firmness and steadiness. In addition, the two-tone color with undertones of blue gives an image of hydrogen and water. The interior, too, uses trim colors with blue undertones, giving an integrated design.



Fig. 1 Exterior view of FCX



Fig. 2 Interior design

3.2. Package Concept and Major Specifications

To create a new power train fuel cell system structure that could be mass-produced, a new platform unique to fuel cell vehicles was developed for the FCX. The package concept was as follows.

- Fuel cell system layout concentrated under the floor.
- A compact body, based on the EV PLUS.
- Sufficient cabin and luggage space for four adults.
- A specially designed chassis with original hydrogen tanks giving advanced cruise performance.
- High reliability and safety measures for the hydrogen systems and the high-voltage electrical system.
- All-directional collision safety, protecting both the occupants and the power train.

We succeeded in fitting the fuel cell system within the same dimensions as the EV PLUS and keeping the weight increase to a minimum. Table 2 gives the FCX major specifications.

Table 2 FCX major specifications

Length / Width / Height (mm)	4 165 / 1 760 / 1 645
Wheel base (mm)	2 530
Vehicle weight (kg)	1 680
Number of passengers	4

3.3. Component Layout

In order to achieve a high level of fundamental functions and performance requirements of a vehicle, such as a generous body size, spacious cabin, collision safety performance, etc., a unique platform was developed for the FCX. Figure 3 shows the placement of major components.

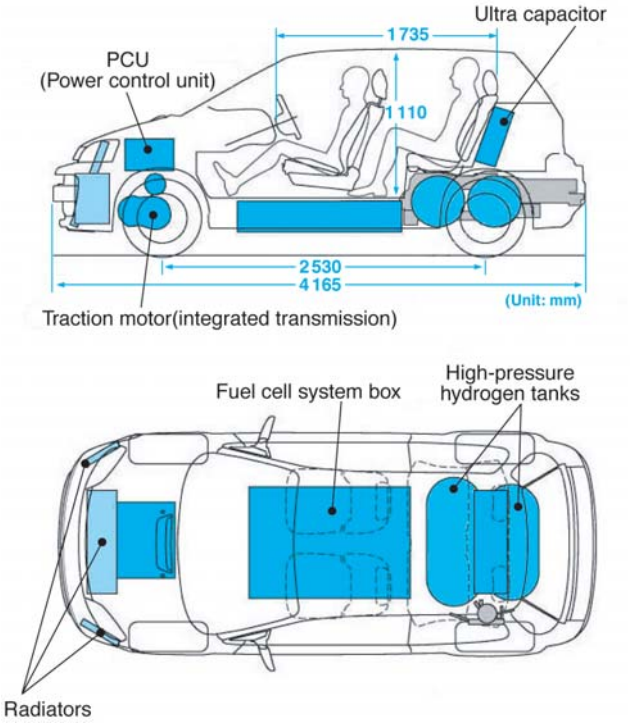


Fig. 3 Placement of major components in FCX

Taking advantage of the freedom allowed by the fuel cell system layout, the high-pressure hydrogen tanks were placed below the rear seats. The fuel cell system placement was concentrated below the cabin floor by giving full considerations to the weight and size. This layout made it possible to maintain a spacious interior while giving advanced collision safety. The Ultra capacitor was placed at an angle behind the rear seat backs, securing sufficient luggage space. In addition, adopted rear suspension uses space efficiently and gives advanced cruise performance. In addition to these innovations, an easy to drive body size was achieved through the use of a compact PCU and a compact transmission. A large fuel cell system radiator was placed in the center, and sub-radiators for the drive train were placed on both sides, giving improved cooling performance. Although it is a fuel cell vehicle with many structural elements, optimal layout enables the vehicle to accomplish a front/rear weight distribution of 55:45, which is an ideal weight ratio for a FF vehicle.

3.4. Major Unit Configuration and Layout

Figure 4 shows the positioning of the major components, and Fig. 5 shows the configuration. All of the major components have a compact layout.

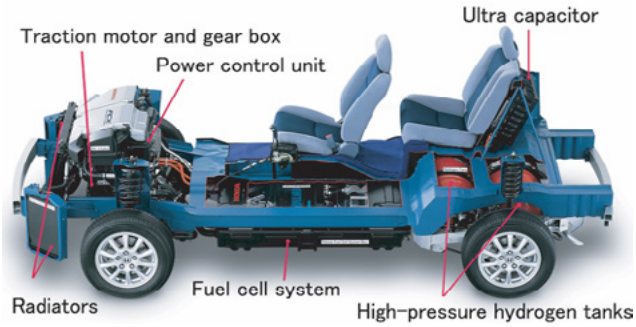


Fig. 4 Positioning of power train

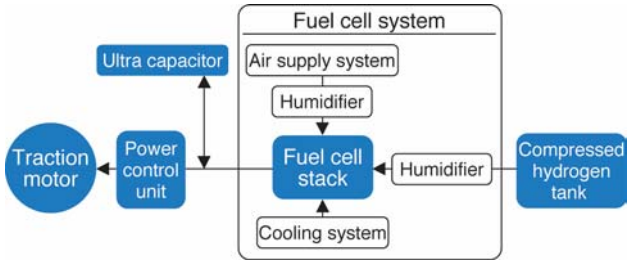


Fig. 5 Simplified diagram of power train system

4. Installed Technologies

4.1. Hydrogen Tank and Installation Structures

In order to improve the vehicle's cruising range, it is necessary that the hydrogen tanks have a large capacity and lightweight structural characteristics. On the FCX, the high-pressure hydrogen tanks have three layers – an aluminum liner, carbon fiber, and glass fiber – giving them strength and corrosion resistance and making it possible to fill at 34.4 MPa. The structure of the hydrogen tank is shown in Fig. 6. Two of these tanks are fitted to the vehicle, yielding a tank capacity of 156.6 L. Together with improvements to fuel consumption, this has resulted in a cruising range of 355 km. In addition, the refueling time using high-pressure charging equipment is approximately 3 minutes, roughly equivalent to that for filling a gasoline vehicle.

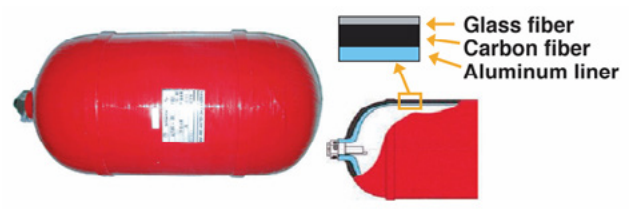


Fig. 6 High-pressure hydrogen tank

As shown in Fig. 7, the two hydrogen tanks are fitted to a sub-frame composed of extruded aluminum members that surround them. A five-link double-wishbone type rear suspension is also fitted to the sub-frame. This configuration makes integrated installation possible, and contributes to efficient use of space.

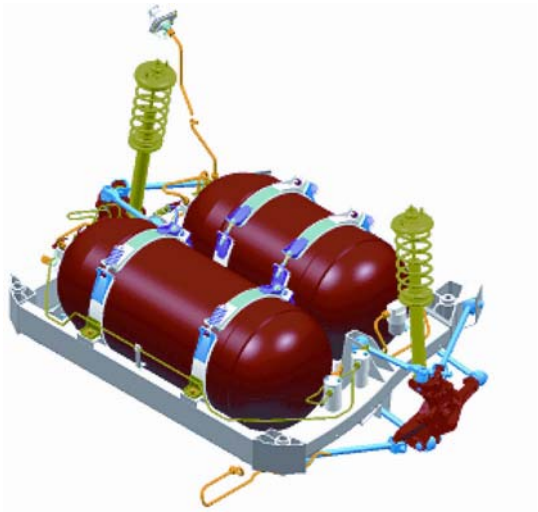


Fig. 7 Rear suspension module

4.2. Hydrogen and High-voltage Safety Measures

As aforementioned, by placing the fuel cell system box under the floor, the structure completely isolates the occupant space from the hydrogen and high-voltage system. In addition, hydrogen sensors were placed in various locations, considering unforeseen hydrogen leaks, and a forced ventilation system is also provided. If a hydrogen leak occurs within the fuel cell system box, the ventilation system will be activated to keep the hydrogen concentration at a safe level. Also provided is a system that automatically shuts off the hydrogen, using the in-tank main valves and shut off valves placed in the hydrogen supply path.

Figure 8 shows the safety system for hydrogen and locations of hydrogen sensors, both important in hydrogen safety. If a hydrogen sensor detects a hydrogen leak with a concentration higher than the specified level, a warning light comes on in the instrument panel, and at an appropriate time, the supply of fuel is cut off.

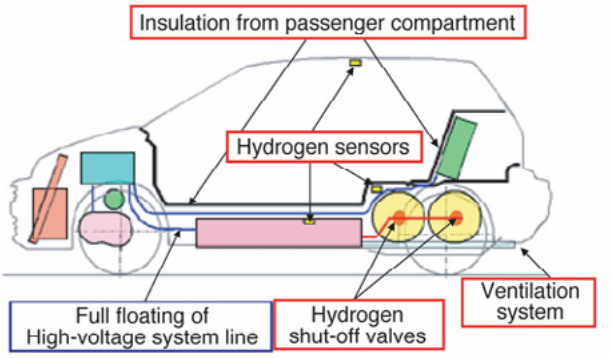


Fig. 8 Hydrogen and high-voltage safety structure and location of the hydrogen sensors

In addition, the high-voltage system is insulated from the body structure. If a ground fault occurs in the electrical systems and the vehicle body, a sensor will give the warning to the occupant, and if a collision occurs, the main power source would be shut off by a circuit breaker. These systems were proven to be safe and highly reliable by repeated floodwater testing, tank fire testing, and others.

Figure 9 shows one example of reliability testing – flood water test in which the vehicle drives through a pool of water.



Fig. 9 Flood water test

4.3. Safety Measures while Charging Hydrogen

The hydrogen charging inlet receptacle provides a good contact with the nozzle, has a highly reliable filter, and has a check valve integrated structure that provides secure sealing of hydrogen. The nozzle geometry prevents the introduction of the wrong type of gas to the vehicle or connection with a nozzle that charges at a higher pressure.

In addition, a grounding system has been adopted that eliminates static electricity from vehicle body prior to hydrogen charging. As shown in Fig. 10, the hydrogen charging inlet lid opener is inside the grounding lid. This safety design feature allows the charging inlet lid opener to be operated only when the grounding lid is open.

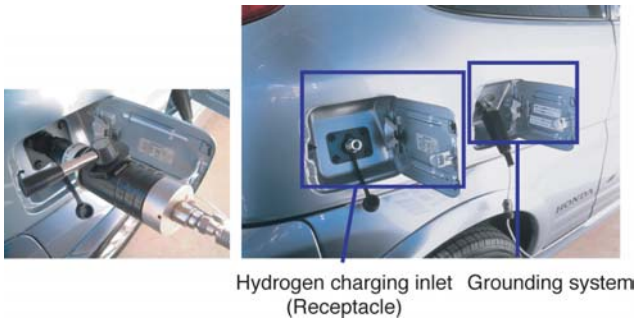


Fig. 10 Hydrogen charging inlet and grounding system

4.4. Body Structure and Collision Safety

4.4.1. Principles of fuel cell system collision safety

In addition to occupant protection, development was carried out to achieve a sufficient safety performance of the fuel cell system and hydrogen tank system against impact and body deformation that may be caused by collisions. The body structure is composed of a shock-absorbing frame, as shown in Fig. 11. The fuel cell's major devices are placed so that they are protected by body frame structures against collision deformation from all sides of the body.

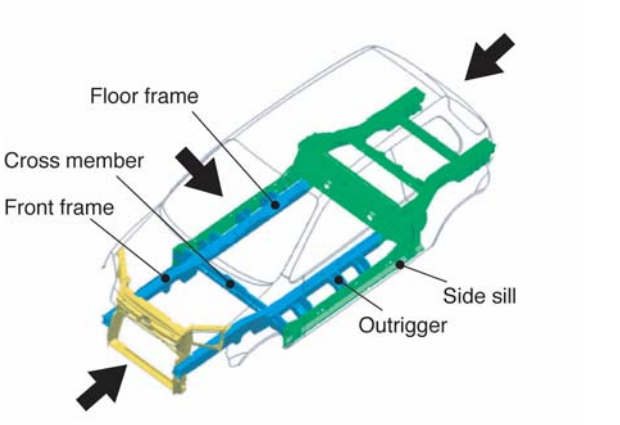


Fig. 11 Basic framework

In the vehicle's longitudinal direction, a sectional straight frame is formed from the front frame to the floor frame, and in the lateral direction, there is a cross member from the floor frame to the side sill and outriggers. The front frame has an impact-absorbing structure, minimizing protrusion into the cabin in a front impact collision. The outriggers effectively absorb the shock of side impact, and minimize the effect of side impact on the cabin and the fuel cell system.

The structure of the box under the body floor storing the fuel cell stacks is a highly secure structure which protects the system against deformation during a collision. Figure 12 shows the rear sub-frame mounting structure and the body structure. The aluminum sub-frame is connected to the rear frame and these two frames above and below form a protective structure for the hydrogen tanks. The Ultra capacitor is placed in the cabin above the hydrogen tanks, and so the body structure forms a firm, protective structure for both the hydrogen and the electrical system.

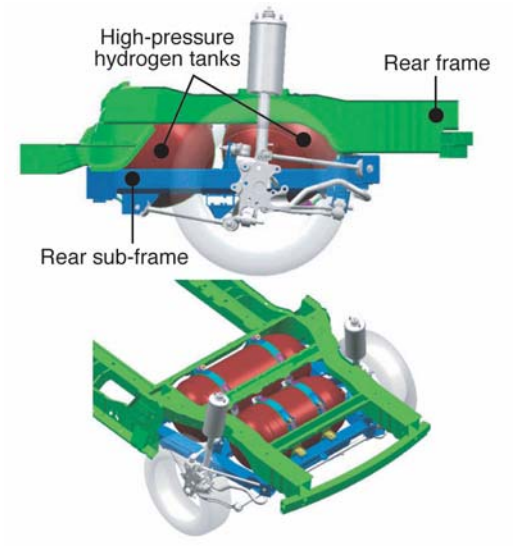


Fig. 12 Rear suspension module & rear sub-frame

4.4.2. Collision test results

In order to verify fuel cell system layout and body structure, collision tests were conducted. Full frontal, front offset, side, and rear impact tests, as shown in Fig. 13, resulted in controlled deceleration acceleration rate and degree of body crush confirming good safety performance for both the hydrogen and electrical systems.

In the collision tests, helium was used as the test gas substitute for hydrogen, because its characteristics are similar. The tests were carried out after charging the hydrogen tanks and piping to approximately 35 MPa.

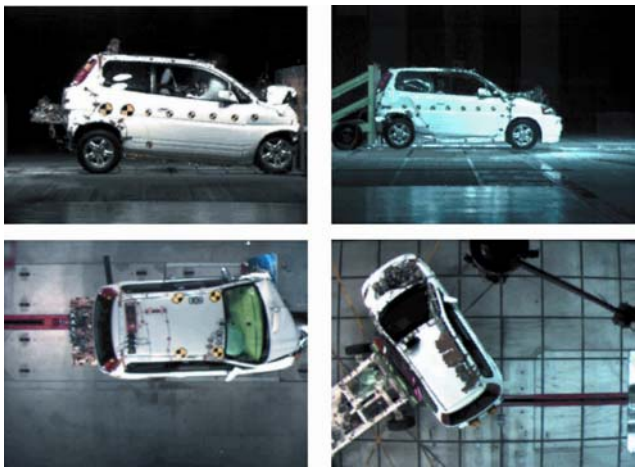


Fig. 13 Crash test images

4.4.3. Shutt off system for electricity and hydrogen during collision

The previous sections explained body structures that provide protection against the collision impact, but to further improve safety, a system is provided to shut off the main power source and the hydrogen supply system during a collision. As in the airbag system that protects occupants from impact acceleration applied to the vehicle body, acceleration sensors are fitted to detect front, side, and rear impact phenomena. This makes it possible to safely stop and isolate the system by shutting off the power source and hydrogen. In order to have collision diagnosis function capable of detecting FR off-set impact as well as local impacts on the side, multiple auxiliary sensors are equipped for improved ability in detecting body deformation.

4.5. Chassis (Suspension, EPS, Brakes)

In addition to a smooth and powerful drive feeling provided by the fuel cell power train, Honda has pursued ride comfort, stability, operating comfort, and etc., with focus on the chassis. From city streets to highways, ease of driving and a comfortable ride have been accomplished.

A McPherson strut was adopted for the front suspension, and for the rear, Honda's five-link double-wishbone type used in the Accord was adopted. They give advanced handling and stability as well as ride comfort.

The steering system is a unique rack assist type electronic power steering system, giving both a natural and smooth steering feel when driving at low speeds, and a feeling of firm stability when driving at high speeds.

The braking force is appropriately assisted by an electric vacuum pump and a master power. In addition, ABS with EBD (electronically controlled brake distribution system) is provided as a standard feature.

4.6. Gauges

An advanced-design original meter cluster for FCV is installed in the FCX to allow the driver to truly experience the system operation when driving the vehicle. The cluster display has the speedometer in the center with the power gauge and hydrogen fuel system indicators on each side. It is a highly effective 3-gauge meter system. Figure 14 shows the display when all the gauges are lit.

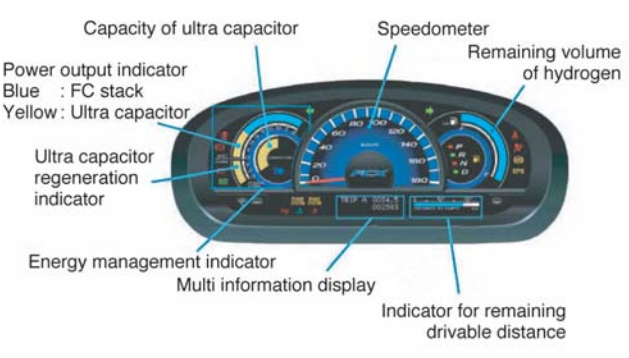


Fig. 14 Cluster design

The output indicator shows various information such as, fuel cell stack output, charged volume of the Ultra capacitor, and the energy management status which changes moment to moment depending on driving conditions. This information is displayed in an easy-to-understand format. Figure 15 is an operation diagram of the output gauges. There is also a remaining drivable distance gauge, which shows the distance the vehicle could travel with remaining hydrogen. Furthermore, in the middle of the bottom there is a multi-information display that can switch between an odometer, trip meter and vehicle status change message display.

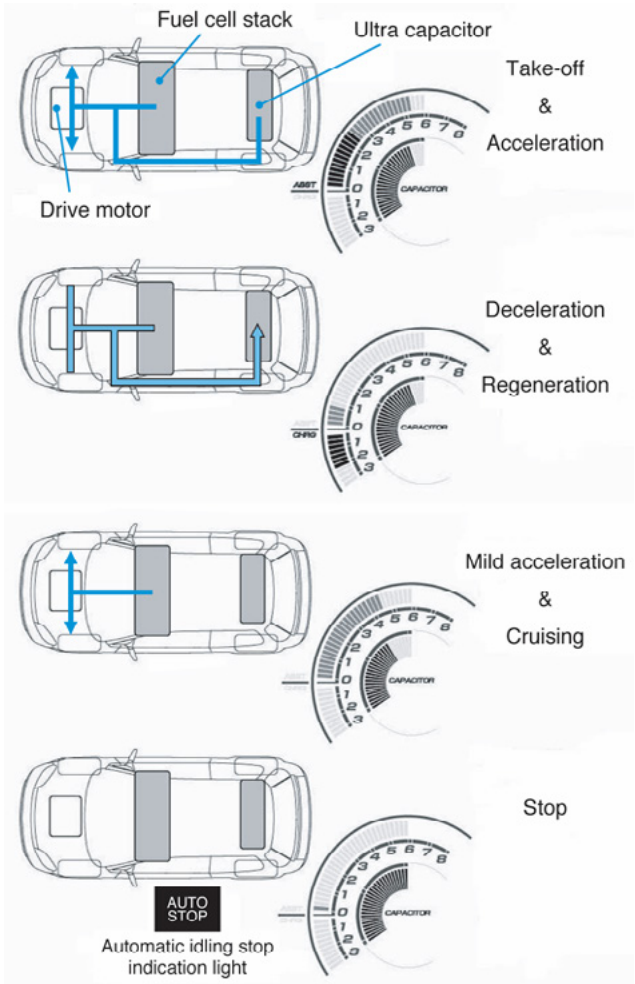


Fig. 15 Graphic images of meter functions

5. Summary

The Honda FCX is the world's first marketed fuel cell passenger vehicle. However, the current version is no more than the beginning of the spread of fuel cell vehicles. Many issues remain, such as low temperature start up, cost reduction, and hydrogen charging infrastructure. These issues must be resolved if there is to be a real popularization of fuel cell vehicles in the near future. Honda will continue to tackle these issues enthusiastically. The more people come to see the wonders of fuel cell vehicles and support their use, the more they will be advanced as the vehicles that are a true response to the environmental issues.

Making the world's first marketing and delivery of a fuel cell passenger vehicle as a milestone, Honda will proceed with even further technological development.

6. Acknowledgments

Finally, the authors would like to express their sincere appreciation to many people who generously gave their cooperation in the sales and delivery of the FCX, including those at each research facility, at the manufacturing plants, and those in the relevant departments in cooperating suppliers.

7. References

(1) Imai, H., Suzuki, S., Hasegawa, O., Matsumoto, K.: Introduction of Electric Vehicle "Clean Urban Vehicle-4", HONDA R&D Technical Review Vol. 7, p. 1-8 (1995)

(2) Ogura, M., Suzuki, S., Matsumoto, K.: Introduction of Electric Vehicle "EV PLUS", HONDA R&D Technical Review, Vol. 9, p. 1-10 (1997)

■ Authors ■


Satoshi KAWASAKI


Masami OGURA


Tohru ONO


Yozo KAMI

Development of New Power Train for Honda FCX Fuel Cell Vehicle

Takayuki OGAWA* Kenichiro KIMURA* Kenji UCHIBORI*
Sachito FUJIMOTO* Kiyoshi SHIMIZU*

ABSTRACT

In response to increasing environmental concerns and demands for clean energy, Honda has developed an emission-free clean power train employing fuel cells. This power train has been fitted in the FCX fuel cell vehicle, which is being simultaneously marketed in Japan and the US in a world first. The new power train is made up of a combined pure hydrogen fuel cell stack and Ultra capacitor system, and a reluctance torque traction motor. In addition to achieving a zero level of emissions of CO_2 and other pollutants, the new power train has raised the energy efficiency of the FCX to 45%, almost 1.5 times that of an electric-gasoline hybrid vehicle (HEV) of equivalent size. The FCX also has higher fuel economy than an HEV, and better acceleration from a standstill compared to a gasoline internal combustion engine vehicle (ICEV).

1. Introduction

In response to environmental issues such as global warming and air pollution, Honda has worked to improve gasoline engine combustion technology through the use of VTEC[(1)] and to develop high-efficiency clean power trains for the Honda EV PLUS electric vehicle[(2)], the Honda Civic GX natural gas vehicle[(3)], and the Honda Civic Hybrid[(4)], a gasoline/electric hybrid vehicle. Now, with the goals of achieving zero emissions, including CO_2, and of utilizing alternative energy sources instead of depending on fossil fuels, the focus has turned to fuel cells using pure hydrogen as their fuel. In combination with a traction motor that utilizes reluctance torque and Honda's proprietary ultra-capacitor, Honda has introduced their independently cultivated electric drive technology, high-pressure gas storage technology, and high-precision hybrid energy management technology, creating a highly efficient, high response clean power train that is installed in the FCX fuel cell vehicle. The FCX is the world's first commercial fuel cell vehicle being delivered simultaneously to Japan and the USA.

This paper explains the power train installed in the FCX.

* Wako Research Center

2. Development Concepts

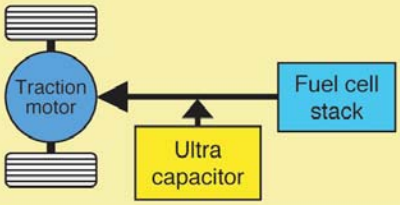
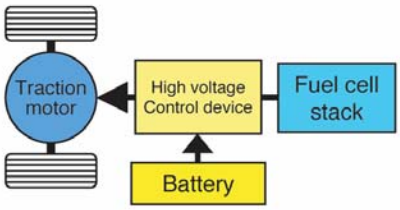
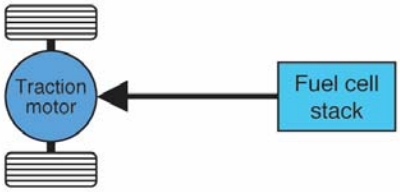
The goals of this development project were not limited to the environmental performance demanded by society of an automobile, but also included those areas which are often sacrificed for environmental performance — acceleration performance and high response, as well as smooth drivability — but are demanded by the customer in terms of marketability. A new, pioneering, next generation power train was realized, achieving all the goals at a high level. The practical development concepts are as follows.

(1) Zero Emissions, CO_2-free
(2) Vehicle energy efficiency which exceeds that of a hybrid vehicle (Tank to wheel)
(3) Standing start acceleration performance that is better than that of a gasoline vehicle.
(4) A compact design that efficiently utilizes space.

3. Power Train System

In actualizing the development concepts, a basic system study was carried out.

Table 1 Comparison of system configurations

	Basic configuration	System configuration	Efficiency	Power performance
Capacitor-assisted system **FCX**		High-voltage distribution system **not required**	Electric transmission efficiency : **HIGH** Braking regeneration : **YES**	Instantaneous high power assist **possible**
Battery-assisted system		High-voltage distribution system **required** for fuel cell stack / battery	Electric transmission Efficiency : **MED** (Losses of high voltage controllers) Braking regeneration : **YES**	Power assist **possible**
Fuel cell direct-supply system		Simple high-voltage system Startup device required	Electric transmission Efficiency : **HIGH** Braking regeneration : **NO**	Power and responsiveness depend on fuel cell stack

First of all, the hydrogen supply was considered, and in order to satisfy the requirements of zero emissions and being CO_2-free, a method was adopted that stored pure hydrogen on the vehicle, rather than using a reforming system. High-pressure hydrogen tanks were adopted as the hydrogen storage method after considering the current infrastructure and equipment situation, vehicle energy efficiency, hydrogen charging time, and the ease of the refueling operation.

The motor drive system utilizes the power from the fuel cell stacks as its drive force. It may be combined with energy storage, such as a battery or capacitor, to provide a regeneration of deceleration energy and power assistance. The results of a drive system comparison, shown in Table 1, led to the adoption of an ultra-capacitor assistance system having the following advanced features.

- Making it possible to efficiently utilize deceleration energy to have good energy transfer efficiency, and therefore to achieve high vehicle energy efficiency.
- Making large power assistance possible instantaneously gives advanced dynamic performance.
- It is not necessary to have an energy distribution system using a high voltage control device, so the system can be made smaller and lighter weight.

3.1. System Configuration

The power train system's configuration is shown in Fig. 1. The power train is comprised of high pressure hydrogen tanks that have a physical volume of 156.6 L and store hydrogen at a maximum pressure of 34.4 MPa, a fuel cell system that generates the electrical power necessary to drive the vehicle, an ultra-capacitor that recovers deceleration energy and assists with maximum power during standing start acceleration, a power control device, and a traction motor that drives the vehicle. Figure 2 shows the power train layout.

3.2. Fuel Cell System

The fuel cell system has many component elements and requires space for installation. However, because it is

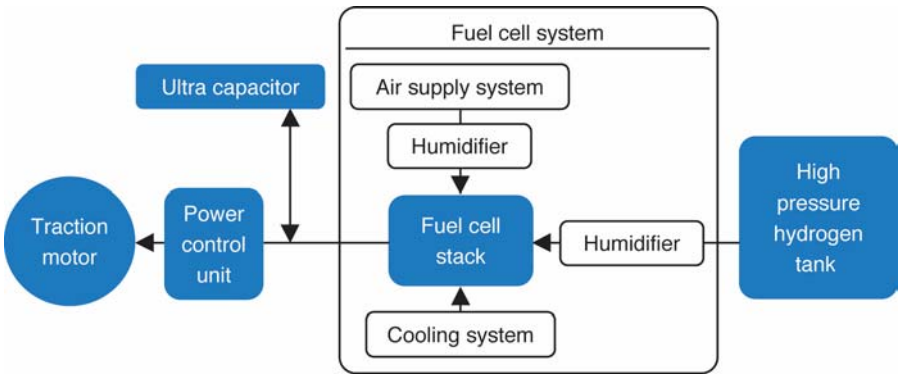


Fig. 1 Power train system configuration

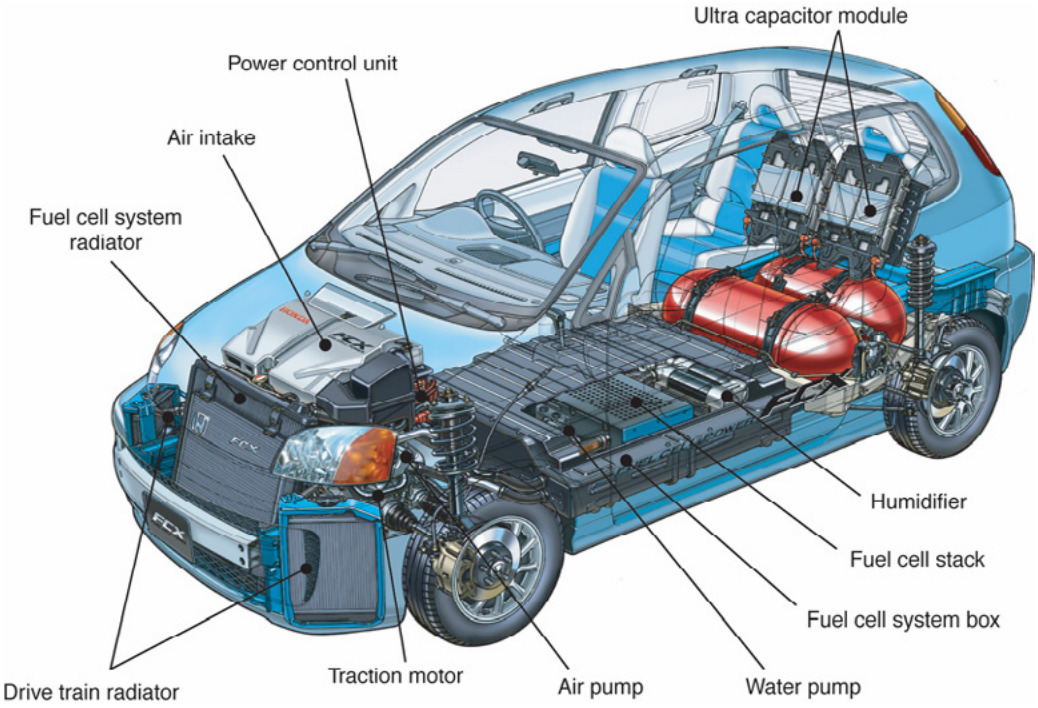


Fig. 2 Power train layout

possible to connect the gas and coolant supplied to the fuel cell stacks using pipes, and the power from the stack using cables, there is a high level of freedom in determining installation locations. Utilizing this freedom, the fuel cell system electrical generating parts are concentrated in a fuel cell system box under the floor. This gives an ideal weight distribution with low center of gravity, and allows the vehicle to have a spacious interior.

3.2.1. Fuel cell stacks

The fuel cell stacks are solid polymer PEMFC (proton exchange membrane fuel cell) type fuel cells, model MK902 made by Ballard Power Systems, Inc., generating a maximum power of 78 kW.

3.2.2. Air supply system

Air is supplied to the fuel cell stacks at the appropriate pressure and flow, through the use of a Lysholm-type air pump driven by a high voltage motor.

Furthermore, the following actions were taken in order to keep air intake noise and air pump vibration noise to a minimum, providing a quiet performance.

- Development of a compact integrated intake module with a muffled resonator chamber.
- Adoption of a double floating mount method that uses rubber mounts to affix the air pump and air pump drive motor onto the traction motor and transmission, which are, in turn, mounted on the vehicle body.

3.2.3. Hydrogen supply system

The hydrogen, stored at a maximum pressure of 34.4 MPa in the high-pressure hydrogen tanks, is supplied to the fuel cell stacks through a regulator, which adjusts it to the appropriate pressure.

3.2.4. Humidification system

It is necessary to humidify the hydrogen and air supplied to a PEMFC fuel cell stack. In order to respond to this requirement, a (completely independent) recycled-water-recovery-type of

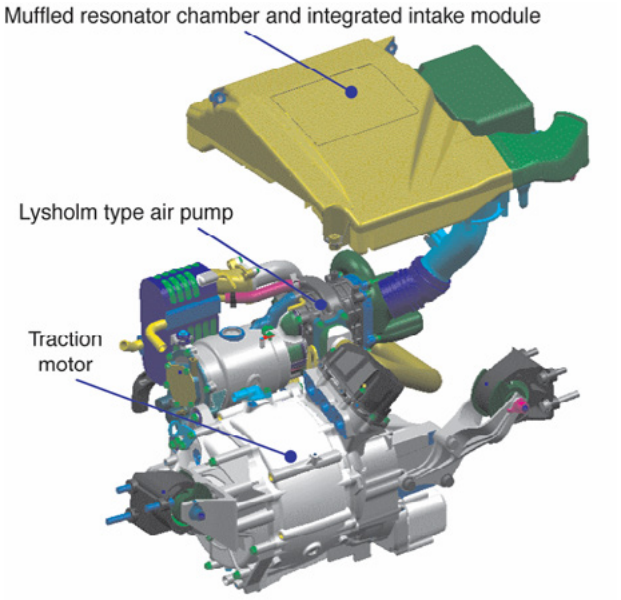


Fig. 3 Power train noise reduction measures

humidification system was developed whereby the water vapor generated as a byproduct of electricity generation by the fuel cell stack is directly re-used to humidify hydrogen and air. This means that neither a condenser nor system to supply water for humidification is necessary, and that the overall system is simple.

3.2.5. Cooling system

Two cooling systems were adopted – a fuel cell cooling system and a drive train cooling system.

The fuel cell cooling system circulates a special fuel cell coolant from the fuel cell through a large radiator developed specially for fuel cell vehicles, making it possible to efficiently release heat from the coolant at a lower control temperature than with a gasoline engine.

3.3. Traction Motor

The new traction motor, which is the major source of driving power, was developed with the aim of greatly improving power performance over that of the EV PLUS.

Power and torque characteristics for the FCX motor and the EV PLUS motor are shown in Fig. 4.

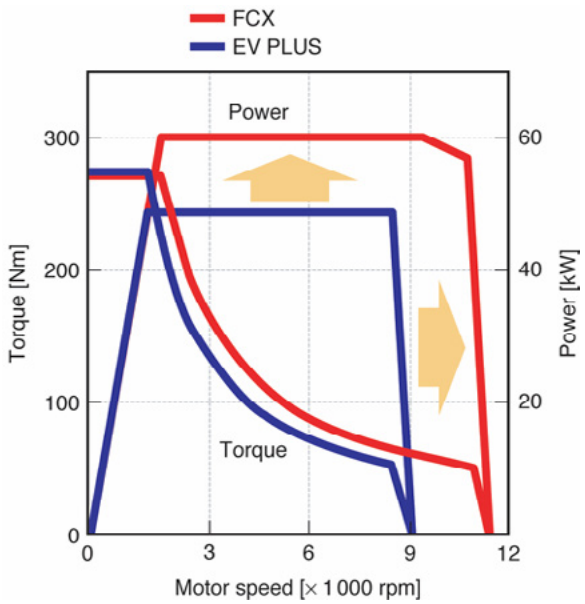


Fig. 4 Power / torque characteristic

First, looking to improve power across the whole range, reluctance torque was also utilized in addition to the magnetic force generated by conventional magnets. Reluctance torque is obtained by letting the magnetic field generated by the stator attract the protruding portion of the magnetic rotor's yoke. In addition, full range full digital controls were adopted.

For the motor to reach maximum speed, it is necessary to have motor heat generation suppression or to make the rotors very heat resistant. At the same time as using highly heat resistant magnets to minimize eddy current loss, which is a cause of magnetic heat generation, the magnets are separated in the rotor shaft direction, and electromagnetic insulation is placed between magnets.

Thanks to these and other measures, such as an efficient mechanism to cool the stator coil heat, the new motor is, as shown in Table 2, smaller than the EV PLUS, and yet achieves a rated power of 60 kW and a CITY mode efficiency of 93% or more.

Table 2 FCX and EV PLUS motor specifications

	EV PLUS	FCX
Max. output (kW)	49	60
Max. torque (Nm)	275	272
Max. revs (rpm)	8 750	11 000
Avg. efficiency in CITY mode (%)	90	93 or greater

4. Fuel Cell + Ultra-Capacitor System Driving Performance

4.1. Power Characteristics

Figure 5 shows an example of fuel cell and ultra-capacitor power characteristics during driving. At a standing start or when accelerating, the ultra-capacitor swiftly assists the fuel cell, giving good responsiveness to the driver's acceleration operation. During deceleration, energy is regenerated, and the ultra-capacitor is charged.

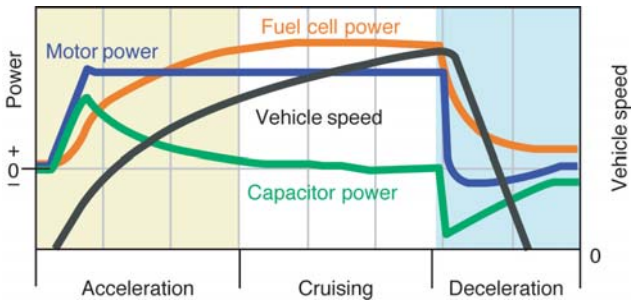


Fig. 5 Fuel cell and capacitor power characteristics

4.2. Acceleration Performance

Figure 6 shows the acceleration rise characteristics during a standing start. Utilizing the power assistance from the capacitor and the traction motor characteristics that generate maximum torque instantly from a standing start, the acceleration rise response time for the FCX is greatly reduced in comparison to that of the ICEV or the HEV. Furthermore, since there is no gear shifting, it is possible to continue that acceleration, and this gives a very smooth superior acceleration feeling.

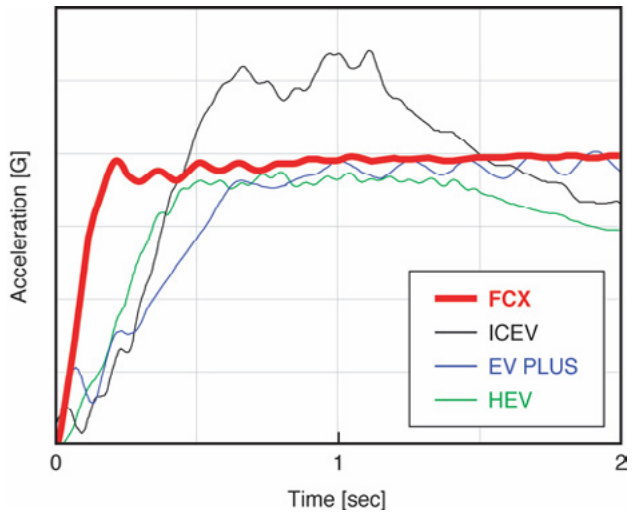


Fig. 6 Standing start performance

4.3. Efficiency and Fuel Consumption Performance

Figure 7 shows fuel cell power, capacitor power and voltage when driving in CITY mode, as used in US fuel consumption certification testing. When the vehicle is stopped, the air supply system and the fuel cell stack electricity generation are stopped by the auto idle-stop system, and the amount of electricity consumed by auxiliary devices is reduced. Thanks to this feature, the amount of hydrogen consumed is minimized. In addition, at the end of driving the ultra capacitor voltage is equal to that of at the beginning, and highly accurate energy give-and-take is feasible, even in CITY mode where assistance and regeneration are repeated.

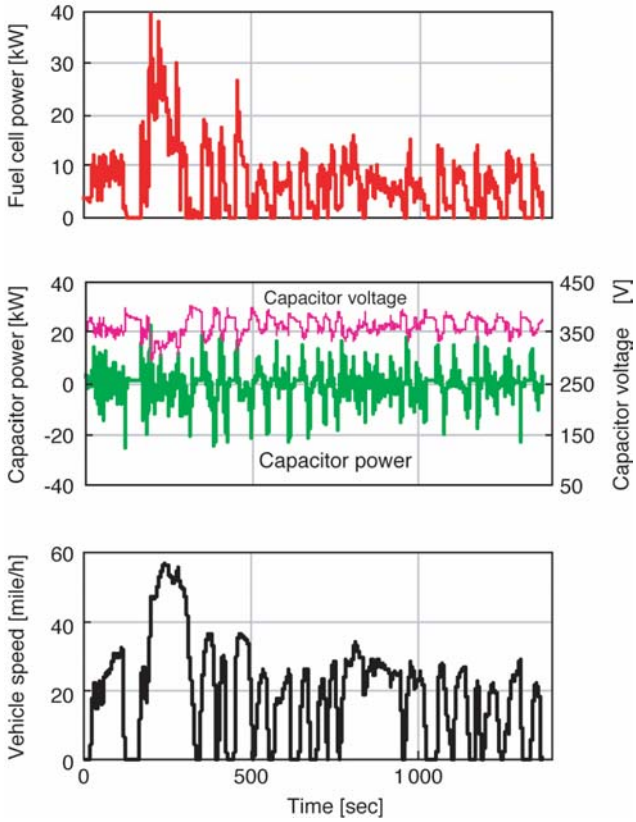


Fig. 7 Speed and power profile in CITY mode

Through the above energy management control, as shown in Fig. 9, the FCX achieves an energy efficiency of 45%, which is twice that of an ICEV, and approximately 1.5 times that of an HEV of equivalent size. The FCX is the world's first fuel cell vehicle to obtain EPA (US Environmental Protection Agency) and CARB (California Air Resources Board) fuel economy certifications[5]. In CITY mode, the certified value is 56.8 miles/kg Hydrogen and the label value is 51 miles/kg Hydrogen, while in highway mode, the certified value is 61.7 miles/kg Hydrogen and the label value is 48 miles/kg Hydrogen. Figure 8 shows the fuel economy label. In interpreting this label, the energy of 1 kg of hydrogen is roughly equivalent to the energy of 1 gallon of gasoline. Figure 10 compares fuel economy in CITY mode, between the ICEV, the HEV, and the CNG (natural gas) vehicles of roughly the same size. The FCX fuel economy is 1.7 times that of the ICEV and the CNG vehicles, and surpasses even the HEV.

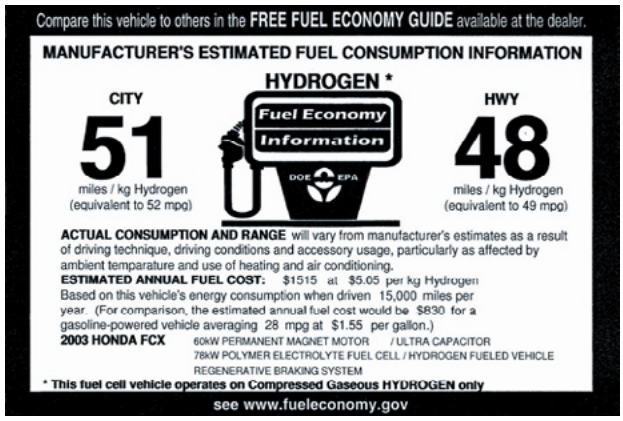


Fig. 8 FCX fuel economy label

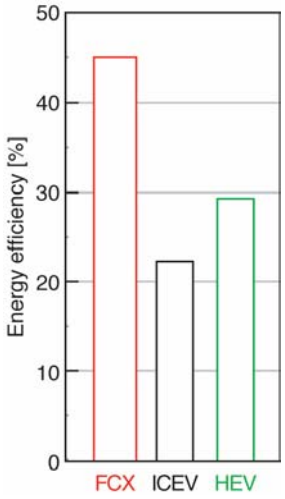


Fig. 9 Efficiency in CITY mode

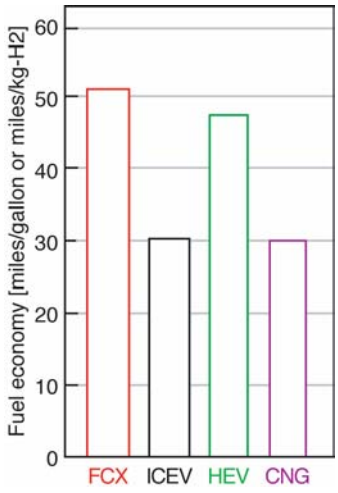


Fig. 10 Fuel economy in CITY mode

5. Summary

A power train system was developed that combines a pure hydrogen fuel cell with an ultra-capacitor, achieving a vehicle energy efficiency of 45%, which is 1.5 times better than that of an HEV of equivalent size, in addition to zero emissions, including CO_2. Moreover, it was possible to reach a fuel economy of 51 miles/kg hydrogen (label value), which surpasses an HEV, and to have a standing start acceleration performance that surpasses an ICEV. As a result, the FCX power plant is truly the next generation power plant that achieves, at a high level, the "drivability, fuel economy, and marketability" demanded of a vehicle by the customer, providing the ultimate in clean driving performance.

However, in looking towards widespread use of fuel cell vehicles, many issues remain, including low temperature start, cost reduction, and cruising range.

Now, with the world's first fuel cell vehicle being on the market and delivered, Honda continues to work on further technological development, in order to address these issues.

6. Acknowledgements

Finally, the authors would like to express their deepest gratitude to the many people, both at Honda and beyond, that generously cooperated in the development of the FCX, its launch, and sales.

References

(1) Niizato, T., Hayashi, A.: Development of New 2.0L Lean-burn Engine, HONDA R&D Technical Review, Vol.12, No.2, p45-54 (2000)

(2) Ogura, M., Suzuki, S., Matsumoto, K.: Introduction of Electric Vehicle “HONDA EV PLUS”, HONDA R&D Technical Review, Vol.9, p1-10 (1997)

(3) Toda, T., Matsuki, M., Ohmori, T., Yamamoto, Y.: Development of a 1.7L CNG Engine for the 2001 Civic GX, Honda R&D Technical Review, Vol.14, No.1, p49-56 (2002)

(4) Matsuki, M., Wakashiro, T., Kamiyama, T., Sato, T., Kaku, T., Kanda, M.: Development of a New Power Train for Civic Hybrid, Honda R&D Technical Review, Vol.14, No.1, p39-47 (2002)

(5) http://www.fueleconomy.gov/feg/feg2000.htm “2003 Fuel Economy Guide”

■ Authors ■


Takayuki OGAWA


Kenichiro KIMURA


Kenji UCHIBORI


Sachito FUJIMOTO


Kiyoshi SHIMIZU

Development of Fuel Economy Measurement Method for Fuel Cell Vehicle

Satoshi AOYAGI* Takuya SHIRASAKA*
Osamu SUKAGAWA** Naoki YOSHIZAWA**

ABSTRACT

A practical fuel economy measurement method has been developed for fuel cell vehicles. The weight method was selected for study from among the various fuel economy measurement methods available for pure hydrogen-type fuel cell vehicles as a direct measurement method, which was accurate and could be produced at a comparatively low cost. Solutions were provided to the drawbacks of measurement deviations caused by pressure variations in the fuel pipes and lowered hydrogen purity due to air entering the pipes. This development project assisted in fuel economy measurements for the Honda FCX, the world's first market-ready fuel cell vehicle; it also provided the measurement system for the Environmental Protection Agency (EPA) tests of the same vehicle, which resulted in the world's first confirmatory test of a fuel cell vehicle.

1. Introduction

In the development of fuel cell vehicles in recent years, there has also been a desire for the development of methods to evaluate performance[(1),(2)]. In the USA, particularly, in order to respond to official confirmatory tests for pure hydrogen fuel cell vehicles carried out by the EPA (Environmental Protection Agency), it was absolutely essential to develop a fuel economy measurement method that was both highly accurate and practical[(3)].

One international standard of fuel economy measurements for internal combustion engines, such as gasoline or diesel engines, is the "carbon balance method" utilizing the fact that the amount of carbon is the same in the intake and exhaust. By measuring the amount of carbon in the exhaust gases, it is possible to determine the amount of fuel consumption. However, with a fuel cell vehicle, that principle cannot be applied, and each manufacturer has adopted their own measurement method. In this development project, a comparative study was made of various fuel economy measurement methods used for pure hydrogen fuel cell vehicles, which are the most desired in development, and an attempt was made to develop a measurement method that can lead to the manufacture of a device that is highly accurate and can be used universally, at a comparatively low cost.

* Wako Research Center
** Honda Motor Co., Ltd.

2. Development Goals

There were four development goals.

(1) Measurement Accuracy
In the US fuel economy measurement modes of City and Highway, measurement accuracy in the SAE-J2572 standards stipulated by the SAE (Society of Automotive Engineers) must be ±1%.

(2) Universal Use
It must be possible to use the method both in Japan and in the USA. It must be possible to measure the amount of fuel consumption for each phase, even in modes composed of multiple phases, such as the US certification fuel consumption mode.

(3) Cost of Manufacture
It must be able to be manufactured at a cost lower than the fuel consumption measurement equipment gasoline vehicles use, the carbon balance method, at no more than ¥2 million.

(4) Standardization
Used for the official confirmatory test, the fuel economy value given in the test results must be recognized as an official value.

3. Selection of Measurement Method

3.1. Representative Measurement Methods

3.1.1. Weight method

This is a method that directly measures the mass of the pure hydrogen fuel, and this principle is used as a calibrated standards method in gasoline vehicle carbon balance methods as well. If one uses a measurement instrument that is highly accurate and does not often cause deviations, one can expect good measurement accuracy. But, there are the issues of deviations caused by pressure changes in the fuel supply pipes and of a drop in hydrogen purity within the pipes due to air contamination when the hydrogen tank was connected. Specifically, the mass of the hydrogen tank, prepared for measurements as shown in Fig. 1, is measured before and after the tests, and the fuel consumption is determined from the difference in the masses. Fuel consumption W (g) is calculated using Eq. (1) below.

$$W = W_i - W_f \tag{1}$$

W_i : Mass of hydrogen tank before test (g)
W_f : Mass of hydrogen tank after test (g)

3.1.2. Flow method

This method measures fuel consumption by continuously measuring fuel supply flow and integrating the measurements. There are no deviations due to pressure changes within the pipes, but there are the issues of accuracy at transient times and at very low flow rate, or when deviations are integrated. Specifically, the value detected by Flow Meter 1 shown in Fig. 1 is integrated, and the fuel consumption W (g) is calculated according to Eq. (2).

$$W = \frac{\Sigma Q}{22.414} \times m \tag{2}$$

Q : Flow rate of fuel (NL/sec)
m : Molecular weight of hydrogen 2.016 (g/mol)

3.1.3. P/T method (pressure method)

Before and after the tests, the hydrogen tank's pressure and temperature are measured, and the fuel consumption is calculated from the ideal gas equation, etc. Specifically, the pressure and temperature of the hydrogen tank are measured before and after the tests using a pressure gauge and thermometer, as shown in Fig. 1. Fuel consumption is calculated using the idea gas equation, etc., from the changes before and after. Deviations occur due to variations of pressure within the pipes, which is a common source of deviation. Fuel consumption W (g) is calculated using Eq. (3) below.

$$W = \left(\frac{P_i \times V}{R \times T_i} - \frac{P_f \times V}{R \times T_f} \right) \times m \tag{3}$$

P_i : Hydrogen tank pressure before tests (Pa)
P_f : Hydrogen tank pressure after tests (Pa)
T_i : Hydrogen tank temperature before tests (K)
T_f : Hydrogen tank temperature after tests (K)
V : Hydrogen tank capacity (m^3)
R : Gas constant 8.314 (J/mol·K)
m : Molecular weight of hydrogen 2.016 (g/mol)

3.1.4. Electrical current method

Utilizing the principle that the electrical current output from the fuel cell stack is proportional to the fuel consumption used in generating electricity, the values detected by the current sensor shown in Fig. 1 are integrated, and fuel consumption calculated. With this method, there are no deviations due to variations in pressure inside the pipes, and accuracy when transient can also be expected. However, depending on the test vehicle, it is also necessary to measure, using a flow method or something similar, the hydrogen that is exhausted without being used to generate electricity, called "purged hydrogen". Therefore, there are many issues such as error integration similar to the flow method, or water elimination in the purged hydrogen, etc. The fuel consumption W (g) is calculated using Eq. (4) when the purged hydrogen portion is measured using Flow Meter 2 shown in Fig. 1.

$$W = \frac{n \times m \times \Sigma I}{F} + \frac{\Sigma Q_p}{22.414} \times m \tag{4}$$

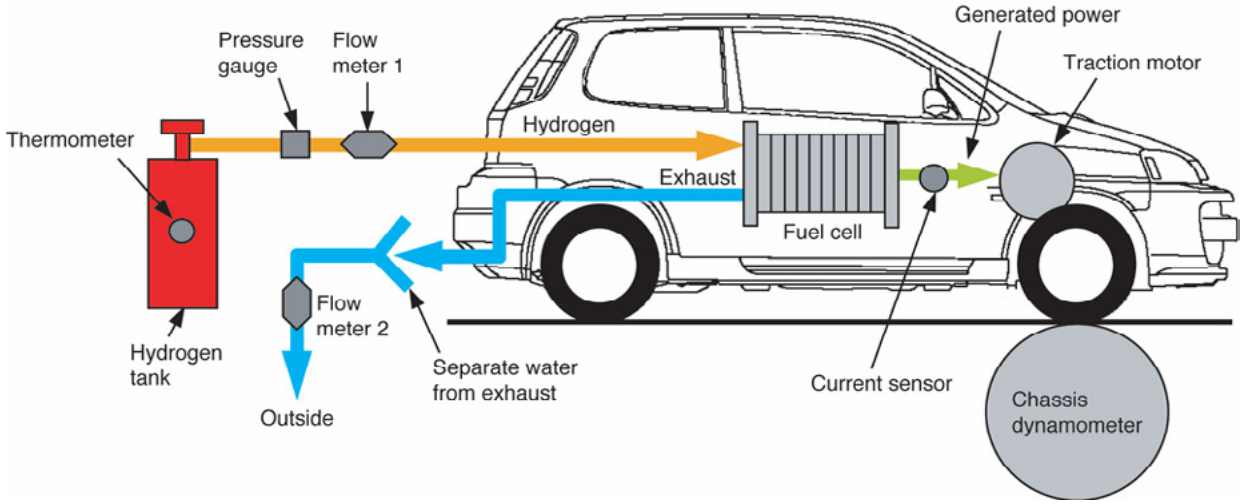


Fig. 1 Comparison of various method

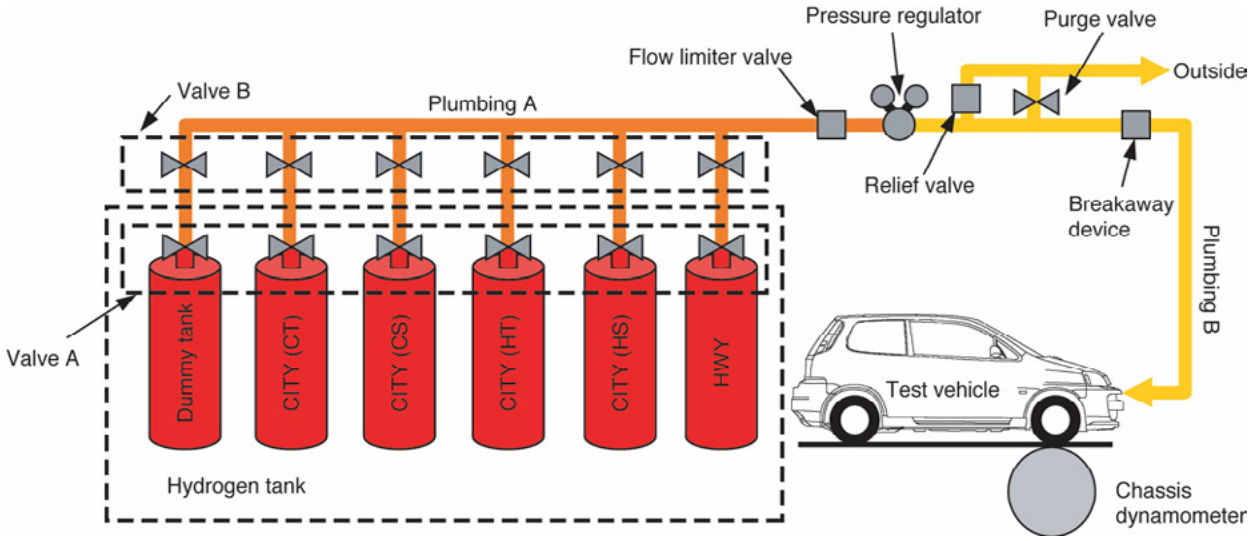


Fig. 2 Configuration of weight method system

I : Fuel cell output current (A)
n : Number of cells in the fuel cell
F : Faraday constant 9.64867×10^4 (C/mol)
m : Molecular weight of hydrogen 2.016 (g/mol)
Q_p : Purged hydrogen flow rate (NL/sec)

3.2. Adoption of the Weight Method

For the following reasons, the weight method was adopted in this development project.

(1) Because the hydrogen being measured is measured only in a direct manner, there is essentially little cause of deviation.
(2) It has become comparatively easy to obtain an accurate measurement device.
(3) The outlook is good for countermeasures concerning the hydrogen remaining inside the pipes.

4. Measurement Accuracy

The major factor affecting weight method measurement accuracy is deviations due to pressure variations within the pipes. In addition, there is the issue of a drop in hydrogen purity due to air contamination in the pipes during hydrogen tank connection. The following countermeasures were taken, for these issues.

Because deviations due to pressure variations within the pipes occur in pressure difference before and after tests, as shown in Fig. 3, deviations can be reduced by maintaining a fixed pressure in the pipes before and after testing. Therefore, as shown in Fig. 2, the pressure in the pipes is raised to a specific pressure prior to the test by using a dummy tank, without using the hydrogen in the measurement tank. By having a pressure regulator in the pipes close to the hydrogen tanks, although pressure variations remain in Plumbing A, as shown in Fig. 2, there is no pressure variation in Plumbing B, and deviation is reduced. The pressure regulator's pressure reduction amount must be set so that supply pressure does not drop below the minimum pressure needed by the vehicle, including that during acceleration and deceleration. It was confirmed that, in both the City and Highway modes shown in Figs. 4 and 5, that the supply pressure for the test vehicle Honda FCX was at least 0.7 MPa, which is the minimum pressure required.

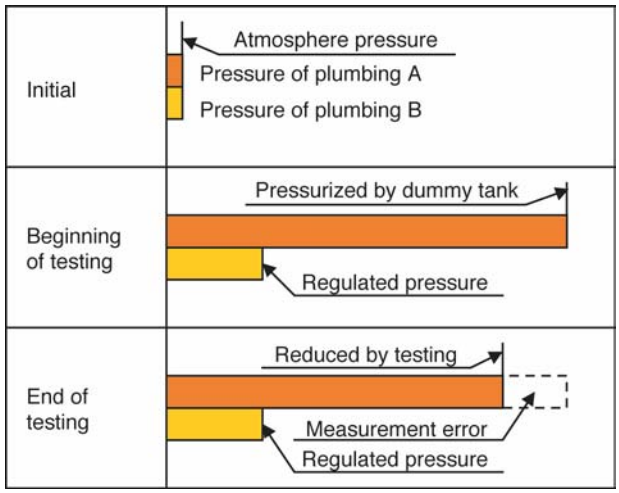


Fig. 3 Plumbing pressure and measurement deviation

By adding a dummy tank and a pressure regulator, measurement deviations caused by pressure variation within the pipes are reduced, and the effects shown in Figs. 6 and 7 are obtained. In the end, it is capable to fully meet the measurement accuracy of ±1% required by SAE standards. As shown in Fig. 8, the measurement accuracy for each phase of the City modes meets the SAE standards. In order to clarify the effect of each of these countermeasures, Figs. 6, 7, and 8 shows the absolute values of the deviations.

Concerning the hydrogen fuel supplied to fuel cell vehicles, because generally an extremely pure hydrogen – 99.99% class – is required, it is necessary to take appropriate countermeasures to prevent even the smallest amount of air penetrating the pipes when the hydrogen tanks are connected. Therefore, as shown in Fig. 2, by repeatedly discharging the hydrogen fuel in the dummy tank to the outside through the purge valve, any air between Valve A and Valve B is eliminated, without using hydrogen from the hydrogen tank used for measurement. Figure 9 shows the number of these air purging cycles and the purity of hydrogen within the pipes. At three or more cycles, the hydrogen purity in the pipes reaches 99.99% or higher, and the required accuracy is roughly achieved.

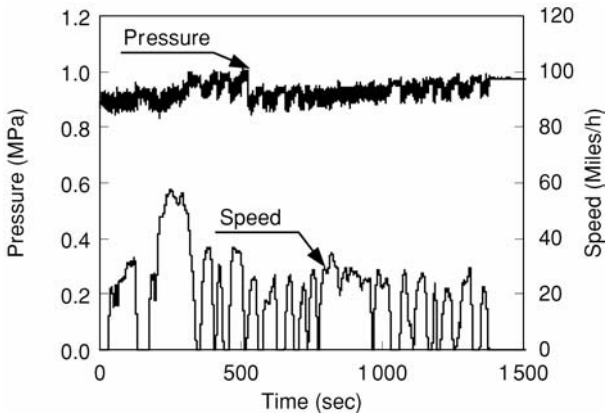


Fig. 4 Fuel supply pressure (CITY)

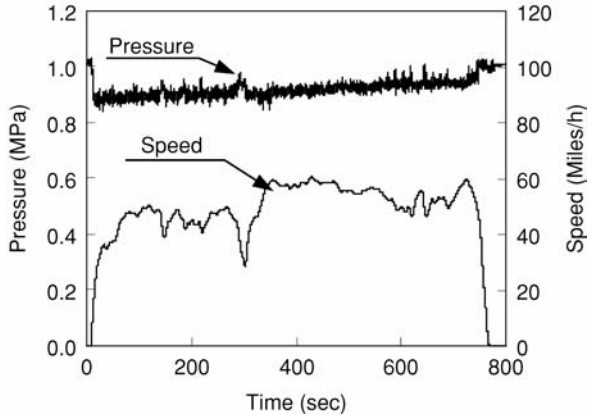


Fig. 5 Fuel supply pressure (HWY)

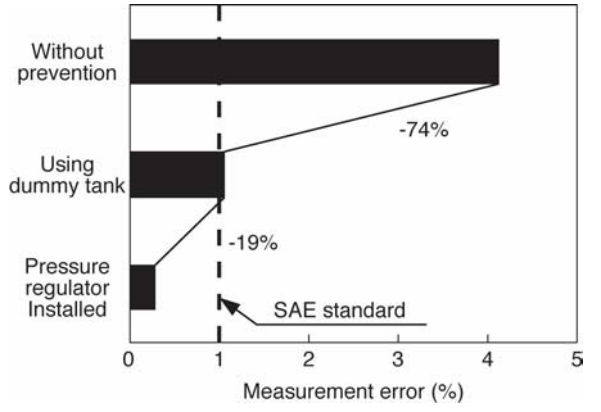


Fig. 6 Measurement deviation (CITY)

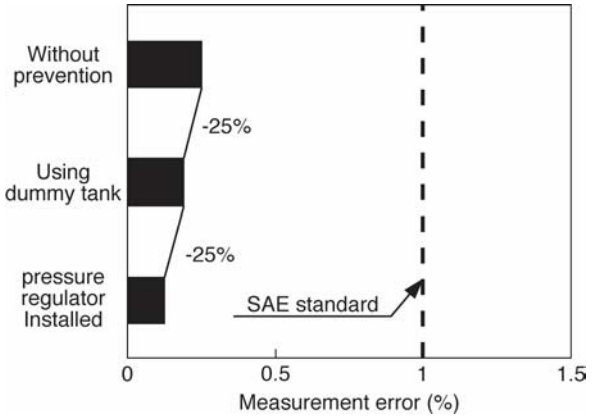


Fig. 7 Measurement deviation (HWY)

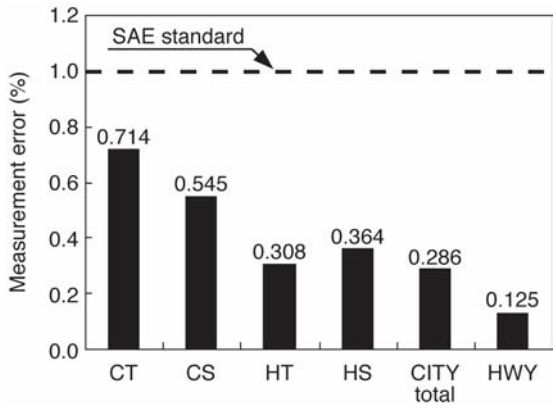


Fig. 8 Measurement deviation for each phase

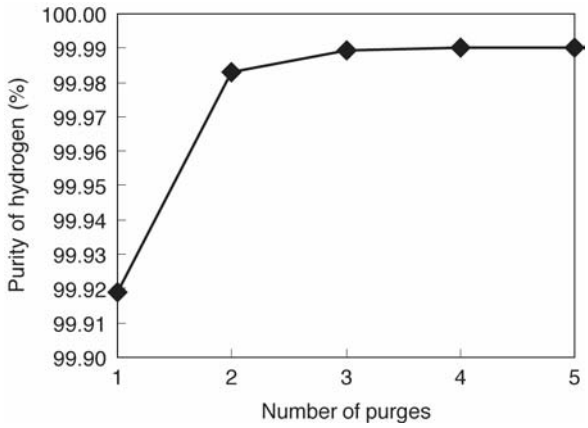


Fig. 9 Purity of hydrogen

In addition, giving due consideration to safety, a flow limiter valve was added to restrict fuel leaks if a pipe disconnects, a pressure relief valve was added to prevent abnormal pressure rise if the pressure regulator fails, and a breakaway device added to prevent fuel leaks if the vehicle moves away. These were added along Plumbing A and B, as shown in Fig. 2.

5. Universal Use

The test apparatus was designed so it was possible to change the height of Plumbing A connecting the hydrogen tanks, as shown in Fig. 2. This made it easy to replace the connectors on the pipe side that connect the pipe to Valve A, which are the tank valves integrated with the hydrogen tanks themselves. Thanks to these measures, it is possible to use, for measurement, hydrogen tanks that are readily available in the USA or in Japan, regardless of their size.

In addition, in order to handle fuel consumption modes that are composed of multiple phases, like the City mode shown in Fig. 10, and so require measurements of fuel consumption for each phase, the number of hydrogen tanks is equal to the number of phases. The hydrogen tanks connected to Plumbing A, as shown in Fig. 2, are placed in a rack, and the tanks can be switched using the B Valves. This arrangement makes it possible to measure fuel consumption for each phase.

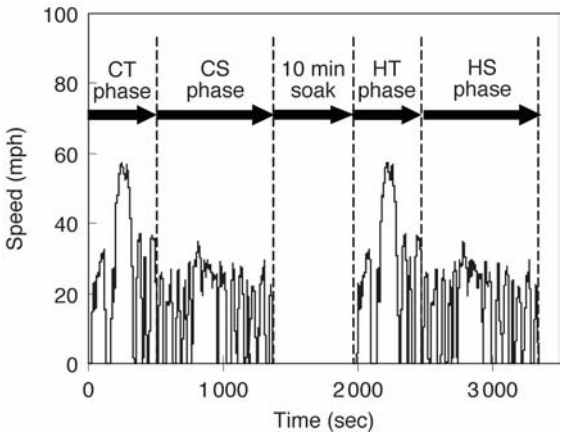


Fig. 10 Phases in CITY mode

6. Cost of Manufacture

Table 1 gives the measurement system specifications. Using readily available parts and avoiding special ones, a simple system was created, that can be manufactured for approximately ¥1.8 million. This has kept the cost to less than that of the carbon balance method used for gasoline vehicles. Figure 11 is a photograph of the measurement system.

Table 1 Measurement system specifications

Type		SUK-1
Dimension (mm)		W 2 000 × D 500 × H 1 940
Fuel supply pressure (MPa)		0.9～1.0
Max. number of tank		6
Safety device		Pressure relief valve
		Flow limiter valve
		Break away device
	Manufacture	A&D
	Type	GP-30K
	Max. mass (g)	31 000.0
	Min. mass (g)	0.1



Fig. 11 Picture of measurement system

7. Standardization

Keeping in mind automotive emissions regulations, a fuel economy measurement method was required that has a high standard measurement accuracy and reproducibility, particularly for use in the USA. In addition, to be used during the official EPA certification fuel economy test indicated what we think would be one of the test methods applied to other models certified in the USA, and therefore should be one of the standard methods.

EPA and manufactures are now working on the evaluation of measurement methods but according to our evaluation results we believe that weighting method achieved the measurement accuracy and reproducibility required of standard test. As a result, this measurement method and measurement system has been used in 2002 the world's first certification fuel economy test for fuel cell vehicles which was implemented on the Honda FCX. The results of this official test are given in Table 2, and Fig. 12 shows the fuel economy label giving the practical fuel economy values calculated from the test results. All vehicles sold in the USA are required to have the fuel economy label attached, giving the vehicle's practical fuel economy value as recognized by the government. The fuel economy unit used in Table 2 and Fig. 12 is the distance traveled, in miles, for each 1 kg of hydrogen fuel.

Table 2 EPA fuel economy test result for FCX

Mode	Fuel economy (miles/kg Hydrogen)
CITY	56.8
HWY	61.7

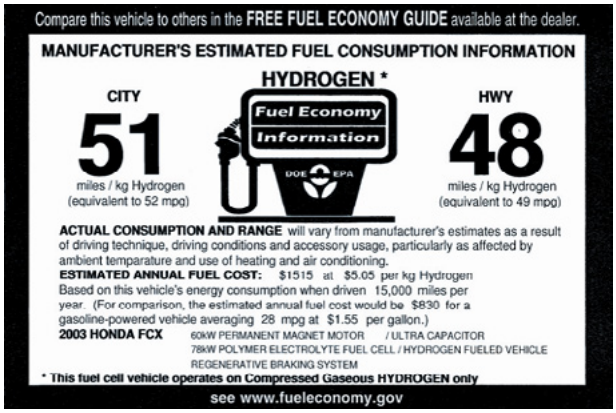


Fig. 12 EPA fuel economy label

8. Summary

By adopting the weight method, reducing measurement deviations, and using the US certification fuel consumption modes, the following results were achieved.

(1) In both the US fuel consumption certification modes of City and Highway, measurement accuracy of total fuel consumed was 0.286% and 0.125%, so this fully satisfies the SAE standard requiring measurement accuracy of ±1%.
(2) It is possible to create a fuel economy measurement system that can use hydrogen tanks that are readily available not only in Japan but also in the USA. By adding a hydrogen tank switching mechanism, it is also possible to measure fuel economy for each phase.
(3) The cost of manufacturing the fuel consumption measurement system is approximately ¥1.8 million, which meets the target of no more than ¥2 million. This is a cost lower than that of fuel economy measurement systems using the carbon balance method for gasoline vehicles.
(4) This measurement method has been used for official fuel economy test method, showing that it can be a standard method.

Acknowledgements

In this development project, many people, including those at Suzuki Shokan Co., Ltd, gave support and cooperation. The authors would like to take this opportunity to express their gratitude.

References

(1) Watanabe, S.: State of the Art of Fuel Cell Vehicle, Journal of Society of Automotive Engineers of Japan, Inc., Vol. 56, No. 1, p. 54-58 (2002)

(2) Seko, T.: Present Status and Future Prospects of Alternative Fuel Vehicle, Journal of Society of Automotive Engineers of Japan, Inc., Vol. 53, No. 5, p.15-20 (1999)

(3) Kuroda, E. et al.: Test Methods to Measure Fuel Economy in Direct Hydrogen Fuel Cell Vehicle, JARI Research Journal, Vol. 24, No. 10, p.49-54 (2002)

■ Authors ■


Satoshi AOYAGI


Takuya SHIRASAKA


Osamu SUKAGAWA


Naoki YOSHIZAWA

Rapid Compressed Hydrogen Filling System for Fuel Cell Vehicle

Yasuki YOSHIDA* Shuichi TOGASAWA* Koichi TAKAKU*
Akira YAMADA* Hirokazu KUWABARA* Yoshio NUIYA*

ABSTRACT

A compressed gas system previously utilized in natural gas vehicles (NGV) was utilized in the Honda FCX. Rapid filling tests of the high-pressure hydrogen tanks of both Type 3 (Aluminum liner) and Type 4 (High Density Polyethylene) were carried out using compressed hydrogen gas. Type 3 tanks showed better performance. This result can be explained in terms of the difference in the heat diffusion coefficient between aluminum and HDPE. The shortest filling time from 1 MPa to 34.4 MPa to enable a gas temperature increase (ΔT) of 45 °C to be observed using Type 3 tanks with a total volume of 156.6 dm^3 was found to be 3.6 min., almost the same as the refueling time of present gasoline vehicles.

1. Introduction

The hydrogen storage methods proposed for use with a direct hydrogen fuel cell vehicle (FCV), up to this time, included compressed gas, liquid hydrogen, and hydrogen-absorbing alloy[1, 2]. The present development project focused on the type of compressed gas storage system that had proven performance in natural gas vehicles. Two types of lightweight compressed gas tanks exist for use on vehicles, one with aluminum and the other with plastic as the liner material. The natural gas automobile standard NGV2-2000 defines the former as Type 3 and the latter as Type 4. The Honda Civic GX natural gas passenger car uses a Type 4 tank, which for a given tank volume, is lighter in weight than a Type 3 tank. The present project approached development from the perspective of rapid filling.

It is desirable, in terms of passenger car usability, for FCV filling time to be equal to the refueling time of current gasoline vehicles. The Interface Working Group of the SAE Fuel Cell Standards Committee is studying a standard that sets the upper limit for gas temperature during filling at 85 °C. The High Pressure Gas Safety Law of Japan stipulates an upper limit for gas temperature while stored in a container at 40 °C. Therefore, the gas temperature increase (ΔT) during filling must not be allowed to exceed 45 °C, which is the difference between these two temperatures.

This report will describe the results from the study of gas behavior during the rapid filling of tanks with compressed hydrogen, simulations of filling behavior, and the factors that affect hydrogen filling mass.

2. Rapid Filling Test with Compressed Hydrogen at 34.4 MPa

Figure 1 shows a filling system from a hydrogen filling station to a high-pressure hydrogen tank (hereafter referred to as a tank). Tests were carried out on a pair of tanks placed side by side, using both a pair of Type 3 and a pair of Type 4

* Wako Research Center

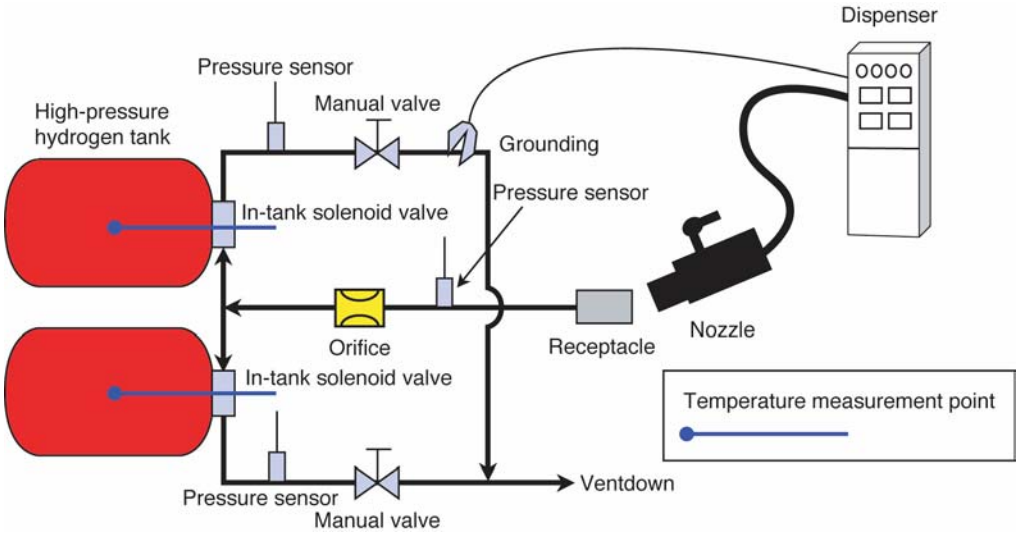


Fig. 1 Schematic illustration of high-pressure hydrogen supply system

tanks. One series of tests was carried out at ambient temperature, with filling speed controlled by an orifice installed before the tanks. The tests were conducted with a hydrogen pressure inside the tanks of 1 MPa (all pressures in this report are gauge pressures) before filling as an initial condition.

Figures 2 and 3 show the gas temperature increase (hereafter ΔT) as the orifice diameter was varied and its relationship to the filling time for both the Type 3 and Type 4 tanks. The Type 4 tank had a high density polyethylene (hereafter HDPE) liner. For both tank types, the time required for filling decreased as the diameter of the orifice was increased, but ΔT showed a tendency to increase. Although the Type 4 tank is lighter weight than the Type 3 tank, it was found that ΔT showed greater change relative to the change in filling time for the Type 4 tank. With the Type 3 tank, on the other hand, it was found that although the filling time grew shorter when the orifice diameter was 0.7 mm or larger, the ΔT showed almost no change.

Figure 4 organizes the findings for both tanks regarding ΔT during filling and the filling time based on the results in Fig. 2 and Fig. 3. Considering that a larger ΔT is associated with a lower filling efficiency, the Type 3 tank has the advantage in rapid filling. In order to keep ΔT below 45 °C, the Type 3 tank allows rapid filling in five minutes or less, but the Type 4 tank requires slow filling that takes 20 minutes or more.

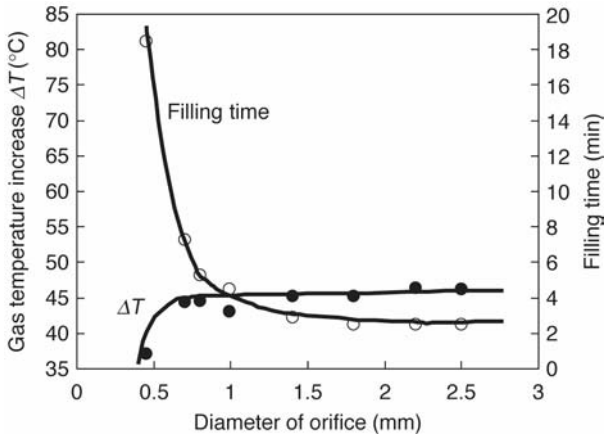


Fig. 2 Effect of diameter of orifice on gas temperature increase (ΔT) and filling completion time (Type 3)

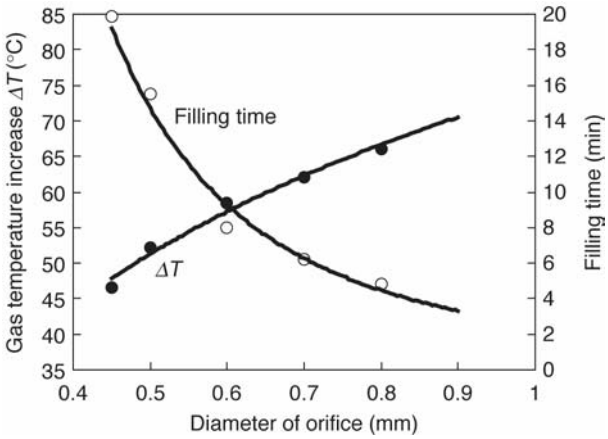


Fig. 3 Effect of diameter of orifice on gas temperature increase (ΔT) and filling completion time (Type 4)

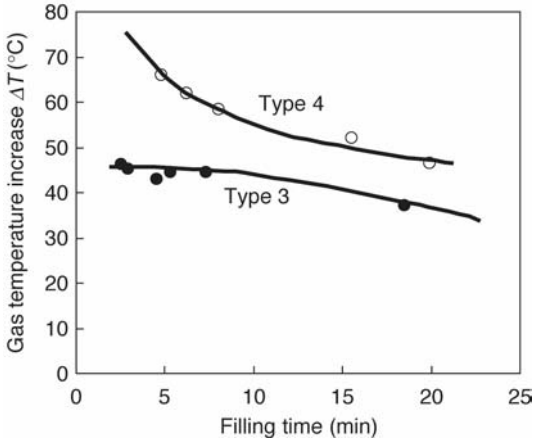


Fig. 4 Relationship between filling time and gas temperature increase (ΔT) for Types 3 and 4 high-pressure hydrogen tanks

3. Influence of Initial Hydrogen Pressure Inside the Tank on ΔT

On the vehicle side, refueling could be envisioned to take place at a variety of different residual hydrogen pressure levels. Therefore tests were carried out with the hydrogen pressure varied over 0 – 15 MPa before filling, and the ΔT was determined for each residual hydrogen pressure. The tests were carried out with a 2.5-mm diameter orifice installed on the filling line into the Type 3 tank, and a 0.7-mm diameter orifice on the Type 4 tank.

The results, as shown in Fig. 5, indicate a tendency for both tanks to have a lower ΔT when the hydrogen pressure in the tanks before filling is higher. The amount of change (slope) of ΔT for increasing hydrogen pressure in the tanks before filling was found to be greater in the Type 4 tank than in the Type 3 tank. In the case of the Type 4 tank, as will be explained below, the heat diffusion coefficient of the HDPE is low, so a larger proportion of the heat that is generated by polytropic adiabatic compression is stored in the hydrogen gas.

Consequently, the Type 4 tank is thought to be affected more than the Type 3 tank by the initial hydrogen pressure inside the tank.

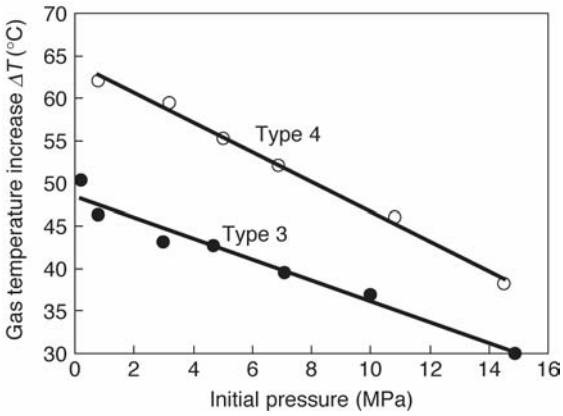


Fig. 5 Dependence of gas temperature increase (ΔT) of Types 3 and 4 high-pressure hydrogen tanks during filling on initial pressure

4. Influence of Ambient Temperature during Filling on ΔT

Similar to that described in the preceding section, refueling could be envisioned to take place under a variety of different temperature conditions on the vehicle side. Therefore the influence of ambient temperature during filling on ΔT was investigated. These tests were carried out only with the Type 4 tank, for which ΔT is larger during filling. The tests were carried out with a 0.7-mm diameter orifice installed and hydrogen pressure in the tank of 1 MPa.

As shown in Fig. 6, the results from testing with ambient temperatures over the range of 4 – 39 °C showed that a higher ambient temperature tends to result in a higher gas temperature peak, while ΔT is not dependent on ambient temperature but remains constant at 62 °C. It was inferred, therefore, that similar results would be obtained with the Type 3 tank.

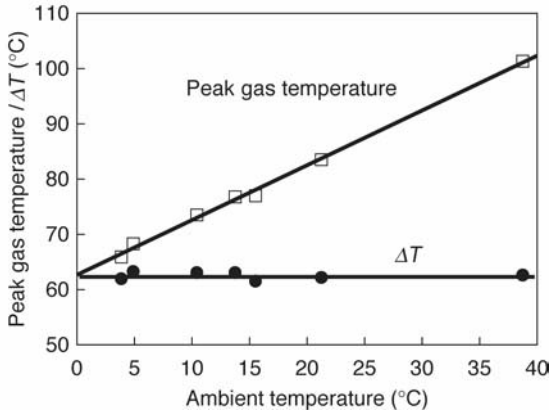


Fig. 6 Effect of ambient temperature on peak temperature and gas temperature increase (ΔT) for Type 4 high-pressure hydrogen tanks

5. Filling Behavior of Hydrogen at 34.4 MPa Pressure in the Type 3 Tank

The Type 3 tank had a total volume of 156.6 dm^3. When filling this tank so that the hydrogen pressure inside the tank rose from 1 MPa to 34.4 MPa, the minimum filling time at which ΔT would remain at 45 °C or lower was found to be approximately 3.6 minutes. Figure 7 shows the changes of pressure and ΔT over time.

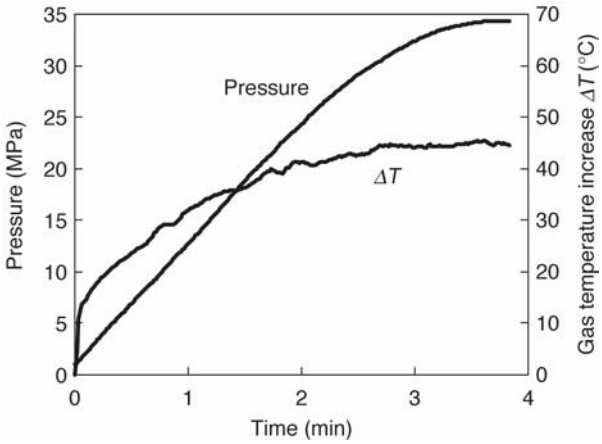


Fig. 7 Filling characteristic from 1 to 34.4 MPa using a Type 3 high-pressure hydrogen tank with a total volume of 156.6 dm^3

Pressure inside the tank increased in a straight line with respect to time up to the vicinity of 20 MPa. After that, the rate of pressure increase showed a tendency to gradually slow. The reason that the rate of pressure increase slows in this way is that the critical pressure of 18 MPa with respect to the filling pressure of 34.4 MPa is exceeded. The critical pressure can be derived using the below formula[3].

$$Pc = P_1 \{2/(\kappa+1)\}^{\kappa/(\kappa-1)} \quad (1)$$

Here, Pc is the critical pressure, P_1 is the initial filling pressure, and κ is the specific heat ratio (in the case of hydrogen, 1.409).

The gas temperature inside the tank shows a sharp increase upon initial filling, after which the rate of temperature increase tends to slow over the course of filling time. This is the result of the decrease in compression ratio as filling occurs, the increase in the heat content of the gas itself, and the occurrence of thermal diffusion to the various materials making up the tank.

6. Simulation of Filling Behavior

Newhouse *et al*. conducted natural gas filling tests with different types of tanks and compared their filling efficiency. Their tests used a Type 1 tank of steel, a Type 3 tank with a thin-walled aluminum liner (3.4 mm thick), a Type 4 tank with HDPE liner, and a Type 4 tank with a nylon 11 liner. From these results, these tanks can be ranked by filling efficiency as follows: Type 1 > HDPE Type 4 = Type 3 > nylon Type 4. Tests were also carried out using a Type 3 tank with a thick-walled aluminum liner (5.6 mm thick) and a Type 4 tank with HDPE liner, showing that the Type 3 tank has a higher filling efficiency[4]. This suggests that filling efficiency varies with the thickness of the aluminum liner.

Simulations were then conducted to investigate the influence of the thickness of the aluminum liner on ΔT. When filling with compressed hydrogen, the tank surface radiates heat, so that the perfectly adiabatic compression (in which PV^{κ} —where P is pressure, V is volume, and κ is the specific heat ratio, which in the case of hydrogen is 1.409— is a constant) does not take place. Moreover, since the temperature inside the tank changes, isothermal change (in which PV is a constant) does not take place. This is, therefore, a polytropic change as expressed by PV^n = Constant. The results in Fig. 7 and the physical properties of the materials in Table 1 were then used in an unsteady heat transfer model to determine the polytropic index n. Accurate approximation was found to be possible when n = 1.2. The filling behavior of four types of tanks was then simulated using this value. The four tanks were (1) Type 4 tank with HDPE, (2) Type 3 tank with liner 7 mm thick, (3) Type 3 tank with liner 3 mm thick, and (4) Type 3 tank with liner 1 mm thick. Their filling efficiencies were calculated from those results. The simulation was carried out using the same constant conditions of 10-minute filling time and 35 MPa filling pressure throughout. As shown in Table 2, the results indicate that ΔT is higher and filling efficiency is lower for thinner aluminum liners. These findings support the test results from Newhouse *et al*[4]. Contrary to their findings, however, the filling efficiency of Type 3 tanks with liners 3 mm and 1 mm thick was found to be higher than that of the Type 4 tank.

Table 1 Mechanical properties of high-pressure hydrogen tank components

	Aluminum	HDPE	CFRP*
Density ($kg\ m^{-3}$)	2680	955	1700
Specific heat ($kJ\ kg^{-1}K^{-1}$)	0.896	2.1	0.9
Heat conductive coefficient ($W\ m^{-1}K^{-1}$)	180	0.41	6.5
Heat diffusion coefficient ($mm^2\ s^{-1}$)	74.96	0.2	4.25

*)Carbon Fiber Reinforced Plastic

Table 2 Comparison of filling efficiency obtained from the simulation method

	ΔT (°C)	Filling efficiency(%)
Type 4	54	86.8
Type 3 (Liner thickness : 7 mm)	40	89.9
Type 3 (Liner thickness : 3 mm)	46	88.6
Type 3 (Liner thickness : 1 mm)	51	87.5

Figure 8 shows the distribution in the hydrogen gas, the various tank parts, and the outside air of thermal energy generated by polytropic compression when the temperature of the hydrogen gas is at its highest. In the case of the Type 3 tanks, it became clear that the heat content of the liners is lower and the temperature of the hydrogen gas is higher when the liners are thinner.

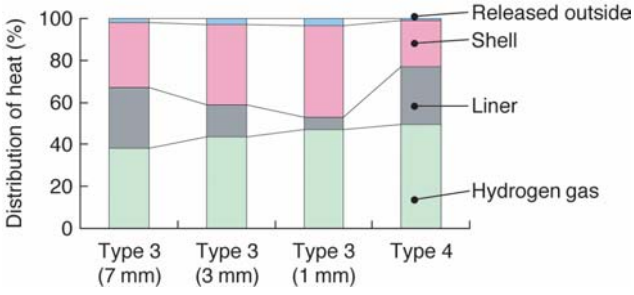


Fig. 8 Distribution of heat generated by the rapid filling of compressed hydrogen gas for various types of tanks

The conspicuous differences in filling behavior that can be recognized even though the heat generated during filling is the same in Type 3 and Type 4 tanks is inferred to be caused by the physical properties of the liner materials. As shown in Table 1, the heat diffusion coefficient α of aluminum is 375 times that of HDPE, and a greater proportion of the heat generated during filling is thought to be distributed to the liner and carbon fibers. It is presumed that the percentage distribution of thermal energy to the hydrogen gas itself is reduced as a result, so that ΔT during filling is lower in Type 3 than in Type 4 tanks.

$$\alpha = \lambda / (\rho \cdot Cp) \qquad (2)$$

Here α is the heat diffusion coefficient, λ is the thermal conductivity coefficient, ρ is the density, and Cp is the specific heat at constant pressure.

7. Comparison with Rapid Filling of Natural Gas (methane)

During rapid filling with methane, the temperature drops conspicuously in the vicinity of the methane inlet in the in-tank solenoid valve upon initial filling. The temperature of the gas in the center of the tank, however, does not drop as much as at the inlet. Figure 9 shows one example of that filling behavior. This is the result of Joule-Thomson expansion (isoenthalpic change) that occurs when high-pressure methane flows into the container from the pressure accumulator at the filling station. After approximately 0.1 minutes of filling time, the temperature of the inflowing gas then tends to rise. This suggests that the temperature drop caused by Joule-Thomson expansion (endothermic heat) is exceeded by the temperature rise (exothermic heat) resulting from the energy generated by compression of methane. Thus the behavior of the gas temperature during rapid filling with high-pressure methane differs significantly from the case of hydrogen, and this is caused by the difference in the amount of temperature change undergone by the two gases in connection with Joule-Thomson expansion.

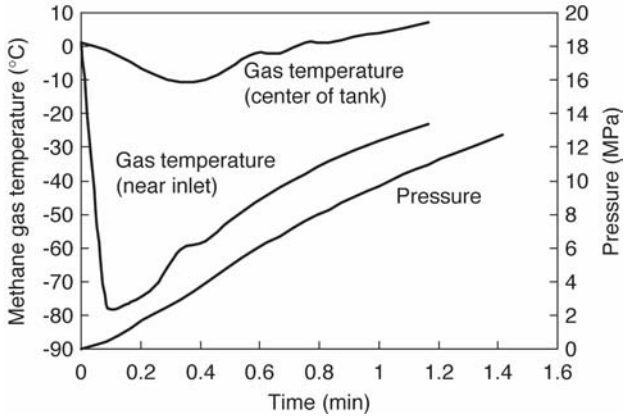


Fig. 9 Changes in gas temperature at the center and near inlet of the tank, and pressure with methane gas filling time

Joule-Thomson expansion is the phenomenon whereby a temperature change occurs in a certain volume of gas under high pressure in a constant flow because the gas passes through a valve or orifice. There are cases when the temperature will rise because of the Joule-Thomson expansion and cases when it will drop, and the boundary temperature between those two cases is known as the inversion point. The inversion point varies with the kind of gas and its pressure. In the case of air at around normal pressure, for example, it is 487 °C, and for hydrogen –72 °C. Above this temperature, passage through a valve or orifice causes the temperature to rise, and below this temperature, it will drop. The drop in temperature results from a decrease in internal energy to the extent of the work done against the intermolecular force. In the case of methane, for example, according to the temperature-entropy curve[5], when methane at 27 °C and 20 MPa undergoes isoenthalpic change to 1 MPa, then a temperature drop of approximately 80 °C will occur. In the case of hydrogen, however, according to the temperature-entropy curve[5], hydrogen in the same pressure region undergoes almost no temperature change even if Joule-Thomson expansion occurs. As a result, the kind of temperature drop observed in the initial stage of filling with methane does not occur, and the gas temperature inside the tank rises over time.

8. Investigation of Hydrogen Filling Mass

Under constant temperature and pressure, hydrogen behaves nearly as an ideal gas, but its behavior diverges from the ideal under lower temperatures or higher pressures. This is caused by intermolecular interaction, whereby the intermolecular force distance becomes shorter under higher pressure, so that the repulsive force increases. As a result, for an actual gas V and ideal gas V_{id} at the same temperature and pressure, the volume ratio $Z = V/V_{id}$ will be greater than 1. Z is known as the compression coefficient, and it describes the deviation of an actual gas from an ideal gas.

Figure 10 shows the relationship between pressure and density of hydrogen at 15 °C in ideal and actual states. At pressures of approximately 10 MPa or above, the density of the actual gas begins to diverge from that of the ideal gas, showing a lower value than the ideal gas. Figure 11 shows the changes of pressure in hydrogen at 34.4 MPa and 15 °C when the temperature is changed. The pressure-temperature property of hydrogen gas in the actual state demonstrates behavior virtually identical to that in the ideal state.

Based on the relationship of Fig. 10 and Fig. 11, the isothermal hydrogen filling mass at an ending pressure of 35 MPa and the rating temperature of 15 °C, and the actual hydrogen filling mass with the filling behavior of Fig. 7 were derived as 3.75 kg and 3.32 kg, respectively. Therefore, the filling efficiency is 88.5%.

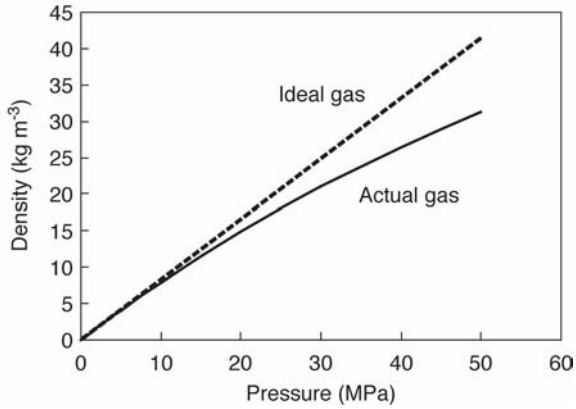


Fig. 10 Relationship between pressure and density of hydrogen gas in ideal and actual states

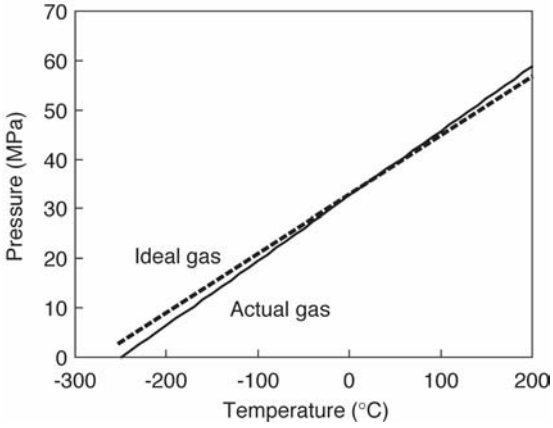


Fig. 11 Pressure-temperature property of hydrogen gas in ideal and actual states

9. Summary

A compressed hydrogen storage system was developed for FCV use and the below findings were obtained. The findings are being utilized in the Honda FCX, which represents the world's first practical application of this technology.

(1) Rapid filling tests of Type 3 and Type 4 tanks with 34.4 MPa compressed hydrogen showed a conspicuous difference in ΔT during filling, and demonstrated that ΔT is smaller for the former type. This is due to the fact that the heat diffusion coefficient of aluminum is 375 times greater than that of HDPE. Based on these results, the Type 3 tank was adopted.

(2) Higher residual hydrogen pressure inside the tank means greater heat content, so that ΔT will be lower. Higher ambient temperature means higher maximum temperature of the gas inside the tank, but ΔT remains constant.

(3) When using a Type 3 compressed hydrogen tank with a total volume of 156.6 dm^3 and filling it from an initial hydrogen pressure of 1 MPa to 34.4 MPa, the minimum time in which the gas temperature increase ΔT would reach 45 °C or less from the initial temperature was 3.6 minutes. This is more or less equal to the refueling time of a gasoline vehicle.

References

(1) Kimura, Y.: Development of Fuel Cell Electric Vehicle, BATTERY TECHNOLOGY, Vol. 10, p. 160-168 (1998)

(2) Hasuike, H.: Report on Clean Energy Vehicles, Kiho Energy Sogo Kogaku, Vol. 23, p. 89-99 (2000)

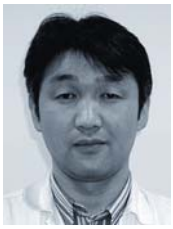
(3) Kurabayashi, T., Terasaki, K., Nagai, N., Ito, K.: Kogyo Netsu Rikigaku, Asakura Shoten, p. 119 (1985)

(4) Newhouse, N., Liss, W.: Fast Filling of NGV Fuel Containers, 6E Paper 1999-01-3739

(5) The Japan Society of Mechanical Engineers: JSME Data Book Thermophysical Properties of Fluids, Maruzen, p. 547 (1991)

■ Authors ■


Yasuki YOSHIDA


Shuichi TOGASAWA


Koichi TAKAKU


Akira YAMADA


Hirokazu KUWABARA


Yoshio NUIYA

Development of Electric Double-layer Capacitor System for Fuel Cell Vehicle

Koji TAMENORI* Koichi YAMAMOTO* Akihiro ANEKAWA*
Takeshi TAGUCHI* Shinya KUBOTA* Makoto KAWAHARA*

ABSTRACT

An electric double-layer capacitor system has been developed for the Honda FCX fuel cell vehicle. This high-power capacitor system offers more than 30% higher output power and more than twice the power density of the nickel-metal hydride batteries used in hybrid electric vehicles (HEV) at an equivalent system voltage, and satisfies automotive power requirements. The new system is equipped with a capacitor cell protection system, which monitors capacitor voltage and provides equalization and malfunction detection functions. Heat insulation and a cooling system control increases in temperature both when the vehicle is parked and when it is moving. The effectiveness of these systems has enabled the new capacitor to satisfy durability and reliability requirements in unit tests and running tests.

1. Introduction

Increasing concern about environmental impact and global warming have made efforts to reduce emissions of exhaust gases, including CO_2, an important aspect of the research agendas of automotive manufacturers. As one solution, Honda has marketed a hybrid car fitted with its proprietary IMA system. In a new innovation aimed at achieving further reductions in emission levels, Honda has developed the FCX, a fuel cell passenger vehicle that releases no pollutants. A capacitor system assists the fuel cells, which form the main power source, by storing energy recovered during deceleration as electricity. This energy is provided when power is required during acceleration. Unlike conventional secondary batteries, the capacitor system contains no heavy metals, and is therefore an environmentally friendlier energy storage system, which, with the fuel cells (FC) also employed in the FCX, is a clean energy technology with considerable future potential. This paper will discuss the concept behind the new energy storage system and the technologies applied in the capacitors it employs.

* Wako Research Center

2. Comparison of Energy Storage

The energy storage system to be used in the FCX was required to compensate for the poor instantaneous response performance of the FC. The assist power required in the FCX is approximately three times that demanded in the CIVIC Hybrid, and it was therefore necessary to achieve a high specific power density from a lightweight unit. As Table 1 shows, Li-ion batteries and capacitors display superior specific power density. At the same mass, the nickel metal-hydride battery utilized in the CIVIC Hybrid provides about half the assist power of a capacitor system. Both nickel metal-hydride and Li-ion batteries utilize chemical reactions to produce electricity, and therefore generate a stable voltage. Capacitors do not employ a chemical reaction, and voltage varies with the status of energy in the units. Because this characteristic enables the capacitor system to synchronize with the voltage of the FC, it is possible to connect it in parallel with the FC without passing the current through a voltage regulator unit, thereby increasing fuel economy.

Capacitors also have lower internal resistance than nickel metal-hydride batteries, and therefore not only display a

Table 1 Power density and voltage of secondary batteries

	Power density (W/kg)	System voltage※ (V)	OCV (V)
Ni-MH	Over 500	400 ~210	320
Li-ion	Over 1 000	400 ~285	340
Capacitor	Over 1 000	400 ~0	——

※Upper voltage fixed 400V

better charge and discharge efficiency across the entire power range, but also demonstrate very little energy loss when charging and discharging (Fig. 1).

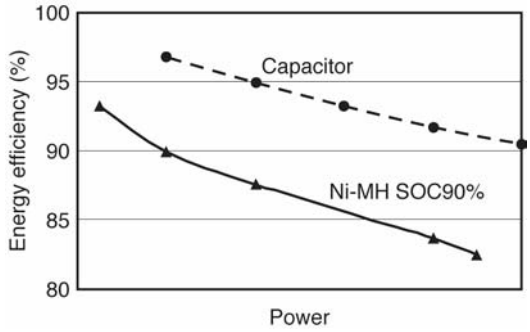


Fig. 1 Energy efficiency

In addition, because capacitors show little decline in performance with repeated charge and discharge, they are able to provide a stable source of power and energy for the life of the FC. There is no memory effect and the state of charge can be determined from voltage, enabling the control system to be simplified. Extremely reliable high-power capacitors are therefore the most suitable energy storage system for use with FC.

3. Development Goals

This development represented the first time in the world that a capacitor system had been utilized in a passenger car, making it necessary to reduce the space required by the unit as much as possible. Development was conducted with a strong focus on the following points, established as necessary prerequisites for achieving compactness and a high level of reliability:

(1) Direct connection to ensure stable mounting of the capacitor units and guarantee the required voltage, while making the system more compact
(2) Minimum space requirements for the heat insulation and cooling systems
(3) Capacitor protection and control systems that increase system reliability in addition to contributing to stable performance

4. Study of Capacitor Module and Vehicle Installation

4.1. Structure of Capacitor Module

As Fig. 2 shows, the capacitor module is made up of 80 capacitors, a protection circuit to monitor their status, and a cooling structure. The newly developed series connection enables the positive and negative electrodes to be positioned on the same side, and the connection structure between the high-voltage capacitors and the protection circuit unit can be compactly organized in an 11.5 mm thick plastic plate, which also serves an electrical insulation function. Module support stays have been positioned at the top and bottom of the central section where functions are concentrated, increasing the strength of the support of the front section of the module, and enabling the capacitor box, which protects the capacitors and ensures cooling air flow, to be constructed from 0.8 mm thick aluminum.

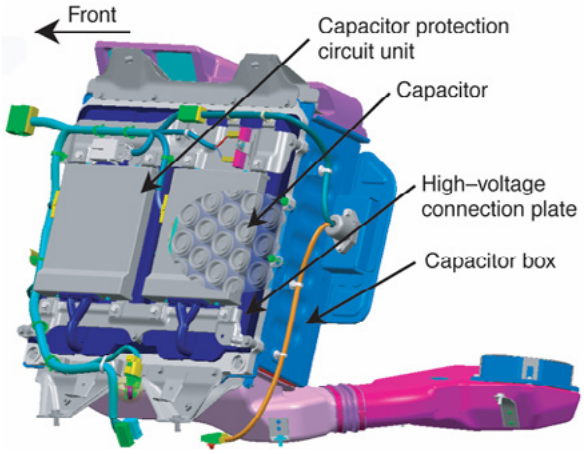


Fig. 2 Structure of capacitor module

4.2. Connection Structure

Welding is standard for conventional battery connections, and was employed for the connection in the CIVIC Hybrid. YAG laser welding must be employed when welding is used to connect capacitors, and control of component tolerances in the welded section is extremely important when utilizing YAG laser welding. The necessity of ensuring weld quality with consideration of the dimensional tolerances of the capacitor cells and possible deviations in assembly makes the technique impractical when connecting multiple capacitors. A low-resistance, lightweight and compact connection that would enable regular and accurate assembly and series connection of multiple capacitors was therefore studied.

Figure 3 shows the new series connection structure. The distinctive characteristic of this connection is that it balances support provided by screws with the achievement of low resistance conductivity through the use of contact washers. In addition, the connection structure has been concentrated at one side to simplify the monitoring of the voltage of individual capacitor cells.

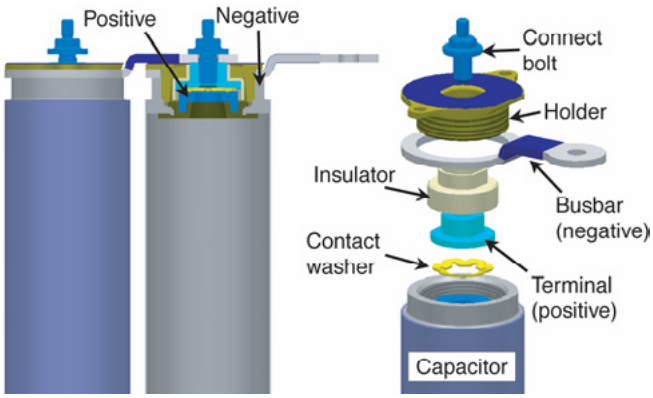


Fig. 3 Structure of capacitor series connection

The torque method was studied for tightening. It was confirmed that at a specified torque resistance stabilizes, enabling the target value for resistance to be achieved (Fig. 4).

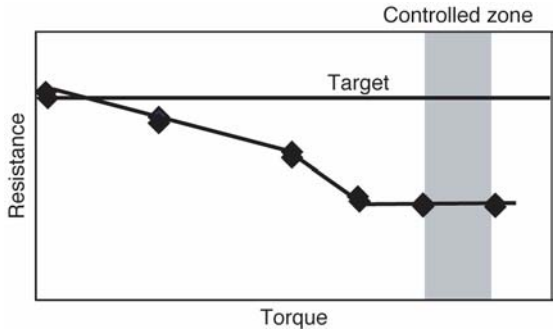


Fig. 4 Torque and electrical resistance

4.3. Controlling Temperature Increase when the Vehicle is Exposed to the Sun

The vertical positioning of the capacitor box behind the rear seat, as shown in Fig. 2, raised concerns that the capacitors in the upper part of the box might become overheated due to exposure to the sun on hot days. The following points were a significant focus during the development of the system of installation in the FCX. Because there is almost no natural ventilation when a vehicle is left exposed on a summer day, the internal temperature rises to more than 100 °C in the sections directly exposed to sunlight, and to more than 80 °C in the sections in the shade. There is no difficulty in protecting the capacitor at even 80 °C if its voltage is zero; the status of the unit's voltage determines the progress of performance decline. If the temperature of the capacitor is maintained at around 60 °C, there is no need to consider the effect of voltage on performance decline, and this was therefore established as a target for temperature control, after which study focused on methods of thermal insulation. The polypropylene foam proven in the CIVIC Hybrid was utilized in the upper duct to provide insulation, while a rubber flap was attached to the inlet of the same duct; the flap blocks the inlet when it is not being used for cooling (Fig. 5). Insulating materials have also been packed around the capacitor module to further contribute to thermal insulation.

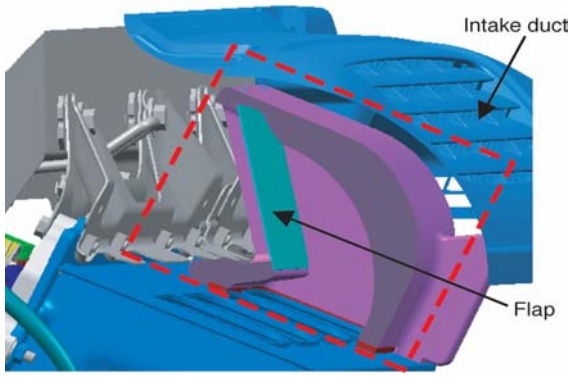


Fig. 5 Structure of upper capacitor box

Figure 6 shows the results of measurements of temperature of an installed module employing the insulating materials and flap described above. The results indicate that the new insulation layout has ensured that the temperature of the capacitors does not exceed 60 °C even if the vehicle is left exposed on a hot day, and functions efficiently to prevent overheating.

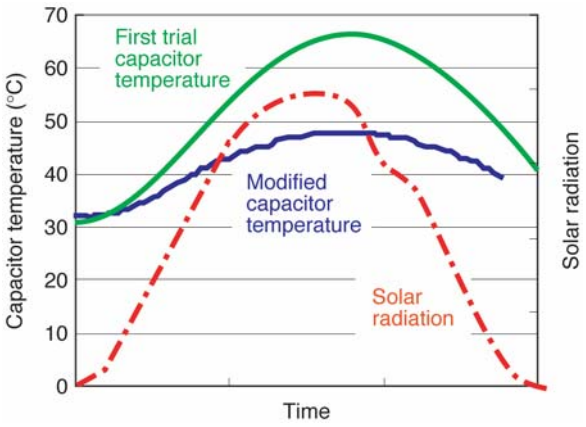


Fig. 6 Effect of heat insulator

4.4. Control of Temperature Increases during Vehicle Operation

The increase in temperature occurring during operation of the vehicle is dependent on the square of current multiplied by resistance during discharge and regeneration. Reduction of the current is effective in controlling temperature increase, but because this is dependent on the driving mode, it cannot be effected on the energy storage system side. The next most effective measures are the reduction of internal resistance and connection resistance. An aluminum case was adopted for the capacitor system in place of the SUS case utilized for the nickel metal-hydride batteries employed in the HEV, and the high heat conductivity of the material has increased cooling efficiency. In addition, as discussed above, the cell connection structure has reduced the level of heat generated by the system. In combination with the increased cooling efficiency provided by the aluminum case, this has enabled the capacitor system to generate half the heat of a Ni-MH battery at an identical system voltage (Fig. 7). The reduction of the heat generated by the system has also enabled the fan to be made more compact, consequently reducing noise.

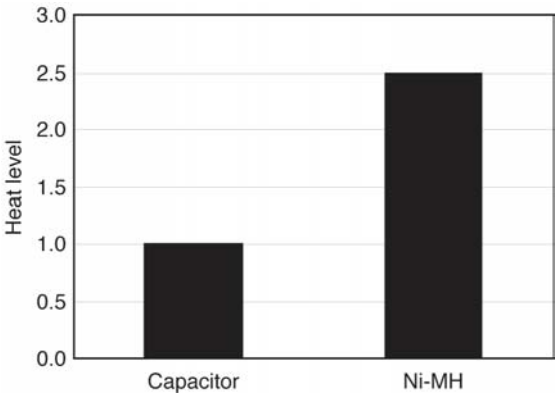


Fig. 7 Heat balance of energy storage

Figure 8 shows the cooling air flow. Cooling air is driven from the top of the module through the duct in the bottom by an axial-flow fan.

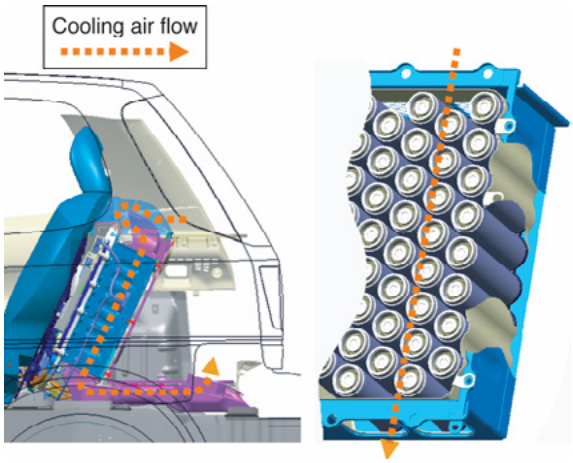


Fig. 8 Cooling air flow

To design the cooling structure for the capacitor box, the driving mode generating the greatest increase in heat value was selected from actual driving data, and the highest increase in heat value occurring in one continuous operation of the vehicle was abstracted from this mode. This was made the test mode (Fig. 9).

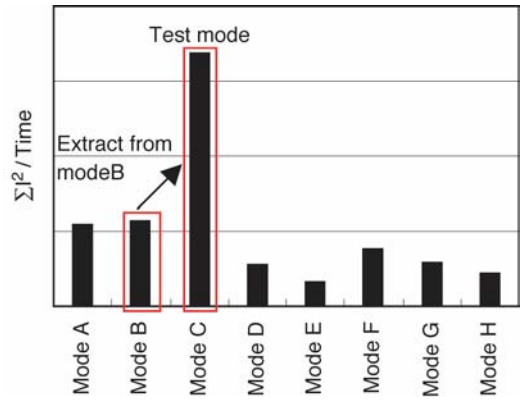


Fig. 9 Heating value in various modes

The temperature of the capacitors during operation of the FCX was measured, and a thermal analysis was conducted on the data. The results are shown in Fig. 10. The measurements were commenced with the temperature of the capacitor and the surrounding ambient temperature at 35 °C. Even in continuous operation in evaluation mode, 45 °C represented the upper limit for temperature increase. This is a result of the balance between the low level of heat generated by the capacitors and the efficiency of the cooling system.

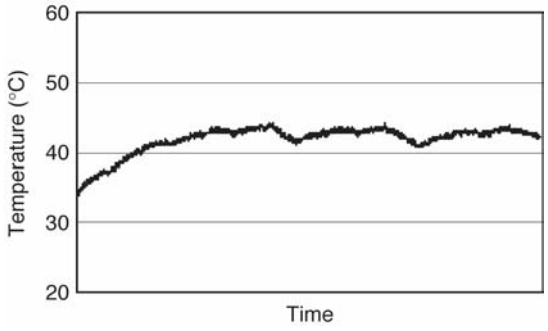


Fig. 10 Temperature transition in continuous mode C

5. Capacitor Protection Circuit

5.1. Configuration of Capacitor Protection Circuit

The electrical system of the capacitor system is made up of the high-voltage capacitors and a 12 V system, which controls them, with an insulating section positioned between them. The capacitor control circuit is composed of a voltage detection circuit and a circuit, which equalizes voltage variations between individual cells. The control circuit processes signals detected in the high-voltage circuit and communicates with the electronic control unit (ECU).

Figure 11 shows a schematic of the system.

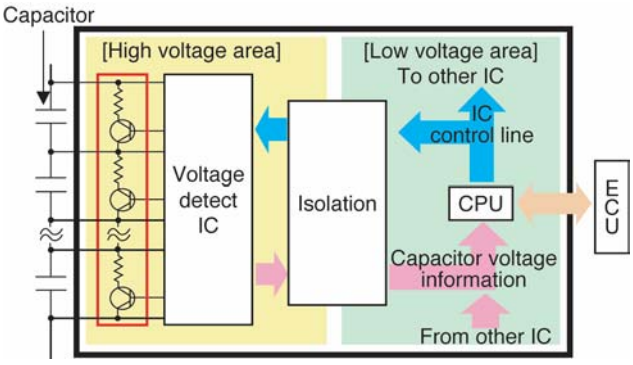


Fig. 11 Capacitor voltage detect system schematic

The functions that have the greatest effect on improving capacitor performance are:

- Capacitor voltage detection
- Equalization of capacitor voltage variations
- Capacitor malfunction detection.

The importance of each of these functions will be discussed below.

5.2. Voltage Detection

The energy of the capacitors reaches its maximum in use at a system voltage close to the upper limit. For this reason it was essential to increase the accuracy of the detection of the voltage of individual cells, leading to the use of integrated circuit (IC) in the voltage detection system. This has enabled the achievement of high-accuracy voltage detection of ±1.5% (0 °C — +80 °C).

Three criteria were established for detected voltage:

1) Upper limit detected voltage = Maximum absolute rated voltage for capacitor
2) Voltage for commencement of equalization ≒ Rated voltage for capacitor
3) Malfunction detection voltage = 0.7 V

The employment of IC has the added advantage of lowering the current consumed by the circuit when the vehicle is stationary (ignition OFF) to approximately 1 μA, enabling capacitor voltage to be maintained at more than 98% over periods of disuse of up to a month.

5.3. Equalization of Voltage Variations

Preventing variations in voltage between multiple capacitors is essential to reducing energy loss and a decline in performance. Figure 12 shows an image of the convergent capacitor voltage achieved by the voltage equalization circuit connected in parallel to the capacitors.

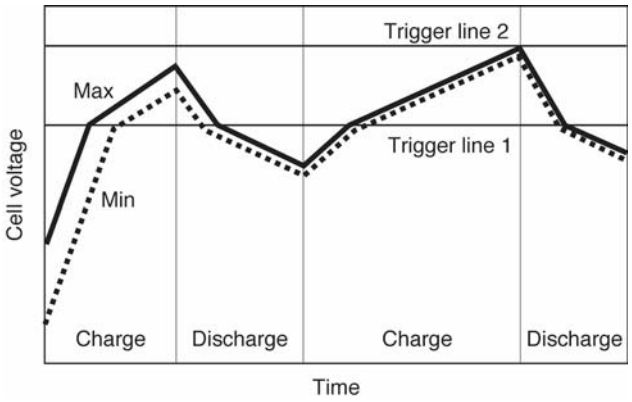


Fig. 12 Image of convergent capacitor voltage

The voltage equalization circuit operates between the voltage established for commencement of equalization and the upper limit detected voltage. When capacitor voltage reaches the level established for commencement of equalization, the equalization circuit connected in parallel operates to render capacitor voltage uniform by allowing part of the current to bypass the circuit. The development of the equalization circuit and the high-accuracy voltage detection circuit discussed above has enabled voltage variations between the capacitors to be controlled to less than 0.1 V, reducing the level of energy loss.

5.4. Malfunction Detection

The total voltage of the series-connected capacitors is considered as source voltage by the new voltage detection IC. If for any reason the voltage of the capacitor system connected to the IC falls below a lower limit, the circuit detects a system malfunction. The malfunction detection circuit can also detect internal shorts in the capacitor, shorts in the connection structures, and disconnections.

6. Verification of Durability

6.1. Changes in Durability towards Voltage and Temperature

By contrast with batteries, because no chemical reaction is involved in the charging and discharging of capacitors, they demonstrate little physical change and show superior durability. However, temperature and voltage affect the durability of capacitors, making the above-mentioned insulating and cooling systems and voltage control essential to the achievement of a stable performance. Figure 13 shows the rate of change of energy retention under different temperature and voltage conditions. It is clear that the level of durability changes as temperature and voltage increase.

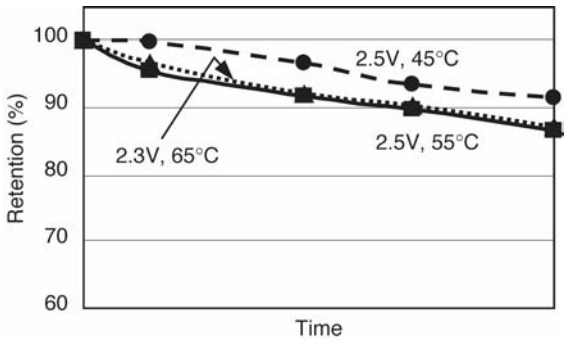


Fig. 13 Energy retention in relation to temperature and voltage

6.2. Establishing a Durability Test Mode

Voltage and temperature were distinguished as factors affecting the performance of capacitor cells. The higher the impressed voltage or the temperature, the more rapid the decline in the performance of the cells. Driving data from prescribed modes and actual modes were therefore focused on, and Mode A in Fig. 14 was abstracted as the durability test mode, because the average voltage in the capacitors and the heat generated by charge and discharge were at their maximum in this mode. By adding an idling time reflecting market data to the durability test mode, it was possible to establish a mode providing a sufficiently accurate representation of the actual conditions of use of the FCX (Fig. 14).

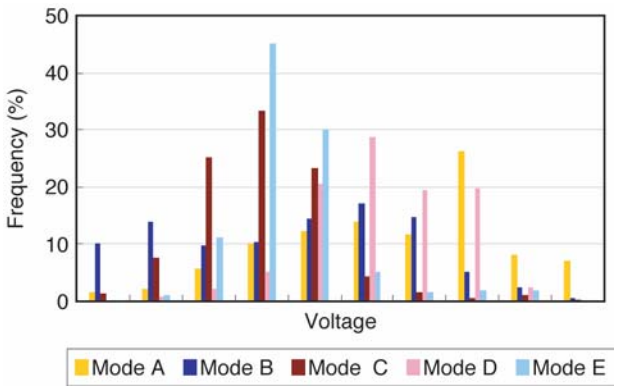


Fig. 14 Voltage frequency

Figures 15 and 16 show changes in performance during durability tests. Although the durability test mode was established on the basis of the most severe use conditions for the capacitors in the FCX, no sharp decline in performance occurred during tests, and the capacitors showed an energy retention rate of more than 90% and an assist time retention rate of more than 80% after tests.

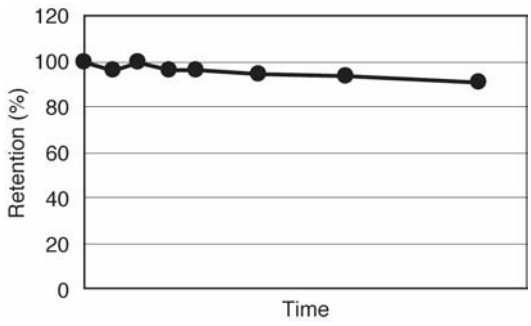


Fig. 15 Energy retention

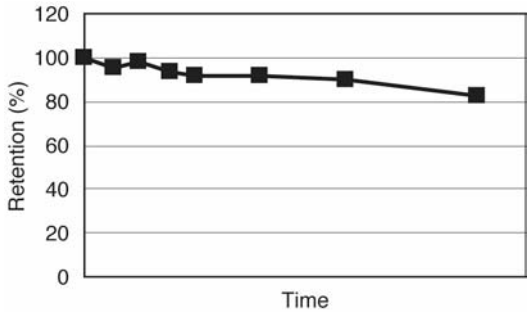


Fig. 16 Assist time retention

7. Current and Voltage Behavior when Installed

Because it is not generated by a chemical reaction, the voltage of a capacitor is not stable, but changes with the status of energy in the cell. For this reason a parallel connection was adopted in the FCX, to enable the changes in voltage in the capacitor cells to synchronize with changes in FC voltage during vehicle operation.

Figure 17 shows changes in FC and capacitor power.

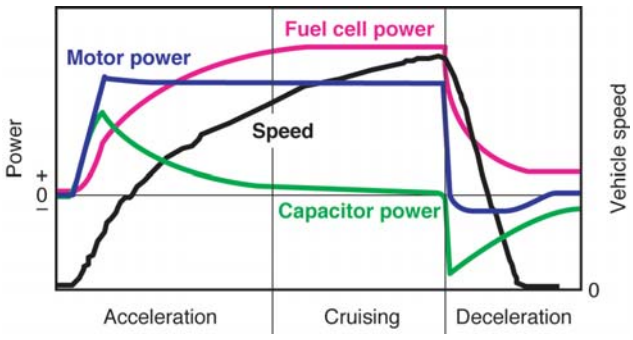


Fig. 17 Fuel cell and capacitor power characteristics

- During acceleration
  The capacitor cells compensate for the poor instantaneous power response of the FC, and provide the vehicle with power according to demand.
- During regeneration
  Part of the energy utilized in deceleration is regenerated in the capacitor system, which instantaneously recharges during deceleration.

8. Summary

An electric double-layer capacitor system has been employed as the energy storage system in the Honda FCX fuel cell passenger vehicle, the first time in the world that this type of system has been utilized in a passenger car. Development focused on the capacitor type most suited to the demands of FC. Series connection was adopted to enable stable mounting and to achieve low resistance, increasing the voltage of the system. In addition, the system has been provided with heat insulation and a cooling structure, to control temperature increases when the vehicle is in operation or is left exposed to the sun. A capacitor protection circuit has also been developed to ensure the reliability of the energy storage system.

Combining these innovations, the system provides power from the capacitors to compensate for the poor instantaneous power response of the FC, contributing to the excellent takeoff and acceleration performance of the FCX.

The capacitor system is not only superior to batteries in terms of power and efficiency, but generates half the heat of the nickel metal-hydride battery employed in Honda's HEV at the same state of charge, confirming that from this perspective too it represents the optimum energy storage system for automotive applications in use today.

Acknowledgments

The authors wish to take this opportunity to offer their sincere thanks to the many individuals from Honda and other companies who generously offered their assistance and support in the development of this system.

Reference

(1) Ohzono, K., Kayano, M.: Development of High Power Storage for the CIVIC Hybrid, HONDA R&D Technical Review, Vol. 14, No. 2, p. 31-36 (2002)

■ Authors ■


Koji TAMENORI


Koichi YAMAMOTO


Akihiro ANEKAWA


Takeshi TAGUCHI


Shinya KUBOTA


Makoto KAWAHARA

Development of High-power Electric Double-layer Capacitor for Fuel Cell Vehicle

Naohiko OKI* Kenji MATSUMOTO* Kenji SATO*
Mitsuru IKEO* Yasuhiro MATSUMOTO* Naoyuki ABE*

ABSTRACT

An electric double-layer capacitor has been developed as an energy storage device for a fuel cell vehicle. This capacitor was utilized in the Honda FCX fuel cell vehicle marketed in December 2002. The capacitor features a rolled electrode housed in a cylindrical case. The aluminum foil at the sides of the electrodes is welded to collector plates with radial U-shaped grooves; the structure is welded together after alignment of the terminals at the center of the collector plates with the holes in the center of the case and case cover. This configuration has enabled the achievement of a fill density of 86% in the electrode and a connection resistance of less than 0.05 mΩ. Due to this packaging the unit displays the highest level of performance for a capacitor cell known to date, with a specific power density of more than 1,500 W/kg and a specific energy density of 3.9 Wh/kg. Tests show that the longevity of the capacitor is equivalent to or greater than that of the vehicle in which it is fitted.

1. Introduction

Honda's continuing commitment to the environment has resulted in the marketing of the Insight[(1)] hybrid vehicle, provided with Integrated Motor Assist (IMA), in 1999, followed in 2002 by the Civic Hybrid[(2)]. Both of these vehicles employed nickel metal-hydride (Ni-MH) batteries as energy storage devices.

In a new innovation, electric double-layer capacitors were utilized as the energy storage system in the Honda FCX fuel cell vehicle. The FCX was first produced in December 2002, and is a zero-emission vehicle with considerable future potential.

This paper will discuss the structure and performance of the capacitor cells utilized in the FCX.

2. Principle and Characteristics of Electric Double-layer Capacitors

An electric double layer is a distribution of positive and negative charges separated by extremely small distances at the interface of a solid and an electrolyte. In an electric double layer, the charge of the electrode is balanced by ions in the electrolyte; for example, a positively charged electrode is balanced by negative ions in the electrolyte.

Figure 1 shows a schematic of charge and discharge for an electric double layer capacitor. One of the characteristics of these capacitors is that the phenomenon of physical adsorption of positive (or negative) ions by the activated carbon in the electrode gives the units lower internal resistance and higher durability under repeated use than chemical batteries. Because no chemical reaction is involved,

* Wako Research Center

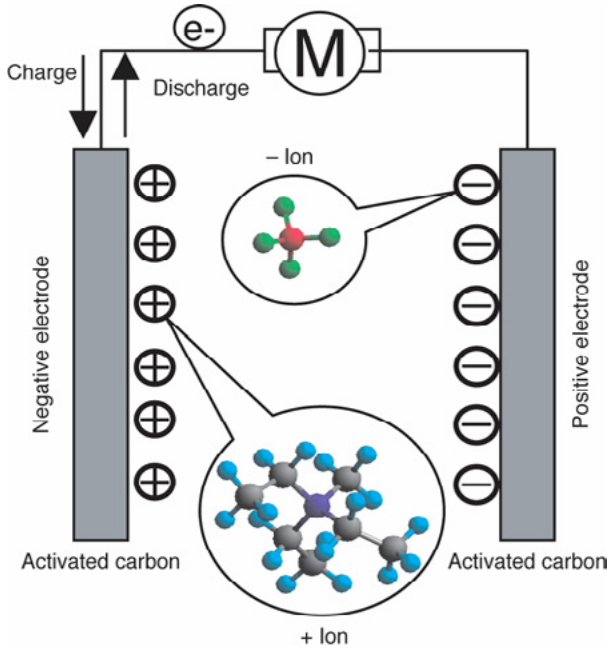


Fig. 1 Schematic illustration of electric double-layer capacitor

they can operate in a wide range of temperatures, from low to high. In addition, they employ no environmentally harmful materials requiring special treatment, such as heavy metals, acids and alkalis.

However, the significantly lower energy storage capacity of current electric double-layer capacitors makes them inferior to chemical batteries from the perspective of practical use.

Figure 2 shows the discharge curve of the new Honda capacitor at a fixed current. Cell voltage drops linearly at discharge. This characteristic indicates that the capacitor can be charged and discharged at a wide range of voltage, and is capable of synchronizing with fuel cell voltage without a voltage regulator.

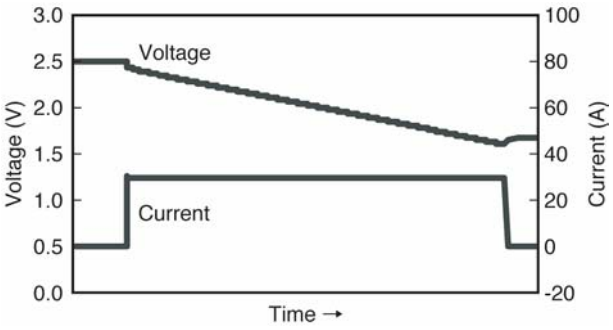


Fig. 2 Discharge curve of Honda Ultra capacitor

3. Development Aims

Targets of 2.5 mΩ for DC resistance and 1,350 F for capacitance were established for the new capacitor cells on the basis of targets for the capacitor system to be employed in the fuel cell vehicle.

The following goals were established to enable these targets to be achieved and to ensure reliability (vibration resistance, etc.):

(1) To achieve a resistance of less than 0.05 mΩ in the conductive connections from the electrode to the terminals (a section not involved in energy storage) in order to ensure that the low resistance characteristic of the capacitor was also displayed by the internal connection structure.

(2) To maximize the ratio of the size of the energy-storing electrode to the interior volume of the cell and minimize the volume required for the connection structure of the collector, which plays no part in storage. This enabled the energy density to be maximized, which was low in comparison to that of chemical batteries (The increase in electrode fill density was more than 80%).

4. Development Concept

4.1. Cell Shape Concept

Excluding small coin-type units, conventional capacitors can be broadly divided into two types. Figure 3 shows one of these, with a rectangular case and a layered electrode. The other type is shown in Fig. 4, and has a cylindrical case and a rolled electrode.

Increasing the width of the collector lead has been considered as a method of reducing resistance in the rectangular type, but because its width must not exceed half the width of the electrode, it is not possible to achieve a target of less than 0.05 mΩ for resistance in the collector section. The further requirement to provide clearance in the direction of the plane to insulate the collector lead from the four sides of the case limits the fill density to 56%, and significant improvements cannot be expected. These considerations led to the selection of a cylindrical case for the new capacitor.

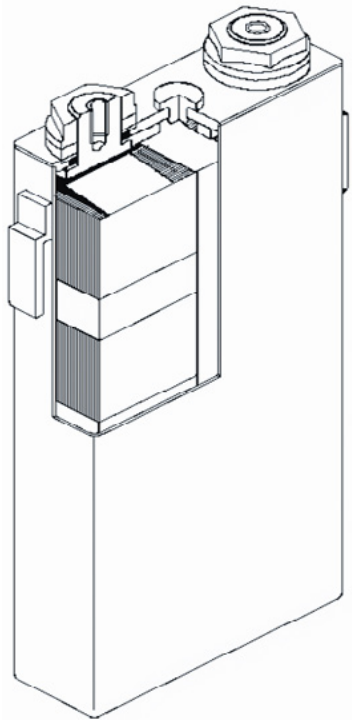


Fig. 3 Rectangular type

4.2. Collection Structure Concept

Various types of collection structures are also possible in a cylindrical cell. The difficulty of significantly reducing the length of the tab connecting the terminal and the rolled electrode in the type with a collector lead made it necessary to reexamine the collector structure to lower resistance and increase the fill density.

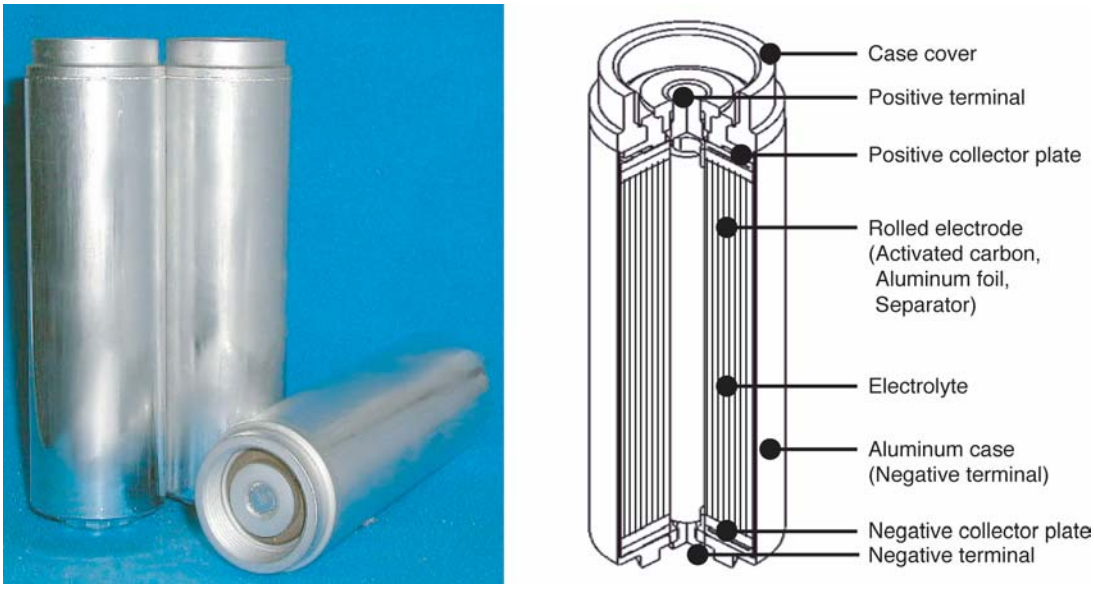


Fig. 4 Photograph and cutaway view of Honda Ultra capacitor

4.3. Concept behind Improvement of Fill Density

This development project focused on the use of the space inside the case, and defined electrode fill density as a function of cell structure as the ratio of the width of the rolled electrode to the internal length of the case. Reduction of the necessary dimensions of the collector structure was the key to increasing the electrode fill density as a function of the ratio of electrode width to available space in the case shown in Fig. 4. The design of the collector structure was studied to enable the establishment of a direct connection between the collector plates and the case and terminals and the minimization of the volume of the collector structure.

5. Study of Structural Design

5.1. Cell Structure

Figure 4 shows an external and a cutaway view of the newly developed cell. The cylindrical rolled electrode is made up of alternately rolled positive and negative poles interleaved with separators. It is immersed in an electrolyte containing positive and negative ions. In consideration of safety during production and normal operation of the cell and in the event of accident, a quaternary ammonium salt dissolved in propylene carbonate was selected as the electrolyte. Collector plates are attached to both ends of the electrode, and the terminals formed by the collector plates are directly connected to the terminal sections of the case and the case cover. To fit the cells to the coupling module in which they are installed in the vehicle, the case cover has the twin functions of sealing the electrolyte and fixing and insulating the positive and negative terminals and is provided with holding screws to fix the cell in place. The case is welded to the case cover, the bottom of which is formed to receive a tightening tool.

5.2. Design and Coupling Method of Collector Section

5.2.1. Shape of collector plates

Connection resistance between the collector plate and the rolled electrode is basically determined by the surface area of the connection between the collector plates and the electrode collector that protrudes from the ends of the rolled electrode. It is possible to establish contact by utilizing a flat collector plate and pressing it onto the ends of the electrode collector. However, if this method is used, the ends of the electrode collector must be formed extremely accurately to ensure uniform contact. In practice, it is difficult to ensure sufficient flatness in the ends of the electrode collector to enable uniform contact with the collector plate, and it is very difficult to achieve the required connection in the welded sections without modification.

To ensure sufficient contact between the electrode collector and the collector plate, U-shaped grooves are formed on the plate, as shown in Fig. 5, and it is pressed onto the electrode to make the grooves bite into the ends of the electrode collector (Fig. 6). The relationship between the flatness of the ends of the electrode collector and the depth of the grooves on the sides of the collector plate is the important factor in achieving this connection.



Fig. 5 Collector plate

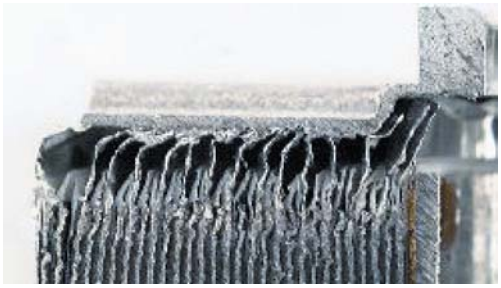


Fig. 6 Detail of welded area on electrical contact points

The accuracy of the formation of the ends of the electrode collector is related to the degree of misalignment in the rolling of the electrode and separators, which constitute it. If there is a large rolling misalignment in the electrode, the positive and negative poles will overlap the separators and the electrode will short itself. If the width of the separators is increased to prevent shorting, the flatness of the ends of the electrode collector is reduced, and the quality of the collector weld connection inevitably declines. Figures of less than 1 mm for deviations in the flatness of the ends of the electrode collector and 1.5 mm for the depth of the U-shaped grooves formed in the collector plate were established as enabling a connection between the plate and the electrode collector (1 mm in width) using a method in which the plates are pressed onto the collector as far as the depth of the grooves.

By positioning weld points at the bottom of the grooves, it was possible to expand the welds from points to surfaces, creating a reliable and low-resistance weld connection. In addition, by making the grooves in the collector plate flat rather than curved, control of variation in the focal point of the YAG laser was achieved, even allowing for some deviation of the welding trajectory from the U-shaped axis, resulting in a consistent weld quality.

Efficient collection is dependent on establishing a sufficient number of collection points at uniform intervals on the electrode collector (collection pitch), but it is difficult to establish collection points at a uniform pitch on a cylindrical rolled electrode. However, by making the grooves on the collector plate radiate out from the center, it is possible to form viable collection points on the inner circumference if the required weld points are ensured at the outermost periphery. Because collection pitch is determined by the number of divisions of the peripheral length, the collection pitch becomes shorter on the inner circumference, and a sufficient connection can be ensured. The relationship between collector connection resistance and weld lines is shown in Fig. 7. Cell resistance reaches a fixed value with three or more weld lines. However, six weld lines have been utilized in the new cells, from considerations of variation in connection quality and to improve safety.

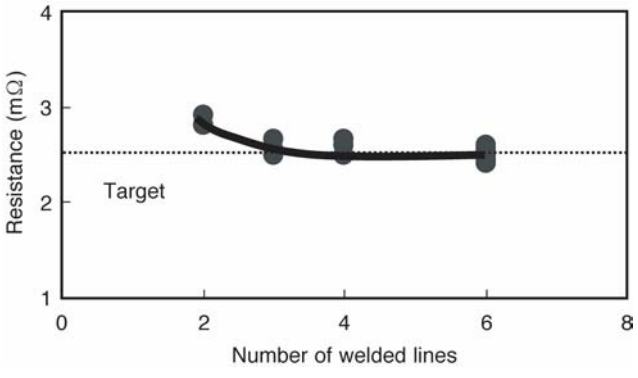


Fig. 7 Relationship between number of welded lines and resistance

5.2.2. Welding in the connector

The operating voltage of the new capacitor necessitated the use of aluminum in the sections in contact with the electrolyte, such as the collector foil and terminals. Brazing and welding (MIG, TIG, spot, YAG, electron beam, etc.) were studied as methods of connecting the aluminum collector foil and collector plates.

The difficulty of controlling the energy of MIG, TIG and spot welding and brazing made it impractical to apply these techniques to welding 40 μm collector foil and collector plates formed from aluminum rolled into thin sheets. While electron beam welding utilizes a high-energy beam, it was not applied because welding must be conducted in a vacuum, making heat dissipation difficult. Production of the new capacitor employs YAG laser welding to generate heat energy on the surface of the collector plate, producing a weld connection with the collector foil.

5.3. Structure of Collector Terminal

A hole is formed in the bottom of the case and case cover of the newly developed cells. The terminal of the collector plates fits over this hole, and a weld connection can be established with the positive and negative poles at the minimum distance. This does away with the need for any structure leading from the collector plate to the outside, and the space required for electrical connection is effectively zero. In addition, because the collector plate is directly exposed and a conducting surface area is therefore guaranteed, this layout is effective in minimizing connection resistance.

5.4. Establishing Collector Width

Reducing the width of the electrode collector enables the distance required for collection to be reduced, increasing the fill density against the internal space available in the case. However, it is not possible to simply reduce the width of the collector in isolation; the width of the separator must be reduced proportionally, which reduces the amount of coverage of the separators on the electrode. As discussed in 5.2.1 (Shape of collector plates), rolling misalignments occur in the separators and the positive and negative poles, and if these misalignments cause the poles to extend beyond the separators, shorting between positive and negative poles will occur. Paying special attention to the accuracy of the formation of the ends of the rolled electrode has enabled the width of the electrode collector to be minimized, resulting in the achievement of an electrode fill density (ratio of electrode width to internal length of case) of 86%.

6. Cell Performance

As Fig. 8 shows, the new capacitor composition and structure discussed in this paper have enabled the achievement of both high specific power density and high specific energy density (Figures shown are based on in-house measurements, and include variations in cell useable voltage).

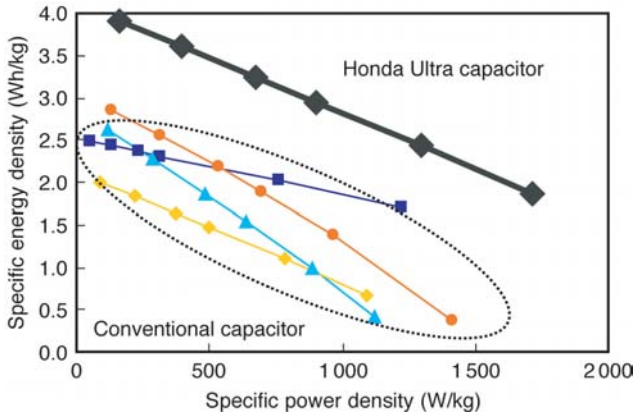


Fig. 8 Ragone plots for conventional capacitors and Honda Ultra capacitor

7. Reliability

7.1. Internal Pressure of the Cell and Reliability

This section will discuss the thinking of the development team with regard to the internal pressure of the cell. The essential structural components of the capacitor are an electrode with positive and negative poles, separators, and an electrolyte. A tightly enclosed space is essential to ensuring adequate performance and durability in a capacitor cell. When the temperature of the cell changes, the various substances sealed in the case (electrode, separators, electrolyte, gases enclosed during production, gases produced in use) expand and contract, causing the internal pressure of the cell to vary. The quality of the weld connections between the case and the cover, the cover and the positive terminal, and the end of the case and the negative terminal are particularly important to ensuring reliability with regard to pressure. The case and case cover have been verified as units to be resistant to pressures of more than 4 MPa and 5 MPa respectively. The welded sections have a margin of mechanical strength, and the strength of the seal is verified during the production process.

The bottom of the cell has been provided with a pressure release valve to guarantee safety when unexpected increases in pressure occur, such as might occur if the cell were thrown into a fire. The pressure resistance of the cell is dependent on the strength of the structural materials in the case and case cover and the strength of the welds. Consideration of the behavior of the valve when opened led to the establishment of the production conditions described below. The maximum internal pressure is determined by the volume of gas produced in the cell until the end of its life and the amount of space initially provided in the cell. Therefore, control of the amount of gas produced in the cell is the key to maintaining internal pressure within a fixed range. To reduce the amount of gas produced in the life of the new cell, impurities have been controlled in the electrode and electrolyte materials and conditions in the production process (temperature and moisture) have been strictly controlled.

7.2. Cell Durability

As Fig. 9 shows, the newly developed capacitor demonstrates excellent durability with little decline in performance in life tests based on hypothetical environmental conditions for actual automotive use. This characteristic is due to the principle of electric double layer capacitor, as described in section 2 of this paper.

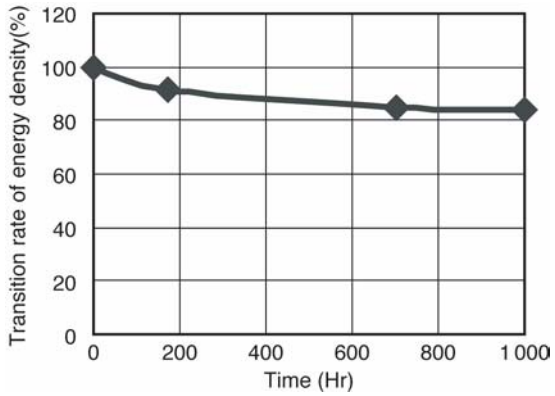


Fig. 9 Life test of Honda Ultra capacitor cell

7.3. Vibration Resistance

Vibration resistance is one of the mechanical characteristics demanded of an automotive energy storage device. During operation of the vehicle, the energy storage device is subjected to amplified and attenuated vibration and shocks, and the load on the unit increases in proportion to its own mass. Sufficient vibration resistance is attained when the device is stably fixed to withstand increased loads, and possesses sufficient resistance to inconsistencies in the mechanical structure (such as issues in electrical conduction or shorting) from occurring. The new capacitors feature collector plates welded onto the electrode collectors. The storage elements are fixed in place by the inner case and the case cover through the intermediary of the welded sections of the electrode collector and the collector plates. The load on these connections is hypothesized as the total mass of the electrolyte and electrode elements multiplied by the acceleration occurring in the holding structures.

The capacitor cells were subjected to vibration tests to verify the mechanical strength of the connection structure. Acceleration settings in vibration tests vary according to the type of vehicle and position of installation of the unit. In the tests of the new cell, the cells were subjected to accelerations in excess of twice those actually measured in the position in which the unit is installed in the FCX. No change in resistance or capacitance was recorded after the tests, verifying the applicability of the cell structure to automotive use.

8. Summary

The development project for the capacitor cell for the Honda FCX established the achievement of low resistance and high energy as its aims. Optimization of the collector structure and the method of connection with the terminals have resulted in the achievement of an internal collector connection resistance of less than 0.05 mΩ and an electrode fill density of 86%.

Individually, the capacitor cells demonstrate the highest specific power density (1,500 W/kg) and specific energy density (3.9 Wh/kg) known to date.

9. Conclusion

The newly developed capacitor cells were installed in the FCX, which has already been produced for the market. Using the new low resistance internal cell structure and electrode fill density design as a base, future development will attempt to respond to demands for increased capacitance, and expand the potential range of application of the cell as an energy storage device to a greater number of vehicles.

In conclusion, the authors would like to express their sincere thanks to the many individuals, in Honda and other companies, who generously offered their assistance during the course of the development project.

References

(1) Ochiai, S., Uchibori, K., Hara, K., Tsurumi, T., Suzuki, M.: Development of the Motor Assist System for a Hybrid Car – INSIGHT, HONDA R&D Technical Review, Vol. 12, No. 1, p. 7-14 (2000)

(2) Ohzono, K., Kayano, M.: Development of High Power Energy Storage for the CIVIC Hybrid, HONDA R&D Technical Review, Vol. 14, No. 2, p. 31-36 (2002)

■ Authors ■


Naohiko OKI


Kenji MATSUMOTO


Kenji SATO


Mitsuru IKEO


Yasuhiro MATSUMOTO


Naoyuki ABE

Development of Activated Carbon Electrode for Advanced Electric Double-layer Capacitor

Manabu IWAIDA* Shigeki OYAMA*
Kenichi MURAKAMI* Eisuke KOMAZAWA*

ABSTRACT

An electrode has been developed for the electric double-layer capacitor utilized in the Honda FCX fuel cell vehicle. Control of the property of the pores of the activated carbon, which is the main material, and efforts to increase electrode density have enabled the achievement of a capacitance per unit volume of 17.6 F/cm^3, while optimization of the electric conductive adhesive has resulted in a surface resistivity of 6.7 Ω·cm^2. Excellent durability has been achieved by controlling residual organic impurities in the production process. As a result, the capacitor cell in which the electrode is utilized has a capacitance of 1350 F and an internal resistance of 2.5 mΩ, is highly durable, and was judged suitable for use in the Honda FCX.

1. Introduction

The Honda FCX fuel cell vehicle (referred to as the FCX hereafter), which was first commercially introduced in December 2002, employs an electric double-layer capacitor used as an energy storage device (referred to as the capacitor hereafter). The capacitor has characteristics different from a conventional secondary battery, and in combination with the fuel cell vehicle, much is expected of these new technologies, looking towards the future.

Unlike a secondary battery that involves an electrochemical reaction during charge and discharge, the charge and discharge of a capacitor are carried out through electron movement due to physical absorption of the ions (Fig. 1). Therefore, the capacitor shows superior characteristics in high rate input and output, which is often restricted with a secondary battery, and in charge-discharge cycle life. However, at the same time, capacitor cells on the market (referred to as cells hereafter) are usually small cells of approximately a few F to tens of F. Cells exceeding 1000 F, such as those used in this development project, are still in the prototype stage. Furthermore, because specific capacitance and specific power are low in these cells, their larger size and increased weight would be unavoidable. These cells are not feasible as the energy storage device for the FCX. This paper reports on the development of an electrode material for a capacitor that achieves both high capacitance and low resistance, for use in the FCX, and on the development of its manufacturing process.

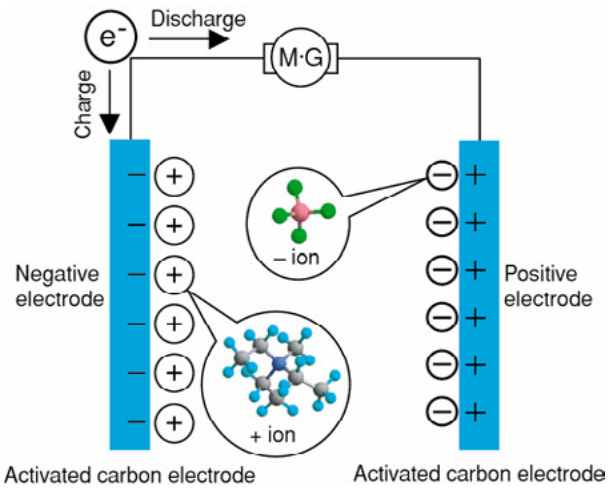


Fig. 1 Model of capacitor

* Wako Research Center

2. Electrode for Capacitor and its Manufacturing Process

2.1. Electrode for Capacitor

The electrode used in the capacitor is mainly composed of activated carbon formed into electric double layers. In addition, conductive admixture was included to improve electrical conductivity, and a binder material was included to maintain the shape (Fig. 2). The electrode is formed in a sheet shape, and attached to the surface of the aluminum foil current collector by an electric conductive adhesive, creating the electrode (Fig. 3). As is clear from the operation principles outlined above, the capacitor uses the same electrode for the positive and negative poles. This means that it is not necessary to separately manufacture the positive and negative poles, like with a secondary battery, and so is of great benefit in terms of cost and quality control.

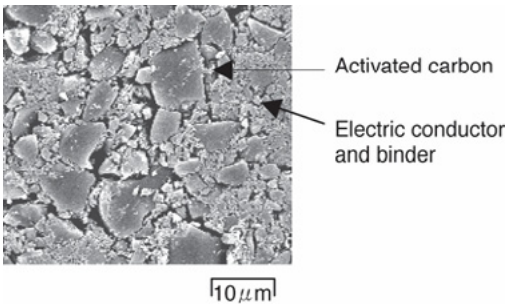


Fig. 2 SEM image of sheet electrode

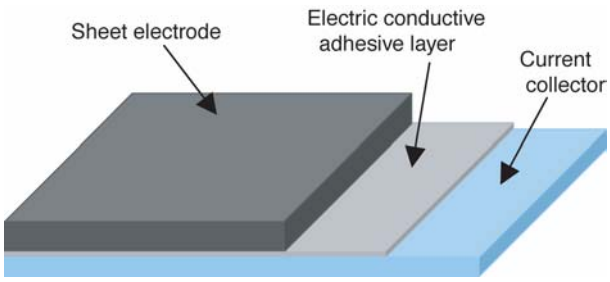


Fig. 3 Structure of electrode

2.2. Electrode Forming Process

Figure 4 shows the electrode forming process in this development process (calender casting method). The details of the process shown in this figure are given below.

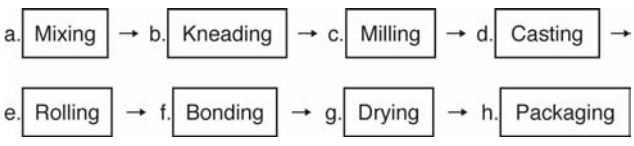


Fig. 4 Production process of electrode for electric double-layer capacitor

(a) Mixing of the raw materials (activated carbon, PTFE binder, conductive admixture)
(b) Pressing and kneading of the mixture, causing fibrillation of the PTFE binder
(c) Crushing, grinding, and milling of the kneaded matter
(d) Adding an organic solvent (referred to as solvent hereafter) to the milled material obtained in step c, and processing into the primary sheet, using a calender casting machine
(e) Rolling the primary sheet, and processing into a sheet electrode of the specified thickness
(f) Bonding the sheet electrode and the current collector to each other using an electric conductive adhesive
(g) Drying, to remove the solvent and water from the electrode
(h) Packaging the product hermetically after drying

Known methods of electrode forming include the doctor blade method, which makes a slurry of the raw materials mixture and coats it, and the extrusion molding method. In making a capacitor with high-capacity, which was one goal of this development project, calender casting was adopted because high-density electrodes can be expected, and because the amount of solvent added can be kept to a minimum.

The features of this manufacturing method are summarized below.

(1) The amount of solvent used in forming is small, and so the burden of removing it is small.
(2) There is plenty of freedom in material combination ratios, and it is possible to raise the amount of the activated carbon, which is the polarizable electrode material.
(3) There is good control of the electrode density.
(4) There is good flexibility in changing the electrode thickness dimensions.

In particular, the solvent noted in (1) changes the liquidity during kneading and rolling, and affects the fibrillation of the PTFE binder, which is a binding component. If this fibrillation is not sufficiently carried out, there is a drop in electrode density and a drop in electrode strength, which may cause poor handling. In addition, because the solvent is absorbed by the activated carbon, it can easily remain inside the electrode, and may cause secondary products due to oxidation and thermal denaturation during the removal process. These materials are dissolved during capacitor operation and cause deterioration.

In this development project, in addition to the goals of high capacity and low resistance, a major focus was to create an electrode manufacturing process that actualizes an electrode with superior durability.

2.3. Development Goals

2.3.1. Capacitor cell performance targets

Characteristics required of an energy storage device for the FCX are high energy storage, high output power, and good durability. In order to actualize high energy storage, the target for the cell was a capacitance of 1300 F or more. In addition, to obtain high output power, an internal resistance of the cell of no more than 3.0 mΩ was the target.

To achieve these targets, the goals for the electrode were as given in the next section.

2.3.2. Electrode performance targets

Performance targets for the electrode were set as follows.

(1) Capacitance per electrode volume (referred to as specific capacitance hereafter): 16.9 F/cm^3 or more
(2) Surface resistivity (referred to as resistivity): 8 $\Omega \cdot cm^2$ or less
(3) Durability: same as vehicle life, or longer

3. Electrode Development Concept

The electrode development concept was determined as follows, in light of the targets (1) through (3) above.

(1) Improve specific capacitance: Optimization of electrode material, and improvement of electrode density.
(2) Reduce resistivity: Optimization of electrode material, collector material, and electric conductive adhesive.
(3) Improve durability: Reduction of the amount of impurities remaining in the electrode.

In addition, emphasis was also placed on stability of the quality of the electrode, and full consideration was given to optimization of the manufacturing process.

4. Tackling Performance Improvements

4.1. High Energy Storage

4.1.1. Selection of polarizable electrode material (activated carbon)

Generally, the material of polarizable electrode is a porous carbon, such as activated carbon fiber or activated carbon powder, as shown in Fig. 5. In the development of a high capacity cell, it is necessary to raise the specific capacitance of the electrode, and therefore high electrode density is required of the electrode.

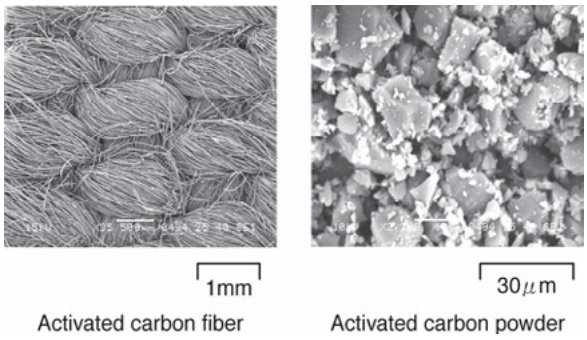


Fig. 5 SEM images of activated carbons

Activated carbon fiber is available as cloth or in a paper form, and it has the benefit of being, in itself, an electrode structure, simplifying the electrode manufacturing processing. However, in terms of its character as a fiber, charging efficiency is low, and it is not possible to expect improvements in electrode density or in specific capacitance. In contrast, it is possible to improve electrode density using activated carbon powder, by controlling grain size and through the electrode forming process. For these reasons, activated carbon powder was adopted for this development project.

Activated carbon powder can be based on natural materials such as coal or coconut shells, etc., or can be based on a synthetic material, such as resin. It is then steam activated. The former is better in terms of cost, but variations in physical properties or residual impurities between manufacturing locations or raw material lots can easily occur. In contrast, the latter is at a slight disadvantage in terms of cost because it is a material chemically synthesized, but in comparison with those based on natural materials, its physical properties are stable and it is superior in terms of control of impurities, making it possible to achieve high specific capacitance.

Figure 6 shows a comparison of specific capacitance of various common activated carbons. Among these, this development project focused on synthetic activated carbon, and in particular on activated carbon powder that uses phenol resin giving high specific capacitance. Studies were made of its application as a capacitor electrode material.

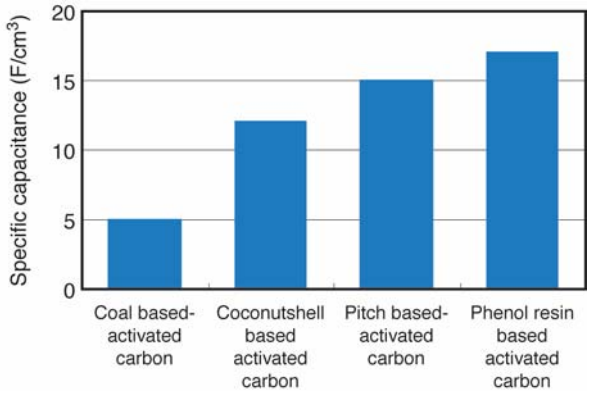


Fig. 6 Specific capacitance of activated carbons

4.1.2. Improvements in specific capacitance

(1) Physical Properties of Activated Carbon

To improve specific capacitance, it is necessary to balance the physical properties of the activated carbon and the electrode forming process. Generally, the physical properties of activated carbon change according to the physical properties of the raw material carbon and according to the steam activation process conditions in the manufacturing process. In particular, the pore forming state not only affects the electrode density incorporating the bulk density of the activated carbon itself, but it also has a close relationship with the specific capacitance and resistivity. In this development project, it was confirmed that the benzene absorption ratio as specified in JIS K1474 is effective as a parameter indicating pore-forming state. With this method, by measuring the benzene vapor absorption ratio against the activated carbon weight, it is possible to specify the raw material's physical properties with higher precision compared to parameters such as specific surface area and pore volume.

Figure 7 shows the relationship between the material's benzene absorption ratio and its specific capacitance. As the material's pore forming progresses, its benzene absorption ratio rises. As this happens, the specific capacitance also changes, becoming largest at 57% and 17.6 F/cm^3. At 59% or more, there is a tendency for the specific capacitance to drop due to excessive pore formation.

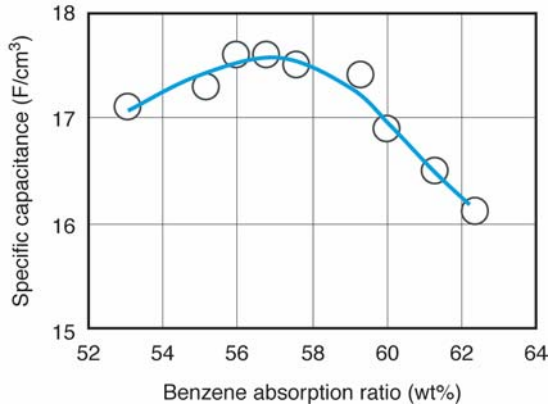


Fig. 7 Relationship between benzene absorption ratio and specific capacitance

(2) Electrode Manufacturing Process

In considering the electrode manufacturing process using this activated carbon, a study was made to raise the electrode density. A solvent is used in this process, to improve formability. A solvent with a low boiling point was used, to reduce the burden of the later elimination process. The solvent is added during (a) mixing, (b) kneading, and (d) the primary sheet forming process using a calender caster (referred to as the calender process hereafter). Among these processes, the most amount of solvent is added in the calender process. Therefore, a study was made of the amount added in this process, and the electrode's physical properties.

In the calender process, the solvent is mixed with the kneaded grain, and machined into a sheet. At this time, the solvent is impregnated with the crushed material, and bonds with the crushed material, improving liquidity. This makes it possible to raise the sheet electrode's density and strength, and also stabilize formability.

Figure 8 shows the relationship between the ratio of solvent added to crushed material weight and the density of the sheet electrode. Figure 9 shows the relationship between the solvent ratio and the tensile strength of the sheet electrode. There is little change in density against the amount of solvent added, but when there is little solvent added there is a tendency for the dispersion to be larger. Concerning tensile strength, too, there is a drop in strength when the additive ratio drops, and there is a tendency for worsening of handling. When the additive ratio exceeds 90 wt%, redundant solvent destroys the shape of the crushed material, causing not only a worsening of formability but also a worsening of mold-releasing from the calender roller. This often leads to forming deviations such as breaking or tearing of the primary sheet. From these results, the solvent additive ratio during the calender process was set at 90 wt% to achieve maximum density and tensile strength.

With this amount of additive, a sheet electrode was manufactured using the actual forming machine, with the set thickness of 150 μm and a length of 150 m. The results of thickness measurements are shown in Fig. 10. Forming deviations during production did not occur, the median thickness was 150 μm, and variation had a standard deviation of $\sigma = 0.18$. The sheet electrode's density was 0.65 g/cm^3, and the standard deviation was $\sigma = 0.0029$.

From these studies, stable and continuous manufacturing was actualized, maintaining a thickness precision of ±5 μm, in a state with high sheet electrode density.

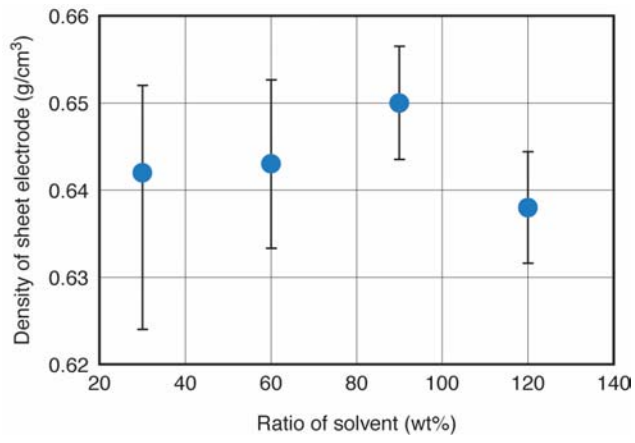


Fig. 8 Sheet electrode density with amount of solvent added

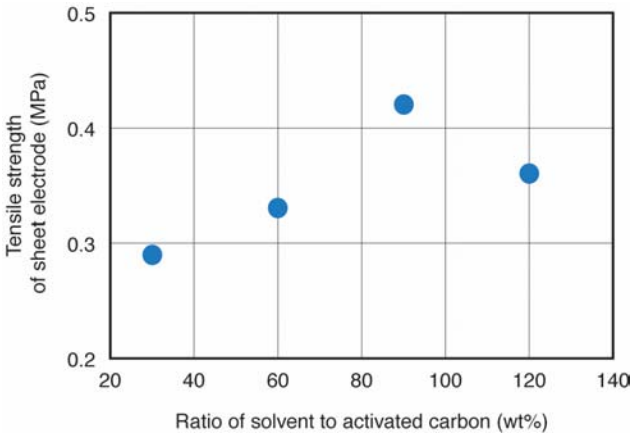


Fig. 9 Tensile strength of sheet electrode with amount of solvent added

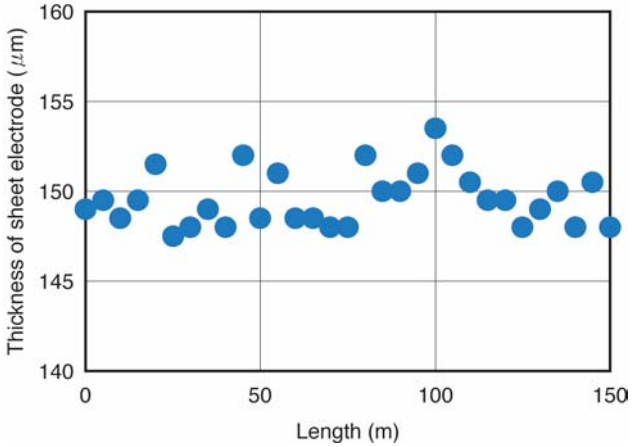


Fig. 10 Thickness distribution of sheet electrode

4.2. High Output Power

4.2.1. Activated carbon's physical properties and internal resistance of capacitor cell

Figure 11 shows the relationship between benzene absorption ratio and surface resistivity. In the range of low benzene absorption, that is to say, the range where pore development is insufficient, there is a rise in resistivity due to inhibition in electrolyte diffusion. Specifically, there is a marked tendency towards this at 55% or less. From the above results, the benzene absorption ratio was stipulated to be between 55.5% and 58% – that being the activated carbon physical property range necessary for specific maximum capacitance and minimum resistivity.

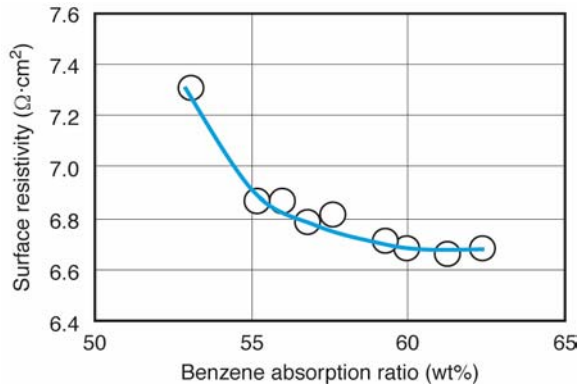


Fig. 11 Relationship between benzene absorption ratio and surface resistivity

4.2.2. Development of an electric conductive adhesive

An electric conductive adhesive is used in the process bonding the sheet electrode and current collector. Generally, a solution of a highly conductive component and an adhesive component distributed in a solvent is used as an electric conductive adhesive. When applied to a capacitor, a mixture of graphite powder and amorphous carbon powder (referred to as carbon black hereafter) is generally used as the conductive admixture, from the point of view of stability and minimization of electrochemical reactions. As for the adhesive component, materials such as those from the poly-imide-amide, silica sol, and polyvinyl alcohol (PVA) groups are used. Table 1 gives a comparison of various adhesive components.

Table 1 Characteristics of adhesive components

Adhesive component	Solvent	Electrolyte resistance	Features
Poly-Imide-amide	N-methyl pyrolidone	Good	· High adhesive strength · Difficulty of solvent removal · Low durability
Silica sol	water	Good	· Fragile and easy to peel with bending
PVA	water	Good	· Good flexibility · Easy to reduce residual solvent

In terms of adhesion strength, the poly-imide-amides are superior, but giving full consideration to the issue of solvent recovery during manufacturing and to the effect of residue on capacitor performance, a PVA and water solvent adhesive was adopted.

Next, the conductive admixture was optimized, with the purpose of reducing resistance between the sheet electrode and the current collector.

For the conductive admixture, the aforementioned graphite and carbon black were used. The surface of the current collector surface shown in Fig. 12 has indentations and protrusions (pits) of 1 to 10 μm. In order that the conductive admixture sufficiently permeates these pits, the diameter of the graphite grain, which forms scaly particles, was set as 3 μm maximum. In addition, the carbon black grain diameter was set as 0.2 μm or less. The adhesive layer after the sheet electrode has been attached reaches the state shown in Fig. 13 and the carbon black fills in the pits and between the graphite particles. In this state the graphite forms the macro conductive path and reduces the resistance of the adhesive layer itself. On the other hand, the carbon black

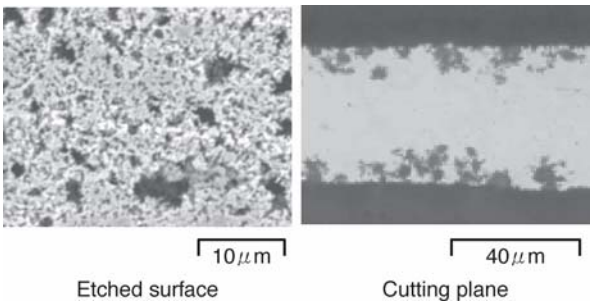


Fig. 12 SEM images of current collector

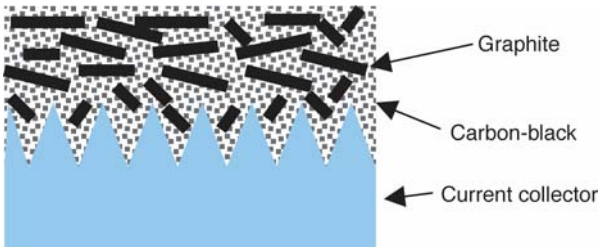


Fig. 13 Image of adhesive layer

serves the function of maintaining conductivity in the space of the graphite particles and with the current collector. Accordingly, the mixture proportions of these two types of carbon material greatly affect contact resistance between the sheet electrode and the current collector.

Figure 14 shows the relationship between the graphite and carbon black weight ratios and the surface resistivity. From these results, it is clear that resistivity is at its smallest when the weight ratio is 1:1. In the range where graphite is rich, conductivity in the space of the graphite particles is insufficient, and resistivity increases. In the range where carbon black is rich, resistivity increases because the macro conductivity paths are insufficient.

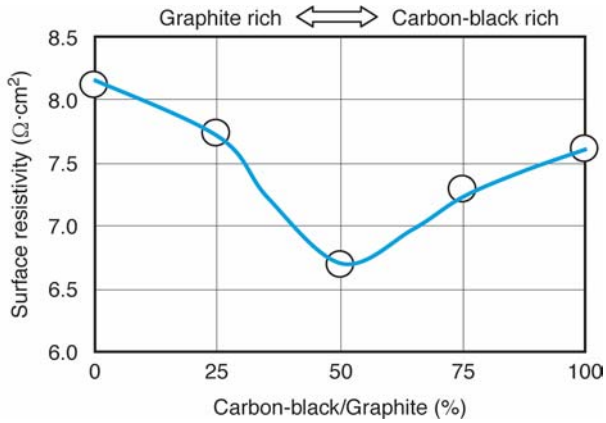


Fig. 14 Effect of carbon-black/graphite composition on surface resistivity behavior

4.3. Durability Improvements

4.3.1. Removal of organic residue inside the electrode

Solvents used during forming, organic matter and water absorbed in the manufacturing process are all causes of performance deterioration during capacitor operation. In order to effectively remove these impurities, drying processes were studied. It is necessary to dry the electrode at no more than 160 °C, due to heat resistance constraints of the electric conductive adhesive and the sheet electrode. A possible method for efficient drying in this temperature range is vacuum drying. In this drying process, the long electrode made by bonding current collector and sheet electrode is rolled up and placed inside a drying oven. Then, the air is removed to create a vacuum and the temperature inside is raised to dry. Placing the whole roll in the vacuum drying oven means that it is batch processing, making it easy to put in airtight packaging after removing it from the oven after drying. This has the advantage of reducing the chance of later

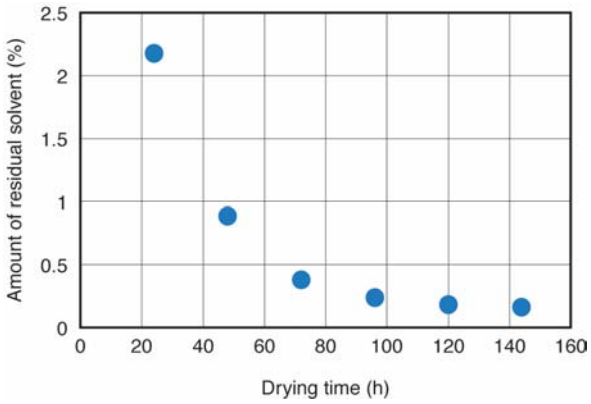


Fig. 15 Relationship between drying time and amount of residual solvent

water absorption or of re-absorption of organic material in outside air. However, it is easy for the temperature inside the vacuum to lose its uniformity, and so it is necessary to establish a sufficient isothermal heating period.

Figure 15 shows vacuum drying time and amount of residual solvent (with the value before drying being 100).

A gas chromatograph was used in quantifying the solvent. A part of the electrode was filled in the test tube of the thermal desorption apparatus, heat was applied while helium gas flowed, and vaporized components were collected in an interior trap. Those components were introduced into the gas chromatograph. The detector uses FID, the quantity is provisionally calibrated from pentene strength, assuming that FID strength is in proportion to the carbon count. Peak qualitative analysis was carried out using mass spectrometry.

From Fig. 15 it is clear that the longer the drying time, the more solvent is removed. However, at the point when vacuum drying is complete, it was confirmed that there were organic impurities, from solvent reactions. These impurities are thought to be organic matter that occur due to oxidation or dehydrate condensation of solvent, which is absorbed or remaining in the pores of the activated carbon. That is to say, when drying is carried out in a rolled state where the concentration of residual solvent is high, impurities are generated secondarily. Accordingly, it is necessary to carry out vacuum drying in the rolled state after the concentration of solvent has been reduced to a certain extent. In order to resolve this issue, prior to vacuum drying in the rolled state, preliminary drying is carried out when the long electrode is still flat. Using this method, the solvent is removed in an open condition.

This has made it possible to reduce the residual solvent and its reaction material, the organic impurities, by 20%.

4.3.2. Control of metallic impurities in the electrode

There are some cases where minute amounts of metal are in the electrode, brought in by the raw material (particularly the activated carbon) or due to contamination during the manufacturing process.

Among these metals, it is known that oxidation-reduction material within the capacitor operation potentially ionizes from the positive electrode, and deposits on the negative electrode. This deposited metal grows on the cathode in the dendrite state, and in the end, penetrates the separator and destroys electrical insulation between the poles. Accordingly, it is necessary to control the raw material manufacturing process and to confirm its content. It is also necessary to avoid metal contamination during the electrode manufacturing process.

5. Confirmation of Electrode Performance

An electrode, produced under the aforementioned conditions, is shown in Fig. 16. When evaluating this electrode, performance such as shown in Table 2 was obtained.

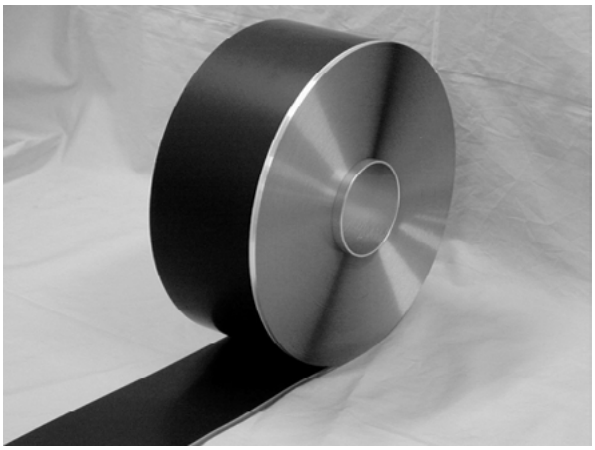


Fig. 16 Electrode coil

Table 2 Electrode performance

Item	Achieved value
Specific capacitance	17.6F/cm^3
Surface resistivity	6.7Ω·cm^2 (per single electrode)

In addition, it was possible to achieve the quality shown in Table 3 as sheet electrode, and continuous production with stable quality was made possible.

Table 3 Sheet electrode quality

Item	Achieved value
Thickness accuracy of sheet electrode	±5μm (σ=0.18)
Density accuracy of sheet electrode	±0.01g/cm^3 (σ=0.0029)

6. Confirmation of Capacitor Cell Performance

When cells were produced using this electrode, performance as shown in Table 4 was obtained.

Table 4 Capacitor performance

Item	Achieved value
Capacitance	1350F
Resistance	2.5mΩ
Durability	longer than FCX life

By improving electrode performance and quality, and by reducing organic impurities, it is possible to manufacture a high output power, high energy storage, high durability cell that can be used in the FCX.

7. Summary

As an energy storage device for the FCX, an electrode was developed for use in a capacitor making possible the actualization of high output power and high energy storage. The results of this project are summarized below.

(1) By controlling the pores of the activated carbon, which is the major material of the electrode, and by improving electrode density, a specific capacitance per electrode volume of 17.6 F/cm^3 was achieved.

(2) By optimizing the electric conductive adhesive composition, surface resistivity of 6.7 $\Omega \cdot cm^2$ was achieved. Full consideration was given to the environment, with the use of a water-based solvent.

(3) By minimizing the residual organic impurities, which affect capacitor durability, in the electrode manufacturing process, an electrode was actualized that surpasses the durability required of an actual vehicle.

(4) A process was established that makes it possible to continuously manufacture large, 1000 F cell grade electrode, with stable quality.

Thanks to these measures, a capacitor cell with a capacitance of 1350 F and an internal resistance of 2.5 mΩ was achieved, making possible the manufacture of a cell with excellent durability, which can be used for the Honda FCX fuel cell vehicle.

8. Acknowledgements

The authors would like to take this opportunity to thank many people, both in Honda and beyond, who gave their support and cooperation in this development project.

■ Authors ■


Manabu IWAIDA


Shigeki OYAMA


Kenichi MURAKAMI


Eisuke KOMAZAWA

Development of Seal Technology for Electric Double-layer Capacitor Covers Using Aluminum-Resin Insert Mold Process

Masato KOMATSUKI* Kazuaki IGARASHI**
Toru OTA* Norifumi YASUDA*

ABSTRACT

Electric double-layer capacitor covers are required to seal in organic liquid electrolyte, to isolate positive and negative electrodes, and to maintain pressure tightness. An insert mold process using chemically combined aluminum and resin and a rib to prevent resin shrinkage have been developed to enable these requirements to be met. In this process aluminum and resin are bonded by insert molding after triazinedithiol electrocoating of the aluminum surface. Optimization of the formation of the triazinedithiol coat and insert mold conditions and the establishment of a rib between the aluminum and resin have enabled the production of covers which satisfy the requirements enumerated above after acceleration tests based on actual use conditions. The long-term sealing performance of the new covers has also been verified.

1. Introduction

The Honda FCX fuel cell vehicle, which was first commercially produced in December 2002, employs an electric double layer capacitor module as an energy storage system. Because the functioning of the capacitors does not involve a chemical reaction, they display higher power output and superior durability towards repeated charge and discharge than batteries. Together with the fuel cell utilized in the FCX, the new capacitors represent a clean energy technology with considerable future potential. The case cover employed in the capacitors was required for reliability against the leakage of electrolyte, for the maintenance of internal pressure of the cells, and for the ability to maintain electrical insulation of the positive and negative electrodes.

The insulating and sealing functions of the case cover are vital to ensuring the reliability of the capacitor cell. This paper will discuss the world's first application of insert molding to a capacitor case cover, and describe the methods used to verify the reliability of the new cells.

* Wako Research Center
** Tochigi R&D Center

2. Development Concept

2.1. Factors Affecting Reliability

The design concept for the capacitor to be employed in the FCX specified a cylindrical shape. The continuing reliability of the seals over long-term use represented another requirement.

Among normal round case covers, aluminum electrolytic condenser covers offered a potential design precedent, but because their structure allows the entry and escape of air, they cannot be used to seal a capacitor employing an extremely osmotic electrolyte.

The following factors were therefore established as being essential to reliability, and the capacitor case cover was developed with a strong focus on long-term reliability:

(1) Ability to seal a highly osmotic electrolyte
(2) Ability to insulate positive and negative electrodes
(3) Sufficient strength to resist increases in the internal pressure of the cell

2.2. Concepts Established for Structure and Materials

Figure 1 shows a perspective view of the capacitor case cover. (1) shows the case cover in the developmental stage, while the cover actually employed in the FCX capacitors is seen in (2). As Fig. 1 demonstrates, the shape of the covers is different, but the concept behind them is the same, in that the outer circumference represents the negative electrode and the center terminal the positive electrode. Aluminum is used for both the outer circumference and the center terminal, with resin employed as an insulating material between them. The outer circumference forming the negative electrode is welded to the cylindrical case, and the terminal representing the positive electrode is welded to the electrode collector plate. This configuration led to the selection of high-purity and high-strength A3003-H112 as the material, to enable both welding and screw-in mounting to be employed. It was essential for the resin to possess high strength in addition to insulating the positive and negative electrodes. The thermoplastic resin polyphenylene sulfide (PPS) was therefore selected, from considerations of heat resistance to enable high-temperature curing in the production process, to remove impurities from the electrode, resistance to organic liquid electrolytes, the ability to form compounds with triazinedithiol (as discussed in section 3), and recyclability. Glass fiber and calcium carbonate is added to the PPS in quantities optimized to coordinate its coefficient of linear thermal expansion with that of aluminum. This reduces the thermal expansion differential of the material with aluminum, even under the rapid heating of welding, ensuring that shearing stress is not generated at the interface of the bonded aluminum and resin, and thus preventing the strength of the bond from declining.

Another reason for mixing glass fiber with the PPS is to increase the material's breaking strength. Glass fiber is anisotropic with regard to contraction after formation, with low contraction in the direction of orientation of the fibers and high contraction in the non-orientation direction. Because formation of the case cover involves injecting resin through three gates, as shown in Fig. 2 (1), glass fiber tends to become oriented around the circumference. Therefore, there is a large post-formation radial contraction, generating shearing forces at the interface of the aluminum and resin, which cause the bond to break down. Once the bond has commenced breaking down, the release of residual stress continues to progress, forming paths through which the electrolyte can leak. To prevent this, 1 mm high ribs are positioned on the positive and negative electrodes to function as resin stoppers and prevent contraction of the resin, as shown in Fig. 2 (2). This reduces post-formation residual stress to zero, ensuring long-term reliability. The presence or absence of the ribs significantly affected the results of the acceleration tests discussed in section 5.

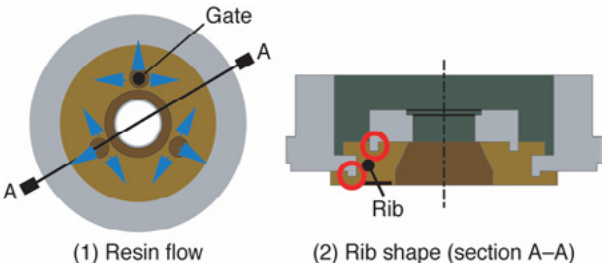


Fig. 2 Resin flow and rib shape

3. Process Concept and Characteristics

3.1. Conventional Resin Insert Molding

In the conventional resin insert molding process, resin is poured into a metal mold after insertion of the aluminum parts, and contraction of the resin forms a physical bond between the aluminum and the resin.

3.2. Concept behind New Process

The newly developed production process is divided into

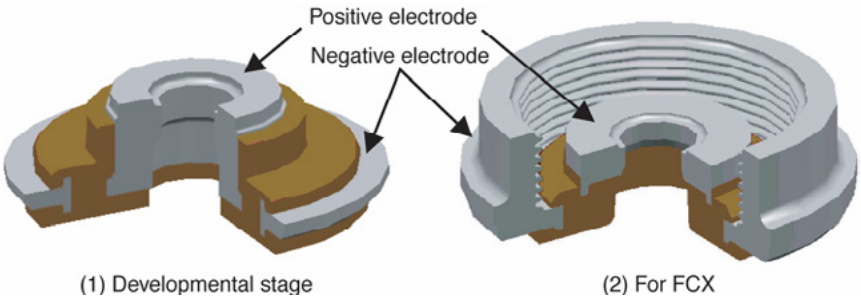


Fig. 1 Perspective view of cover

three stages: Cutting of the aluminum parts to be inserted in the mold, a surface treatment process in which triazinedithiol is electrodeposited to create a chemical bond between the aluminum and the resin, and the molding process, in which the resin is injected into the mold, producing the finished case cover. Figure 3 illustrates the difference between this process and the conventional process. The innovation in the new process is the addition of surface treatment (triazinedithiol treatment).

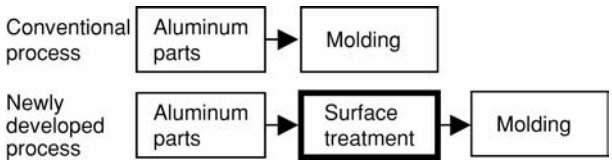


Fig. 3 Comparison of insert mold processes

3.2.1. Cutting

The aluminum employed in the outer circumference of the case cover and the terminals is conventionally rolled and cast, after which it is cut to the required dimensions. The change in dimensions during etching in the surface treatment process and the changes occurring due to contraction in the forming process must be taken into consideration in this initial process.

3.2.2. Surface treatment

To activate the aluminum surface, it is neutralized with acid after alkali etching. It is then subjected to triazinedithiol electrocoating treatment (organic coating), after which drying under reduced pressure represents the final stage of the process (Fig. 4).

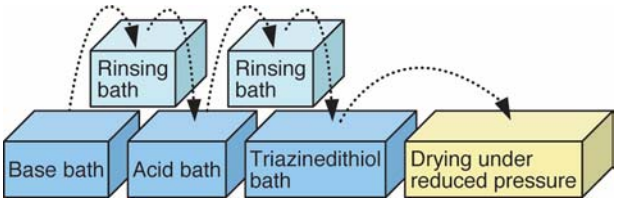


Fig. 4 Treatment process

In the electrocoating process, a film of approximately 150–250 nm is formed by bonding of the triazinedithiol with the positively charged side of the aluminum and the formation of bonds between triazinedithiol molecules, as shown in Fig. 5[(1)].

3.2.3. Molding

Having undergone surface treatment, in the forming process the aluminum parts are inserted into a metal mold into which PPS is then injected. The sulfur and R components in the triazinedithiol chemically bond with the sulfur in the PPS, forming a seal at the interface of the aluminum and the resin and unifying the outer circumference, resin and terminals.

The adhesive strength of the formed product varies greatly with conditions during production. The factors affecting the adhesive strength are the ease of chemical bonding between the functional groups in the film and the PPS, and the soundness of the weld at the interface of the melted PPS. The ease of chemical bonding is increased by raising the temperature, and increased pressure guarantees the soundness of the resin. However, if the temperature of the mold is increased too much, expansion of the aluminum causes galling with the mold, and too great an increase in the internal pressure of the mold causes deformation of the aluminum parts. Optimization of the conditions has enabled a balance to be maintained in the molding process.

3.3. Analysis of the Film during Triazinedithiol Treatment

It has conventionally been difficult to observe the condition of the film without damaging it. In this project, the following method was used to examine the condition and thickness of the film:

First, after coating with platinum to prevent surface damage to the film, test cross-sections were irradiated by a gallium ion beam (focusing ion beam: FIB). They were then observed using a field emission scanning electron microscope (FE-SEM). Results showed that uniform triazinedithiol layers of approximately 200 nm with no pinhole imperfections had been formed on the aluminum (Fig. 6).

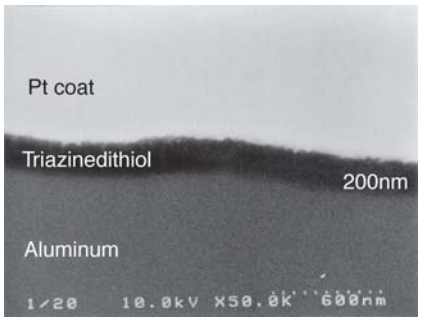


Fig. 6 Cross-section of aluminum and triazinedithiol layer

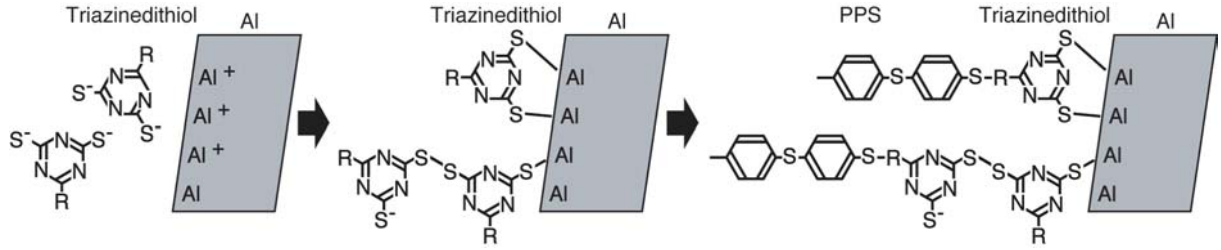


Fig. 5 Sealing mechanism aluminum-triazinedithiol-resin

3.4. Characteristics of the New Process

The high adhesive strength ensured by the firm chemical bond between the aluminum and resin achieved in this process is highly durable towards increases in internal pressure, which may be caused by changes in temperature, etc., during operation of the cell. A reliable seal is formed, ensuring insulation and preventing shorting caused by leakage of the extremely osmotic electrolyte.

Another advantage of the new production process is that the use of insert molding means that there is little restriction on the shapes that can be formed.

3.4.1. Film specifications

As Fig. 7 shows, film thickness increases with treatment time. A stable film is formed after a specific period of time, enabling the establishment of a treatment time guaranteeing the viability of the film.

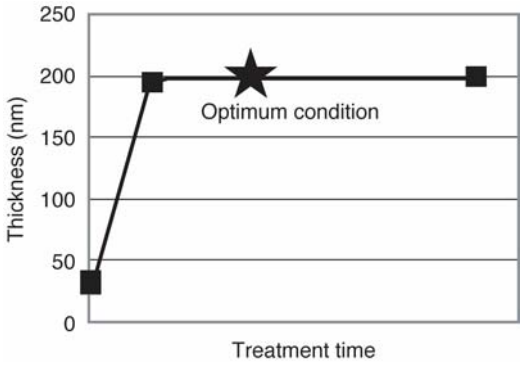


Fig. 7 Thickness of triazinedithiol coating

There is a great deal of aluminum and oxygen in the film that is formed, and traces of sulfur and carbon of triazinedithiol have also been detected (Fig. 8).

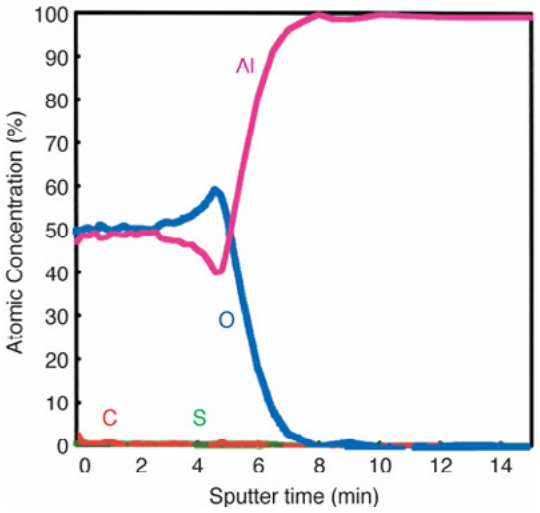


Fig. 8 AES analysis of triazinedithiol coat

3.4.2. Base conditions for molding

Conditions for molding were optimized as shown in Fig. 9, to prevent galling or deformation of the aluminum parts and produce high adhesive strength. Figure 10 shows a cross-section of a case cover formed under these conditions. It is clear that a reliable bond has been formed between the aluminum parts and the resin.

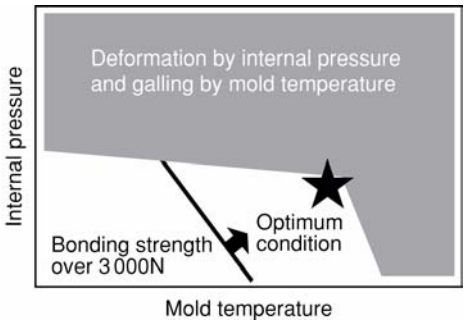


Fig. 9 Insert mold condition



Fig. 10 Cut section of cover

4. Verifying the Quality of the Seal

4.1. Concepts behind Verification

4.1.1. Chemical verification

According to Arrhenius' principle (Eq. 1), the speed of a simple reaction is normally dependent on temperature. If the temperature increases 10 K, the reaction speed doubles.

$$k = A \exp(-Ea / RT) \quad (1)$$

k : Reaction speed
A : Frequency factor
Ea: Activation energy
R : Gas constant
T : Absolute temperature

To determine whether the degradation of the strength of the new case cover obeyed Arrhenius' principle, units were immersed in electrolyte liquid at different temperatures, and the time taken for a 20% decline in adhesive strength to occur was plotted. The results of these tests are shown in Fig. 11, and verify that the strength of adhesion in the case cover degrades in accordance with Arrhenius' principle. High-temperature acceleration tests were conducted on the basis of these results to determine whether the functional life of the cover would satisfy automotive requirements and no malfunctioning of the seal was demonstrated. The quality of the seal remained excellent even under acceleration tests corresponding to 1.5 times the life of the vehicle.

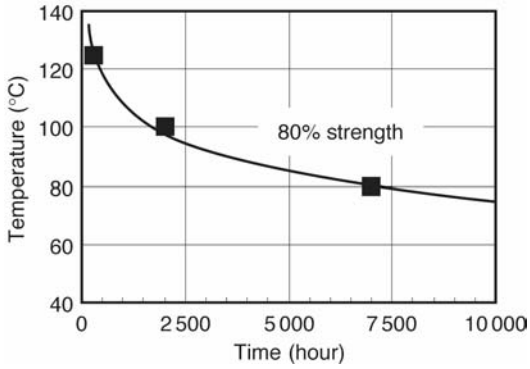


Fig. 11 Degradation of bond strength

4.1.2. Mechanical verification

The conditions established for mechanical verification of seal quality are that the seal should show no change after thermal shock or vibration. Thermal shock characteristics were measured by putting a case cover through the thermal cycle shown in Fig. 12 1,000 times. To test characteristics under vibration, test equipment was used to subject the covers to prescribed levels of vibration. The seal demonstrated no change in quality after either of these tests.

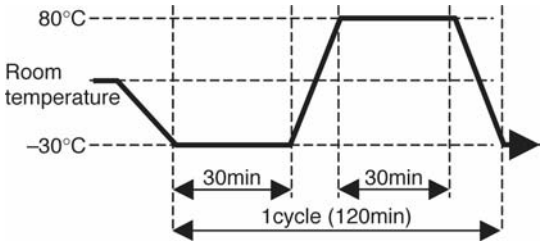


Fig. 12 Thermal shock test cycle diagram

4.2. Quality Inspection

One major issue in the production process is to ensure that the seals that allow electrolyte to leak do not get through the system. Three tests are used to inspect quality during production: Measurement of the infrared spectrum to analyze the components of the film after surface treatment, ultrasonic inspection to enable non-damaging inspection of the adhesion, and pressure inspection to check seal quality and pressure resistance.

After completion of surface treatment of the aluminum parts, the infrared spectrum is measured using a Fourier transform infrared spectrophotometer. The absorbance of the triazinedithiol is measured in the 1,125 cm^{-1} absorption band, enabling confirmation that the film has been formed according to specifications.

After forming, the completed product is inspected using an ultrasonic detector, as shown in Fig. 13. Ultrasonic inspection examines for structural imperfections through separate inspection of the bonded sections of the outer circumference and terminals. This method is used to inspect for pinholes and micro-cracks in the welded sections. Measurements taken using this method were cross-referenced with measurements from other equipment and compared with test data to confirm that it was sufficiently accurate to evaluate the soundness of the interface between the aluminum and the resin.

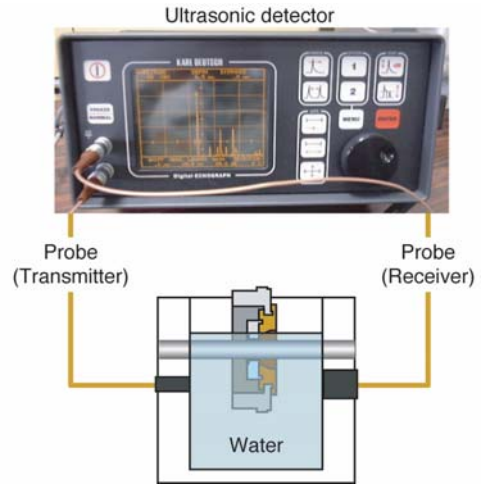


Fig. 13 Ultrasonic inspection

Pressure inspection utilized the set-up shown in Fig. 14, and verified that there were no paths for potential leakage under a back pressure of 5 MPa.

These three inspection methods effectively prevent faulty units from going into distribution.

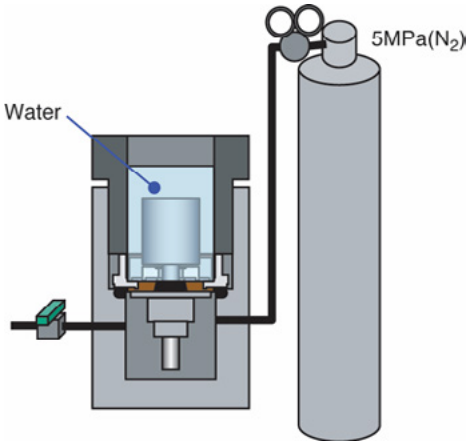


Fig. 14 N_2 pressure inspection

5. Results of Durability Evaluation

5.1. High-temperature Electrolyte Immersion Test

Figure 15 shows the results of measurements of bond strength after the acceleration test discussed in section 4. The units maintained a high level of bond strength. The absence of any paths for leakage to occur in the interface between the aluminum and resin, as shown in Fig. 16, confirms that the seal will remain viable for the life of the vehicle.

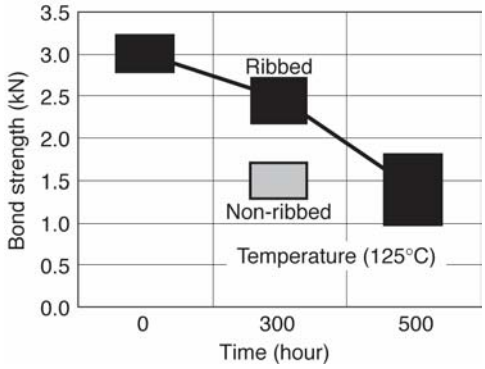


Fig. 15 Bond strength after acceleration test

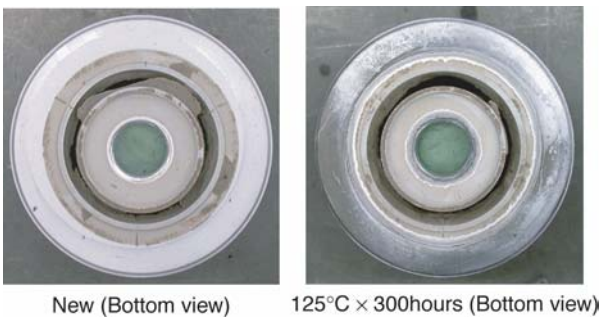


Fig. 16 Adhesion condition after acceleration test

5.2. Endurance Test under Actual Use Conditions

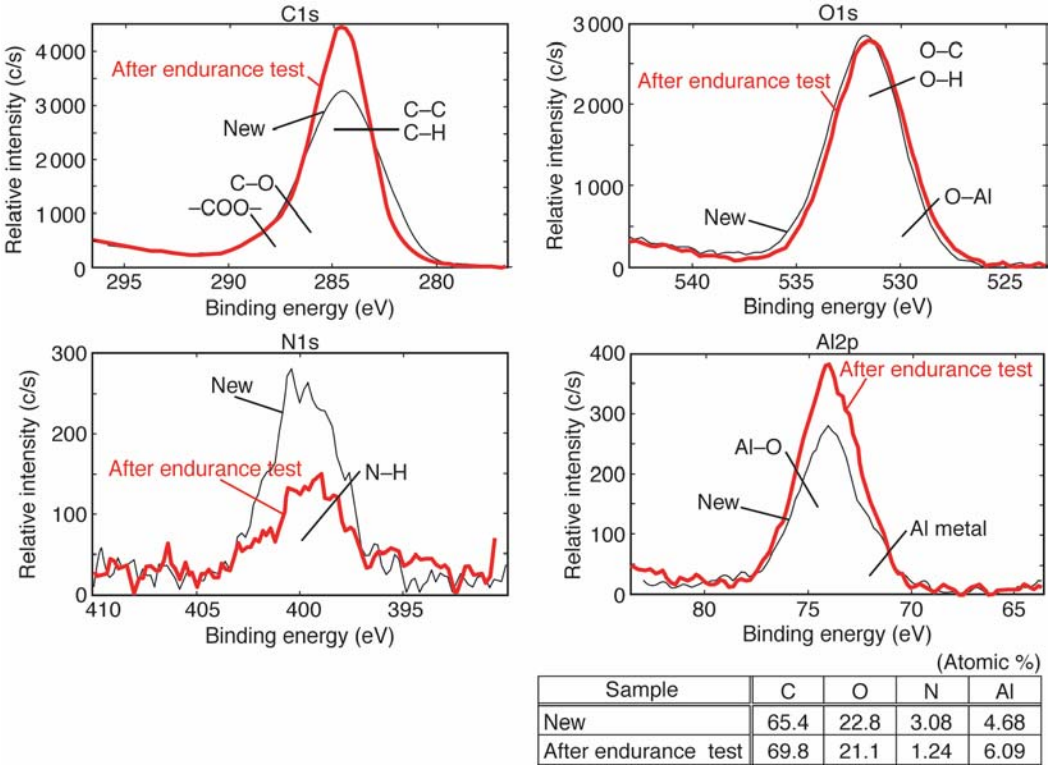
Capacitor cells were subjected to continuous testing under constant DC voltage at 45°C to verify their lifetime in actual use. No leakage occurred for the specified period, and analysis of the film after the tests demonstrated virtually no change in the distribution of carbon, oxygen, nitrogen and aluminum (Fig. 17), confirming that the seal will remain viable for the life of the vehicle.

5.3. Pulse Pressure Endurance Verification Test

A pulse pressure test apparatus was constructed to confirm the durability of the case cover against pressure. This test apparatus enables confirmation of durability in a short period by inducing changes in pressure. Figure 18 shows a schematic of the device.

An extremely tiny pressure sensor is positioned in the cell to measure the maximum change in the internal pressure. The results of these tests are shown in Fig. 19. With a change of temperature from –20°C to 80°C, the internal pressure of the capacitor cell increased 0.13 MPa. The change in internal pressure when the cell was charged and discharged was also measured, but the figure was negligible. These results enabled a target value to be established for the number of times internal pressure would increase to a maximum of 0.13 MPa over the lifetime of the cell.

Durability tests show that even under extreme conditions considerably in excess of the target value there was no breakdown of the aluminum/resin interface, and confirm the reliable durability of the case covers.



(Atomic %)

Sample	C	O	N	Al
New	65.4	22.8	3.08	4.68
After endurance test	69.8	21.1	1.24	6.09

Fig. 17 XPS analysis after endurance test

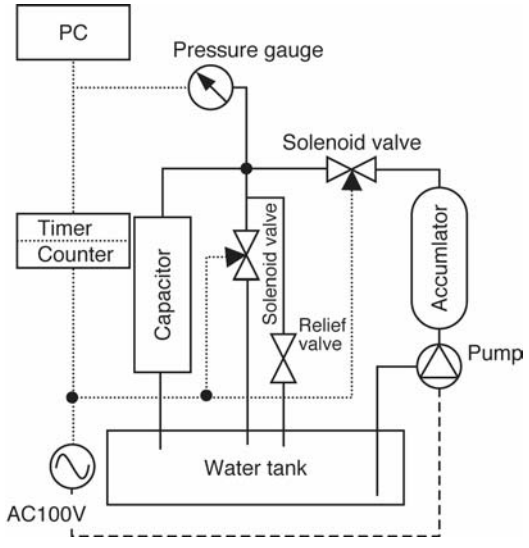


Fig. 18 Pulse pressure test

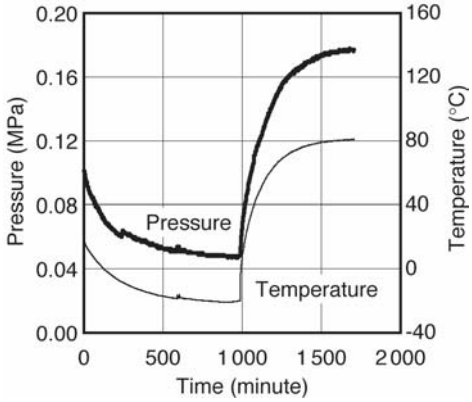


Fig. 19 Inner pressure of capacitor with temperature change

6. Summary

An insert molding process has been developed and utilized for the production of capacitor case covers for the first time in the world. The aluminum parts used are fitted with ribs to prevent contraction of the resin. Electrocoating of triazinedithiol at the interface of the aluminum and resin has enabled the achievement of a very reliable bond, and the applicability of this process to capacitor case covers was verified.

The reliability of the cover has been ensured by optimization of the conditions for treatment of the triazinedithiol and the insert mold conditions during forming, and by post-formation analysis of the composition of the film, ultrasonic inspection and pressure testing. In addition to acceleration testing, methods of analysis of the condition of the ultra-thin film (which has conventionally been difficult) and of degradation of the strength of the bond have also been developed.

Acknowledgments

In closing, the authors would like to take the opportunity to thank all those, representing Honda and other companies, who contributed to the success of this project.

Reference

(1) Sasaki, H., Kobayashi, I., Sai, S., Omoto, T., Mori, K.: Direct Adhesion of Nylon Resin to Stainless Steel Plates Coated with Triazine Thiol Polymer by Electropolymerization during Injection-Molding, Kobunshi Ronbunshu, Vol. 55, No. 8, p. 470-476 (1998)

■ Authors ■


Masato KOMATSUKI


Kazuaki IGARASHI


Toru OTA


Norifumi YASUDA

Introduction of Micro Combined Heat and Power Generation Unit for Residential Use

Toshimitsu TAKAISHI* Masato ARA* Kazuhiro TOGAWA*

ABSTRACT

The Micro-cogeneration unit (MCHP1.0) for residential use has been developed. The unit produces both hot water and electricity. This process is carried out in an extremely efficient manner. By fueling the system with cleaner burning natural gas, carbon-dioxide emissions can be further reduced. Electrical power from the units can be connected to the electricity grid. The Honda MCHP1.0 has reached 85% (LHV) of total energy efficiency, has a 380 mm width of enclosure, and a 46 dB (A)/1 m operating noise level due to advanced small engine technology and inverter generator technology accumulated in Honda's power equipment business. The unit is the smallest commercialized cogeneration unit.

1. Introduction

There is an increase in efforts across a range of sectors to reduce energy consumption and to utilize new forms of energy in response to global environmental issues. In striving to achieve the targeted reduction in CO_2 emissions by 2010 (6% less compared to 1990), which was proposed at the 1994 Kyoto Protocol Symposium (COP3), a range of measures are being explored by the industry, the social, and the transportation sectors. Nevertheless, the current restriction levels pose an extremely tough challenge.

Of particular note, is the dramatic rapid increase in energy consumption among residences, which is now a major cause of the overall increase in energy consumption.

A law in Japan concerning the rational use of energy has been established for addressing the efficient consumption of energy in residences. This law is based on the so-called top runner method, which is the principle of adopting the most efficient energy consumption levels achieved by specific electronic products such as TVs, air conditioners, automobiles and so forth. In addition, housing and construction design have adopted principles of lower energy consumption to help reduce the level of energy consumed through air conditioning and heating systems. Still, in spite of these improvements, changing lifestyle patterns and a greater number of home electric appliances have led to a continued increase in energy consumption.

In addressing the supply of energy, the shift toward cleaner fuels that emit less CO_2 as well as continual improvements in energy consumption efficiency are both

* Asakahigashi R&D Center

essential to achieving the targeted emission levels. Cogeneration systems supply both heat and electric energy and by 2010 the total power production from cogeneration systems is expected to reach approximately 10 GW. These cogeneration systems are expected to make increased inroads in addressing the requirements for reduced levels of energy consumption.

Cogeneration systems have, until recently, been used in large-scale facilities such as factories, hotels and retail shops. However, with the recent revision of the Electricity Utility Industry Law, gas engine generators with a maximum power of less than 10 kW are treated as small electric equipment. This deregulation has lead to an increased impetus in the development of micro-cogeneration units.

The Micro Combined Heat and Power Generation System described in this report is an energy supply system for residential use designed and achieved through joint development participation. The micro-cogeneration unit was developed by Honda while the combined hot water storage tank and supplementary boiler sub units were developed jointly by a city gas company, along with some manufacturers of hot-water supply systems. This report introduces the main features of the micro-cogeneration unit.

The micro-cogeneration unit is the world's first system to adopt electric interconnection sine wave inverter technology[(1)].

2. Development Concept

The following requirement conditions were focussed on in the development of the unit.

(1) Must be able to minimize efficiency loss of city gas supplies while maintaining balanced environmental conditions.
- Effective use of such a direct source of energy
- Reduce CO_2 and nitrogen oxide (NO_x) emissions

(2) Must be able to be set up in a typical residential environment
- A compact packaging
- Low noise
- High quality power supply
- Connection to hot water supply and heating systems

(3) Must be able to integrate the various subsystem standards.
- Meet standards of the Japan Gas Appliances Inspection Association
- Simplify discussion with electric power companies regarding Electric Interconnection. (Meet guidelines of electric interconnection technology requirements in the future.)
- Conform to Fire Prevention Standards

3. Specifications and Features

3.1. System Configuration and Specifications

Figure 1 shows the micro-cogeneration system layout in a residential setting. The system is set up outside the house. The power generated by the micro-cogenerator is consumed by the various electric products used in the house via the distribution panel. Heat produced along with the electricity is used first to warm water in hot water storage. Then it is used efficiently for hot water supply, floor heating and dehumidification in the bathroom.

Figure 2 shows an external view of the micro-cogeneration unit consisting of a gas engine, electric generator, heat exchanger and electric interconnection inverter. Table 1 lists the unit's specifications.

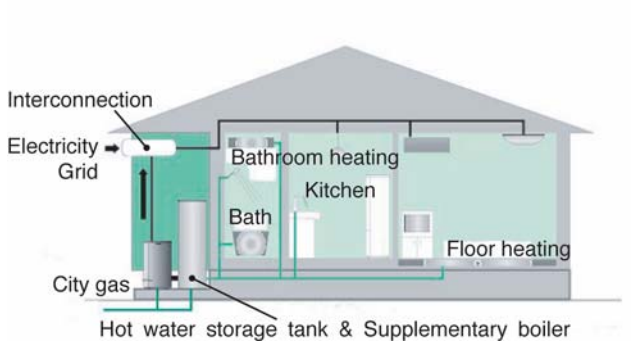


Fig. 1 General view of micro-cogeneration system



Fig. 2 External view of micro-cogeneration unit

Table 1 Specifications

Output	Electricity	1Φ3W 200V/100V 50/60Hz 1 kW
	Heat	3.25 kW
Power supply		Grid connection by inverter
Heat recovery		80°C Hot water
Efficiencies (LHV)	Electricity	20%
	Heat	65%
Dimensions (LxWxH)		635 × 380 × 940 mm
Weight(kg)		81
Noise		46dB(A)
NOx		Max 60 ppm
Engine	Type	Liquid cooled 4-stroke OHV vertical single cylinder
	Displacement	163 cm^3
Starting system		Starter generator

3.2. Differences with Conventional Micro Electric Generators

The micro-cogeneration unit differs significantly from conventional micro electric generators with its combined interconnected electricity grid. The power produced by the micro-cogeneration unit is synchronized to the frequency of the electricity grid and is supplied to the house, monitoring potential voltage trouble and power failure occurrences. Also, heat loss that would normally occur in typical micro engine generators is recovered by the engine coolant and converted to heating water in the hot water storage tank and supplementary boiler. The heat of exhausted gas including latent heat is also recovered by a heat exchanger unit shown in Fig. 6. Figure 3 shows the internal layout of the micro-cogeneration unit.

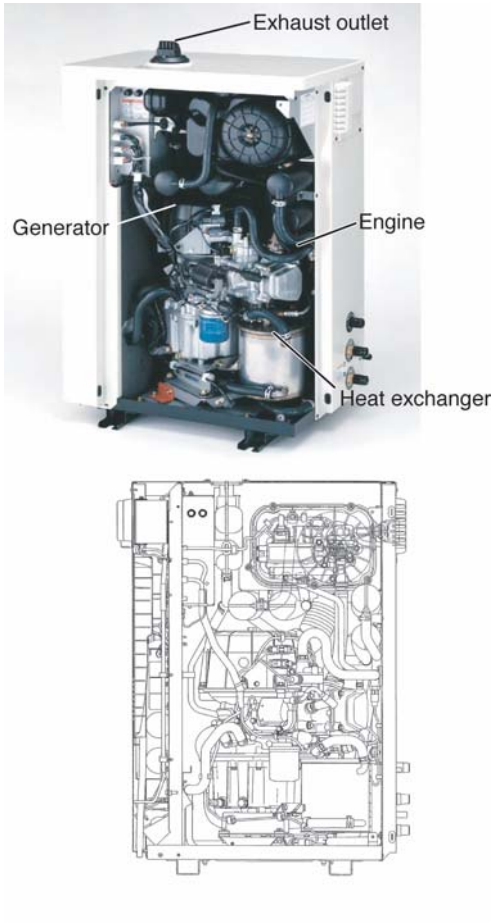


Fig. 3 Layout of micro-cogeneration unit

4. Technological Achievements

4.1. Effective Use of Primary Energy and Low Emissions

Usually, when power is supplied by electric power companies, there is a significant line of distance between the source of power generation and the areas where the power is in demand. Heat energy generated along with electricity cannot be used and is inevitably lost. After the transmitted energy loss is deducted, usable energy would account for an energy utilization ratio of 39%. On the other hand, as the micro-cogeneration unit generates power in the house, the heat can be used efficiently for heating water. Figure 4

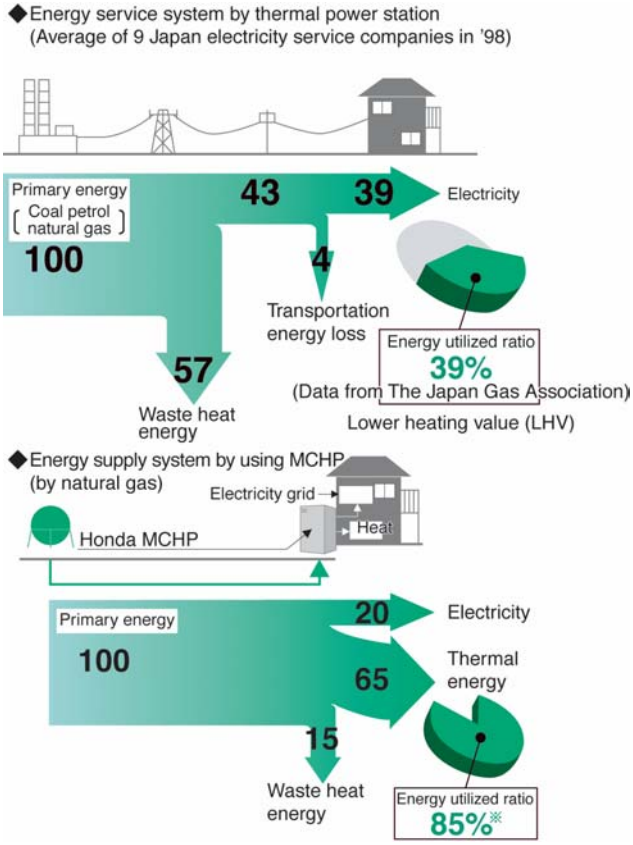


Fig. 4 Comparison of total energy efficiency

provides a comparative illustration of energy utilization ratio between conventional energy supply systems and the micro-cogeneration system.

The efficiency of power production at 1 kW of power output is 20%. The overall rate of efficiency, which is equal to (power output + amount of heat recovery) / gas supplied energy, reaches 85% of the lower heating value (LHV) standard. Figure 5 shows the multi-pole sine wave generator used in the micro-cogeneration unit.

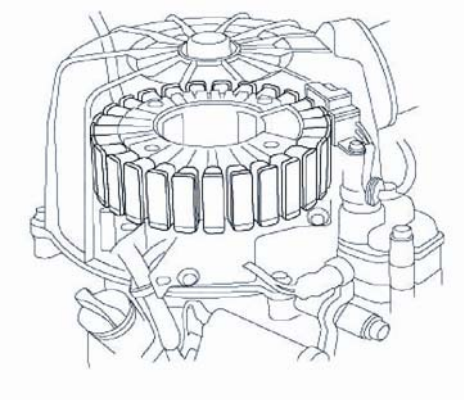


Fig. 5 Generator unit (27 pole)

The heat is recovered up to 65% of the LHV by using a heat exchanger unit, which is capable of recovering both sensible and latent heat. Figure 6 provides a structural representation of the heat exchanger unit.

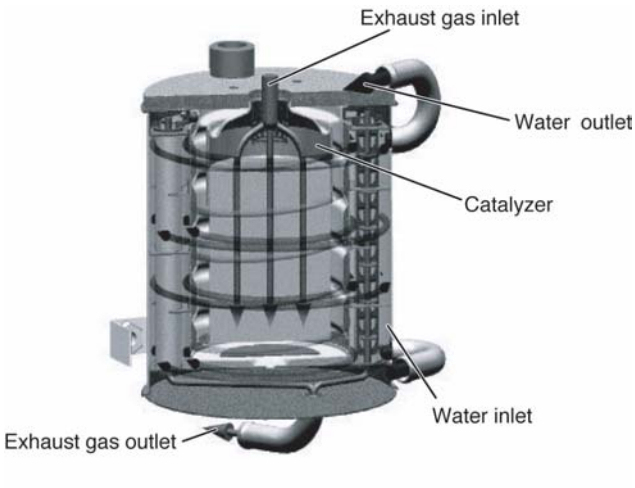


Fig. 6 Heat exchanger with a built-in catalyzer

The temperature of the engine coolant through which heat recovery is delivered ranges between 75°C and 80°C. The hot water storage tank and supplementary boiler unit can produce hot water, which is achieved through heat conversion from the engine coolant with clean water. For supplementary terminals using heated water, such as floor heating or bathroom dehumidifier, existing commercial products can be used without modification.

Heat, power output and the heat-electricity ratio, which is equal to heat output/power output, are all taken into account for system operation. The system operates according to heat demand while the amount of electricity generated is subsidiary. The engine operation time is adjusted depending on domestic heat demand. The system enables efficient use of any heat recovered from the engine.

The daily heat requirement and duration of heat use are calculated for the hot water storage tank and supplementary boiler unit. The calculation is then used to determine the start time and run duration of the micro-cogeneration unit. In effect, the system conducts a learning control routine to extract the most efficient level of energy consumption by running the units mainly when the radiation heat loss from hot water storage is low and electric loading is high. The remote controller for the supplementary boiler unit displays the current amount of stored hot water and power being consumed. The remote controller also incorporates a navigation function to enable scheduling of bathing time for the most effective energy consumption.

Regarding the emission, the internal exhaust gas heat exchanger discussed above has a three-way catalyst for controlling exhaust emissions and uses an O_2-feedback controller to enable fuel consumption at a stoichiometric air-fuel ratio to attain levels of NOx ≤ 20 ppm, CO ≤ 100 ppm.

4.2. Compact Packaging Suitable for Typical Residential Space Layouts

The micro-cogeneration unit incorporates numerous design controls in a compact size suitable to the general home environment. Installation floor space and compact format are of particular merit, especially from the viewpoint of the limited residential space conditions in Japan. A large volume oil tank along with a vertical engine has been incorporated in a unified layout design to enable the smallest possible floor space. Figure 7 shows the vertical engine layout with a multi-pole generator in comparison with a conventional generator. The vertical engine design contributes to the unit's reduced footprint size and facilitates installation in the smallest of locations. The multi-pole sine wave inverter generator has been designed without a fly wheel and has achieved a compact format approximately 1/2 the size and weight of a conventional generator. When starting, the generator acts as a starter motor for the engine by introducing net electricity (starter-generator). This configuration has eliminated the need for heavy and large independent starter motors. Figure 8 shows a comparison of the planar dimensions for an installed micro-cogeneration unit and other installed domestic appliances. The micro-cogeneration unit incorporates a smart compact design suitable for installation in typical residential environments.

When the system is started, the starter generator transmits power to the generator and initiates engine operation.

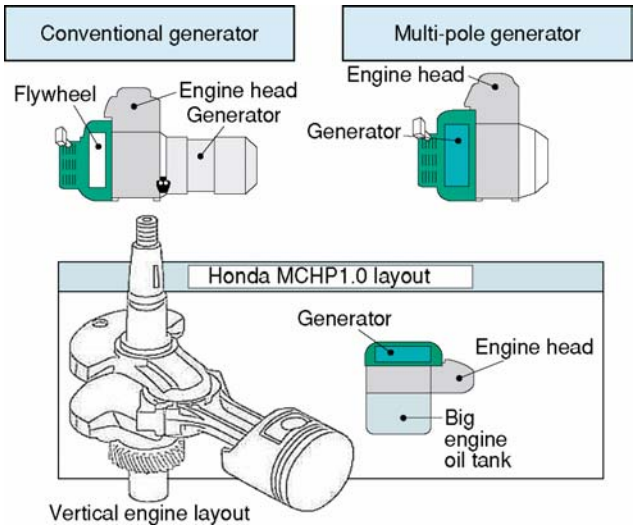


Fig. 7 Comparison of layout

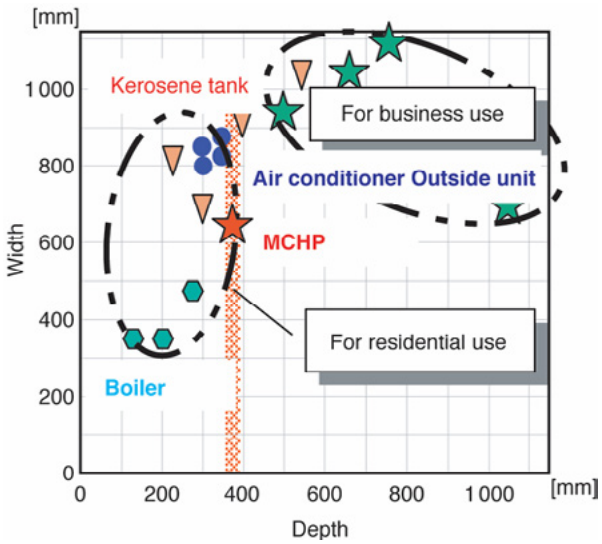


Fig. 8 Comparison of installed planar dimension

4.3. Noise Reduction

Potential noise sources are engine intake air and exhaust noise, ventilation noise inside the unit, engine combustion noise and mechanical noises. A multistage intake and exhaust silencer has been fitted to moderate engine intake air and

exhaust noise. Similarly, a silencer has also been fitted to reduce ventilation noise within the unit. To reduce overall internal noises including engine-generated noise, the inner walls of the unit have been covered with sound insulator.

These sound reduction measures have enabled a reduction in noise level to 46 dB (A) / 1 m (measurements conducted according to JIS GHP standards) during rated operation conditions and have attained low noise levels such as that for outdoor air-conditioners. Figure 9 shows a comparison of noise levels evaluated for the micro-cogeneration unit and other appliances.

The previously discussed multi-pole generator enables a silent start without engagement.

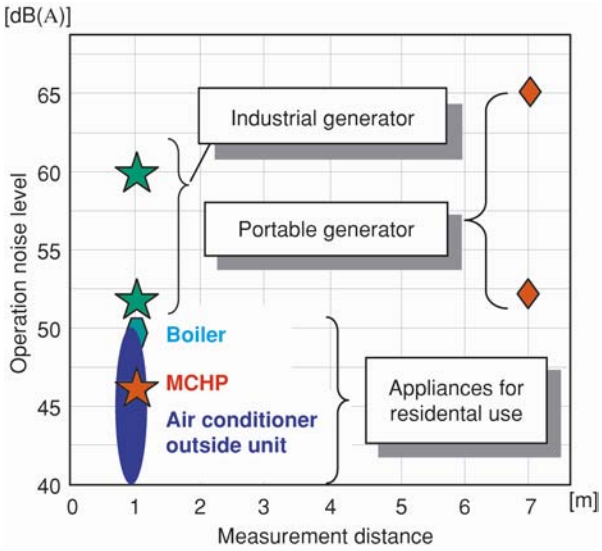


Fig. 9 Comparison of noise level

5. Summary

The newly developed micro-cogeneration unit is the world's first model for residential use that has successfully achieved an environmentally friendlier application by optimizing the saving of primary energy.

(1) The sine-wave inverter generator and exhaust gas heat exchanger used in the unit have enabled an overall efficiency of 85% LHV ((power output + amount of heat recovery) / gas supplied energy.)

(2) The sine wave inverter generator, which avoids the use of a fly wheel, a vertical engine and starter generator contribute to reducing the overall weight and size of the unit, highly suitable for residential use.

(3) Mechanical noise and internal noises such as engine intake and exhaust noise, etc. have been reduced to a maximum operating noise level of 46 dB (A) / l m making the system ideally suited to residential application. This has been achieved by adopting a multistage silencer and by covering the entire inner surface of the unit with sound insulator.

6. Acknowledgements

The authors would like to thank the Japan Gas Association and Osaka Gas Co., Ltd. for their cooperation in the development of the micro-cogeneration unit. Also, without the newly developed supplementary boiler unit achieved by NORIZ Corporation and Chofu Seisakusho Co., Ltd., this system would not have been adapted to its current product profile.

For socially acceptable environmental controls, the authors would like to thank the Japan Gas Appliances Inspection Association and the Japan Electrical Safety & Environmental Technology Laboratories for their support in developing suitable standards for this new product category. The authors would also like to express their appreciation to the Fire and Disaster Management Agency and Agency for Natural Resources and Energy.

Additionally, there were many specialists of energy technology who strongly supported the development of this system. The authors would like to express their sincerest gratitude to all of those specialists, both at Honda and those from other organizations, for their valuable contributions to the successful development of this system.

The issue of efficient energy consumption and reduced levels of CO_2 emissions are topics of concern shared on a global scale. In designing the co-generation system, although the principles of compactness and application to residential use were conceived at an early stage, these were not readily attained due to various technical issues and a range of social constraints.

Reference

(1) Kotani, Y., Shinogi, Y., Nakada, Y., Nakagawa, Y.: Interconnection Technology for Engine Generators, Honda R&D Technical Review vol. 15, p. 145-150 (2003).

■ Authors ■


Toshimitsu TAKAISHI


Masato ARA


Kazuhiro TOGAWA

Introduction of the “RINCON TRX650FA” ATV

Yoshiaki HORI* Bunzo SEKI* Hideaki SUZUKI*
Michio NAKAMURA* Kazuhiro KUDO*

ABSTRACT

The “RINCON TRX650FA” ATV, a new concept that provides an enjoyable and comfortable ride for use mainly in recreation, was developed as Honda’s flagship model of the utility oriented ATV (All Terrain Vehicle) series. An electronic controlled three speed automatic transmission with torque converter was employed in an ATV for the first time in the world. A powerful and comfortable running performance was realized by combining the transmission with a newly developed 648 cm^3 single-cylinder engine of a flat torque type. Moreover, riding comfort and smoother handling were achieved by adopting a rear independent suspension, a first for Honda, and radial tires. Some weight reduction technologies, such as an aluminum alloy forged suspension arm, were effective for achieving higher maneuverability during running on rough roads. As a result, these advanced technologies along with an original new design using an SUV concept, realized an impressive running performance.

1. Introduction

The ATV market, centered predominately in North America, is expanding year by year. Along with this growth, there are a growing range of performance criteria and functional requirements. In 2000, Honda released the first automatic transmission equipped utility ATV, the RUBICON TRX500FA. In response to the intense market competition in the large class vehicle displacement and the expanding lineup of automatic models, Honda has developed its ATV flagship, the RINCON TRX650FA.

2. Development Aims

In addition to the power and high running stability required by conventional large displacement ATVs, a balanced higher level of riding comfort and ease of handling have been achieved to retain the successful riding performance accomplished to date while providing an enjoyable and sporty ride. Figure 1 shows an external view of the vehicle and Table 1 lists the main specifications.

3. Engine

The engine size has been designed to take into account the rider’s comfort when sitting astride the vehicle and has adopted the same level of forward projection design as the TRX500FA while distributing the vehicle’s overall mass evenly. The engine design has successfully achieved a less than 60 kg format. Figure 2 shows the engine’s forward projection profile in comparison with that of the TRX500FA and Fig. 3 shows a sectional view of the entire engine. Parts used in the XR650R motorcycle were taken into consideration to achieve a 648 cm^3 displacement with a bore × stroke setting of 100 mm × 82.6 mm. The maximum output is 27.3 kW/5,500 r/min and achieves a maximum torque of

* Asaka R&D Center



Fig. 1 External view of TRX650FA

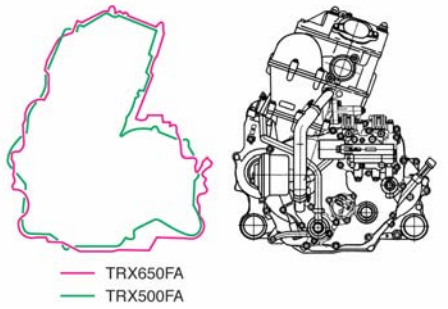


Fig. 2 Comparison of engine profiles

Table 1 Main specifications

Items		Specifications
Overall length (mm)		2 113
Overall width (mm)		1 189
Overall height (mm)		1 207
Wheelbase (mm)		1 289
Tread (mm)	Front	915
	Rear	945
Seat height (mm)		875
Ground clearance (mm)		234
Vehicle dry mass (kg)		273
Engine type		Liquid cooled 4-stroke single cylinder
Displacement (cm^3)		648
Bore × Stroke (mm)		100 × 82.6
Compression ratio		9.2 : 1
Valve layout		OHV 4-valve
Max. Output (kW/r/min)		27.3/5 500
Max. Torque (Nm/r/min)		49.9/4 500
Torque converter		3-element, 2-phase
Creep control system		Direct hydraulic controlled system by linear-solenoid
Transmission type		Constant-mesh type 3-speed automatic
Fuel tank capacity (L)		17
Tire size	Front	AT25 × 8R12
	Rear	AT25 × 10R12
Brake system	Front	Hydraulic drum
	Rear	Hydraulic disk
Suspension	Front	Double wishbone
	Rear	Double wishbone

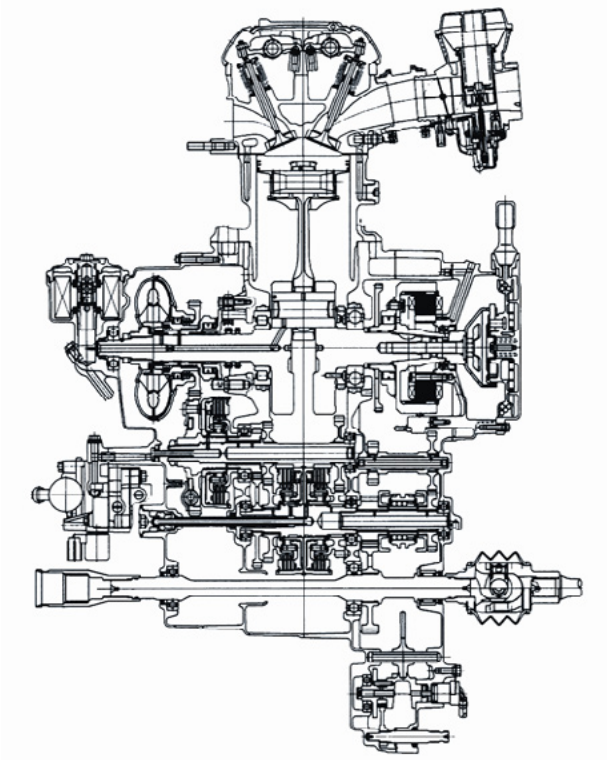


Fig. 3 Main section of engine

49.9 Nm/4,500 r/min to attach importance to the torque in the low speed range. To enable the 4-valve configuration for the vertical crankshaft placement, the same chain drive camshaft to cylinder configuration used in the TRX500FA has been adopted. A unique configuration has been implemented to drive the valves via the push rods and rocker arms. Figure 4 provides an illustration of the engine performance curve.

This vehicle is the world's first ATV to have successfully employed a three-speed automatic transmission configuration that makes use of a torque converter to achieve a powerful and comfortable ride to match the SUV concept. The creep phenomenon commonly associated with torque converters has been eliminated through the implementation of a newly developed creep control system to achieve a take off similar to that achieved by a conventional automatic wet type centrifugal clutch.

3.1. Built-in Oil Tank

The crankcase has a built-in oil tank which improves the vehicle's handling by providing for a lighter configuration and concentrating the mass centrally. Figure 5 provides a structural view of the crankcase oil tank location.

To stabilize the hydraulic supply to the hydraulic mechanical CVT (HFT) transmission in the TRX500FA, a separate oil tank has been positioned in the forward part of the engine. By utilizing a three-speed automatic transmission, the TRX650FA is able to allocate the lower central portion of

the crankcase, which accommodates the mechanical shift fitted to conventional ATVs, for the oil tank. This has achieved approximately a 2 kg weight reduction over a separate oil tank.

3.2. Multi Scavenger Oil Pump

The crankcase is divided into three separate chambers and consists of the centrally positioned oil tank, the laterally positioned crankshaft, and the transmission chamber. The oil pump draws the oil from these three chambers independently. Figure 6 shows the structure of the oil pump.

The oil pump is fitted with three trochoid rotors and a built-in relief valve. The oil drawn from the crankshaft and transmission chambers is cooled as it passes through the forward positioned oil cooler and is then returned to the oil tank. The oil from the oil tank is supplied to the engine and transmission system. The TRX650FA adopts a three-speed automatic transmission, which embodies a torque converter and three hydraulic clutch units. To preserve the same degree of maintenance commonly associated with conventional ATVs, one type of engine oil is used to lubricate all of the hydraulic driven parts.

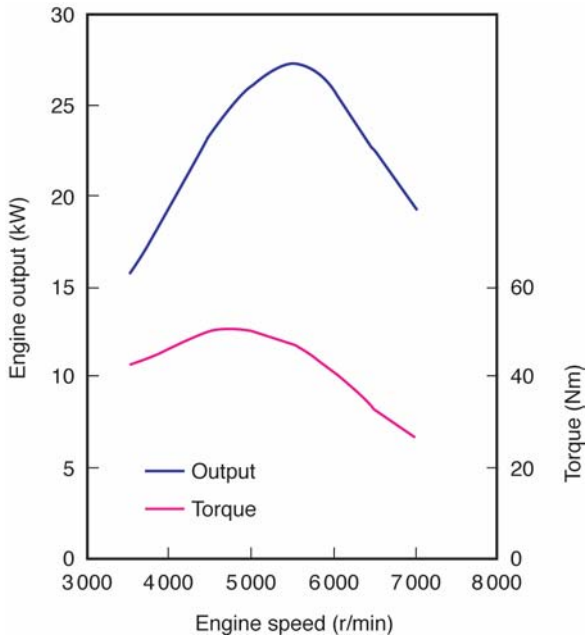


Fig. 4 Engine performance curve

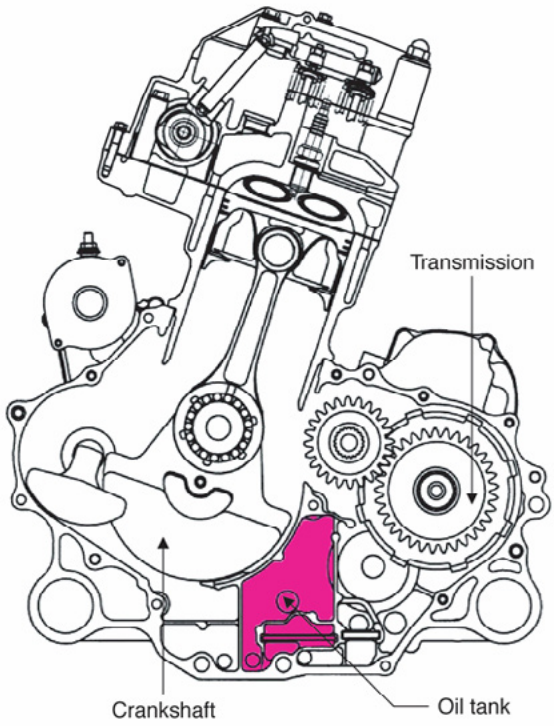


Fig. 5 Location of oil tank

3.3. Torque Converter

Instead of the automatic centrifugal clutch used in conventional ATVs, a torque converter is positioned on the crankshaft. The primary gear is welded into a single unit providing a configuration unique to ATVs and not typically found in an automobile. Figure 7 provides an external view of the torque converter.

The creep phenomenon, commonly associated with

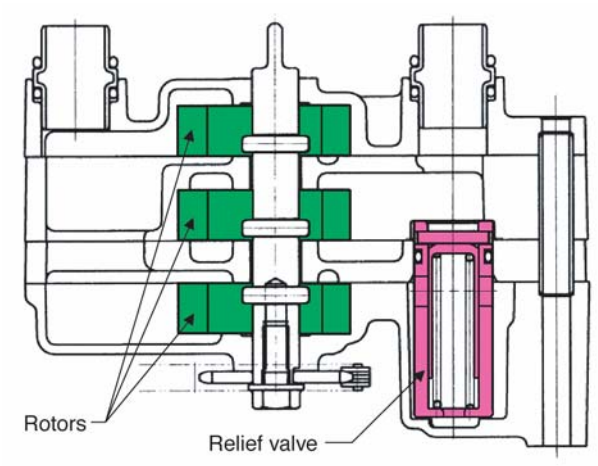


Fig. 6 Structure of oil pump



Fig. 7 External view of torque converter

torque converters, has been controlled by the oil pressure of the hydraulic clutch to maintain a similar degree of drivability as with conventional ATVs. The hydraulic controller, which uses a linear solenoid valve, enables the clutch to engage continuously to deliver the correct oil pressure as required by the vehicle speed, throttle opening, engine speed and oil temperature.

3.4. Transmission

The transmission utilizes three parallel shaft units. The main primary shaft unit accommodates the low clutch and the counter shaft unit accommodates the 2nd and 3rd clutch. The rear end of the counter shaft is fitted with a drive and reverse range switching mechanism. The drive force is transmitted to the front and rear propeller shaft from the final drive shaft unit via the final reduction gear.

To attain the same degree of vehicular drive rolling load as conventional ATVs, the selection of the neutral gear is mechanically effected and is set on the drive and reverse switching mechanism close to the propeller shaft.

Operating oil for the hydraulic clutch is supplied from the main shaft and counter shaft units via a typical feed pipe. All high pressure passage circuits, including the hydraulic controller, are concentrated under the engine front cover. Under the front cover an oil filter cartridge and the hydraulic controller valve body has been pre-assembled inside a clean room to prevent contaminants from entering the hydraulic circuit. Also, since processing along the assembly line has been simplified, the unit can be assembled on the same assembly line as that used for conventional ATVs.

Additionally, hydraulic clutches have been incorporated into the main and counter shaft units, respectively. The longer feed pipes for the counter shaft unit have been designed to enable the removal of an individual pipe from the outer engine surface. Figure 8 illustrates the structure of the transmission unit.

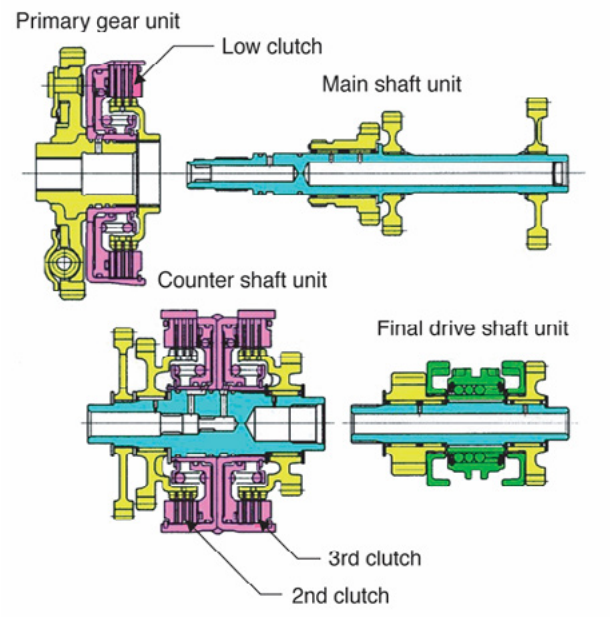


Fig. 8 Structure of transmission unit

4. Vehicle Body

The body design of the RINCON TRX650FA was developed along the lines of the SUV concept. SUVs are an extremely popular category in the North America automobile market. The RINCON TRX650FA has incorporated a balance of utility and recreational characteristics typically associated with SUVs to establish this as a new vehicle category in the ATV market. As Honda's flagship ATV, the TRX650FA incorporates a large range of original technology features to make it a benchmark vehicle design for future Honda ATVs offering a solid and sporty riding experience with a sense of quality and sophistication.

4.1. Exterior

Honda's characteristic ATV body carries a hybrid bumper design, which has eliminated the previously incorporated round piping. The new design employs steel piping set in blow molded plastic. By combining specially designed large integrated headlights, Honda has successfully captured the design concept of a SUV while creating a revolutionary new sporty look. A particular feature of this vehicle is the rear mounted independent suspension, offered for the first time on a Honda ATV. In addition to a superior quality aluminum alloy forged suspension arm, the vehicle adopts a uniquely configured dual tail lamp design. Figure 9 shows the front and rear view of the TRX650FA. Figure 10 show a view of the operator controls. The instrument panel has been allotted high priority to provide visibility for off road running and incorporate a new styling that matches the exterior character, all packaged in a highly usable and balanced configuration. All of the switches to be operated while the vehicle is running have been positioned and designed to provide ease of operation without requiring the driver's hands to be removed from the handle bars. The lever for operating the vehicle forward or reverse adopts a column style controller to provide the same feeling as an automotive driving experience.

4.2. Fender Molding

Weight reduction has been emphasized in the development of this vehicle. To achieve a lighter exterior, all of the exterior parts have been constructed in a completely new format. In conventional approaches to development, it can take an inordinate amount of time to achieve the desired specifications for reducing weight.

In the design of this vehicle, computer graphics (hereafter, referred to as CG) were employed where basic design sketching would have traditionally been used to develop a clay model representation. CG was used in the development of the exterior design of the vehicle and to design the exterior mounted parts. This was instrumental in improving the



Fig. 9 External view of TRX650FA's front and rear



Fig. 10 External view of operator controls

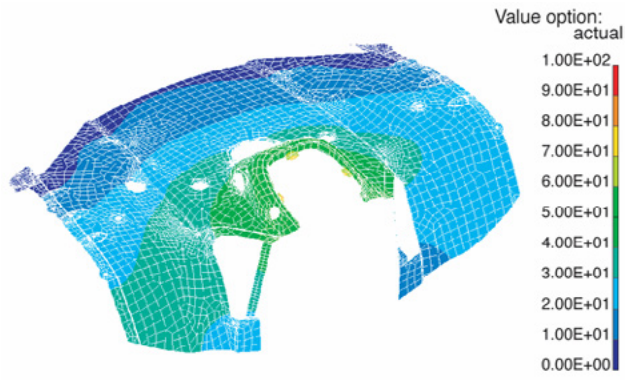


Fig. 12 Calculation results of flow analysis

accuracy of the specifications at the initial development stage. Figure 11 shows an external view of the vehicle under development with CG.

Using the external view data, a numerical flow analysis was conducted to estimate the plastic molding configuration and the appropriate thickness of each part. This approach finally enabled a thickness of only 2.8 mm, which was virtually inconceivable up to this point. This has resulted in a 20% weight reduction in fender weight compared to previous designs. Figure 12 shows the calculation results of the numeric flow analysis.

4.3. Transverse Muffler

Usually, the muffler is located on the left or right rear side of the vehicle and is mounted longitudinally. However, if a rear independent suspension was to be adopted, it would impinge on the operating range of the shock absorbers and impair the lightweight suspension unit’s design. To address this issue, priority was given to the suspension’s freedom of movement while achieving an overall weight reduction to the vehicle by extending the exhaust pipe to the rear of the vehicle and positioning the muffler transversely. Adopting this configuration has provided greater freedom in the selection of exhaust pipe length while achieving the desired level of engine performance. Also, centralizing the muffler positioning has made it easier to balance the weight along the lateral direction and has enhanced the layout flexibility of the overall vehicle. Figure 13 shows the location of the muffler.



Fig. 11 External view by “CG”

5. Chassis

Conventional Honda ATVs have typically employed full time 4WD and a swing arm type rigid axle rear suspension. To provide Honda’s flagship TRX650FA with the ideal underbody specifications, it has been designed with an independent rear suspension and a selectable 2WD/4WD system.

In addition to these specifications, the vehicle employs a range of weight reduction technologies, never used before in ATVs, to achieve a vehicular weight of 273 kg. This has limited the weight increase of the underbody to 1.2 kg in comparison to the full time 4WD and swing arm mechanism. In addition to reducing the vehicle weight, it provides for an easy to handle, comfortable ride, both of which have been key development concepts.

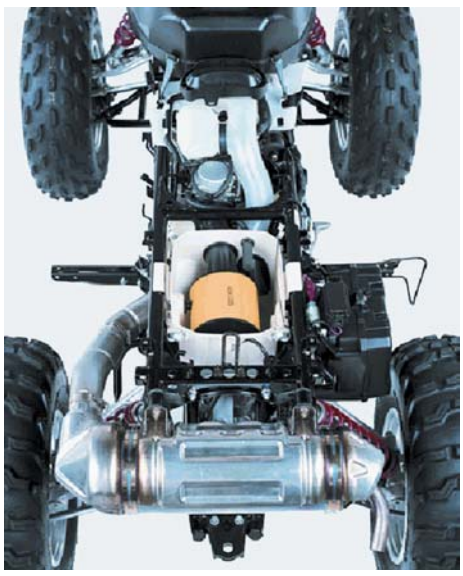


Fig. 13 Location of muffler

5.1. Independent Rear Suspension

The rear suspension employs a double wishbone type independent suspension, another first for Honda ATVs. A conventional swing arm type rigid axle utilizes a riding style where the rear of the vehicle slides while turning. Such a method is, however, limited in its capacity to enhance comfort when travelling over severe bumpy and rough road surface conditions. While the independent suspension system enhances driver comfort, it has contributed to an overall weight increase, and the increased horizontal rolling pitch tends to reduce the turning performance.

By taking a radical new approach to the entire body construction, the TRX650FA has incorporated an innovative suspension placement design and achieved a balanced set of specification settings for each component. Figure 14 shows a view of the rear suspension.

The parts attached to the lower side of the shock absorbers and the upper arm fulcrum are set along the same axis. This transfers the reaction force from the trail surface directly to the shock absorbers. The upper arm and lower arms have been designed to bypass any flexural load exerted by the trail's reaction force and have achieved reduced weight to the entire system. To maintain a sufficient axle stroke, a twin chamber type single tube damper has been adapted. The built-in twin chamber enables a high degree of packaging flexibility and increases the angle for the damper. To enhance this angle setting, the upper part of the damper is positioned close to the main frame. By repositioning the damper in this way, smaller sized brackets can be used to attach the damper. This has achieved a lighter rear suspension system that offers highly efficient operability while preserving an axle stroke of 203 mm. When addressing the issue of rolling as the vehicle turns, comfort and vehicular balance need to be taken into account. An independent suspension system is more effective than a rigid axle for ground contact of the inner wheel as the vehicle turns. To reduce the degree of rolling, it would be better to increase the stabilizer load, yet conversely, that would not contribute favorably to riding comfort.

This has been resolved in this new vehicle by setting a certain degree of tow out to the rear tire. Also, radial tires have been adopted, another first for a utility ATV. An improved balanced load setting to the stabilizer has provided greatly enhanced riding comfort and sporty handling performance compared with conventional rigid axle systems. Along with the changes made to the suspension system, the increase in weight has been addressed by applying aluminum alloy forgings on the upper and lower arms and knuckle to achieve targeted weight reduction. Figure 15 shows an external view of these parts.

5.2. Separate Rear Frame Construction

The independent rear suspension system uses a greater number of components than conventional rigid axle systems. The same production line used for the conventional rigid axle system is used for the new suspension system. The assembly of such a large number of parts has contributed to a reduced level of efficiency along the production line. To resolve this issue, the rear frame has been designed in a modular construction so that all the components on the rear suspension and rear final drive are assembled on an independent production line in a sub frame unit. This has greatly reduced the number of assembly processes on the main production line and increased efficiency in the combined manufacturing of other machines on the main production line. Figure 16 shows the sub frame unit.

5.3. Rear Final Drive System

A Birfield type constant velocity joint has been employed in the rear power train, which transfers the drive from the rear final shaft to the wheel. The ratio of the axle stroke to the tread is large in ATVs compared with usual passenger vehicles. This increases the angle of the constant velocity joint, which in turn leads to the generation of heat thereby contributing to endurance related issue. To resolve this issue, it required that the length of the left and right drive shafts were made equal and that the angle to the constant velocity joint be reduced to a minimum. To achieve this, the rear final gear needed to be positioned closer to the center of the vehicle. This however would cause a misalignment of the propeller shaft, which connects the engine and the final gear case. This is normally resolved by using a pair of yoke joints. In the TRX650FA, because the engine is positioned close to

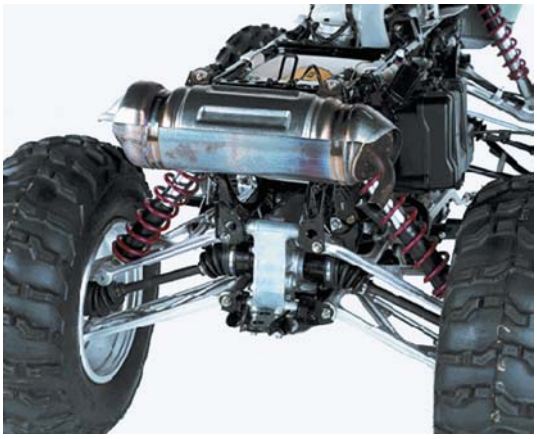


Fig. 14 External view of rear suspension



Fig. 15 Rear upper and lower arm & knuckle



Fig. 16 Rear sub frame unit

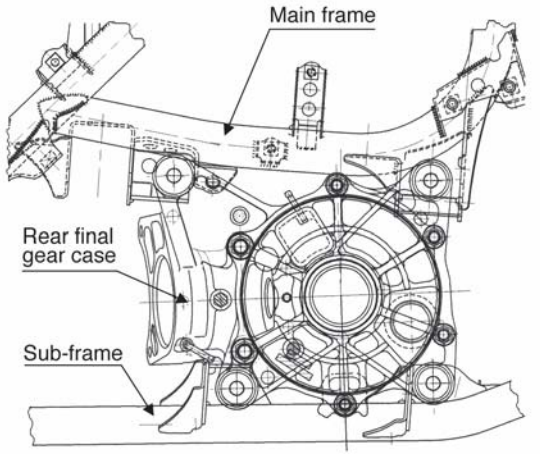


Fig. 18 Rear final gear case and rear frame

the rear final gear case, if a pair of yoke joints were to be used, it would increase the angle setting which would decrease the efficiency of power transfer and would generate heat. The engine output shaft has been set in a direct line from the front final gearbox to avoid using a yoke joint on the front propeller shaft. The change in the positioning of the engine output shaft however makes it difficult to reduce the velocity joint angle. By setting the cross angle on the rear final bevel gear to 77°, the propeller shaft is positioned in an angle to the vehicle body to enable the use of a simple drive system which uses only the yoke joint coupled to the engine side. Figure 17 shows the structure of the final drive system. Additionally, the rear final gear case, described in Section 5.2, is used to strengthen the connection between the main frame and sub frame units. By fixing the rear brake system directly to the gear case, the entire weight of the overall vehicle has been reduced. Figure 18 shows the integrated sub frame unit.

5.4. Rear Brake

The rear brake is fitted with a brake disk 170 mm in outer diameter on the propeller shaft and the caliper is clamped on to the rear final gear case. This enhances the operation efficiency of the cushion by greatly reducing the weight of the movable parts on the rear suspension. It also enhances the maneuverability as the vehicle travels over rough road conditions. Since the input torque load exerted to the brakes is reduced according to the reduction ratio of the rear final gear, the diameter of the brake disk has been decreased and the weight of the entire vehicle reduced.

However, the propeller shaft to which the brake disk is mounted is less exposed to air flow as the vehicle is being driven in comparison to a wheel mounted brake. A continued application may cause insufficient heat radiation. By insulating the brake pads and using a floating type of brake disk, the rear brake system is able to overcome these issues. Figure 19 shows an external view of the rear brake system. The rear brake on the ATV utility vehicle has two

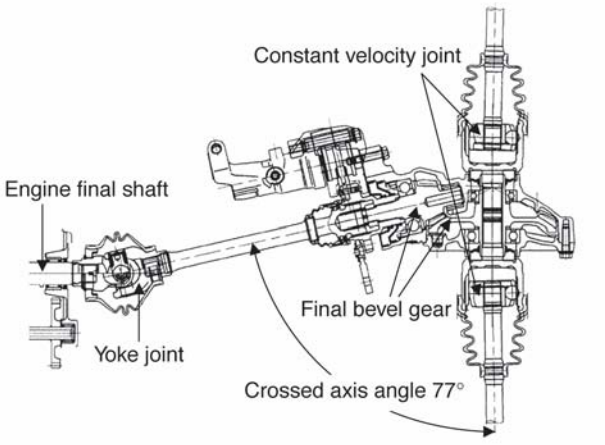


Fig. 17 Structure of rear power train

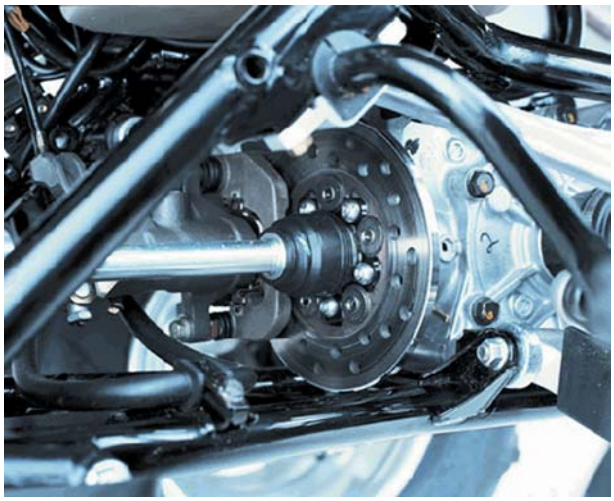


Fig. 19 Rear brake system

independent operating input positions: one on the right foot pedal and the other on the left handle bar. The handle bar is fitted with a parking brake function for securing the vehicle position. A rear brake on conventional vehicles typically uses a mechanical drum brake. In the dual brake system described above, two input cables are connected to a single brake arm to operate the brake. In conventional vehicles, a brake adjustment screw fitted to the cable ends had to be manually adjusted to modify any play in the brake. The TRX650FA employs a collet type caliper that is fitted with a mechanical piston to enable automatic brake adjustment. Figure 20 shows the structure of the rear brake caliper. The caliper piston is operated by input from the foot pedal, which is converted by hydraulic pressure in the master cylinder via the brake hose. Brake control input from the handle bar uses the cable to operate the mechanical piston. Enabling the rear brake input conditions to be set independently has brought greater control to the braking function and enabled automatic brake adjustment on both braking systems.

5.5. Front Suspension

The front suspension employs the same basic structural design and wishbone configuration with an axle stroke of 175 mm as that used in the TRX500FA. However, to provide ease of handling for both 2WD/4WD operating conditions, the alignment of the main kingpin angle has been redesigned. This new design employs an aluminum alloy forged upper arm, a first for ATVs, to achieve the targeted weight reduction. Figure 21 shows an external view of the aluminum forged front upper arm.

5.6. Front Final Drive System

The front final gear assembly comprises an electromagnetic controlled mechanical clutch unit[1] (hereafter referred to as MCU) for 2WD/4WD switching control; a torque sensitive cam differential; and a near net forged straight bevel gear. Figure 22 shows the structure of the front final gear assembly. The electromagnetic MCU has an electromagnet and a two-directional roller clutch assembly and was adapted to the TRX450FE ATV utility vehicle in 2001. The MCU operates by intermittently controlling the electromagnet current to provide easy and instantaneous roller clutch switching to the drive and idling running modes. When the roller clutch is engaged, 4WD is operational and when disengaged, 2WD is operational. Figure 23 shows the structure of MCU. When no current is flowing to the electromagnet, a switch spring load causes the retainer to hold the roller position in the center of the cam ring. Since a clearance is maintained between the outer ring and roller in the center of the cam ring, the transfer of the drive force from the propeller shaft is cancelled which switches the vehicle to 2WD. In 4WD, the electromagnet attracts the armature. The electromagnet is connected to the propeller shaft and the armature rotates at the same speed as the retainer. When the electromagnet and armature come in contact, the retainer tends to slip from the center of the cam ring. This creates a rotational difference between the retainer and cam ring and creates a torque to override the force of the switch spring. The retainer moves the roller from the center of the cam ring to a locked position thereby transferring the drive force. Figure 24 illustrates the MCU torque force transfer.

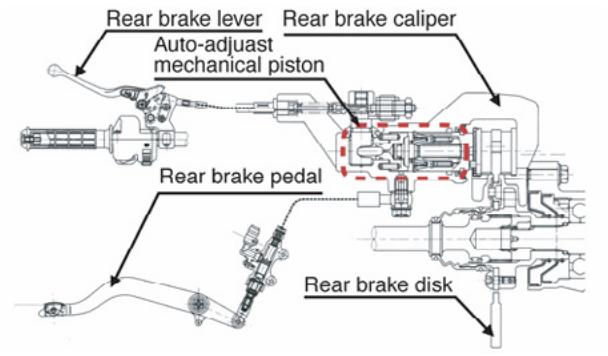


Fig. 20 Structure of rear brake caliper



Fig. 21 Aluminum forged front upper arm

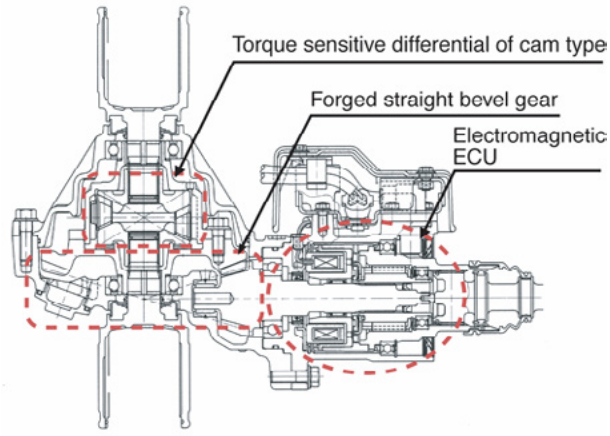


Fig. 22 Structure of front final gear assembly

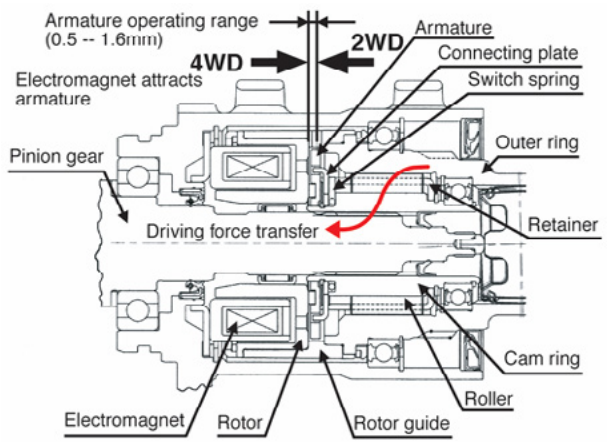


Fig. 23 Structure of MCU

The TRX650FA has a cam type torque sensitive differential built onto the front drive system as shown in Fig. 25. Unlike typical limited slip type differentials, which use friction disks, multiple cams are constructed so that when the power force is transferred, friction control is also applied. The integration of these functions has enabled weight reduction and reduction of the horizontal width. It also incorporates advantageous system features for narrow treaded ATV vehicles. The TRX650FA is configured with a maximum torque displacement of 1:3.9 to the left and right wheels to free the vehicle from muddy road conditions. Also, by employing a different ratio to the front and rear final gear,

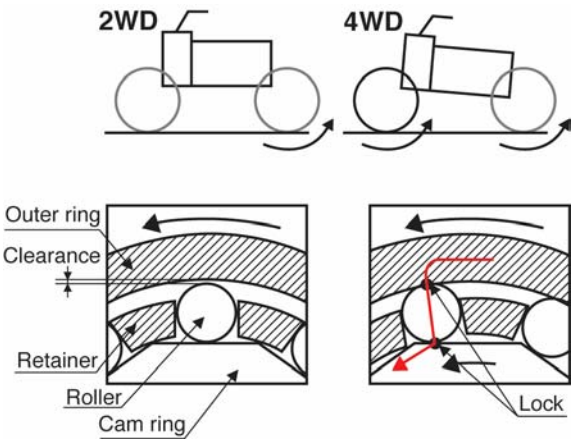


Fig. 24 Structure of MCU

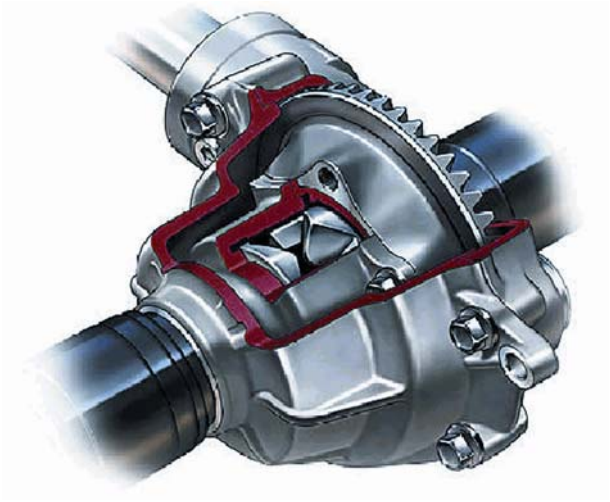


Fig. 25 Cam type torque sensitive differential

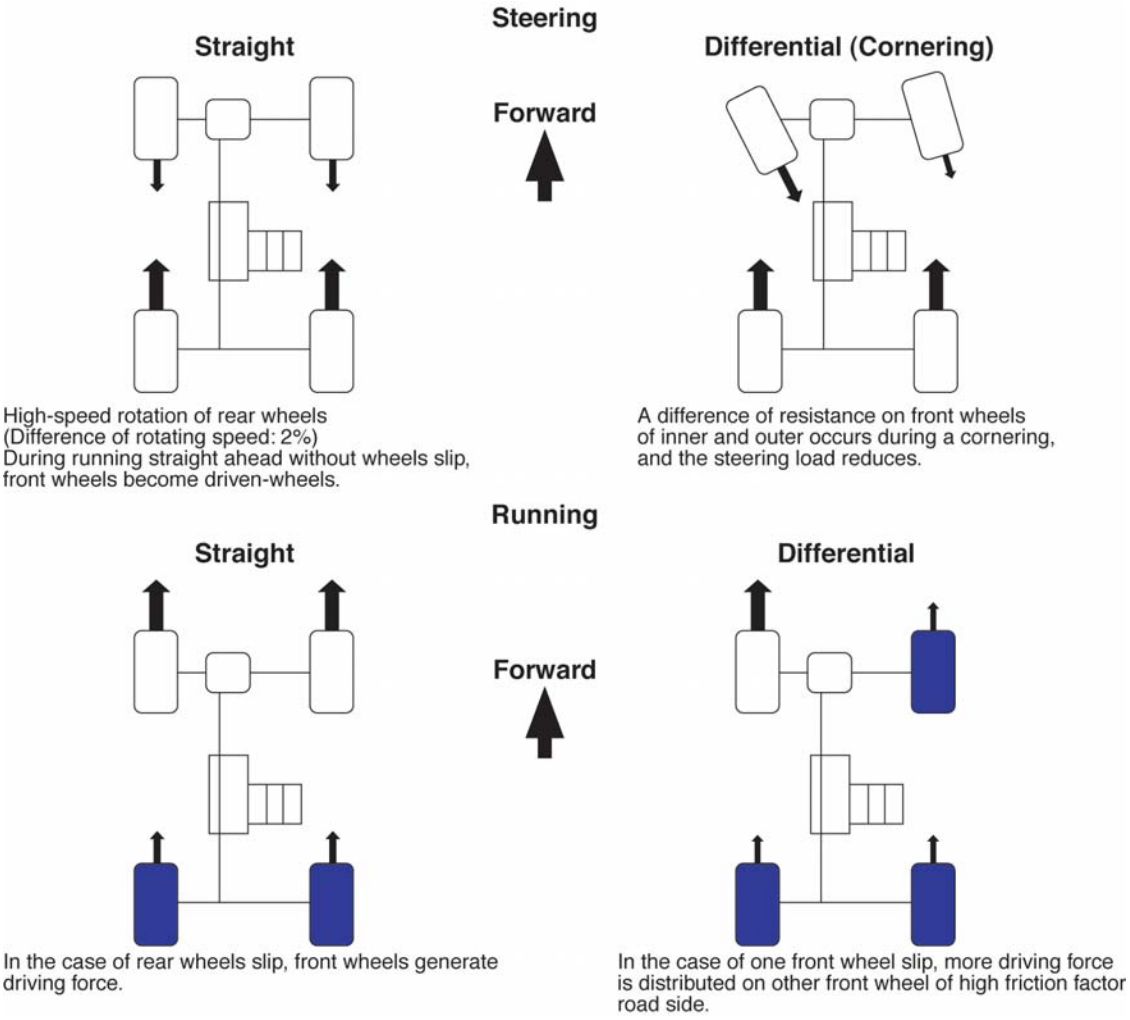


Fig. 26 Characteristics of vehicle

the front wheels rotate 2% faster than the rear wheels. Figure 26 shows the drive power distribution in different driving conditions. The front wheels become driven-wheels in normal straight drive conditions and are subject to resistance. When the handle bar is turned in such conditions, the front inner wheel with a lower rotation speed takes on a greater amount of resistance than the outer wheels because of the differential's torque distribution ratio. This results in a significantly improved turning performance. Furthermore, on low resistant road conditions, such as muddy roads and severe rough road surface conditions, the torque distribution ratio contributes to making the course more drivable. The combined front torque sensitive type differential and the front/rear wheel rotation differential provide comfortable handling and a smooth riding course. Even in the 2WD drive mode, the differential influences vehicle handling and the inner electromagnetic MCU friction is set to the optimal integrated handling specifications.

The ATV final gear has conventionally employed a straight bevel gear made of a near net forging and has achieved a lower degree of cost compared with a machined spiral. To further this technology, an optimal sized gear has been adopted to contribute to weight reduction. This has resulted in a 0.4 kg reduction in weight in the front final assembly compared to the TRX450FE, which employed the same system. Figure 27 shows the gear set used in the assembly.



Fig. 27 Forged straight bevel gear

6. Summary

The TRX650FA is an ATV based on new SUV concepts and incorporates a new vehicular design and numerous new configurations that are summarized below.

(1) Employs an engine with a maximum output power of 27.3 kW/5,500 rpm and a maximum torque of 49.9 Nm/4,500 rpm in addition to achieving an overall vehicular weight of 273 kg, which have contributed to a balanced running performance, ease of handling, and a high level of maneuverability.
(2) Constructed with an original design that incorporates a solid and sporty riding experience with a sense of quality and timeless sophistication.
(3) Incorporated operational stability and comfort into a balanced easy to handle and comfortable riding experience.

Acknowledgements

The authors would like to express their deepest gratitude to NTN Ltd. for their cooperation in the development of the electromagnetic MCU and FCC Ltd. for their cooperation in the development of the cam type torque sensitive differential.

Reference

(1) Goto S., et al.: Development of an Electronically Controlled Two-way Roller Clutch for Transfer Case Applications, SAE 2001-01-0866.

■ Authors ■


Yoshiaki HORI


Bunzo SEKI


Hideaki SUZUKI


Michio NAKAMURA


Kazuhiro KUDO

Development of an Engine with a 3-speed Automatic Transmission for the “TRX650FA”

Yoshiaki HORI* Seiji HAMAOKA*
Hideyuki TAWARA* Takeshi NAKAZAWA*

ABSTRACT

The world’s first engine with a torque converter has been developed for the paramount TRX650FA in Honda’s utility oriented ATV (All Terrain Vehicle) line-up. A linear solenoid valve and a hydraulic clutch control the creep phenomenon at idling peculiar to the torque converter. The start-ability is equal to a wet automatic centrifugal clutch for conventional ATVs. A pleasant running condition, similar to an automobile, was achieved by employing an electronically controlled 3-speed automatic transmission. Assembly of the transmission and the engine using an existing production line was made possible because the lubrication systems of both the transmission and the engine were designed in common. A substantial weight reduction was achieved by optimizing the design of each part.

1. Introduction

The ATV market centered predominately in America is experiencing an accelerated trend toward large vehicle displacement and automated features in order to provide greater comfort and running performance. In 2000, Honda released its TRX500FA featuring a hydraulic mechanical CVT[(1)]. In achieving its line-up of automatic models, it was necessary to design models with a larger vehicle displacement. In addition, weight reduction is highly desirable for improving maneuverability for off road driving conditions required by ATVs. In addition to achieving a larger engine displacement configuration and improved specifications including 4-wheel independent suspension and a selectable 2-wheel/4-wheel drive mechanism, the TRX650FA has also retained the superior features and weight of the TRX500FA. Figure 1 shows the exterior view of the TRX650FA. In addition to achieving a lighter weight engine, and to provide the appropriate torque to provide the standard of running stability required by ATVs, a 3-speed automatic transmission with an in-built ATV-specific micro torque converter was developed.

2. Development Goals

This vehicle has achieved a balance of riding comfort and running stability, at higher performance levels, suitable to the top fleet model series. Also this new model focuses on ease of handling for the leisure driver while incorporating a revolutionary design concept.

The engine, together with its uniquely configured torque converter, provides a smooth and powerful starting level of performance highly suited to such large displacement vehicles. A 3-speed automatic transmission was also adopted to provide the novice ATV driver with ease of handling and a sporty gearshift feeling similar to a manual transmission.

The torque converter has a unique output torque character which delivers a powerful starting through its effect of torque amplitude. Accordingly, as the vehicle increases in speed, the rate of torque converter slippage is minimized to provide a reduced torque output. This serves to stabilize the tire grip over loose off-road or dirt conditions. The torque output provides an enjoyable drive sensation during times when the throttle opening is frequently adjusted to provide a stable ride over uneven off-road conditions. The basic engine

* Asaka R&D Center

configuration employs a crankshaft design which sits longitudinally to the vehicle's traveling direction and is unique to Honda 4-wheel drive ATVs. Adopting this configuration in which the crankshaft and final output axial are set parallel to one another, has achieved an effective means of eliminating the necessity for a bevel gear for the engine's final reduction mechanism. This has been effective in promoting weight reduction.

3. Engine Overview

The layout of the main engine parts has been designed with due consideration to assembly on the manufacturing line and employs a similar configuration to that used in the conventional ATV engines. The generator and starter motor have been positioned on the rear part of the engine, and the torque converter, oil pump and water pump etc. have been positioned on the forward part of the engine. Oil beneath the crankshaft is scavenged by the oil pump. This configuration lowers the oil surface and the positioning of the crankshaft center. This design has contributed to reducing the size of the forward projecting configuration to approximate that of the TRX500FA. Figure 2 shows an external cutaway model view of the TRX650FA engine.



Fig. 1 External view of TRX650FA

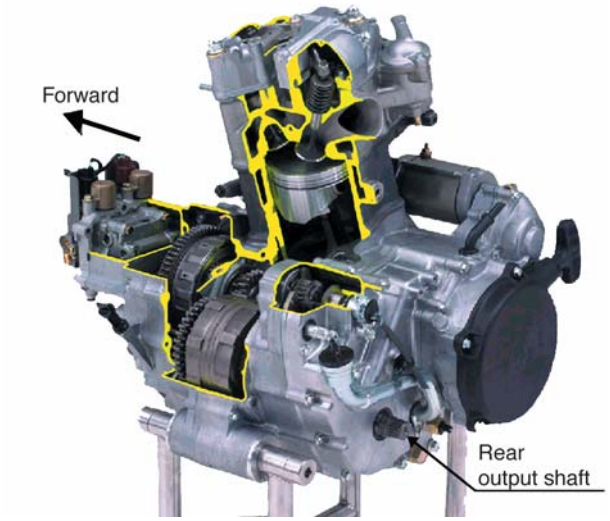


Fig. 2 Cutaway model of TRX650FA engine

Parts used in the XR650R motorcycle were taken into consideration to achieve a 648 cm^3 displacement with a bore × stroke setting of 100 mm × 82.6 mm. The maximum output is 27.3 kW/5500 r/min and the maximum torque is 49.9 Nm/4500 r/min to emphasize a low speed torque that matches the torque converter specifications and provides ease of handling. Figure 3 provides an illustration of the engine performance curve and Table 1 lists the main specifications.

4. Torque Converter

4.1. Basic Specifications

In typical automobiles, the torque converter is positioned in a dry chamber located between the engine and transmission. The input and output positions on the torque converter are set at opposite ends of the main torque converter unit.

As shown in Fig. 4, instead of the automatic centrifugal clutch found in conventional ATVs, the torque converter adopted in TRX650FA is positioned on the crankshaft.

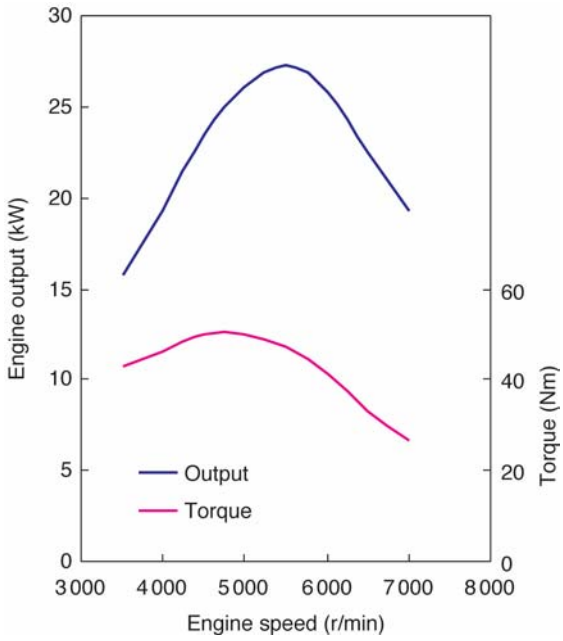


Fig. 3 Engine performance curve

Table 1 Specifications of engine

Engine type		Liquid cooled 4-stroke single cylinder
Displacement	(cm^3)	648
Bore × Stroke	(mm)	100 × 82.6
Compression ratio		9.2 : 1
Valve layout		OHV 4-valve
Max. output	(kW/r/min)	27.3/5500
Max. torque	(Nm/r/min)	49.9/4500
Engine mass	(kg)	59.8
Torque converter		3-element, 2-phase
Creep control system		Direct hydraulic controlled system by linear-solenoid
Transmission type		Constant-mesh type 3-speed automatic

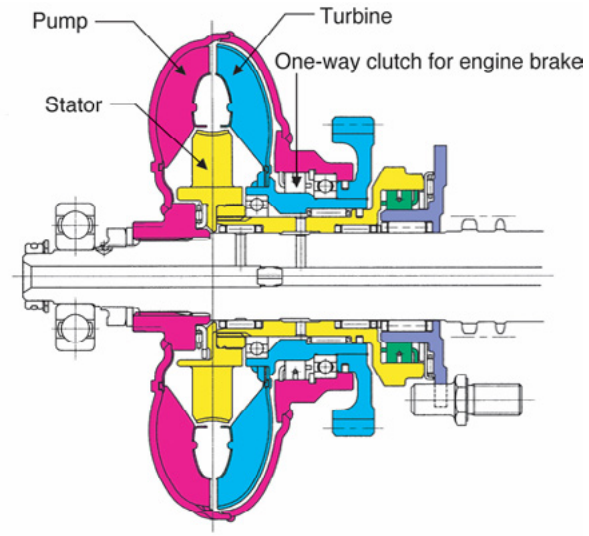


Fig. 4 Structure of torque converter

Therefore, the input and output positions of the torque converter have been positioned on the same side. Additionally, because the torque converter is positioned in the wet chamber inside the crankcase, the seals have been designed with a simple finish to allow slight oil leaking to lubricate the shaft bearing. On the other hand, the shaft bearing has been designed with a complex dual capability to accommodate input-output functionality. As shown in Fig. 5, the torque converter adopts a typical 3-element, 2-phase type configuration while the pump is fixed to the crankshaft with a nut and the primary drive gear is welded to the turbine. The stator rotation is transferred to the stator one-way clutch via the inner shaft. When coupling occurs, the stator normally rotates freely. When the unit stalls, the reverse stator rotation sends a reactive force via the inner collar to the lock pin, which is bolted to the crankcase, causing the torque to increase. Table 2 lists the main torque converter specifications and Fig. 6 illustrates the performance curve of the torque converter. Because ATVs are significantly lighter than typical automobiles, they do not require a large torque ratio. The maximum drive power and maximum drive force from the low pressure tires required for ATVs, are set to a



Fig. 5 Cutaway model of torque converter

Table 2 Specification of toque converter

Hydraulic diameter	(mm)	146.5
Number of blades	Impeller	28
	Turbine	23
	Stator	15
Torque converter dry mass	(kg)	3.0
Max. torque	(Nm/r/min)	49.9/4 500
Vehicle dry mass	(kg)	273
Torque mass ratio	(kg/Nm)	5.5
Used oil type		Engine oil

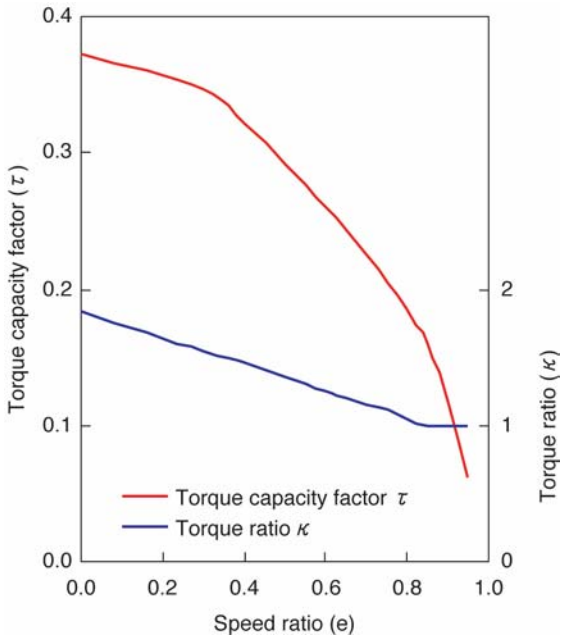


Fig. 6 Torque converter performance curve

low ratio with the torque ratio $\kappa = 1.8$ for a speed ratio $\varepsilon = 0$. A balanced engine torque has been achieved by setting the torque capacity factor τ to 0.38 for a speed ratio $\varepsilon = 0$.

When ATVs are running over uneven off-road conditions there is a large variation in the running resistance that affects the ability to keep a constant cruising speed and this could cause a throttle open-close operation. To reduce gear-shifting frequency and promote a smooth running performance under such running conditions, the torque capacity factor curve is lowered slightly to the right in relation to the increased speed ratio. Figure 7 illustrates the variation in the turbine torque performance curve in respect to the engine speed. As the torque amplitude decreases, the engine speed and vehicle speed increase slightly to yield a smoother acceleration.

4.2. Compact Light Weight Design

In appraising the drivability of a vehicle, both the stationary and transitional characteristics must be taken into consideration. To find the ideal torus for the previously described setting conditions, a 3-dimensional CFD[(2)] was conducted. In addition, three different torque converters were made according to the specifications listed in Table 3 and illustrated in the capacity factor curves shown in Fig. 8. Calculations and fine adjustment tuning was conducted repeatedly to achieve the particular specifications for this

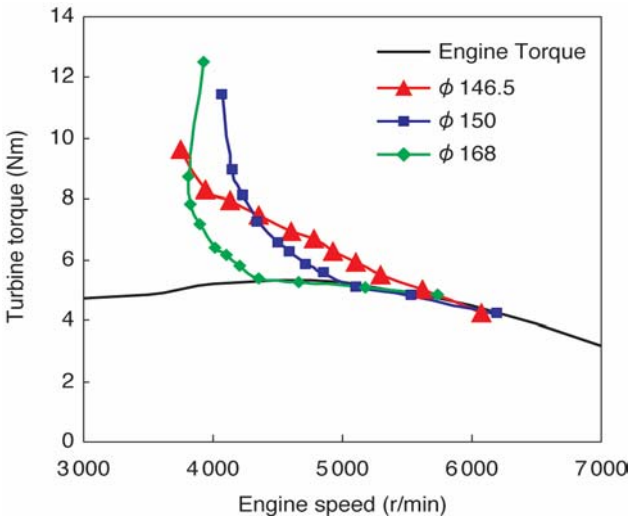


Fig. 7 Turbine torque performance curve

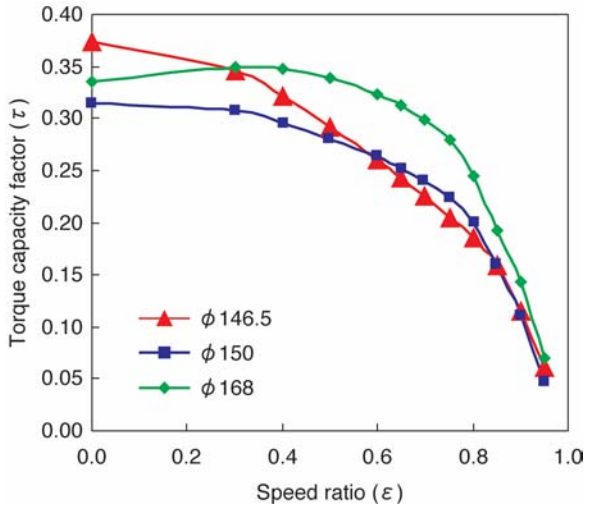


Fig. 8 Torque capacity factor curve

Table 3 Comparison of toque converter size

Hydraulic diameter (mm)		146.5	150	168
Number of blades	Impeller	28	23	23
	Turbine	23	21	21
	Stator	15	11	11
Torque converter dry mass (kg)		3.0	3.3	4.0

model unit. The hydraulic diameter was set at 146.5 mm to achieve the targeted settings.

A blade thickness of 0.5 mm was attempted to improve driving efficiency and facilitate weight reduction. A balance of strength, pressing, welding, wax adhesion, etc. were utilized in the manufacturing to achieve the most suitable levels of thickness for each part. This has resulted in a 25% reduction in weight compared with the initial specifications.

4.3. One-way Clutch for the Engine Brake

The performance of the engine brake according to the gear ratio is important to promote easy handling for ATVs. Typical hydraulic controlled lock-up mechanisms have a more complex configuration for supplying oil pressure to the control system and torque converter. Also, the actuating responsiveness of a hydraulic clutch is instrumental in facilitating the engine brake just as the throttle is closed. The currently developed system embodies a simple configuration which ensures a reliable performance and has adopted a mechanical one-way clutch adapted for the engine braking system and is built into the torque converter. The one-way clutch has been adopted to the automatic centrifugal transmitting clutch in most ATV engine brakes for its highly reliable performance. Figure 9 shows an external view of the one-way clutch.

4.4 Integrated Lubrication System

Oil used for operating the torque converter is supplied from inside the crankshaft and also serves to lubricate the connecting rod bearing. The quantity of oil drawn from the oil pump is regulated as it passes the orifices positioned along the upper side passage of the crankshaft and the oil pressure is also reduced. The lubricated passages leading from the inside of the crankshaft are divided into separate passages that lead to the torque converter and the connecting rod. The amount of oil flow is also distributed as it passes over the respective orifices. Oil expelled from the torque converter is returned to the crankshaft and in combination with the oil separated by the orifices, is supplied in total to the connecting rod bearing. Oil supplied to the connecting rod bearing is also used to lubricate the support bearings for the pistons and crankshaft branches. After the oil accumulates in the oil pond located beneath the crankshaft, it is scavenged to the oil tank by the exclusive oil pump. This configurational design has enabled a simple lubrication passage to the torque converter while providing a means of effective oil scavenging.

5. Creep Control System

5.1. Structural Overview

Creep phenomenon promotes smooth drive torque transition as the vehicle starts and is effective in improving torque output as the vehicle starts on loose off-road surfaces and on inclining off-road conditions. In typical automobiles, the creep phenomenon is peculiar to torque converters. Mechanical automatic centrifugal clutches are typically used



Fig. 9 External view of one-way clutch

as the drive clutch on ATVs. When the engine is idling, the vehicle does not move by drag torque of the clutch.

Creep phenomenon is effective for drive performance. However, to ensure a similar degree of handling performance as other ATVs on the market, a creep control system was developed to eliminate creep when the vehicle is in the stationary idling position. Figure 10 illustrates a structural diagram of the transmission. The TRX650FA incorporates three hydraulic clutches for the 3-speed automatic shifting. When shifting gears, the electronic controller switches the hydraulic circuit to the clutch and transfers the drive force to each gear setting. When the engine is idling and the vehicle is stationary, just as when the vehicle is in neutral position, the control system shuts the hydraulic pressure to the clutches to prevent any creep from occurring.

5.2. System Overview

As shown in Fig. 11, the hydraulic circuit including the gearshift control system, is configured with the linear solenoid valve set to the upper aspect of the hydraulic switching valves for gear-shifting. The parameters for controlling the vehicle speed, the degree of throttle opening, the engine speed, oil temperature, etc. gradually generate the hydraulic pressure as required. To control on and off of creep without any sense of irregularity, it is essential to improve the responsiveness of the clutch engagement in respect to the engine speed. To enable this, the hydraulic circuit has been set to as short as possible a length leading up to the low clutch. A highly responsive free-ball type check valve has been adopted to the clutch. A minimal amount of hydraulic standby is supplied from the linear solenoid valve and fills the circuit to the low clutch with oil. Furthermore, to stop creep at low oil temperatures and eliminate any sensation of connection as the oil temperature changes, the standby hydraulic pressure is controlled by oil temperature. This has enabled responsiveness to intermittently occurring creep and a characteristic connection feeling equivalent to an automatic centrifugal clutch. Figure 12 shows the creep engage performance curve.

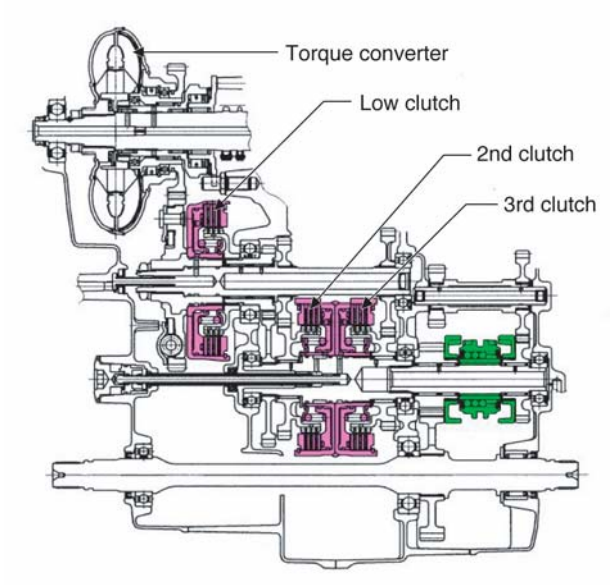


Fig. 10 Structure of transmission

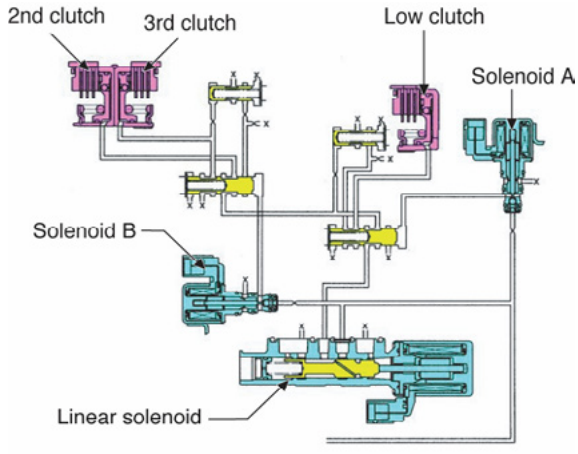


Fig. 11 Structure of hydraulic circuit

6. Automatic Gearshift System

6.1. Basic Configuration and Structure

The newly developed transmission comprises four elements engaged, three clutches, and a mechanical gear-shifter. In forward gear, the respective clutches engage with three speeds each to transfer the drive force. In reverse gear, the low clutch and mechanical gear-shifter are engaged in the ‘R’ position. Table 4 lists the relevant gear levels and clutch operations. Convex dogs and dogs holes are used to mechanically switch drive ranges between the ‘N’ neutral, ‘D’ drive and ‘R’ reverse gears. A switching mechanism located on the lower side of the clutch is operated via the control cable leading from the column lever, which is situated close to the driver’s hands. As there is no creep occurrence before and after the switching and all of the clutch hydraulic pressure is shut by the linear solenoid valve, a smooth switching range is enabled.

6.2. Overview of Gearshift Control System

The gearshift control hydraulic circuit is basically the same as that employed in typical automobiles but has been further simplified for a more balanced adaptation required by ATV vehicles. Low pressure tires unique to ATVs are highly suited to drivability over uneven off-road conditions and

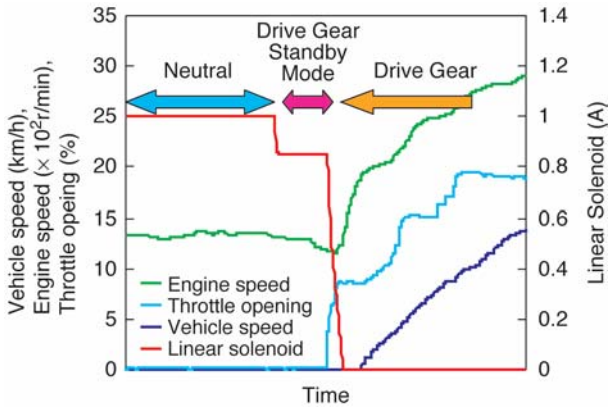


Fig. 12 Creep engage performance curve

contribute significantly to softening the shock from gearshift changing. Consequentially, the need for parts such as the accumulator, which is used to control hydraulic changes during clutch switching and thereby reduces the gear-shifting shock, has been reduced. Gear-shifting acts as a controller along with the two on-off solenoid valves. Table 5 lists the on-off solenoid valve application controls according to the gear-shifting. When a system malfunction occurs, power to the solenoids is shut by the relay causing the A and B solenoids to shut off and sets the gear position to 2nd. In case the solenoid drive circuit is in an unknown condition, the circuit is configured so that solenoid A is set to 'Off' when solenoid B is 'ON'. This configuration prevents a jumping gearshift from 3rd gear to low gear. Figure 13 illustrates the solenoid circuit diagram.

Table 4 Operating conditions

Elements engaged	Clutch			Mechanical shifter
Actual gear	Low	2nd	3rd	D/N/R
Neutral				N
Low	○			D
2nd		○		D
3rd			○	D
Reverse	○			R

Table 5 Solenoid application and actual gear

	On-Off Solenoid	
Actual gear	A	B
Low	On	Off
2nd	Off	Off
3rd	Off	On

6.3. Hydraulic Control Valve Body Unit

The valve body unit which controls gear-shifting is best to be assembled in a clean room while preserving quality control to prevent any operational damage that may be caused by contaminants from the hydraulic switching spool valve. The engine is manufactured on an existing assembly line which is not sufficient to manage the introduction of contaminants on the production line. For this reason, the linear solenoid valve, on-off solenoid valve, and the gear spool valves have all been incorporated into a single unit. This has then been assembled inside a clean room to ensure functional integrity of the unit. The valve body unit and the oil filter element have been assembled within the clean room on the front cover which forms the central high pressure oil passage to prevent the introduction of any contaminants to the upper side passage of the valve body.

Service maintenance has also been taken into consideration in the design of the valve body unit to enable easy removal from the outer engine. Figure 14 shows an external view of the valve body.

6.4. Hydraulic Clutch

The basic configuration of the hydraulic clutch incorporates successfully applied elements of the automatic transmission used in typical automobiles. The pistons have been constructed of aluminum die-cast, which contributes to weight reduction. To reduce the load build-up to the pistons, the maximum level of hydraulics being used and the return spring load have been reduced. Also, the pistons have been set to the same space as that for accommodating steel pistons to achieve a 0.6 kg weight reduction for the three clutches. Figure 15 shows an external view of the clutch piston. Figure 16 illustrates a comparative structural diagram of a conventional steel piston and an aluminum piston.

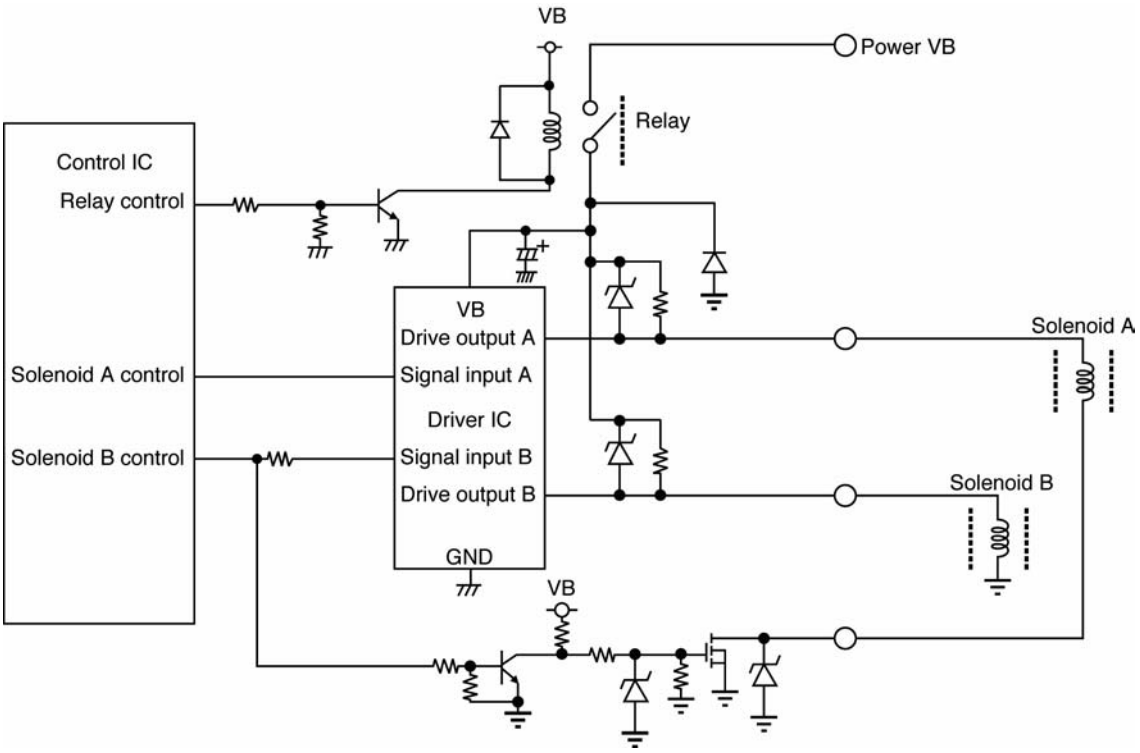


Fig. 13 Solenoid circuit



Fig. 14 External view of the valve body

The check valve emphasizes responsiveness during intermittent creep occurrence and has adopted a free-ball type configuration. In automobiles, in order to reduce the degree of gearshift shock it is necessary to provide greater clutch control. This has been achieved by changing from the free-ball type check valve to a leaf-valve type to decrease the centrifugal pressure. Also, a centrifugal hydraulic cancellation type[3] has been adopted to improve the functionality.

As previously described, low pressure tires are invaluable in reducing the degree of gearshift shock in ATVs. Particularly, when running at high speeds, the influences from vehicular acceleration are greater than the gearshift shock, which presented no particular concern in the product profile. At the time of starting the vehicle, on the other hand, the responsiveness during creep engagement is readily transmitted to the rider due to enhanced tire gripping and less vehicle acceleration. To emphasize this responsiveness at low speeds, a free-ball type check valve has been adopted. Figure 17 shows the acceleration character at gear-shifting.

7. Gear-shifting Control System

7.1. Control Unit

The motor drive gearshift[4] specifications and basic ECU in mass produced ATVs have been combined and a slave unit has been added for creep and automatic gearshift control. By conducting interactive transmissions between the ECU and slave unit, greater extension flexibility to exclusive parts and a more compact and lightweight configuration design have been achieved.

7.2. Slip Determination

In running over uneven off-road conditions, the variance in the throttle opening increases to stabilize the vehicle positioning. Furthermore, if tire slippage occurs at too great of a frequency this may cause the wheels to lock on loose off-road conditions. Under such conditions, the difference in vehicle speed and speed sensor detection value increases causing up/down gear-shifting. This shifting might contribute to some decrease of the running performance. To accurately determine the vehicular speed and achieve accurate gear-shifting, the vehicle speed acceleration rate has been set according to a time variable setting. This enables accurate



Fig. 15 External view of clutch piston

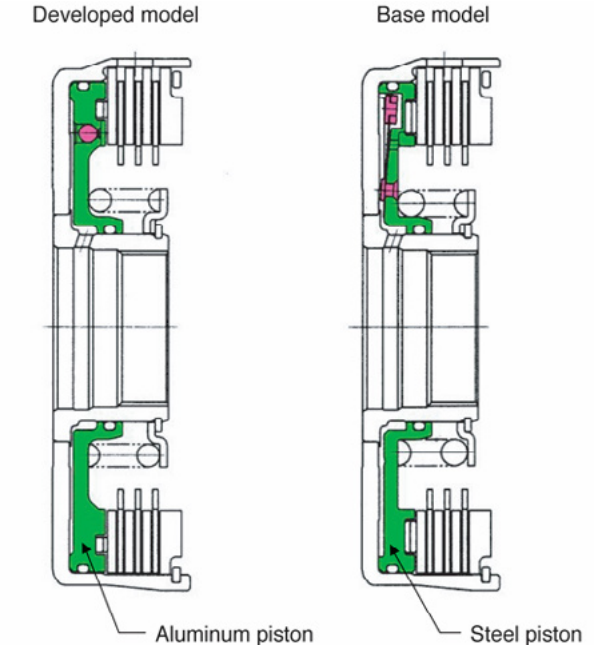


Fig. 16 Structure of clutch piston

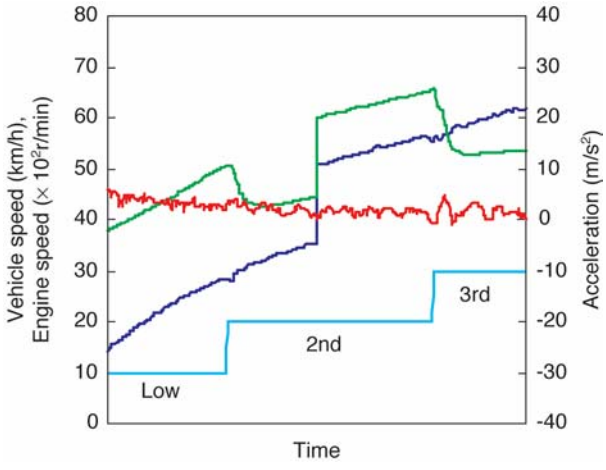


Fig. 17 Acceleration character at shifting

speed increase and decrease readings. Sharp increases in vehicle speed detection values determine tire slipping while drastic decreases in the vehicle speed detection value determine wheel locking. Then, control to set the gear to the current level is implemented to prevent unwanted gear-shifting.

7.3. Cornering Mode

In running conditions ranging from where the throttle opening is large to a cornering scenario in which the throttle closes completely, sometimes the vehicle is shifting up in accordance with the gearshift map. One way to help prevent this from occurring is to determine the running condition and fix the degree of gear-shifting. For ATVs running over uneven off-road conditions, it is quite difficult to determine the degree of off-road surface variance. By focusing on the throttle opening rate, a control has been added for fixing the gearshift level when a sudden throttle closure occurs. In addition, when the throttle opening is less than 20%, the gearshift point is transferred to the higher vehicle speed range.

This helps prevent an unwanted gear-shifting up when the throttle closes. Even if a low throttle opening is maintained, it also helps prevent unwanted shifting up. Therefore, a constant running speed is stabilized at a minimal load.

7.4. Descent Mode

For travelling on a descending off-road conditions, a customized gearshift map for enacting early downshifting in response to brake signaling is provided to increase engine braking and enable acceleration after deceleration. Figure 18 shows the performance curve of the shift control map.

8. Summary

The newly developed TRX650FA engine has adopted numerous new mechanisms to achieve the following.

(1) An engine weight of 59.8 kg with a maximum output power of 27.3 kW/5,500 r/min and a torque of 49.9 Nm/4500 r/min.
(2) A similar degree of engagement as conventional automatic centrifugal clutches by employing a creep control system that uses a linear solenoid valve.
(3) Accurate recognition of slip conditions by calculating the rate of change in throttle opening and vehicular speed. Have achieved a gearshift control characteristic highly suited to ATV running performance.
(4) A gearshift control characteristic highly suited to ATV running performance.

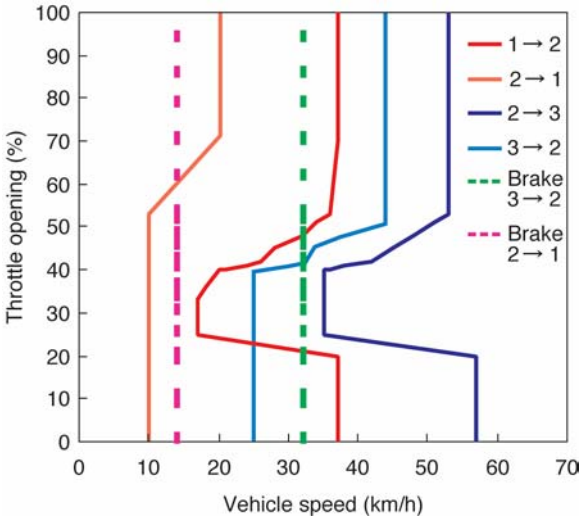


Fig. 18 Shift control performance curve

Acknowledgements

The authors would like to express their deepest gratitude to Mr. Imasaka and Mr.Makita from Yutaka Giken, Ltd., and Mr. Kagawa and Mr. Ryuen from Keihin Corporation, and Mr. Nishide from F.C.C. Co., Ltd., in addition to the large number of people who cooperated in the development of the transmission described herein.

References

(1) Saito, M.: Introduction of PGM-HMT System for ATV, Autumn Seminar 2001, Japan Fluid Power System Society, p. 43-50 (2001)

(2) Abe, H., Maruyama, T., Sakatou, M.: Development of Super Squared Torque Converter by Applying Three-Dimensional CFD, Honda R&D Technical Review, Vol. 13, No. 1, p. 75-80 (2001)

(3) Ohashi, T., Tanisawa, S., Asatsuki, S., Moriya, H., Mochizuki, T.: Development of One-Way Clutch-less 4-speed Automatic Transmission, Honda R&D Technical Review, Vol. 9, p. 61-69 (1997)

(4) Ota, A., Narita, S.: Utilization of Motor-Driven Gearshift System, SAE Paper 99PC-129 (1999)

■ Authors ■


Yoshiaki HORI


Seiji HAMAOKA


Hideyuki TAWARA


Takeshi NAKAZAWA

Development of a 4-stroke Engine for Small Motorcycles with Low Fuel Consumption and Low Emissions for Thailand

Yoshinobu SAWAMURA* Norio SAITO* Bunichiro SAKAMOTO*
Hideo KOBAYASHI* Yoshihisa HIROSE*

ABSTRACT

Concerns about environmental protection and energy savings continue to grow, including in Thailand where the market is requiring improvements in fuel consumption and emissions for motorcycles. Therefore, we developed a 125 cm^3 4-stroke engine with revolutionized fuel consumption and emissions for the Thailand market. To enhance the fuel consumption, the friction of contact surfaces of the rocker-arm and piston and the mechanical input of the generator were reduced. Also, the combustion efficiency was enhanced by changing the ignition timing according to the throttle opening. To reduce the emissions, a secondary air pulse induction system, which introduces fresh air into an exhaust port, was employed. As a result, the fuel consumption was enhanced 30% in ECE40 mode compared to the 108 cm^3 engine of the previous model. The emissions were reduced 55% in CO and 60% in HC + NOx against the value of Thailand's 4th emission regulation.

1. Introduction

The small motorcycle market in Thailand has shifted toward motorcycles with 4-stroke engines since the second half of the 1990s, as shown in Fig. 1. In order to deal with Thailand's market conditions, such as a depressed economy and the 4th emission regulation, Honda is actively introducing motorcycles with 4-stroke engines that are both economical and offer superior environmental performance.

A 125 cm^3 4-stroke engine for small motorcycles, which makes full use of the advantages of 4-stroke engines with the goal of further improving fuel consumption and reducing emissions, has been developed for the Thailand market. This paper describes the fuel consumption improvement and emissions reduction technologies applied to this engine.

* Asaka R&D Center

2. Development Goals

The development goals were set as follows from the viewpoint of energy savings and environmental protection.

(1) Energy savings: Improve fuel consumption in ECE-40 mode by 30% compared to the previous model
(2) Environmental protection: Half or less of the Thailand 4th emission regulation values (4th emission regulation values = CO: 4.5 g/km, HC + NOx: 3.0 g/km)

3. Engine Overview and Major Specifications

Figure 2 shows a structural drawing of the developed engine, and Table 1 lists the main specifications.

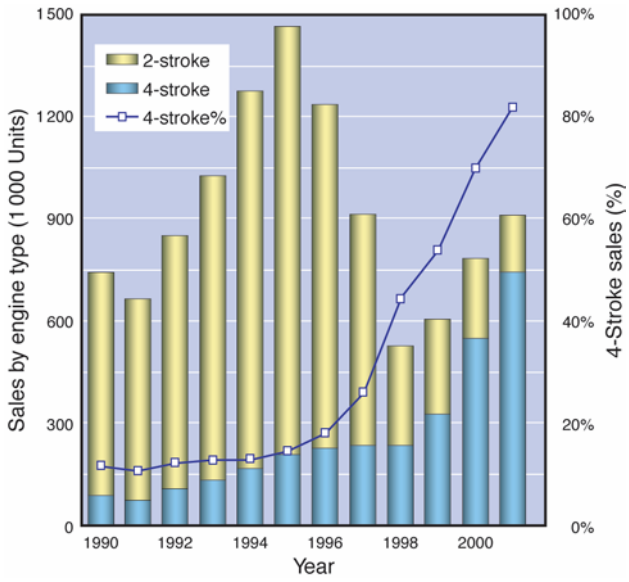


Fig. 1 Motorcycle market demand in Thailand, share by engine types

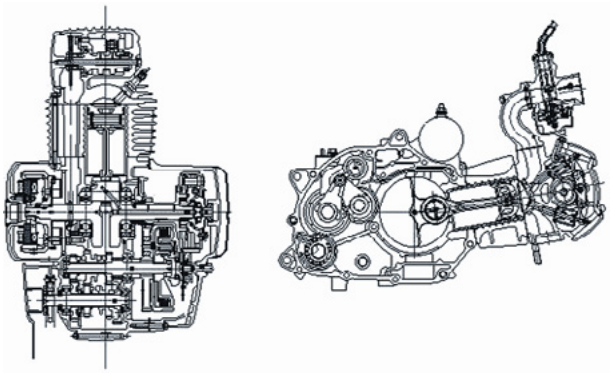


Fig. 2 Sectional drawing of developed engine

The developed engine is an OHC 2-valves, air-cooled, single-cylinder, 4-stroke engine. The displacement was increased to 125 cm^3 from the 108 cm^3 of the previous model. The included valve angle was changed from 66° to 49°. The intake valve diameter has been changed from 23 mm to 24 mm, and the exhaust valve diameter from 20 mm to 21 mm. In addition, the compression ratio was changed from 9.0 to 9.3.

4. Fuel Consumption Improvement Technologies and Effects

The technologies employed to improve fuel consumption and their effects are described below.

4.1. Employment of a Roller Bearing Type Rocker-arm

A roller bearing type rocker-arm was employed to reduce the sliding friction of the cam and the rocker-arm. However, simply adding a roller bearing to the same layout as the previous model would increase the inertia equivalent mass of the valvetrain system. Increasing the inertia equivalent mass of the valvetrain system would impair durability due to bounce at high engine speeds, and increasing the valve spring load to suppress bounce would increase the friction. Therefore, the included valve angle was changed from the 66° for the previous model to 49°, and the rocker-arm size was reduced. In addition, the weight was reduced by offsetting the valves and using a straight rocker-arm shape as shown in Fig. 4. As a result, the rocker-arm weight was kept the same as the previous model even with the addition of a roller bearing.

Offsetting the valves also made it possible to increase the valve diameters, thus securing sufficient air-fuel mixture volumetric flow without increasing the valve lift.

These developments reduced the friction due to valve drive at an engine speed of 4,000 rpm by approximately 13% as shown in Fig. 5.

Table 1 Major specifications of engines

Items		Developed engine	Previous engine
Engine type		4-stroke, single-cylinder	4-stroke, single-cylinder
Bore × Stroke	(mm)	52.4 × 57.9	50 × 55.5
Displacement		125	108
Compression ratio		9.3	9
Valve train		SOHC 2-valves	SOHC 2-valves
Valve diameter	(mm)	IN 24, EX 21	IN 23, EX 20
Included valve angle	(deg)	49	66
Clutch type		Automatic centrifugal	Automatic centrifugal
Transmission		4 speed constant mesh	4 speed constant mesh

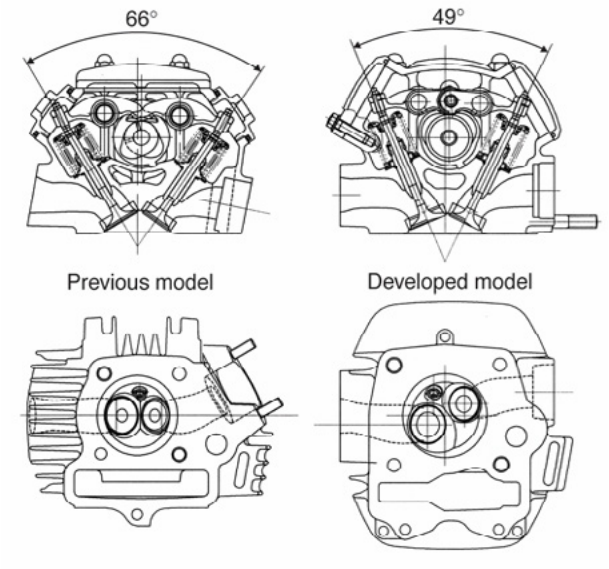


Fig. 3 Comparison of valve systems

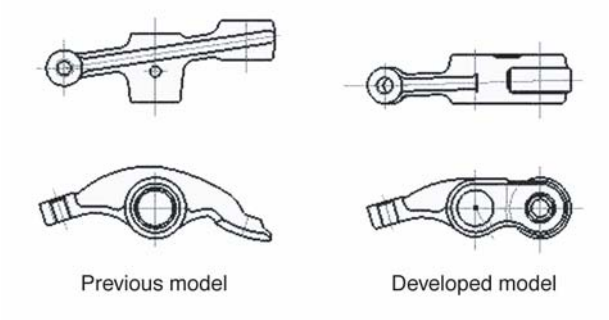


Fig. 4 Comparison of rocker-arms

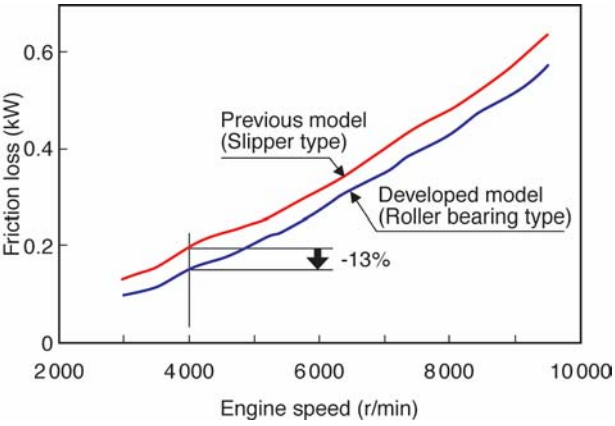


Fig. 5 Result of friction reduction by roller bearing type rocker-arm

4.2. Reduction of Piston Sliding Friction

A molybdenum disulfide resin coating[(1)] was applied to the piston skirt as shown in Fig. 6 to reduce the piston sliding friction. In addition, striation machining was performed to create oil collection grooves in order to improve lubrication performance. Furthermore, the piston ring plate thickness of the TOP, 2ND and OIL rings was reduced from 1.0 mm, 1.0 mm and 2.0 mm of the previous model to 0.8 mm, 0.8 mm and 1.5 mm, respectively. This reduced the piston ring tension by 22% compared to the previous model.

As a result of these developments, the total piston height was reduced by 8 mm compared to 125 cm^3 class engines of existing models, thus reducing the piston system weight by 28%. The employment of these friction reduction technologies reduced friction at an engine speed of 4,000 rpm by 5% as shown in Fig. 7.

4.3. Reduction of Friction by Lowering the Normal Cruising Engine Speed

In order to reduce the friction, which increases together with the engine speed, a high gear ratio was set to increase the displacement and achieve a low-speed, high torque type engine. This made it possible to set a low normal cruising engine speed. As shown in Fig. 8, the engine output was increased by approximately 20% compared to the previous model, and the engine speed at the same cruising speed was also reduced by approximately 20% compared to the previous model.

As a result, lowering the engine speed reduced the engine friction produced at the same cruising speed by approximately 23% compared to the previous model.

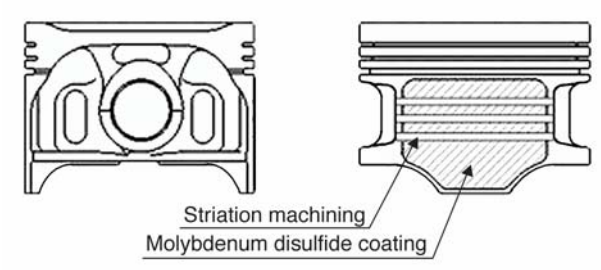


Fig. 6 Sectional drawing of developed piston

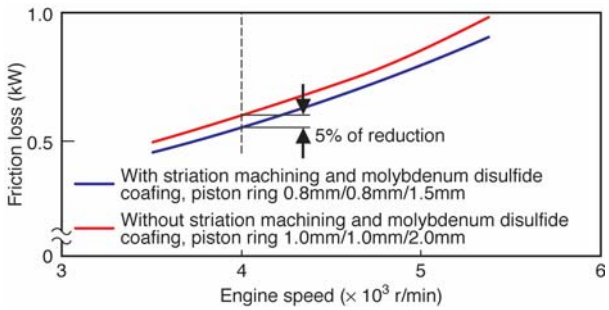


Fig. 7 Result of friction reduction by developed piston

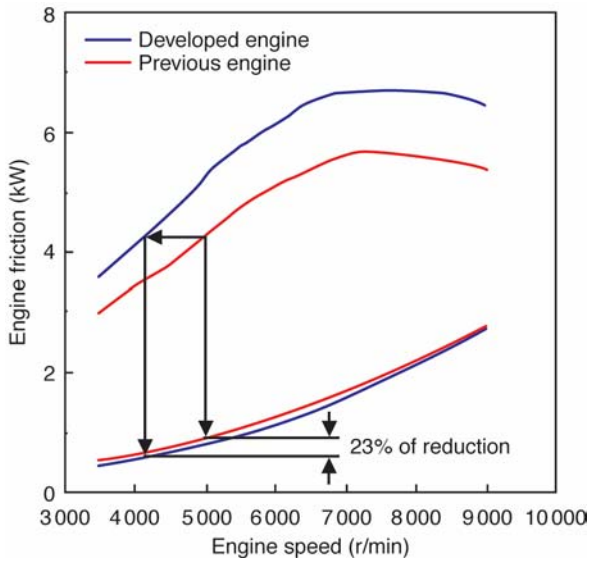


Fig. 8 Engine output and friction

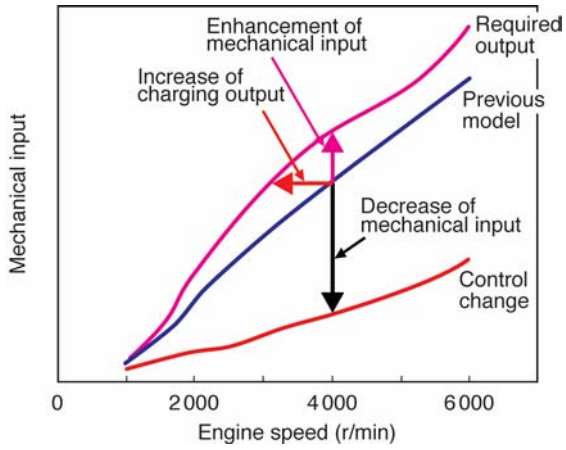


Fig. 10 Reduction of mechanical input

4.4. Reduction of Mechanical Input to the Generator

Reducing the engine speed also made it necessary to increase the charging output of the generator at low speeds.

However, simply increasing the generation capacity caused the mechanical input to the generator to rise due to the increased magnetic force. As a result, the mechanical input at an engine speed of 4,000 rpm increased by 20% compared to the previous model.

Therefore, the control system was changed as shown in Fig. 9 to reduce the generator friction. This system de-energizes voltage in excess of the prescribed voltage for the lighting side that was formerly short-circuited and became heat loss with conventional generation voltage control.

This made it possible to reduce the mechanical input to the generator even when increasing the charging output as shown in Fig. 10. As a result, the mechanical input value at an engine speed of 4,000 rpm could be reduced by 67% compared to the previous model.

4.5. Improvement of Combustion Efficiency by Optimizing the Ignition Timing

Simply advancing the ignition timing and increasing the compression ratio to improve combustion efficiency produces the knocking[(2)], which is undesirable. Therefore, control must be performed to change the ignition timing as required according to the throttle opening and the engine speed. To achieve this, a throttle opening detection switch was provided to the side of the carburetor throttle valve to detect the throttle opening. This switch is used to switch the ignition timing at a throttle opening of around 40%. Controlling the ignition timing as shown in Fig. 12 made it possible to avoid knocking which occurs easily at a throttle opening of 40% or more, and allowed the compression ratio to be increased from the 9.0 of the previous model to 9.3. As a result, BSFC at an engine speed of 4,000 rpm increased by 17%. Figure 13 shows a comparison of BSFC when the ignition timing is changed.

4.6. Fuel Consumption Improvement Results

Reducing friction in each part and increasing the combustion efficiency improved fuel consumption by 30% compared to the previous model. Figure 14 shows the measurement results for fuel consumption in ECE-40 mode.

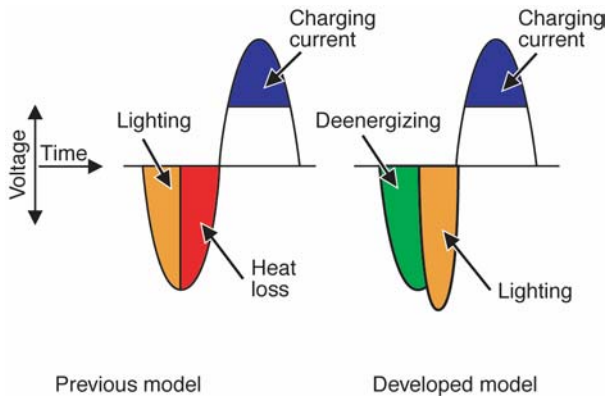


Fig. 9 Comparison of charging characteristics

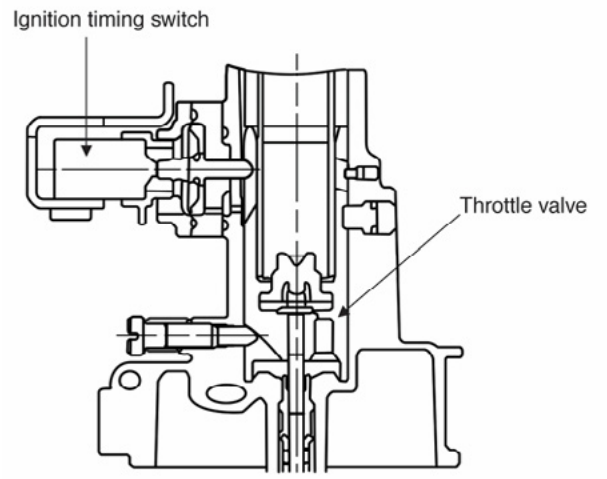


Fig. 11 Sectional drawing of developed carburetor

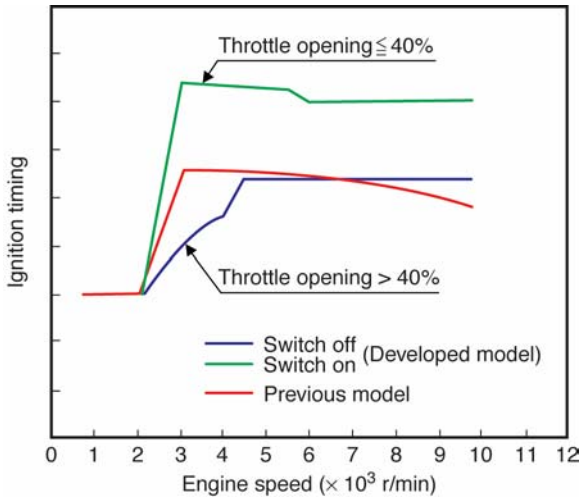


Fig. 12 Characteristic of ignition timing

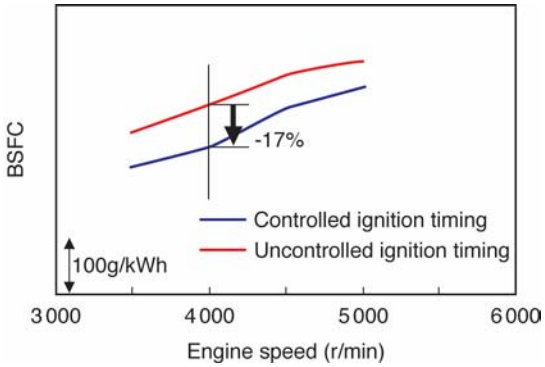


Fig. 13 Result of BSFC reduction by controlling ignition timing

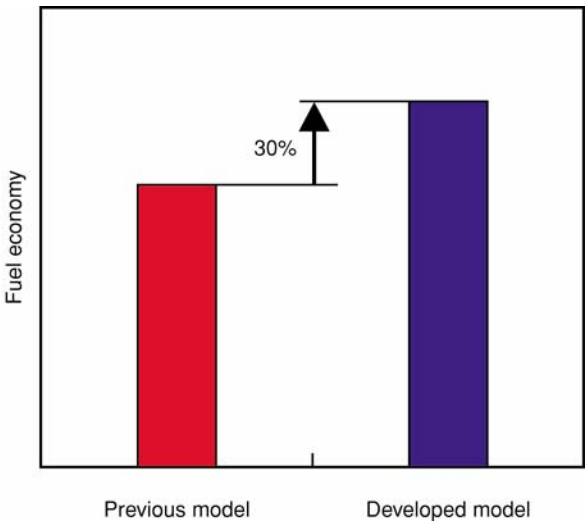


Fig. 14 Result of fuel consumption in ECE-40 mode

5. Reduction of Emissions

A secondary air pulse induction system[3] was added to the exhaust port to combust the unburned gas discharged from the combustion chamber to the exhaust port. Figure 15 shows the structural drawing. This system leads fresh air to the exhaust port with an air suction valve (ASV) utilizing the negative pressure generated at the exhaust port.

The employment of a secondary air pulse induction system reduced CO by 55% and HC + NOx by 60% from the Thailand 4th emission regulation values as shown in Fig. 16.

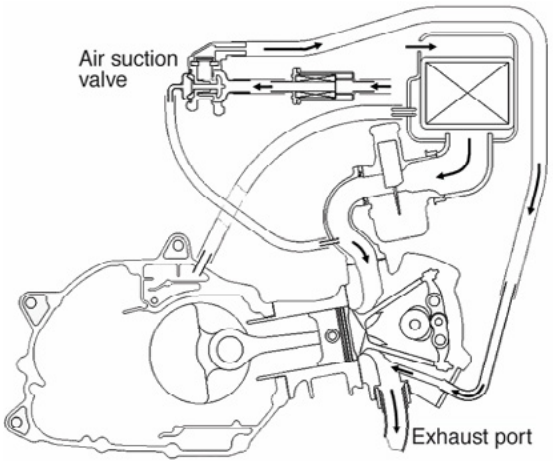


Fig. 15 Diagram of secondary-air pulse induction system

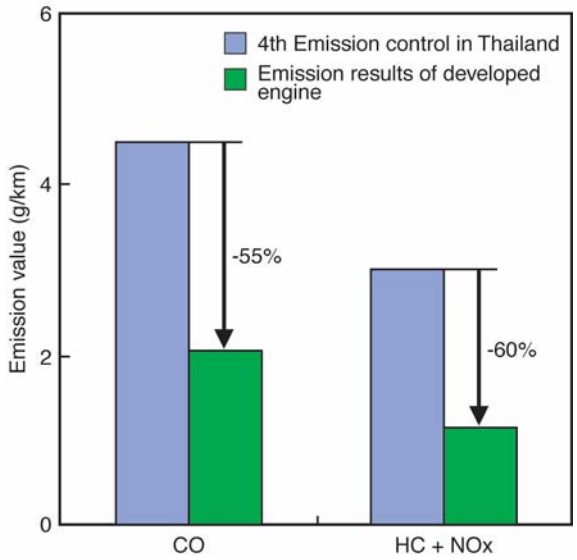


Fig. 16 Results of emission

6. Summary

The newly developed engine introduced technologies to reduce engine friction, improve combustion efficiency and reduce emissions. The following was achieved.

(1) Friction at an engine speed of 4,000 rpm was reduced by 23% compared to the previous model.
(2) Fuel consumption in ECE-40 mode was improved by 30% compared to the previous model.
(3) CO emissions were reduced by 55% and HC + NOx emissions were reduced by 60% from the Thailand 4th emission regulation values.

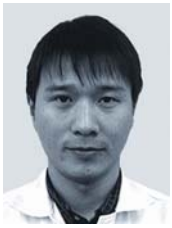
References

(1) Editorial Committee for Automobile Piston: Surface Treatment of Automobile Piston, Sankaido, Tokyo, p. 167-173 (1997) (in Japanese)

(2) Nakajima, Y., Muranaka, S.: Chapter 2 Enhancement of Fuel Consumption, Revision: Automobile Gasoline Engine, Sankaido, Tokyo, p. 29-31 (2001) (in Japanese)

(3) Nakajima, Y., Muranaka, S.: Chapter 4 Cleaning of Exhaust Gas, Revision: Automobile Gasoline Engine, Sankaido, Tokyo, p. 109-110 (2001) (in Japanese)

■ Authors ■


Yoshinobu SAWAMURA


Norio SAITO


Bunichiro SAKAMOTO


Hideo KOBAYASHI


Yoshihisa HIROSE

Development of an ECU Integrated Throttle Body System Module for a Compact Fuel Injection System Used in Small Motorcycles and Scooters

Nobuhiro SHIMADA* Shunji AKAMATSU* Minoru UEDA*
Akira HAYASHI* Yoshiaki HIRAKATA*

ABSTRACT

Concerns about environmental conservation continue to grow, increasing the demand for the reduction of exhaust emissions and enhancing fuel economy for small motorcycles. Therefore, electronic control fuel injection systems, which can finely control an air-fuel ratio, are being utilized. This time, the ECU integrated throttle body system for the electronic control fuel injection system, which is compact and low-cost, was developed for a small displacement engine. Features of this system include combining two modules. The modules are the throttle body module with several bore sizes in series and the ECU module with an electronic control unit, sensors, and an idling-air-control device. As a result, the complex wiring and piping were minimized, miniaturization was achieved, and a system that can be applied to single cylinder engines from 50 cm^3 to 250 cm^3 was achieved.

1. Introduction

Concerns about environmental issues have increased the demand for the reduction of exhaust emissions and increased fuel economy for small motorcycles. For example, Level 5 emission limits as shown in Table 1 are scheduled to take effect from 2003 in Thailand, one of the major markets for small motorcycles. These limits are predicted to become even stricter in the future. For this reason, electronically controlled fuel injection systems (hereafter referred to as “FI systems”), which can accurately control the air-fuel ratio, are increasingly being utilized to effectively reduce exhaust emissions and improve fuel economy. However, most FI systems thus far have only been mounted on large motorcycles with multi-cylinder engines[(1), (2)]. This raised the issues of higher costs and the size being too large for mounting on small motorcycles[(3)]. This study aimed to consolidate functions into a unit the size of a conventional carburetor and reduce both the size and cost by integrating the throttle body, various sensors and the engine electronic control unit (hereafter referred to as “ECU”) as a system module.

* Asaka R&D Center

2. Aim of Integrating the Throttle Body and ECU into a Single Module

In conventional FI systems for large motorcycles, the ECU is generally mounted on the chassis. In addition, the sensors needed to detect the information for control are positioned independently as separate units. Figure 1 shows an example of this layout. Therefore, many wire harnesses were required to connect these sensors with the ECU. As a result, these systems became quite complex, and application to small motorcycles was difficult. Integrating the throttle body, which controls the air intake volume, and the ECU module, which controls the engine operating status, eliminated the need for these wire harnesses. The module size was also reduced to the size of a conventional carburetor.

3. Test Engine Overview

An example of applying a European specification 4-stroke engine with a displacement of 125 cm^3 as the test engine is described below. The main specifications are shown in Table 2.

4. System Overview

Figure 2 shows the configuration of the ECU integrated throttle body system module. Splitting the structure into two parts, the throttle body and the ECU module, as shown in Fig. 3, made it possible to change the throttle body to the appropriate bore size to support engines with different displacements. This created a FI system configuration with a general-purpose and a high flexibility for application. The

Table 1 Current emission limits for motorcycles

	CO (g/km)	HC (g/km)	NOx (g/km)
Euro-3(<150cm^3)	2.0	0.8	0.15
Thailand Level 5	3.5	1.8	

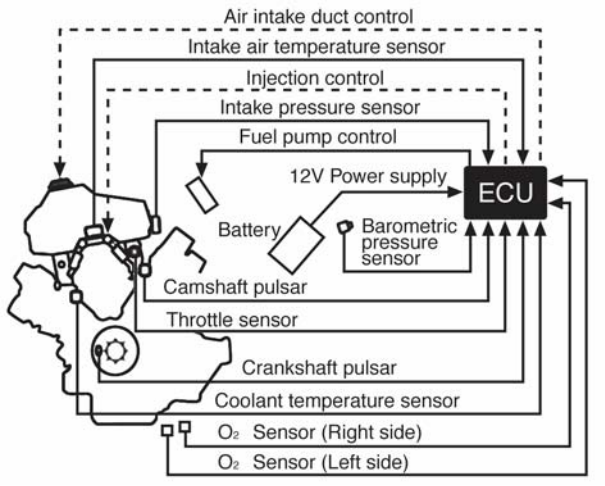


Fig. 1 VFR800FI system

Table 2 Test engine specifications

Items		Specifications
Bore × stroke	(mm)	52.4 × 57.8
Displacement	(cm^3)	124.6
Compression ratio		11.0
Valve system		OHC 2 valves
Max power	(kW/r/min)	9.66/9 000
Max torque	(Nm/r/min)	11.4/7 500

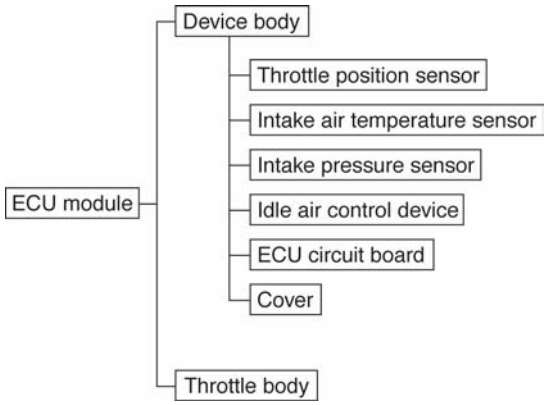


Fig. 2 ECU module components

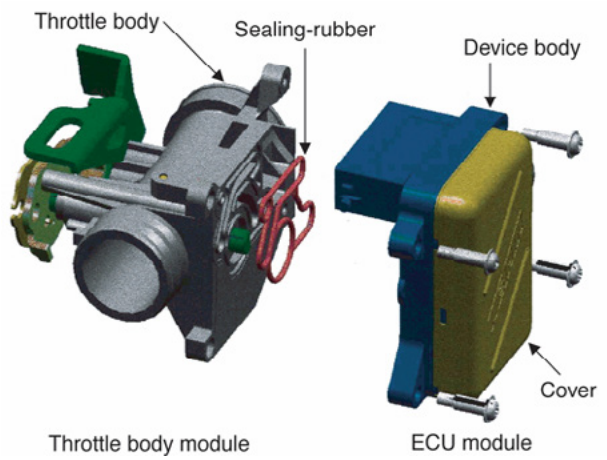


Fig. 3 ECU integrated throttle body system module

throttle body and the ECU module, which incorporates various sensors, are joined by four screws as shown in Fig. 3. In addition, grooves forming idle air passages are provided on the fitting plane on the throttle body side as shown in Fig. 4. These grooves are sealed between the ECU and throttle body with sealing-rubber. The ECU module is comprised of a plastic housing (hereafter referred to as “device body”), the ECU circuit board, and a cover. The device body incorporates various sensors, and the ECU circuit board is connected directly to the input-output terminals of these sensors. After the cover is set on the device body, the inside is filled with potting resin to secure and waterproof the sensors, circuit board and other parts.

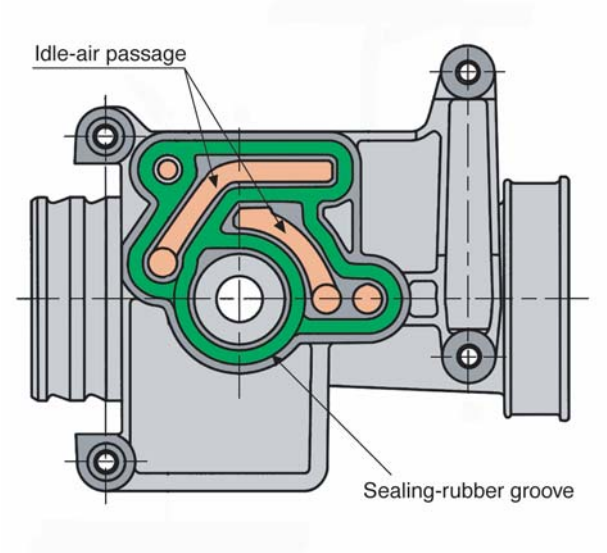


Fig. 4 Throttle body module fitting plane

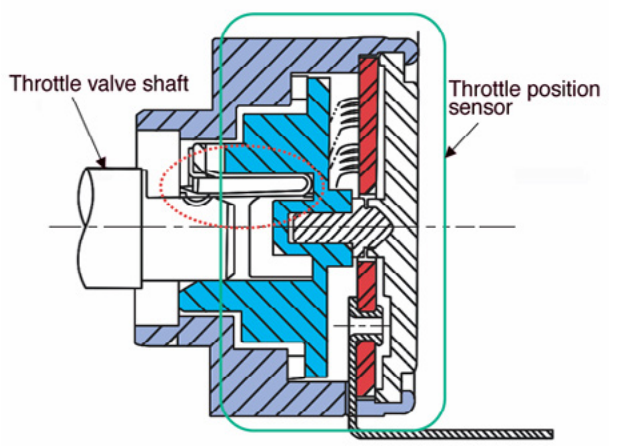


Fig. 6 Structure of throttle position sensor

4.1. Sensor Layout

This throttle body system module contains three sensors inside the device body. Figure 5 shows the sensor arrangements.

(1) Intake air temperature (Ta) sensor: The sensing element at the tip of the sensor is positioned, protruding from the inner surface of the intake air passage upstream from the throttle valve to allow measurement of the intake air temperature. A compact size is achieved by connecting the sensor terminals directly to the ECU circuit board.

(2) Throttle position sensor (TPS): This sensor is located at the end of the throttle shaft as shown in Fig. 6, and directly detects the throttle opening. The throttle shaft and the sensor rotor are joined via a spring that presses them in the direction of rotation in order to eliminate working hysteresis caused by the joint clearance. This TPS is fitted directly into the device body, and the external seal is secured by potting.

(3) Intake pressure (Pb) sensor: The sensor element is mounted directly on the ECU circuit board, and is connected to the communicating hole provided downstream from the throttle valve of the throttle body.

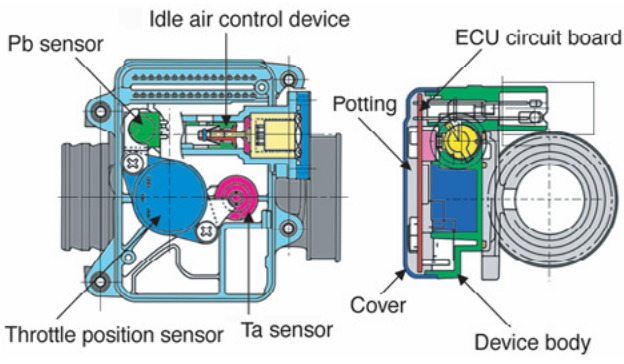


Fig. 5 ECU module components

4.2. ECU Circuit Board

The ECU circuit board utilized by this system was designed specially for single-cylinder engines. That is to say, designing a fuel injector drive circuit and an ignition circuit for a single cylinder made it possible to reduce the size and locate the ECU circuit board on the side of the throttle body. A 16-bit CPU was used as the controller. In addition, large elements such as the condenser in the power supply are positioned in the gaps between the various sensors inside the device body. This helped keep the overall width the same dimension as a conventional carburetor. The ECU circuit board has a 3-layer design with circuits on each of the four sides to reduce the area for each element circuit. In addition, the wire harness connector which accounted for a large space in the conventional ECU was changed to a 32-pin connector with a pin pitch of 2.6 mm, thus reducing the size to approximately half the conventional one as shown in Fig. 7. This pin pitch reduction was made possible by using an adhesive gel sheet for the connector waterproof structure. The number of pins was set at 32 to support the addition of future functions such as an immobilizer.

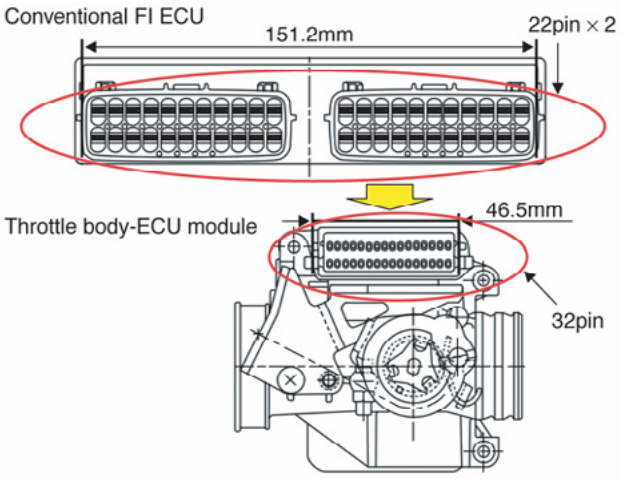


Fig. 7 Comparison of ECU size

4.3. Idle Speed Control Device

Engines for small motorcycles must control the intake air volume in smaller increments than large motorcycles. In addition, fine control capability is also required to support even stricter emissions limits. At the same time a small size is important to allow this system to be used. In order to meet these demands, this system employed a slide-valve-type air-control valve (hereafter referred to as "SACV") driven by a stepping motor. As shown in Fig. 8, the conventional direct-drive type needed a stepping motor with a diameter of 20 mm to ensure sufficient operating torque against the intake pressure. However, the developed SACV uses a slide type valve structure, which made it possible to reduce the stepping motor size to a diameter of 14 mm. There were concerns that using a SACV with a slide structure would produce hysteresis in the air volume due to the reciprocating action, but this was dealt with by eliminating the clearance in the valve thrust direction. Figure 9 shows the SACV idle-air volume characteristics. This graph shows that there is extremely little hysteresis in the idle air volume when the valve opens and closes, which indicates adequate control performance.

5. Mounting on an Actual Motorcycle

Figure 10 shows the overall layout of the test motorcycle. A plastic fuel tank is located in the center of the test motorcycle chassis, and a return-less type in-tank fuel pump unit is mounted inside this fuel tank. Fuel is sent from the pump at a pressure of 300 kPa through a high pressure fuel hose to the fuel injector mounted to the intake manifold. The throttle body system module is mounted to the intake manifold, which extends to the rear from the cylinder head via a rubber insulator. The unit swing type engine mount used in the test motorcycle is subject not only to its own vibration, but also the running vibrations from the road surface. Most

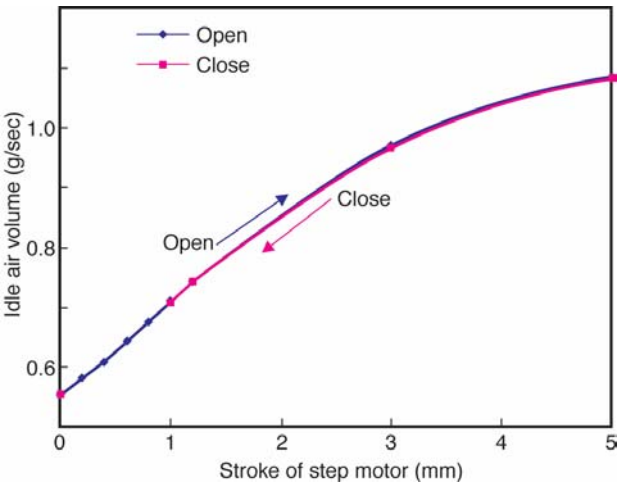


Fig. 9 Characteristics of idle-air volume

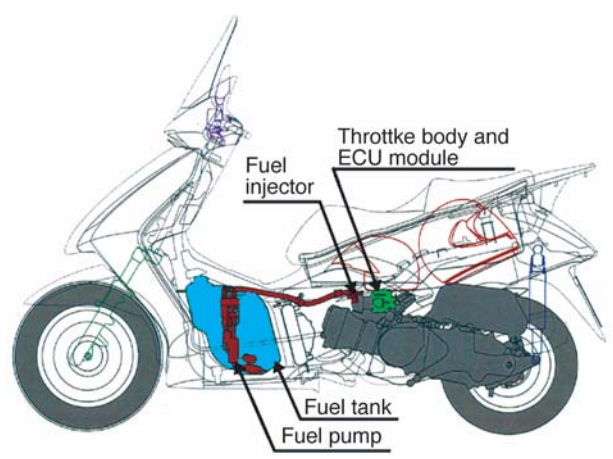


Fig. 10 Location of ECU integrated throttle body system module

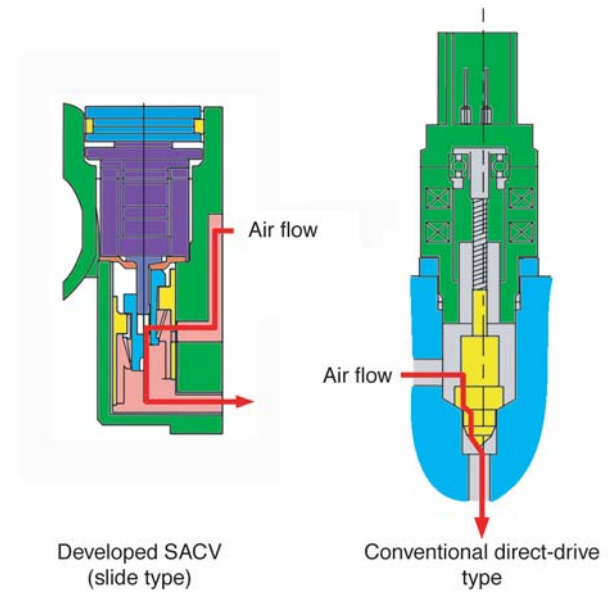


Fig. 8 Comparison of idle-air control valve

ECU thus far had been rubber-mounted to the frame body, and none had been mounted directly to the engine.

Figure 11 shows the engine vibration acceleration. This ECU module achieves high reliability under continuous high vibrations by securing the ECU circuit board, the sensors and the SACV stepping motor inside the device body with potting resin. In addition, the issue of heat was raised as a potential problem from mounting on the engine. Figure 12 shows the measurement data for temperature around the throttle body during running. The ECU reached its maximum temperature when the engine was returned to the idling state after full throttle operation. Therefore, a heat resistant plastic insulator was inserted between the engine and the intake manifold as a countermeasure to ensure ECU module heat resistance. Heat generation from the SACV stepping motor also caused the ECU temperature to rise, but the effects of this heat generation were canceled by stopping power to the SACV motor after the engine warmed up.

The test motorcycle employed an O_2 sensor and a 3-way catalyst as countermeasures for reducing emissions in order to support stricter emissions limits.

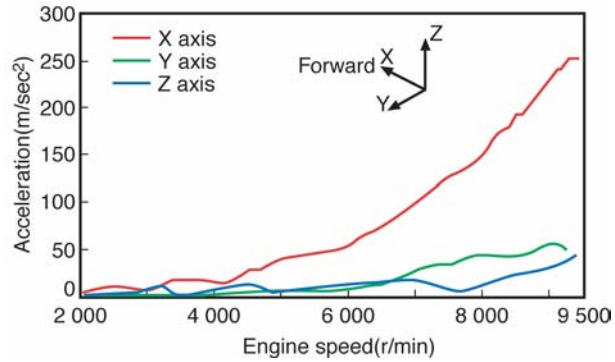


Fig. 11 Vibration acceleration on throttle body during no-load condition

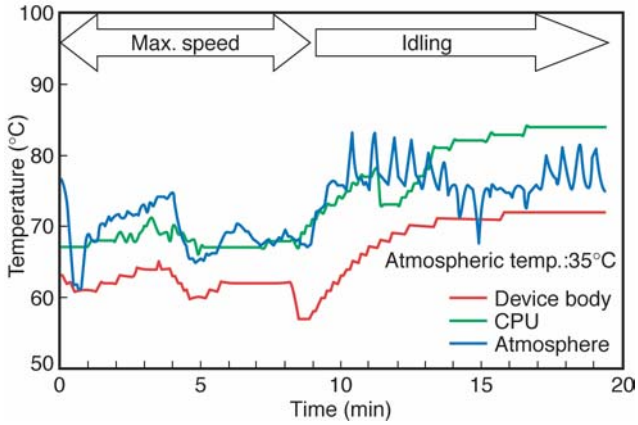


Fig. 12 Temperature rise characteristics (V max. to idle)

6. FI System Control

6.1. Control Outline

The developed FI system controls the fuel injection volume, injection timing and ignition timing based on the signals from the TPS and Pb sensors located inside the ECU module and the crank position sensor, which detects the angle of rotation. Compensation is also performed according to the coolant temperature, the intake air temperature and the atmospheric pressure to control the fuel injection volume, injection timing and ignition timing to the optimum values with respect to changes in environmental conditions.

6.2. Fuel Injection Control

The fuel injection volume control method consists of switching between two different injection volume maps according to the throttle opening and the engine speed.

(1) Under low load conditions minute changes in the throttle opening are detected by the engine intake pressure and it uses the intake pressure injection volume map determined by the engine intake pressure and the engine speed.

(2) Under high load conditions it uses the throttle opening injection volume map determined by the throttle opening and the engine speed.

6.3. Ignition Timing Control

The ignition timing is controlled to achieve the optimum ignition timing using a map determined by the throttle opening and the engine speed.

6.4. O_2 Feedback Control

In order to efficiently utilize the performance of the 3-way catalyst mounted inside the exhaust muffler, a feedback system using an O_2 sensor is employed to control the air-fuel ratio to the stoichiometric ratio.

6.5. Control of Idle Speed Control Device

The SACV controls the intake air volume according to each operating condition of starting up, warming up and idling. As shown in Fig.13, when starting up, the intake air volume is increased to improve the start-up performance by opening the idle air control valve according to the engine coolant temperature. Then, as the engine coolant temperature rises, the valve opening is adjusted to control the intake air volume to the optimum value.

After the engine coolant temperature reaches the set value, the intake air volume is controlled using engine speed feedback control to maintain a constant idling speed. This feedback control eliminates the need for maintenance to cope with changes in the idling speed over time, which formerly required adjustment.

7. Results of Employing the New FI System

A test motorcycle using the new FI system achieved the following results compared to a model using a conventional carburetor, the introduction of secondary air to the exhaust port, and an exhaust catalyst system.

(1) Exhaust emissions: CO and HC emissions were reduced by approximately 50% as shown in Fig. 14.

(2) Fuel economy: Fuel economy was improved by approximately 10% compared to the conventional model as shown in Fig. 15.

(3) Cold start-up and warm-up performance: The new FI system and air control device achieved excellent engine start-up and warm-up performance as shown in Fig. 16.

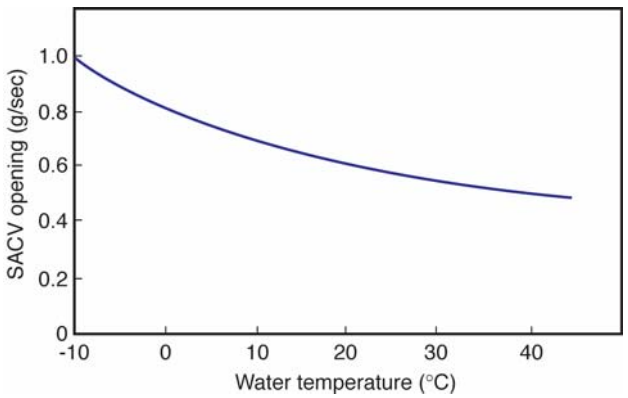


Fig. 13 SACV opening characteristics

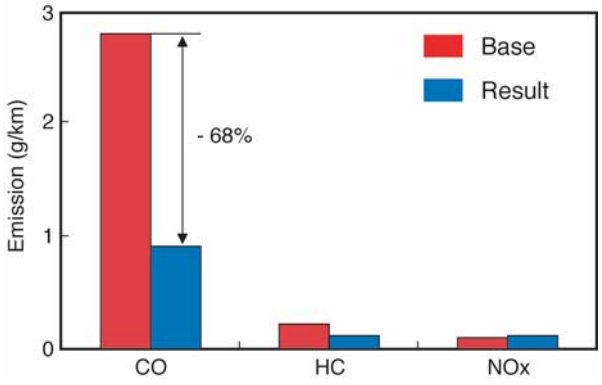


Fig. 14 Test results of ECE40 mode emission

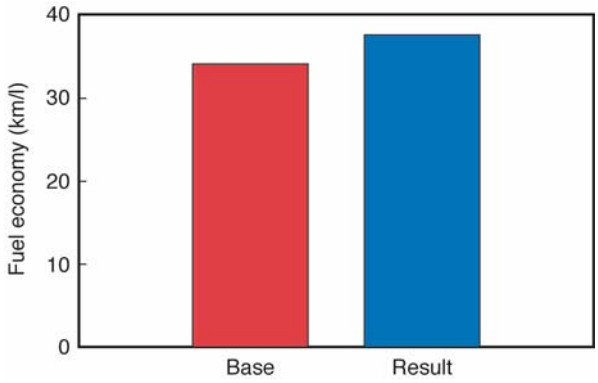


Fig. 15 Test results of fuel economy by ECE40 mode

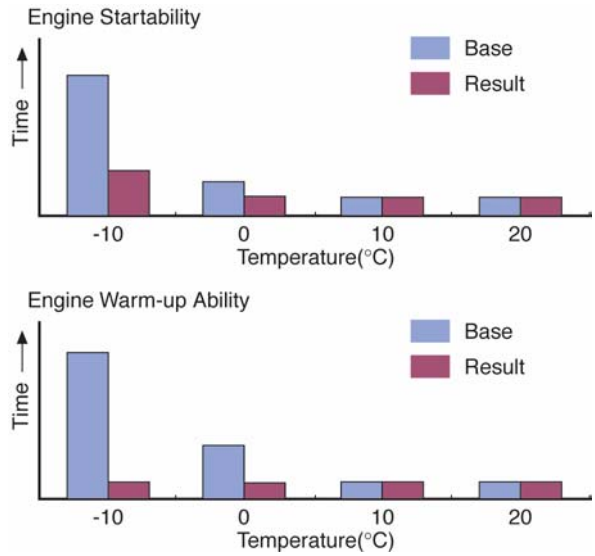


Fig. 16 Result of engine startability and warm-up ability

8. Summary

Development of this ECU integrated throttle body system module realized the following results.

(1) Integration into a module made it possible to eliminate the wire harnesses for the sensors, ECU and other parts that have become quite complex in recent years, and allowed the ECU module size to be reduced to the same size of a conventional carburetor. In addition, the system cost was also approximately the same as a conventional carburetor system.

(2) CO and HC emissions were reduced to approximately half that of conventional carburetor systems, and fuel economy was improved by approximately 10%.

(3) The newly developed compact SACV assembled into the module achieved stable and excellent start-up and warm-up performance.

The use of these technologies made it possible to employ a FI system to small motorcycles, which account for the majority of the market, without substantial changes to the layout. This is expected to accelerate the application of FI systems to small motorcycles, thus further improving emission purifying and fuel economy.

References

(1) Horiike, S., et al.: Exhaust emission reduction technology for the VFR800FI, HONDA R&D Technical Review, Vol. 10 (1998)

(2) Horiike, S., et al.: Exhaust emission reduction for the VFR800FI, International Motorcycle Conference “Safety, Environment and Future II”, p. 459-475 (1998)

(3) Akamatsu, S., et al.: Research of an Emission Reduction System for Small Motorcycles, International Motorcycle Conference: Safety, Environment and Future III, p. 291-309 (1998)

■ Authors ■


Nobuhiro SHIMADA


Shunji AKAMATSU


Minoru UEDA


Akira HAYASHI


Yoshiaki HIRAKATA

Development of Engine Rock Dampers for the Manual Transmission 2003 Acura 3.2CL Type-S

Michael THOMPSON* Atsushi YONEYAMA*

ABSTRACT

Engine mount development for the manual transmission 2003 3.2CL Type-S included the use of engine rock dampers, a new technology for Honda. A damper mounted between the engine and subframe with isolation rubber to control engine-roll motion was developed as a countermeasure to improve shock hunt. Engine rock dampers are found to be an effective means of controlling engine roll stiffness for transient torque input. Shock hunt targets are achieved, sports coupe drivability is maintained, and marketable noise and vibration levels are preserved.

1. Introduction

The goal of the engine mount development for this vehicle was to achieve a marketable throttle tip-in acceleration feeling without compromising the drivability expectations of the sporty coupe driver. Shock hunt describes the undesirable acceleration feeling upon throttle tip-in. These phenomena would be commonly described as jerkiness under acceleration. The initial jerk after applying the throttle is shock. The 'back and forth' feeling after the shock is hunting. Generally the primary engine mount technical concern for front-engine front-drive manual transmission vehicles is shock hunt.

The 3.2CL presented certain challenges from a shock hunt standpoint. The powertrain generates 232 lb-ft of torque, more than any other Honda with a manual transmission. The drivetrain layout, front drive with a transverse front engine, is fundamentally weak for shock hunt. Reducing shock hunt levels imparts the vehicle with a stable and secure feeling under acceleration.

This report will detail the development of engine rock dampers as part of an engine mount system that is compatible for shock hunt as well as noise and vibration.

2. Shock Hunt Mechanism

The shock hunt time history data below (Fig. 1) shows the longitudinal acceleration experienced upon abrupt and heavy throttle application. Average acceleration is the rate of the vehicle acceleration forward. Overshoot equals the difference between peak acceleration and average acceleration. Overshoot describes shock. Hunting is the sinusoid portion of the acceleration time history as it decays to steady state.

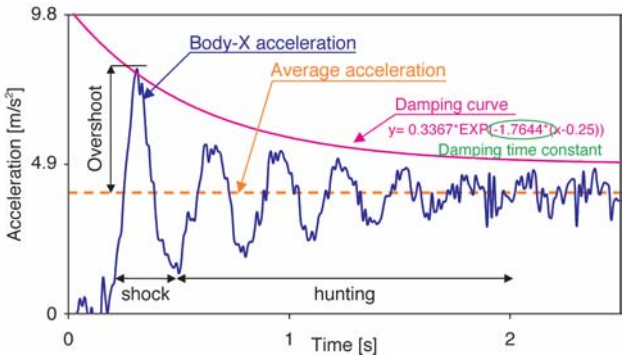


Fig. 1 Shock hunt acceleration time history

* Honda R&D Americas, Inc.

The main cause of shock hunt is the powertrain 1st order torsional resonance. As the simplified model below illustrates (see Fig. 2), the primary springs for this system are the driveshaft, clutch spring, and engine mounts. Important masses include engine mass and flywheel inertia. The input for this system is transient engine torque. If the mounts have nonlinear characteristics, the engine roll resonance and sometimes the suspension's unsprung resonance can also contribute to shock[1].

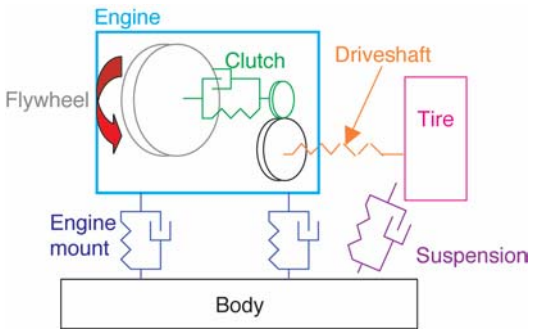


Fig. 2 Simple powertrain model for shock hunt

Generally the primary shock hunt concern is coupling of engine front to back motion and powertrain torsional resonance. The frequencies of engine roll and suspension resonances are higher than powertrain 1st order, but their effect can be seen in multiple peaks within the main shock peak. Figure 3 shows the typical frequency ranges of areas important for shock hunt.

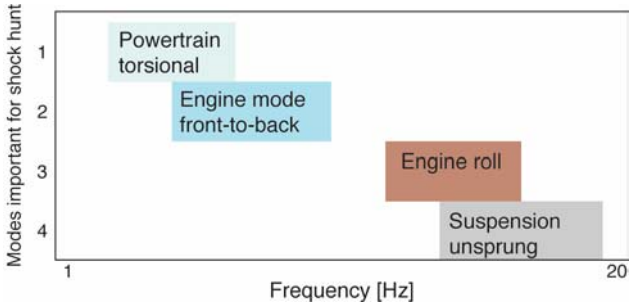


Fig. 3 Shock hunt primary and secondary modes

For the 3.2CL engine roll stiffness is very important. Since engine torque is high, drive reaction force at the mounts are much larger than a typical car. Therefore, it is very important to control roll stiffness with engine mounts.

3. Typical Shock Hunt Countermeasures

Typical shock hunt countermeasures can be broadly grouped into three categories: software, powertrain, and chassis. Software countermeasures include ignition retard and throttle response control. Relying solely on software to meet shock hunt targets would result in a vehicle that feels sluggish. Other countermeasures offered a better solution for the 3.2CL Type-S sporty image.

On the powertrain side, the 3.2CL applied a dual mass flywheel. This imparted the vehicle with a very flat clutch-spring characteristic, which is a good direction for shock hunt. The negative of the dual mass flywheel is lighter engine-side mass as compared to a conventional flywheel. Increasing the mass of a conventional flywheel reduces shock hunt level, but can result in a vehicle that feels slow to respond.

Finally, chassis countermeasures, including engine mount stiffness, damping, and stopper characteristic tuning are available to control shock hunt. Mount characteristics are especially important if the engine roll mode is contributing to shock. Increasing engine mount stiffness reduces powertrain peak acceleration and also helps keep the movement within the linear segment of the mount's stiffness characteristic (see Fig. 4). However, increased mount stiffness also reduces isolation between the engine and body, resulting in higher noise and vibration levels. Mount damping can also be used to diffuse shock hunt, but effectiveness is limited. Increasing damping is basically limited to changing material, typically up to 10% due to other engine constraints.

Stopper characteristic tuning is important if the mount is contacting its stopper in the shock hunt driving mode, targeting smooth and linear engagement.

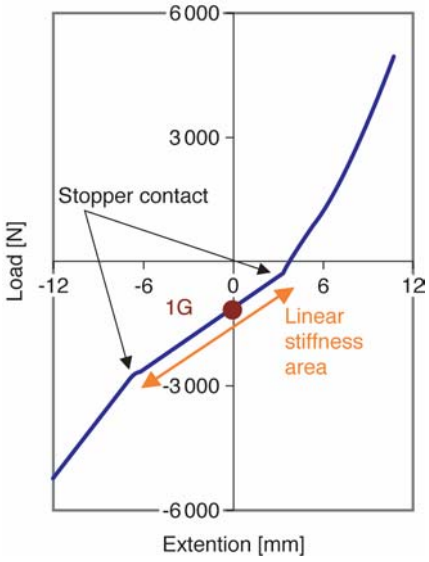


Fig. 4 Engine mount and stopper characteristic

Every countermeasure has tradeoffs. A new chassis countermeasure to improve shock hunt was required. To maintain a sports car image, a limited reliance on ignition retard and minimizing flywheel inertia were important for this vehicle. Therefore, the 3.2CL applied a new chassis countermeasure to meet shock hunt targets.

4. New Shock Hunt Countermeasure

Engine rock dampers offer the opportunity to dramatically increase stiffness and damping in a dynamic event while maintaining relatively low stiffness under

conditions where engine movement and velocity are small. Of the typical shock hunt countermeasures, only increasing powertrain roll stiffness would maintain the vehicles sporty character and have enough impact to meet shock hunt target. However, in order to maintain noise and vibration performance, the engine mount system could not be stiffened sufficiently by conventional means to meet the shock hunt target. Therefore, engine rock dampers were considered as a new countermeasure. The engine rock damper is a dashpot/absorber mounted between the engine and subframe (see Fig. 5).

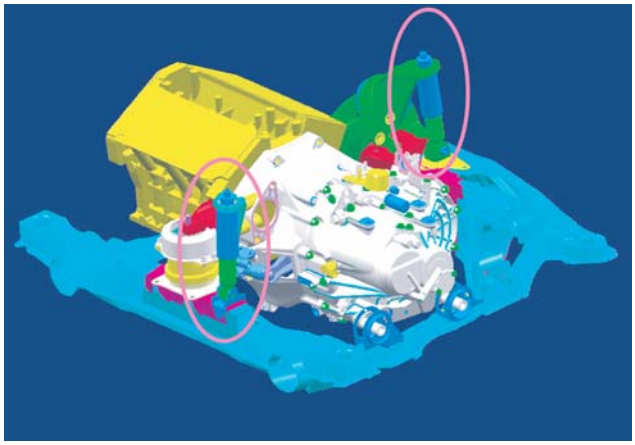


Fig. 5 3.2CL engine mount layout

The engine rock damper (Fig. 6) consists of a soft upper bushing which sandwiches a bracket attached to the engine. Engine movement compresses the upper bushing and displaces the damper piston. The lower bushing is very stiff and experiences little deflection. This construction is very advantageous for 3.2CL application. At shock hunt driving mode, the damper experiences large displacement at approximately 3 Hz where damping force is high. Under steady-state conditions, the damper is not moving and the relatively soft upper bushing offers isolation.

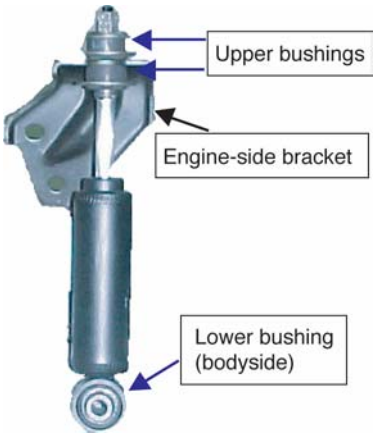


Fig. 6 Engine rock damper

In a dynamic event with large gross engine displacement, engine rock dampers provide additional stiffness to the engine mount system. Figure 7 shows the load borne by the rock damper peaks 0.03 seconds before that of the engine mount. The rock damper distributes the shock to the body over a longer period than conventional engine mounts. This smoothes the peak acceleration experienced by the body.

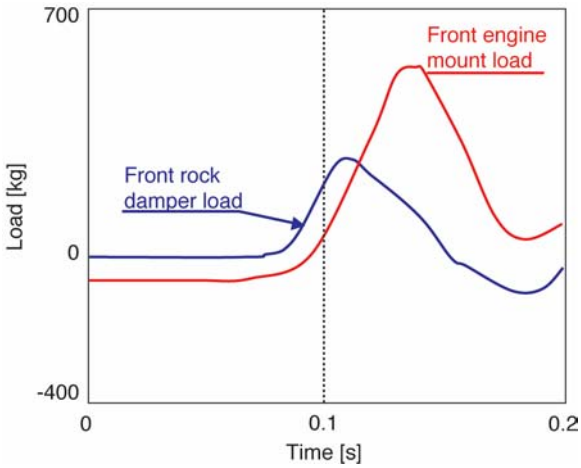


Fig. 7 Rock damper and engine mount loads in shock

The damping characteristic, not including the upper bushing, has the shape seen in Fig. 8. Positive damping force is bump or compression. The plot illustrates the peak damping force value for each velocity. At lower piston velocities, and for those in the shock hunt driving mode, bump and rebound have similar stiffness characteristics. Over 200 mm/s stiffness in bump remains flat, while stiffness in rebound continues to increase. However, this is outside of the shock hunt driving mode.

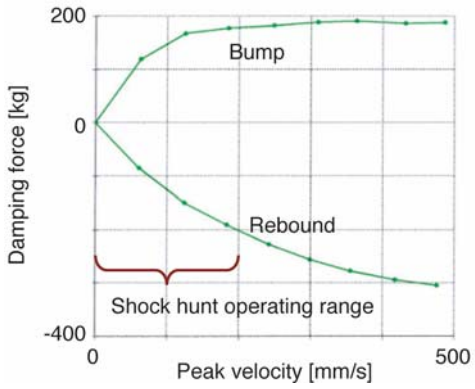


Fig. 8 Rock damper damping force

Rock dampers offer a large increase in stiffness and damping of the engine mount system in engine dynamic events, like shock hunt. When the rock damper piston is not moving, static friction effectively makes the damper rigid. The upper bushing affords isolation between the engine and the body.

5. Shock Hunt Result

Using engine rock dampers, engine dynamic roll stiffness and damping were increased to meet shock hunt targets. Peak body acceleration was reduced by 25%. Target of 3 [m/s^2] overshoot for shock and –1.6 hunting time constant was achieved (see Fig. 9 and 10). Adding rock dampers increased peak dynamic roll stiffness of the engine mount system 45% in shock. In hunting, dynamic roll stiffness is increased approximately 30%.

Below on the shock judgment chart (Fig. 9), the vertical axis is overshoot, the height of the first peak over average acceleration. The vertical axis on the hunting chart (Fig. 10) is the time constant of an exponential curve fit to the hunting peaks (see Fig. 1).

Rock dampers increase powertrain transient natural frequency by 5%, from 3.25 to 3.42Hz. Steady-state movement does not change. Peak overshoot movement is reduced 45%. See Fig. 11. Rock dampers are velocity devices and have little static stiffness. Final engine position under acceleration does not change, but transient movement is reduced. Stiffness of the rock damper in shock is very high due to high engine velocity.

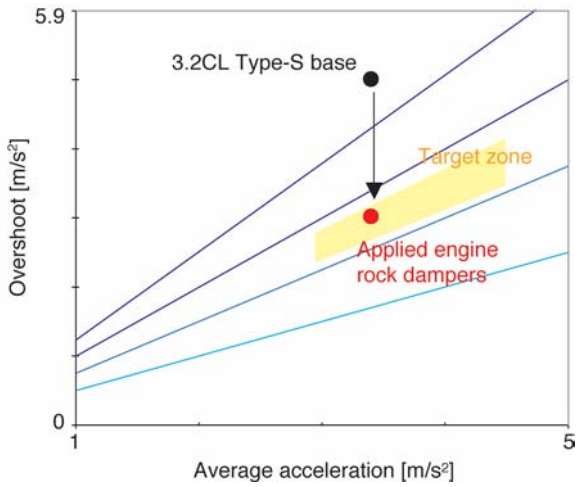


Fig. 9 Shock judgment chart - 2nd gear WOT

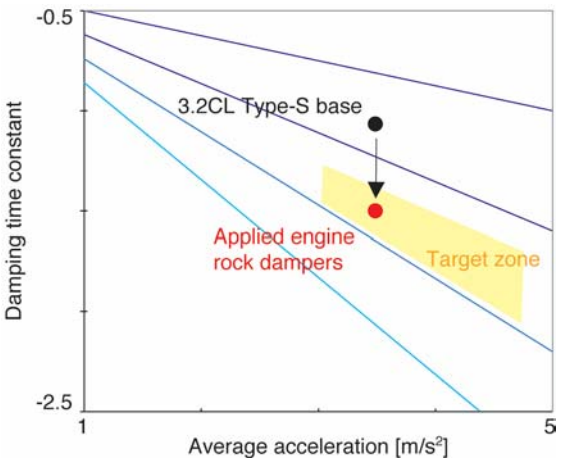


Fig. 10 Hunting judgment chart - 2nd gear WOT

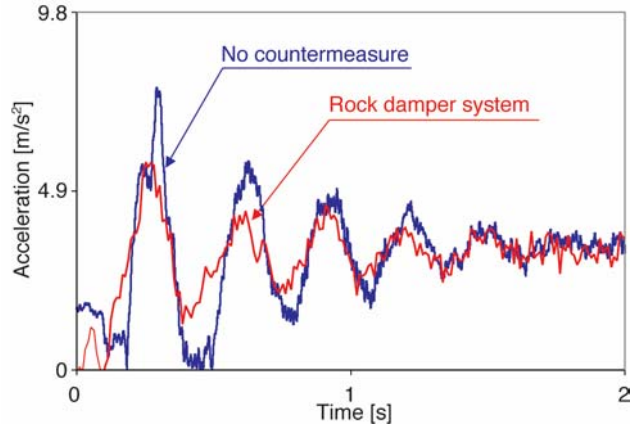


Fig. 11 No countermeasure vs. rock damper system shock hunt time history

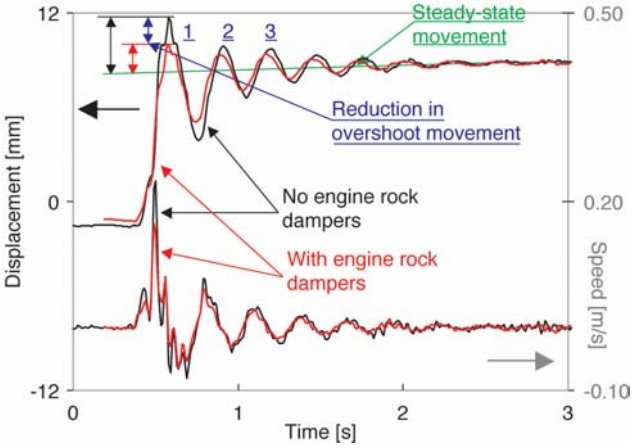


Fig. 12 Rock damper displacement and velocity - 2nd gear WOT

Rock dampers add roll stiffness and damping to an engine mount system in dynamic events. Applying engine rock dampers reduces engine overshoot movement. Figure 12 shows the effect of rock dampers on the first three cycles of engine overshoot movement. Figure 13 expresses the reduction in movement for the first three cycles as a percent increase in stiffness. The percent increase in stiffness for each point is plotted against roll frequency. Roll frequency for each cycle is analyzed from measured data using the inverse of time from peak-to-valley divided by two.

In shock, engine mount dynamic roll stiffness is increased 45% by adding engine rock dampers (Fig. 13). Damping force drops off as engine movement slows down and damper displacement is reduced. At steady state, when the rock damper is no longer moving, static friction locks the damper and the upper bushings alone contribute to mount system stiffness.

To achieve shock hunt target, the 3.2CL requires a rock damper rate of 1500N at 120 mm/s (see Fig. 14).

Although roll stiffness is significantly higher in a dynamic event; any increase in static stiffness in steady-state conditions comes only from the upper bushing. Shock hunt body acceleration levels experienced by the driver achieve targets.

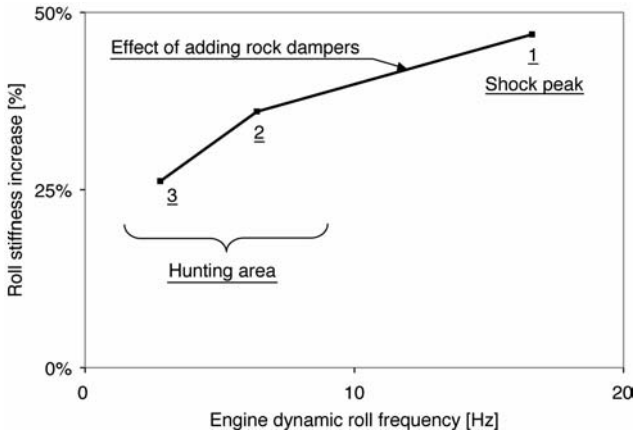


Fig. 13 Dynamic stiffness increase to engine mount system by adding rock dampers

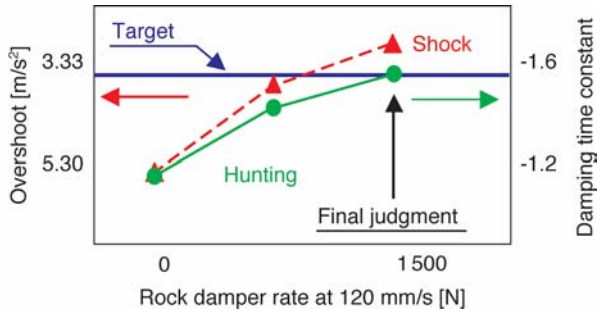


Fig. 14 Rock damper rate effect

6. Engine Rock Damper Tradeoffs

6.1. Idle Vibration

Idle vibration in the seat and steering wheel is heavily influenced by the engine roll mode in vehicles with V6 engines. Rock dampers reduce isolation between engine and body by 4dB. The 3.2CL required additional countermeasures for idle noise and vibration. Sporty car idle targets were achieved with the following countermeasures: bumper beam dynamic damper, idle engine speed increase to 790 rpm, and tuning of the steering dynamic damper. See Fig. 15.

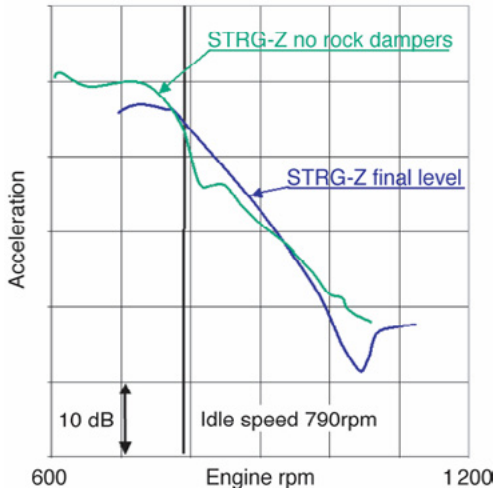


Fig. 15 3rd order steering vibration

6.2. Engine Noise

Engine noise during acceleration increased throughout the engine speed range but no bad feeling peaks were created. The increase in noise was judged acceptable for a sporty car.

7. Conclusion

Rock dampers are a very effective countermeasure for shock hunt. Rock dampers are able to provide a significant increase in engine roll stiffness in a dynamic event while remaining relatively soft at steady state. Shock hunt acceleration levels experienced by the driver are reduced to meet targets. Acura 3.2CL Type-S shock hunt feeling improved to an acceptable level by applying engine rock dampers without compromising drivability expectations of the sporty car driver. Marketable noise and vibration levels are preserved.

Reference

(1) Inoue, M.: “Analysis on Acceleration / Deceleration Shock and Vibration in FF Vehicle”, Proceedings Journal of Society of Automotive Engineers of Japan 921087 (1992)

■ Authors ■


Michael THOMPSON


Atsushi YONEYAMA

Gesture Recognition Algorithm for Understanding Man-Machine Interaction and Its Adaptation for New ASIMO

Nobuo HIGAKI* Taro YOKOYAMA* Kikuo FUJIMURA**

ABSTRACT

An image-based gesture recognition module has been developed as a part of the biped walking humanoid robot ASIMO's man-machine interaction function in order to enhance its autonomy. ASIMO recognizes human gestures based on statistical analysis, using spatio-temporal variance of the three-dimensional (3D) positions of the face and hand. It is able to distinguish 10 kinds of gestures and postures on both the left and right side. It is also able to recognize a position pointed to by an operator from the relative position of the operator's head and hand and from the direction of the arm. This is calculated by PCA (Principal Component Analysis) on a 3D-point set observed in the proximity of his arm. These components are implemented in a layered structure to reduce complexity, and in an optimally designed communication structure to minimize processing resources. This effort has resulted in a comprehensive image processing system in ASIMO's onboard computer.

1. Introduction

At the end of October 2000, Honda introduced an upgraded version of ASIMO, a small humanoid robot that could adapt to the human living environment[(1)]. The objective was to develop a robot that would actually serve a useful role in close proximity to human beings. This ASIMO was then improved and a new model equipped with a man-machine interaction function and network connectivity was announced in December 2002 (Fig. 1).

ASIMO has previously served in various ways as an attraction and performed reception duties at a variety of locations, thereby gradually gaining acceptance in human society. The former ASIMO, however, performed such actions as walking and shaking hands through handling by an operator who used a remote terminal or portable controller. The robot was not able to interpret human pointing and perform interactive actions autonomously. ASIMO will need to understand human actions and perform actions in collaboration with human beings if it is to evolve into a robot that can be useful to human beings in human society.

Now the previous ASIMO's systems have been expanded by equipping it with a man-machine interaction function using image processing in order to make it a humanoid robot

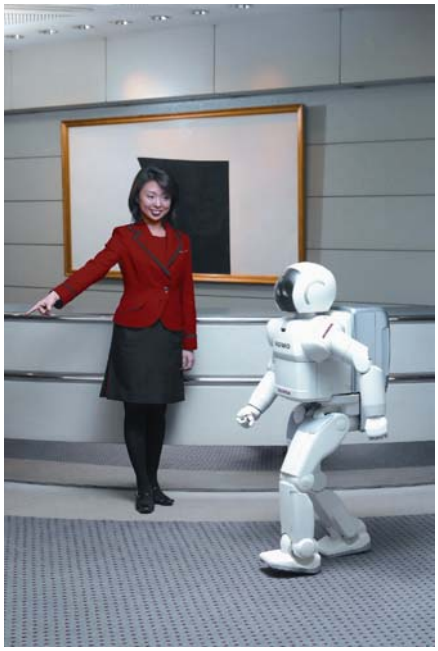


Fig. 1 New ASIMO

* Wako Research Center
** Honda Research Institute USA, Inc

that is endowed with autonomy[2].

In general, people find it easier to understand what a robot is doing if it has a humanoid configuration, which also suits the robot for coexistence with human beings in ordinary environments. When giving movement instructions to a humanoid robot by pointing, however, people tend to deal with it in the same way they deal with other people, because it does have a human-like shape. This means that greater value is placed on the capability for communication with human beings than is the case for robots with other configurations.

The means of communication most used among human beings is the voice, whereas communication using gestures fulfills a role of nearly equal importance. Communication by gesture becomes even more important when pointing to a general location, when verbal expression would tend to become wordy, and in cases when the voice would not reach the recipient. Communication using gestures is also effective in conveying nuances that are not easily expressed in words.

Many different proposals have been made for research on gesture recognition. A natural interface with a robot would best be achieved by a means of recognition through non-contact sensors that use image information and so on, since these do not require wearable sensors such as magnetic sensors and data gloves, which impose bodily restraints[3]. The methods of gesture recognition using image processing that have been proposed so far, however, have involved such issues as fixed cameras[4, 5], numerous limitations with respect to backgrounds and human images[6], high computation costs and the need for dedicated processing systems[7], and so on.

The image processing system installed in ASIMO, in particular, demands high-speed techniques that can carry out actions at the same time it handles image processing for face recognition, obstacle recognition, and so on, as well as the gesture recognition that is the subject of the present report. Although this does have the advantage of being able to utilize other processing results, the combination of multiple image processing functions generally makes processing more complex. Even if it were possible to provide greater functional variety and higher reliability, the computation costs become very high, as noted above, and these issues hinder real-time processing. Moreover, even if the different processes could be carried out by single functions, it would be extremely difficult to deal with those functions in an integrated manner.

This paper reports on gesture recognition processing as a real-time and on-board operation that is conducted together with image processing, including face recognition and obstacle recognition.

2. Overview of the Image Processing System

Figure 2 shows an overview of the image processing system installed in the new ASIMO.

The image processing system is made up of two CCD cameras installed in ASIMO's head and a frame grabber and PC board that performs image processing that are installed in ASIMO's body. The angles of each of ASIMO's joints and other such posture information required to compute camera positions and angles and other such camera parameters used during image processing are held in memory on an electronic control unit (ECU) board.

The computer used for image processing is a commercially available PC board with a CompactPCI bus.

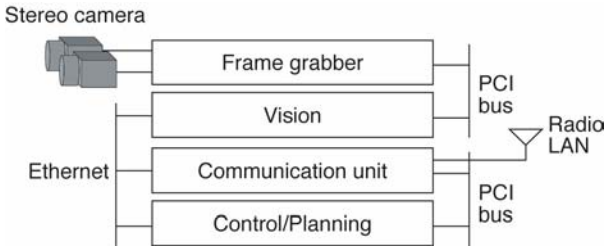


Fig. 2 Image processing system

The computer CPU is a 1.2-GHz Intel Pentium III-M.

A pair of CCD cameras are used to capture images in order to obtain depth information by stereo vision.

A frame grabber is used to capture the image signals output by the cameras. When using stereo vision to identify the location of an object in real space, the frame grabber must acquire the camera parameters matched to each image. For this reason, the frame grabber was designed with the capability for a synchronization signal to synchronize each image with its camera parameters. This makes it possible to perform accurate image processing of time-varying images captured by moving cameras without a need for complex processing.

3. Image Processing Algorithm

3.1. Overview

Figure 3 shows the software configuration of the image processing unit.

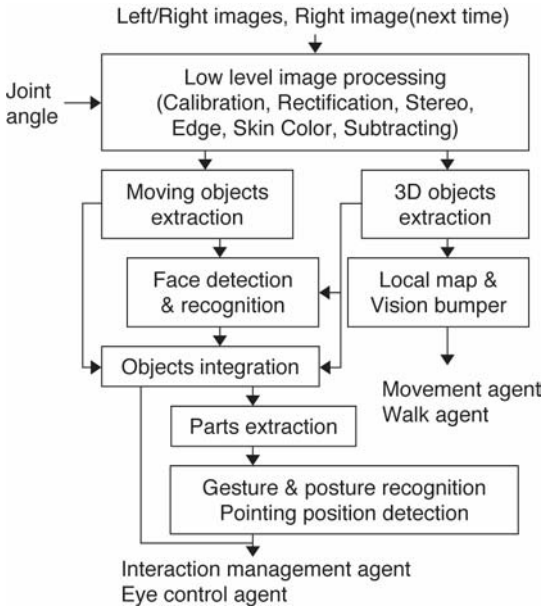


Fig. 3 Vision system software configuration

The images input from the cameras are processed by a low-level image processing unit to correct distortions (upper left row in Fig. 4). This is then followed by computation of depth information (right middle row in Fig. 4), edge information (left lower row in Fig. 4), skin color region information (right lower row in Fig. 4), and movement region information (left middle row in Fig. 4).

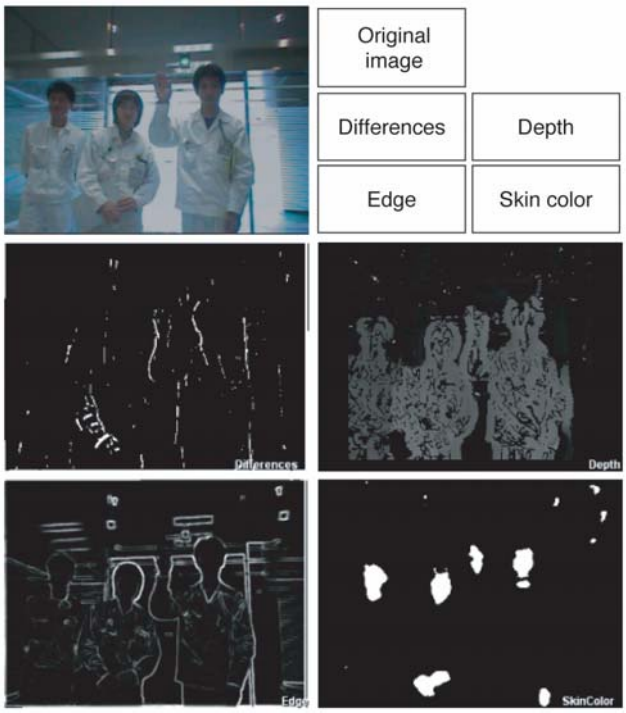


Fig. 4 Preprocessing images

Depth information is obtained by stereo processing using block correlation. Edge extraction is carried out using a Sobel operator. The skin color region is extracted by threshold value operation over the HLS (hue, lightness, saturation) space. Movement region information is extracted by a finite difference calculation after background movement has been estimated from the variance between the image and the camera parameters and the image has been aligned with the background.

These items of information provide the basis for moving object extraction, 3D object extraction, and face detection object extraction processing. At that point integrated processing of the object is carried out in order to integrate the objects within each frame and to process the objects across frames accordingly.

Next, extraction processing is performed on each object or on each object that is subject to tracking, and finally recognition processing is performed for gesture and posture recognition and pointing position detection. After this, the processing results are sent to the human-machine interaction processor and fed back into action by the robot.

Thus the processes in this system are layered through the object extractor, parts extractor and recognition unit, and the process results are put together at each layer in order to keep the processing from becoming complex. At the same time, information from other processes is used effectively so that the search area for each process is kept limited. Means such as these were used to reduce the computation costs and achieve operation at 100 – 200 msec/frame with on-board equipment.

The various processes from object extraction to gesture and posture recognition and pointing position detection are described below.

3.2. Moving Object Extraction

This process performs extraction of the person (moving object) who is the object of gesture recognition. First, the depth, edge, and movement information obtained by low-level image processing are used to establish an approximate rectangular solid region that covers the moving object. Then more detailed shape and position information are extracted from the image information within that region.

In the depth direction, the depth d is extracted from the depth information and movement information taken from the camera that has the largest number of edge points in motion. That value is used as a reference in setting the object depth range for processing.

Next, the pixels within this object depth range (or the pixels for which the edge has been extracted (the pixels shown in blue in Fig. 5)) are extracted and the number of pixels extracted from the image along the vertical axis is counted. The line for which that number is largest is taken as the centerline of the processing region (Fig. 5). A distance corresponding roughly to human shoulders is marked off to the left and right of this centerline, according to the depth d, and the left and right processing regions are established accordingly.

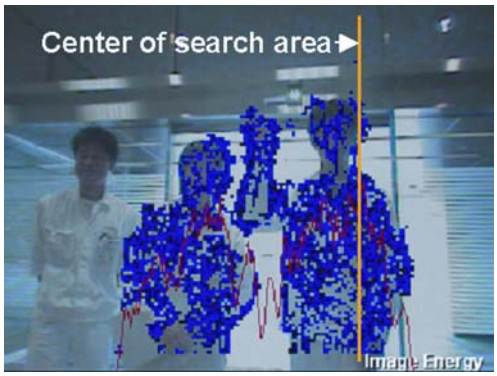


Fig. 5 Center of search area (left-right)

Finally, the vertical processing region is established from the processing depth d and the camera parameter values as the range from the floor to a height above the floor that can fully cover a human body.

The more detailed shape and position of the moving object are extracted from the image information inside the search areas established by the above processes.

Methods for extracting target objects from image information include the segmentation method, which is based on clustering of characteristic features, the contour extraction method[8], which links together the detected edges, and the dynamic contour model (Snakes[9]), which deforms closed curves so as to minimize a predefined energy.

This system must be able to extract detailed portions of target objects such as faces and hands from complex scenes. Here, therefore, extraction of moving bodies is done using Snakes, which is tolerant of noise and can extract the contour shapes of target objects.

The Snake is a contour model based on the principle of minimized energy. It changes the contour expressed as $v(s) = (x(s), y(s))$ so that the energy calculated in Eq. (1) will be a minimum value.

$$E_{snake} = \int_0^1 E_{int}(\mathbf{v}(s)) + E_{image}(\mathbf{v}(s)) + E_{con}(\mathbf{v}(s))ds \qquad (1)$$

The calculation here of the image energy $E_{image}(v(s))$ uses the intensity of the edges in the search areas described above.

The position of the center of gravity (x_i, y_i) of the moving object is calculated from the positions of the points on or inside of the contour of the extracted moving object i and the angle θ_I of the moving object is determined. The distance d_I to the moving object is calculated from the depth information in the pixels for the points inside the contour, and the position of the moving object in real space is determined. The depth information in the pixels inside the contour of the moving object, which was already extracted, is then updated (the parallax is set to zero), and the process is repeated according to the set processing range in order to extract multiple people.

Figure 6 shows the results for multiple moving objects extracted using Snakes. The rectangles represent the search areas for moving objects within the image, and the points inside the contours represent the centers of gravity of each moving object in the image. The figures to the side express the distance and angle to each moving object.

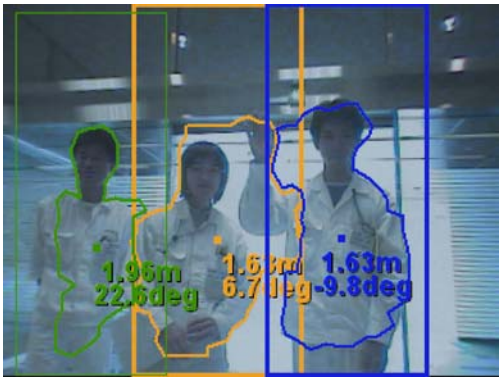


Fig. 6 Extraction of humans

In this way, this method establishes a general rectangular solid region that covers the moving object, and then extracts its more detailed shape and position. Consequently, the method is capable of extracting individual moving objects at high speed even in a scene that has more than one person in a row.

3.3. Parts Extraction

Next the system extracts the parts of the people (positions of faces and hands) to be used in gesture recognition.

3.3.1. Face position extraction

Face position extraction extracts the head from the contour information for the extracted moving object. Using that head as a reference point, it establishes a search area and performs the extraction. The position of the head that serves as a reference is defined as the point located at the highest part of a contour within an area expanded laterally for about the width of a human head to the left and right of the center of gravity of the moving object. This point is used as a reference to establish a search area for the face. The size of the search area on the image varies with the distance d_i to the moving object. The search area in the depth direction is defined as the approximate area that would cover a human face with its center at the moving object distance d_i.

The face position (x_f, y_f) in the image is defined as the center of gravity of the skin color region in the above search area. The face position (X_f, Y_f, Z_f) in actual space can be calculated using (x_f, y_f), the moving object distance d_i and the camera parameters.

For the purposes of later hand position extraction, the face position following face position extraction is used to further establish an area where the face is estimated to have moved, and skin color information inside that area is deleted.

3.3.2. Hand center position extraction

The hand center position (x_h, y_h) is also defined, in the same way as the face, as the center of gravity of the skin color region within the search area.

The hand search area is defined as the area where the hands can reach, taking the face position (x_f, y_f) as a reference. In some cases there may be another moving object close to the target moving object. In such cases, the center of gravity of the adjacent moving object is set as the boundary of the search area in order to prevent false detection of the hands or face of a moving object that is not a target.

The hand center position (X_h, Y_h, Z_h) in real space is calculated in the same way as the face position.

3.3.3. Tip of hand position extraction

This method for extracting the hand center position (x_h, y_h) derives only the approximate hand position. Therefore, this position is next used to estimate the tip of hand position (x_{ht}, y_{ht}), which is required for gesture recognition.

First, the hand center position (x_h, y_h) determined in section 3.3.2. is set as the center for defining a tip of hand search area. This search area is defined to be large enough to fully cover a human hand. The size of the region in the image changes according to the distance moved, as in the preceding processes.

Next the system extracts those points within this region that are the top, bottom, left, and right-most points with skin color information in the image. The hand is considered to be extended in the direction of the longer of the distances between the top and bottom-most points and the left and right-most points. The tip of hand is presumed to be the endpoint, either the top or bottom (or left or right).

Finally, it is decided which is the tip of hand —top or bottom (or left or right)— from the relationship between the hand center position (X_f, Y_f, Z_f) and the face position (X_h, Y_h, Z_h). Specifically, when the hand center position is distant from the face, the hand is considered to be extended, and the end farther from the face is considered to be the tip of hand position. When the hand center position is close to the body, the elbow is considered to be bent, and the end closer to the face is considered to be the tip of hand position. The tip of hand position (X_{ht}, Y_{ht}, Z_{ht}) in real space can be calculated from the coordinates (x_{ht}, y_{ht}) of the point in the image extracted as the tip of hand position and the depth of that point (the parallax).

Figure 7 shows the hand and face search areas and the results of extraction. The red outlines show the respective search areas. The search areas vary in size on the left and right because when the hand is extracted in one frame, that hand position is used as the center of the search area in the following frame, and this narrows the search area.

The use in this way of the extraction results from the previous frame or the moving object extraction results for the search area makes it possible to extract the face and hands with accuracy and high speed.

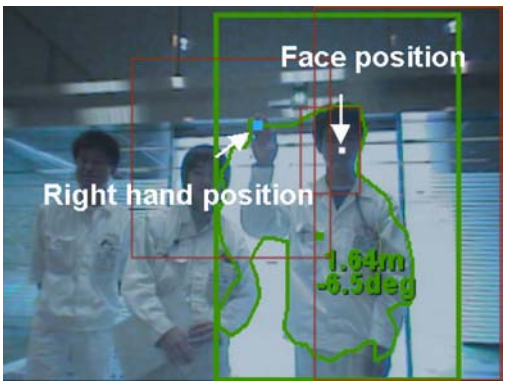


Fig. 7 Extraction of face & hands position

3.4. Gesture and Posture Recognition

The face position and tip of hand position in real space extracted in section 3.3 are used for recognition of gesture and posture by observation of the temporal variance in the relationships of those positions.

Gesture recognition methods include use of the hidden Markov model (HMM)[4], but this involves various problems. It requires large amounts of learning data[3] to improve the recognition rate, and real-time processing is difficult when the data are extended to 3D[10]. The present system, therefore, extrapolates gestures using the Bayesian method[11], a method of statistical analysis that allows high-speed processing and statistically optimum judgement, so that it tends not to result in misjudgment. The vector of characteristics x used to characterize a gesture is made up of six parameters, the averages ($\overline{X}$, $\overline{Y}$, $\overline{Z}$,) across several frames of the tip of hand position (X_{ht},' Y_{ht},' Z_{ht}')=($X_{ht}-X_f$, $Y_{ht}-Y_f$, $Z_{ht}-Z_f$), which has the face position in real space as its origin, and the standard deviations (σ_x, σ_y, σ_z).

When the vector of characteristics x is given, the probability density $p(\omega_i|x)$ that it presents is a gesture i can be found through Bayes' theorem using Eq. (2).

$$p(\omega_i|\mathbf{x}) = \frac{p(\mathbf{x}|\omega_i)p(\omega_i)}{p(\mathbf{x})} \tag{2}$$

Here $p(x|\omega_i)$ is the conditional probability density that when gesture i is given, the image will include the vector of characteristics x. It is expressed in Eq. (3).

$$p(\mathbf{x}|\omega_i) = \frac{1}{2\pi\sqrt{|\Sigma|}} e^{-(\mathbf{x}-\bar{\mathbf{x}},\Sigma^{-1}(\mathbf{x}-\bar{\mathbf{x}}))/2} \tag{3}$$

The vector of characteristics x is defined as having covariance matrix Σ and to follow the normal distribution of the expectation value $\overline{X}$.

Furthermore, $p(\omega_i)$ expresses the probability density of the prior probability of ω_i. When $p(\omega_i)$ is the normal distribution of the expectation value ω_{i0} and distribution $V[\omega_{i0}]$, then $p(\omega_i)$ can be written as in Eq. (4).

$$p(\omega_i) = \frac{1}{\sqrt{2\pi V[\omega_{i0}]}} e^{-(\omega_i-\omega_{i0})^2/2V[\omega_{i0}]} \tag{4}$$

Since the denominator of Eq. (2) does not depend on ω_i, the probability density of the posterior probability of ω_i, following Eqs. (3) and (4), can be expressed as in Eq. (5).

$$p(\omega_i|\mathbf{x}) \propto p(\mathbf{x}|\omega_i)p(\omega_i) = \frac{1}{\sqrt{2\pi}^3\sqrt{|\Sigma|V[\omega_{i0}]}} e^{-(\omega_i-\omega_{i0})^2/2V[\omega_{i0}]-(\mathbf{x}-\bar{\mathbf{x}},\Sigma^{-1}(\mathbf{x}-\bar{\mathbf{x}}))/2} \tag{5}$$

Equation (5) is used to determine, for a given extracted vector of characteristics x, the probability relative to all gestures that it is gesture i. The vector with the highest probability is taken as the gesture recognition result for that frame. The final output result is obtained from results across several frames.



Fig. 8 Gesture & posture recognition results

The system using this method is currently capable of recognizing ten kinds of gesture and posture separately for the left and right hands. These are the handshake, hand circling (moving the hand in a circle beside the body), bye-bye (waving the hand from side to side in front of the body, upper left in Fig. 8), hand swing (waving the hand from side to side above the head), high-hand (raising the hand, upper right in Fig. 8), side-hand (extending the hand out beside the body), low-hand (extending the hand diagonally downward beside the body, lower left in Fig. 8), come here (beckoning by waving the hand up and down with palm down in front of body), stop (holding out the hand palm-forward in front of the body, lower right in Fig. 8), and face-side (raising the hand to the side of the face). The postures and gestures shown in red on the right and left sides of Fig. 8 are recognition results.

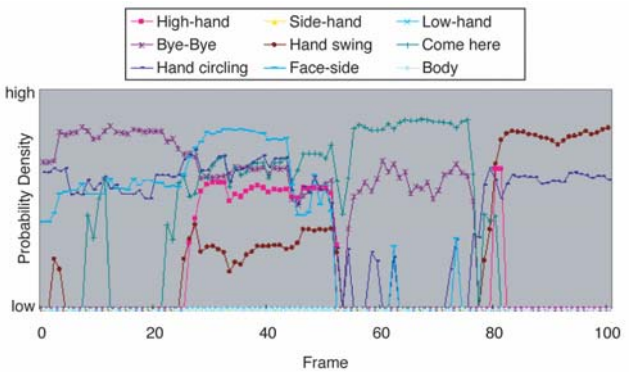


Fig. 9 Probability density

Figure 9 shows the probability densities for the bye-bye, face-side, come here, and hand swing gestures and postures. The graph indicates that the probability densities for gestures and postures performed at that time are clearly higher than the probability densities for other gestures and postures. It is clear that correct recognition is taking place.

3.5. Pointing Position Detection

Pointing position detection processing takes place by the procedure shown in Fig. 10.

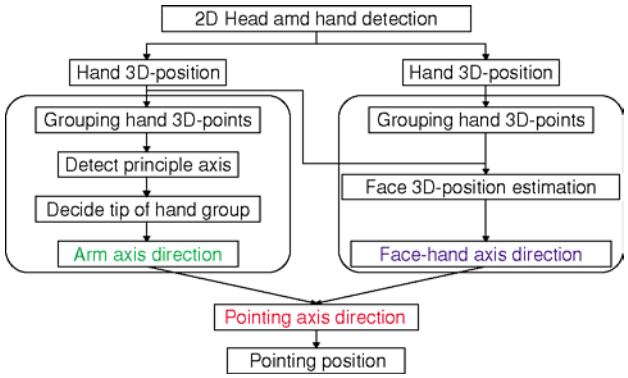


Fig. 10 Flowchart of pointing position detection

First, the tip of hand and head positions obtained by parts extraction from certain image acquisition frames are used as a reference to obtain points corresponding to the head and ends of the arms in a stereo image. Specifically, objects within a certain range by 3D distance from the reference position are taken as the head and ends of the arms. These are called the head group and hand group, respectively.

For the head group, the center of gravity is taken as the head center. For the hand group, the principal axis is determined through principal component analysis of the values of the 3D coordinates. This calculation is performed as follows. There are N points in the group. The average of the coordinate values for these points normalized to 0 is A_n. The normalized group is expressed as a matrix, in the form $A=[A_1, A_2, ..., A_N]$. The distribution covariance matrix for this matrix is determined, and its eigenvalues and specific vectors are calculated. The specific vector corresponding to the largest eigenvalue is taken as the largest principal axis of the hand group distribution.

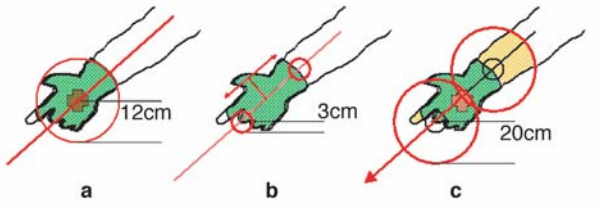


Fig. 11 Arm direction detection

The direction of the end of the arm is sought for the principal axis thus obtained. The method employed is to search for locations in two directions along the principal axis and within a radius of 3 cm from the center of gravity where there are no 3D points (Fig. 11b). The direction in which there are fewer 3D points within 20 cm from the location within 3 cm where there are no 3D points is taken as the end direction (Fig. 11c).

Finally, the relationship of the head group and hand group positions is confirmed, and when the selected direction is not possible in terms of body structure, it is corrected to the reverse direction. If the reverse direction is also not possible, then it is determined that processing could not be accomplished with that image acquisition frame.

The same kind of process is applied to three or more frames, and when the total distribution of the head center position, the arm axis direction and the arm positions lies within certain values, the arm and head posture is considered to have been identified. Arm processing is carried out on both the right and left arms, and the hand on the side that is identified first and that is identified as being farther away is considered to be the pointing hand.

After the arm and head posture has been identified, the face position is estimated on the supposition that the person pointing will be looking at the pointing hand. The head is supposed to be a sphere with a radius estimated from the body height. The surface of the head in the direction from the head center toward the pointing hand is determined. The neck is considered to have rotated perpendicularly to the Z axis, and the value of Z set back to the value of the head center is considered to be the eye position (see Fig. 12 for the coordinate system).

The vector linking the eye position and the hand position is the face-hand vector ($V_{face\text{-}hand}$), and the vector in the arm direction is the arm vector (V_{arm}). The composite of the face-hand vector and arm vector is the pointing vector ($V_{pointing}$) (Fig. 12). The composite is as shown in Eq. (6).

$$V_{pointing} = \frac{\frac{V_{arm}}{|V_{arm}|} + \frac{V_{face\text{-}hand}}{|V_{face\text{-}hand}|}}{2} \quad (6)$$

However, if the distance from the head to the pointing hand is 70% or less of the full arm length as estimated from body height, then the elbow is considered to be bent. In this case, the arm vector is taken as the pointing vector.

The location where the line extended from the pointing vector that has the hand position as its origin intersects with the floor surface is considered to be the pointing position (the red line in Fig. 12).

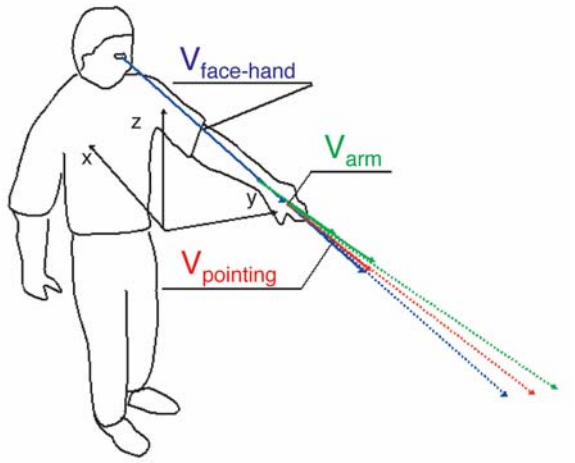


Fig. 12 Pointing gesture overview

The above algorithms were incorporated into the system equipment and the accuracy of this method was verified. The stereo cameras were installed 1.5 m in front of the test subject (ASIMO was stood 1.5 m in front of the test subject).

Images of the subject pointing to seven lateral points at a distance of 1 m in front of the test subject were used. The pointing position was detected using three methods, extrapolation of the pointed floor surface using only the arm vector, using the face-hand vector, and using the pointing vector. Figure 13 shows the detection results.

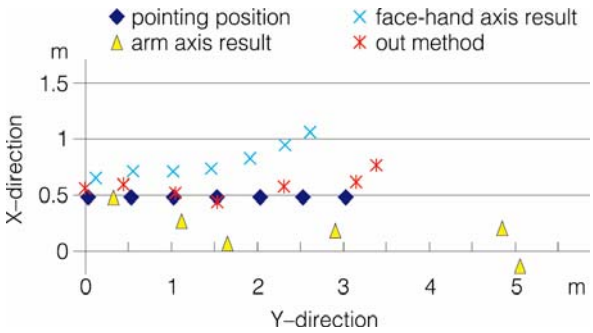


Fig. 13 Result of pointing position detected by each vector

The average error was 0.93 m when the pointed floor surface was extrapolated using only the arm vector, 0.34 cm when using the face-hand vector, and 0.25 cm when using the pointing vector. It is clear that the recognition results are improved by use of the pointing vector, which is a composite of the face-hand vector and arm vector.

During this testing, the test subject simply pointed toward the floor without any deliberate attention to the detection method. By using this method, the system became able to detect a point closer to the intended position indicated by the pointing in a natural manner than just the position derived from the arm vector and face-hand vector.

The accuracy of detection was also determined using six test subjects (S1-S6 in Fig. 14), who each extended an arm to point toward nine points diagonally to the left (1.4 to 4.2 m ahead). They did this three times (Fig. 14).

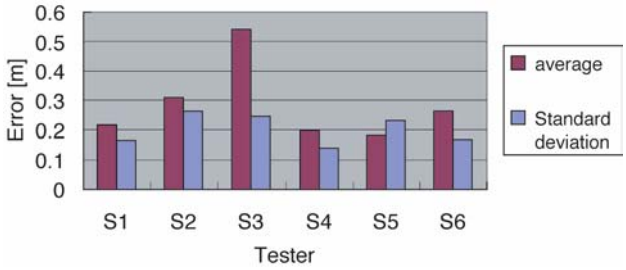


Fig. 14 The detection error for every subject

The average error for all points was 0.28 m (broken down by pointing distance, this was an error of 0.15 m for 1-2 m, 0.25 m for 2-3 m, and 0.45 m for 3-5 m). The range extended from an error of 0.54 m for the test subject with the largest error, to 0.18 to 0.31 m for the other test subjects. There was some individual variation, but this is considered to indicate a largely stable detection capability.

Figure 15 shows an example of pointing position recognition results. The left side of Fig. 15 is an illustration of a stereo image overlaid by recognition results, and the right side is an overhead view of those recognition results.

In this way, the system became capable of extracting a stable, highly accurate pointing position through use of the relationship between the head and arm positions in addition to the direction of the arm.

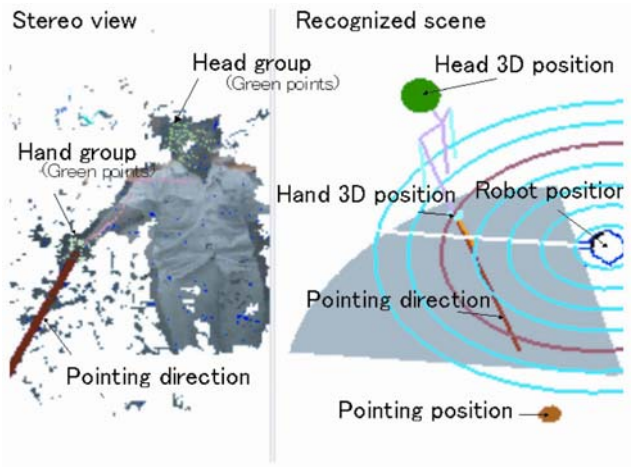


Fig. 15 A Pointing gesture recognition result

4. Test Results

Installation of these gesture recognition functions in ASIMO enabled it to come to where it was called over by a gesture or move to a pointing position.

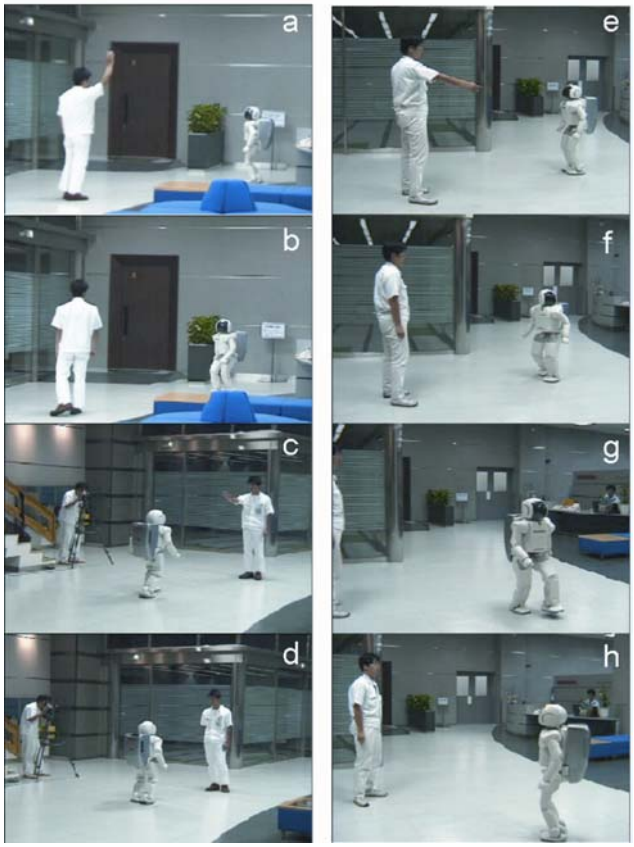


Fig. 16 Demonstration images a: recognize “high-hand” posture, b: start to follow, c: recognize “stop” posture, d: stop walking, e: recognize pointing position, f: start to walk, g: walk to pointing position, h: arrive and stand by

Specifically, ASIMO has become able to obey a person when it sees a person raising a hand high or gesturing to come. In addition, when the person gestures ASIMO to stop, it is able to stop on the spot. (See examples on left in Fig. 16.)

When a person tries to shake hands with ASIMO, it will extend its right hand to shake, and in response to other gestures and postures, it will perform the same gestures and postures as a person.

In addition, when ASIMO receives voice input that requests it to move, such as by saying "go over there," it has been enabled to recognize the position where the person is pointing, and to move to that location. (See examples on right in Fig. 16.)

5. Conclusion

A gesture recognition function using image processing was installed on the biped walking humanoid robot ASIMO in order to enhance ASIMO's autonomy.

1) The system extracted people (moving objects) that are the objects of gesture recognition on the basis of movement information, and further used color information to extract the human head and hands. From the temporal variance in the 3D positions of the head and hands, it used statistical analysis to carry out gesture and posture recognition, and has become able to recognize ten types of gesture and posture.
2) Further, the direction of the arm was determined by principal component analysis of the 3D point set observed in the vicinity of the hand. Then the direction a person was pointing and the point being indicated were extracted from the relationship between the positions of the head and arm and the direction of the arm.

This made it possible to use gestures to give ASIMO some instructions for actions that up to now had been provided by an operator using a remote terminal to execute operating instructions one by one. This enhanced ASIMO's operability and autonomy.

The present system implements object extractor, parts extractor, and recognition unit functions in a layered structure. The results of the processes are put together at each layer, and the system has thus avoided complexity in the processing. Furthermore, information from other processes is used effectively so that the search area for each process is kept limited. Means such as these were used to reduce the computation costs. As a result, this system realized a comprehensive image processing system that was the first in the world capable of operating at a speed of approximately 100 – 200 msec/frame with on-board equipment.

References

(1) Hirose, M., Takenaka, N.: Development of Humanoid Robot ASIMO, Honda R&D Technical Review, Vol. 13, No. 1, p. 1-6 (2001)

(2) Sakagami, Y., Watanabe, R., Aoyama, C., Matsunaga, S., Higaki, N., Fujimura, K.,: The intelligent ASIMO : System overview and integration, IROS, p. 2478-2483 (2002)

(3) Yachida, M., Iwai, Y.: Human Motion Analysis and Recognition for Interaction, Technical Report of IEICE, PRMU99-142 (1999)

(4) Takahashi, M., Ogura, N., Watanabe, S.: Recognition of mixture motions using Hidden Markov Model, Technical Report of IEICE, PRMU 2000-151 (2001)

(5) Takahashi, K., Sakaguchi, T., Ohya, J.: Remarks on a Real-Time, Non-contact, Non-wear, 3D Human Body Posture Estimation Method, Trans. IEICE (D-II), Vol. J83-D-II, No. 5, p. 1305-1314 (2000)

(6) Ishii, H., Mochizuki, K., Kishino, F.: A Motion Recognition Method from Stereo Images for Human Image Synthesis, Trans. IEICE (D-II), Vol. J76-D-II, No. 8, p. 1805-1812 (1993)

(7) Takahashi, K., Seki, S., Kojima, H., Oka, R.: Spotting Recognition of Human Gestures from Time-Varying Images, Trans. IEICE (D-II), Vol. J77-D-II, No. 8, p. 1552-1561 (1994)

(8) Ballard, D., Brown, C.: Segmented Images, Computer Vision, p. 147-205 (1987)

(9) Kass, M., Witkin, A., Terzopoulos, D.: Snakes: Active Contour Models, Proc.of 1st ICCV, p. 259-268 (1987)

(10) Muller, S., Eickeler, S., Rigoll, G.: Crane Gesture Recognition Using Preudo 3-D Hidden Markov Models, In 4th IEEE International Conference on Automatic Face and Gesture Recognition, p. 398-402 (2000)

(11) Kanatani, K.: Bayesian estimation, p. 149-150 (1995)

■ Authors ■



Nobuo HIGAKI



Taro YOKOYAMA



Kikuo FUJIMURA

Establishment of an Intake Port Design Support Tool Using CFD

Yasushi TAKAHASHI* Yasuo MURAKAMI*

ABSTRACT

An intake port design support tool using CFD (Computational Fluid Dynamics) software based on the PCC (Partial Cells in Cartesian coordinate) computational mesh method was applied during the development of a motorcycle engine. CFD analyses were performed with a relatively quick turn around time due to the reduced mesh generation time. To ensure sufficient accuracy in actual applications, the CFD results have been validated against measurement data. In addition, recommendations for the mesh setup and details of implemented post processing improvement are described. In the present report, it has been confirmed that the developed CFD software is a robust design support tool.

1. Introduction

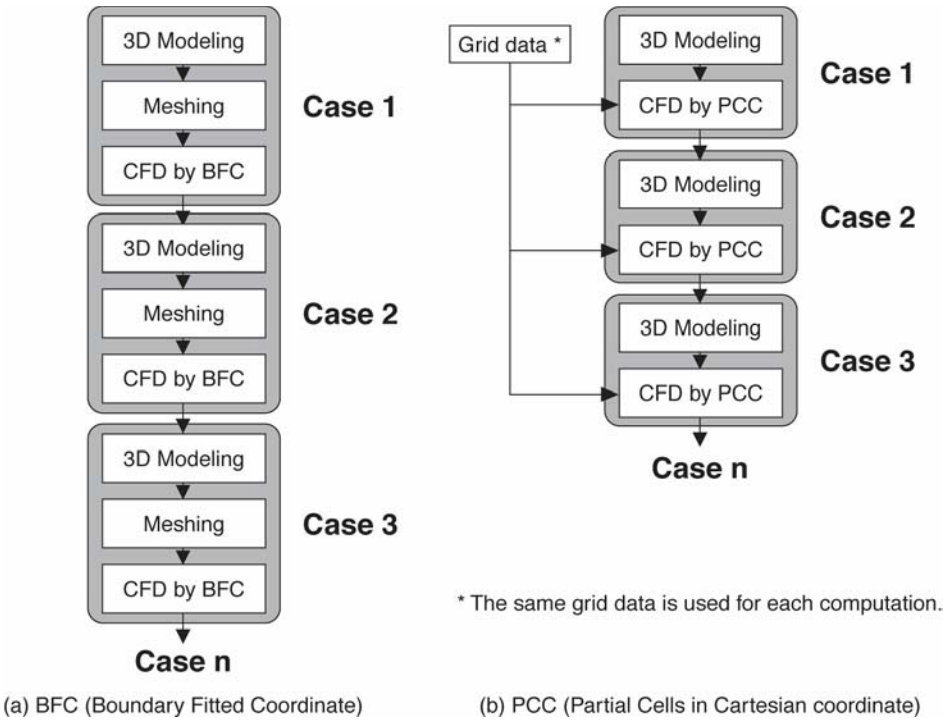
Since the shape of the intake ports of an engine greatly influences the characteristics of power output and adjacent components, it should be determined at the early stage of engine development. Therefore, developing a design support tool capable of evaluating flow features prior to prototyping has been desired to replace the conventional method employing steady state flow test rig. Rapid improvement of computer performance in recent years has made it possible to perform CFD calculations of port flows with desktop computers. However, most commercial CFD codes require much time for mesh generation and are not suitable as a design support tool for motorcycle engines because such engines are usually developed in an extremely short term. To address that issue, the authors have developed a PCC (partial cells in Cartesian coordinate) method which employs an orthogonal grid of straight lines and enables shortening mesh generation time[(1)]. This work aims to construct a support tool for an intake port design with the PCC method.

2. Overview of Tools

The intake port is the component to introduce the air fuel mixture into the engine cylinder, so flow resistance through the port is used as one of the indicators for engine power output. For port flow resistance calculations in most CFD codes, a series of tasks shown in Fig. 1 (a) are necessary and a new mesh must be created for each geometry shape. The general process of mesh generation consists of the following tasks: initial mesh generation → mesh quality check →improvement. Recently, the initial mesh generation has been automated, and not much human labor is required. On the other hand, the mesh quality check and improvement tasks have a profound effect on calculation stability and accuracy, and highly depend on the know-how of an operator. These considerations have been an obstacle to the full automation of mesh generation. In such a situation, by using the PCC method shown in Fig. 1 (b), a great deal of reduction in mesh generation time has been accomplished.

In the PCC method, calculations of fluid dynamics are carried out with an orthogonal grid of straight lines among any geometric shape, for example as shown in Fig. 2. Though many cell shapes other than hexahedron cells appear around a wall surface, mesh update is not necessary because the CFD calculation has been enabled among these cell shapes. Therefore, the grid data also can be applied for other calculations such as similar shapes and each valve lift.

* Asaka R&D Center



(a) BFC (Boundary Fitted Coordinate) (b) PCC (Partial Cells in Cartesian coordinate)

Fig. 1 Comparison of work flow between BFC and PCC

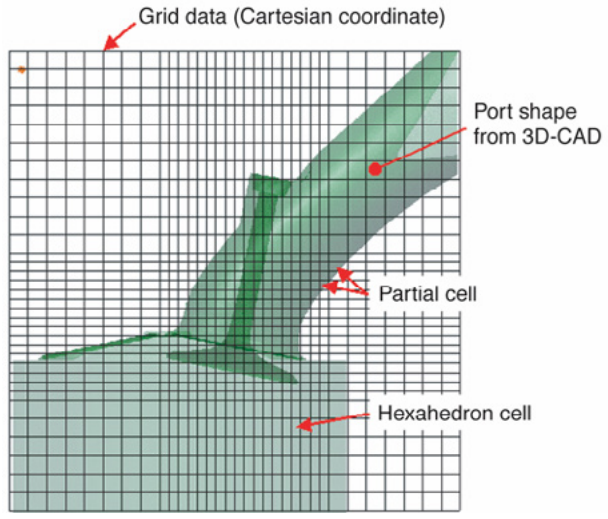


Fig. 2 Example of port shape and Cartesian coordinate

3. Evaluation Parameters for Intake Port Characteristics

Effective valve opening area (Z) defined in Eq. (1) is employed as a parameter indicating ease of air flow through the port.

$$Z = \frac{\dot{m}}{\sqrt{2\rho\Delta p}} \quad (1)$$

Here, $\dot{m}$ is mass flow rate, ρ is density of air, and Δp is pressure drop over the port.

In addition, SUM(Z) defined in Eq. (2) is used to consider a valve lift curve, which affects engine volumetric efficiency.

$$SUM(Z) = \int_{\theta 1}^{\theta 2} Z d\theta \quad (2)$$

Here, $\theta 1$ and $\theta 2$ are the crank angles at valve opening and valve closing, respectively.

Since the power output characteristics are predicted using these parameters during engine development, in this paper the effective valve opening area (Z) has been selected as the indicator to evaluate intake port characteristics.

4. Preparations for Application of Tools

In practical use as a design support tool, the main theme is to achieve both short analysis time and sufficient accuracy. Short analysis time was achieved in the PCC method. However, general orthogonal grid methods by straight lines show considerable concerns in calculation accuracy[2), 3), 4)]. Therefore, verifications of the accuracy of the effective valve opening area (Z) were carried out using several types of ports. In addition, to improve the utility of the software as a design support tool, several functions of post-processing were added. Note that the code in this paper is an upgraded version combining “logarithmic law of the wall” and a low Reynolds number k-ε turbulence model[5)].

4.1. Comparison with Measurement Values

First of all, a verification of the calculation accuracy concerning the details of port geometry was carried out. Figure 3 shows the base port shape, and Figs.4 (a) and (b) show improvement rate of the effective valve opening area (Z) in increasing +2 mm and +3 mm port diameter each, and comparison between measurement and calculation values are presented. The effective valve opening area (Z) improves in the whole valve lift by increasing port diameter. Since the improvement rate between measurement values and

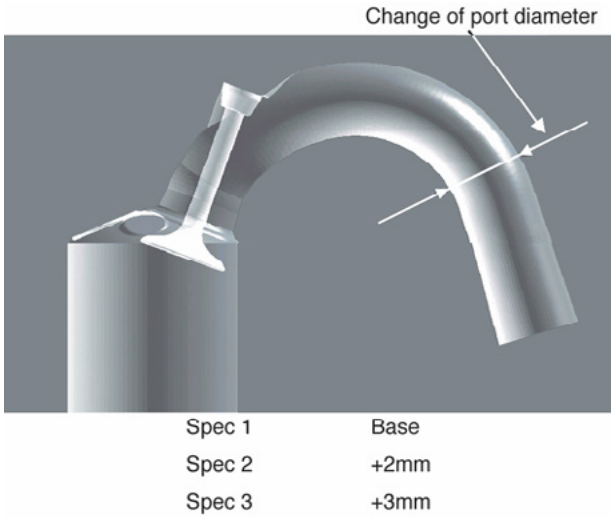


Fig. 3 Port shape for verification by changing port diameter

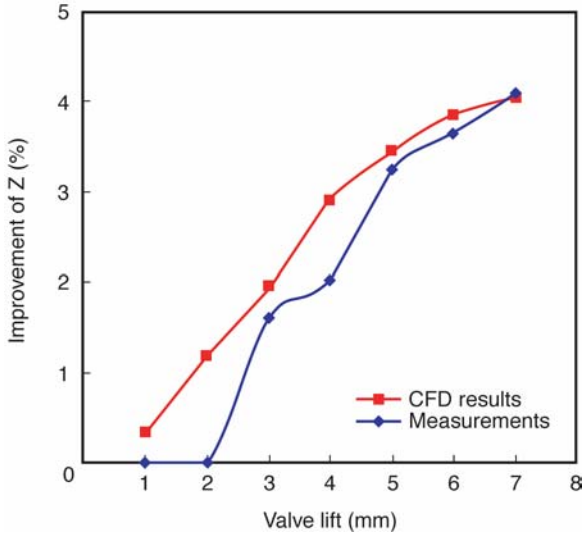


Fig. 4(a) Improvement of Z for Spec 2 port (diameter +2 mm) compared to Spec 1 port

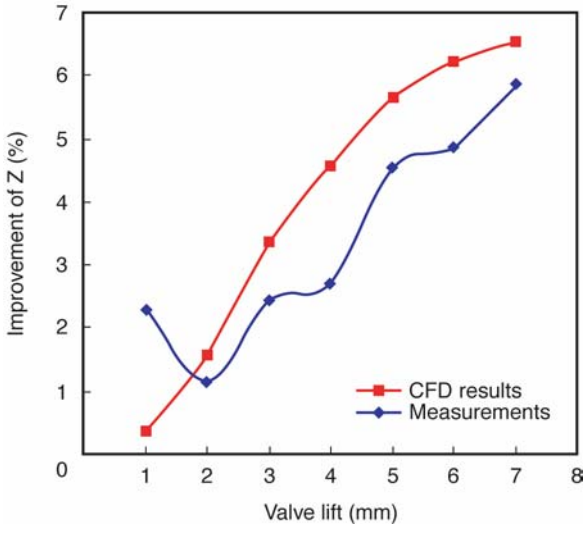


Fig. 4(b) Improvement of Z for Spec 3 port (diameter +3 mm) compared to Spec 1 port

calculation values agreed, it was confirmed to have much potential for examining geometry changes in detail.

Next, the calculation accuracy with a big port geometry change was examined. Figure 5 shows two port shapes used in the verification. Figure 6 shows comparison of measurement and calculation results in terms of the effective valve opening area (Z) at each valve lift. Although the two ports differ greatly in several dimensions such as port length, port bend angle, existence of a hollow around the injector tip, etc., the correlation between measurement values and calculation values was almost good. A difference between the two was observed around 5 mm of valve lift; these are considered due to differences in the scale of separation vortices in the calculations and measurements[5].

Thus, it was confirmed that the issues of calculation accuracy concerning the orthogonal grid by straight lines were resolved by employing the PCC method.

4.2. Setting of Recommended Grid Data

To guarantee the calculation accuracy as a design support tool, a minimum standardization was needed to provide a fine grid size at places of sudden changes in flow. In addition, it was necessary to use the same grid data to avoid the issue of grid dependence of results[6]. The recommended grid data was provided mainly around the valves.

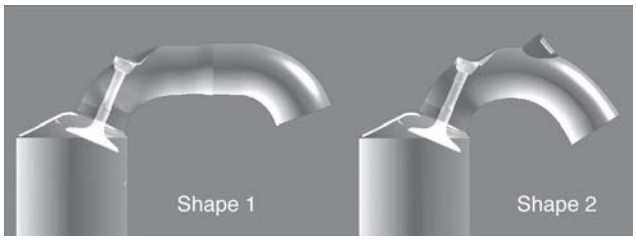


Fig. 5 Port shapes for the following comparisons

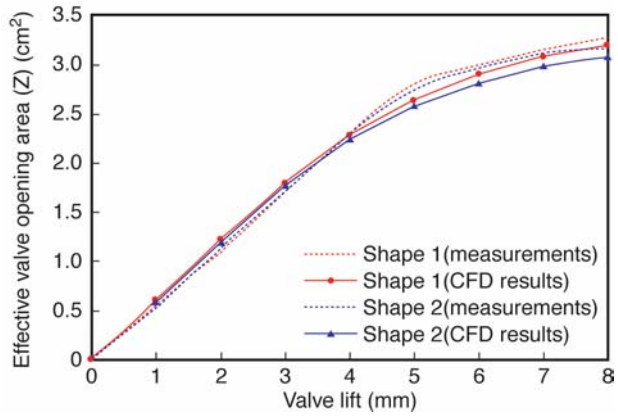


Fig. 6 Comparison between measurement results and CFD results for Shape 1 port and Shape 2 port

Figure 7 shows comparisons between measurement and calculation values of SUM(Z) of 16 engines with displacements from 50 cm^3 to 500 cm^3 per cylinder. By setting the recommended grid data, the differences between the measurement and calculation values were held within ± 4%. Thus, it has become possible to guarantee sufficient accuracy as a design support tool.

Some calculation values in the figure are estimated rather high from the correlation line. However, since these were limited cases caused by large separation vortices inside the ports or just under the valves, it appears that an issue remains with the current turbulence model. Note that the recommended grid data established here were two sets for small-displacement engines and for large-displacement engines, and the grid size around the valves was set between 0.8 mm and 1.2 mm.

4.3. Automation of Calculation of Effective Valve Opening Area

Pressure measurement points of the steady state flow test rig are in a chamber with a large volume and at a point open to the atmosphere, so that the static pressure is equal to the total pressure. To make calculation conditions correspond to the measurement conditions, a chamber to imitate the atmosphere was added at the port inlet of the CFD geometry model. By adding a large chamber, the flow velocity in the chamber is ignored, so the conditions correspond to the experiment. However, there is a drawback that large volume of the chamber requires a longer calculation time by increasing total mesh numbers. On the other hand, small size of chamber derives the necessity to calculate the total pressure from the static pressure and the flow velocity. Therefore, both the expressions to calculate the total pressure and Eq. (1) were incorporated into the CFD code to easily obtain correct values of the effective valve opening area (Z), regardless of the size of the chamber.

4.4. Equipment of Function to Indicate Vortex Magnitude

Because only the Z value is provided from the conventional steady-state flow tests, the only way to optimize the port shape has been to depend on the designer's experience and instincts for finding the place and method. Improving the effective valve opening areas means reduction of pressure drop over the port. However, it is difficult to identify the locations of momentum losses by examining the pressure distribution. In order to make it easier to identify those locations, the vortex magnitude ($|\omega|$) defined in Eq. (3) was considered, and its graphic display function has been equipped in a post processing program. Strictly speaking, the vortex magnitude does not quantitatively express pressure drops, but it smooths the way for further work, since it identifies the locations that need to be optimized.

$$|\omega| = \left(\left(\frac{\partial w}{\partial y} - \frac{\partial v}{\partial z} \right)^2 + \left(\frac{\partial u}{\partial z} - \frac{\partial w}{\partial x} \right)^2 + \left(\frac{\partial v}{\partial x} - \frac{\partial u}{\partial y} \right)^2 \right)^{\frac{1}{2}} \quad (3)$$

Above, x, y and z are the coordinate axes, and u, v and w are the flow velocity in each direction.

Next, the utility of the vortex magnitude display will be shown. Figure 8 (a) displays the vortex magnitude distribution of the base shape. Vortices due to flow separation are visible in the red on the lower surface of the curve. Although modifications to the port bend angle are desired to reduce the pressure drop, the separation on the bottom surface of the port curve was controlled by increasing port diameter due to engine layout. As shown in Figs. 8 (b) and (c), vortex magnitude decreases with the increase in port diameter by +2 mm and +3 mm, and as shown in Figs. 4 (a) and (b), the effective valve opening area (Z) was improved.

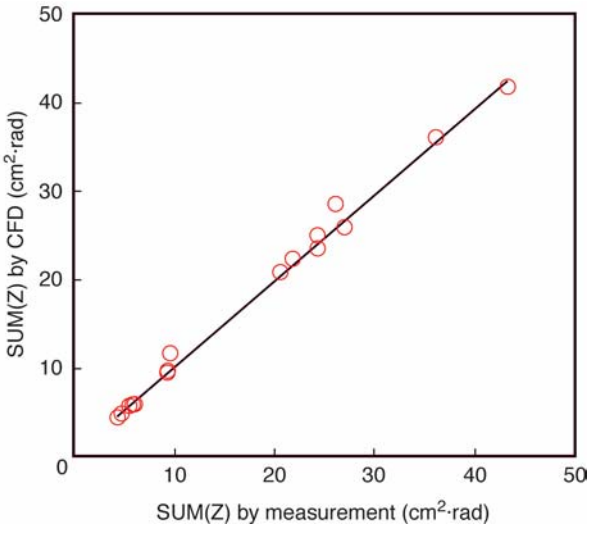


Fig. 7 Comparisons of SUM(Z) between CFD results and measurement results

5. Examples of Application in Motorcycle Engine Development

An example will be described that aims to improve both power output and throttle response simultaneously by intake port modifications in a 4-valve engine. The smaller port volume between the throttle valve and the intake valves help to obtain the higher engine acceleration rate by throttle control. Therefore, 5% reduction of port volume against base ports was aimed while maintaining the effective valve opening area (Z).

Figure 9 presents a cross-sectional view of the base ports, and Fig. 10 (a) shows its vortex magnitude. By the indication of high vortex magnitudes in three locations of A, B and C, it was found that these places should be modified.

For location A, it is well known that small radii of the valve stems are helpful to reduce the pressure drop. However, in this example improvements were attempted only by modifying port geometry. Figures 10 (b) and (c) show the velocity magnitude distributions in section D – D and section E – E in Fig. 9. At the downstream of the bifurcation, it is visible that flow speed of port center becomes rather high. Generally, it is desirable to create a flow velocity distribution in a port as uniform as possible, but flow in a port is also governed by the shape of the combustion chamber and the shape of insulator which connects a carburetor to the ports. Therefore, attempting a uniform flow distribution by only port geometry revisions often results in the increase of pressure drop. As shown in Fig. 11, the change of the port bifurcation position and optimization of port sidelines increased the flow toward the centerline of the ports. Thus, the colliding flow to the valve stems could be reduced.

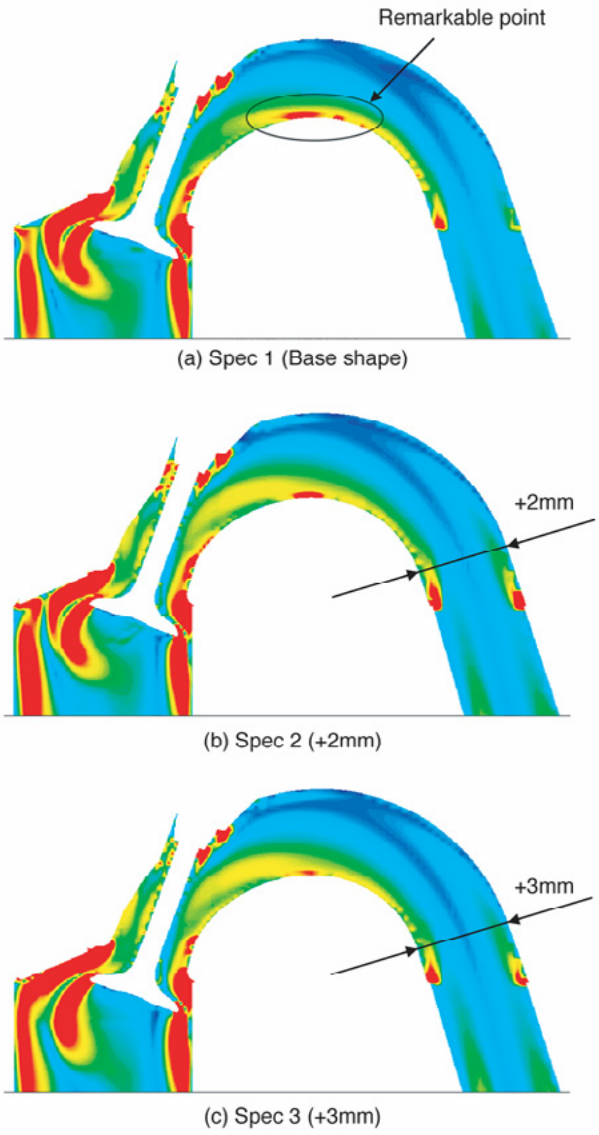


Fig. 8 Display of vortex magnitude for finding defective shape

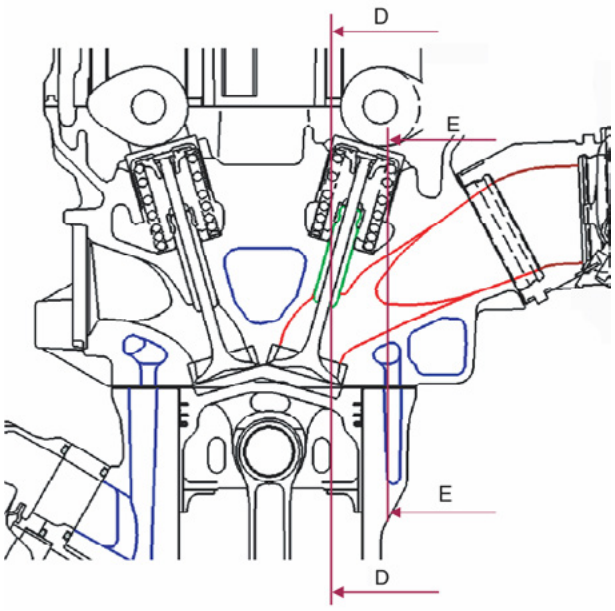


Fig. 9 Drawing of intake port

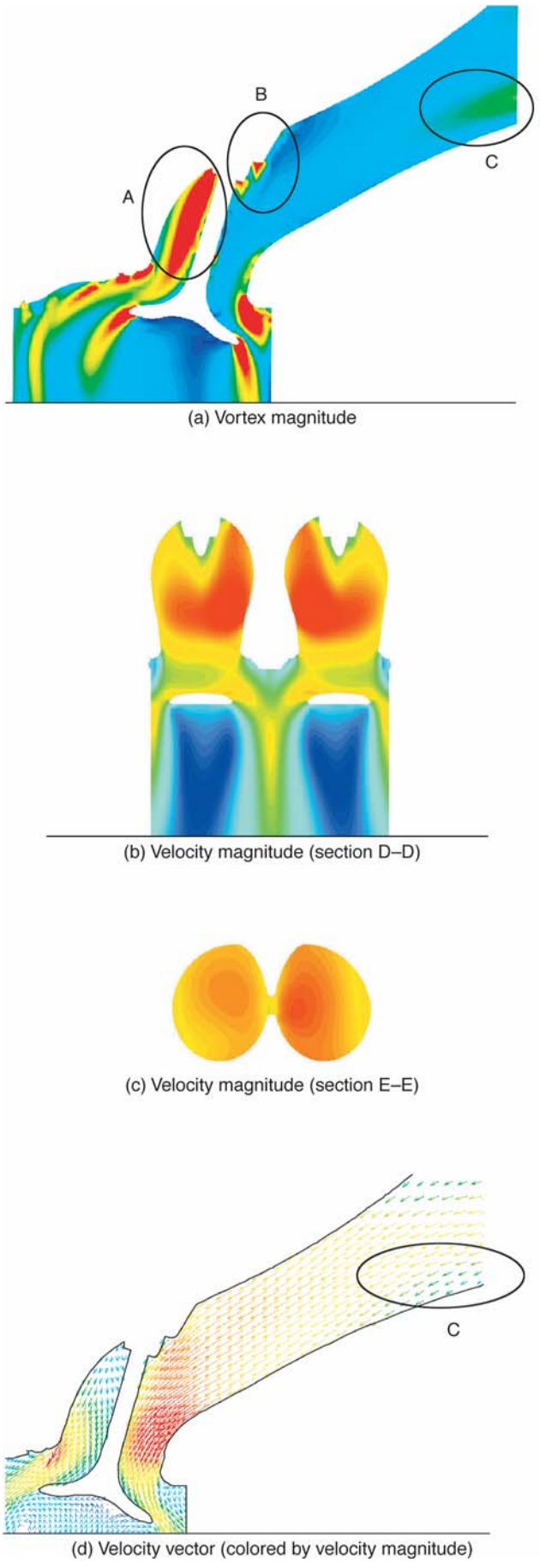
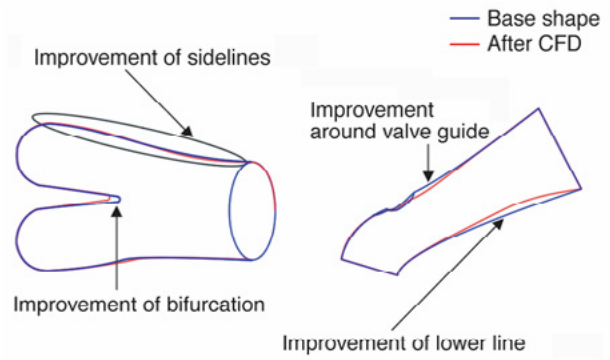


Fig. 10 Display for analyzing port shape

For the location B, a decrease of the inflow angle of the ports was first attempted to reduce the protrusion distance of the valve guides. However, a weak separation occurred at the lower port wall on the curve, and the calculation result of the effective valve opening area (Z) was decreased against expectation. Instead, shapes around the valve guide were smoothed as shown in Fig. 11.

At the location C, the reasons for the vortices were examined together with the velocity vector display shown in Fig. 10 (d). The results indicated separation at the lower wall of the insulator because the ports and the insulator were not smoothly connected; the flow tended toward the upper side of the port (toward the valve guide). Thus, port volume was reduced while optimizing the lower wall of the port to smoothly connect to the insulator.

As mentioned above, countermeasures with CFD allowed a 4.2% reduction in port volume and a 2.4% improvement in SUM(Z). In an engine performance test of the prototype engine, it was confirmed that both the maximum power output and the throttle response characteristics were improved compared with the base port configurations. Thus, the utility of this tool was confirmed.



Port volume	SUM(Z)	Engine power output
-4.2%	+2.4%	+0.4kW

Fig. 11 Examination points and results

6. Summary

(1) A design support tool for intake ports was constructed by verifying calculation accuracy of the PCC method, by setting recommended grid data and by improving the post processing functions.
(2) The utility of the tool was verified for use in development of motorcycle engines and in the tuning of engine specifications prior to prototyping.

By the establishment of a quick and convenient design support tool that significantly reduces mesh generation time, its applications have rapidly spread for various examinations of intake port design at several stages of engine development. Especially, the applications in the initial design stage are increasing, because the tool proves to be very helpful to shorten design optimization time.

References

(1) Takahashi, Y., Fukuzawa, K., Fujii, I.: Numerical Simulation of Flow in Intake Ports and Cylinder of Multi-Valve S. I. Engine using PCC Method, International Symposium COMODIA, p. 529-534 (1994)

(2) Ichikawa, O., Fujii. K.: Study of boundary conditions on solving flow field around arbitrary shape by using Cartesian grid (in Japanese), The 13th Japan CFD Symposium, F03-3 (1999)

(3) Matsunaga, N., Himeno, R.: An approach of finite difference method for general boundary in orthogonal coordinates (in Japanese), The 13th Japan CFD Symposium, F03-5 (1999)

(4) Ono, K.: Product Design using Cartesian Mesh method (in Japanese), Nagare (Journal of The Japan Society of Fluid Mechanics), 21, p. 16-25 (2002)

(5) Takahashi, Y., Nomura, T., Ishima, T., Obokata, T.: Analysis on Flow Around a Rectangular Cube by the Numerical Simulation of PCC Method with LDA Verification (in Japanese), Transactions of The Japan Society of Mechanical Engineers, 68-666, B, p. 331-337 (2002)

(6) Takahashi, Y., Fujii, I.: Numerical Simulation of Gas Flow in Cylinder with PCC (Partial Cells in Cartesian coordinate) Method (in Japanese), The 12th Internal Combustion Engine Symposium, p. 91-96 (1995)

■ Authors ■


Yasushi TAKAHASHI


Yasuo MURAKAMI

Practical Examples and Future Directions for CAE-Based Development for Automobile Transmissions by Designers

Takanao UCHIDA* Shigeru NAGAI* Shigeru KOYAMA*

ABSTRACT

Three-dimensional (3D) CAD systems have been used for design and development of automobile transmissions for several years. These systems have been improved to the point that they can be used to design sand castings, which have the precision equivalent to that mass-produced from die molds. Since automatic meshers for CAE analysis have improved so much, it has become increasingly common practice for designers to use, as is, the 3D models of prototype parts and mass products in CAE analyses to make decisions on the detailed specifications of components. The next step in this revision of CAE systems is to re-create them as a more designer-friendly environment, and allow designers to use these systems to perform CAE analyses not only of individual components, but also of assemblies, a much more difficult task.

1. Introduction

Recent years have seen developments in design using 3D CAD systems, and it is becoming normal design procedure to use 3D methods from the beginning of the design process, rather than creating 2D drawings for conversion into 3D models. It is also increasingly customary to use 3D models including detailed fillets and draft angle (hereafter 3D detail modeling) for design investigations of die molds for manufacturing engines, transmissions and other forgings[(1)]. It has also become possible to use 3D detail models directly for CAE analysis[(2)]. This has made it a simple matter for the designers themselves to carry out design investigations employing CAE analysis. Here, some examples will be provided to show how effective 3D design methods are for development of automotive transmissions and to indicate directions of future developments in CAE as it will be used by designers.

2. 3D Detail Modeling and Precision of Prototype Parts

Mass production of components such as transmission cases and engine cylinder blocks is by forging with die molds, but initially, small lots of prototype parts are produced with sand molds to investigate specifications. Before the 3D detail modeling-based development shown in Fig. 1 came into use, the sand molds were produced by hand on the basis of 2D drawings. This often resulted in some discrepancies between the designers' intent and the shape of the actual parts. One of the reasons for this is that the designers' intent could not be completely expressed in 2D drawings. Another was that the designers themselves sometimes failed to provide complete specifications of the shape of the mass-products from die molds forging in their 2D drawings. Due to these factors, it sometimes happened that prototype parts were of different shapes than the intentions of the designers and than the mass-

* Tochigi R&D Center

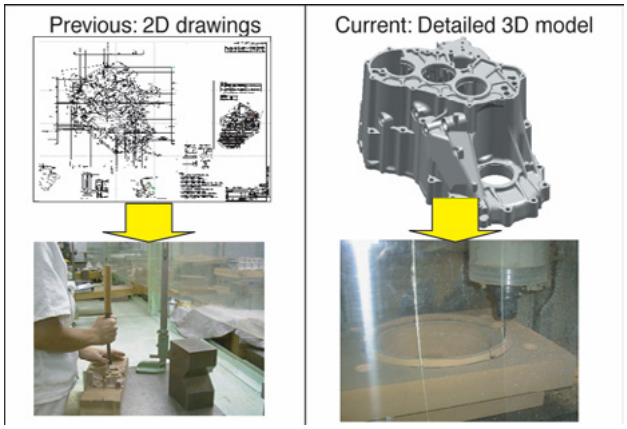


Fig. 1 Comparison of designing methods for sand mold manufacturing

products. Currently, since the design process at the leading manufacturers is based on 3D detail modeling, from the early stages of development to mass production, prototype parts are constructed with vastly improved precision. This is because it is possible to capture the intent of the designers and the full benefit of the ideas and experience possessed by the manufacturing department in specifications at the early stage of design and to represent them directly as complete 3D detail models[1]. As shown in Fig. 1, the shape of the prototype cast in a sand mold made with numerically controlled (NC) equipment according to the 3D detail model is nearly a 100% match with the intentions of the designers and the experience of the manufacturing division.

Figure 2 shows the result of a comparison of estimated weights (design weights) and actual weights of a sand-mold prototype made in the traditional method and of a sand-mold prototype made in the 3D design process. The vertical axis is the amount in percent by which the design and actual weights differed.

Conventional sand mold castings weighed about 10% more than the design weight, but those made from sand molds formed in NC equipment on the basis of the 3D detail models weighed within ±2% of the design weight, a very close correspondence to design. Thus, 3D detail models enable creation of forged components at the prototype stage with weights and shapes virtually identical to those mass-produced from die molds.

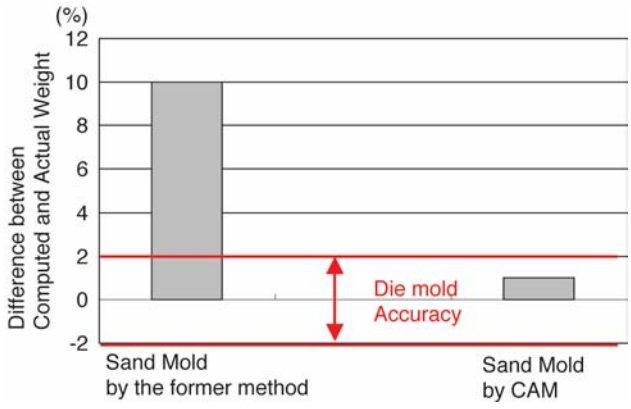


Fig. 2 Comparison of error in prediction of casting Weight

3. CAE Analysis of Single Components in 3D Detail Models

Formerly, both CAE analytical software (hereafter a CAE solver) and a technology for creating a CAE model compatible with the CAE solver were necessary in order to carry out analysis. Besides designers and test development engineers, there is a third specialty called ‘CAE experts’. CAE experts used the 2D drawings or 3D data provided by the designers to create CAE models incorporating fillets, draft angles, bolt holes and other features, as shown in Fig. 3, and carried out analysis with these models. Also, at times, CAE experts acted in place of the designers in assessing the results of the analyses.

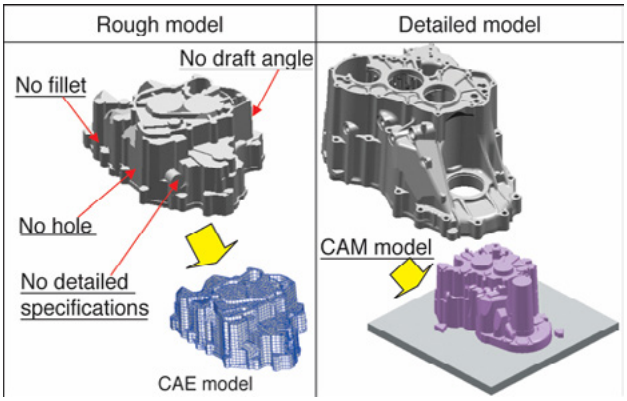


Fig. 3 Definition of rough & detailed models

One goal of simplification of model shape was to minimize the size of the CAE model in order not to exceed the capacity of the computer. Therefore, hexahedral elements, which provide comparatively high precision in calculations, have always been used to obtain the best precision in results with the smallest possible number of elements and nodes. Shell elements, which can provide acceptable precision while reducing solving time, were also incorporated in parts of the models to reduce the labor time of the CAE experts[3]. These measures were necessary in order to extract the most effective possible results, within the limits of the computers. Thus, it was necessary for CAE modeling technology to not only allow specialized operations and settings for analytical conditions but also to account for the calculation capacity of the host computer. This was an obstacle to the use of CAE analysis as a numerical tool aiding designers in design specification decisions.

Figure 4 shows the flow from development to mass production, using a transmission as an example. CAE techniques are generally used to investigate specifications during the development up to creation of the prototype. As explained in Section 2, now that a sand-cast prototype can be obtained with nearly identical precision to that of mass products from die molds assessments based on tests employing these prototype parts are of the same level of confidence as assessments from tests of mass produced parts. Shape adjustment based on the test results requires the same level of precision as direct revision of mass production parts

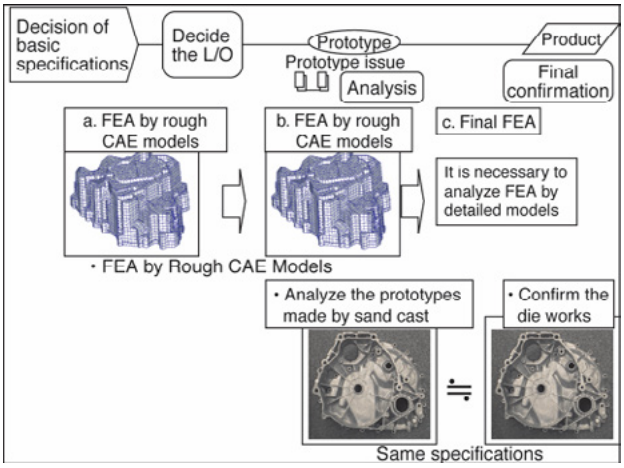


Fig. 4 Transmission development flow and models

do. "Final FEA" in Fig. 4c indicates that it is not possible to assess the influence of component shape details by analysis of the simplified CAE models made by the CAE experts. Full, un-simplified models must be used. It is concluded that the more precise the prototype becomes, the stronger the demand becomes for precision in the shape of CAE models after prototype testing.

3.1. Aim of 3D CAD-CAE

An automatic meshing (automesh) function capable of inserting meshes into fine details is necessary for finite element (FE) analysis of 3D detail models. The automesh function has been described in previous reports[(2), (4)] so no explanation will be given here.

Thus, for the effective use of CAE analysis at the development stage, fast FE analytical functions must be incorporated within the same 3D design tool to be used during the design process with 3D model. Figure 5 shows how the functions allow CAE analysis while providing a 3D representation of the designer's intent.

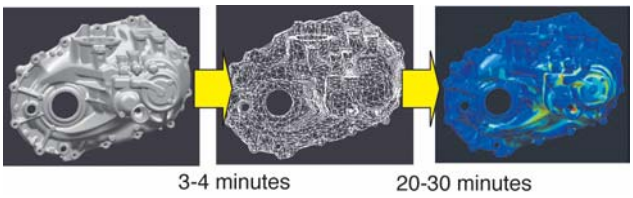


Fig. 5 The detailed model and the result

3.2. Examples of Stress Analysis by Designers

Here, some examples of actual use of component automeshing and stress analysis performed by designers are provided[(2), (4), (5)].

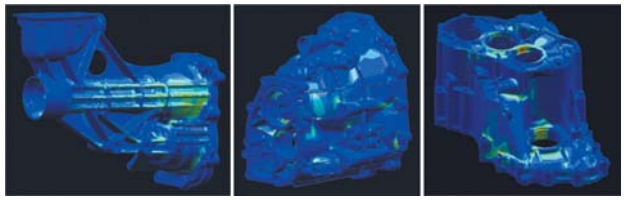


Fig. 6 Examples of FEA in detailed models

Figure 6 shows an actual stress analysis. There was absolutely no simplification of the component, such as elimination of fillets or shape revision, before the FE analysis. The 3D detail model also allowed application to die molds, including die mold draft angle.

The model consisted of about 90,000 2nd-degree tetrahedral elements with 150,000 nodes.

Formerly, a CAE expert would have required over 80 man-hours to perform only the manual meshing of the transmission case with about 2,000 nodes without fillets. To perform the analysis of this 3D detail model, it took about 10 minutes to apply the boundary conditions, and the analysis on a workstation, including automeshing, required about 30 minutes. The meshing task only required 3 – 4 minutes.

3.3. Examples of Eigenvalue Analysis

Here are some examples of the 3D detail model applied to eigenvalue analysis[(5)].

Tests of this component revealed intense 2.3 kHz radiation noise, which would considerably degrade noise from the vehicle. Based on the noise test results, CAE analysis of a 3D detail model of the component was employed to examine the effects of the ribs and other features on the eigenvalues, as depicted in Fig. 7. The 2.3 kHz eigenvalue was raised to 4.1 kHz, resulting in a large improvement in radiation noise.

CAE was already employed for eigenvalue analysis, but it was not possible for designers to use 3D detail models as is, including draft angle for die molds, for CAE models.

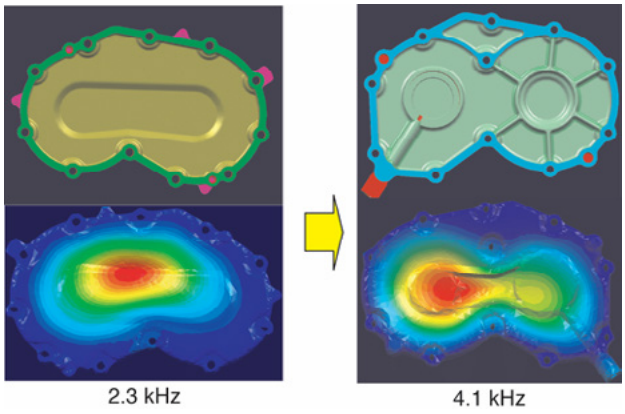


Fig. 7 Modal analysis by FEA

Figure 8 displays examples of the usefulness of CAE analysis by designers during transmission development. The number of design modifications was cut to about 1/3 of its previous level by the direct use of 3D detail models as CAE models.

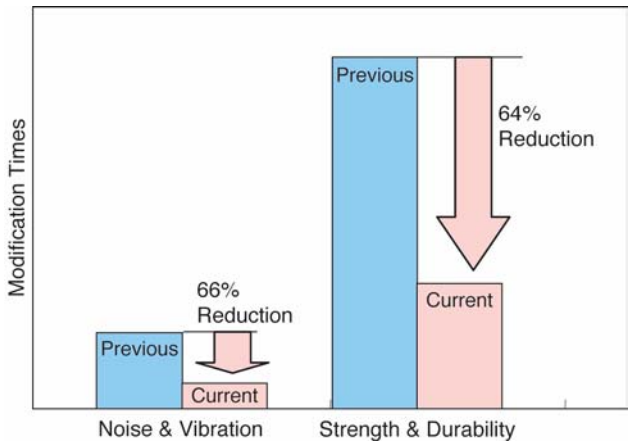


Fig. 8 Revised specifications of the transmission die mold parts at start of production

4. CAE Analysis of Assembled Models by Designers

4.1. Aim of CAE Analysis of Assembled Models

Section 3 described examples of decisions on single component specifications made by designers and test-development engineers after their own CAE analyses of components for strength, stiffness and eigenvalues.

The biggest concern in functional assessments of single components at the designer's desk is the selection of analytical conditions. These are set on the basis of the design requirements and the results of past tests. These analytical conditions are usually considered not on the basis of a single independent component, but on the assembly of several components. For example, the load applied on each bearing or other component and its direction are calculated from the input transmission torque; this sets the analytical conditions for each component. There is much controversy about CAE precision, but the investigation of precision in the analytical conditions is usually left up to the analyst. There are not many research papers or reports which serve as references on the subject. Originally, designers themselves calculated the loads applied to each component and the resulting deflections, and used previous examples to set design specification. The better the designer was at accurately predicting the forces applied on the component, the lighter and more compact he could design it. CAE analysis will allow all designers the ability to investigate analytical conditions in order to make more precise choices of conditions. However, in new L/O design and design of components with new functions, it is difficult to predict the forces on the component. Sometimes, CAE experts were summoned to create very roughly meshed CAE models for analysis of simplified assembled models in order to estimate analytical conditions such as forces on individual components. These models were also used for investigations of analytical conditions for single components, using the forces estimated from the assembly models. If it is possible to perform CAE analysis of assemblies using 3D detail models, very high precision can be obtained in analytical results such as strength and eigenvalues for components while taking the analytical conditions of single components into consideration.

For example, when finding the stiffness of a transmission case, CAE analysis of the case itself is easy, but one of the analytical conditions which must be taken into account is the load on the joint between case halves. If it is possible to carry out a CAE analysis of an entire transmission unit, the load on the joint will be available as one of the analysis results. Of course, CAE experts have always been employed to carry out these large-scale, time-consuming analyses of assembled models. Transmission analyses are common as examples of CAE analysis. However, it was extremely rare for designers to use this at the design stage with assemblies using 3D detail models, due to high-precision CAE analytical techniques and the time needed for analysis.

Thus, one of the next steps in this technology will be construction of a CAE analytical environment for assembled models. This will enable rapid analysis of 3D detail models by designers in the design stage.

4.2. Examples of CAE Analysis of Assembly Models and Their Effectiveness

Practical testing of CAE packages allowing analysis of assemblies of multiple components began just as CAE analytical methods were becoming available for analysis of single components by designers. An example is provided in Fig. 9.

This transmission had two outer cases which were fastened together. A CAE analysis of the assembled model was carried out with separately created cylindrical gears and gear shafts. This kind of analysis was already the established method for CAE experts. The great difference between the earlier analysis and the new analysis was that the several hours required for preprocessing items such as contact definition was cut by a factor of about 10 through use of the CAE solver. With CAE analysis software embedded in 3D CAD systems (hereafter CAD-CAE systems), the simplified preprocessing and the fact that it is all performed on the same CAD system results in great reductions of man-hours. Design investigation by designers by CAE analysis of assembled models has entered the realm of possibility.

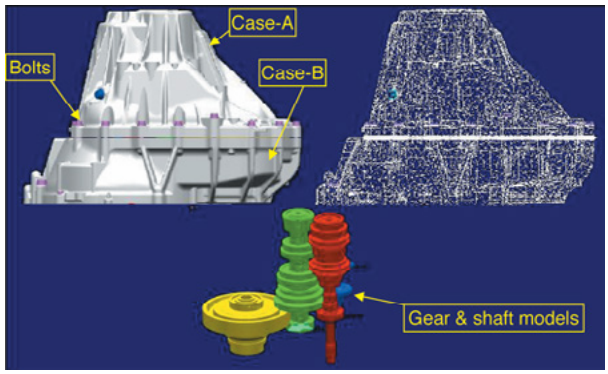


Fig. 9 Assembled models

Figure 10 presents the results of designers' investigations of eigenvalues with CAE analysis of the transmission assembly in order to reduce radiation noise from the case. Figure 11 shows some additional details of the countermeasures. The designers were able to assess the effects of details of shapes of some of the components in a coupled situation, without the help of specialists.

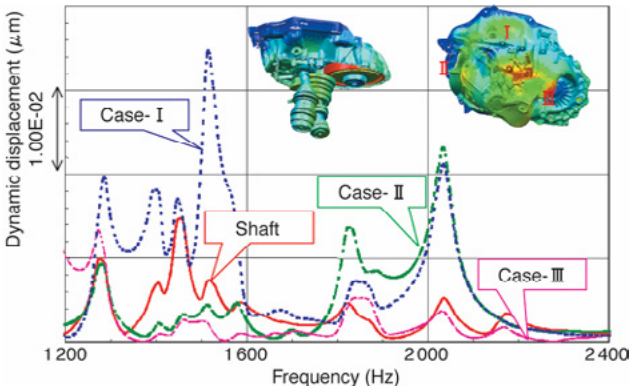


Fig. 10 Dynamic displacement of an assembled model

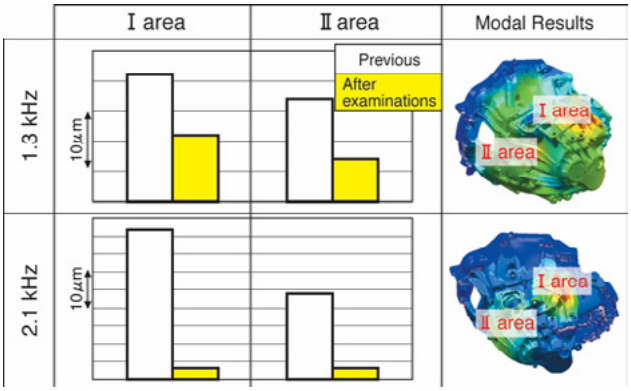


Fig. 11 Results of countermeasures

4.3. Future of CAE Analysis of Assembly Models by Designers

CAE analysis of assembled models with CAD-CAE systems is expected to spread throughout the industry, just like the CAE analysis of the single components explained in Section 3, due to the convenience of using CAD models directly as CAE models and the much more user-friendly definitions of contact conditions than in previous CAE solvers. It is believed that the labor involved in using CAE in the next generation of CAD-CAE systems will be greatly reduced, requiring only about one tenth the time necessary in current CAD-CAE systems. While designers have seen the utility of CAE analysis of assembled models with their own eyes, demands have naturally grown for greater capabilities in modeling of details in gears, shafts and similar components, as described in Section 4.2. Due to the huge size of the files involved and the current numerical capacities of computers and CAD systems, it is not yet possible to prepare 3D models with the shape details of every component in an automobile for CAE analysis of an assembled model. Also there are certain differences between systems, so it is impossible to give a 'correct' value for the calculation limits of currently used CAD-CAE systems, but a plausible estimate for current analytical models is 1 million degrees of freedom and 2,000 – 3,000 contact elements. Further improvements to systems and to CAD-CAE software will be necessary in order to carry out the CAE analyses of assembled models that designers, including the authors, would really like to carry out. The authors are certain that all designers share a desire for stress-free, easy calculations for this region.

5. Summary

The following advances have been made, thanks to the development of 3D detail shape modeling.

(1) The precision of sand-cast prototype parts was improved to that of mass products with die molds.
(2) Since the precision of prototype parts allows nearly the same confidence in assessments of the test results as after tests of mass products, it is necessary to develop CAE analysis employing 3D detail models that allow assessment of details in CAE analysis of prototype part tests.
(3) Designers are now able to use CAE analysis employing 3D detail models during the design process.
(4) Designers now realize that they are able to use CAE analysis of assembled models, a task formerly entrusted to CAE experts, during the design process.

6. Afterword

Thanks to the development of 3D detail models, not only has it become possible to incorporate manufacturing technologies in the early stages of the design process, designers themselves can also use FE analysis. The tools of FE analytical techniques have been placed in the hands of designers. Thus, technologies and information formerly available only to manufacturing technologists and CAE experts have been provided to designers at the early stages of product development, allowing them to assess products and make adjustments to specifications. Now that CAD-CAE operations have been simplified so that designers can employ CAE analysis, it is clear that the next step will be to provide CAE analysis capabilities for assembled models. The obstacle to this is the limitations on model size in CAD-CAE systems. The key to future developments in design technologies will be the sharing of this issue by CAD vendors and designers and the rapid improvement of CAD-CAE analysis environments.

References

(1) Shimada, H., Ishihama, Y., Kubota, N., Uchida, T.: Establishment of Design Method for Transmission by 3D Media, Honda R&D Technical Review, Vol. 14, No. 2, p. 107-114 (2002)

(2) Nagai, S., Uchida, T.: Application of finite element analysis using 3D auto-mesher to transmission development, Honda R&D Technical Review, Vol. 13, No. 1, p. 117-124 (2001)

(3) Takahashi, K., Takahashi, Y., Semba, K.: Use of a Supercomputer for Analysis of Power Plant Vibrations, Society of Automotive Engineers of Japan, preprint for lecture 901, p. 65-68 (1990)

(4) Uchida, T., Nagai, S.: The examples of Virtual Development for Automobile's Transmission, Journal of Society of Automotive Engineers of Japan Vol. 56, No. 6, p. 71-76 (2002)

(5) Kiku, K., Sekine, A., Ryoukata, M.: Prediction technique for gear noise transfer in engine mounting systems, Honda R&D Technical Review, Vol. 13, No. 1, p. 145-150 (2001)

■ Authors ■



Takanao UCHIDA



Shigeru NAGAI



Shigeru KOYAMA

Development of a Thin, Lightweight Aluminum Wheel by the Multi-gate LPDC Process

Satoshi TAKAHASHI*

ABSTRACT

The characteristics required for wheel function were clarified and a thin, lightweight aluminum wheel was developed. The method adopted to reduce wheel thickness involved improving the mechanical properties of the materials by modification of the die layout. In the newly developed die layout, the gates that are set at the periphery of the outer rim are positioned at the bottom of the slide die so that the number of gates, their locations, and their shapes can be changed freely as needed. This arrangement made it possible to reduce the thickness of the material and increase the cooling rate. The faster cooling rate resulted in a finer structure, yielding greater elongation, which improved the fatigue strength and increased the toughness of the material. As a result, the thickness of the product in the inner rim and spoke portions was reduced 25%, achieving a 10% reduction in the weight of the wheel. This also shortened the casting cycle time and eliminated the need for a straightening process, therefore improving productivity.

1. Introduction

Demand for aluminum wheels is increasing due to design and weight reduction needs. Die casting processes, which have a high degree of design freedom and allow low cost manufacturing account for the majority of aluminum wheels currently being manufactured. Of these methods, the low pressure die casting (LPDC) process ranks alongside the gravity die casting (GDC) process as a typical manufacturing process for die cast aluminum wheels. Demands to address environmental and energy issues are increasing, and further weight reduction is also required of aluminum wheels.

Against this background, the developed multi-gate LPDC process makes it possible to further reduce the thickness and weight of aluminum wheels without major changes to the existing LPDC process facilities. At the same time, a higher productivity is also achieved by shortening the casting cycle time. These approaches toward weight reduction and the newly developed LPDC method are introduced below.

2. Weight Reduction for Aluminum Wheels

2.1. Characteristics Required of Aluminum Wheels

When investigating weight reduction for aluminum wheels, first the characteristics required of each part were clarified. Figure 1 shows the name of each wheel part.

In order to ensure the wheel functions of strength and

* Tochigi R&D Center

endurance, bench tests such as that shown in Fig. 2[(1)] are generally used. These tests evaluate the characteristics required of wheels separately for each part.

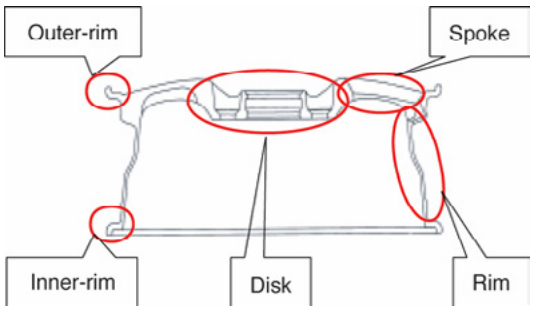
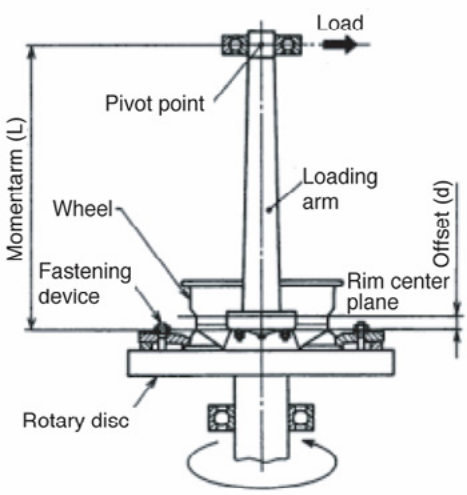


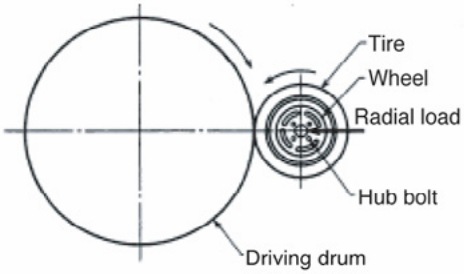
Fig. 1 The part name of the wheel

The rotary bending endurance test (Fig. 2-a) evaluates wheel endurance; it tests the fatigue strength for the area where the spokes meet the disk. The drum endurance test is used to evaluate the fatigue strength for the area where the spokes meet the disk as well as the rim as shown in Fig. 3-b. The drop impact test (Fig. 2-c) evaluates the impact resistance; it tests the toughness in the outer rim area and the area where the inner rim meets the rim as shown in Fig. 3-c.

When investigating thickness and weight reductions, the outer rim was excluded from thickness reductions due to a priority on styling and limitations of the tire bead assembly design. In addition, the disc was also excluded from thickness reductions due to limitations of the hub mounting layout. Therefore, investigation of thickness and weight reductions focused on the spokes, inner rim and rim.

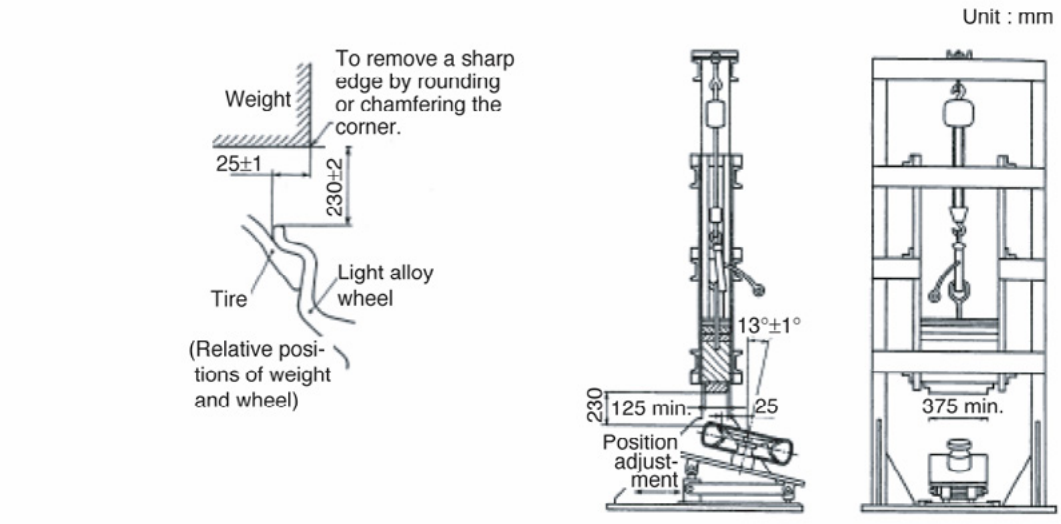


a) Bending endurance test apparatus (example)



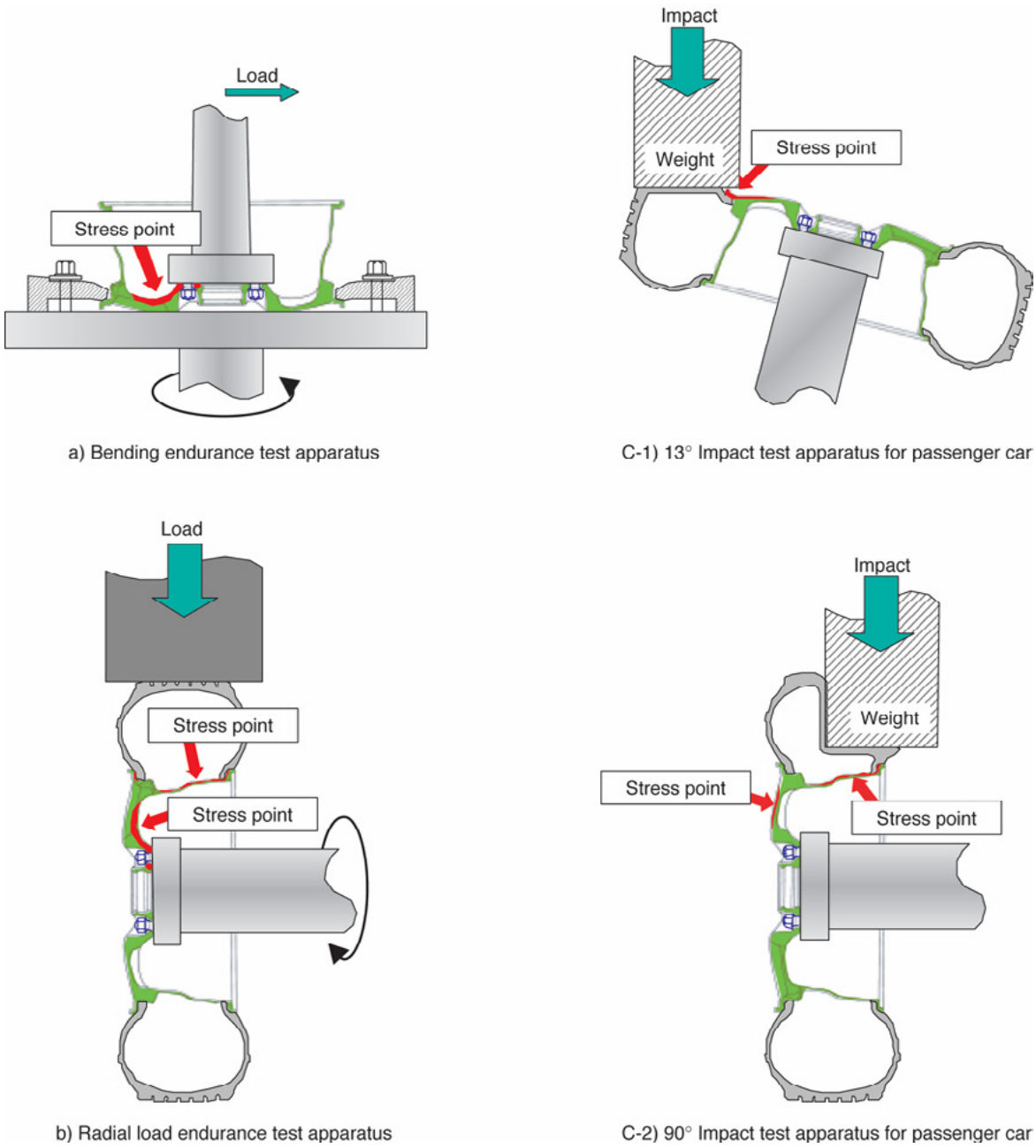
Remarks 1 The width of the drum shall be provided with a surface flat and wider than the overall width of the tire to be used in the test of the wheel.
2 The diameter of the drum shall be, at least, 1 700mm.

b) Radial load endurance test apparatus (example)



c) Impact test apparatus for passenger car (example)

Fig. 2 Test apparatus for the wheel



a) Bending endurance test apparatus

C-1) 13° Impact test apparatus for passenger car

b) Radial load endurance test apparatus

C-2) 90° Impact test apparatus for passenger car

Fig. 3 Stress point by the wheel test apparatus

2.2. Improvement of Mechanical Properties

In order to reduce the thickness and weight while maintaining the wheel strength and endurance, it is essential to improve the mechanical properties of the materials.

This development assumed that the melting furnace and heat treatment furnace would be shared in order to utilize existing LPDC facilities. Therefore, the material used was the AC4CH-T6 material that is generally used for die cast aluminum wheels. Table 1 shows the typical chemical composition of the AC4CH material used in this development.

Refining the structure is known to be an effective method of improving the mechanical properties without changing the material or the heat treatment. The mechanical properties of elongation and impact energy value increase significantly as the dendrite arm spacing (hereafter "DAS II")[2], which represents the structure size, decreases[3]. This tendency is also clearly evident in the manufacture of aluminum wheels, with elongation increasing greatly as DAS II becomes finer as shown in Fig. 4. In addition, increasing the cooling rate results in a finer DAS II[4], so increasing the cooling rate is an effective method for improving the mechanical properties.

Increasing the elongation normally leads to greater toughness, so using a finer DAS II to increase the elongation in the outer rim and area where the inner rim meets the rim is effective for improving the wheel performance in the drop impact test.

On the other hand, it has been reported that there is also a correlation between fatigue strength and elongation[5]. The test results in this development also showed a correlation between fatigue strength and elongation as shown in Fig. 5,

Table 1 AC4CH chemical composition

(wt.%)

	Cu	Si	Mg	Zn	Fe	Mn
JIS standard	0.20 Max	6.5 ~ 7.5	0.25 ~ 0.45	0.10 Max	0.20 Max	0.10 Max
A representative example	0.003	7.10	0.320	0.005	0.121	0.016
	Ni	Ti	Pb	Sn	Cr	Al
JIS standard	0.05 Max	0.20 Max	0.05 Max	0.05 Max	0.05 Max	Bal.
A representative example	0.005	0.120	0.005	0.000	0.001	Bal.

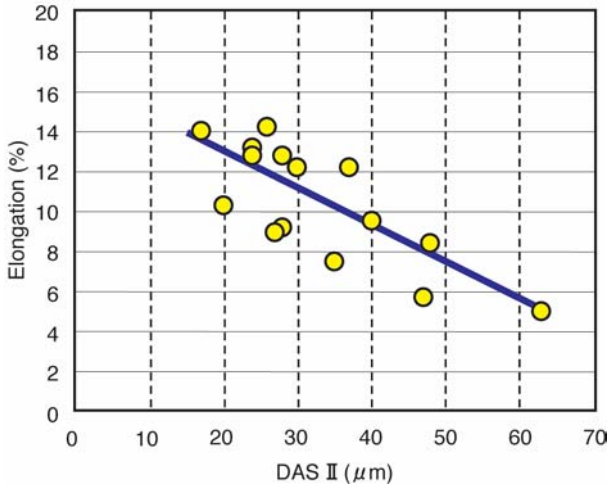


Fig. 4 Relation between DAS II and elongation of the Aluminum wheel

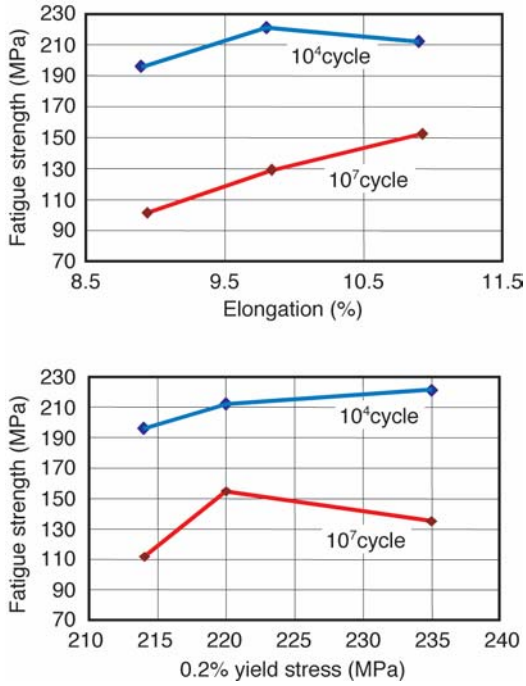


Fig. 5 Relation between fatigue strength and 0.2% yield strength/elongation

and the high cycle fatigue strength in particular was found to be more dependent on elongation than yield strength. The fatigue strength required for aluminum wheel durability is mainly the high cycle fatigue strength, so increasing the elongation is effective for improving aluminum wheel durability.

These results show that increasing the elongation for the area where the inner rim meets the rim and in the spokes is effective for reducing aluminum wheel weights. That is to say, efficient thickness and weight reduction can be achieved by increasing the cooling rate to improve the fatigue strength and toughness in these areas.

3. Issues for LPDC Process Aluminum Wheels

3.1. LPDC Process Issues

Using a finer DAS II is effective for improving the mechanical properties of die cast aluminum wheels including those made using the LPDC process, and to achieve this it is necessary to increase the cooling rate.

Figure 6-a shows schematic drawings of the center-gate systems most commonly used with the aluminum wheel LPDC process. The center-gate LPDC process uses a system that fills the entire product with molten metal from a single gate located in the center of the wheel. This requires a thick section to ensure metal flow and also directional solidification for excellent internal quality. This thick section not only lowers the cooling rate, but also increases the molten metal filling time.

The side-gate system shown in Fig. 6-b provides gates in two locations on the rim in order to increase the cooling rate compared to the center-gate system. However, there is a limit to how thin the section can be made due to the need to ensure metal flow from the rim to the center portion of the disc.

3.2. Conventional Multi-gate LPDC Process

Using multiple gates has been considered as an improvement method that both increases the cooling rate and shortens the filling time in the LPDC process. Figure 7 shows an example that further expands the above-mentioned side-gate system to pursue the merits of multiple gates. Molten metal is filled from four gates located on the outer

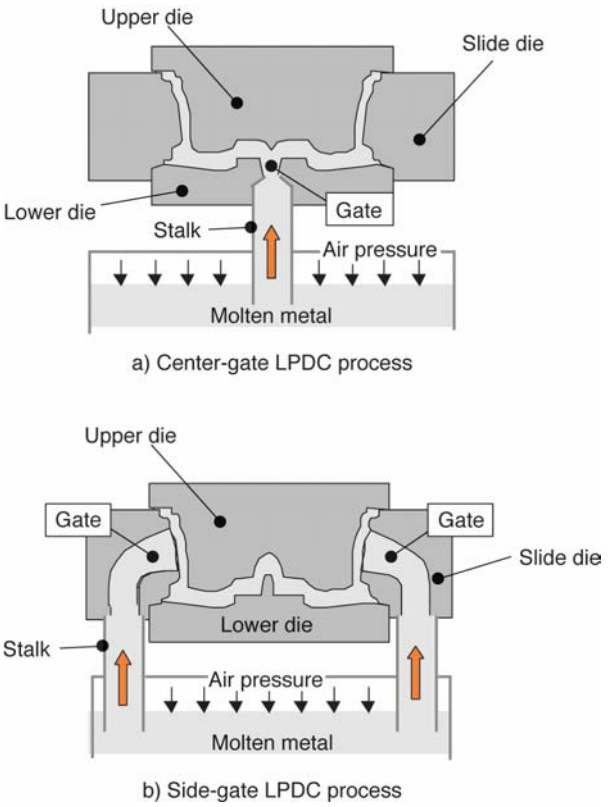


Fig. 6 Schematic illustration of the LPDC process

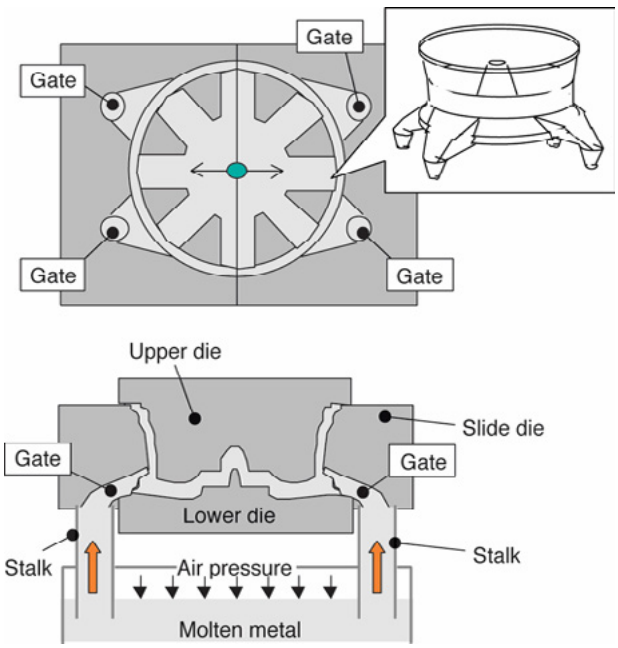


Fig. 7 4-gate LPDC process

rim, so metal flow is easily ensured and a thin section can be used. As a result, the cooling rate can be increased and at the same time the die filling time is also shortened, so this is expected to improve both the mechanical properties and productivity.

However, when using multiple gates with the conventional LPDC process, there are numerous limitations on the gate positions, such as number and shape in order to avoid interfering with the sliding motion of the slide die when the gating system opens. This meant that conventional multi-gate systems had to be designed in full consideration of productivity. This was a major issue for the LPDC process, which offers a superior degree of design freedom, and is why there are few examples of mass production using a multi-gate system.

Thus, the issues for reducing the weight of LPDC process aluminum wheels can be summarized as follows.

- The thick section makes it impossible to increase the cooling rate, which is a factor hindering improvement of both mechanical properties and productivity.
- Using multiple gates has been attempted as an improvement measure, but the gate settings are subject to limitations, so these effects were insufficient.

4. New Multi-gate LPDC Process

4.1. Overview of the New Multi-gate LPDC Process

The new multi-gate LPDC process was developed as a new process that is capable of solving the above-mentioned issues forwheels produced by the LPDC process. Figure 8 shows a schematic drawing of the new multi-gate LPDC process.

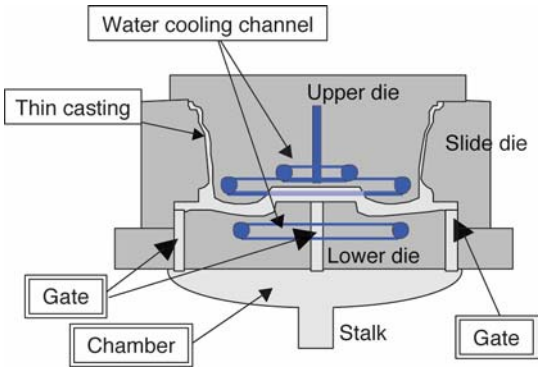


Fig. 8 New multi-gate LPDC process

This multi-gate system allows sliding without the gates interfering with slide die separation by using the bottom surface of the slide dies as the upper surface of the gates that are set at the periphery of the outer rim as shown in Fig. 9. As a result, the gate positions and the number of gates can be set freely as needed, thus improving metal flow which was an issue for using multiple gates with the LPDC process. In addition, in order to use multiple gates freely in the desired locations, a chamber was provided between the stalk and the die, allowing molten metal to be supplied to each gate without increasing the number of stalks. Furthermore, a high cooling rate was obtained by enhancing the water cooling capability of the upper die in order to reduce DAS II.

This new multi-gate system makes it possible to shorten

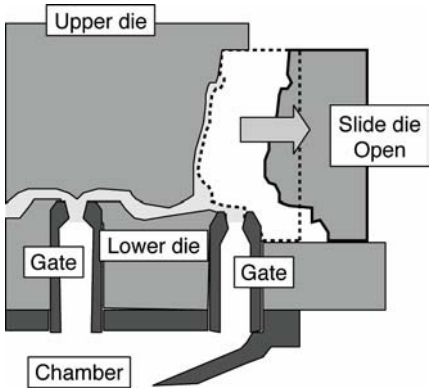


Fig. 9 Gating system of new multi-gate LPDC process

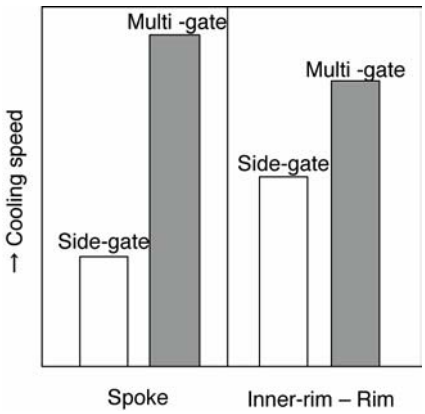


Fig. 10 Comparison of cooling speed



a) New multi-gate LPDC process



b) Side-gate LPDC process

Fig. 11 The section of the castings by LPDC process

the molten metal flow length, ensuring sufficient metal flow even when a thin section is used compared to the side-gate system. The use of thin sections and improved die cooling capability achieved a cooling rate approximately three times faster in the spokes. (Fig. 10)

Using this type of process made it possible to improve the mechanical properties by reducing DAS II.

4.2. Weight Reduction Effects of the New Multi-gate LPDC Process

Figures 11-a) and 11-b) show section photographs of castings manufactured using the new multi-gate LPDC system and the side-gate LPDC system. Compared to the side-gate LPDC system, the new multi-gate LPDC system reduced the material thickness of a 15-inch × 6.5 JJ aluminum wheel by 33% in the rim and 25% in the spokes, and also reduced the casting weight by 37%.

The non-material effects of the new multi-gate LPDC system are described below in comparison with the side-gate LPDC system.

4.2.1. Mechanical properties

Figure 12 shows the refinement effects on the DAS II size, which is important for improving toughness in order to reduce weights.

The area where the inner rim meets the rim and the spokes provide large weight reduction effects, and DAS II refinement effects of approximately 30% and 20%, respectively, were seen in these areas. As a result, elongation also increased by approximately 50% and 70%, respectively.

4.2.2. Weight reduction effects

These improvements in toughness made it possible to reduce the product thickness by 25% in the spokes and by 7% to 25% in the rim as shown in Fig. 13. This made it possible to reduce the total product weight by 10% without sacrificing strength performance.

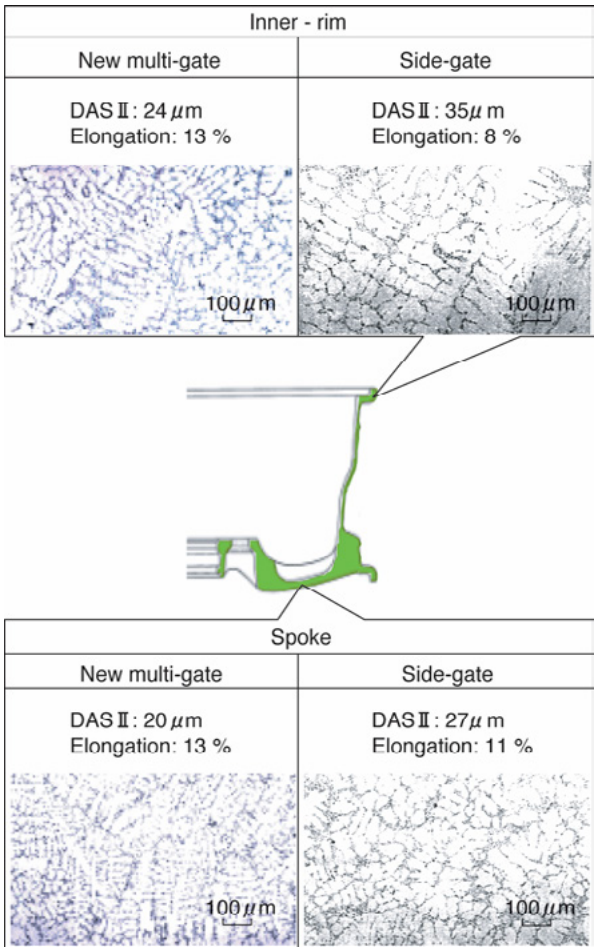
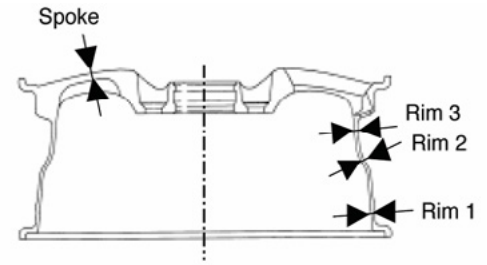


Fig. 12 Relation between DAS II and elongation



Part		Reduction ratio (%)
Thickness	Spoke	25
	Rim 1	25
	Rim 2	19
	Rim 3	7
Total weight		**10**

Fig. 13 Comparison of the thickness

4.3. Improvement of Productivity

In addition to the effects described above, the new multi-gate LPDC process also produced the following effects related to productivity.

4.3.1. Cycle time

Figure 14 shows the casting cycle time reduction effects. The long casting cycle time is a major issue related to LPDC process productivity. In particular, the long die filling time and cooling time are the main factors.

The new multi-gate LPDC process has a thin section, reduced casting weight and short cooling time. This means that of the casting processes from the pressure rise process to the clamping process, the filling, feeding and cooling process times are shortened, thus shortening the total time to 75% of the conventional casting cycle time.

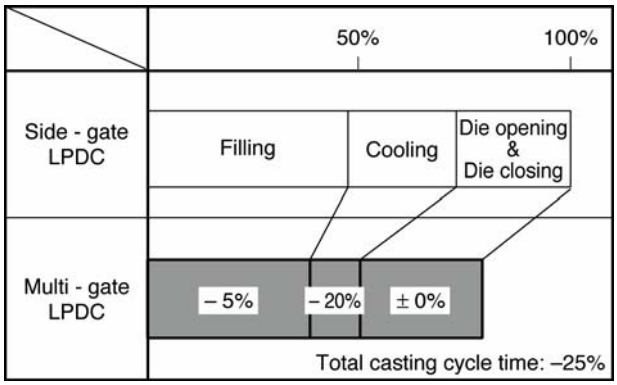


Fig. 14 Comparison of the thickness

4.3.2. Other effects

The multi-gate system also reduced the temperature gradients during solidification, thus effectively reducing the residual strain induced during solidification. This eliminated the need for a straightening process after casting which had been necessary for the LPDC process thus far.

5. Conclusion

Aluminum wheels manufactured using the new multi-gate LPDC process take advantage of the gates located at the periphery of the outer rim positioned at the bottom of the slide die, so the gates can be freely designed as needed, and the thickness of the material can be reduced. This has provided the following results.

(1) An increased cooling rate produced a finer structure, which improved the mechanical properties. As a result, the thickness in the inner rim and spoke portions was reduced by 25%, achieving a 10% reduction in the total weight.

(2) A 25% reduction in the casting cycle time and elimination of the straightening process improved productivity.

This paper described the new process using the example of a 15-inch × 6.5 JJ size wheel, so these results will vary depending on the wheel size and design. Recent wheels are tending toward larger diameters, so application of this multi-gate LPDC process can be expected to provide even greater weight reduction effects in the future.

6. Acknowledgements

The author wishes to express his deepest thanks to Asahi Tec Corp. for its enormous cooperation with this development.

References

(1) JIS D4103 Automobile Parts — Disc Wheels — Performance requirements and marking

(2) Kamio, A. et al.: Dendrite Arm Spacing SOKUTEITEJUN, Aluminum NO Dendrite Arm Spacing TO REIKYAKUSOKUDO NO SOKUTEIHOUHOU, Tokyo, The Japan Institute of Light Metals, p. 46-52 (1988)

(3) Kitaoka, S. et al.: Al-Si-Mg KEIGOUKIN NO SOSIKI TO KIKAITEKISEISITU, Aluminum NO SOSIKI TO SEISITU, Tokyo, The Japan Institute of Light Metals, p. 242-245 (1991)

(4) Adachi, M.: IMONO·Diecast, Aluminum NO SEIHIN TO SEIZOUGIJUTU, Tokyo, The Japan Institute of Light Metals, p. 384 (2002)

(5) Honma, U.: KEIGOUKINMONO NO SEIHOU TO ZAISITU, IMONO BINRAN, Tokyo, Maruzen, p. 931-936 (1986)

■ Author ■



Satoshi TAKAHASHI

Development of a Plastic Mold Technology for Bus Rings in a DC Brushless Motor

Kazuo TAKEUCHI* Kotaro TANAKA*
Tatsuro HORIE* Akihiro OKAMURA*

ABSTRACT

To improve the layout and increase the mass productivity of Hybrid Electric Vehicles (HEV) drive motors, integrated molding of high voltage distribution parts using plastic insulation material was investigated as a method to reduce the number of parts and increase ease of assembly. The enlargement of part dimensions, occurring with the change to molding plastic from the former cure coat-type fluoropolymer insulator material, was minimized and waterproofing performance was increased. Selection of materials on the basis of measurements of heat strain in plastic molded parts and full molding using floating over molding ensure waterproofing. Study of the design basis for high-voltage insulation clarified the minimum insulation distance, enabling the development of an integrated bus ring molding technology, which allows mass production without increasing the dimensions of the parts.

1. Introduction

As part of the continuing effort to address automotive environmental issues, expectations have been high concerning the market penetration of hybrid electric vehicles (HEV hereafter) as technology to further improve fuel economy.

In order to work towards true market penetration of HEV, it is necessary to resolve issues of making the systems additional to those of a conventional gasoline vehicle, such as a driving motor and battery, etc., smaller and lighter, and improving mass productivity of these systems.

In addition, the motor drive voltage (generally 200 V or more) for HEV, EV and FCV is higher than the voltage of a conventional gasoline vehicle's electrical component (12 – 24 V). Therefore, the reliability of insulation against the high voltage of the electrical conponents is very important, and when insulation is guaranteed using plastic molding, the selection of plastic material and the structure design of the molding are important in determining the quality of insulation. Therefore, a study was made, working towards making the unit smaller and improving mass productivity, by reducing the number of parts through integrated mold forming of the multiple bus rings, having a current distribution function used to drive the DC brushless motor, with plastic insulation material. In addition, studies were performed on integrated molding structures and molding technologies. Bus ring integrated plastic mold technologies were developed with high insulating reliability. This is a report on those technologies.

2. Development Aims

Figure 1 shows the structure of the DC brushless motor being used in the IMA (Integrated Motor Assist) system for the Honda Insight. The motor uses three copper conductors (bus rings) to distribute three-phase current to 18 stator coils used for motor drive.

The bus rings are required for not only an electrical distribution function, but also for inter-phase insulation and external insulation, so a cure coat type of insulation material is used. In the cure coat type of insulation material, generally an epoxy cured coating is used, but because of the engine bay

* Tochigi R&D Center

high temperature environment around the motor for HEV, a highly heat resistant flouro-polymer cured resin coating was used.

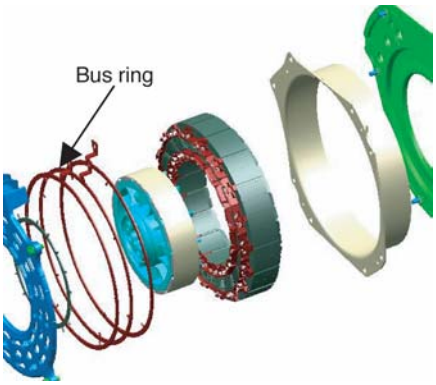


Fig. 1 Motor components and bus ring

The flouro-polymer cured resin coating is not only high in raw material cost, but also, as shown in Fig. 2, it is easy for the coating to become thinner at the corner edges and in areas of burrs of the pressed copper conductors. Furthermore, because of coating imperfections, such as pin holes, conductivity contaminants, coating film separation, etc., it is necessary to have rigorous quality control in order to maintain insulation performance. Therefore, yield is poor and it is difficult to expand the scale of manufacture.

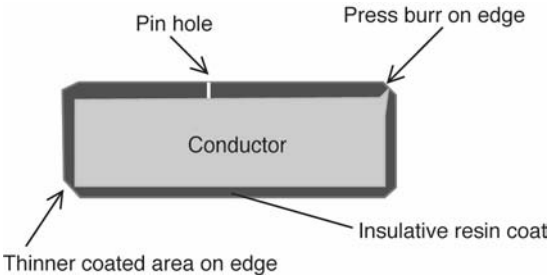


Fig. 2 Typical concerns of resin coated bus rings

In this development project, a study was done to see if it were possible to expand the scope of manufacturing through the use of copper conductors, over-molded with plastic insulation material, as insulation material instead of cured resin coating.

3. Technological Issues in Changing to Plastic Molding

3.1. Technological Issues in Changing to Plastic Molding

When over-molded with plastic and used as insulation material, by improving yield, an expansion of manufacturing scale can be expected. Yet the following technological issues must be addressed.

(1) Thinning of the insulation layer
With a cure type insulation layer, everything is fine as long as the minimum thickness necessary for insulation is maintained (10's of μm). However, in contrast, with plastic molding, it is necessary to have a thickness of approximately 1 mm in order to maintain plastic flow during forming. Therefore, when using three bus rings together, additional space of 5 or 6 mm is needed in the stacking direction, in comparison with the cure type resin insulation material coatings.

(2) Durability and reliability against heat cycles
With cured resin coating, a comparatively flexible plastic coating is thinly formed on the conductor surface. Therefore, the plastic coating follows the thermal expansion of the copper conductor and it is able to absorb thermal strain. In comparison, when using plastic molding, the thermal expansion difference from the copper conductor cannot be absorbed because the molded plastic is hard and the layers thick. This means there is cracking of the molded plastic due to thermal cycles creating a water penetration passage and resulting in a drop in insulation performance. In particular, weld lines, which are one type of plastic forming flaw or imperfection, give low strength characteristics and easily form the point of origin of thermal cycle cracking.

3.2. Methods for Responding to These Issues

In order to resolve these issues, the following countermeasure methods were studied.

(1) Achieving a smaller size through integrated molding
Rather than plastic molding the three copper conductors separately, work to make it more compact with integrated plastic molding of the three conductors. At the same time, while coming up with ideas for an integrated molding structures and forming methods, maintain insulation reliability by firmly establishing principles for design of insulation against high voltage.

(2) Maintaining durability and reliability against heat cycles
The optimum plastic material is selected by directly evaluating thermal strain that occurs in the plastic during thermal cycles and comparing it with material strength characteristics. In addition, through forming method proposals and molding structure ideas, structurally prevent water penetration and avoid a drop in strength characteristics, which can be caused by flaws or imperfections such as weld lines.

4. Studies of Structure and Forming Method Proposals

4.1. Studies of Forming Method Proposals

When integrated, the major functions of the plastic molded parts are insulation between the integrated copper conductors and insulation from external parts. Accordingly, in order to maintain insulation performance, it is essential to accurately maintain the thickness of the molded plastic between the conductors and around the outside. Conductors are subject to a large plastic filling pressure during plastic molding. Therefore, as shown in Fig. 3, there is a conductor position misalignment which causes the insulation performance to drop.

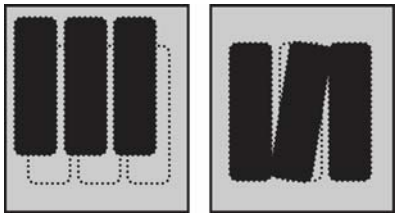


Fig. 3 Position shift in resin mold

Generally, in order to prevent insert part position misalignment during molding, forming manufacturing ideas are used, as shown in Fig. 4.

a) The mold is formed in two separate stages (two-step injection).
b) Conductor misalignment is prevented by holding them inside the mold using a mold holding pin.

Use of the two-step molding shown in “a” has the advantage of being able to firmly support the insert part. However, even when using the same plastic material for the 1st and 2nd injections, at the time of the 2nd injection the 1st mold has already cooled to a solid state, and at a position away from the injection gate, it is easy to have an incomplete interface fusion (cold joint). A cold joint on the outer surface of a part is a cause of loss of insulation function, due to water penetration.

In contrast, when using a holding pin, no cold joints are created. But in order to guarantee full waterproofing performance, it is necessary to add a process, such as waterproof potting application, etc., in the holding pin tracks, as shown in Fig. 4b.

A method that gives a seamless mold not requiring an additional waterproofing process is floating over mold, which removes the holding pin in the forming process. However, because the holding pin is removed before the plastic filling is complete, it becomes difficult to balance plastic filling pressure during the molding of complex shapes and to maintain insert position accuracy.

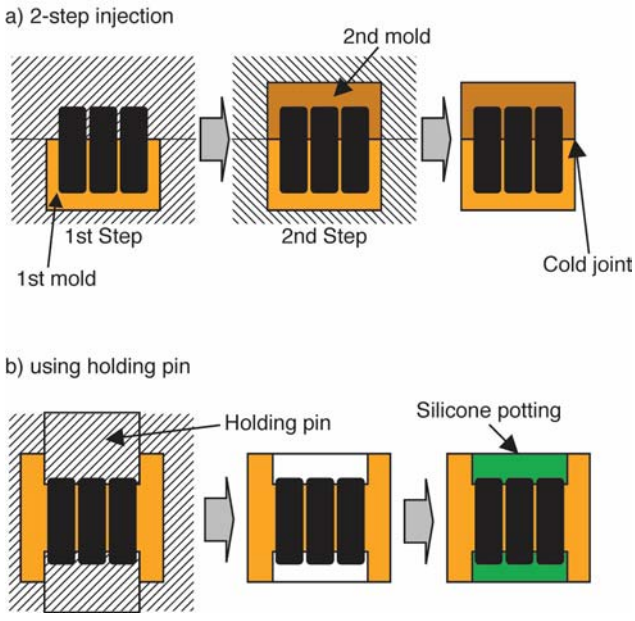


Fig. 4 Schematic drawing of full mold method

Therefore, this development project combines two-step injection (a) and float over mold (b), as shown in Fig. 5.

(1) The copper conductor is held by a previously formed 1st mold, and in addition to maintaining the accuracy of relative positions between phases, there is an over-mold over the whole (two-step molding).
(2) By molding over the 1st mold that holds the copper conductors, using floating over molding, no cold joints are created on the external surface and waterproofing performance is maintained (floating over mold).

This structure and the forming method proposal separate the functions to be guaranteed.

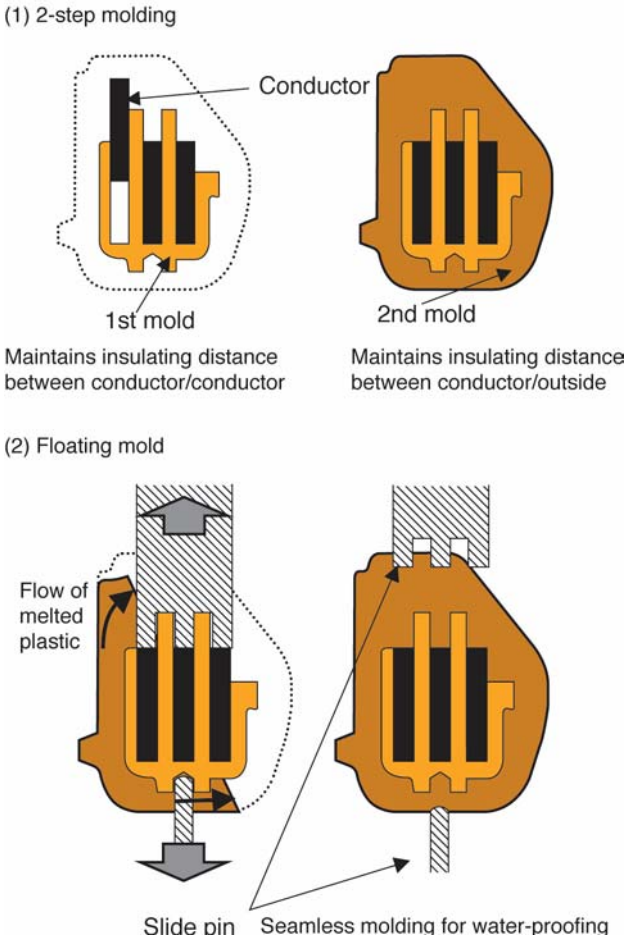


Fig. 5 Seamless molding method for a bus ring

4.2. Molded Bus Ring Structure

The basic structure of the plastic molded bus ring is shown in Fig. 6. Three copper conductors are bent into a cylindrical shape. After securing insulating distance between conductors held by the 1st mold (holder), waterproofing performance and insulation between the conductors and the outside are secured with a 2nd mold (over-mold).

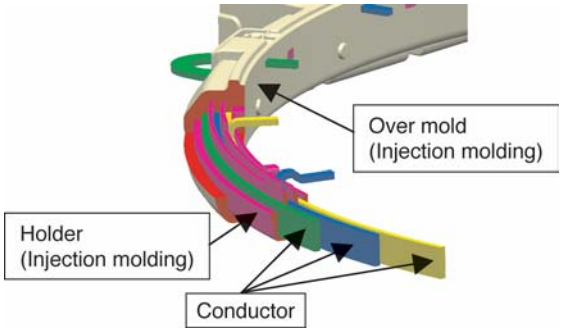


Fig. 6 Structure of a plastic molded bus ring

5. Selection of Optimum Material

5.1. Selection of Study Materials

In this development project, because the part usage environment temperature is high (150 °C or higher), and because shape accuracy and stiffness are necessary for the parts during assembly, the mold materials studied included PBT reinforced with glass fibers (PBT-GF hereafter), PPS reinforced with glass fibers (PPS-GF hereafter) and PPS reinforced with glass fibers and minerals (PPS-GF/M hereafter). The PPS-GF/M is a special grade with low thermal expansion anisotropy.

The thermal expansion coefficients for these materials are given in Table 1.

Table 1 Thermal expansion coefficient of investigated materials

		PBT-GF	PPS-GF	PPS-GF/M
Thermal expansion coefficient (10^{-6}/K)	Flow direction	35	15	19
	Transverse to flow direction	80	51	29

5.2. Evaluation of Thermal Stress

Plastic molded parts formed with metal inserts have thermal stress generated due to differences in thermal expansion when there is a temperature change. To select materials, the thermal strain is evaluated and a comparison is made of fatigue strength characteristics of the materials. With material such as metals showing isotropic thermal expansion behavior, a simple method for evaluating thermal strain is to use a self-temperature compensated strain gauge, compensating for a certain level of apparent strain occurring due to simple thermal expansion. However, with plastic insulation material, there is a large difference in thermal expansion behavior between the plastic flow direction and the direction perpendicular to the flow direction. In the case of plastic with anisotropic filler such as glass fibers, etc., the anisotropy is heightened, making it difficult ordinarily to correct apparent strain due to thermal expansion.

Even in this development project, in order to reduce the difference in thermal expansion with the copper conductor, studies were done on ordinary glass short fiber filler material and of glass filler + mineral filler material, called improved anisotropy material. However, even with the improved anisotropy grade, as shown in Table 1, there is anisotropy in the thermal expansion behavior.

Therefore, in this development project, two bus rings were formed under the same conditions, one being cut and used as a reference for free thermal expansion and the other being used for thermal strain evaluation in the part shape. By measuring them at the same temperature, it was possible to measure the thermal strain while eliminating the thermal expansion effect of the material itself.

The measurement method is shown in Fig. 7.

a) A strain gauge is attached to one of the bus rings, and another strain gauge attached to the same area of the other bus ring, which has been cut. With the strain gauge on the cut bus ring as reference, the two-gauge method was used to create a bridge.
b) The temperature was changed so that the temperature of the two bus rings became the same and a temperature to strain (measured strain) diagram was obtained.
c) At normal temperature, the completed part bus ring's cut release strain was measured and the temperature to strain diagram was shifted to calibrate, so that it passed through the measurement points, and the temperature to strain graph (calibrated strain) was obtained.

The temperature to strain diagram thus obtained shows the absolute value of thermal strain generated due to thermal expansion differences, at each temperature.

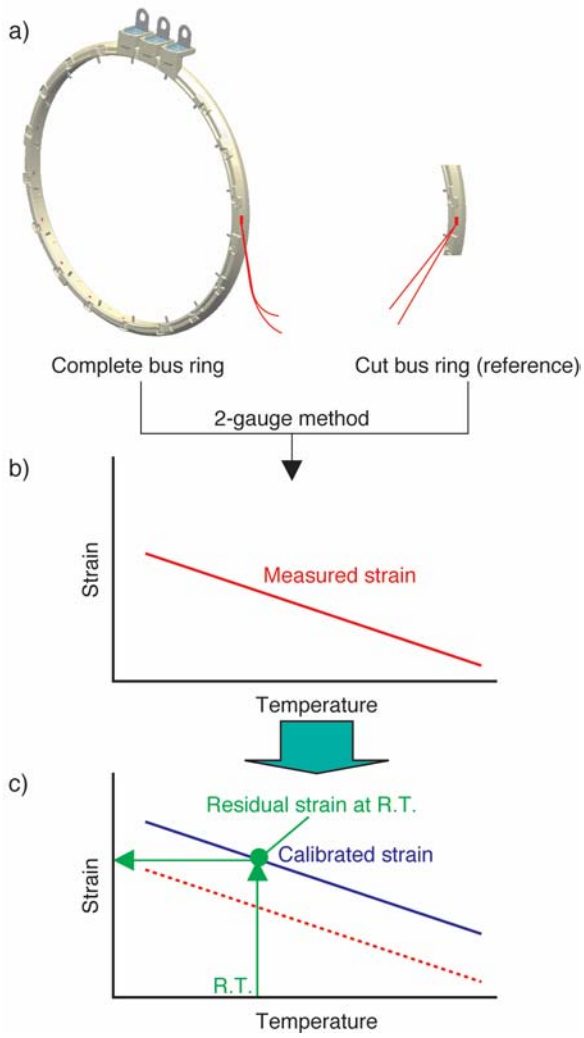


Fig. 7 Thermal strain measurement method

An example of bus ring thermal strain evaluation results obtained in this way is shown in Fig. 8.

Thermal strain occurring in bus rings is predicted from the thermal expansion behavior. It was confirmed that thermal strain is roughly zero near the temperature where plastic flow stops, and as the temperature lowers, it increases in a roughly linear manner. Accordingly, it is thought that bus ring heat cycle life is controlled by fatigue strength on the low temperature side, when thermal strain value is large and plastic elongation after fracture is low.

In addition, making predictions by comparing material thermal expansion rate, compared to the PBT-GF material, the PPS-GF ordinary grade material's thermal strain is approximately 30% smaller and the PPS-GF/M improved anisotropy grade material's thermal strain approximately 40% smaller.

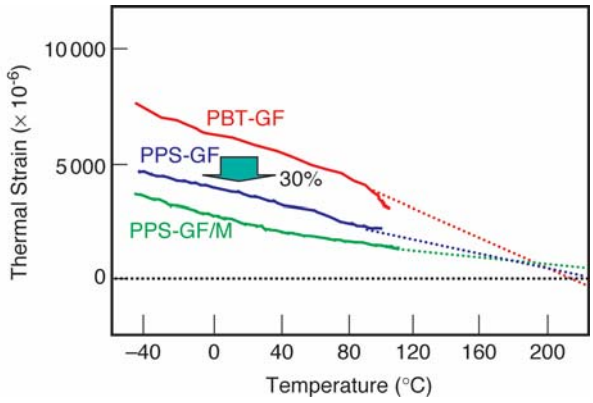


Fig. 8 Temperature dependence of thermal strain

Since this part's guaranteed low temperature limit is –40°C, when selecting material, the bus ring thermal strain amount at –40°C and the fatigue strength at the target cycles established are measured, and comparisons are made.

As shown in Fig. 9, with the PBT-GF material, thermal strain is generated that is roughly equivalent to test piece material strength. Ordinarily, because an actual formed part has forming flaws or imperfections such as weld lines that show lower physical properties than material test piece strength characteristcs, the safety ratio of the actual formed part is expected to be less than 1. In contrast, with the PPS-GF ordinary injection molding grade and the PPS-GF/M improved anisotropy grade material, it is predicted that the thermal strain is sufficiently small in comparison with the fatigue strength (strain value), and heat cycle life can sufficiently be maintained.

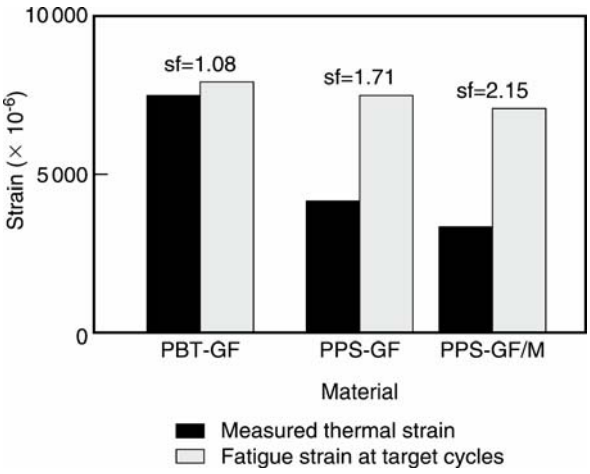


Fig. 9 Thermal strain and fatigue strain

Figure 10 shows the actual heat cycle life of bus rings molded with the various plastics.

The PPS-GF ordinary injection molding grade material and the PPS-GF/M improved anisotropy grade material, which have little thermal strain and a sufficient safety ratio against material strength, were confirmed as having at least three times the heat cycle life of the PBT-GF material, even with actual formed parts.

From these facts it was learned that ordinary PPS-GF injection molding grade material could be applied as molded plastic material.

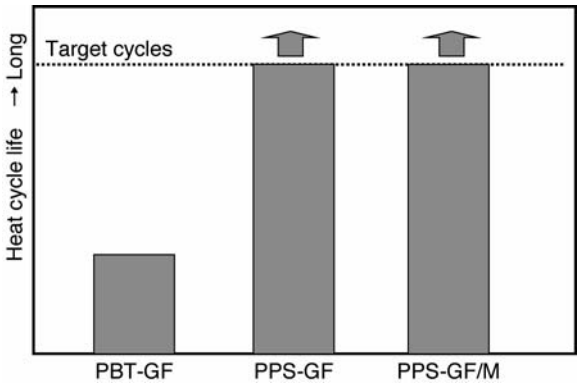


Fig. 10 Heat cycle life of bus ring

6. Insulation Design Technology

In order to achieve both insulation reliability against high voltage and a reduction in part size, insulation design principles were created.

With this structure, as shown in Fig. 11, the following two dielectric breakdown paths can be imagined.

a) Dielectric breakdown at interface between 1st and 2nd mold
b) Dielectric breakdown in the plastic thickness direction

Concerning these two dielectric breakdown paths, mold tests were carried out, and from the relationship between the insulation distance against the various dielectric breakdown paths and the dielectric breakdown voltage, the required insulation distance was determined.

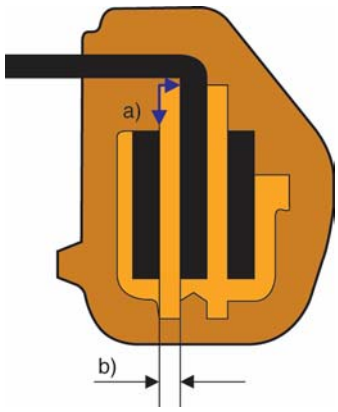


Fig. 11 Insulating distance a)interface, b)bulk

Figure 12 shows the relationship between the plastic material's bulk and surface insulation distance and the dielectric withstanding resistance, for the molded plastics studied.

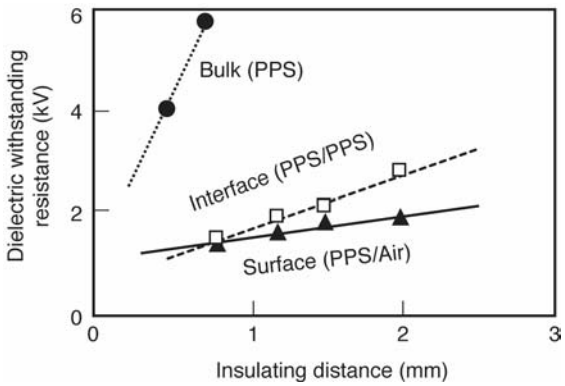


Fig. 12 Dielectric withstanding resistance

Generally, plastic surface resistance is lower than the internal plastic parts, due to the effect of water absorption in the plastic surface and electrostatic concentration on the vapor side[(1)], caused by differences in dielectric constant. The results of model tests also showed that plastic bulk insulation resistance is much greater than the insulation resistance of the plastic interface and plastic surface. And in terms of insulation design, a key point is to establish the insulation distance against the surface resistance at the interface.

In particular, concerning the insulation guarantee at interface "a)" it is necessary to establish a distance that guarantees insulation even when there is no interface fusion because it is not possible to expect fusion across the entire interface even when using the same plastic.

From these facts, it was learned that the distance between the copper conductors along the interface between the 1st and 2nd molds (creepage distance for insulation), as shown in Fig. 13, is the design value that guarantees insulation.

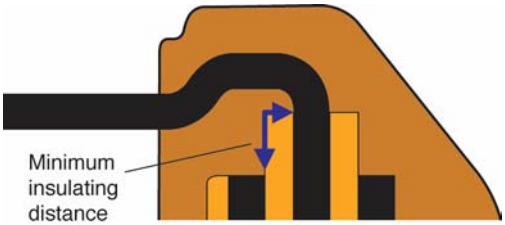


Fig. 13 Minimum insulating distance

7. Plastic Integrated Molding Technology

In this development project, the following principles were applied when making integrated molding of the three conductors.

(1) Guaranty inter-phase insulation between the conductors in the structure
(2) No exposure of the interface on the surface for waterproofing performance

In order to actualize these, floating over mold technology was applied, so that the 1st mold guarantees inter-phase insulation and the 2nd mold insulates against the outside and maintains waterproofing performance.

7.1. Overview of Floating Over Mold

Floating over mold is a technology that forms a seamless, multi-layer structure.

(1) The first mold is inserted into the 2nd molding die and supported by holding pins.
(2) At an appropriate time during the 2nd mold plastic filling process, the holding pins are removed and the support pin tracks are filled with molding plastic. This gives a plastic molded part without joints.

An overview of the floating over mold process is given in Fig. 14.

Because a high plastic filling pressure (generally 10 – 30 MPa or more) is applied to the 1st mold and the copper conductors during the 2nd mold filling, it is necessary to prevent deformation of or position misalignment of the copper conductor and the 1st mold during 2nd mold forming.

In this development project, in order to support the shapes of the 1st mold and the copper conductors, and to maintain position accuracy in the 2nd mold, the 1st mold is supported by slide pins from above and below, in the direction that divides the 2nd mold die.

The process can roughly be divided into three steps.

a) The 1st mold and the copper conductors are set into the 2nd mold die, and supported.
b) Injection of the 2nd mold plastic.
c) At an appropriate time, the slide pins supporting the 1st mold are removed, and the slide pin tracks are filled with insulation plastic.

7.2. Establishing the Timing for Holding Pin Removal

Figure 15 shows the relationships between degree of cavity plastic filling after the start of filling, holding pin removal timing, copper conductor shift amount, and holding pin removal track weld line actual strength.

If the timing of the 1st mold holding pin sliding is early in comparison with the 2nd mold plastic filling, the 1st mold hold is insufficient and during the 2nd molding the 1st mold and the copper conductors shift due to injection pressure. This gives rise to variation in the 2nd mold thickness and to the mold warp accompanying it.

If the removal is late, there is a drop in temperature and pressure of the plastic that flows to fill the tracks of the pins removed, and this is a cause of filling flaws or imperfections around the pins and of weld line strength drop.

Accordingly, the timing of pin removal must be controlled after a certain level of plastic filling in the cavity and within the range of primary filling pressure.

In this development project, by optimizing the gate position and number of gates, according to CAE flow

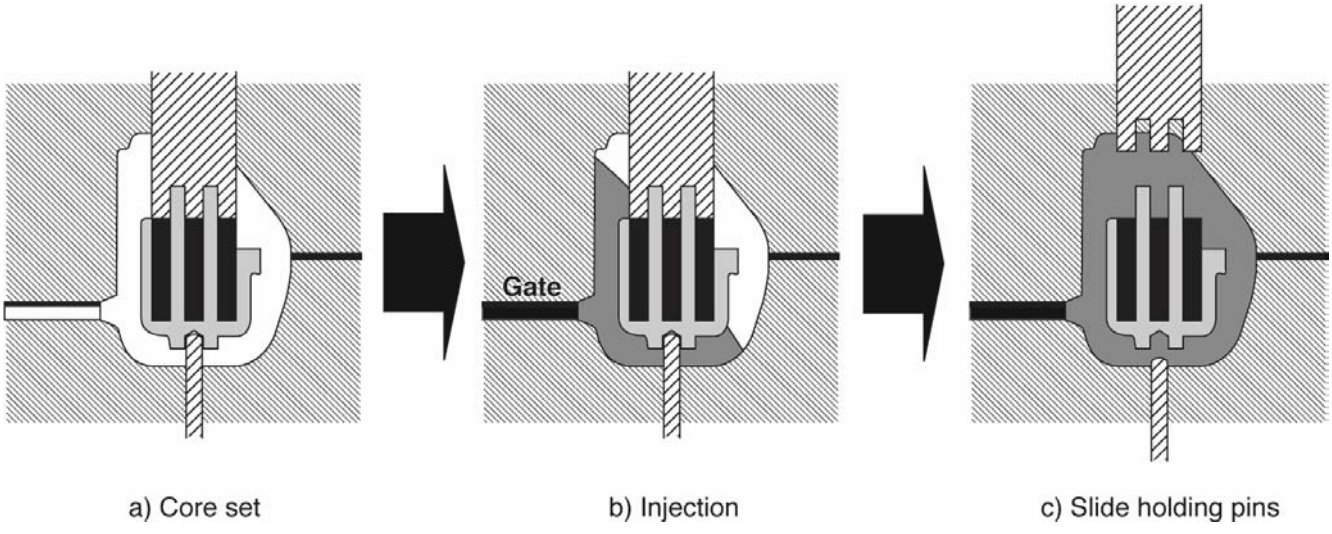


Fig. 14 Seamless injection molding process

analysis, and by establishing the removal timings for upper and lower pins separately, it was possible to simultaneously achieve stability of the 2nd mold thickness distribution and to maintain reliability of the strength of the weld line along the tracks of the pins.

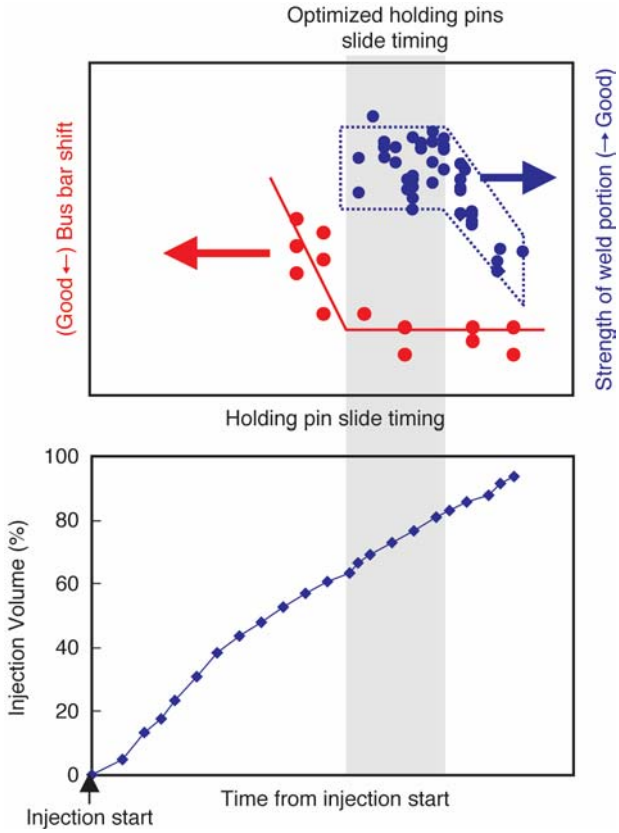


Fig. 15 Holding pin slide timing chart

8. Summary

Bus ring plastic integrated molding technology was developed in order to simultaneously achieve mass productivity advancement and a smaller size of a DC brushless motor.

(1) It is now possible to select material by evaluating the thermal strain occurring in the plastic molded bus rings and comparing it with material fatigue strength characteristics.
(2) Design technology for insulation against high voltage was firmly established, maintaining insulation reliability and at the same time achieving a smaller size.
(3) Through the utilization of float over mold technology and the optimization of holding pin removal timing, it was possible to simultaneously achieve improvement through the integration of multiple parts, to shorten assembly time[(2)], and to maintain waterproofing reliability and strength reliability.

Acknowledgements

The authors would like to express their gratitude to all those who gave their support in the progress of this development project, including Components Group of Sumitomo Wiring Systems Ltd., Atryz Yodogawa, Inc., and Kuroda Kagaku Co., Ltd.

References

(1) Utsunomiya, T. et al: Dictionary of Electrical Engineering, Tokyo, Gihodo Syuppan Co. Ltd., p. 226 (1988)

(2) Ogawa, H., Fukuda, K.: Development of the Motor for the Civic Hybrid, Honda R&D Technical Review, Vol. 14, No. 2, p. 25-30 (2002)

■ Authors ■


Kazuo TAKEUCHI


Kotaro TANAKA


Tatsuro HORIE


Akihiro OKAMURA

Method of Controlling Arc Welding on an Ultrathin Sheet

Koji UEDA* Akira YANAGITA*
Takeshi YAMAGAMI* Manabu MURAKAMI*

ABSTRACT

A positive proportional relation between arc length and arc illumination was found to apply in arc welding. By applying this relation, a control technology was developed that maintains arc length at a constant fixed value during welding. This control is able to maintain a fixed arc length of 1.0 mm or less, a result which is not possible with conventional arc voltage control. This method produces a stable, uniform melting on ultrathin sheets 0.5 mm thick or less through the application of low-current, low-voltage welding.

1. Introduction

The conventional steel sheet used in automobiles is about 0.6 – 1.6 mm thick. Energy saving and environmental measures increasingly call for a change to ultrathin sheets primarily for use in vehicle body and exhaust assembly components and in the reforming system parts used in fuel cell development. The effort to improve weld quality is important for the use of ultrathin sheets.

The use of ultrathin sheets 0.5 mm thick or less is more likely to result in burn through, lack of fusion, deposition on the electrode, and the like. Consequently, the stable provision of an appropriate welding heat input becomes an issue. This also necessitates use of a clamping jig during welding procedures to fix the base material firmly in place so that it does not deform under the heat input. There are many shapes, however, that cannot be fixed in place with a clamping jig.

2. Concerns with Conventional Technology

In arc welding, it is important to maintain stability of the arcing that is the heat source. It requires control that brings the electrode extremely close to the base material and holds a constant fixed arc length. This arc length is a crucial technical element for the stability of weld quality on an ultrathin sheet. It has been considered extremely difficult, however, to control this length accurately.

Current methods for measuring the arc length include laser and photographic sensors. However, there are concerns with these techniques, since a laser sensor tends to malfunction when its receiver picks up the powerful arcing light and camera sensors cannot accurately measure distance. Figure 1 shows experimental results for welding currents of 20 A, 50 A, and 80 A using the conventional detection control method of arc voltage. The arc voltage becomes unstable

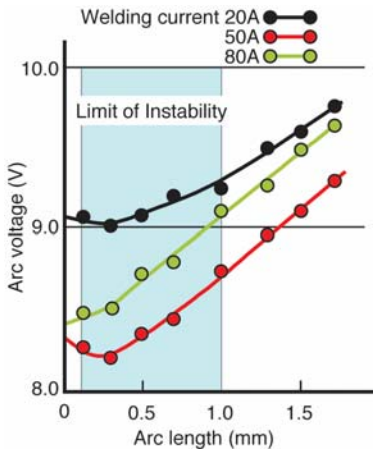


Fig. 1 Relation between arc length and arc voltage

* Tochigi R&D Center

when the arc length is 1.0 mm or less, so it is clear that the arc length cannot be fixed during those times.

3. Relationship between Arc Length and Size of the Melton Pool Caused by Arcing

Figure 2 shows the relationship between the arc length and the diameter of the molten pool (the diameter of melting metal) when the current is constant and the arc length is varied to 0.25, 0.50, 0.75, 1.00, and 1.25 mm. Table 1 shows the welding conditions during those measurements.

Measurement of the melting diameter on the front and back sides of the sheet shows that the melting diameter becomes larger when the arc length is shorter, and there is little difference between the melting diameter on the front and reverse sides. This shows that the thermal energy of the arcing is consumed more efficiently in melting the base material when the arc length is shorter.

Table 1 Welding condition

Base material	SUS316L
Thickness	0.5mm
Material of electrode	Tungsten
Diameter of electrode	1.6mm
Welding current	27A
Welding time	0.25s
Welding method	TIG

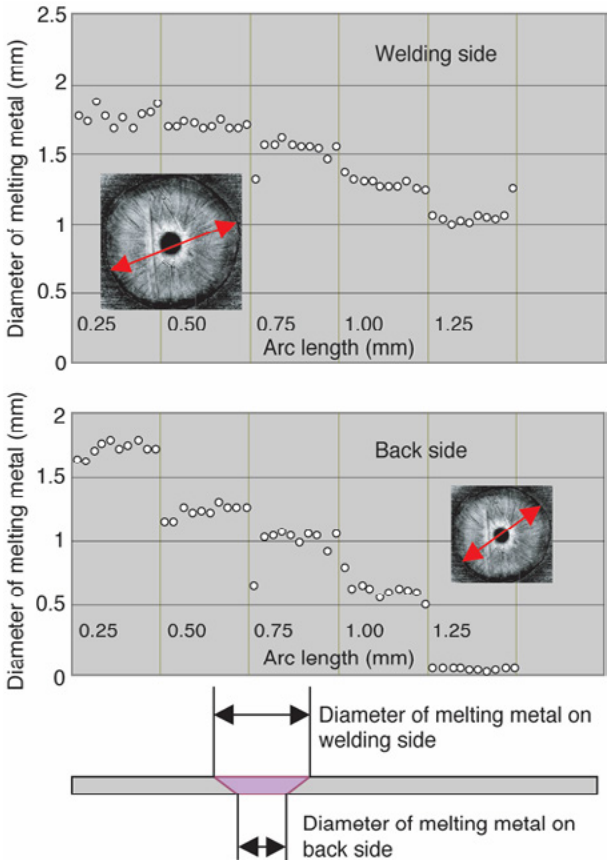


Fig. 2 Relation between arc length and diameter of melting metal

4. The Characteristic of the Relationship Between Arc Optical Illuminance and Arc Length

During the investigation of potential control technologies to replace conventional arc length control and arc voltage control, it was noticed that changing the arc length would cause minute changes in the arcing light. An experiment was therefore conducted on the relationship between arc optical illuminance and arc length using the experimental TIG welding apparatus shown in Fig. 3. An illumination meter was placed at a distance of 150 mm from the center of the welding electrode in order to measure changes in the arcing light. The welding current was set at the minimum of 20 A and maximum of 81.25 A for which past hand welding results were available. A stainless steel sheet 1.6 mm thick was selected in order to avoid burn through or deformation during measurement. Table 2 shows the other conditions.

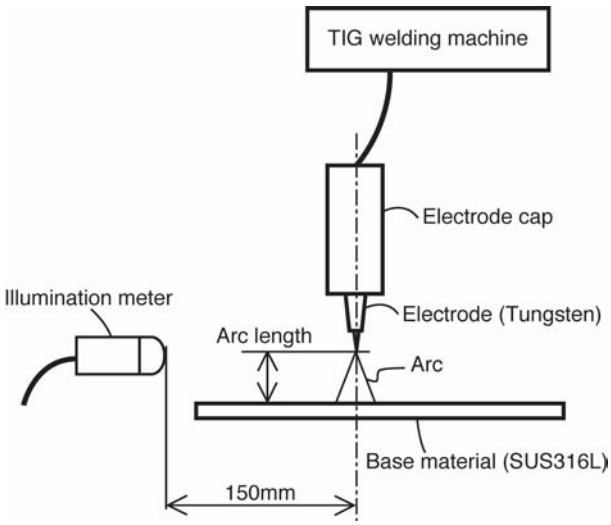


Fig. 3 Experimental apparatus of arc length change and arc optical illuminance

Table 2 Condition of arc length change and arc optical illuminance experiment

Base material	SUS316L
Thickness	1.6mm
Material of electrode	Tungsten
Diameter of electrode	1.6mm
Extension of electrode	16mm
Distance of electrode and illumination meter	150mm
Welding method	TIG

Table 3 shows the results of the experiment. Figure 4 shows the relationship between arc illuminance and arc length with the welding current at 20 A and 81.25 A. It was found that arc illuminance and arc length remained in a directly proportionate relationship even when the arc length was 1 mm or less, where it had previously been thought difficult to control. It was reasoned from these results that it may be possible to control arc length by keeping the welding current fixed and monitoring the illuminance.

Table 3 Result of experiment

Arc length at welding current 20A

Arc length (mm)	0.17	0.39	0.61	0.98
Illuminance (Lx)	36.7	399	449	564

Arc length at welding current 81.25A

Arc length (mm)	0.25	0.5	1.0	2.0	3.0
Illuminance (Lx)	2006	2650	4620	8315	12649

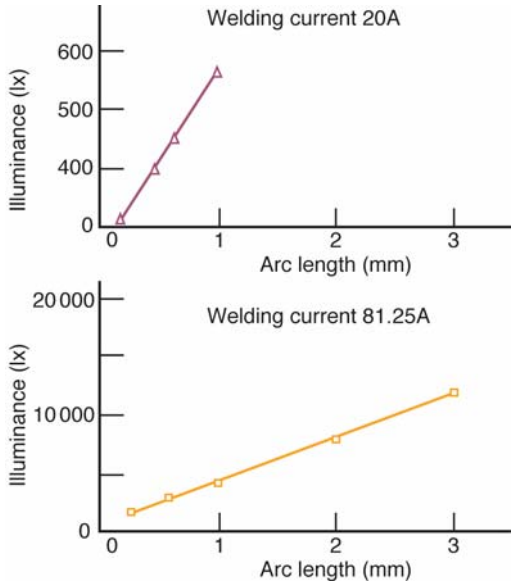


Fig. 4 Relation between arc length and illuminance

5. Control Using Arc Illuminance

Figure 5 shows the method of control using arc illuminance as described above. The information from the arc illuminance sensor undergoes analog/digital conversion and is taken as the illuminance voltage signal. This is sent to the CPU and judged for its difference from a preset standard voltage. The mechanism then controls the arc length by moving the torch and electrode vertically to a fixed height. Figure 6 shows the control flow. ST stands for program step.

1) The optimum arc length is set according to the base material and the arc illuminance voltage at that point is input to the CPU as the standard voltage V_{st} (ST01).
2) Arc illuminance is measured using the illuminance sensor after welding begins (ST02).
3) That voltage signal V_{ac} is sampled (ST03).
4) V_{ac} is compared with the reference voltage V_{st} (ST04).
5) If $V_{ac}<V_{st}$, then the torch is raised (ST05).
6) If $V_{ac}>V_{st}$, then the torch is lowered (ST06).
7) If $V_{ac}=V_{st}$, then the arc length can be judged to be correct, so that torch height is maintained (ST07).

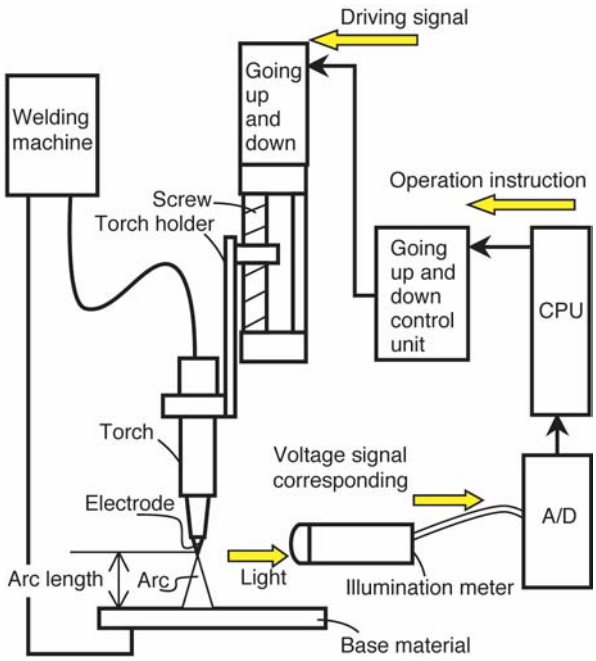


Fig. 5 Arc length controller

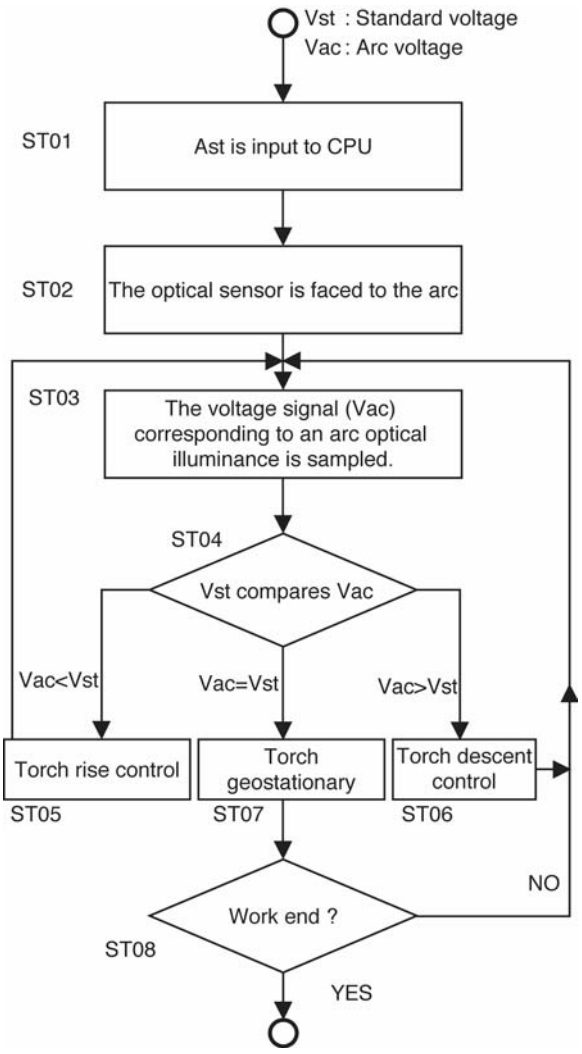


Fig. 6 Arc welding control flow chart

8) If the welding work end signal is received, the flow is terminated (ST08).
9) If a work end signal is not received, then the flow returns to ST03 and control continues.

The above flow was implemented in an arc welding robot used for actual welding. The test specimen was given a wave form at the welding point to make it easier to confirm correct control of the arc length and vertical control of the torch. Figure 7 shows how the movement was observed with the arc length set to 0.5 mm and the torch moved straight across the workpiece at a fixed speed. As a result, the above control was able to produce a weld with a uniform melting width by moving the torch at a fixed arc length maintained relative to the wave-formed base material, as shown in Fig. 8.

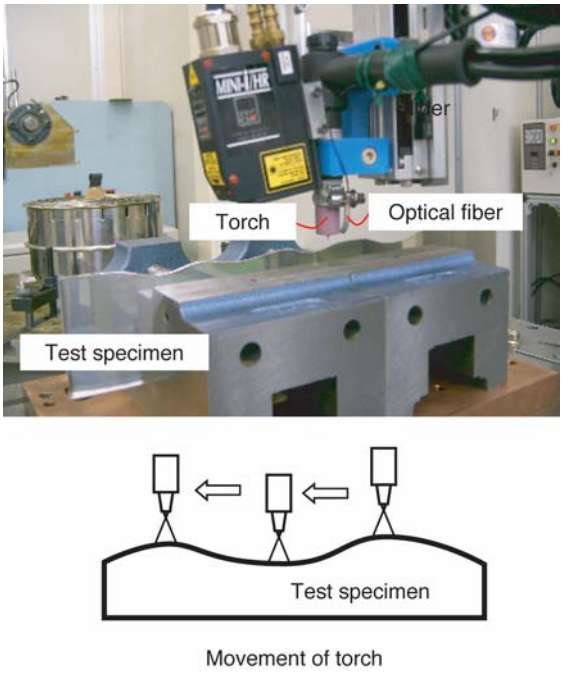


Fig. 7 Arc length control experiment

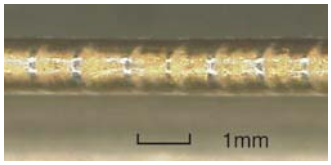


Fig. 8 Form of weld state

Next, Fig. 9 shows the welding experiment conducted using a sheet 0.5 mm thick. The workpiece was made in an L shape and the torch was run over it at a constant speed without using a clamping jig. The results show that a melt form with a uniform, stable appearance could be welded. This was achieved despite the ultrathin sheet and the complex shape. This is shown in Fig. 10.

Figure 11 is an illustration of the welding of a prototype heat exchanger. The sheets of 0.3 mm thick stainless steel sheet were joined together using an edge joint and welded in a loop. The arc length stays stable with a welding current of



Fig. 9 Experiment without jig

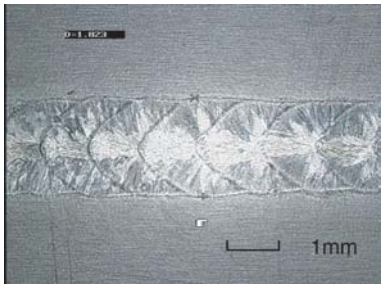


Fig. 10 Form of weld state



Fig. 11 Welding and observation of weld

20 A, and the result obtained shows that heat input was kept uniform in the weld area and no irregularity was found in the weld freezing structure.

6. Study and Experiment in the Use of Arc Illuminance

It was known through experimentation up to this point that arc illuminance has a correlation with arc length. This study and experiment was carried out to determine whether arc illuminance would change when the weld joint form was different.

Figure 12 shows the workpiece made for the experiment. The joint for Sec A-A had a butt joint cross-section, while Sec B-B had a butt joint with a groove forming a gap. Figure 13 shows the illuminance converted to a voltage value on the vertical axis and the weld length on the horizontal axis. The illuminance voltage can be seen to rise from the point where there is a groove. These results suggest that arc illuminance can be applied to detect whether the joint form is a butt joint, a groove joint, and so on.

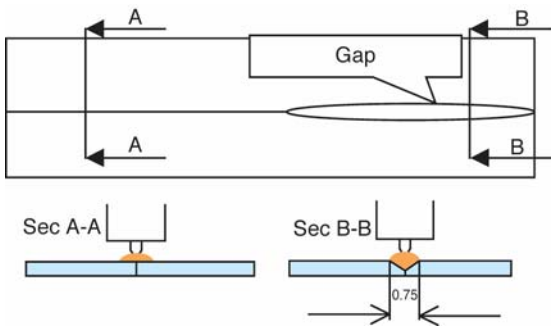


Fig. 12 Experiment sample

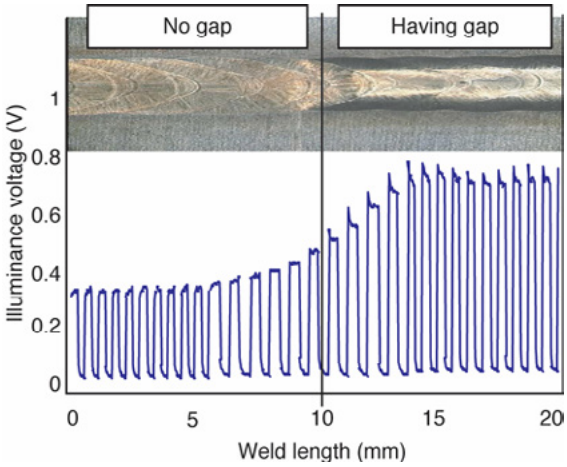


Fig. 13 Relation between gap and arc illuminance

7. Summary

This method of arc length control enabled automatic welding of ultrathin sheet 0.5 mm thick without using powerful clamps.

1) It was determined that arc illuminance has a positive proportional relationship to arc length when the arc length is 1 mm or less.
2) Development of arc length control technology making use of the above relationship achieved stable, uniform melting quality with ultrathin sheets 0.5 mm thick or less.
3) Changes in arc illuminance can be used to detect gaps and different forms of joint.

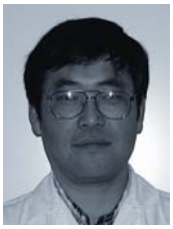
This technology is being utilized on prototype parts for reforming systems in fuel cell development.

Acknowledgements

The authors received much cooperation from the people of DAIHEN Corporation in carrying out the present research, and would like to take this opportunity to express their gratitude.

■ Authors ■


Koji UEDA


Akira YANAGITA


Takeshi YAMAGAMI


Manabu MURAKAMI

Two-Stroke Gas Exchanging Method for Controlling Auto-Ignition : Activated Radical Combustion

Yoichi ISHIBASHI* Kenji NISHIDA*
Yukio SAKAI* Hisashi SAKUYAMA*

ABSTRACT

The auto-ignition is focused as a combustion process, where improving efficiency and lowering NOx emission could be compatible. A current subject would be controlling combustion process. Honda demonstrated a method to control the auto-ignition, i.e. Activated Radical (AR) combustion, in several commercial motorcycle engines.

Through the experimental analyses of the AR combustion, this article shows that control of the gas exchange generates a temperature for the auto-ignition in the end of compression stroke, due to heat exchange between residual and new mixture. It is also revealed that its combustion speed is affected by the engine speed, scavenging efficiency, and etc.; however, 10% to 90% mass burn timing is settled on the same crank-angle duration as a result regardless of the engine operating conditions. This is owing to the dualism of the residual gas, i.e. combustion promotion action as heat energy potential and the inhibitory action as the inert gas. Both actions should balance for the two-stroke gas exchanging method for controlling auto-ignition.

1. Introduction

Simultaneously improving fuel economy and reducing emissions is a theme for engines. In particular, improving the thermal efficiency of automotive engines, which are said to account for 20% of the total CO_2 emitted by developed countries, is an important issue. Theoretically, thermal efficiency should be improved by a higher compression ratio and lean operation; however, practically, it has limits. A higher compression ratio is limited by the occurrence of knocking and the structure of the engine. And again, lean operation is also limited by the ignitability of the mixture and the NOx deoxidization by the catalyst. Even direct injection diesel engines, which are known as the most effective internal combustion engines, due to their higher compression ratio, have not become mainstream in automotive engines due to the issue of reducing NOx and soot produced by stratified combustion. Gas direct injection engines, which aim to improve fuel economy owing to the super lean burn operation and its lower pump loss results from non-throttle operation, also basically face these similar issues.

Recently, auto-ignition is focused as a new combustion process that aims to simultaneously improve fuel economy and clean emissions[(1), (2), (3)]. This type of combustion, which does not have a flame propagation process, should be extremely promising as a means of simultaneously improving fuel economy and reducing emissions. This is because it provides superior ignition stability with a lean mixture or

* Asaka R&D Center

large amounts of diluted inert gas, which expands the lean burn limit, reduces the combustion temperature, reduces NOx emission, avoids knocking, increases the compression ratio limit, and so on. However, in terms of combustion control this technology is still incomplete, because producing auto-ignition itself is a primary barrier, especially for four-stroke gas engines. Heating the intake air and using a higher compression ratio were tried in the initial research stages, and the prescribed effects were confirmed in specific operating states[4), (5)]. However, in this case the operation used to produce auto-ignition acted to simultaneously accelerate the combustion speed. This meant that the ignition timing and the combustion speed changed both together, which greatly limited the operating conditions under which ideal combustion could be achieved.

On the other hand, in cases where auto-ignition is applied to a two-stroke gas engine, the ignition timing is controlled by varying the gas exchange state using a throttle valve located in the exhaust system[6)]. Honda has already applied a controlled auto-ignition system, named Activated Radical (AR) combustion to commercial motorcycle engines, and has demonstrated a significant fuel economy improvement and emissions reduction effects[7), (8)]. This AR combustion is generated by changing the percentage of inert gas in the cylinder by varying the opening area of the exhaust port with a valve, which is to heat or reform[9)] the fresh air by using the thermal energy of the inert gas. In this case, the dualism of the inert gas, that is to say its thermal energy and inertness, act differently on the generation of auto-ignition and the subsequent combustion. In other words, the thermal energy of the inert gas causes the gas inside the cylinder to reach the auto-ignition temperature at the end of the compression stroke, whereas the increase in the inert gas works as a factor to suppress the combustion speed and the combustion temperature.

This paper introduces an example of auto-ignition control in two-stroke engines, and clarifies the combustion control mechanism peculiar to these types of AR combustion engines through the experiments concerning the combustion speed. It aims to deepen understanding of the two-stroke engine gas exchange process[10), (11), (12)], which is recently focused as a means of the auto-ignition also in the four-stroke gasoline engines, and to investigate further application possibility of gasoline auto-ignition combustion in the future.

2. Experimental Engine

In the case of conventional two-stroke engines, there is a unique relationship between the amount of inert gas and the amount of short-circuiting fresh air in the cylinder. AR combustion is controlled by varying the rate of inert gas in the cylinder, consequently the amount of short-circuiting fuel also changes with the combustion state, which complicates the analysis of individual phenomena. Therefore, these experiments used a pneumatic direct injection (PDI) engine in order to eliminate the effects of short-circuiting fuel as much as possible. The experimental engine shown in Fig. 1 has a rotary type mechanical injection valve in the cylinder wall. After the scavenging process using air only, the pre-measured fuel for one cycle is injected directly into the cylinder using the gas pressure in the accumulator chamber. Therefore, the fresh air short-circuited to the exhaust does not include the fuel. The principle of this PDI engine has already been reported in detail[13), (14)], so these details are omitted here. A valve, which varies the opening area in order to change the amount of inert gas for the AR combustion is installed in the exhaust port.

Two types of experimental engines were used in the experiments: engine A with a displacement of 250 cm^3, and engine B with a displacement of 400 cm^3 as shown in Table 1. The PDI assist gas supply method differs according to the operating speed range of each engine. The high-speed engine A (12,000 r/min) supplies the assist gas by using a special air pump, while the medium speed engine B (8,000 r/min) supplies it by using the in-cylinder gas accumulated in the chamber at the compression stroke. Therefore, engine A has a higher degree of freedom for

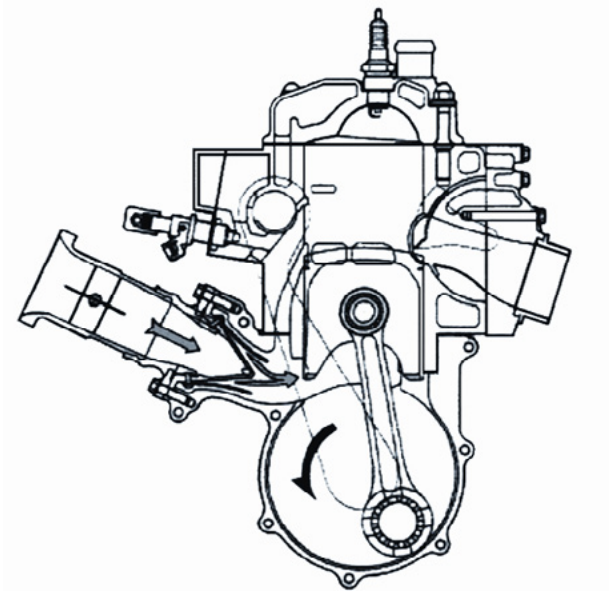


Fig. 1 Overview of the experimental engine B

Table 1 Principal specifications of the Experimental Engines

Specifications	Engine A	Engine B
Bore × Stroke	68mm × 68.8mm	80mm × 80mm
Displacement	249.9cm^3	402cm^3
Compression ratio (Trapped)	7.2	6.3
Compression ratio (Geometric)	12.4	10.5
Exhaust opening duration	194deg.C.A.	188deg.C.A.
Exhaust opening area	2437cm^2 deg	2159cm^2 deg
Scavenging opening duration	130deg.C.A.	113deg.C.A.
Scavenging opening area	1712cm^2 deg.	1449cm^2 deg.
Charge means for PDI	Air pump	In-cylinder gas
Exhaust opening rate	100%–5%	100%–5%

adjusting the amount of assist gas. Other basic structures and operation principles are exactly the same, so that there should be no significant difference in the auto-ignition combustion itself between these two engines.

3. AR Combustion Control Analysis from the Gas Temperature Aspect

3.1. Estimation of Auto-ignition Temperature

When the exhaust port is throttled in order to generate the auto-ignition by maintaining a constant indicated mean effective pressure, the exhaust recirculation increases, and a rise of in-cylinder pressure is observed at the exhaust port close timing. The scavenging efficiency (η s) is assumed to deteriorate due to this increase in the relative charge (Crel). In order to predict a change in the in-cylinder gas temperature of this case, the enthalpic balance models of the working gas during the exhaust process and the scavenging process are constructed.

For simplification, models stand on the following assumptions;

(1) The temperature of the fresh air, inert gas, exhaust and the in-cylinder gas after scavenging are typified by the average temperatures T_f, T_r, T_e and T_i, respectively.
(2) Labeling the isobaric specific heat of each gas as cp_f, cp_r, cp_e and cp_i, respectively, $cp_f = cp_r = cp_e = cp_i$.
(3) Heat exchange between each gas is performed adiabatically and instantly.
(4) The compression stroke is polytropic change.

Labeling the mass of the fresh air and inert gas in the cylinder as M_f and M_r, respectively, the mass of the fresh air and inert gas in the exhaust at a trapping efficiency of η_{tr} are $M_f(1/\eta_{tr} - 1)$ and M_f, respectively.

From the enthalpic balance of the exhaust process:

$$M_f cp_r T_r + M_f(1/\eta_{tr} - 1)\, cp_f T_f = M_f/\eta_{tr}\, cp_e t_e$$

From the enthalpic balance of the scavenging process:

$$M_f cp_f T_f + M_r cp_r T_r = (M_f + M_r)\, cp_i T_i$$

The scavenging efficiency $\eta_s = M_f/(M_f + M_r)$, thus,

$$T_r = (T_e - T_f)/\eta_{tr} + T_f \quad (1)$$

$$T_i = T_r - (T_r - T_f)\,\eta s \quad (2)$$

$$T^* = T_i\,(\varepsilon^*)^{n-1} \quad (3)$$

Here, T* and ε* are the in-cylinder gas temperature and specific volumeat the ignition point, respectively and n is the mean polytropic index of the compression stroke.

3.2. In-cylinder Gas Temperature in the AR Combustion Engine

The experimental PDI-engines control the exhaust valve opening by using a computer so that auto-ignition always occurs at the point several degrees before the top dead center (TDC), where the combustion efficiency is the best[4]. That is to say, the exhaust valve opening for the AR combustion is pre-programmed in the ECU, according to each engine speed and throttle opening.

This AR combustion control system was analyzed from the in-cylinder gas temperature aspect, using experimental engine B. Figure 2 shows an example of varying the load at a speed of 3,000 r/min, and Fig. 3 shows the gas exchange state at that time.

The residual gas temperature and the in-cylinder gas temperature at the end of the compression stroke were obtained successively, according to the method introduced in the previous section, by using the direct measurement results such as the average exhaust gas temperature, average scavenging gas temperature, intake air amount, exhaust O_2 concentration, indicator diagram, power output and the model test results of Blair's single cycle gas exchange rig[15] for the scavenging efficiency characteristic of the experimental engine.

As gradually decreasing the load from the full load, the exhaust temperature peaks at a brake mean effective pressure (BMEP) of 400 kPa and decreases thereafter. This phenomenon occurs because the inert gas is diluted by the short-circuiting fresh, while the estimated residual gas temperature peaks at the full load and then decreases according to the load decrease as shown in Fig. 2. This drop in the residual gas temperature is understood that the combustion temperature decreases as the inert gas increases, and also it is due to a decrease of the total heat release to the heat loss.

On the other hand, the in-cylinder gas temperature after the gas exchange depends on the heat exchange between the residual gas and the fresh air. As shown in Fig. 3, decreasing the load, the scavenging efficiency decreases, the rate of the residual gas increases, thus the in-cylinder gas temperature rises. When the gas temperature reaches 1,000 K + α the AR combustion occurs. After that, the exhaust valve controls the gas exchange state so as to maintain this temperature constant at 1,000 K + α, as seen in the dotted line enclosed area in the

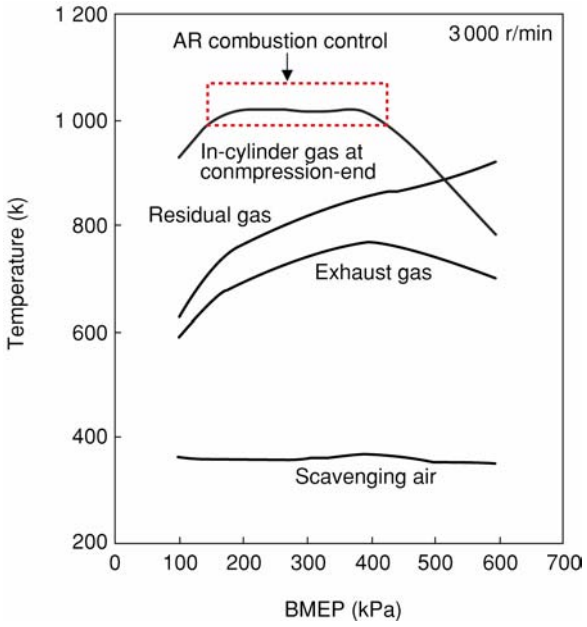


Fig. 2 In-cylinder gas temperature in the AR engine

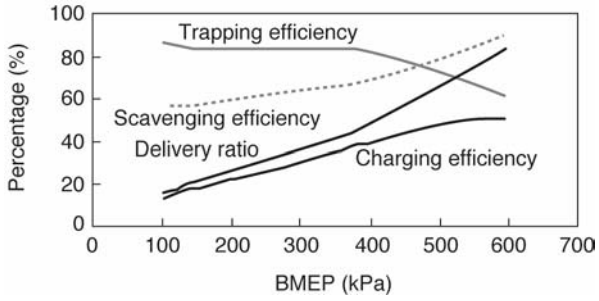


Fig. 3 Gas exchange state in the AR engine

figure. This area is the AR combustion zone for the experimental engine at 3,000 r/min. Note that the value of α is a constant depending on the engine speed, which tended to rise on the order of 10-odd K in accordance with each 1,000 r/min engine speed rise. Decreasing the load further from this AR combustion zone, the residual gas temperature drops excessively so that the in-cylinder gas temperature can no longer be maintained. However, the exhaust valve controls the scavenging efficiency, which is the AR combustion lower limit. Irregular combustion occurs in the load area below this lower limit.

3.3. AR Combustion Zone

The exhaust valve controls the mixing state of the residual gas and fresh air, i.e. scavenging efficiency, so as to reach an in-cylinder gas temperature which induces the AR combustion. Such gas exchange state for the AR combustion is obtained in the range of the scavenging efficiency approximately from 30% to 70%[4]. There occurs the irregular combustion in the scavenging efficiency range of approximately 30% or less. Figure 4 compares the AR combustion operating zones for experimental engines A and B. The upper limit load for AR combustion operation is a BMEP of less than 400 kPa, regardless of differences in the engine output characteristics, and the lower limit load characteristics exhibit similar tendencies. In addition, AR combustion was observed up to the extremely high-speed range.

The AR combustion lower limit mechanism was explained in the former section as a drop in the residual gas temperature. When the coolant temperature and other adiabatic conditions vary, the lower limit load fluctuates 10-odd kPa order due to the change of the residual gas temperature. In addition, the effect of change in the compression ratio on the residual gas temperature is canceled by the change in the expansion ratio, it only affects the fresh air temperature rise. Thus, there is a little effect on the AR lower limit load, as far as the normal compression ratio range, which allows the full load operation. However, an exceedingly higher compression ratio would enlarge the lower limit load, and the upper limit load. The auto-ignition zone can be expanded in this manner, however it would be limited by the occurrence of the knocking in the higher load side.

3.4. Ignition Timing Control

In the AR combustion zone, the ignition timing can be controlled in a stable manner by changing the scavenging efficiency. The spark ignition does not affect the AR combustion timing in this zone. Exhaust valve operation for experimental engine B was switched to manual, and the scavenging efficiency was changed by both the throttle and the exhaust valve opening, while maintaining a constant load of BMEP = 300 kPa and a constant speed of 3,000 r/min. Lowering the scavenging efficiency, that is to say increasing the inert gas, the mass fraction burnt curve against the crank angle advances, as shown in Fig. 5. This advance in the combustion timing is limited by the onset of detonation or misfiring. Conversely, increasing the scavenging efficiency retards the combustion timing, and it is limited by the onset of irregular combustion. Incidentally, Under the Fig. 5 conditions, the maximum thermal efficiency was marked at a scavenging efficiency of 0.54. The figure also represents that, in a scavenging efficiency more than 0.59, auto-ignition cannot be maintained and irregular combustion results. The adjustment width of the auto-ignition timing gradually narrows toward the retardation side around the surrounding AR combustion zone. In addition, a typical auto-ignition combustion, namely “semi-AR combustion”, which occurs with the assistance of the spark ignition is seen in a narrow range of the outer surroundings of the AR combustion zone.

4. Auto-ignition Combustion Speed

The previous section explained the mechanism of the auto-ignition timing control, however combustion speed control is another important factor of the combustion control. For example, in spark ignition (SI) engines the flame propagation speed increases in accordance with the engine speed, therefore combustion always takes place approximately at the same crank angle. This is an extremely important characteristic for the OTTO cycle, and thanks to this, constant volume combustion is performed from the several hundred r/min of idling state up to the racing engine’s speeds as high as 20,000 r/min. It is explained that as the engine speed rises, due to the increase of the in-cylinder turbulence, the flame propagation also speeds up. It would naturally come to raise a question in the case of auto-ignition, which does not involve the flame propagation process.

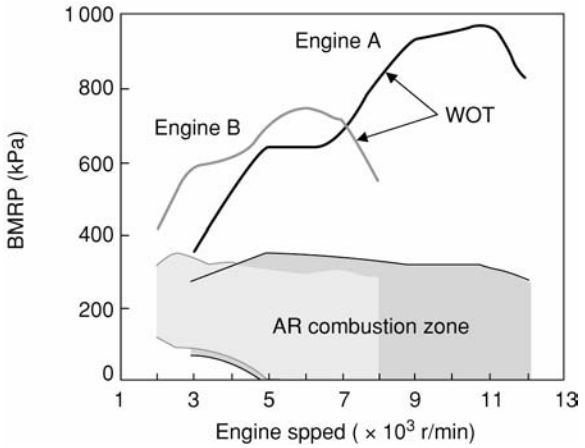


Fig. 4 AR combustion zones of the experimental engines

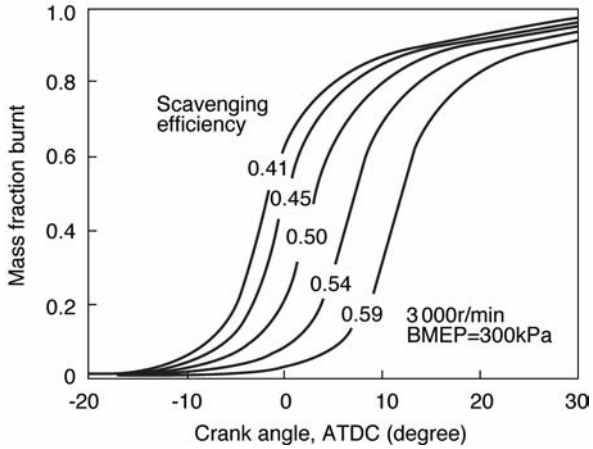


Fig. 5 Effect of scavenging efficiency on mass fraction burnt curve

4.1. Relationship between Load and Combustion Speed

Figure 6 shows the heat release curve variations against the load variations of the 250 cm^3 experimental engine A. The combustion form shifts from SI combustion to AR combustion as the load decreases. The pressures noted on the heat release curves represent the respective indicated mean effective pressures (IMEP). The stoichiometric in-cylinder air to fuel ratio is given for all loads and the ignition timing for the SI combustion is the minimum advance for best torque (MBT). Expressing the amount of PDI assist gas as a mass-rate, which symbol is Las, of the assist gas against the air required to fill the swept volume under the reference condition, Las of 5% is given at all examined loads. The upper two curves, dotted lines, are SI combustion. The third dotted curve of 420 kPa is semi-AR combustion, which requires assistance of the spark ignition, and the lower four curves by the solid lines are AR combustion. According to the slopes of these heat release curves, which indicate the combustion speed, Fig. 6 shows a general tendency that the combustion speed decreases as the load decreases for both SI and AR combustion. This could be explained that deterioration in the scavenging efficiency, i.e. increase in the in-cylinder inert gas, controls the combustion speed. However the graph also shows that combustion speeds up in accordance with the onset of the AR combustion.

Reading the crank angles for the mass burnt fraction of 10% and 90% of each curve, the same data are rearranged on the IMEP – crank angle axes in Fig. 7. The 10% mass burnt fraction timing for AR combustion is controlled, so that it is the same as that of the SI combustion applying MBT. According to this graph, when the combustion shifts from SI to AR, the 90% mass burnt fraction timing advances. Which means that a degree of constant volume combustion increases in the AR combustion. The combustion speeds down as the load decreases, however at the same time the mass to be burnt also decreases, consequently, combustion always takes place at the same crank angle regardless of the load. In the case of SI combustion, the initial combustion time from the ignition timing up to the 10% mass burnt increases as the load decreases, which would be also related to the increase of inert gas concentration.

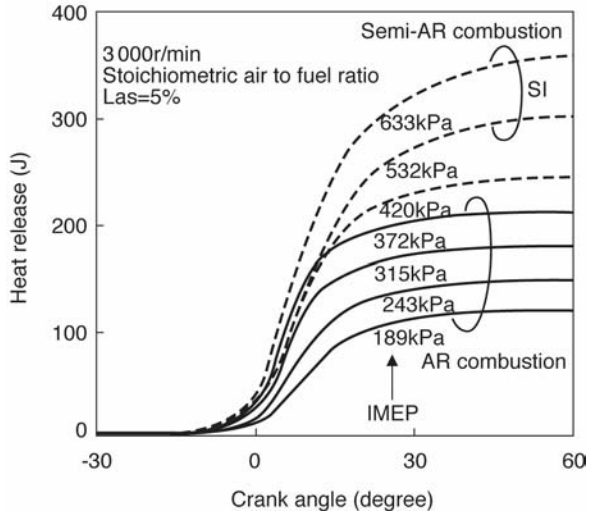


Fig. 6 Heat release variations against the load

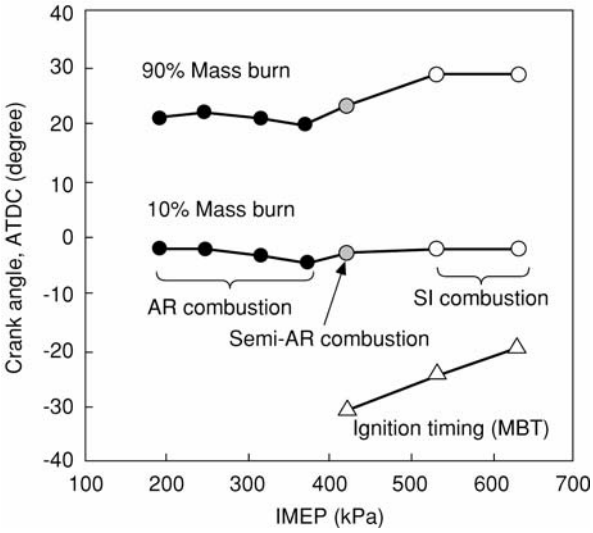


Fig. 7 Combustion duration on the crank angle against IMEP

4.2. Relationship between Engine Speed and Combustion Speed

The next issue is the influence of the engine speed on the AR combustion speed. Experimental results thus far indicate ;

(1) The scavenging efficiency is adjusted to induce the AR combustion, i.e. the exhaust enthalpy performs the auto-ignition at the end of the compression stroke.
(2) The scavenging efficiency itself affects the AR combustion speed.

As it had been empirically known that in the case of the constant IMEP, the scavenging efficiency for inducing the AR combustion was also constant in rough. Therefore, the relationship between the engine speed and the AR combustion rate was tested at a constant IMEP. Figure 8 shows the heat release curve variations of the engine speed from 3,000 r/min to 6,000 r/min at a constant IMEP of 300 kPa, using experimental engine A. The horizontal axis is the time from TDC. The in-cylinder air to fuel ratio is the stoichiometric condition for all engine speeds, and the amount of assist gas is held constant at Las = 5%. This data reveals that the AR combustion speeds up as the engine speeds up.

The same data is rearranged in Fig. 9, showing the crank angles for the mass burnt fractions of 10% and 90%. AR combustion occurs at approximately the same duration as the crank angle, regardless of the engine speed.

This result shows that the AR combustion speeds up with the engine speed, in the same manner as the SI combustion, however it does not have a flame propagation process. This remarkable feature allows the auto-ignition to maintain the ideal constant volume combustion even in the high-speed range.

4.3. Relationship between Mixture Formation and Combustion Speed

In order to investigate the influence of homogeneousness of the in-cylinder mixture on the AR combustion, the amount of PDI assist gas were varied. PDI of the experimental engine shows a tendency that with a larger amount of assist gas it promotes diffusion of the spray and promotes the homogeneousness of the mixture, and inversely with a smaller amount of assist gas, it becomes biased spray.

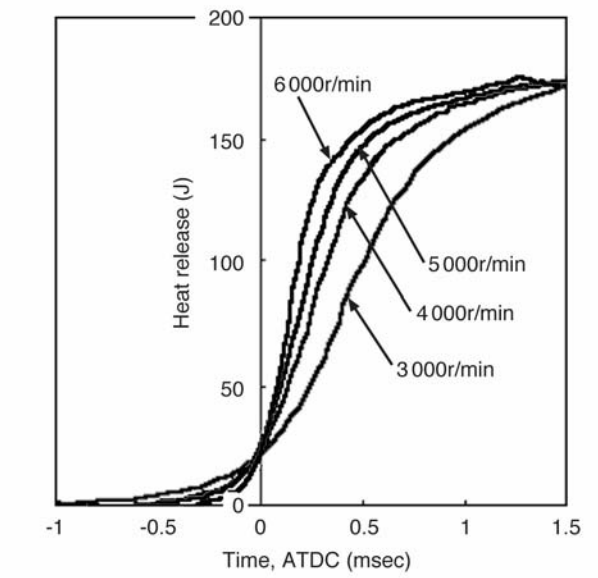


Fig. 8 Heat release speed variations against r/min

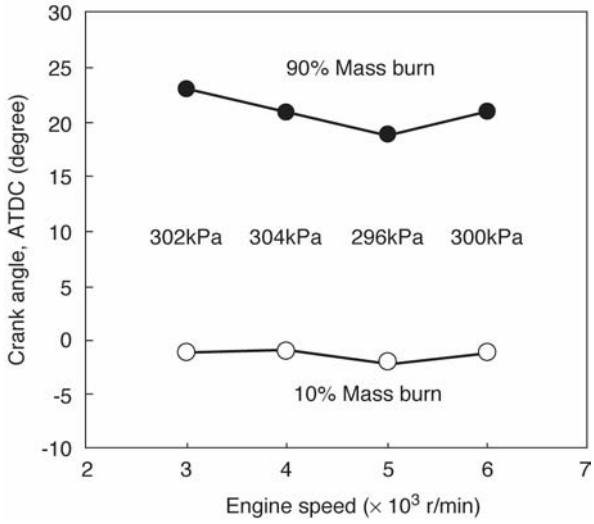


Fig. 9 AR combustion duration against the engine speed

The amount of PDI assist gas was varied between 1%, 8% and 16%, while maintaining a constant IMEP of 300 kPa at an engine speed of 4,000 r/min using experimental engine A. The stoichiometric in-cylinder air to fuel ratio was applied. There is no significant change in the exhaust valve opening required for the AR combustion in all cases of assist gas amounts, consequently, it is estimated that the scavenging efficiency would also be approximately the same in all cases. As increasing Las, BMEP decreases due to increase of the pump loss, and the brake mean specific fuel consumption ratio (BSFC) also increases accordingly as shown in Fig. 10. In this case, the indicated mean specific fuel consumption ratio (ISFC) remaines roughly constant. Which means that the AR combustion efficiency remains unchanged and the mechanical loss simply increases. However, as shown in Fig. 11, the emission composition between HC and NOx is affected markedly according to the difference in the assist gas amount.

From the indicated pressure data aspect, a remarkable difference in the heat release between the cases of Las = 1% and Las = 16% was observed, as shown in Fig. 12. In case of Las = 16%, the heat release reaches the maximum value at 20° after top dead center (ATDC). In contrast, in case of Las = 1%, it reaches the maximum value around 40° ATDC. From this result, the difference in the amount of PDI assist gas, that is to say heterogeneousness of the mixture formation is also a factor, which affects the AR combustion speed, like other factors such as the scavenging efficiency and engine speed.

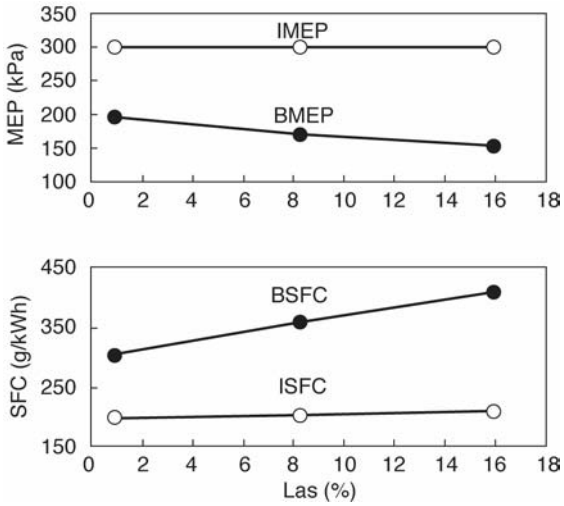


Fig. 10 Effect of assist gas of the PDI on BMEP and SFC in the AR combustion

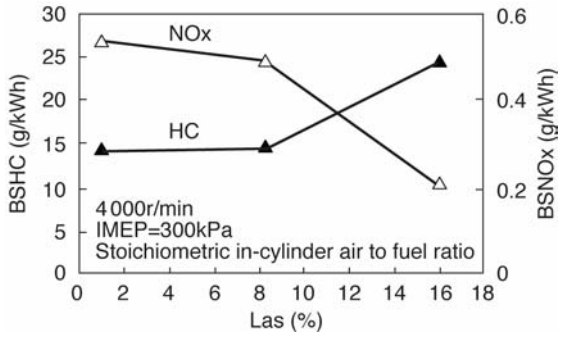


Fig. 11 Effect of assist gas of the PDI on HC NOx emissions in the AR combustion

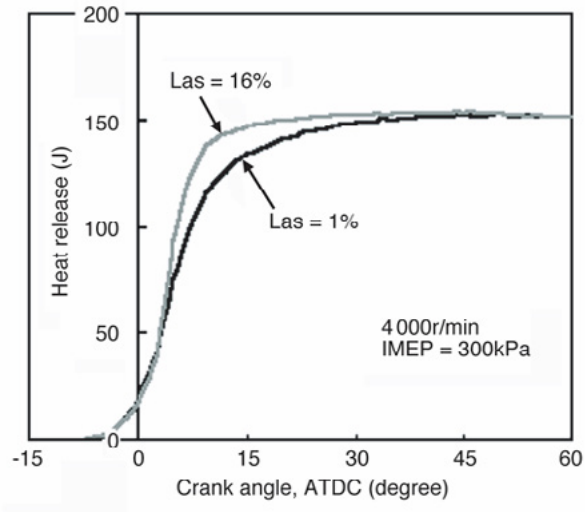


Fig. 12 Effect of assist gas of the PDI on the combustion speed of the AR combustion

5. Conclusion

(1) The AR combustion ignition timing is controlled according to the in-cylinder gas temperature at the end of the compression stroke.
(2) This gas temperature is maintained at a constant degree during the AR combustion zone, by varying the gas exchange with an exhaust valve and utilizing the enthalpy of the residual gas.
(3) The auto-ignition combustion speed depends on the scavenging efficiency, engine speed and other factors, but the combustion duration always comes about a constant crank timing, regardless of the operating condition.
(4) A heterogeneousness of the mixture formation also affects the heat release characteristic and the exhaust gas composition in a PDI engine.

These experimental data thus reveal that the controlled auto-ignition applying the two-stroke gas exchanging method is a result of a well balance in the dualism of the inert gas, i.e. combustion promotion due to its thermal energy and combustion control due to its inertness. An unbalanced state of it results in irregular combustion. As a methodology for the controlled auto-ignition, it is becoming a trend to apply the two-stroke engines' gas exchanging process to four-stroke gasoline engines.

References

(1) Takeda, Y. et al.: The 73rd JSME Fall Annual Meeting Proceedings (Ⅲ), p. 188 (1995)

(2) Aoyama, T.: Premixed-Charge Compression Ignition Gasoline Engine, Journal of Society of Automotive Engineers of Japan, Vol. 53, No. 9, p. 39-44 (1999)

(3) Lavy, J. et al. (14 authors): Innovative Ultra Low NOx Controlled Auto Ignition Combustion Process for Gasoline Engines, the 4th SPACE Project, SAE Paper 2000-01-1837 (2000)

(4) Aoyama, T. et al.: An Experimental Study on Premixed-Charge Compression Ignition Gasoline Engine, SAE Paper 960081 (1996)

(5) Urushihara, T. et al.: Parametric Study of Gasoline HCCI with Various Compression Ratios, Intake Pressures and Temperatures, IFP International Conference Preceding, p. 77-83 (2001) Rueil-Malmaison France

(6) Ishibashi, Y. et al.: A Trial for the Stabilising Combustion in Two-Stroke Engines at Part Throttle Operation: A New Generation of Two-Stroke Engines for the Future, EDITIONS TECHNIP, p. 113 (1993)

(7) Asai, M. et al.: Analysis on Fuel Economy Improvement and Exhaust Emission Reduction in a 2-Stroke Engine by Using an Exhaust Valve, SAE Paper 951764 (1995)

(8) Ishibashi, Y., Asai, M.: Improving the Exhaust Emissions of Two-Stroke Engines by Applying the Activated Radical Combustion, SAE Paper 960742 (1996)

(9) Hiratani, K., Kakukata, S., Urushihara, T., Ito, K.: Study on Compression Auto-Ignition Gasoline Engine, JSAE Proceedings, No. 70-02, p. 1-6, (2002)

(10) Morikawa K., Kaneko, M., Ito, H., Motokubi, Y.: Study on Premixed-Charge Compression Ignition Gasoline Engine - First Report, JSAE Proceedings, No. 51-01, p. 5-8 (2001)

(11) Kaneko, M., Morikawa K., Ito, H., Motokubi, Y.: Study on Pre Premixed-Charge Compression Ignition Gasoline Engine - Second Report, JSAE Proceedings, No. 51-01, p. 9-13 (2001)

(12) Allen, J., Law, D.: Advanced Combustion Using a Lotus Active Valve Train Internal Exhaust Gas Recirculation Promoted Auto-Ignition, IFP International Congress Preceding, p. 85-100 (2001)

(13) Ishibashi, Y., Asai, M. and Nishida, K.: An Experimental Study of Stratified Scavenging Activated Radical Combustion Engine, Small Engine Technology Conference, SAE Paper 972077 (1997)

(14) Ishibashi, Y., Asai, M.: A Low Pressure Pneumatic Direct Injection Two-Stroke Engine by Activated Radical Combustion Concept, SAE Paper 980757 (1998)

(15) Blair, P. G. et al.: Single Cycle Gas Testing Method for Two-Stroke Engine Scavenging, SAE Paper 790501 (1979)

■ Authors ■


Yoichi ISHIBASHI


Kenji NISHIDA


Yukio SAKAI


Hisashi SAKUYAMA

Interconnection Technology for Engine Generators

Yoshiaki KOTANI* Yoshihisa SHINOGI*
Yasuhiro NAKADA* Yoshinori NAKAGAWA*

ABSTRACT

The development of the 1 kW-class inverter unit with a small engine generator that conforms to “Guideline for the interconnection technology requirements” has succeeded. To connect distributed electrical sources such as wind power generation, photovoltaic generation, or cogeneration to the utility grid, it is necessary to detect demand-side problems including the distributed sources (short circuit, ground fault, troubles in generated voltage or frequency) and to detect problems in the grid (power failure and troubles of voltage or frequency). It is also necessary to protect electric power systems, distributed sources, and electrical appliances. The inverter unit uses both passive and active islanding detection methods. Total distortion factor is reduced to less than 1% by applying two kinds of input current to the power supply unit. Efficiency of the interconnection inverter unit has achieved 91% and total efficiency of power generation of the cogeneration unit has achieved 20%.

1. Introduction

The micro-cogeneration unit described in this report differs from typical portable generators in that it can be connected directly to the power utility grid. This capability is referred to as interconnection. Both grid supplied electricity and electricity from micro-cogeneration units are supplied to electrical appliances. To insure human safety as well as safety to load installations inside the home and appliances – whether inside or outside of the home – while maintaining the quality of residential distribution lines, it is imperative that a standard of rational technology requirements be adopted to govern the connected operation of various power supplies.

The “Guidelines for Interconnection Technology Requirements”[(1)] issued by the Agency of Natural Energy and Resources, describe the necessary technological requirements for interconnecting distributed power sources, methods for detecting power failures, and procedures for detecting problems with distributed power sources such as wind power generation and photovoltaic generation, as well as problems emanating from the power grid.

These requirements however do not take into account connectivity of rotary generators to low-voltage distribution feeders and do not provide testing details for evaluating whether a connection is appropriate or not. To address this shortfall, the Investigation Committee on Interconnection Technology has issued the “Testing Methodology Guide for Protection of Interconnection with Gas Engine Cogeneration Systems”.

This report introduces the interconnection inverter technology for 1 kW-class inverter units, which conform to the “Guidelines for Interconnection Technology Requirements”.

2. Development Concept

The inverter used in the micro-cogeneration unit has numerous technology features that enable interconnection and set it apart from typical portable generator inverters. The development of the micro-cogeneration unit was first started to establish autonomous technologies when testing for determining conformity with the interconnection guidelines, which were not yet available.

In adapting the interconnection inverter for the micro-cogeneration unit for residential use, the following conditions were focused on.

(1) Must conform to the interconnection guidelines, including the implementation of two methods of power failure detection.
(2) Must embody a high quality power that is generated at low noise levels.
(3) Must perform at high levels of efficiency.
(4) Must be able to be integrated into the main cogeneration unit.

* Asakahigashi R&D Center

3. Specifications and Features

3.1. Interconnection Inverter Unit Specifications

The interconnection inverter unit adopts a 32-bit CPU control circuit and is comprised of a system for monitoring power supplied by the grid and a controller to enable the inverter unit to convert power from the generator to high-grade power. Table 1 lists the specifications for the inverter unit and Fig. 1 shows a block diagram of the control system.

Table 1 Specifications

Type of inverter	Self-exciting and voltage type power current control system
Type of switch control	PWM
Type of insulation	Non-insulating non-transformer type
Rated capacity	1.0kW
Type of interconnection	Single-phase three-line
Rated voltage	AC 202V (AC101V two-phase)
Rated frequency	50/60Hz
Output power factor	Over 0.95
Total output current distortion	Under 5 %
Type of electric power controlling system	Regulating output electric power
Protective measures	Over voltage protection
	Under voltage protection
	Over frequency protection
	Under frequency protection
	DC injection protection
Type of anti-islanding protection	Passive: Detecting saltatorial drift of voltage phase
	Active: Phase shifting system
Type of Restraining power output	Effective power controlling system



Fig. 2 Inverter unit

4. Component Technology

4.1. Interconnection Inverter Controller

The following functions are requirements for the interconnection inverter.

1) To enable grid connectivity and output

In connecting to the utility grid, the inverter unit must adopt specifications that conform to the “Guidelines for Interconnection Technology Requirements” issued by the Agency of Natural Resources and Energy, a division of the Ministry of International Trade and Industry in 1986.

Table 2 provides an overview of these guidelines.

2) Accommodate Regional Variations

There is some variation in utility voltage depending on regional location. Also, utility power sources may experience short interruptions, voltage dips and voltage phase variations. To enable follow-up operation for these variations in power standards, the unit must be able to accommodate a threshold of 7 different protective functions that can be set at 5 levels. A customized communication software package has been developed for PC-based application to enable multiple settings according to regional variation.

3) Allocate Priority to Environmental Issues

Cogeneration systems have been designed to provide efficient use of energy and are highly efficient. Running cogeneration systems at a constant level of power output and

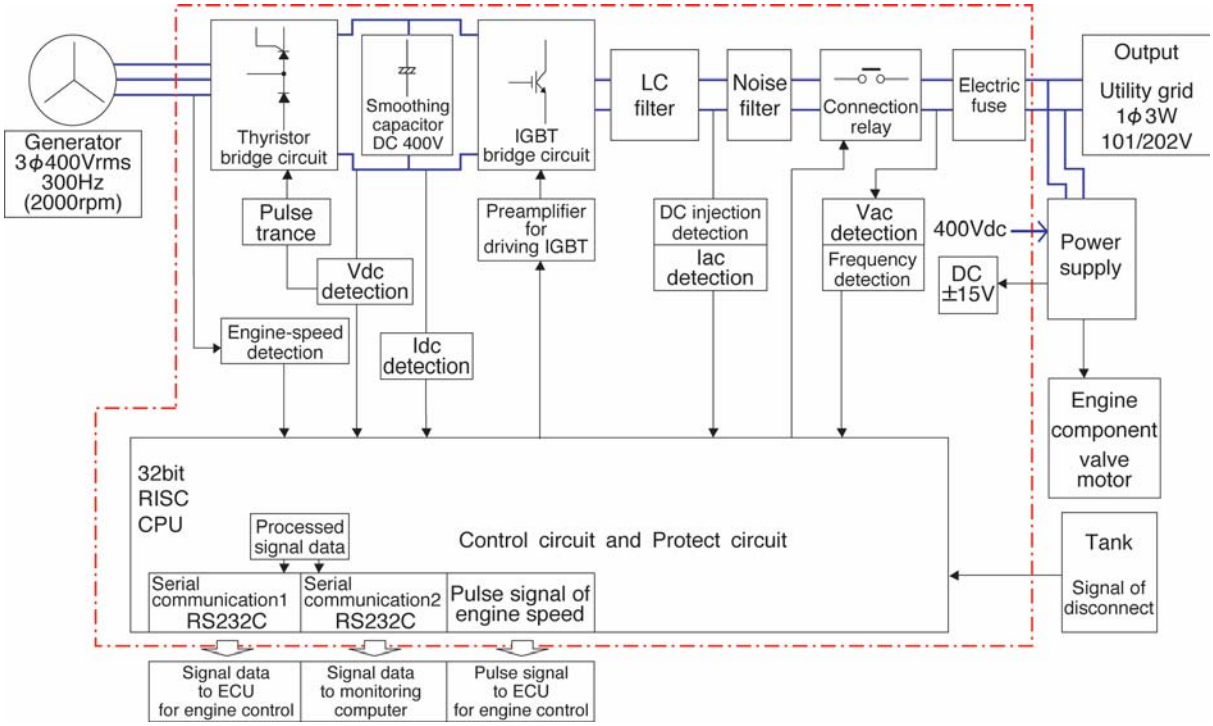


Fig. 1 Control system diagram

Table 2 Guideline for utility-interconnection

Test term	Benchmark			
	Action	Protect level	Operating time	Action after a utility disturbance
Over current protection.	Disconnect from a utility grid.	Setting level ±0.2% Max. Setting level is below 150% of rated current	0.5 sec Max.	–
Over/Under DC current protection.	Disconnect from a utility grid.	–5% Min. +5% Max. against working voltage.	0.5 sec Max.	–
Detecting DC injection.	Disconnect from a utility grid.	1% Max. against rated AC current.	0.5 sec Max.	–
Over/Under AC voltage protection.	Disconnect from a utility grid.	Setting level –0.2% Min. +0.2% Max.	Setting time –0.1sec Min. +0.1sec Max.	Do not reconnect after a period.
Over/Under frequency protection.	Disconnect from a utility grid.	Setting level –0.1Hz Min. +0.1Hz Max.	Setting time –0.1sec Min. +0.1sec Max.	Do not reconnect after a period.
Active detecting islanding.	Disconnect from a utility grid.	–	0.5sec Min. 1sec Max.	Do not reconnect after a period.
Passive detecting islanding.	Disconnect from a utility grid.	–	0.5 sec Max.	Do not reconnect after a period.
Blocking after a utility disturbance in a period.	–	–	–	Do not reconnect after a period.
Detecting instantaneous over voltage.	Disconnect from a utility grid.	Setting level –5% Min. +5% Max. Only 135V Max.	1 sec Max.	–
Restraining rising output voltage	Restraining power output under 107V when working voltage is 100V.	–	–	–

implementing optimal design settings for inverter efficiency along with the incorporation of an efficient engine design have enabled a high level of unit efficiency.

4.2. Islanding Detection

A key feature of interconnection technology is that when a malfunction in a cogeneration unit or a defect in the source side power is detected, the generator is halted and the connection is immediately interrupted. It is essential that the system embody detection functions to monitor malfunctions caused by leakage currents or over current occurrences, as well as the ability to detect abnormalities in distribution line voltage or frequency problems.

When a problem occurs in the source side power, the generating appliance is autonomously halted and the connection is immediately interrupted. The unit will not establish connectivity until the source side power has recovered.

When the power distribution line is disconnected from the main source due to power failures, malfunction, or for some other reason, the power from the cogeneration unit and power being consumed from the distribution line tend to create a static state of equilibrium. If this occurs, the cogeneration unit will only carry the loading from the distribution line and resume operation with the distribution feeder as it is being charged. This phenomenon is called islanding. Since there is no change in the distribution line voltage or frequency when islanding occurs, the normal protection relay is not able to detect the islanding occurrence.

Islanding conditions are potentially dangerous to distribution line technicians and may also cause large over currents caused by the difference in voltage phase between the line experiencing islanding and the main source when the connection with the main source is closed again. Islanding ultimately causes undesirable damage to distribution line equipment and appliances. For this reason, the system must be able to autonomously halt the generator when the distribution power line is disconnected.

4.2.1. Passive islanding detection

Passive islanding detection picks up small fluctuations in line voltage frequency, voltage phase, or harmonic voltage that are brought on by vacillating current and loading levels, which occur during islanding. Although this detection mode is noted particularly for its rapid detection capability, it has a low level of detection capability when the generated power and loading levels are at perfect equilibrium. The principles adopted in the passive islanding detection mode used by the interconnection inverter unit are described below. This detection mode uses what is referred to as voltage phase-skip detection, which detects the amount of change in frequency.

Although electric loading conditions in residences change for a variety of conditions, when loading requiring reactive power is connected where the power factor $\neq 1$, the voltage frequency is normally stabilized at 50/60 Hz. When a power failure occurs, the interconnection inverter generates a constant rate of AC power. When a power load is connected where the power factor $\neq 1$, the voltage phases are advanced or delayed according to the loading reactive power value. The voltage frequency before or after a failure occurrence varies greatly at points where the failure occurs. Looking closer at

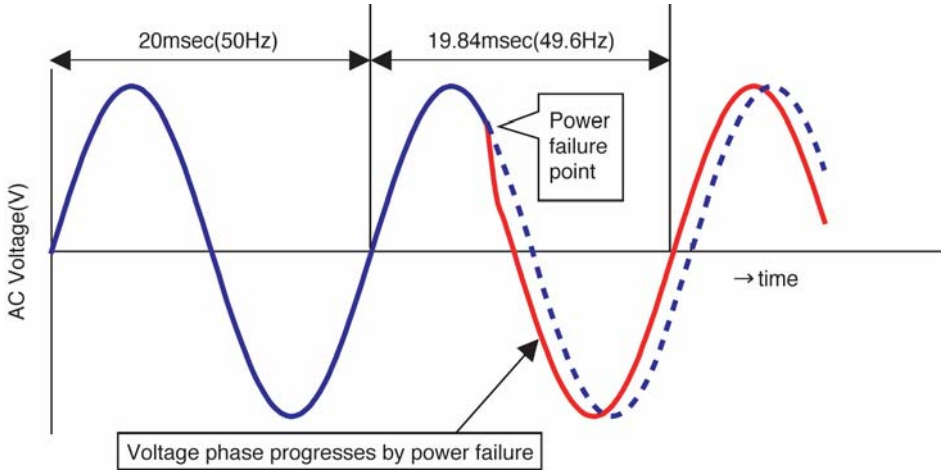


Fig. 3 Voltage wave pattern in power failure with connected inductance load

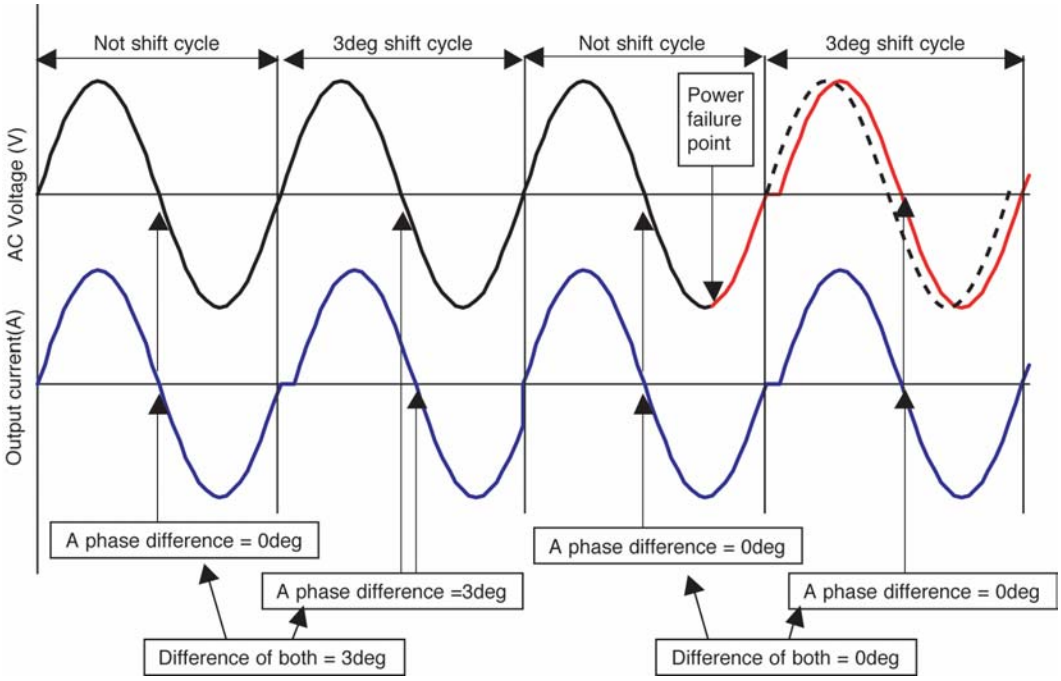


Fig. 4 Control method of active islanding

this phenomenon, when the change in voltage frequency is greater than 0.8%, a power failure is presumed to have occurred and power output is halted. The threshold can be adjusted in 5 different levels ranging in 0.2% ~ 1.0%.

Noise generated from large power loading associated with appliances, whether ON/OFF, tends to cause changes in voltage frequency. The passive detection mode is able to detect this variation. When the variation is detected, the inverter CPU is turned OFF for 5 seconds (gate blocking) without causing the interconnection relay to turn OFF. If an actual power failure were to occur, the AC under voltage protection (UVR) function is initiated and the interconnection relay is turned OFF. If there is no power failure, the relay is automatically re-established in 5 seconds.

Although the principles governing the passive islanding method of detection have been discussed, there are, logically speaking, conditions in which passive islanding detection is not able to detect a power failure.

When a connection is established at a residence with power loading ≅ 1 kW and a loading power factor = 1, there is no change in voltage and also no change in frequency because of phase skipping. Therefore power failure cannot be detected. The active islanding detection method has been implemented to compensate for such conditions.

4.2.2. Active islanding detection

Active islanding detection creates small fluctuations in generated power voltage, frequency or voltage phase and works to break the static equilibrium between the generated power and loading levels that occur with islanding. This ultimately leads to some voltage and frequency malfunctions but stops the occurrence of islanding. The active islanding detection mode is effective in instances where a static state of equilibrium has occurred between the generated power and loading levels.

The principle adopted in the active islanding detection mode used by the interconnection inverter unit is described below. This detection mode uses what is referred to as phase shift mode of detection.

Figure 4 shows the deliberate changes to current and voltage phase that alternate at fixed cycles from 0° to 3° (where a delay has occurred). Normally, the difference between a 0° phase and a 3° phase is 3°. When a power failure occurs, a loading with a power factor of 1 is

connected, and the current from the cogeneration unit is equal to the voltage waveform. So even if the displacement is 3°, the voltage phase remains 0° as no phase change occurs.

The active islanding detection mode recognizes a power failure when the phase differential is less than 3°.

When the active islanding detection function is active, the gate blocking setting and interconnection relay are turned OFF. After verifying that the voltage and frequency during a fixed interval are within a range of operational normalcy following power recovery, the connection is re-established. The fixed interval can be set at 5 different stages within a period of 120 ~ 300 seconds in accordance with guideline specifications.

4.3. Power Quality

The system has been designed to filter out reactive power transmission from the engine generator and to avoid exerting any changes in voltage on the distribution line. Additionally, the system harnesses the highest quality power by suppressing harmonic currents and preventing interference to other electrical components or appliances, and prevents any occurrence of electromagnetic interference.

4.3.1. Harmonic currents

The interconnection inverter adapted to the cogeneration unit, adopts the following technological principles. The cogeneration unit's main power supply and auxiliary units and controller exert the same degree of electrical load on the interconnection inverter as on domestic appliances. When the power from the interconnection inverter has passed through the cogeneration unit's main power supply and auxiliary unit load, the power factor from the cogeneration unit is reduced thereby creating distortion in the current. To avoid this malfunction, the power supply unit has been designed to accommodate 2 types of power input, the grid supply and converted DC current, which takes place within the inverter unit. Figure 5 shows how the grid supply is consumed when the engine is started. The figure also shows how the power and auxiliary units operate with only DC current from the generator when the cogeneration unit is generating power. After the AC/DC conversion takes place, quality power sent from the inverter output channel is transmitted to the distribution line without passing through the main power supply or auxiliary unit.

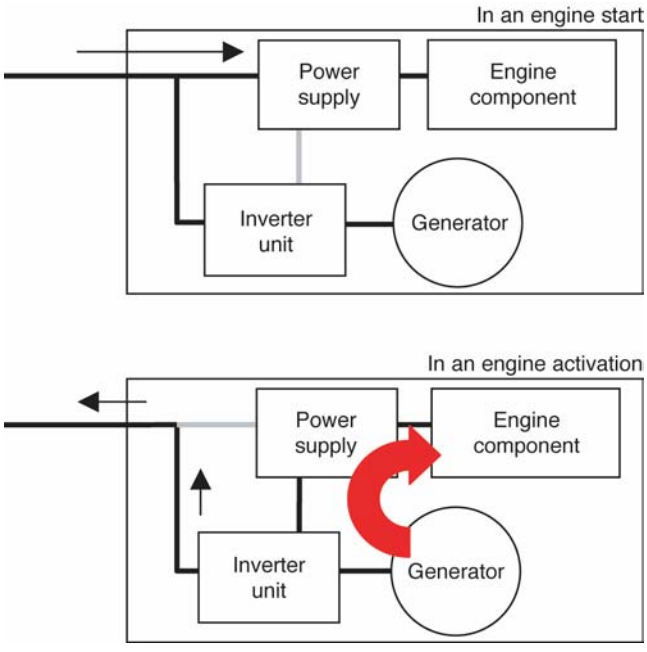


Fig. 5 Explanation of this technique

By implementing this method of power generation, the control power supply is preserved when the engine is started even if a short interruption were to occur on the grid power side.

A comparison was conducted on the single circuit system in which the power passes through the main power supply and auxiliary unit and the two-circuit system. Figure 6 shows the results of this comparison. As shown in the figure, the distortion factor reaches a level high of 3.86% in the single circuit system while the two-circuit system registers a low distortion factor of 0.89%.

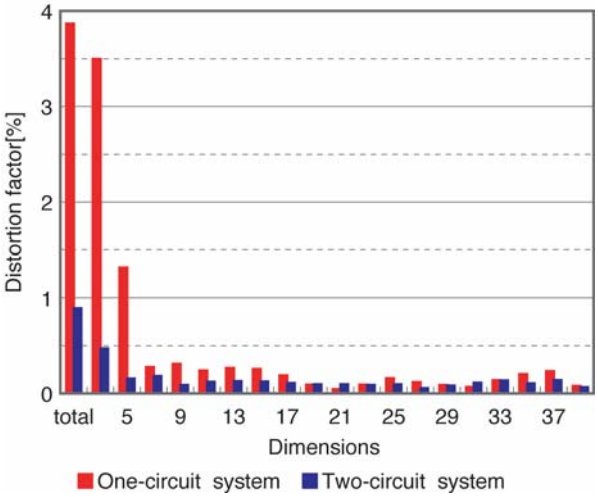


Fig. 6 Test results of distortions factor

5. Applications to the Cogeneration Unit

For details regarding the cogeneration unit with inbuilt interconnection inverters, refer to the technical report published by Takaishi et al[(2)].

Based around a 1 kW power output unit, which is suitable for the typical residence, Fig. 7 shows the interconnection inverter efficiency level at a peak of 91%, which provides a power efficiency level of 20%. Figure 8 provides a general view of the installed micro-cogeneration system. Power produced from this unit is sent to electrical appliances throughout the house by the interconnection supply. The overall level of efficiency, including the heat output, reaches a maximum peak of 85% and suppresses consumption of the

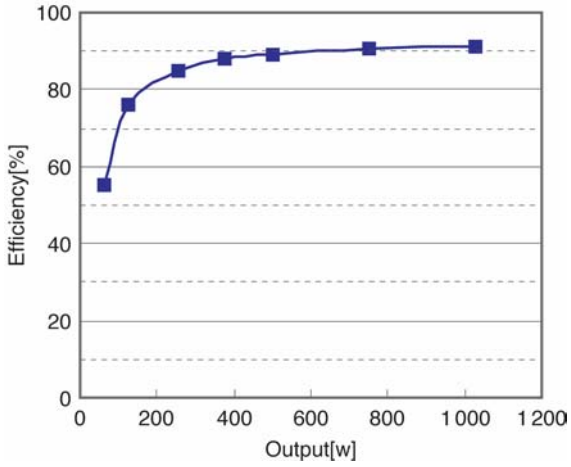


Fig. 7 Test results of inverter efficiency

primary energy within the house.

The interconnection inverter has been incorporated and adapted to the cogeneration unit. The high voltage distribution line running from the generator is connected to the interconnection converter within the shortest possible distance. This contributes to the reduction of the number of parts required for the configuration. See Fig. 9 for an overview of the inverter unit for interconnection.

Figure 10 provides an overview of the newly developed micro-cogeneration unit.

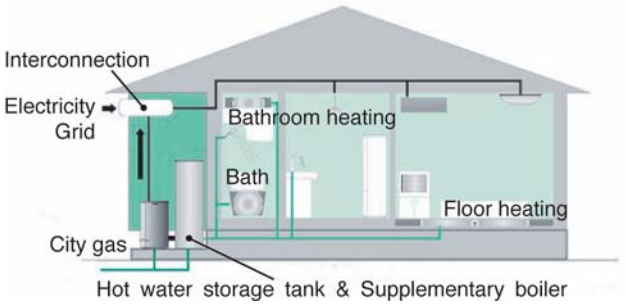


Fig. 8 General view of micro cogeneration system

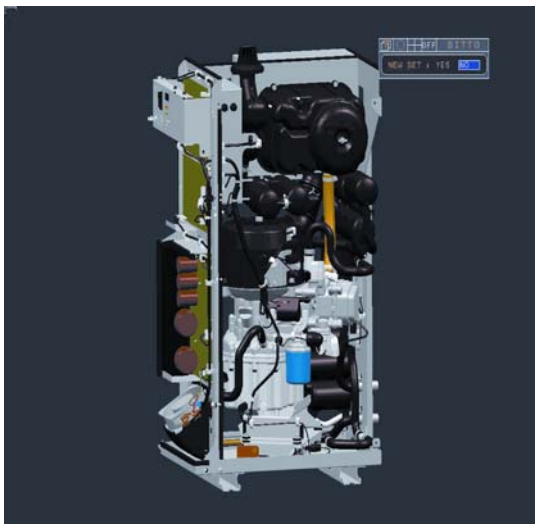


Fig. 9 Inverter unit for interconnection



Fig. 10 Overview of micro cogeneration unit

6. Summary

The interconnection sine wave inverter has been successfully adapted to the product profile and conforms to the "Guidelines for Interconnection Technology Requirements".

(1) The system satisfies all technological principles described in the "Testing Methodology Guide for Interconnection Maintenance Appliances for Gas Engine Cogeneration Systems".

(2) Applying 2 types of input power supply in accordance with technology measures for suppressing harmonic currents has produced a low 0.89% distortion factor and enabled the supply of high quality power for domestic applications.

(3) Optimal settings have been adapted to the inverter unit to achieve a 91% level of efficiency for the interconnection unit.

The interconnection inverter, which is based on the configuration principles described herein, has been installed in a typical residential environment for purposes of field testing and monitor testing to provide a working example of interconnection.

The authors would like to take this opportunity to express their gratitude to the many people who have cooperated in the development of this unit.

Reference

(1) Electricity Technology Standard Investigation Committee: Guidelines for the Distributed Power Source Technology Requirements, JEAG 9701 (1993)

(2) Takaishi, T., Ara, M., Togawa, K.: Introduction of Micro Combined Heat and Power Generation Unit for Residential Use, Honda R&D Technical Review, Vol. 15, No. 1, p. 53-58 (2003)

■ Authors ■



Yoshiaki KOTANI



Yoshihisa SHINOGI



Yasuhiro NAKADA



Yoshinori NAKAGAWA

Research on Noise Reduction for Pinion Shift-type Starters

Mikihiro TAKANO* Masashi TANAKA*
Nobuyuki HIRAMATSU* Takashi AOKI*

ABSTRACT

The mechanism that generated of noise was analyzed and research on noise reduction was conducted in pinion shift-type starters for idle stop systems. Both pinion shift noise and cranking noise are components of the noise generated during engine start; vehicle tests demonstrated that cranking noise is produced for a longer period and causes greater discomfort to driver and passengers, and countermeasures were therefore devised against this form of noise. Bench tests revealed that gear whine was a more significant factor in cranking noise than gear rattle, and countermeasures therefore targeted this source of noise. The spur gears conventionally used in pinion shift-type starters were replaced by helical gears and the contact ratio was increased, reducing noise by 7 dB. When establishing gear specifications, analyses of stress in the sections making contact were conducted to enable judgment of the ease with which damage occurs to gear end faces during pinion gear shifting. The relation between angle and stroke of the pinion gears during shifting was optimized to achieve superior shift performance.

1. Introduction

Idle stop systems, which automatically shut off the engine when a vehicle idles at traffic lights, etc. are being increasingly employed as a means of reducing emissions of the greenhouse gas CO_2. Various methods are used to restart the engines of vehicles provided with these systems. The majority restart the engine instantaneously using a high-power electric motor, as in the hybrid cars shown schematically in Figs. 1-a and 1-b. The use of high voltages increases the cost of these systems. The system shown in Fig. 1-a positions the motor between the engine and the transmission, while the system in Fig. 1-b locates the motor on a separate shaft. This positioning increases the width of these systems (by the width of the motor and the belt respectively), making it difficult to fit them in the engine compartment.

Figure 1-c shows a system employing a conventional pinion shift-type starter to restart the engine. These systems are lower in cost than those discussed above, and are employed in comparatively less expensive vehicles with low displacement engines and manual transmissions. However, because these systems are very loud when starting the engine, noise reduction measures are required to enable them to be fitted in idle stop vehicles, in which the engine is constantly stopped and restarted. The project discussed in this paper therefore analyzed the mechanism that generated noise in pinion shift-type starters and conducted research on methods of noise reduction to develop a less expensive, low-noise idle stop system.

* Tochigi R&D Center

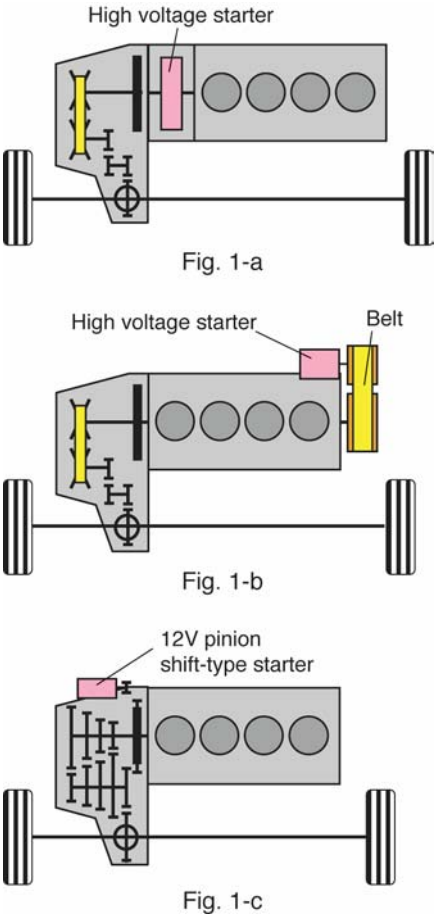


Fig. 1 Starter types for idle stop system

2. Analysis of Noise at Engine Start

Figure 2 shows the configuration of the pinion gear shift-type starter used in this research. Spur gears are employed in pinion gear shift-type starters to reduce costs. The operation of this type of system is shown in Fig. 3. (1) The command to start the engine causes current to flow to a magnetic switch, which in turn draws in a plunger. The pinion gears are connected to the plunger by the drive lever. The movement of the plunger pushes the pinion gears towards the ring gears, and they strike the end faces of the ring gears. (2) The closure of the main switch causes battery voltage to be transmitted directly to the motor, rotating the pinion gears. (3) The rotation of the pinion gears causes them to mesh with the ring gears. The pinion gears are pushed farther into the ring gears until they completely mesh and the engine is cranked.

Figure 4 shows changes in the level of cabin noise during engine start over time. Noise during engine start is composed of pinion shift noise generated as the pinion gears shift to the ring gears, and cranking noise generated by the meshing of the pinion and ring gears when shifting is completed and the starter motor drives the engine. The noise level of cranking is low in comparison to that of shifting, but it is produced for a longer period, and tests demonstrated that it therefore causes occupants of the vehicle a greater level of discomfort. This research project therefore restricted its focus to the reduction of cranking noise.

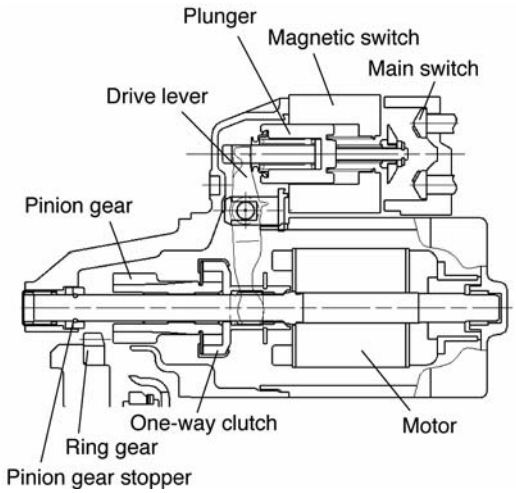


Fig. 2 Pinion shift-type starter

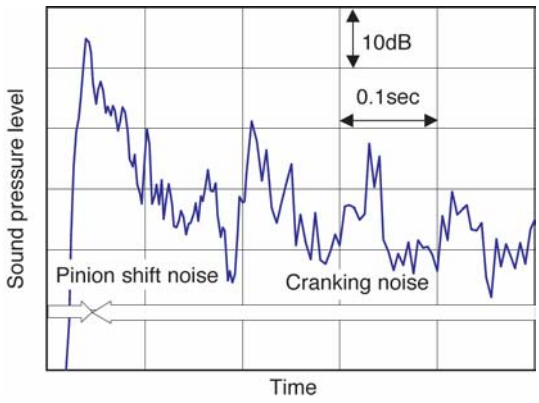


Fig. 4 Cabin noise during engine start

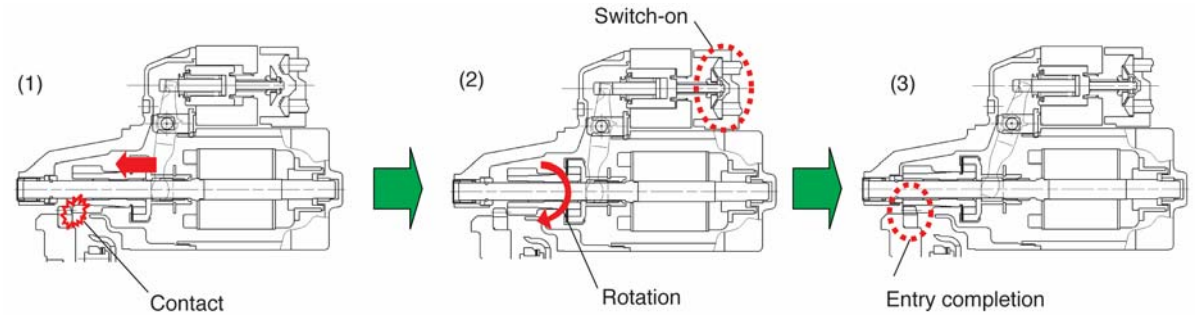


Fig. 3 Operation of pinion shift

Figure 5 shows changes over time for engine speed (Ne) and starter motor speed multiplied by the reduction gear ratio between the pinion gears and ring gears (Nm') during cranking. Engine speed fluctuates periodically during cranking. An almost complete cycle is shown in Fig. 6. Figure 7 shows motor torque over the same cycle, and Fig. 8 shows longitudinal vibration of the vehicle in the starter motor. In Fig. 7, there is a time zone during which the starter motor is not driving the engine, and torque is close to zero. This corresponds to time zone 1, from a to b, in Fig. 6. During this period engine speed exceeds motor speed. In time zone 1, the pinion gears are driven by the ring gears, and the opposite tooth surfaces, which are not in contact when the pinion gears drive the ring gears, are in contact with the surfaces. During this period the one-way clutch is over-running. Time zone 2 is represented by b to c in Fig. 6. During this period, backlash is reduced in the pinion gears because the motor speed exceeds the engine speed. Finally, at c, the pinion gear drive side tooth surfaces and the ring gear driven side tooth surfaces make contact, generating gear rattle.

As can be seen from Fig. 8, after c, when the starter motor is generating torque, i.e., driving the engine, there is a higher amount of vibration than when it is not driving. This vibration is gear whine generated by the mesh of the gears, and is dominant over gear rattle.

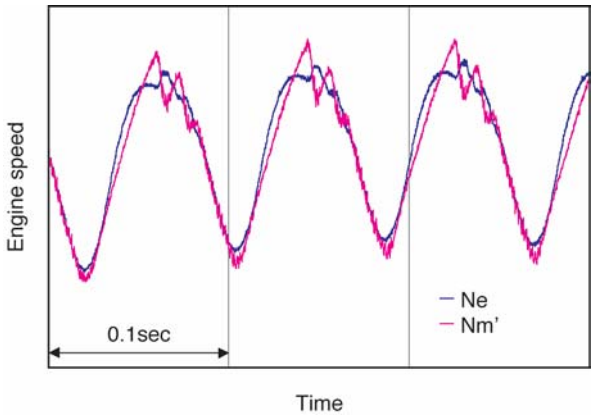


Fig. 5 Engine speed and starter motor speed during engine start

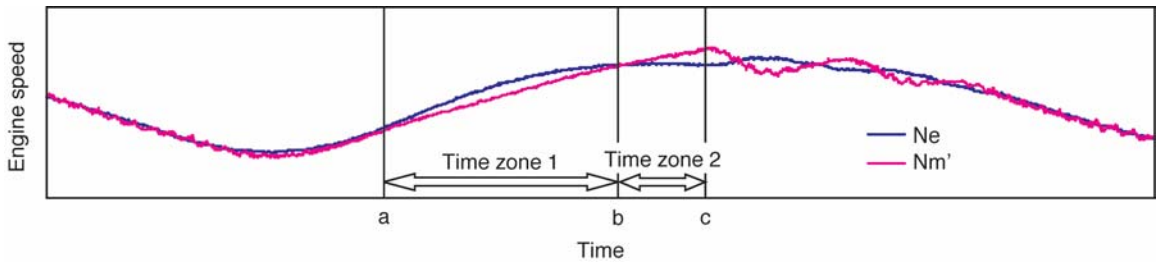


Fig. 6 Engine speed and starter motor speed during engine start

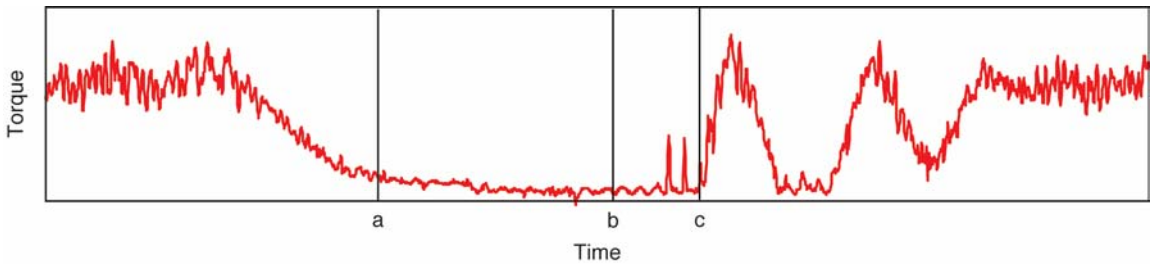


Fig. 7 Torque produced by the starter motor during engine starter

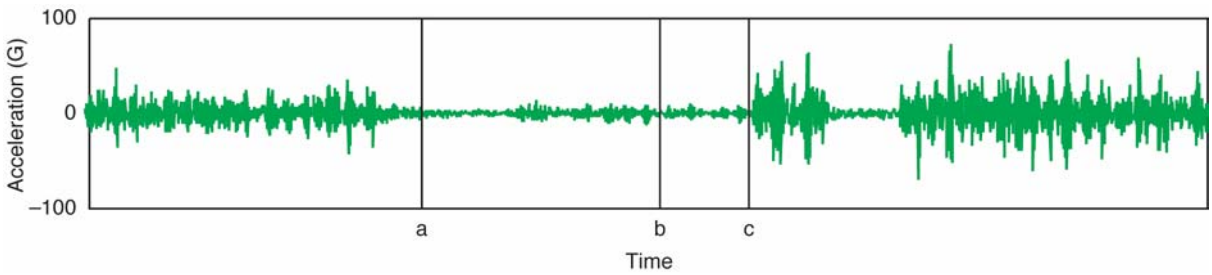


Fig. 8 Vibration of starter during engine start

3. Analysis of Cranking Noise

To analyze cranking noise, tests were first conducted on a test stand to determine the relationship between gear tooth profile, backlash, gear contact width, contact ratio, and gear whine. Gear specifications producing superior results in these tests were then evaluated in a test vehicle. As Fig. 9 shows, for tests on the test stand the pinion gears and ring gears were meshed in advance, and the behavior of each section of the gears and the amount of noise generated was measured with the starter motor driving.

3.1. Tooth Profile

To determine the effect of improving the tooth profile on cranking noise, tests were conducted using two types of ring gears with different profiles, and noise levels were compared. The 'spur gear' column in Table 1 shows the specifications of the gears, and Table 2 shows the results of measurements for the different tooth shapes driven by the starter motor. A in Table 2 is a mass-produced tooth profile, while B represents an improved profile over the mass-produced model. The figures for waviness represent the highest value obtained from measurements of four teeth; other figures are averages. It is clear from a comparison of the maximum figures for waviness and the averages for profile slope deviation and helix slope deviation that the tooth profile of gear B is more accurate than that of gear A.

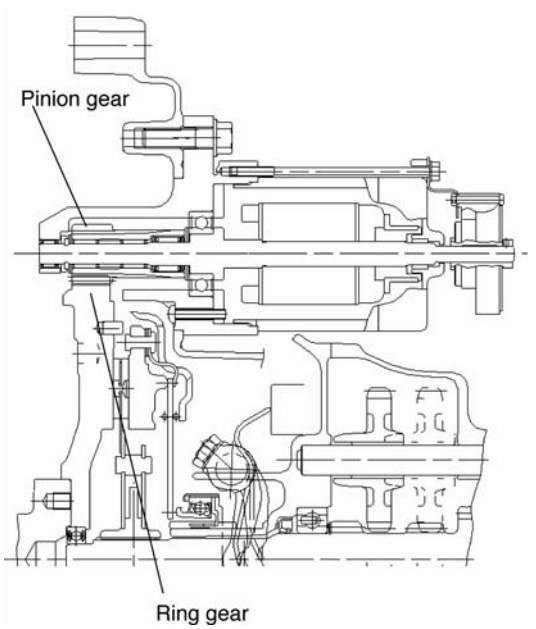


Fig. 9 Constant mesh type starter motor

Table 1 Gear specifications

Item	Total contact ratio	Normal module	Helix angle (deg.)	Contact width (mm)
Spur gear	1.09	2.54	0	9
Helical gear	1.25	2.5	4	9
	1.45	2.25	12	9
	1.80	2.25	28	9
	1.84	2	20	9
	1.91	1.75	20	9
	1.97	2	28	9
	2.33	2	20	18.7
	2.39	2.25	28	18.7
	2.45	1.75	20	18.7
	2.64	2	28	18.7
	2.68	2.25	36	18.7
	3.62	1.5	36	18.7

Figure 10 shows the results of test stand measurements of sound pressure level during cranking. There is only a 0.5 dB difference between the sound pressure levels for tooth profiles A and B, demonstrating that improving the tooth profile is largely ineffective in reducing cranking noise.

Table 2 Teeth profiles data

		Teeth profiles A		Teeth profiles B	
		Pinion gear	Ring gear	Pinion gear	Ring gear
Involute	Profile slope deviation	3.1	–4.3	2.3	8.7
	Bulge	–2.5	4.5	0.3	0
	Waviness of profile	9.2	19.6	1.6	1
	Tip relief	8.6	4.3	7	8.1
	Profile slope bias	–3.8	–4.3	–0.2	–0.7
Lead	Helix slope deviation	–7.5	–2.7	–2	5.1
	Crowning	–0.5	–3.2	4.9	5.3
	Waviness of helix	11.3	14	1.4	0.9

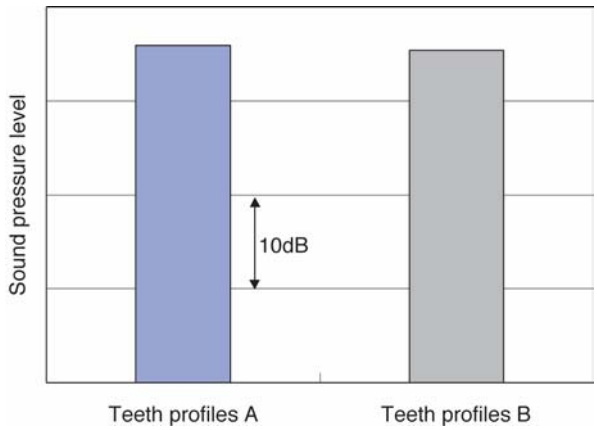


Fig. 10 Comparison of sound pressure level during engine start for different teeth profiles on test stand

3.2. Backlash

Next, to determine the effect of gear rattle, a gear with variable backlash was constructed, and cranking noise was compared. The specifications of the gears remained the same, as shown in Table 1 (spur gear); only backlash was varied from 0.15 mm to 0.45 mm in 0.1 mm increments. The results of test stand measurements of cranking noise are shown in Fig. 11. As shown there, the lowest measurement for cranking noise was taken at a backlash of 0.35 mm. When backlash is small, power transmission causes the teeth to deform, and the tooth surfaces on the side that is not driving contact each other, and when backlash is large, gear rattle

increases. Test results demonstrated that the minimum cranking noise is generated at specific levels of backlash, but these levels match backlash settings in mass-produced gears, and adjustment of backlash is therefore ineffective as a noise reduction measure.

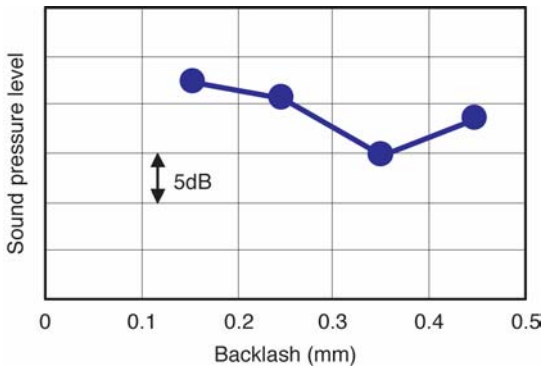


Fig. 11 Relationship between backlash and noise level of engine cranking on test stand

3.3. Gear Contact Width

Tests were conducted with gears of the same specifications to determine the effectiveness of increasing contact width in reducing cranking noise. As Fig. 12 indicates, the sound pressure level during cranking decreases as contact width increases. This is thought to be because increased flexural rigidity of the teeth reduces the amount of deformation occurring at power transmission. However, increasing the contact width in the vehicle required making the stroke longer during pinion gear shift, increasing the cost and weight of the starter. Increasing the contact width could therefore not be considered an effective method of reducing noise. The next stage of this research therefore examined the effect on cranking noise of using helical gears to increase the contact ratio, enabling the amount of deformation of the teeth to be reduced without increasing contact width.

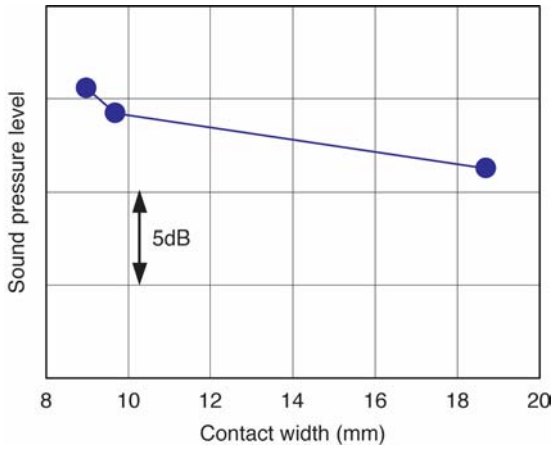


Fig. 12 Relationship between contact width and noise level of engine cranking on test stand

3.4. Gear Contact Ratio

Table 1 shows the specifications of the helical gears. The reduction ratio of the pinion gears and ring gears was set as equivalent to that of the spur gears. As in the analyses of the spur gears, the pinion gears were meshed with the ring gears before noise tests were conducted. Figure 13 shows the results of test stand measurements of cranking noise. The results demonstrate that cranking noise is reduced by approximately 8 – 16 dB by increasing the contact ratio, but that the effect is small at a contact ratio of 2.5 and above.

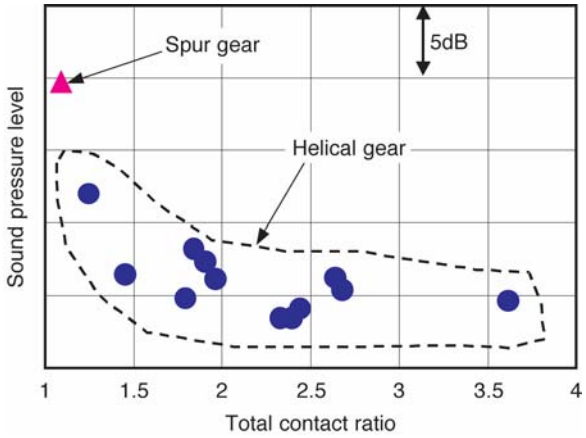


Fig. 13 Relationship between total contact ratio and noise level of engine cranking on test stand

3.5. Cranking Noise in a Vehicle Cabin

Having demonstrated in test stand tests that increasing contact ratio by utilizing helical gears is effective in reducing cranking noise, the project proceeded to vehicle testing. The specifications of the helical gears used in these studies were selected from Table 1. Figure 14 shows a comparison of the sound pressure level in a vehicle cabin when using mass-produced spur gears and helical gears, which increased the contact ratio to 1.84. In the test vehicle, increasing the contact ratio reduced cranking noise by 7 dB. A pinion gear shift-type starter was employed in the test vehicle. There were concerns that this would cause gear damage and rebounding during shift, therefore, gear specifications were established on the basis of the analyses described in sections 4 and 5.

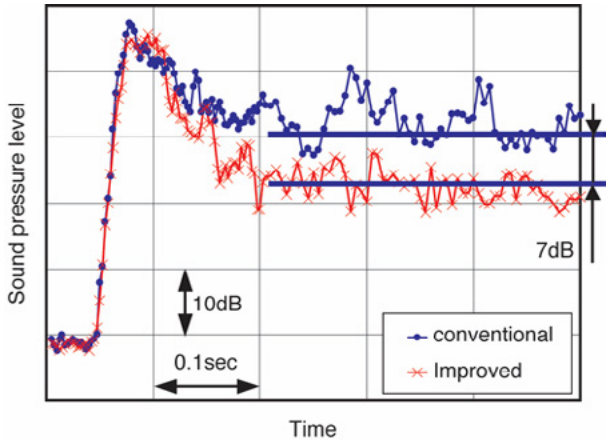


Fig. 14 Cabin noise during engine start

4. Analysis of Ring Gear Stress

The tests discussed above demonstrated increasing contact ratio to be the most effective method of reducing cranking noise. In practical terms, this involved reducing the size of the module to increase the number of teeth, and making the helix angle greater. Because this reduced the size of the gears and produced acute angles at the end faces, there were cases in which the end faces were damaged when the pinion gears made contact with the ring gears. The stress generated in the sections of the gears in contact was therefore analyzed using the finite element method. Figure 15 shows a pinion gear end face brought into contact with a fixed ring gear end face. The pinion gear was rotated until its drive side tooth surfaces made contact with the ring gear driven side tooth surfaces. This was taken to be a pinion gear angle of zero. The range of α in equation (1) from a pinion gear angle of zero was calculated. As Fig. 16 shows, the maximum stress was generated in the edge of the end face. Figure 17 shows the relationship between pinion gear angle and maximum stress on the ring gear. The stress generated in the ring gear increases as the pinion gear angle becomes smaller, because the area in contact decreases. No matter what specifications were tested, the end faces struck each other, causing plastic deformation. The rate at which the elastic limit was exceeded, t, is defined by equation (2). Gear specifications were selected using t as an indicator of end face damage.

$$\alpha = \frac{360}{Z} \tag{1}$$

$$t = \frac{\beta}{\alpha} \tag{2}$$

Z : Number of pinion gear teeth
β : Pinion gear angle at which elastic limit is exceeded

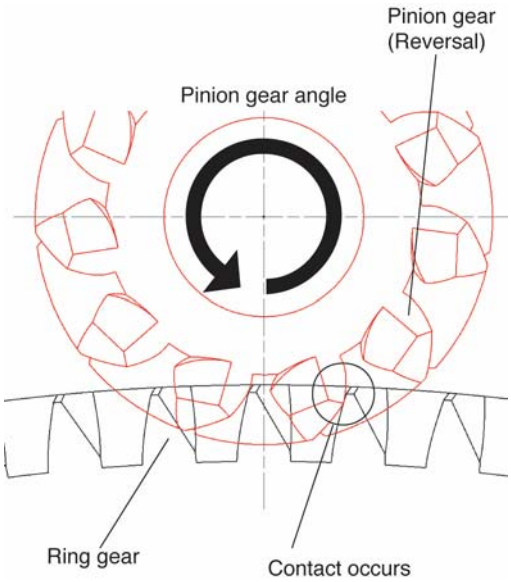


Fig. 15 Condition at pinion gear angle=0

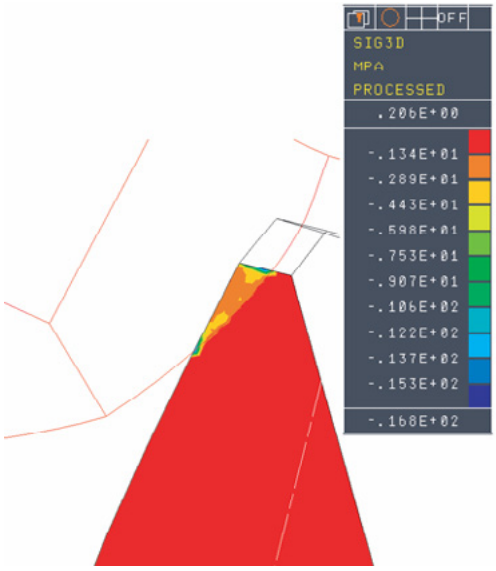


Fig. 16 Stress analysis results for ring gear

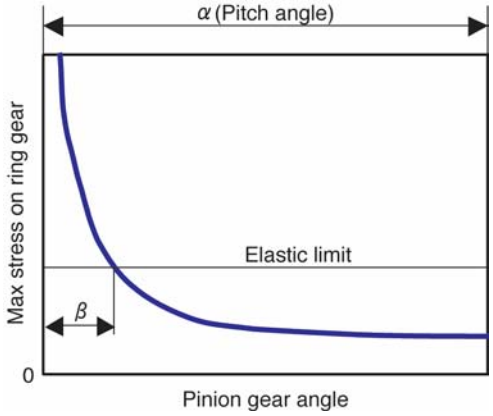


Fig. 17 Relationship between pinion gear angle and ring gear stress

5. Pinion Gear Shift Performance

The changes made to the specifications of the gears against mass production specifications, such as the size of the module and the helix angle, resulted in changes to the chamfering of the end face. These changes made the pinion gear unable to shift; the effect of pinion gear angle on stroke was therefore analyzed using mechanical system analysis software. Figure 18 shows the direction of pinion gear angle and stroke. Figure 19-a shows specification E, which was unable to shift, and Fig. 19-b shows the results of the analysis. It was determined that in this gear specification there was a certain range of angles during pinion gear shift (d in Fig. 19-b) at which the stroke did not increase even though the angle was increasing. This occurred when the gear in contact was changed from No. 1 to No. 2 (Fig. 18), and this is estimated to be the origin of the difficulty in shifting. Figure 20-a shows specification F, an improved chamfered form designed to enable the pinion gear stroke to increase with increasing angle, even when the gears in contact change (Fig. 20-b). Specification F displayed excellent shift performance in vehicle tests.

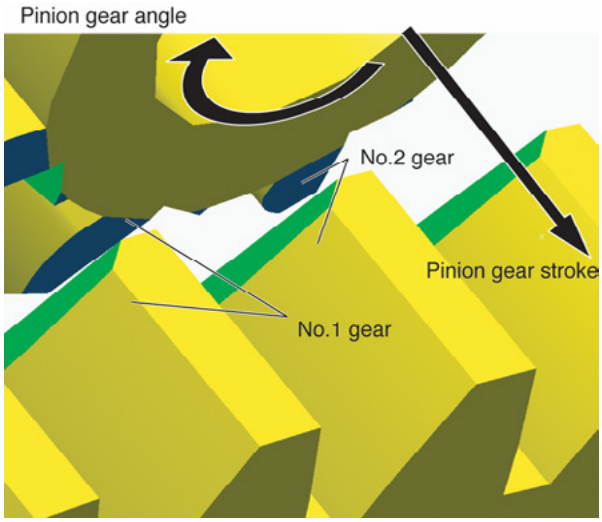


Fig. 18 Direction of pinion gear angle and stroke

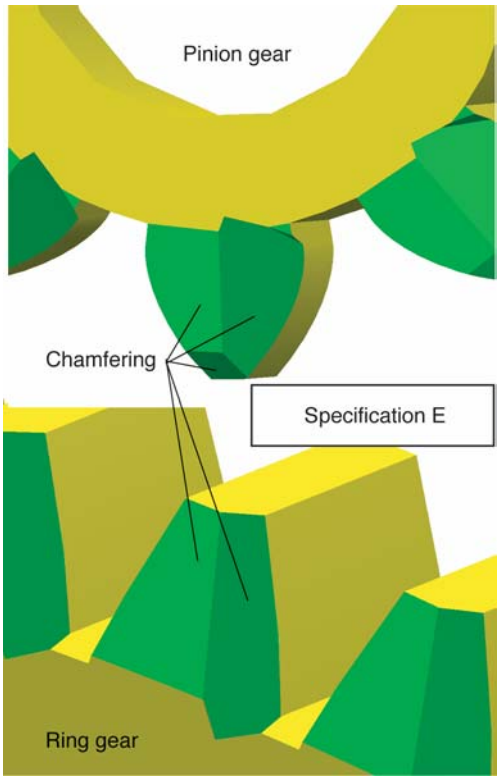


Fig. 19-a Chamfering form of gear end face

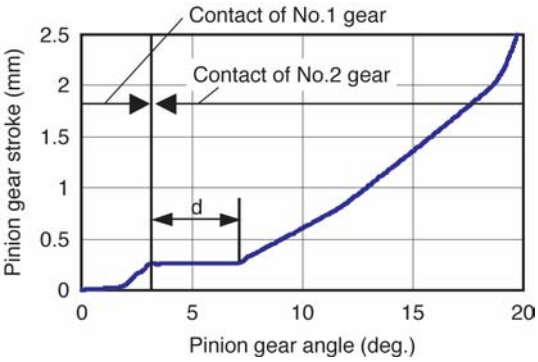


Fig. 19-b Relationship between pinion gear angle and stroke

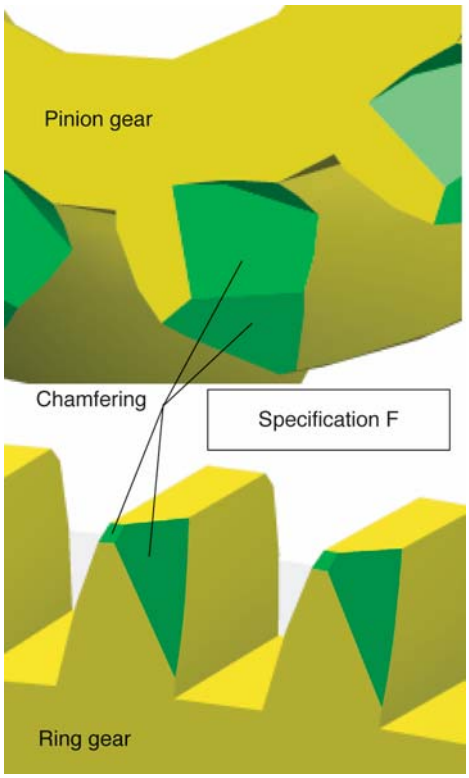


Fig. 20-a Chamfering form of gear end face

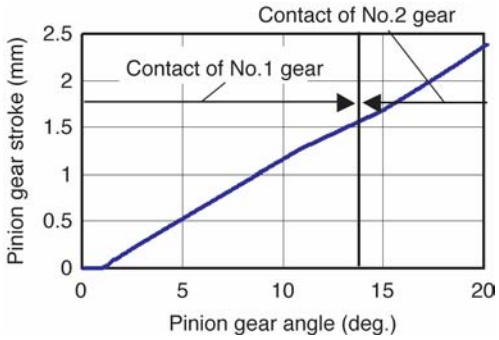


Fig. 20-b Relationship between pinion gear angle and stroke

6. Summary

Research conducted on noise reduction for pinion gear shift-type starters produced the following results:

(1) Pinion shift noise and cranking noise are both elements of noise at engine start; cranking noise is produced for a longer period, and therefore generates a higher level of discomfort for occupants of the vehicle.

(2) Cranking noise is composed of gear rattle and gear whine, but gear whine is dominant.

(3) Measures to decrease cranking noise in spur gears have little effectiveness, and are therefore impractical.

(4) Employing helical gears to increase contact ratio decreased cranking noise in the cabin by 7 dB.

The following methods were utilized to establish gear specifications:

(1) Stress analyses were conducted for the sections making contact when the end faces of the pinion gears and ring gears strike. The rate of generation of stress exceeding the elastic limit was established as an indicator of potential damage to the end faces.
(2) Excellent shift performance was achieved by establishing a setting at which pinion gear stroke increased with increasing angle during shift.

7. Acknowledgments

The authors wish to take this opportunity to thank all those from Honda and other companies who offered their assistance in this project.

■ Authors ■


Mikihiro TAKANO


Masashi TANAKA


Nobuyuki HIRAMATSU


Takashi AOKI

A Computer Simulation for Motorcycle Rider-Motion in Collision

Hideo NAMIKI* Toyokazu NAKAMURA* Satoshi IIJIMA*

ABSTRACT

Through computer simulation of the motion of a motorcycle rider, as a result of a collision between a motorcycle and car, we have validated the computer simulation results in two cases. In each case a motorcycle hits the side of a running car, one at an angle of 45 degrees and the other at 90 degrees. The simulation software of explicit finite element method (FEM) was selected because of its capability for expressing accurate shapes and deformation. The mesh size was determined by considering the simulation accuracy and calculation time. Then, FEM models of a motorcycle, airbag, dummy, helmet and passenger car were built. To shorten the calculation time, a part of the model was regarded as a rigid body and eliminated from the contact areas. As a result, highly accurate dummy posture and head velocity at ground impact time were simulated in the two cases of collision. Calculation time of the two cases was about 50 hours using a computer with a performance of 14.4 Gflops.

1. Introduction

Honda has been researching studies on protection of motorcycle riders since the 1960's[(1)]. A recent study described one of the rider protection techniques, a motorcycle-mounted airbag system[(2)]. In this research, airbag systems including sensors were developed and installed on the GL1500, a large touring model, for actual vehicle collision tests. Such tests require exclusive use of a test facility for long periods of time and are very expensive. It has, therefore, long been desired to develop computer simulation techniques that are usable in motorcycle airbag research. The goal of this study was to establish a collision simulation method that permits behavior estimates until the moment the dummy contacts the ground within a practical length of calculation time.

This report describes the results of two test cases. The reliability of computer simulations of rider motion in collisions with opposing vehicles was examined. The two cases were collisions of a motorcycle moving at 13.4 m/s into the side of an opposing vehicle moving at 6.7 m/s at angles of 45° and 90°. Figures 1 and 2 show the impact configurations. The accuracy of the simulations were assessed by observing the rider motion parameters of head velocity and torso angle. Methods for reducing calculation time were also investigated while pursuing simulation accuracy.

2. Selection of Simulation Software

Simulation software for collision analysis can be roughly classified into two types: the Multibody type and the FEM type. The software of Multibody type is advantageous due to its short calculation time. The FEM type is more suitable for more accurate crash simulation until the dummy's ground hit, because it can generate the accurate shapes easily,

* Asaka R&D Center

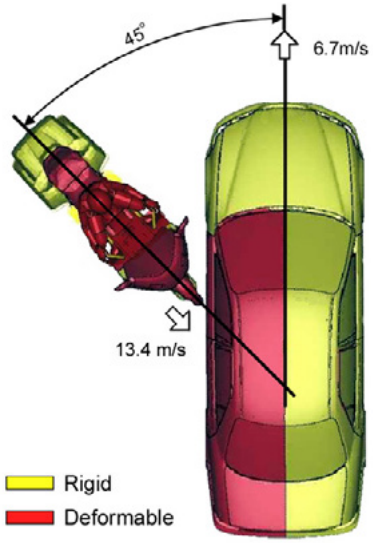


Fig. 1 Impact configuration of 45-degree

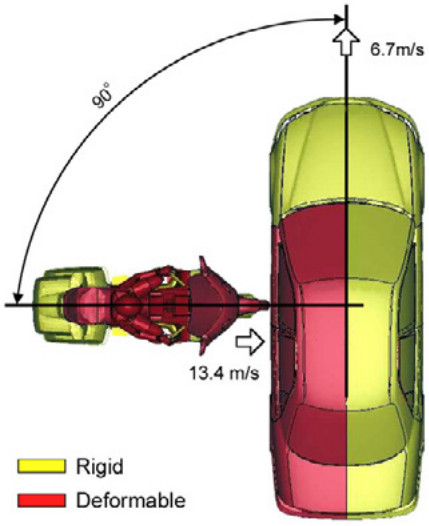


Fig. 2 Impact configuration of 90-degree

deformation and reaction force direction resulting from a deformation. Based on the above reasons, the finite element method, i.e., the explicit FEM software (LS-DYNA), was used for this study.

3. Creation of Model

3.1. Principles on Mesh Size and Model

Models of the motorcycle, airbag, dummy, helmet and the passenger car were handled simultaneously in the computer simulation in this study. Since the number of elements can be very large in this kind of simulation, the mesh size has a large influence on the calculation accuracy and the time needed for the calculation. A finer mesh is desirable for higher calculation accuracy, but the smaller the mesh size, the longer the required calculation time. It is also necessary to avoid having meshes of very different sizes where the models interfere with each other, to obtain the best stability and accuracy in the calculation. Thus, the mesh size is a critical parameter. The mean mesh size in the dummy model was set as the standard size in this study; meshes were never created smaller than this. The sizes of the various models created are shown in Table 1. The validity of each model was verified in unit tests before the simulation of the motorcycle-opposing vehicle collision.

3.2. Motorcycle Model

The motorcycle model made for this study was exclusively for frontal collision simulations. It accounted for deformation of the front wheel, and the tire model reproduced a certain internal air pressure. Since the steering mechanism is forced to high steering angles at the time of the collision with the opposing vehicle, the model was constructed to reproduce steering. Some motorcycle component models were made deformable where interference with the opposing vehicle or dummy and deformation were expected, and other components were made rigid in order to save calculation time. The resulting motorcycle model is illustrated in Fig. 3. The red portions were deformable, and the yellow portions, rigid.

For validation of the motorcycle model, the results of a simulated collision with a fixed barrier at 13.4 m/s were compared with those of an actual model. Those are shown in Fig. 4. The pitching angle of the body and the deformation results around the front wheel and headlight resembled the actual model well. Figure 5 shows the predicted and test waveforms acceleration of the body center of gravity. Overall, the waveforms coincide well.

3.3. Airbag Model

The airbag is supported by the motorcycle body through a connection to the retainer box and two belts behind the airbag. There are several tethers inside the airbag to help maintain its intended shape. These structures are essential for a motorcycle airbag and were modeled in shapes faithful to those of the originals. Figure 6 shows the airbag model.

Table 1 Numbers of nodes and elements

	Motorcycle	Dummy	Airbag	Opposing Vehicle	Total
Number of nodes	25618	34962	4768	178329	243677
Number of elements	34821	35567	4692	168916	243996

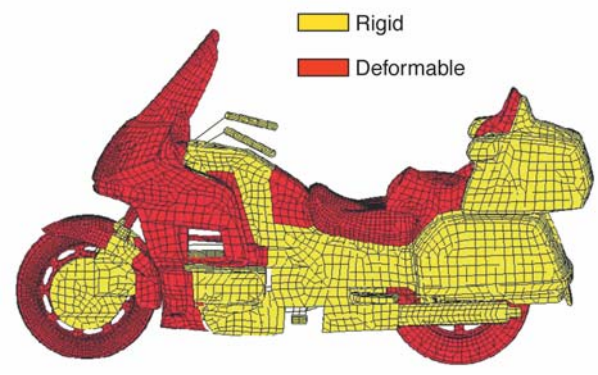


Fig. 3 Motorcycle model

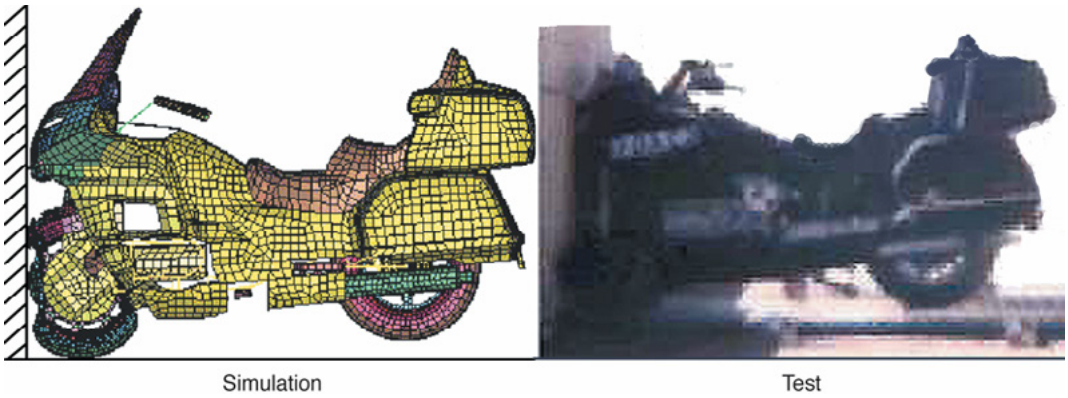


Fig. 4 Comparison of motorcycle motion between the simulation and the test in a rigid barrier collision

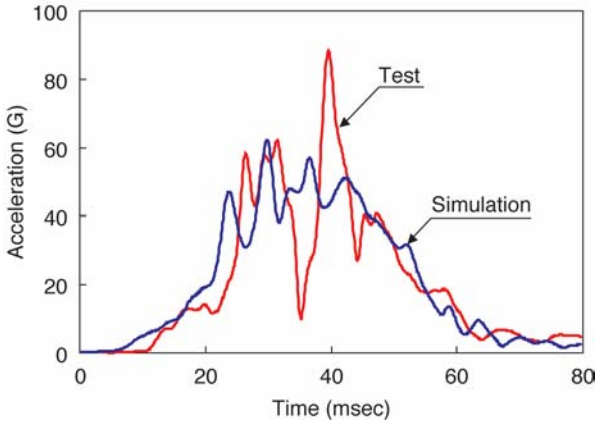


Fig. 5 Comparison of acceleration of motorcycle's center of gravity

For validation of the airbag model, the pressure waveforms during a static inflation of the test and simulation were compared; the waveforms are shown in Fig. 7. A high pressure spike occurred at the beginning of the test, but this was not indicated in the simulation. This is because folding of the airbag was not expressed in the model. Reproduction of this phenomena at the initial stage of inflation was not necessary in the present airbag model, which was made for assessing its effect on the rider after unfolding. Thus, folding of the airbag and the pressure spike at the initial stage of inflation were not included in the model.

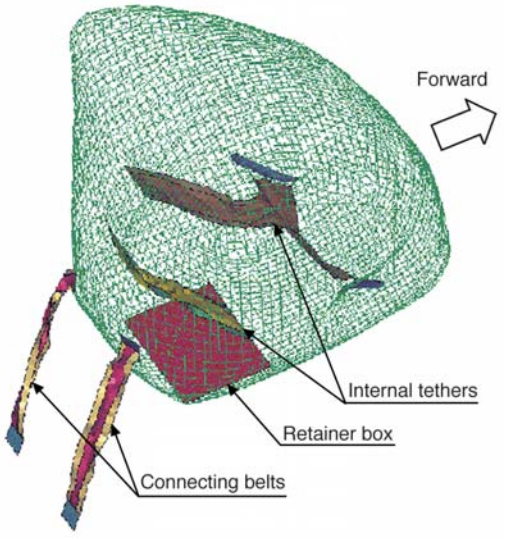


Fig. 6 Airbag model

3.4. Dummy

The dummy model has to be a deformable model because any part of the dummy body is subjected to a potential impact. Therefore, the LS-DYNA hybrid III 50th percentile model was selected as the base. It was created identically with the MATD dummy specified in ISO 13232[3]. The dummy model is shown in Fig. 8. The parts that were modified are shown in red; these were the head, neck, chest, abdomen, pelvis and legs. The model characteristics met the ISO 13232 criteria. The dummy also wore boots meeting ISO 13232.

3.5. Helmet Model

The helmet consists of a shell and a liner. The shell is a hard exterior and the liner is a shock-absorbing interior. Both the shell and liner were modeled with deformable elements. The helmet model is depicted in Fig. 9.

The helmet model was checked for validity according to JIS T8133-2000[4] for the pileum, temporal, forehead and occipital regions. As an example of such verifications, both acceleration determined by test and simulation when the pileum of the helmet was dropped from a height of 1 m are compared in Fig. 10. The peak acceleration and the timing match well; the reaction forces of the shell and liner were well reproduced.

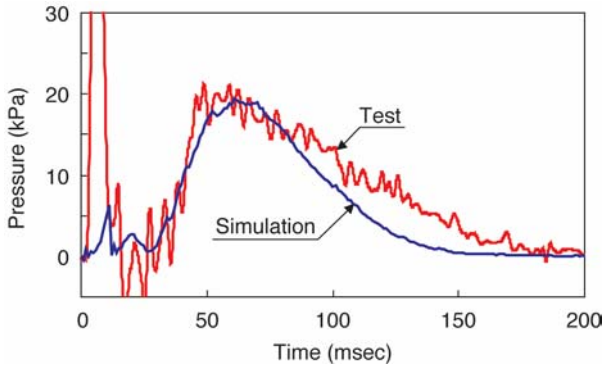


Fig. 7 Comparison of pressure in airbag inflating test

3.6. Opposing Vehicle Model

Rigid models were used for the portions of the opposing vehicle body where no impact with the motorcycle, deformation due to impact with the motorcycle, or contact with the dummy was expected. This was in order to reduce calculation time, as in the motorcycle model. Since this study concerned collisions with the side panel of a moving passenger car, the portions of the frontal part of the vehicle body and half of the vehicle body on the opposite side from the motorcycle were rigid models. The red portions of the model illustrated in Fig. 11 were deformable and the yellow portions were rigid. The results of the simulation and the test were compared to verify validity of the opposing vehicle model. Figure 12 shows the comparison of velocity on the side of the vehicle body that moves while deforming. The value of peak speed and the timing were well reproduced in the simulation.

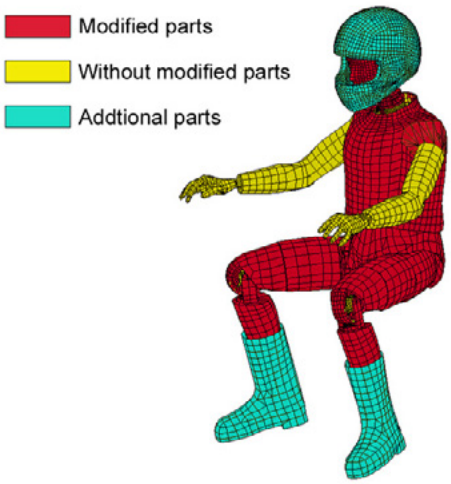


Fig. 8 Dummy model

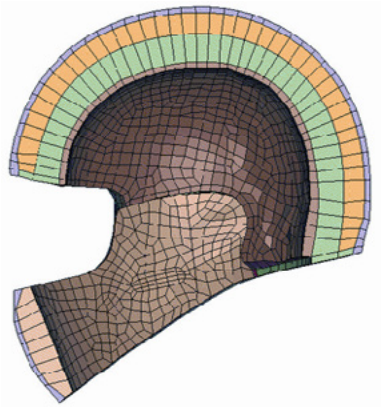


Fig. 9 Helmet model

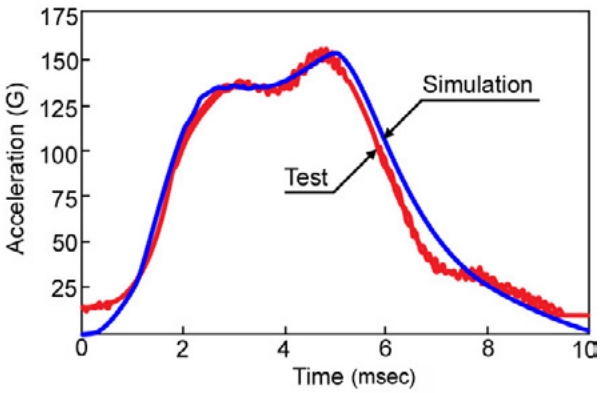


Fig. 10 Comparison of acceleration in helmet drop test

4. Method for Reduction of Required Calculation Time

Several investigations were carried out on methods for reducing required calculation time. It was found that the locations with the highest weights of required calculation time were the locations searched for object-to-object contact (impact) and the locations undergoing deformation[5]. These *contact search* and *deformation* calculations are carried out at every step for every model where they have been defined, whether or not there actually has been contact or deformation. Thus, an effective way to reduce required calculation time without degrading calculation accuracy is to eliminate the *contact search* and *deformation* calculations for locations which see no contact or deformation throughout the collision and for time domain where, temporarily, no contact or deformation occur during collision. A limited definition of contact and changing to rigid modeling were used as these methods in this study.

The limited definition of contact was performed in two stages. First, contact was not defined between locations and components that had no possibility of contact. In other words, contact was only defined between locations where it was expected. The second stage was to limit the time domain where contact was defined. For example, contact was not defined for internal components of the opposing vehicle from

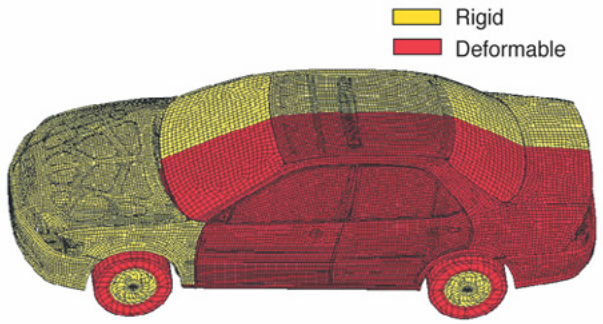


Fig. 11 Opposing vehicle model

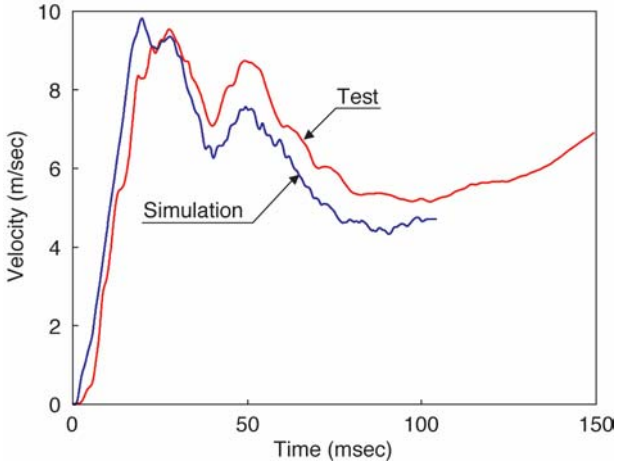


Fig. 12 Comparison of absolute velocity on the side of vehicle body in side impact test

0.300 s after start of calculation, i.e., after start of collision. Also, contact between the passenger car and the dummy was not defined until 0.050 s after the start of calculation. These two means were quite effective in shortening required calculation time.

The change from deformable to rigid modeling was also performed in two stages. In the first, prior to calculations, locations in the motorcycle and opposing vehicle, which were not expected to suffer collision or deformation, were modeled as rigid. Secondly, all the opposing vehicle models were considered as a rigid model after the halfway of the calculation process. This employment of a rigid model is applicable at the time both the motorcycle and the dummy disengage from the opposing vehicle. In the simulation of the two examples reported here, all the deformable portions of the opposing vehicle were changed to rigid at 0.300 s after the start of calculation. As the dummy does not disengage from the motorcycle until the very end of collision, a rigid model is not employed for the motorcycle in the process of simulation calculations. The employment of a rigid model for the opposing vehicle was very effective in the reduction of calculation time because the model size was large.

Overall, the calculation time was reduced by approximately 30% as a result of both the above mentioned secondary stages effects.

5. Simulation Results and Validation

Simulations for the aforementioned two examples (Figs.1 and 2) were carried out on an identical model, and the head velocity and the torso angle from the simulation were compared to those from the actual vehicle collision test. The coefficients of friction between the motorcycle and the opposing vehicle and between the rider and the airbag were investigated and selected during the validation of the correlation between the actual and numerical models. These characteristics are difficult to measure directly in real objects.

The results obtained in the simulations are explained below. Figures 13 and 15 show the test results and simulation results where the dummy is in contact with the airbag after the motorcycle has collided with the opposing vehicle at 45-degree and 90-degree angles. Figures 14 and 16 show the posture of the dummy just before falling on the ground in the same collision examples. The data from the simulation and actual test for the head velocity and torso angle at time of contact with the ground are shown in Table 2. Both in the 45-degree collision and in the 90-degree collision, the simulation results have coincided with the actual vehicle collision tests. Since the opposing vehicle model was changed to rigid after 0.300 s, the opposing vehicle behavior is not verified. A computer with a theoretical performance of 14.4 Gflops was used for calculation from collision until contact of the dummy with the ground; the required calculation time was 47 hours for the 45-degree collision case and 52 hours for the 90-degree case.

6. Conclusion

- Highly accurate simulations have been attained for dummy behavior (until falling on the ground) in the two cases of collision using the explicit FEM software.
- Rigid models and limited areas of contact were effective

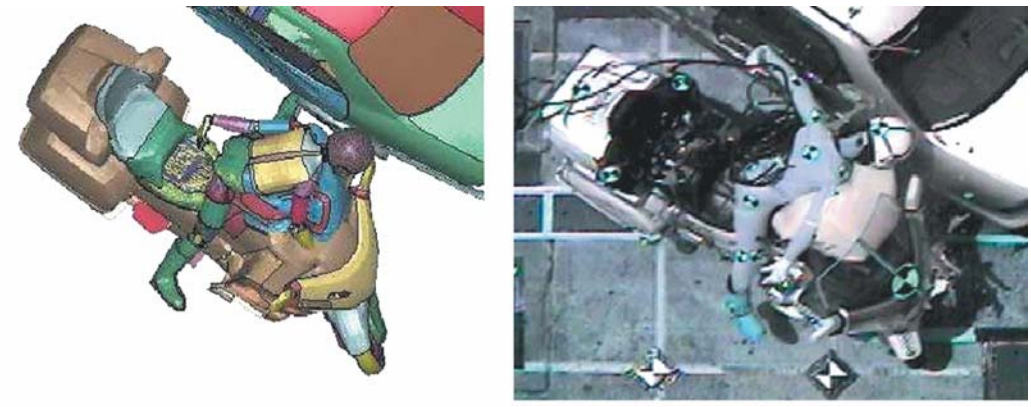


Fig. 13 Comparison of rider and motorcycle motion in 45-degree collision

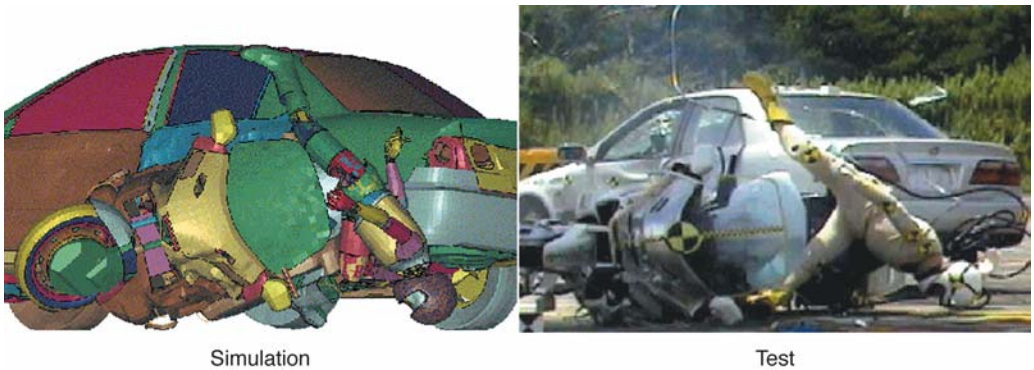


Fig. 14 Comparison of rider motion during fall in 45-degree collision

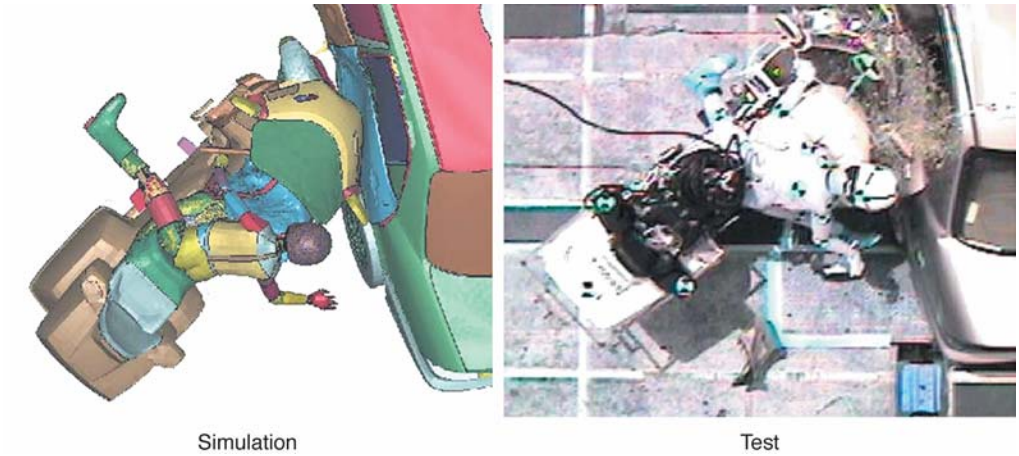


Fig. 15 Comparison of rider and motorcycle motion in 90-degree collision



Fig. 16 Comparison of rider motion during fall in 90-degree collision

Table 2 Comparison of torso angle and head velocity of dummy

45 degree collision

		Test	Simulation
Torso angle	deg	41	48
Head velocity	m/s	7	6

90 degree collision

		Test	Simulation
Torso angle	deg	31	34
Head velocity	m/s	4	5

methods for reducing required calculation time.

- The required calculation times were 47 hours for the 45-degree collision and 52 hours for the 90-degree collision.

Future research will focus on establishing methods for assessing rider injuries and for reducing calculation time.

Acknowledgements

The authors express their deep appreciation to Livermore Software Technology Corporation, ARUP, Hitachi Ltd., and The Japan Research Institute Limited for their great assistance with this project.

References

(1) Inoue, T., Miura, K., et al.: Experimental Collision Test on Motorcycles with Passenger Car, Paper No.15 of the Safety Research Tour in the USA from the Viewpoint of the Vehicle Dynamics, Society of Automotive Engineers of Japan, October 1969

(2) Iijima, S., et al.: Exploratory Study of Airbag Concept for a Large Touring Motorcycle, Paper No. 98-S10-O-14, Sixteenth International Technical Conference on the Enhanced Safety of Vehicles, Windsor, Canada, 1-4 June 1998

(3) ISO 13232 Motorcycles Test and Analysis Procedures for Research Evaluation of Rider Crash Protective Devices Fitted to Motorcycles, 1996-12-15

(4) JIS T8133-2000: Protective helmets for drivers and passengers of motorcycle and mopeds, (in Japanese)

(5) LS-DYNA User's Manual: Livermore Software Technology Corporation

■ Authors ■


Hideo NAMIKI


Toyokazu NAKAMURA


Satoshi IIJIMA

Novel Formulation of the 3D Large Deformation Beam Element for Dynamic Crash Analysis

Kenji TAKADA* Wlodek Abramowicz**

ABSTRACT

This paper presents a new Object Oriented Formulation of the FE algorithm that encompasses traditional FE, Super Element, experimental data and rigid body mechanics in a single calculation environment. The new formulation is implemented in a software for the dynamic crash simulation of an arbitrary 3D frame structure discretized into Super Elements and subjected to large dynamic crash loading. This paper presents basics of the general algorithm and element formulation. The theoretical portion of this paper is followed by a discussion of benchmark tests and results of the application to the real world structures.

1. Introduction

In recent years, it has become possible to use 3-dimensional (3D) CAD data to quickly create large-scale finite element models (FEM) that offer highly accurate reproductions of a physical component, due to the progress in capabilities of preprocessors and computers[1]. Nonetheless, strength of materials-based beam models are still a quite effective method for preliminary calculations at the layout stage, when 3D CAD data have not yet been established.

Beam elements must fulfill the following requirements when used to analyze beam models of behavior during frame collapse in a collision:

- Consideration of elastic plastic issues
- Consideration of large deformation issues
- Consideration of dynamic issues
- Consideration of interactional collapse combining axial forces, bending, and torsion[2]
- Consideration of deformation of component cross section and high accuracy post-collapse (post-buckling)
- Simple data creation and short calculation times.

It is impossible to obtain all the considerations listed above in standard FEM formulations. The authors have proposed a new formulation which combines FEM, the Super Element method, and rigid body mechanics.

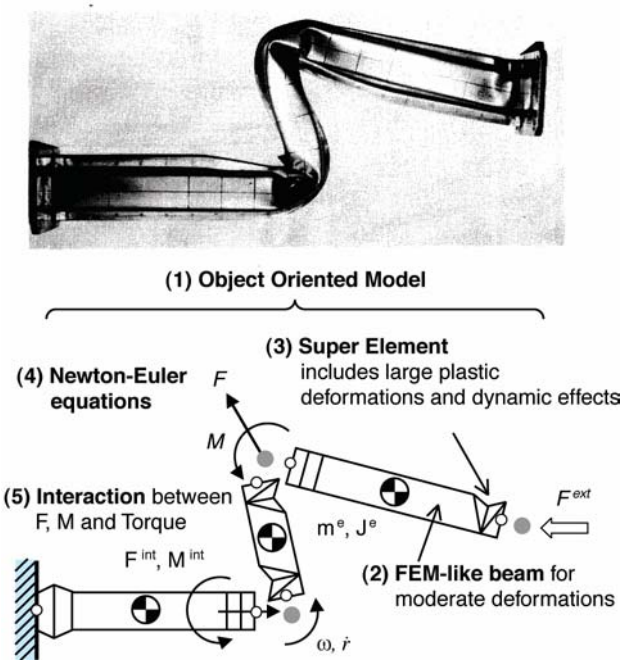


Fig. 1 Object oriented discretization of a thin-walled S-frame

* Tochigi R&D Center
** Impact Design, EUROPE

In addition, programming is done in an Object-Oriented Formulation (OOF)[3] in order to ease the handling of non-linear issues. In this report, the formulation of what we call a 'superbeam' is explained, its utility and effectiveness are shown in comparisons of results with experiments and FEM.

2. Overview of Formulation

Figure 1 shows an overview of this formulation with an example of the bending of a thin walled curved beam.

(1) Three numerical beam element models were created using OOF. A time integration scheme was employed with a central difference method.
(2) Beam behavior in the elastic region was calculated using the Euler-Bernoulli beam theory.
(3) Results were included with the Super Element method to provide results on beam elastic plastic issues, large deformation issues and dependence of yield stress on strain rate.
(4) The Newton-Euler equations of motion were employed for considerations of dynamic issues. However, new nodes were established in different locations from the initial model nodes for use in calculating dynamic behavior and posture angle.
(5) Interactional collapse combining axial force, bending, and torsion was modeled by constructing an element stiffness matrix based on the co-rotational method in continuous-body dynamics. Serial updating of the collapse surface was included in order to obtain high accuracy in the post-collapse region.

3. Solution of Equations of Motion

The principal of virtual velocity[4]–[7] (or the principal of virtual work) shown in Eq. (1) was used to handle non-linear issues in this formulation.

$$\delta W(\delta u, u) \equiv \delta W^{in} - \delta W^{ext} + \delta W^{kin} = 0 \qquad (1)$$

Here, δW^{in} is virtual internal work, δW^{ext} is virtual external work, and δW^{kin} is virtual kinetic energy. The equation of motion in Eq. (2) was obtained by discretizing Eq. (1).

$$M\ddot{u} = f^{ext} - f^{in} \qquad (2)$$

Here, M is the mass matrix, $\ddot{u}$ is the nodal acceleration vector, and f^{in} and f^{ext} are the nodal internal force and nodal external forces, respectively.

Ordinarily, when Eq. (2) is solved with the central difference method, each element is treated in a step routine at each time step (element-by-element method). In this formulation, a method is proposed where each node is treated, and each element is treated, with complete separation between the two processes (Node-by-Node/Element-by-Element method).

Figure 2 shows how this method is related to the equation of motion. The inertia term on the left side of Eq. (2) is treated on a node-by-node basis according to the Newton-Euler equations of motion; the load terms on the right side are treated on an Element-by-Element basis by the Super Element method.

This method allows the two approaches of rigid body mechanics and the Super Element method to be combined.

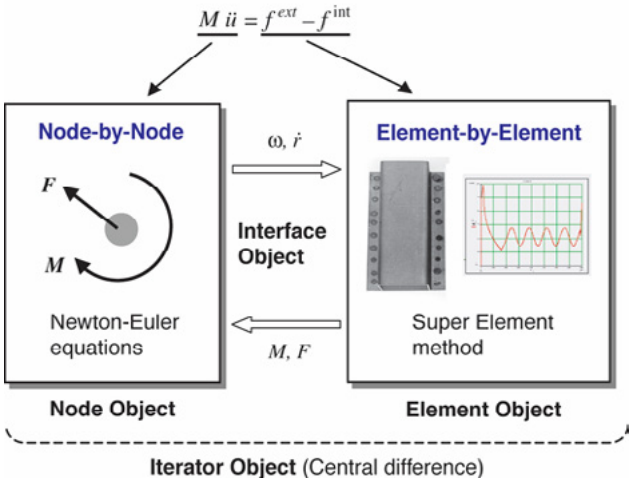


Fig. 2 Relationship between the equation of motion and Node-by-Node/Element-by-Element technique

4. Description of Objects Comprising OOP

Object-Oriented Programming (OOP)[8] is an extremely effective way for programming non-linear programs. The present program is comprised of the four objects shown in Fig. 2. This chapter describes the operations in each of the objects.

4.1. Node Objects

When both forces and moments work on a node, the Newton-Euler equations of motion in Eq. (3) and (4) can be obtained[9], [10].

$$m\ddot{r} = F \qquad (3)$$

$$J\dot{\omega} = M - \omega J\omega \qquad (4)$$

Here, F and M are the forces and moments exerted on the node, m is the nodal mass, ω is the angular velocity, J is the inertial tensor, and $\ddot{r}$ is the nodal acceleration in the global coordinate system. The rotational motion in Eq. (4) is expressed in the local coordinate system.

For updating of new nodal locations, angular velocity ω, transformed to global coordinate, is found, and the instantaneous increase in angular position $\Delta\theta$ is calculated in Eq. (5).

$$\Delta\theta = \omega\Delta t \qquad (5)$$

If this increase in angular position is used, the new location of the node can be expressed as a unit vector, as shown in Eq. (6).

$$\begin{aligned}\vec{i}_n &= \vec{i}_{n-1} + (a\times\vec{i}_{n-1})\sin(\Delta\theta_n) + 2[a\times(a\times\vec{i}_{n-1})][1-\cos(\Delta\theta_n)]\\ \vec{j}_n &= \vec{j}_{n-1} + (a\times\vec{j}_{n-1})\sin(\Delta\theta_n) + 2[a\times(a\times\vec{j}_{n-1})][1-\cos(\Delta\theta_n)]\\ \vec{k}_n &= \vec{i}_n\times\vec{j}_n\end{aligned} \qquad (6)$$

4.2. Element Objects

When an object has deformed, the complete potential energy of the object J is defined as shown in Eq. (7) by the principal of the stationary potential energy[11), (12)].

$$\frac{\partial J}{\partial \dot{q}_i}\delta\dot{q}_i \equiv 0 \quad (i = 1...N) \tag{7}$$

Here, $\dot{q}$ is the generalized velocity and N is the total degrees of freedom. The complete potential energy J of the beam element is expressed in Eq. (8) using the principal of virtual work.

$$J(q, \dot{q}, \hbar) = Q\dot{q} - P(L_t, \dot{L}_t, \hbar)\Delta L(q, \dot{q}) - M_\alpha(\phi_i, \dot{\phi}_i, \hbar)\phi_\alpha(q, \dot{q}) \tag{8}$$

Here, Q is the external force (generalized force), P and M_α are the axial force and bending moment acting on the cross-section of the component, q is the generalized displacement, L_t is the component length after deformation, ϕ_k is the rotation, and $\hbar$ is a parameter expressing the condition of the axial force P and bending moment M_α.

In this formulation, the axial stiffness/bending stiffness matrix corresponding to the axial force and bending moment shown in Eq. (8) were derived using the co-rotational method used in continuous body dynamics. The ultimate element stiffness matrix was calculated using the principle of superposition.

4.2.1. Axial stiffness matrix

Figure 3 shows the post-deformation component length L_t defined in Eq. (9) using the local coordinate system.

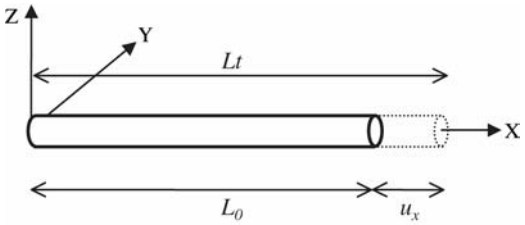


Fig. 3 Three-dimensional rod fixed at one end and subjected to large rotations and deformations

$$L(t) \equiv L_t = \sqrt{(L_0 + u_x)^2 + u_y + u_z} \tag{9}$$

Here, L_0 is the initial component length, and u_x, u_y and u_z are the deformations of the component in the local coordinate system. The principle of virtual work shown in Eq. (10) is applied to these deformations u_x, u_y and u_z.

$$P\frac{\partial \Delta L}{\partial u_x}\delta u_x = 0,\ P\frac{\partial \Delta L}{\partial u_y}\delta u_y = 0,\ P\frac{\partial \Delta L}{\partial u_z}\delta u_z = 0 \tag{10}$$

The axial stiffness matrix shown in Eq. (11) can be derived using the results of Eq. (10)[13]. $P(t)$ in Eq. (11) is an axial collapse characteristic of the cross-section calculated with the Super Element method. While the beam is in the elastic region, an element stiffness matrix is constructed using the Euler-Bernoulli beam theory, but once the beam enters the plastic region, this is replaced with Eq. (11).

$$K_a(t) = \frac{P(t)}{L(t)}\begin{bmatrix} \dfrac{(L+u_x)}{u_x} & 0 & 0 \\ 0 & 1 & 0 \\ 0 & 0 & 1 \end{bmatrix} \tag{11}$$

4.2.2. Bending stiffness matrix

According to the co-rotational method, the local coordinate system is defined at each point within an object and rotates with rotation of the object. Using a rotating local coordinate system eliminates the need to consider terms concerned with solid body rotation, such as the angular velocity tensor; only the deformation rate tensor must be included. The deformation speed tensor $\hat{D}_y$ is defined in Eq. (12)[4].

$$\hat{D}_{ij} = \frac{1}{2}\left(\frac{\partial \hat{v}_i}{\partial \hat{x}_j} + \frac{\partial \hat{v}_j}{\partial \hat{x}_i}\right) \equiv sym\left(\frac{\partial \hat{v}_i}{\partial \hat{x}_j}\right) \equiv v_{\hat{i},\hat{j}} \tag{12}$$

Here, $v_{\hat{i},\hat{j}}$ the velocity in the local coordinate system. The bending stiffness matrix shown in Eq. (13) was derived from Eq. (12). Only 1/4 of the actual matrix is shown for simplification.

$$K_b(t) = \begin{bmatrix} \kappa u_y^2 & \kappa L_o u_y & 0 & 0 & 0 \\ 0 & -\kappa L_{xz}^2 & 0 & 0 & 0 \\ 0 & 0 & \kappa u_y^2 & 0 & 0 \\ 0 & 0 & 0 & \dfrac{M(\phi_y, \alpha_y)\cos(\alpha_y)}{\phi_z} & 0 \\ 0 & 0 & 0 & 0 & \dfrac{-M(\phi_y, \alpha_y)\sin(\alpha_y)}{\alpha_y} \end{bmatrix} \tag{13}$$

Here, M (ϕ,α) is the bending collapse characteristic obtained by the Super Element method, ϕ and α are the rotational displacements, L_{xz} is the deformed length of the beam, and κ is the quantity defined in Eq. (14). The displacement vector q (t) corresponding to Eq. (13) is shown in Eq. (15). The ultimate element stiffness matrix is obtained by combining Eq. (11) and Eq. (13) by the principle of superposition. That matrix allows expression of interactional collapse involving axial force and bending.

$$\kappa(t) = \frac{-M}{\sin(\theta)L_t^3 L_{xz}} \tag{14}$$

$$q(1)^T = \{u_x\ u_y\ u_z\ \phi_z\ \alpha_y\} \tag{15}$$

4.3. Interface Objects

Here, the interface object using a model of the combination of the two beam elements shown in Fig. 4 is explained. In the standard FEM, the characteristics of beam elements A and B are discretized at their common node I, and ultimately, the stiffness, displacement, velocity, internal forces, etc. are expressed at node I. If, in addition, it is attempted to enter equations for rigid body kinetics at I, it is very difficult to set up these equations. Therefore, in this formulation, as shown in Fig. 5, a new node J was established in addition to node I. Rigid body mechanics were expressed using this node J. Also, posture angle was calculated using this node J.

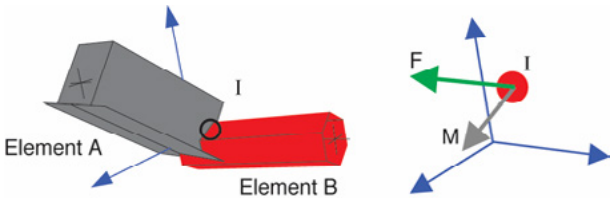


Fig. 4 Illustration of the basic paradigm of the FEM

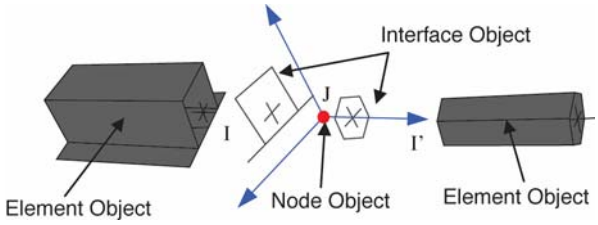


Fig. 5 Concept of the interface objects

Since the loads F and moments M were set constant at each time step when using a central difference scheme, as a result, it was possible to handle node J as a rigid body with no coupling with other locations.

This set of operations was carried out with node objects. Meanwhile, since element deformation was expressed at node I, calculations were handled to preserve equilibrium between the two nodes I and J using interface objects.

4.4. Iterator Object

An iterator object is a routine for carrying out time integration based on a central difference scheme. Figure 6 presents the overall flow.

(1) The initial values are set for the mass and moment of inertia at the center of gravity of each element.
(2) The initial values for velocity and angular velocity of each node are set and the mass and moment of inertia are calculated.
(3) Treatment of each element is carried out on an element-by-element basis. From the velocity and angular velocity of each node, the resulting nodes and moments F^n and M^n are calculated and handed off to the next node-by-node step.
(4) Treatment of each node is carried out on a node-by-node basis. Using the F^n and M^n values provided by step (3), the translational accelerations and angular velocities of each node are calculated according to the Newton-Euler equations and provided back to step (3).

5. Overview of Super Element Method

Beam plastic issues, large deformation issues and dependence of yield stress on strain rate are calculated using the Super Element method[14] – [18] and combined into the stiffness matrices shown in Eq. (11) and (13).

Formulation of the Super Element method is basically comprised of three steps. The first step consists of assuming a plastic folding wavelength 2H, a hinge line rolling radius r, and the deformation mode of wall faces and hinge lines indicated by 1-5, using data from the thin walled frame

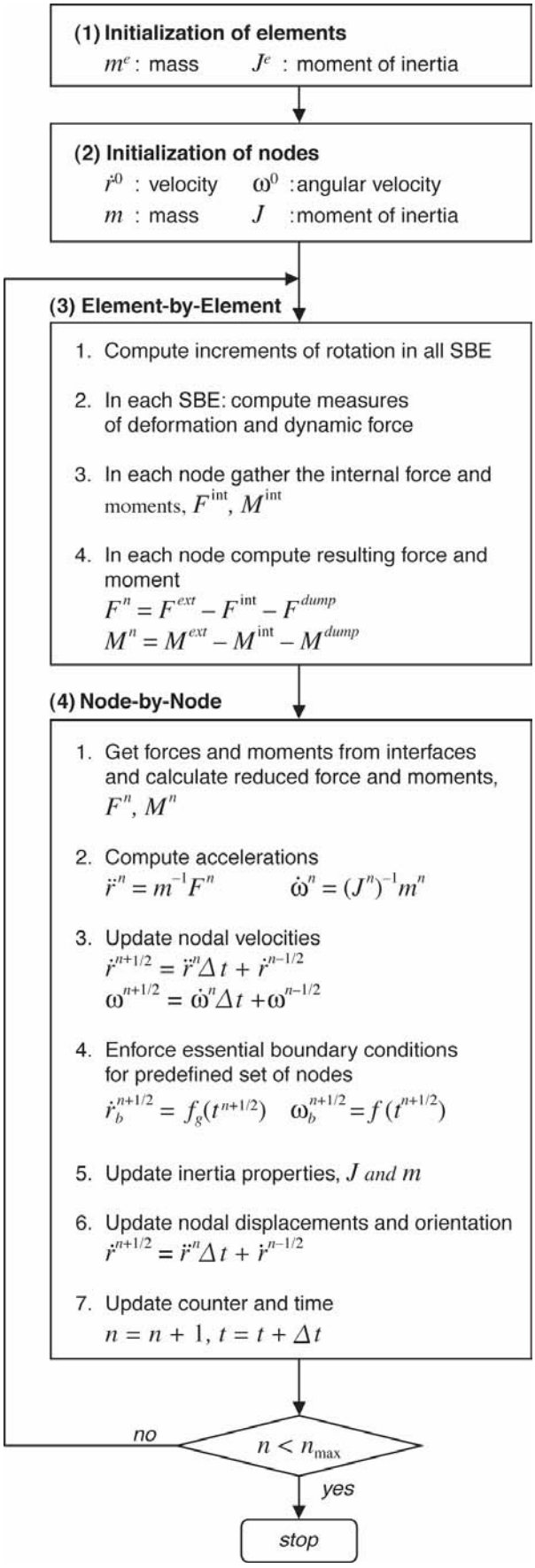


Fig. 6 Flow diagram of numerical procedure

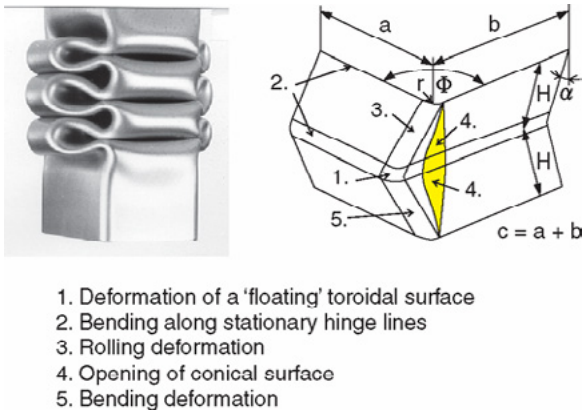


Fig. 7 Idealized deformation mechanisms

crushing test shown in Fig.7. In the next step, the expression for the internal energy is assumed, as shown in Eq. (16), on the basis of plastic shell theory.

$$\dot{E}_{\text{int}} = \int_s N_o \dot{\varepsilon}_1 dS + \sum_{i=1}^{n} \int_{L^i} M_o^i \left[\dot{\theta}_i\right] dl^i \qquad (16)$$

Here, L^i is the length of the i^{th} hinge line, n is the total number of plastic hinge lines, N_0 is the axial stress, and $M^i{}_0$ is the bending stress. The first and second terms in Eq. (16) are calculated using Eq. (17) and (18).

$$E_{\text{int}}^N = \sigma_0^N(\bar{\varepsilon}) \int_0^{\alpha} d\alpha \int_s t\dot{\varepsilon} dS \qquad (17)$$

$$E_{\text{int}}^M = \sum_{i=1}^{n} \sigma_0^M(\bar{\varepsilon}) \frac{t}{4} \int_0^{\alpha} d\alpha \int_{L^i} \left[\dot{\theta} i\right] dl^i \qquad (18)$$

Here, $\sigma_0{}^N$ and $\sigma_0{}^M$ are the flow stress[19], α is a variable indicating the deformation process, and t is the sheet thickness. The mean crushing force P_m is defined as shown in Eq. (19), which is calculated using Eq. (16), (17) and (18).

$$P_m = \frac{t^2}{4}\{\sigma_0^N(\bar{\varepsilon}_1)A_1\frac{r}{t} + \sigma_0^M(\bar{\varepsilon}_2)A_2\frac{C}{H} + \sigma_0^M(\bar{\varepsilon}_3)A_3\frac{H}{r} + \\ + \sigma_0^M(\bar{\varepsilon}_4)A_4\frac{H}{t} + \sigma_0^N(\bar{\varepsilon}_5)A_5\}\frac{2H}{\delta_{eff}} \qquad (19)$$

Here, δ_{eff} is the effective crushing distance and A is a cross-sectional shape coefficient. In the last step, the mean crushing force P_m in the frame is obtained from Eq. (20), which is based on the principle of stationary potential energy.

$$P_m(H) = \frac{2H}{\delta_{eff}}\left(2\pi M_0 \frac{H}{t} + \frac{4\pi c M_0}{H}\right) \qquad (20)$$

Here, M_0 is the fully plastic bending moment. The axial collapse characteristics and bending collapse characteristics can be calculated from the mean crushing force P_m in Fig. 8.

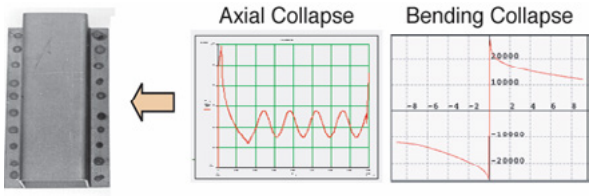


Fig. 8 Schematic illustration of the Super Element characteristics

5.1. Assessment of Collapse

Collapse assessment of beam elements in the pre-collapse region is carried out using Eq. (21).

$$\left(\frac{P}{P\max}\right)^a + \left(\frac{My}{My\max}\right)^a + \left(\frac{Mz}{Mz\max}\right)^a + \left(\frac{T}{T\max}\right)^a = 1 \qquad (21)$$

Here, *P max*, *My max*, *Mz max* and *T max* are the maximum values for, respectively, the axial collapse force, bending collapse moments about the Y and Z axes, and torsional collapse moment in the beam. *P*, *My*, *Mz* and *T* are the loads occurring in the beam. Coefficient *a* is a variable determined by the thickness width ratio of the sheet. It is assumed that collapse occurs in the beam element when the left side of Eq. (21) reaches a value of 1.

Since *P max*, *My max*, *Mz max* and *T max* decrease in the post-collapse region due to deformation of the beam, Eq. (21) cannot be used here. Therefore, Eq. (22) was assumed for collapse assessment. Figure 9 shows the relationship between the collapse surface and the collapse force.

$$\left|\frac{P}{P\max(u)}\right| + \left|\frac{My}{My\max(\phi)}\right| + \left|\frac{Mz}{Mz\max(\phi)}\right| + \left|\frac{T}{T\max(\phi)}\right| = 1 \qquad (22)$$

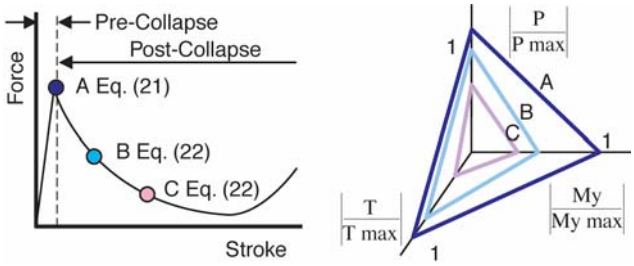


Fig. 9 Relationship between the interaction surface and the crushing characteristic

5.2. Analytical System

Figure 10 shows the analytical system for this beam model.

(1) The axial collapse and bending collapse characteristics of the frame cross section are calculated using the cross section design software Crash Cad[18] and the data are stored.
(2) A 3D CAD model is created in the preprocessor. The element characteristics are set to the data saved in Crash Cad.
(3) Once the boundary conditions have been set, the solver is set in operation.
(4) The beam collapse behavior is investigated using the postprocessor.

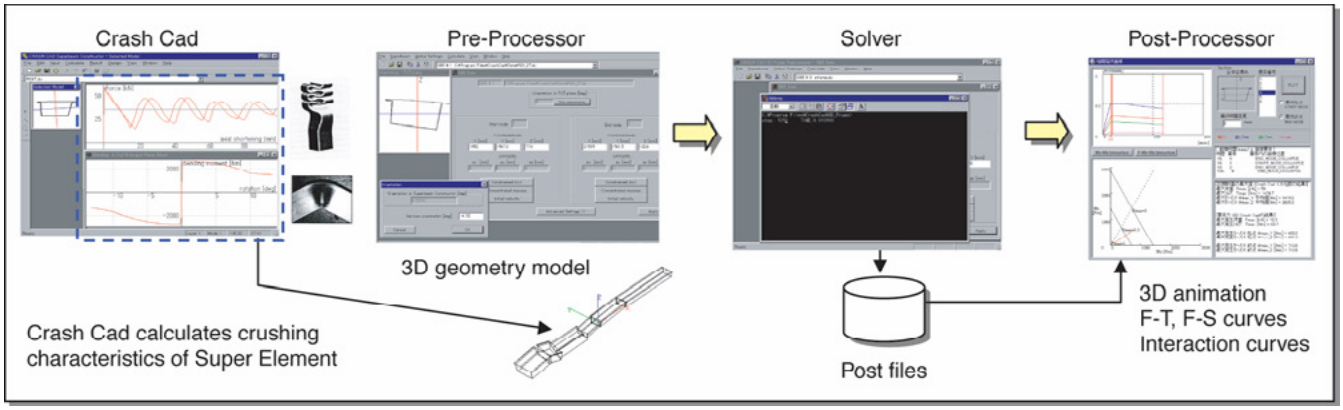


Fig. 10 Organization of the design/calculation environment for 3D large deformation beam systems

6. Examples of Use

6.1. Quasi-static Issue in an Aluminum Extrusion[20]

Bending collapse under quasi-static load was analytically examined in an extruded aluminum specimen with both ends connected with a pin joint, as presented in Fig. 11. Two cross sections were used, designated A and B. The sheet in both was 2 mm thick. The material was series 6,000-T5, with a proof stress of 186 MPa, E = 69 MPa, and ν = 0.33.

Force-stroke diagrams of the test and analytical results are shown in Fig. 12. It is clear that there is a high correlation between the test results and the results in this beam element for both the maximum force and the post-collapse region.

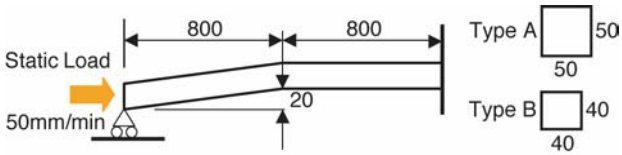


Fig. 11 Dimensions of the crooked extruded aluminum beam

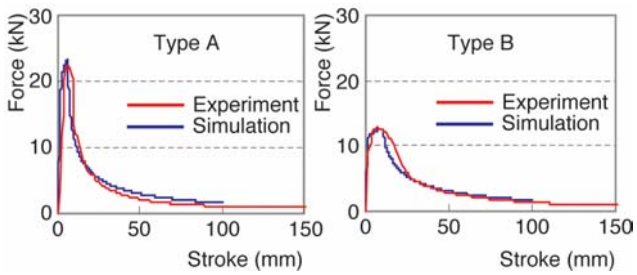


Fig. 12 Correlation of experimental and simulation results for the crooked aluminium beam shown in Fig. 11

6.2. Quasi-static Issue in Thin Walled Curved Beam[21],[22]

This was an analysis of a thin-walled curved specimen with both ends completely fixed under a quasi-static load. The component shape and cross section are shown in Fig. 13. A hat section and flat plate were spot-welded to a flange of the component and end plates were full-perimeter arc-welded onto each end of the component for attachment of the component to the test apparatus. The bend angles θ were 15° and 30°, wall thickness was 1.2 mm and the material was SPC.

Figure 14 shows a deformation mode test of a 15° bend specimen with a 100 mm stroke. It is clear that this beam element showed a high correlation with the specimen in results for collapse location and deformation angle.

Figure 15 shows force-stroke diagrams for the 15° and 30° bend specimens. Good accuracy was also found in this issue for maximum force and behavior in the post-collapse region.

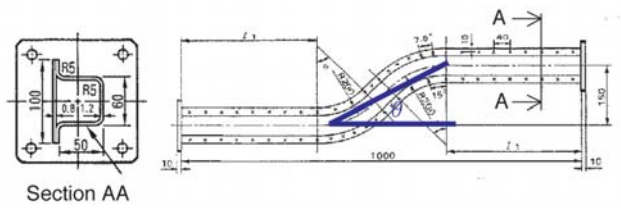


Fig. 13 Dimensions of the thin-walled steel S-frame

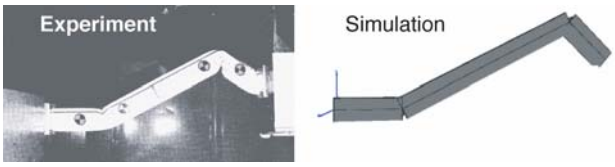


Fig. 14 Comparison of deformed modes at 100 mm stroke

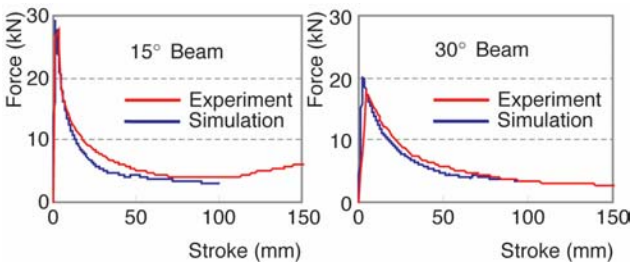


Fig. 15 Correlation of experimental and simulation results for the thin-walled S-frame shown in Fig. 13

6.3. Quasi-static Issue in Rear Frame

A quasi-static issue was analyzed using the rear frame from an actual automobile structure. The results of the beam element were compared with those from a FE model. Figure 16 illustrates the FE model and the superbeam model. The FE model was made completely from shell elements. The superbeam model was made from six elements.

Figure 17 shows the results for the predicted deformation modes in the FE and superbeam models after a stroke of 50 mm. It is clear that both models show good agreement in the deformation location and deformation mode. The maximum force during collapse was predicted at 19.5 kN in the FE model and 18.4 kN in the superbeam model, quite close predictions.

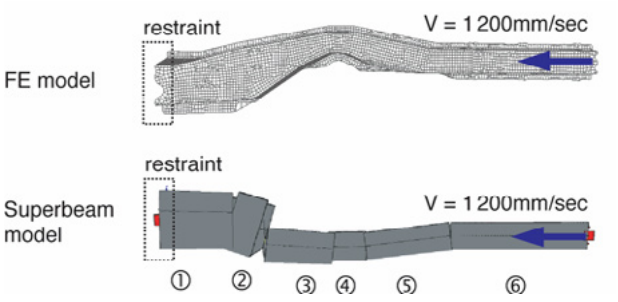


Fig. 16 Boundary and loading conditions for FEM and Superbeam models

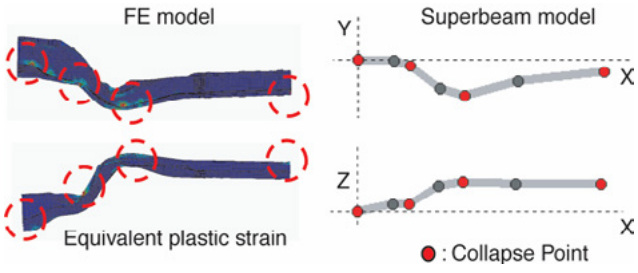


Fig. 17 Deformed configurations of FEM and Superbeam

6.4. Dynamic Torsion Issue in Box Frame

An analysis was performed with a 90° frame corner made of two square cross section beams, subjected to a dynamic load (Fig. 18). The purpose of this analysis was to test the accuracy of this formulation in a collapse issue where torsional deformation is a dominant factor.

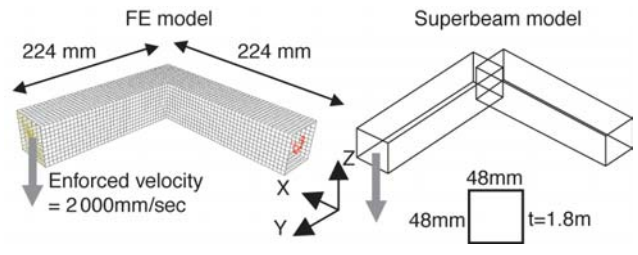


Fig. 18 Boundary and loading conditions for the FEM and the Superbeam model of a thin-walled torque box

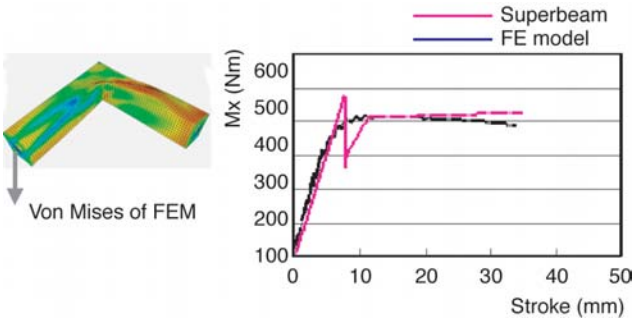


Fig. 19 Correlation of FEM and Superbeam results for the thin-walled torque box shown in Fig. 18

Figure 19 shows the force-stroke diagram. A fairly good correlation was found with the FEM. The superbeam model showed a vibration at a stroke of 8 mm, but this was caused by the modeling of the structure with two beam elements. This issue was solved when the model was divided more finely.

6.5. Dynamic Issue in Thin Walled Curved Beam[23]

A dynamic issue was analyzed using the same model as in 6.2. Figure 20 shows a schematic view of the dynamic test apparatus. Components with a 45° bend were fixed to the front of a dolly and crashed into a barrier at 30 kph.

Figure 21 shows the force-stroke diagram. The measurement of the initial maximum force in the test was affected by the weight of the plate attached to the tip of the test specimen[23], by the sampling pitch of the load cell and perhaps by other factors. It differed from the result for maximum force given by the beam model. A good correlation between the results was found in the post-collapse region, however.

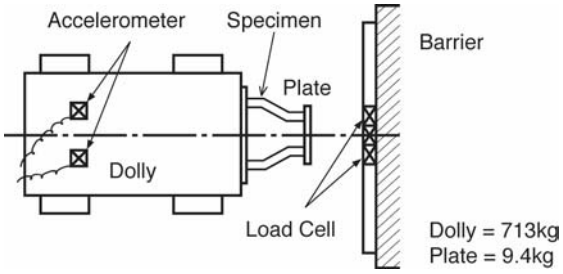


Fig. 20 Schematic diagram of dynamic experiment

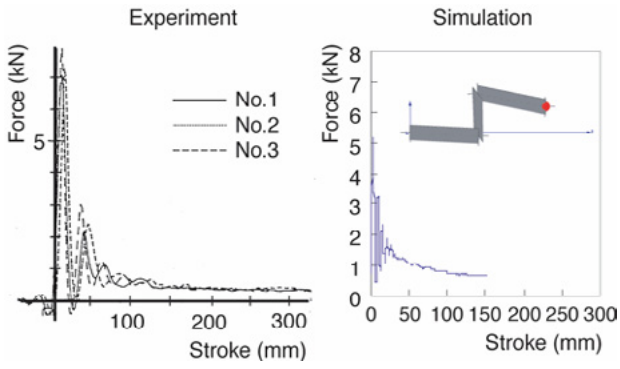


Fig. 21 Results of experiments and Superbeam model simulation for an S-frame shown in Fig. 20

6.6. Comparison of CPU Time

The calculation times for the rear frame test in 6.3 were compared. The FE model was comprised of about 5,000 shell elements. On a supercomputer, a calculation time of about 22 h was necessary for a deformation of up to 200 mm.

The superbeam model required 68 seconds for calculations for deformation of up to 200 mm on a PC.

7. Summary

For this report, a new formulation combining FEM, the Super Element method, and rigid-body mechanics was created to analyze dynamic collapse issues in a beam element. The results of this formulation were as follows:

(1) It was confirmed that this 'superbeam' element accorded well with experimental models. At the same time, it was proved that the Super Element method is effective.
(2) A tool was developed which enables preliminary investigation, at the layout stage, of component collapse characteristics using cross section data.
(3) By using this formulation, it was judged possible to develop non-linear shell elements which provide calculation results in short times.

References

(1) Takada, K., Matsuura, N., Nakano, F., Iwamoto, A.: Development of New Pre-processor for Car Body Analysis, Proceedings of the Conference on Computational Engineering and Science, Vol. 7, p. 263-266 (2002)

(2) Kawai, T., Nogami, K.: Analysis of Discretized Limits in Stiff Structural Components and Frames (in Japanese), Tokyo, Baifukan, p. 93-119 (1991)

(3) Abramowicz, W.: Object Oriented, Reduced Operation Set Formulation of the Multi-Body Macro and Finite Element Method, Impact Design Europe Report 2/2001, p. 238 (2001)

(4) Belytschko, T., Liu, W, K., Moran, B.: Nonlinear Finite Elements for Continua and Structures, New York, John Wiley, p. 650, (2000)

(5) Belytschko, T., Hughes, TJR.: Computational Methods for Transient Analysis, Amsterdam, North-Holland, p. 523 (1983)

(6) Cook, RD., Malkus, DS., Plesha, ME.: Concepts and Applications of Finite Element Analysis, New York, John Wiley, p. 630 (1989)

(7) Zienkiewicz, OE., Taylor, RL.: The Finite Element Method (Vol. 1) The Basis Oxford, Butterworth-Heinemann, p. 689 (2000)

(8) MSDN (the Microsoft Developer Network), ©1991-2000 Microsoft Corporation, http://msdn.microsoft.com/

(9) Rosenberg, M, R: Analytical Dynamics of Discrete Systems, New York, Plenum Press, p. 424 (1977)

(10) Blajer, W.: Methods of Multibody Dynamics, Monographs of Radom Technical University (in Polish), p. 184 (1998)

(11) Kawai, T.: Outline of Discretized Limit Analysis (in Japanese), Limit Analysis with Computers Series 1, Tokyo, Baifukan, p. 23-52 (1991)

(12) Washizu, K., Miyamoto, H., Yamada, Y., Yamamoto, Y., Kawai, T.: Finite Element Method Handbook I, Fundamentals (in Japanese), Tokyo, Baifukan, p. 443

(13) Abramowicz, W.: Limitations of the matrix method in the FEM formulation for large deformations and strains, Impact Design Europe Report 1/2001, p. 327 (2001)

(14) Abramowicz, W.: Macro element method on crashworthiness of Vehicles in Crashworthiness energy management and occupant protection (Ambrosio J., Editor), Wein New York, Springer-Verlag, p. 85-138 (2001)

(15) Abramowicz, W.: Extremal Paths in Progressive Plasticity, Int. J. Impact Engng, Vol. 18, No. 7-8, p.753-764 (1996)

(16) Abramowicz, W., Wierzbicki, T.: Axial crushing of multi-corner sheet metal columns, J. App. Mech., Vol. 56, No. 1, p. 113-120 (1989)

(17) Wierzbicki, T., Abramowicz, W.: The Manual of Crash-worthiness Engineering Vol. I-IV, Center for Transportation Studies, Massachusetts Institute of Technology, P. 542 (1987-1989)

(18) Abramowicz, W., Wierzbicki, T.: Crash Cad Manuals-Superbeam Constructor, Boston, MA, Impact Design, P. 73 (1998)

(19) Taira, S.: Modern Plastic Dynamics (in Japanese), Tokyo, Ohmsha, p.13 (1982)

(20) Egawa, Y., Satoh, T.: Effects of Main Frame Bending and Wall Collapse During Collisions, Journal of Society of Automotive Engineers of Japan, Vol. 52, No. 4, p. 49-54 (1998)

(21) Society of Automotive Engineers of Japan, Inc. Structural Strength Commission: Collapse Characteristics of Thin-walled Curved Beams, Vol. 1 Test Methods and Results, p. 1-222 (1986)

(22) Ohkami, Y., et al: Collapse of Thin Walled Curved Beam with Closed Hat Section – Part 1, Study on Collapse Characteristics, SAE, 900560 (1990)

(23) Society of Automotive Engineers of Japan, Inc. Structural Strength Commission: Characteristics of Thin-walled Curved Beams, Vol. II Considerations and Simulation of Test Results, p. 106-125 (1989)

■ Authors ■



Kenji TAKADA



Wlodek Abramowicz

Research on Stick-Slip Noise around Hub Bearings in Driven Wheels

Mikio KASHIWAI* Haruo SHINOHARA* Nobuo NIWA**
Ikuo YAMAKAWA** Shigeki OIDE** Kunio MIZUNO**

ABSTRACT

Micro-slippage occurs in the metal contact surfaces between the hub bearings and surrounding parts of automotive driven wheels when driving torque is applied. A stick-slip noise can accompany this slip motion. Analysis of the occurrence of stick-slip has shown that it is caused by a combination of factors. The research described in this paper has discovered previously unknown causes. Excess insertion load or axial force causes non-uniform strain in the bearing inner race. This strain builds up even after the load is released. Changes occur in the lubrication conditions of the press-fit face of the hub and the bearing inner race with varying insertion speed and humidity conditions, leading to the generation of excess insertion load. An effective method for prevention of stick-slip is proposed on the basis of this analysis.

1. Introduction

The typical fastening structure around the hub bearings of automotive driven wheels is one where the hub unit bearings and the constant velocity joint (CVJ) are press-fit, serration-fit and then screw-fastened using a hub and spindle nuts.

When driving torque is transmitted from the CVJ, twisting and slipping occur in the fastening structure in accordance with the magnitude of that torque. In order to eliminate this twisting and slipping, an extremely thick serrated shaft must be selected and the serration must be fit snugly so there is no play. However, this method is limited in consideration of the space layout and ease of assembly and disassembly work. Therefore, the fastening structure must take into account twisting and slipping when driving force is applied.

The CVJ tends to rotate toward the direction of the driving torque due to the twisting of the CVJ spline and the gap between the CVJ spline and the hub spline. This shifting must be absorbed by the slipping of the metal contact surfaces. Slipping may occur in multiple locations, and these slipping surfaces have various lubrication conditions. Normally, no special measures have been taken for this slipping surface lubrication.

In contrast to recent increases in the driving torque due to improved automotive engine output, the torsional rigidity of the serrated shaft has not increased, so slipping occurs more easily. If the lubrication conditions of these slipping surfaces cannot be controlled, stick-slip noise may occur. This stick-slip noise may on rare occasions be viewed as an abnormal noise (called “Paki” or “Kakkin” noise) during operation. This study investigated the conditions under which this noise occurs, and clarified the factors. An effective method for preventing this noise is proposed on the basis of this analysis.

2. Conditions under which Stick-Slip Noise Occurs

2.1. What is Stick-Slip Noise?

The noise that is the focus of this research is the stick-slip

* Tochigi R&D Center
** Honda Motor Co,. Ltd.

noise produced when micro-slippage occurs in the metal contact surfaces. This slip motion occurs in the metal contact surfaces when driving torque is applied to the serrated CVJ shaft. The conditions under which slipping occurs can be broadly divided into an initial type noise, when stick-slip occurs in the new vehicle condition, and an enduring type noise produced by roughness of the slipping surface. This surface roughness can be due to repeated slipping in the metal contact surfaces or caused by a change in the lubrication conditions. In either case these noises are not symptomatic of a situation that might damage the fastening structure of the hub bearings.

2.2. Locations where Stick-Slip Occurs

Research has been performed for some time to determine the locations where stick-slip occurs. Stick-slip has been confirmed to occur in all locations that contact the inner race of the bearings. Analysis results showed that the stick-slip location that should be given the most attention is the contact face between the CVJ and the bearing inner race as shown in Fig. 1. When driving torque is applied, the hub and serration-fitted CVJ attempt to twist in the driving direction. The stick-slip produced by this twisting can be divided into two types. The first is stick-slip that occurs when the CVJ undergoes relative micro-motion at the contact face with the bearing inner race end. The second is stick-slip that occurs when there is large static frictional force at the contact face between the CVJ and the inboard bearing inner race end. In the second case there is relative movement at the contact face between the two bearing inner races, and at the press-fit face between the bearing inner race and the hub, causing high level stick-slip noise to occur at this time.

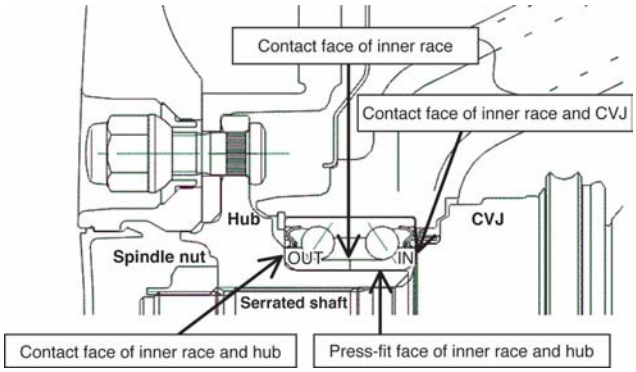


Fig. 1 Basic configuration around hub bearings in driven wheel

3. Factor Analysis of Noise Occurrence

3.1. Analysis of Initial Type Stick-Slip Noise

First, factor analysis was performed on the initial stick-slip noise that occurs in the new vehicle assembly condition. As a result, multiple factors were found.

3.1.1. Finished condition of the bearing contact faces

(1) Lathe turning and grinding

There are two types of machining processes for the contact face between the CVJ and the bearing inner race: lathe turning and grinding. This contact face is generally used as the reference surface for machining the inside of the CVJ, and in this case the finished surface roughness after lathe turning or grinding must be 6.3 S or less. However, some CVJ are known to provide a separate CVJ machining reference surface, so the roughness of the contact face with the bearing inner race is increased up to approximately 25 S, and concentric lathe turning finish lines (Fig. 2) remain.

Figure 3 compares the effect on stick-slip of the difference in the above two types of contact face finished conditions. The contact faces were degreased to eliminate the influence of lubrication, and torque equivalent to the driving torque was applied from the CVJ at a cycle of one time each in the forward and reverse directions to produce repeated twisting. The degree of acceleration of the vibration produced at that time was measured and compared up to 1,000 cycles. The results confirmed that the concentric finish lines were advantageous with respect to stick-slip. This showed that grinding processed parts had a high noise level in the initial condition when the lubrication condition was poor.

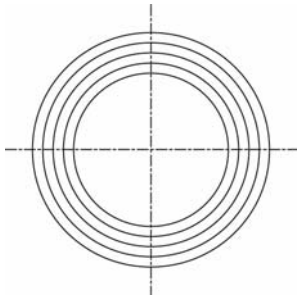


Fig. 2 Concentric finish line

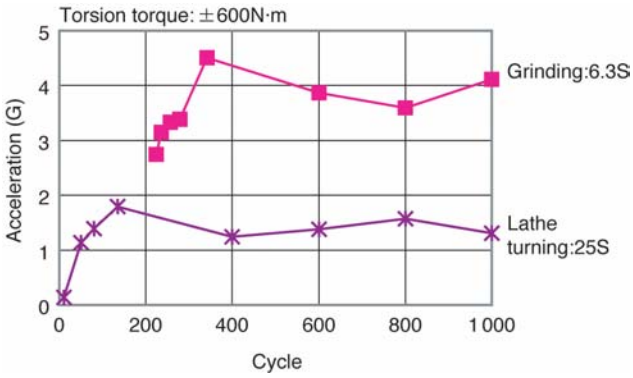


Fig. 3 Acceleration level for stick-slip and the machining process of CVJ

(2) Grinding waves

In the grinding process, care must be taken to manage the bearing play of the grinder main spindle and the grinding wheel feed rate. Depending on these management conditions, waves appear on the above-mentioned CVJ grinding finished surface, and the number and height of these waves varies. The true contact area changes according to the number and height of the waves, causing the static frictional force of the contact face to also change. As a result, stick-slip may occur at the contact face with the bearing inner race, and the CVJ and bearing inner race may also slip together. When the CVJ and bearing inner race slip together, stick-slip occurs at the press-fit face of the bearing inner race and the hub. Thus, factors causing stick-slip were found to be the CVJ waves, and the static frictional force between the hub and the bearing inner race that prevents the bearing inner race from slipping together with the CVJ.

Figure 4 shows an example of the number of waves on the contact face between the CVJ and the bearing inner race produced by different grinding conditions. To ensure a flat surface, the bearing play of the grinder main spindle and the grinding feed rate must be reduced. The wave height was greatest when there were seven waves.

Figure 5 shows the change in the slipping location due to the differences in the number of CVJ waves and the press-fit interference of the bearing inner race and the hub. When there were seven waves, the static frictional force at the contact face between the CVJ and the bearing inner race exceeded the frictional force provided by a press-fit interference of 25 μm or less between the bearing inner race and the hub, causing slipping to occur at the press-fit face. Setting a press-fit interference of 40 μm increased the static frictional force of the press-fit face, and slipping occurred at the contact face between the CVJ and the bearing inner race.

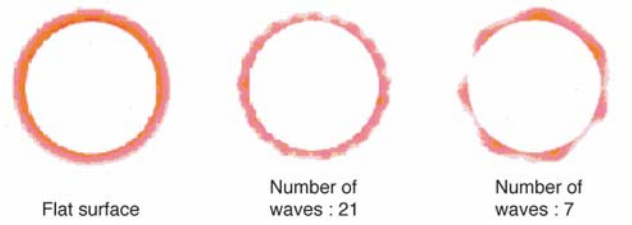


Fig. 4 Surface condition of CVJ

H : Slip at inner race and hub
C : Slip at inner race and CVJ

Interference of hub/bearings	Number of waves		
	Flat	21	7
10μm	C	H	H
25μm	C	C	H
40μm	C	C	C

Fig. 5 Waves and interference for various fitting dimension of hub/bearings

3.1.2. Changes in the dynamic frictional force due to the lubricant

The fastening structure around the hub bearings of the driven wheels shown in Fig. 1 is generally assembled in the condition with only cutting oil or rust-proof oil applied to the metal contact surfaces, and without using lubricant. However, the following test results showed that stick-slip prevention effects cannot be expected for some types of applied oils with regards to slipping at the metal contact surfaces.

A reciprocating type friction tester (Fig. 7) was used with a ϕ 10 steel ball (Fig. 6) as the test piece to measure the coefficient of dynamic friction under high surface pressure.

Tested lubricants

Rust-proof oil A : Refined kerosene used as the base oil

Rust-proof oil B : Lubricant used as the base oil

When the contact face load was 300 N in the degreased condition (Fig. 8), the coefficient of dynamic friction was confirmed to increase over time. Unlike rust-proof oil B (Fig.10), the coefficient of dynamic friction increased over time for rust-proof oil A (Fig. 9), which does not contain a lubricant. This resulted in an unstable lubrication condition that produces dynamic frictional force similar to the degreased condition (Fig. 8).

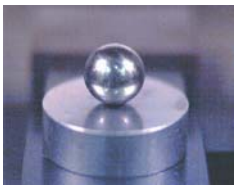


Fig. 6 Test piece for dynamic friction

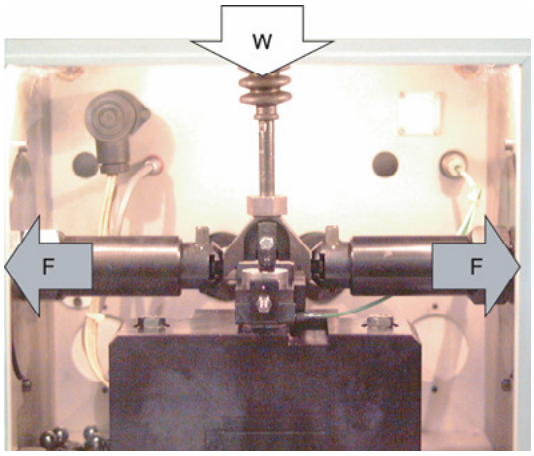


Fig. 7 Coefficient of dynamic friction

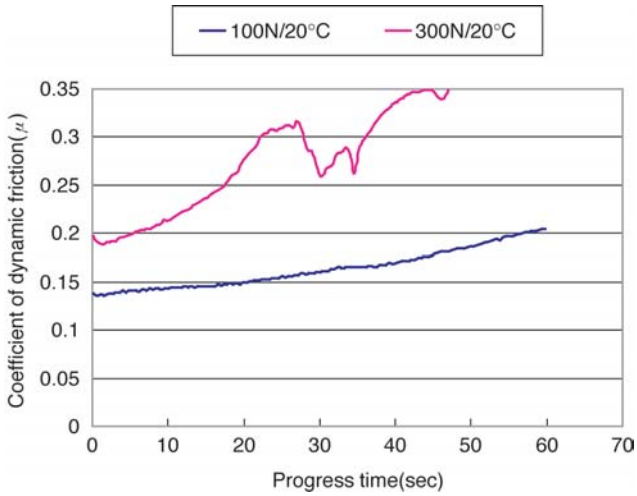


Fig. 8 Coefficient of dynamic friction when degreased

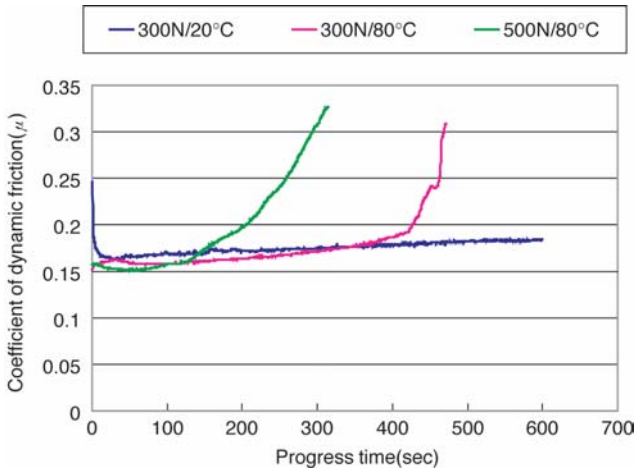


Fig. 9 Coefficient of dynamic friction with rust-proof lubricant type A

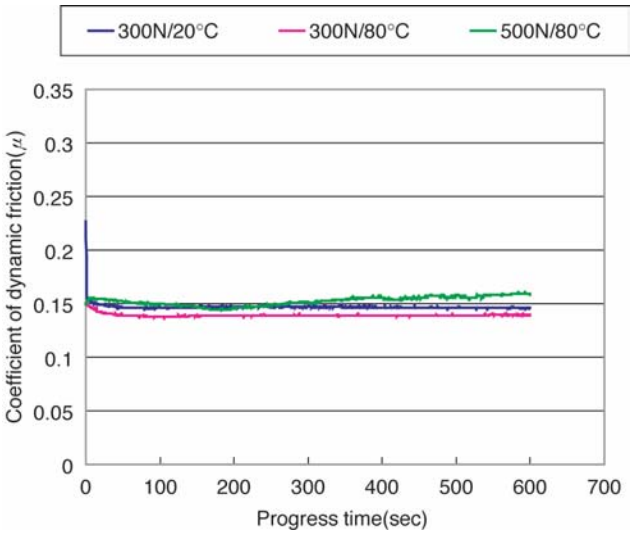


Fig. 10 Coefficient of dynamic friction with rust-proof lubricant type B

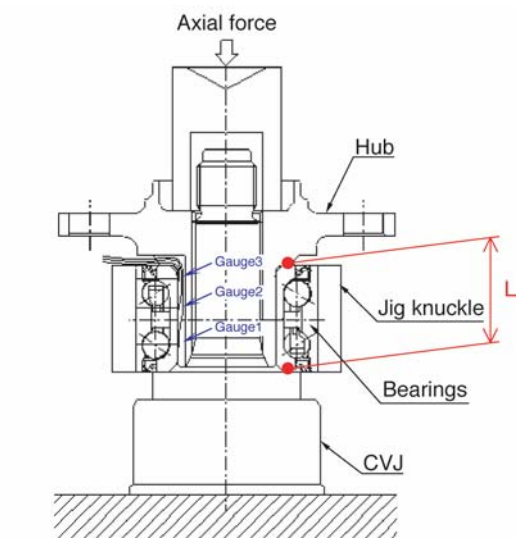


Fig. 12 Measuring strain of inner race of bearings

3.1.3. Non-uniform strain at the bearing inner race

Figure 11 shows the results of measuring the inner race length (L in Fig. 12) in the no-load condition after press-fitting the hub to the bearing inner race and applying a load equivalent to the axial force. The inner race length of 40.96 in Fig. 11 is the length after contact of the inboard and outboard inner races, and a length shorter than 40.96 represents the accumulation of strain in the no-load condition. In addition, Fig. 12 and Fig. 13 show the strain of the bearing inner race measured by attaching strain gauges to the bearing inner race and applying a load equivalent to the axial force. Figure 13 shows that gauge 3 changes toward the tension side regardless of whether a load is applied. In addition, the strain was confirmed not to change even when the load was removed. When this type of non-uniform strain of the bearing inner race occurs, the true contact area at the contact face between the inner race and the hub decreases, so the static frictional force drops and slipping is thought to occur more easily. Figure 14 shows a CAE representation of non-uniform strain of the bearing inner race. The bearing inner race is normally a non-uniform thickness, so when an excessive load is applied, the strain easily becomes non-uniform.

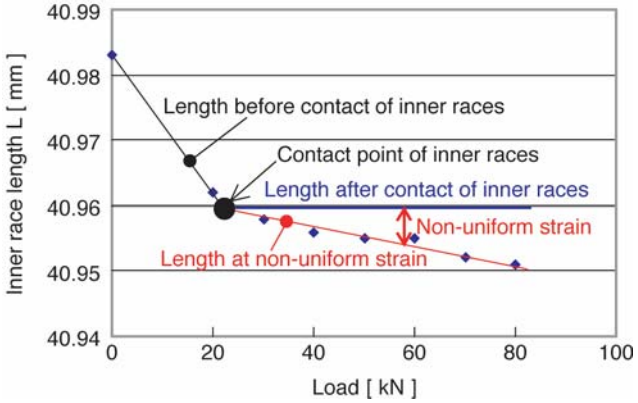


Fig. 11 Insertion load and inner race length

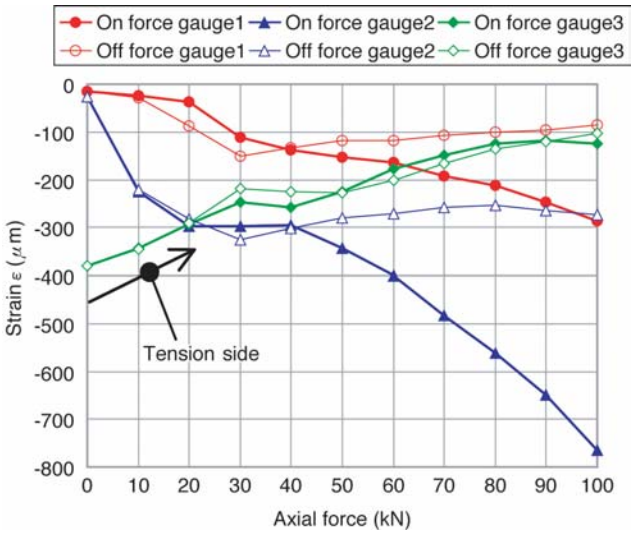


Fig. 13 Axial force and strain

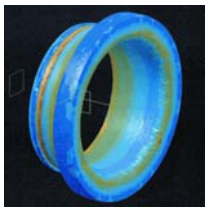


Fig. 14 Non-uniform strain of inner race

3.1.4. Effects of humidity

(1) Humidity and torque coefficient

A phenomenon was reported where stick-slip noise occurred when this fastening structure was manufactured during rainy weather. Investigations of vehicles exhibiting this phenomenon showed that the spindle nut tightening torque had changed, so factor analysis was performed.

First, the change in the torque coefficient with respect to humidity was investigated. The torque coefficient was found to change according to the tapered shape of the spindle nut seat and the humidity as shown in Fig. 15. In the humid condition the torque coefficient tended to become higher and the axial force tended to drop.

However, a clear correlation between the weather and the rotation angle of the spindle nut after contact was confirmed as shown in Fig. 16. Factories where this phenomenon occurred used a press-fitting machine structure where the maximum load was set by hydraulic control. This led to the hypothesis that, like the above-mentioned correlation between the insertion load and the strain of the bearing inner race, the effects of humidity caused an excessive load in the process to press-fit the hub to the bearing inner race, which resulted in non-uniform strain of the bearing inner race.

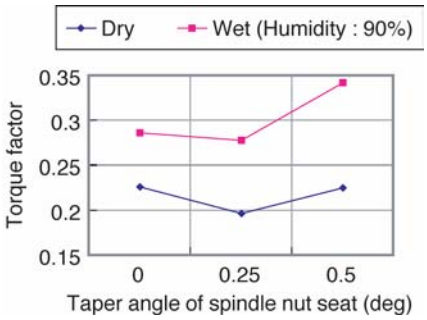


Fig. 15 Torque factor with variation in nut seat angle

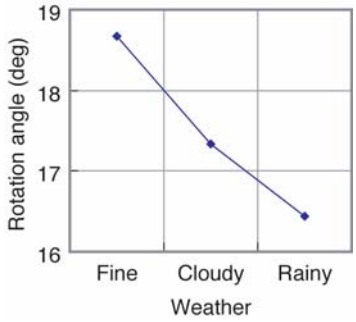


Fig. 16 Change of spindle nut rotation angle with change in weather

(2) Humidity and lubrication condition

Based on this hypothesis, the humidity and the insertion load were measured. This measurement used a mass produced press-fitting machine and changes in the insertion load over time were recorded as shown in Fig. 17. The hub was press-fit to the bearing inner race and the change in the load due to humidity was compared, focusing on the load (contact load) at the load rise point when the hub contacts the inner race and the peak insertion load.

The humidity around the press-fitting machine during rainy weather was approximately 60% and the measurement results confirmed a high correlation (coefficient of correlation: – 0.912) between the contact load and the peak insertion load as shown in Fig. 18. Here, the peak insertion load increases as the contact load decreases. The humidity around the press-fitting machine during fine weather was approximately 20% and the coefficient of correlation at this time dropped to a level that was hardly noticeable (coefficient of correlation: – 0.280), as shown in Fig. 19.

These results show that the dynamic frictional force drops when the humidity is high and the bearing inner race contacts the hub with a small insertion load. The cause for this is thought to be that the lubrication performance of the water-soluble cutting oil used when machining the hub changes according to the humidity. The contact load is small, but the insertion load control has a time lag, which causes the peak load to increase. The dynamic frictional force drops so the actual load applied to the bearing inner race increases. This causes the strain of the bearing inner race to increase and assembly enters the next spindle nut tightening process with this strain accumulated even in the no-load condition. Tightening is performed at the reference torque, but the bearing inner race which contracts with the tightening already has strain due to the excessive insertion load so the specified torque is reached with a small rotation angle. This fastening condition is thought to be the same as excessive tightening of the spindle nut. If the parts are assembled into a vehicle in that fastening condition, the application of driving torque from the CVJ causes the bearing inner race to move together with the CVJ so slipping occurs at the press-fit face between the bearing inner race and the hub. This slipping phenomenon produces stick-slip noise.

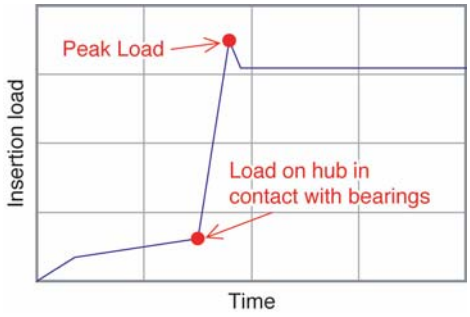


Fig. 17 Insertion load with time

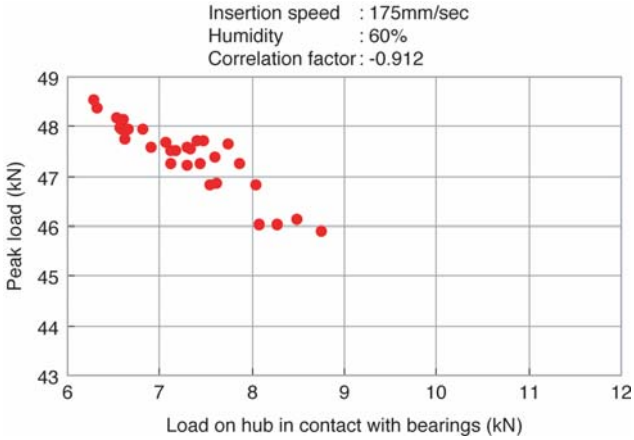


Fig. 18 Peak load and load on hub in contact with bearings in the case of a rainy day

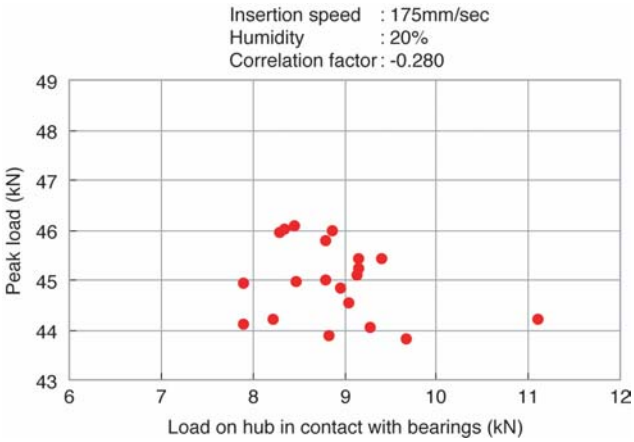


Fig. 19 Peak load and load on the hub in contact with bearings in the case of a fine day

(3) Maximum set insertion load and insertion speed

The peak load of the above-mentioned press-fitting machine can be set, but normally that setting is not changed even if the size of the bearings flowing along the line changes. Therefore, the set load becomes larger than the required insertion load as the bearing size decreases and the insertion speed also increases in this case.

The experiment shown in Fig. 20 compared the coefficient of correlation between humidity and the contact and peak loads at insertion speeds of 175 mm/s and 80 mm/s. At an insertion speed of 80 mm/s, a stable press-fit condition was obtained for all humidity ranges. In contrast, the correlation with humidity was confirmed to change greatly at an insertion speed of 175 mm/s. At an insertion speed of 175 mm/s, the lubricant was found to spread to the press-fit face, which is thought to have changed the lubrication condition.

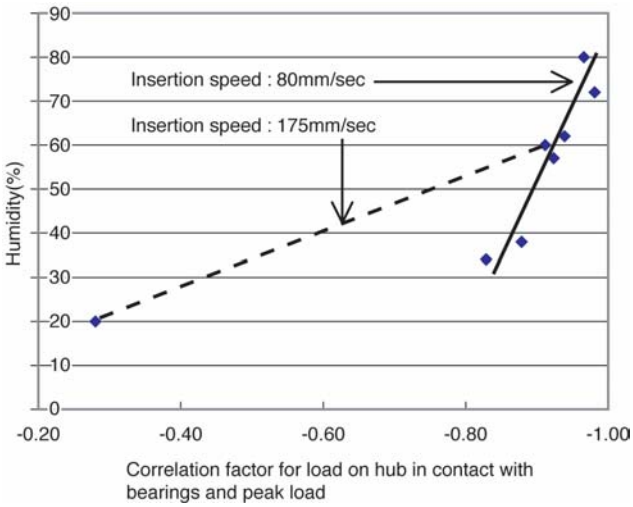


Fig. 20 Humidity and correlation factor

3.2. Enduring Type Stick-Slip Noise

3.2.1. Surface roughness

Stick-slip noise includes noise produced when running for long periods causes the contact face to become rough due to slipping of the contact face between the CVJ and the bearing inner race. Figure 21 shows a contact face that has been roughened by actual running. When the contact face becomes rough, stick-slip may occur at this face, or it may occur at the press-fit face between the bearing inner race and the hub when the CVJ and the bearing inner race move together because the roughness increases the static frictional force of this face.

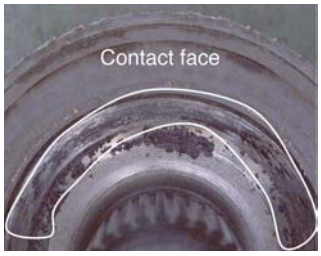


Fig. 21 Rough face of CVJ

3.2.2. Contact face lubrication

Methods for preventing stick-slip based on the adhesion theory of friction were investigated. The conditions for selecting the lubrication method for the contact face between the CVJ and the bearing inner race were as follows.

Selection conditions

- The lubricant should not attack the bearing seals or other rubber materials.
- Performance should be maintained even under conditions of a poor protective environment for the contact face.
- The lubricant should be easy to obtain and allow refilling after its life span is reached.

In consideration of the above conditions, solid lubrication utilizing the molecular level shearing of molybdenum disulfide (MoS_2) interposed on the contact face was deemed suitable.

Figure 22[1] shows a photograph of shearing in the MoS_2 crystal orientation viewed at a magnification of 6 million times. MoS_2 has a micaceous molecular structure, so when the metals move relative to each other, the MoS_2 interposed between the metal contact surfaces shears and reduces the adhesive force between the metals.

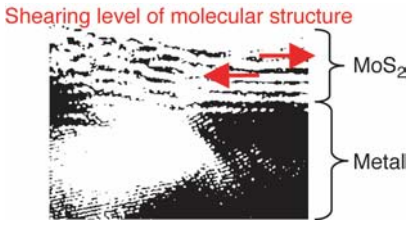


Fig. 22 Crystal structure orientation

The coefficient of dynamic friction of the MoS_2 grease was measured using the method described in section 3.1.2 above. The results confirmed that a stable coefficient of dynamic friction can be obtained even when the temperature changes under high surface pressure.

The coefficient of dynamic friction was confirmed to drop slightly when the contact face load was raised from 100 N to 300 N at a temperature condition of 20°C as shown in Fig. 23. The coefficient of dynamic friction at a contact face load of 300 N was also confirmed to drop at a temperature condition of 80°C as compared to a temperature condition of 20°C. Likewise, the coefficient of dynamic friction at a temperature condition of 80°C was confirmed to drop further and stabilize at 0.05 after 200 s when the contact

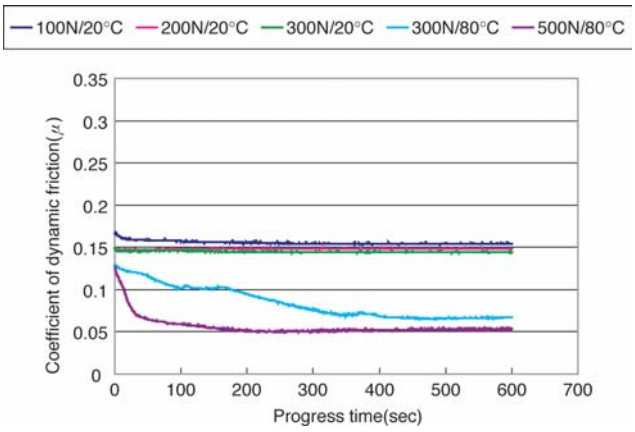


Fig. 23 Coefficient of dynamic friction with MoS_2 grease

face load was raised to 500 N. The high surface pressure and temperature rise are thought to improve the fluidity of the grease, so the MoS_2 spreads over a wide area and reduces the coefficient of dynamic friction.

Summarizing the above results, the easy-to-shear characteristic of MoS_2 is strongly manifested when the MoS_2 grease spreads widely over the metal contact faces. This easy-to-shear characteristic can be used to prevent stick-slip around the hub bearings of driven wheels.

3.2.3. Lubrication and surface roughness

When fastening portions experience repeated slipping, the contact face becomes rough. These limit conditions and the effects of lubricants were confirmed using a torsion tester.

Torsion test conditions

- Lubricants applied to the contact face

(1) MoS_2 grease
(2) Rust-proof oil
(3) Degreased

- Torsion torque : ± 1,300 N
- Number of repeated cycles : 8,000 cycles

Figures 24, 25 and 26 show the test results.

(1) MoS_2 grease : No roughness
(2) Rust-proof oil : Roughness
(3) Degreased condition : Surface roughness of a worse degree than (2) above.

This confirmed that use of a lubricant was effective even under life operating conditions.



Fig. 24 Damage of contact face with MoS_2 grease



Fig. 25 Damage of contact face with rust-proof lubricant



Fig. 26 Damage of contact face when degreased

4. Methods for Preventing Stick-Slip

Stick-slip around the hub bearings of driven wheels occurs due to an increase in the static frictional force at the contact face between the CVJ and the bearing inner race, and a decrease in the static frictional force at the press-fit face between the bearing inner race and the hub. Therefore, methods for preventing stick-slip include reducing the static frictional force at the contact face between the CVJ and the bearing inner race to ensure slipping, and ensuring that the static frictional force at the press-fit face between the bearing inner race and the hub exceeds the static frictional force at the contact face.

4.1. Ensuring Slipping at the Contact Face between the CVJ and the Bearing Inner Race

The static frictional force can be reduced by managing the finishing process for the contact face between the CVJ and the bearing inner race to prevent waves and by leaving concentric lathe turning finishing lines. In addition, when applying rust-proof oil to the contact face between the CVJ and the bearing inner race, excellent lubrication conditions can be obtained by selecting an oil that uses a lubricant as its base oil. As a more active measure, applying MoS_2 grease can ensure sliding at the contact face between the CVJ and the bearing inner race. When the lubrication condition deteriorates after long periods of use, the lubrication condition can be improved by refilling the MoS_2 grease.

4.2. Ensuring Static Frictional Force at the Press-fit Face between the Bearing Inner Race and the Hub

Increasing the press-fit interference between the bearing inner race and the hub can elevate the static frictional force at the press-fit face. In addition, increasing the rigidity of the bearing inner race also increases the static frictional force at the press-fit face that is obtained from the interference. When the load used to insert the hub to the bearing inner race is excessive, or when the axial force produced by tightening the spindle nuts is excessive, non-uniform strain occurs in the bearing inner race. In this case the true contact area at the press-fit face between the bearing inner race with non-uniform strain and the hub decreases, and the static frictional force also decreases. Increasing the rigidity of the bearing inner race suppresses the occurrence of non-uniform strain and ensures static frictional force at the press-fit face between the bearing inner race and the hub.

5. Summary

Factor analysis of stick-slip noise around the hub bearings of driven wheels revealed multiple factors and the following previously unknown special factors were found.

(1) Excessive axial force due to spindle nut tightening and an excessive insertion load produced non-uniform strain in the bearing inner race and this strain accumulated even when the load was removed. This non-uniform strain of the bearing inner race was a factor causing stick-slip at the press-fit face between the bearing inner race and the hub.
(2) If a fast insertion speed is used when inserting the hub to the bearing inner race, the coefficient of dynamic friction of the press-fit face (friction face) is easily

affected by a rise in humidity during insertion. When the humidity rises, the coefficient of dynamic friction falls. When fast insertion is performed in a high humidity environment, the coefficient of dynamic friction decreases and insertion is possible with a small load. This results in the same excessive insertion load condition as in (1) above, and is a factor causing stick-slip.

Stick-slip noise can be prevented by eliminating the above special stick-slip factors, managing the finishing process of the contact face between the CVJ and the bearing inner race, and increasing the press-fit interference with the hub after first ensuring the rigidity of the bearing inner race. However, the most effective method for preventing stick-slip noise proposed by this paper is to ensure an excellent lubrication condition at the contact face between the CVJ and the bearing inner race. As a concrete method, an excellent lubrication condition can be maintained and stick-slip noise can be prevented by applying MoS_2 grease to the contact face between the CVJ and the bearing inner race.

Afterword

With regards to the stick-slip around the hub bearings of driven wheels that is the subject of this research, in addition to the noise level, the noise recognition level also changes depending on differences in automotive sound insulation performance. Even when it is not recognized as abnormal noise, if the structure is such that slipping occurs at the contact face between the CVJ and the bearing inner race when driving torque is applied, MoS_2 grease should be applied to that contact surface to maintain an excellent lubrication condition and prevent changes in the stick-slip noise level.

Acknowledgements

The authors wish to express their deepest thanks to all related parties at Yanagawa Seiki Co., Ltd., NTN Corp., Fuserashi Co., Ltd., and Sumiko Lubricant Co., Ltd. for their immense cooperation with this research.

Reference

(1) Takahashi, N., Kashiwaya, S.: High resolution transmission electron microscopy observation of the MoS_2-Au interface formed due to Stick-Slip of MoS_2 sliding on Au in relation to the friction trace, Wear, 206, p. 8-14 (1997)

■ Authors ■


Mikio KASHIWAI


Haruo SHINOHARA


Nobuo NIWA


Ikuo YAMAKAWA


Shigeki OIDE


Kunio MIZUNO

Prediction of Vehicle SEA Model Input Parameters for a Sound Package

Kazuhito MISAJI* Hiroko TADA* Yuji KURUHARA*
Yoshihiro NOGUCHI* Tsuyoshi YAMASHITA*

ABSTRACT

This paper describes a method for the prediction of automotive sound package acoustical characteristics. This method is based on the transfer matrix approach and is applied to calculate the transmission loss (TL) and absorption of multi-layered insulation components from the acoustical impedance of each layer. The predicted results are necessary as fundamental input parameters of SEA vehicle models. The accuracy of this method was verified by comparing the predicted TL and absorption values of trimmed components with measurement results.

1. Introduction

Statistical energy analysis (SEA) has come into wide, general use for analysis of high-frequency sound propagation, especially through air. A key point in constructing SEA models related to air-propagated sound is to find coupling loss factors (CLF), which express the acoustic insulation characteristics between acoustic fields, and the damping loss factors (DLF), which express the acoustic absorption characteristics of a single acoustic field. It is possible to calculate the CLF and DLF from the acoustic characteristics (transmission loss, absorption coefficient) of a sound package. It is also possible to measure the acoustic characteristics of a sound package, but this is not realistic in an automobile at the development stage. In order to accomplish both weight savings and sound-proofing of an automobile in a short time frame and at low cost, it is necessary to have the technology for predicting the acoustic characteristics of a sound package and for creating SEA models of the situation in an actual vehicle at stages when no test vehicles yet exist (initial stages of development).

The CLF and DLF of an acoustic system are especially important for setting the specifications of noise insulation. Therefore, in this study, a method was proposed for predicting the transmissibility τ (for the transmission losses TL) and the absorption coefficient α from the specifications of multi-layered automotive trim (composition, thickness and material characteristic). The validity of the method was verified by comparing predicted values with measured values.

2. Relationship between Acoustic Characteristics of Noise Insulation and SEA Parameters

The CLF between acoustic fields η_{12} can be found using Eq. (1) with the transmissibility τ_{12} found using the method described in this paper. Here, A is the area of the interface between acoustic fields V the combined volume of the acoustic fields. Additionally, c_0 is the speed of sound in air and ω is the angular velocity of the sound.

- CLF of acoustic fields:

$$\eta_{12} = \frac{A \cdot c_0}{4\omega V} \tau_{12} \tag{1}$$

In the same way, the DLF of an acoustic field η can be found using Eq. (2) with the absorption coefficient α found using this method and the area A and volume V of the acoustic field.

- DLF of acoustic system:

$$\eta = \frac{A \cdot c_0}{4\omega V} \alpha \tag{2}$$

Using these expressions allows investigation of the sound-insulating specifications of the floor, and sound-absorption specifications of various acoustic cavities in the automobile. Knowing these parameters can permit efficient reduction of road noise in the initial stages of development of an automobile.

* Tochigi R&D Center

3. Method for Prediction of Acoustic Characteristics of Multi-layered Trim

Prediction of the acoustic characteristics of multi-layered trim is based on the transmission matrix method. This allows prediction of the acoustic characteristics of multi-layered trim consisting of both porous materials and vibration-damping materials. In this method, a model consisting of the subject trim material is constructed of multiple areas, of which each can be considered a laminated body of uniform thickness. The transmission losses TLi and the absorption coefficient αi of trim layer i are calculated. Then, the calculated values of TLi and αi are used to find the mean TL and mean α for the whole area.

3.1. Method for Estimating Transmission Losses in Multi-layered Trim of Uniform Thickness

As shown in Fig. 1, the structure of a general multi-layered trim of uniform thickness is a triple lamination, consisting of the first layer, an impervious barrier; the second layer, a porous medium; and the third layer, a plate.

p_I is the acoustic pressure of the incident wave, ϕ is the incident angle, and p_T is the acoustic pressure of the transmitted wave. The impedance of each interface is found in sequence.

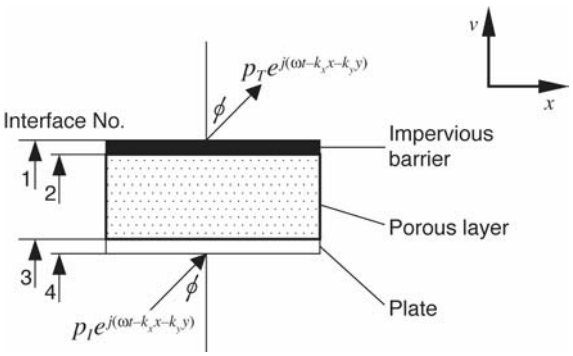


Fig. 1 Three layers in contact in a multilayer material

First, the impedance Z_1 of the first interface (at air) is calculated using Eq. (3) and (4). Here, k is the wave number.

$$k_x = k_0 \sin\phi \tag{3}$$

$$Z_T = Z_1 = \frac{\rho_0 c_0}{\cos\phi} \tag{4}$$

Next, the impedance Z_2 of the second interface (at impervious barrier) is calculated using Eq. (5), (6), (7) and (8). Here, the surface density, thickness, Young's modulus, Poisson's ratio, and loss factor at each interface are denoted by ρ_i, t_i, E_i, ν_i and η_i, respectively.

$$Z_2 = Z_1 + j\left[\omega\rho_s - \frac{D^c k_x^4}{\omega}\right] \tag{5}$$

$$P_x = P_B t_B \tag{6}$$

$$D^c = D(1 + j\eta_B) \tag{7}$$

$$D = \frac{E_B t_B^3}{12(1-\nu_B^2)} \tag{8}$$

The impedance Z_3 at the third interface (at porous barrier) is calculated using Eq. (9), (10), (11) and (12). The subscript 'PL' indicates that the variable applies to the porous layer; R_{PL} is the flow resistance of the porous layer.

$$Z_3 = Z_0 \frac{K}{k_y} \frac{\left(1 + \frac{Z_0 K}{Z_2 k_y}\right) e^{jk_y t_{PL}} + \left(1 - \frac{Z_0 K}{Z_2 k_y}\right) e^{-jk_y t_{PL}}}{\left(1 + \frac{Z_0 K}{Z_2 k_y}\right) e^{jk_y t_{PL}} - \left(1 - \frac{Z_0 K}{Z_2 k_y}\right) e^{-jk_y t_{PL}}} \tag{9}$$

$$Z_0 = \rho_0 c_0 \sqrt{1 - j\frac{R_{PL}}{\rho_0 \omega}} \tag{10}$$

$$K = k_0 \sqrt{1 - j\frac{R_{PL}}{\rho_0 \omega}} \tag{11}$$

$$k_y^2 = K^2 - k_x^2 \tag{12}$$

The impedance Z_4 at the fourth interface (at plate) is calculated from Eq. (13), (14) and (15).

$$Z_4 = Z_3 + j\left[\omega\rho_s - \frac{D^c k_x^4}{\omega}\right] \tag{13}$$

$$P_x = P_{p\,p}^{\,t} \tag{14}$$

$$D^c = D(1 + j\eta_p) \tag{15}$$

The transmission loss in a multi-layered trim of uniform thickness, $TL^{w/trim}$, is found in Eq. (16) – (22) using impedances $Z_1 - Z_4$.:

$$\tau_R^{w/trim}(\omega) = \int_0^{\pi/2} \tau_R^{w/trim}(\omega, \phi) \sin 2\phi \, d\phi \tag{16}$$

$$TL^{w/trim} = 10\log\frac{1}{\tau_R^{w/trim}(\omega)} \tag{17}$$

Here, $$\tau_R^{w/trim}(\omega, \phi) = \frac{|p_T|^2}{|p_I|^2} \tag{18}$$

$$p_T = p_1 = \frac{Z_1}{Z_2} p_2 \tag{19}$$

$$p_2 = \frac{p_3}{2}\left[\left(1 + \frac{Z_0 K}{Z_3 k_y}\right) e^{-jk_y t_{PL}} + \left(1 - \frac{Z_0 K}{Z_3 k_y}\right) e^{jk_y t_{PL}}\right] \tag{20}$$

$$p_3 = \frac{Z_3}{Z_4} p_4 \tag{21}$$

$$p_4 = \frac{2\alpha}{\alpha + 1} p_I, \quad \alpha = \frac{Z_I}{Z_T} = \frac{Z_4}{Z_1} \tag{22}$$

(p_i is the acoustic pressure at each interface)

3.2. Method for Estimating Acoustic Absorption Coefficient in Multi-layered Trim of Uniform Thickness

Here, the method for finding the absorption coefficient α in a multi-layered trim of uniform thickness is explained. The multi-layered trim of uniform thickness used as the object of this analysis is shown in Fig. 2.

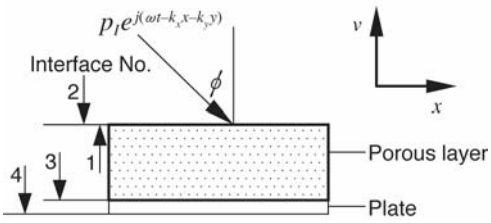


Fig. 2 Two layers in contact in a multilayer material

The first layer of this 2-layer structure is a porous material and the second is a plate. p_I is the acoustic pressure of the incident wave and ϕ is the incident angle.

The absorption coefficient in this case is calculated with the following expression:

$$\hat{\alpha} = 2\int_0^{\phi_{lim}} d\phi \sin\phi\cos\phi\,\alpha \tag{23}$$

Here, $$\alpha = \frac{\text{Absorption energy}}{\text{Incident energy}} = 1 - |R|^2 \tag{24}$$

R : reflection factor

When noise impinges on an interface at a right angle, the reflection factor and absorption coefficient are found using the characteristic impedance Z_2 for perpendicular incident energy in the sound-absorbing layer (Interface 2) and the characteristic impedance Z_1 at the air surface (Interface 1) in the following relation:

$$R = \frac{Z_2 - Z_1}{Z_2 + Z_1} \tag{25}$$

Here, Z_2 is found using Eq. (26) – (29).

$$Z_2 = Z_0 \frac{K}{k_y} \frac{\left(1 + \frac{Z_0 K}{Z_3 k_y}\right) e^{jk_y t_{PL}} + \left(1 - \frac{Z_0 K}{Z_3 k_y}\right) e^{-jk_y t_{PL}}}{\left(1 + \frac{Z_0 K}{Z_3 k_y}\right) e^{jk_y t_{PL}} - \left(1 - \frac{Z_0 K}{Z_3 k_y}\right) e^{-jk_y t_{PL}}} \tag{26}$$

$$Z_0 = \rho_0 c_0 \sqrt{1 - j\frac{R_{PL}}{\rho_0 \omega}} \tag{27}$$

$$K = k_0 \sqrt{1 - j\frac{R_{PL}}{\rho_0 \omega}} \tag{28}$$

$$k_y^2 = K^2 - k_x^2 \tag{29}$$

The impedance Z_3 at the surface of the plate (Interface 3) is found in the same way as shown in Eq.(5) shown in Section 3.1.

3.3. Method for Estimating Transmission Loss in Actual Automotive Trim

Here, the method for estimating the transmission loss in a multi-layered trim of uniform thickness shown in Section 3.1 is used to estimate the transmission loss in a real floor carpet of non-uniform thickness.

The following expression (30) is obtained when sections A_1 – A_n of a floor carpet can be assumed to have uniform thickness with transmissibilities τ_1 – τ_n. Here, τ is the mean floor carpet transmissibility and A is the total floor area.

$$\tau A = \tau_1 A_1 + \tau_2 A_2 + \ldots + \tau_i A_i + \ldots \tau_n A_n \tag{30}$$

τ is found by the following procedure: τ_i is calculated by the method for predicting transmission losses in multi-layered trim of uniform thickness shown in Section 3.1 for each section of the floor which can be considered of uniform thickness. Then, these are substituted into Eq. (30) and the sum is divided by total floor area A. The overall transmission loss is then found using the mean transmissibility τ and Eq. (16), (17) and (18).

The estimated TL is shown in Fig.4.

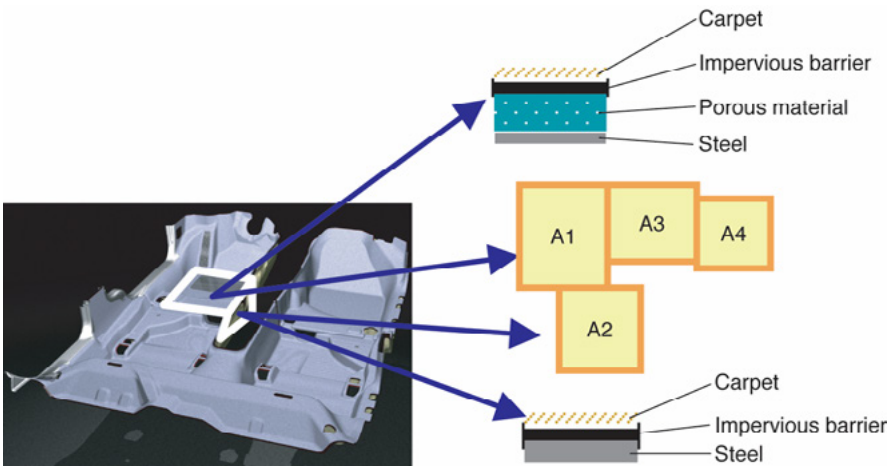


Fig. 3 Definition of the floor carpet model

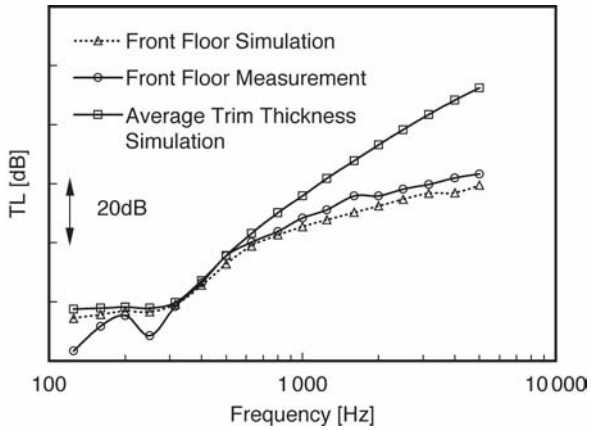


Fig. 4 Measured and simulated TL for the floor

3.4. Method for Estimating Absorption Coefficient in Actual Automotive Trim

Here, the method for estimating the absorption coefficient is shown for a real seat of non-uniform thickness, using the method described in Section 3.2 for estimating the absorption coefficient α in a multi-layered trim of uniform thickness.

Like the method for predicting the floor carpet transmission losses explained in Section 3.3, the following expression (31) can be obtained when areas $A_1 - A_n$ of a floor carpet can be assumed to have uniform thickness with absorption coefficients $\alpha_1 - \alpha_n$, as in the method for transmissibilities. Here, α is the mean absorption coefficient of the seat and A is the total seat area.

$$\alpha A = \alpha_1 A_1 + \alpha_2 A_2 + \ldots + \alpha_1 A_1 + \ldots \alpha_n A_n \qquad (31)$$

α is found by the following procedure: α_i is calculated by the method in Section 3.2 for each section of the seat which can be considered of uniform thickness. Then, these are substituted into Eq. (31) and the sum is divided by total seat area A. The seat absorption coefficient is then found using the mean seat absorption coefficient α and Eq. (23), (24) and (25). The estimated α are shown in Fig.5.

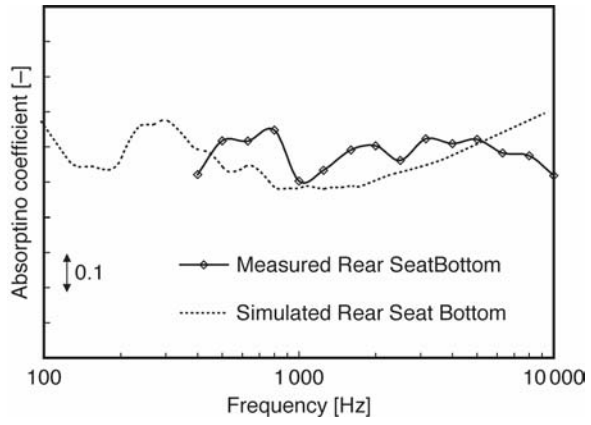


Fig. 5 Measured and simulated α for the seat

4. Verification of Precision of Estimates of Acoustic Characteristics

4.1. Measurement of Acoustic Characteristics

1) Measurement of transmission loss in floor carpet

The TL values in Fig. 4 observed in an actual floor carpet were measured using the acoustic property measurement equipment shown in Fig. 6. The upper chamber in the equipment in Fig. 6 is the reception cabin (reverberation chamber), and the lower chamber is the emission cabin. The test sample was placed between the two chambers. Noise was generated by the speakers on the floor of the lower chamber, and the transmission loss was calculated from the acoustic pressures in the upper and lower chambers. This equipment was used to measure the TL in the floor carpet shown in Fig. 7. The TL observed in the floor section is shown in Fig. 4.

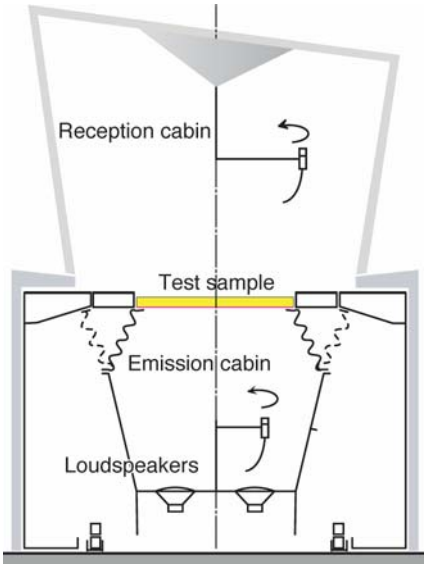


Fig. 6 The acoustic property measurement equipment



Fig. 7 The front floor as an example

2) Measurement of absorption coefficient of a seat

α values were measured in the actual seat shown in Fig. 8 with the equipment shown in Fig. 6, as described in part 1) above. The upper chamber in the equipment in Fig. 6 is the reverberation chamber and the test sample is placed between the two chambers. Noise was generated at the speakers toward the upper chamber, and the absorption coefficient was calculated from the reverberation time. This equipment was used to measure α of the portion of the seat under measurement. The observed α are graphed in Fig. 5.

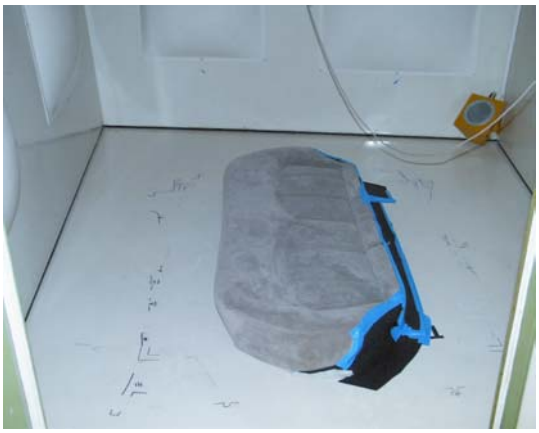


Fig. 8 The rear seat bottom cushion as an example

4.2. Comparison of Predicted Values and Measured Values

1) Transmission losses in floor carpet

The measured values for transmission loss in the floor carpet observed by the method described above are shown in Fig. 4 for comparison with the values predicted by the method shown in Section 3. It is clear that there was over a 10 dB difference between the results for TL using the mean thickness of trim in the floor plate as the equivalent plate thickness and the results for TL using actual plate thicknesses shown in Section 3.3, in the region over 1000 Hz. Also, the latter predicted results matched well with the observed TL in the actual floor plate. The analytical accuracy was within ± 3% dB.

Thus, these results indicate that the method of dividing the floor areas into sections which can be considered of equal thickness, calculating the overall mean floor transmissibility from the values for each section, and calculating the floor TL from this transmissibility is superior to the method of calculating TL from average plate thickness.

2) Absorption coefficient of a seat

By comparing the value for seat absorption coefficient estimated by the method in Section 3.4 with the observed absorption coefficient in Section 4.1, it is confirmed that the prediction method proposed in this paper yielded an analytical precision within ± 0.15 (Fig.5).

5. Summary

Methods were presented for estimating the transmission loss characteristics and absorption coefficient of automotive trim with varying thickness and structure. The validity of the methods was verified by comparison with measured values. Accordingly, the following results were found.

1) The transmission losses in floor carpet were predicted with an accuracy of ± 3 dB at frequencies over 400 Hz by the demonstrated method.
2) The seat absorption coefficient was predicted with an accuracy of ± 0.15 at frequencies over 400 Hz by the demonstrated method.
3) This method enables prediction of the SEA parameters CLF and DLF by calculation of transmissibility and absorption coefficient at the early development stage of automobiles, when there are no physical models yet.
4) The above results indicate that the demonstrated method is effective for the investigation of specifications of sound packages in the development of automobiles.

References

(1) Lyon, R.H.: Statistical Energy of Dynamical Systems, Theory and Applications, MIT Press (1975)

(2) Lauriks, W., Mees, P., Allard, J.F.: The acoustic transmission through layered systems, Journal of Sound and Vibration, Vol.155, p.125-132 (1992)

(3) Semeiuk, B.: The Simulation of the Acoustic Absorption and Transmission Characteristics of Automotive Material Configurations: The New Sisab Software, Rieter Automotive Conference Proceedings (1999)

(4) Chappuis, A.: Small Size Devices for Accurate Acoustical Measurements of Materials and Parts Used in Automobiles, SAE paper n. 931266

(5) Delany, M.E., Bazley, E.N.: Acoustical properties of fibrous absorbent materials, Applied Acoustics, Vol.3, p.105-116 (1970)

■ Authors ■


Kazuhito MISAJI


Hiroko TADA


Yuji KURUHARA


Yoshihiro NOGUCHI


Tsuyoshi YAMASHITA

Development of CAE Technology Applicable to the Concept Stage of BIW

Takayuki FUJII* Shigeo FUJITA* Yasushi YOSHIZAWA*

ABSTRACT

A CAE technology was developed which can be applied to the BIW concept stage in the design of lightweight, high-performance vehicle bodies. This technology utilizes a parametric FE model formulated from design lines and frame cross-sections, and enables analysis of body performance for static, dynamic and side impact characteristics. Because this technology does not require CAD drawings, designers can quickly evaluate numerous ideas in FE models, enabling the creation of new frame structures. Comparison of analysis results with conventional high-accuracy large-scale models has confirmed correlation between the methods, and verified that it is possible to predict performance from the concept stage of BIW using the new technology. This paper discusses the application of CAE at the concept stage of BIW to examine frame structure and predict performance when altering the design of a vehicle.

1. Introduction

As a part of the continuing effort to address automotive environmental issues, there has been a demand for technology to decrease the weight of the BIW (body in white) while not reducing safety or marketability. CAE (computer aided engineering), which is a core technology in the development of a lightweight BIW, together with improved computer performance, makes it possible to predict performance more accurately. However, the current CAE process is mainly focused on CAD (computer aided design) drawing based FE (finite element) models, and at the concept stage of BIW (stage at which there are no CAD drawings), performance evaluation of the frame structures being considered by the designer cannot be carried out in a short period of time. This paper reports on the newly developed FE model creation technology that does not require CAD drawings[(1), (2)], and on CAE technology that enables quick evaluation of frame static, dynamic and collision performance characteristics, using the FE model created with the new method.

* Tochigi R&D Center

2. Overview of Concept Stage CAE Technology

2.1. Timing of CAE Application in Vehicle Development

Conventionally, CAE has been applied after CAD drawing creation, at the stage of making vehicle performance predictions. The CAE method proposed in this paper is suitable for the BIW concept stage, as shown in Fig. 1. This stage is the period from design sketch through the creation of clay models. The aim is to incorporate a lightweight and high-performance frame structure into the styling design. During this period, it is possible to propose lightweight and high-performance frame structures, by predicting body characteristics and taking countermeasures. However, because there are frequent design changes during this period, it is very important to make model corrections and to rapidly carry out characteristics predictions. The goal of this technology was therefore to determine the direction of the design, rather than analysis accuracy.

There are two types of vehicle development flow; new model vehicle development, and existing model carryover.

(1) In the case of new model vehicle development, a new frame structure study is carried out, and the frame structure of an existing vehicle is not available to be used. From when the sketches are started, CAE is applied and many frame structures are proposed, that can be lightweight and high-performance.
(2) In the case of an existing vehicle carry-over, performance changes that accompany upper body styling changes are predicted by the CAE technology proposed in this paper, and countermeasure proposals are made. The requirement is to propose the most effective countermeasure spec within the existing layout.

In both development flows (1) and (2), as shown in Fig. 1, the application of concept stage CAE technology proposed in this paper makes development of lightweight, high-performance frame structures possible.

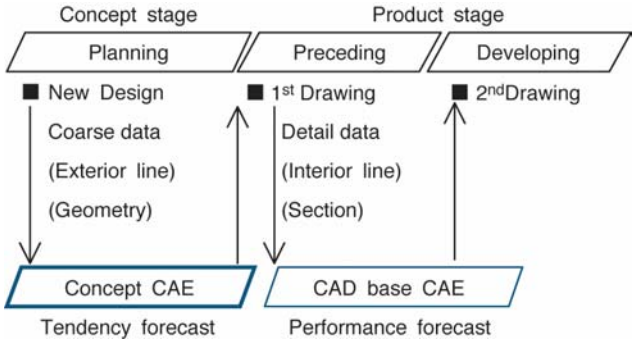


Fig. 1 Car development flow & CAE

In addition, after the design has been determined and CAD drawings issued, the application of conventional, large-scale CAE technology based on CAD drawings is used for NV (noise vibration), stiffness and impact performance predictions.

2.2. Modeling Concept

With conventional CAE, detailed FE models are necessary for vehicle performance predictions. The part shapes are created with CAD drawings, and the detailed, large-scale FE model is created using FEM (finite element method) pre-processors. Highly accurate analysis is expected of detailed, large-scale models. However, because CAD drawings are used, much time is needed for modifications, depending on the area of change, or the shape.

In contrast, with the parametric geometry model used in this project, it is expected that a simplified FE model will be able to deal with spec studied for frame structure proposals, in a short period of time. The simplified FE model is created using the drawing-free modeling technology proposed in this paper, utilizing design data and section shape data. This model can quickly respond to model changes that accompany frame structure and design studies without the creation of CAD drawings and is suitable to frame structure studies.

2.3. Drawing-free Modeling Technology

Figure 2 shows the model creation flow utilizing the drawing-free modeling technology.

- Establishing the body frame member layout, from design shapes
- Establish cross-sections on frame layout lines
- Create beam elements

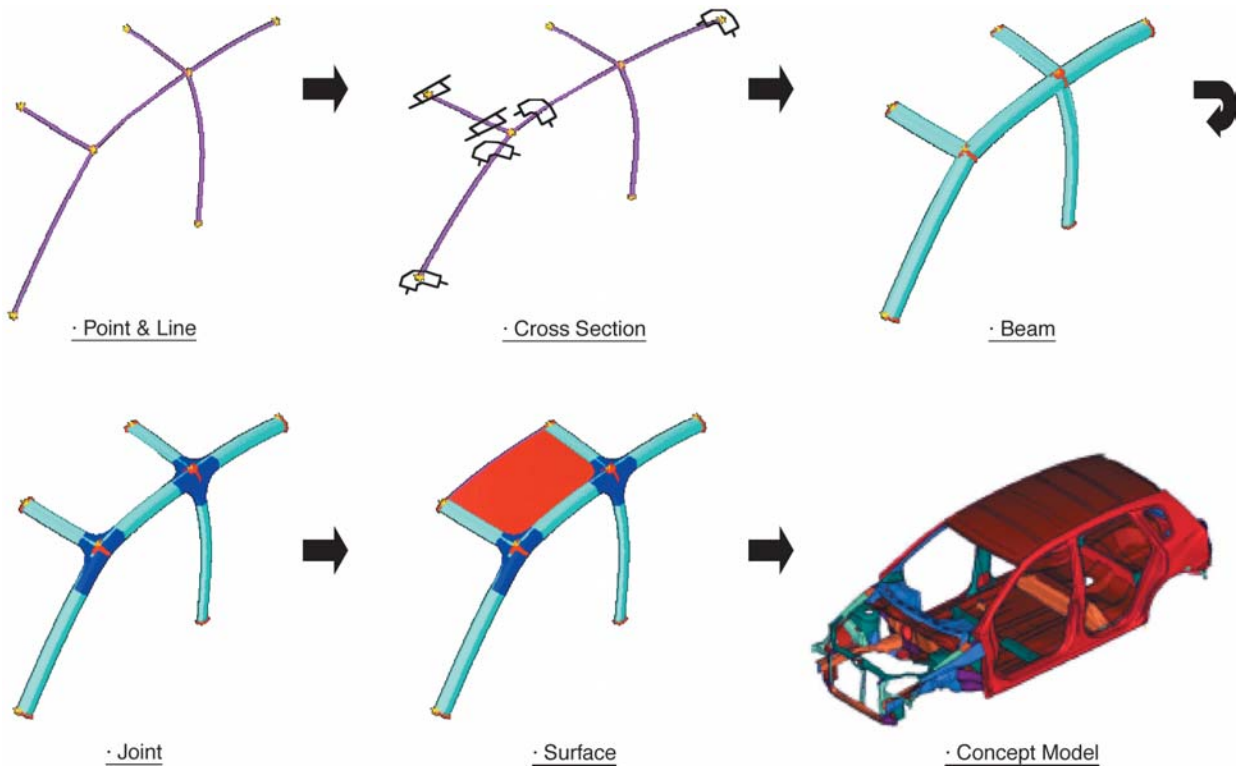


Fig. 2 Concept modeling flow for body structure

- Create joint elements in connection areas where multiple beam elements come together
- Create surface elements between frames

By repeating the work outlined above, it is possible to create a frame model for the whole body (referred to as the concept model hereafter) without creating CAD drawings.

2.4. Parametric Technology

With the concept model, it is possible to change the shape or structure at will. As shown in Fig. 3, if overall height dimensions are input, changing the design of the base concept model, then it is changed to a new model. It is possible to implement body performance prediction analysis in a short period, if the frame layout or section shape changes. In the case of a topology change, if the changed part only is newly created, it is possible to immediately apply parametric technology. Utilizing drawing-free modeling and parametric technology, a new method has been actualized that creates frame structure models without the making of CAD drawings. This enables quick checks of the effect of design changes, making it possible to study structure spec differences within a short period of time.

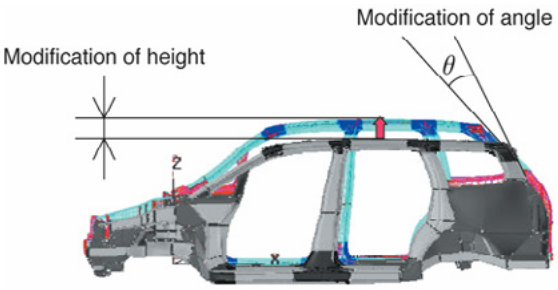


Fig. 3 Model modification using parametric technique

3. Verification of Concept Modeling

Using the analysis model created through the use of the drawing-free modeling and parametric technology, BIW performance evaluation is implemented. In this example, a verification of the concept model was carried out, by comparing it with a conventional detailed model, concerning side impact performance and body stiffness (dynamic, static).

3.1. Time Required for Model Creation

Figure 4 shows the hours taken to create a model with a modification to the concept model pillar angle. In comparison with the conventional method, there was a large reduction in the time taken when utilizing parametric technology. When implementing a frame structure study within a limited development period, it was confirmed that, in comparison with the CAD drawing based modeling technology, many more frame structure studies are possible.

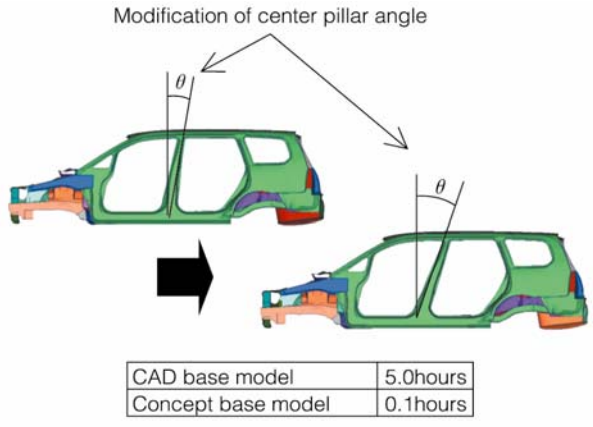


Fig. 4 Man-hour comparison for modeling

3.2. Verification of Impact Analysis

Carrying out side impact analysis using the concept model, verification was made of predictions of major deformation at impact. A comparison was made of the side impact analysis results using actual vehicle crash testing, CAD based FE models, and side impact analysis results using the concept model. When implementing the side impact analysis, a concept model was created for the body and door, and an existing model was used for the dummy and seat, etc. In order to judge the appropriateness of the analysis results, a comparison was made of three items – amount of center pillar penetration, center pillar penetration mode, and body reaction. The amount of center pillar deformation when the center pillar and the dummy come into contact is taken as the center pillar penetration amount, and the amount of deformation determined from the bend angle is the center pillar penetration mode.

Figure 5 shows the center pillar deformation results before and after side impact. Comparing the results of concept modeling and CAD drawing based modeling with results from an actual vehicle, there is good correlation between the amount of center pillar penetration and the amount of deformation determined from center pillar bend angle. Figure 6 shows the body reaction force. Comparing the body reaction force of the concept model and the CAD based model shows good correlation in reaction force values. Through these comparisons it was confirmed that by carrying out side impact analysis with a concept model it is possible to predict BIW performance.

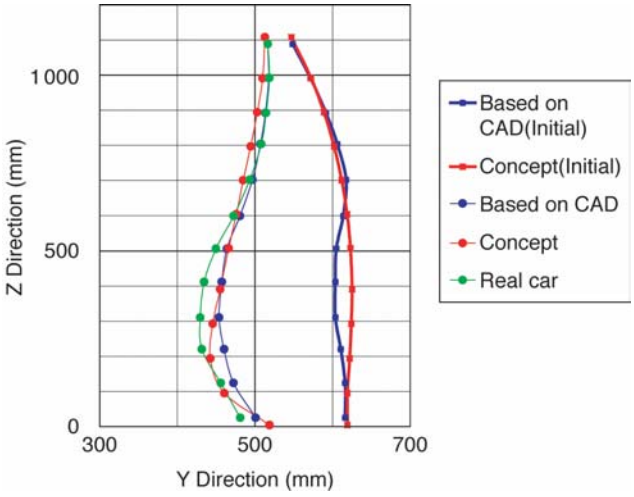


Fig. 5 Deformation of the center pillar in a side impact test and simulation results

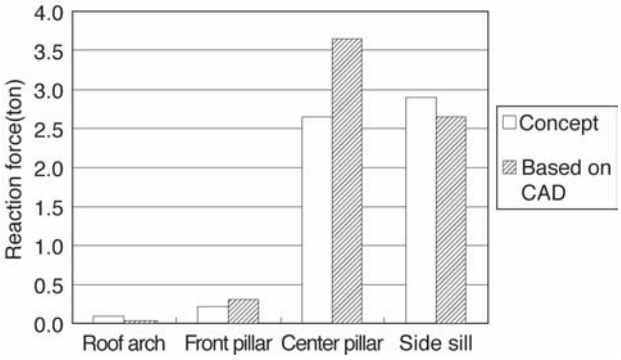


Fig. 6 Reaction force

3.3. Verification of Body Eigen Value Analysis

Carrying out eigen value analysis using the concept model, verification was made of frame characteristics predictions in the low order mode of 30 – 80 Hz. The focus on low order mode is due to the fact that its characteristics are determined by BIW. Things other than BIW, such as panel surface stiffness, etc, more often determine higher order mode characteristics.

In order to judge the appropriateness of the analysis results, eigen value analysis was carried out using the concept model and the CAD based model, and a comparison made of mode generation order and eigen value accuracy.

The results are given in Fig. 7. For both the concept model and the CAD based model, the mode generation order was the same – torsion, front lateral bending, bend, and shear bending. As for the eigen values, in comparison with the CAD based model, the concept model showed a tendency to be higher, and that difference was +14% maximum. Because the order of mode generation can be predicted, it was confirmed that it is possible to predict frame characteristics using the concept model.

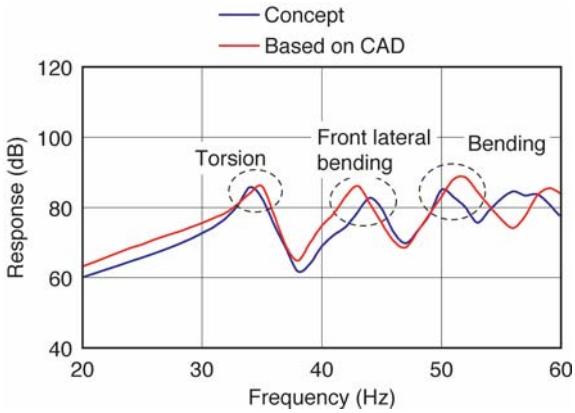


Fig. 7 Result of eigen value analysis

3.4. Verification through Body Static Stiffness Analysis

A comparison of bend and torsion body static stiffness was made, between values measured on the vehicle and values calculated from the CAD drawing based model and the concept model. The results are given in Fig. 8. For both bend and torsion stiffness, the concept model calculated values showed a tendency to be higher than the vehicle measurements and the CAD drawing based model. As shown in Fig. 9, the CAD drawing based model more accurately expresses the vehicle shape, while in contrast the concept model intentionally simplifies the detail shape expression, so the calculated values become higher.

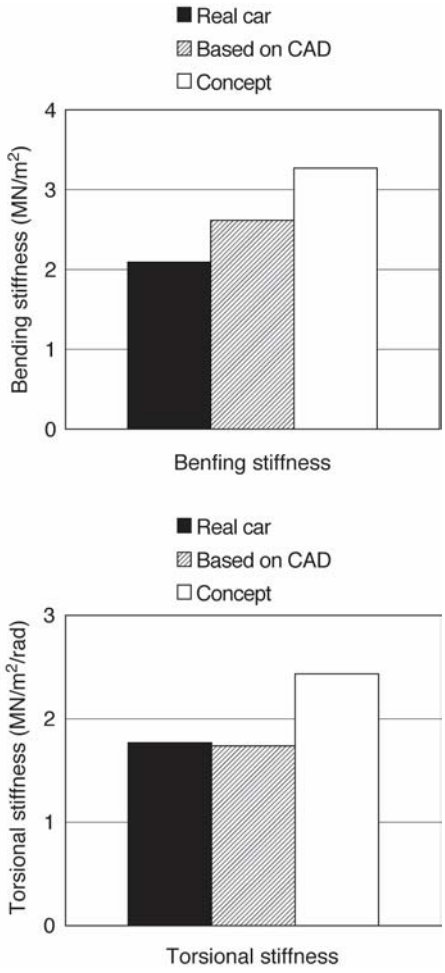


Fig. 8 Comparison of static stiffness with real car

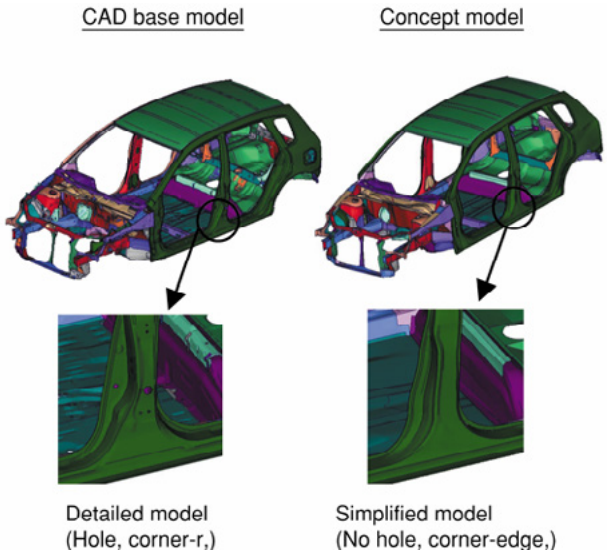


Fig. 9 Comparison of detailed CAD base model and concept model

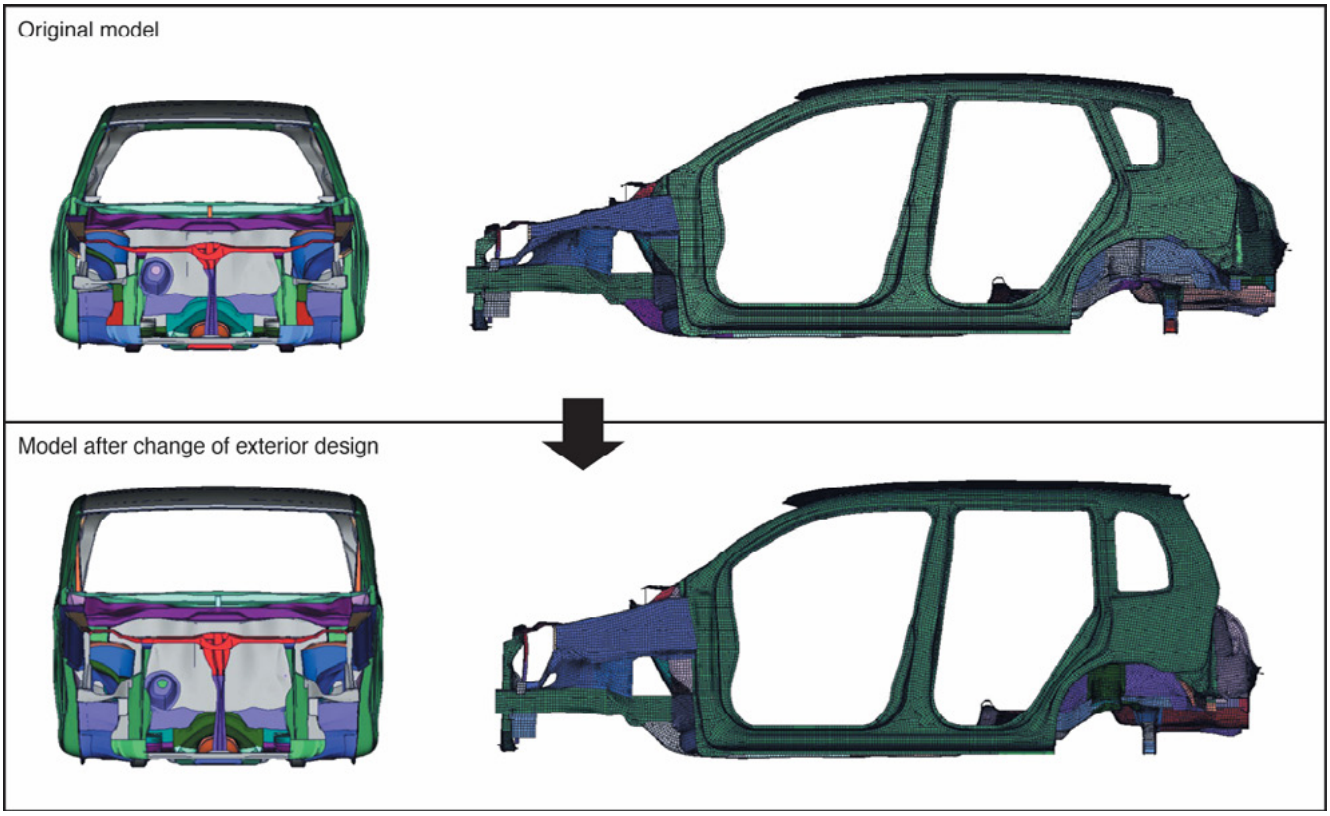


Fig. 10 Original model and model after change of exterior design

4. Examples of Application in Development

This technology was applied to a vehicle with a common BIW platform. A base model was created, using parametric technology then, the model is changed to incorporate the exterior design. The model incorporating external design is updated in a frame structure study model which reflects each pillar and side sill's section shape, fully considering the packaging. Figure 10 shows the original model and the model after the design changes. Figure 11 shows a comparison of section shapes, between the frame structure study model and the original model.

Using the three concept models above, a performance prediction analysis was carried out for side impact, eigen values and body stiffness. The effect of exterior design and section shape changes on BIW performance was determined.

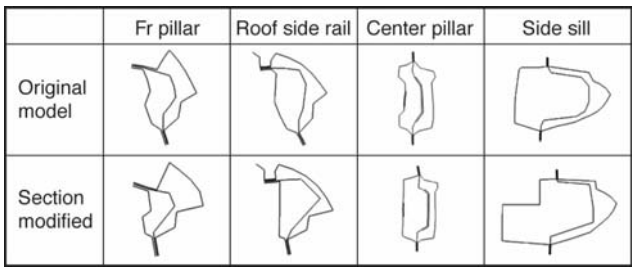


Fig. 11 Sections before and after modification

4.1. Application to Side Impact Analysis

Figure 12 shows the amount of center pillar penetration obtained through analysis, and Fig. 13 shows the displacement amount determined from the center pillar penetration bend angle. Due to exterior design changes, the center pillar penetration amount increased, and the displacement amount determined from center pillar penetration bend angle increased. Due to section shape changes, the center pillar penetration amount further increased, and the displacement amount determined from center pillar penetration bend angle increased.

According to this model's side impact analysis results, the cause of the amount of center pillar penetration is estimated, a model is created that implements section changes, and analysis is carried out. These results are included in Fig. 12 and Fig. 13. Due to the countermeasures, in comparison with the original model, the amount of the center pillar penetration is reduced, and the displacement determined from center pillar penetration bend angle is increased. From the results, BIW performance against side impact is expected to be equivalent to the original vehicle, or better.

4.2. Application to Eigen Value Analysis

Next, the results of eigen value analysis are shown in Fig. 14. As for transmission characteristics, the rear floor frame end vertical response is shown for the original model and the frame structure study model.

From analysis results, it is expected that there will be a dramatic worsening of rear torsion mode in comparison with the original model, as shown in Fig. 15. As a result of making countermeasures, it was learned that improving tailgate opening stiffness is effective, and so a model was created with countermeasures to improve tailgate opening stiffness, and an eigen value analysis carried out. The results are shown in Fig. 16. It was confirmed that by making section changes, the rear torsion mode was improved to be equivalent to a vehicle having the original model platform.

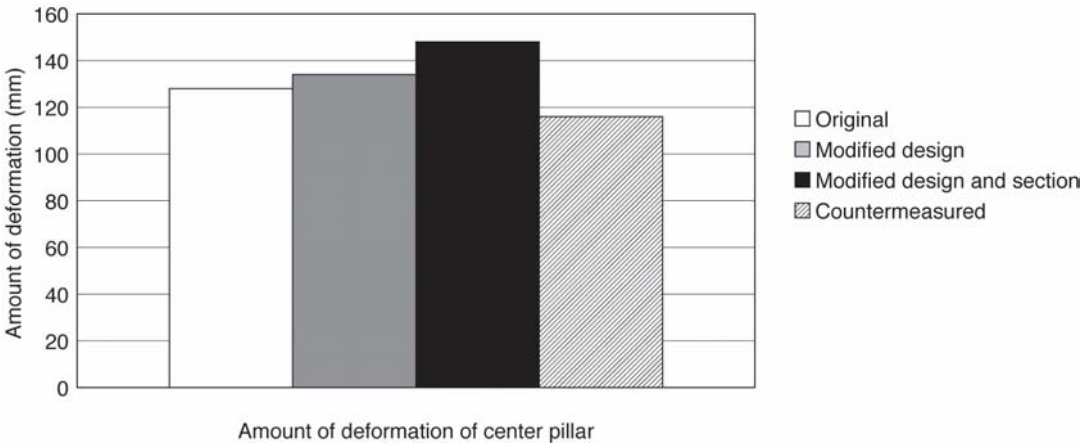


Fig. 12 Result of analysis of amount of deformation

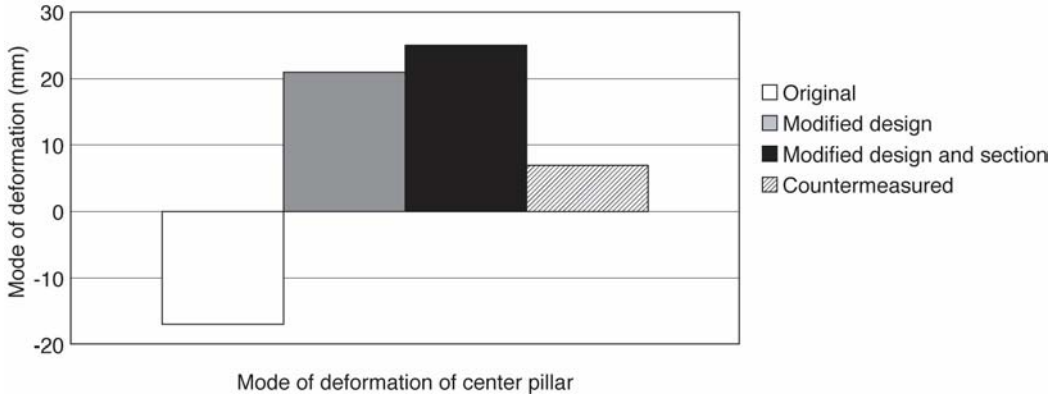


Fig. 13 Mode of deformation results

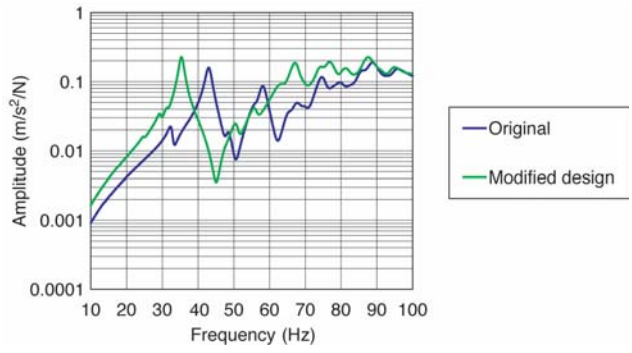


Fig. 14 Response of rear floor frame end

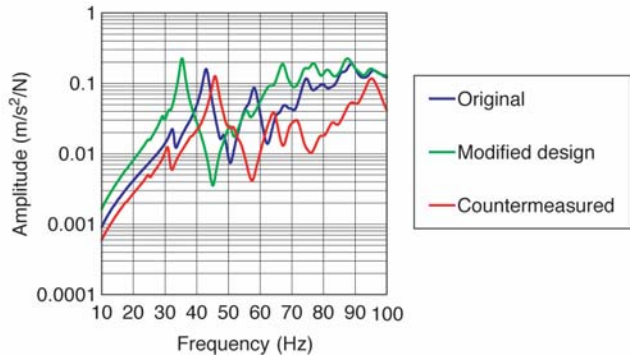


Fig. 16 Response of rear floor frame end after modification

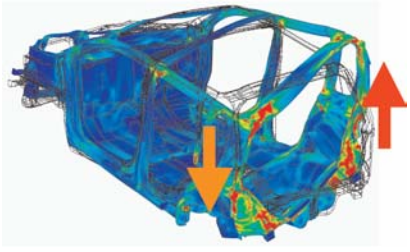


Fig. 15 Rear torsional mode

4.3. Application to Vehicle Static Stiffness Analysis

The static stiffness analysis results are given in Fig. 17. With the model incorporating exterior changes with respect to the original model, it was learned that both the bending and torsion were lower. Due to the section shape change and tailgate opening stiffness improvement countermeasures, it was confirmed that stiffness is improved and that it is equivalent to models with the original platform.

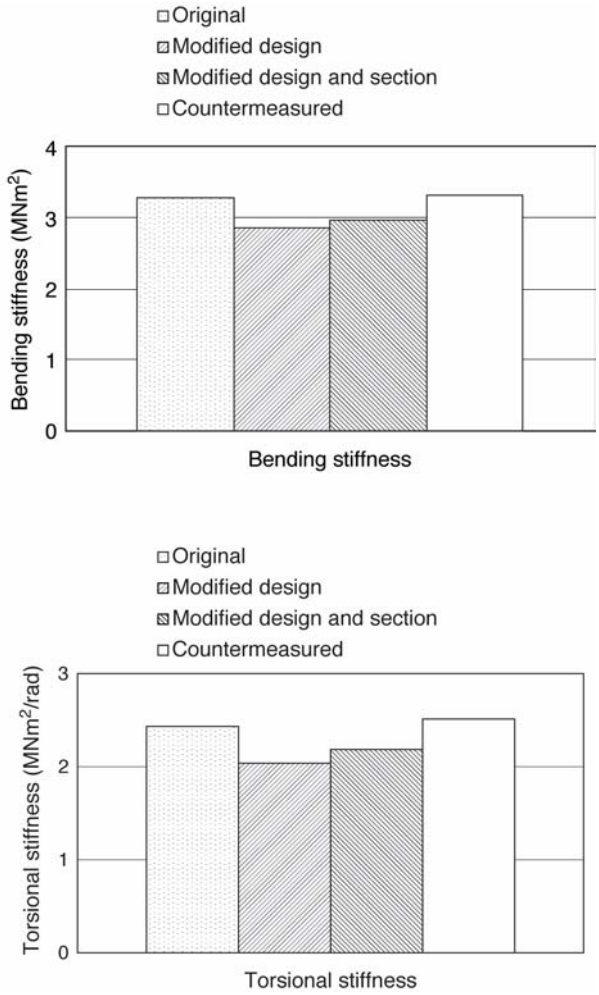


Fig. 17 Static stiffness of concept models

5. Summary

The following results were obtained through the development of CAE technology that uses concept modeling.

(1) Using drawing-free parametric model technology, it is possible to make CAE BIW performance predictions for side impact, eigen values, and stiffness, at the BIW concept stage before CAD drawings are created. A frame structure can then be made into a CAD drawing, having the performance predicted by CAE.

(2) By applying structural analysis at the same time as design studies, it is possible to make repeated performance analyses, with a variety of frame structure proposals concerning BIW structures which greatly affect vehicle development, leading to the appropriate frame structure.

References

(1) Zimmer, H., Hovelmann, A., Schmidt, H., Umlauf, U., Frodl, B., Hanle, U.: Concept development tool Flexible generation of parametric virtual Prototypes in car body design, VDI Report Nr. 1559-2000

(2) Schelkle, E., Elsenhans, H. H.: Integration of Innovative CAE-Tools in the Concept Stage of Vehicle Development, VDI Report Nr. 1559-2000

■ Authors ■


Takayuki FUJII


Shigeo FUJITA


Yasushi YOSHIZAWA

Analysis of Suspension Characteristics Considering the Elastic Deformation of Parts

Makoto TSUKAGOSHI* Takuya SHUDO*

ABSTRACT

Taking the elastic deformation of parts into account in calculations to simulate the characteristics of suspension alignment was confirmed to improve prediction accuracy. Taking the elastic deformation of the main elements of the overall suspension, the sub-frame, and the body into account made it possible to accurately determine the side force compliance at the tire contact point with the ground, and also to clarify the contribution made by each of those parts. Development of an elastic body modeling method that accounts for significant deformation made it possible to improve the accuracy of alignment prediction, even in parts such as the twist beam axle that undergo significant deformation. Software was developed to assist with design analysis so that these prediction methods could be utilized in practical design work.

1. Introduction

Multi-body simulation software used to be employed for analysis of alignment characteristics when designing suspension geometry. Since the use of multi-body simulation software by designers imposed a heavy data origination load, a simple data entry tool for use by designers was developed. This made it a simple matter to perform analysis of alignment characteristics by inputting the coordinates for the main suspension points and the non-linear spring characteristics of the bushings.

The model for multi-body calculation up to this time, however, considered all suspension parts to be rigid bodies. Thus the elastic deformation of parts was not taken into consideration, and this is known to result in discrepancies between alignment calculation results and actual measurements.

Here, an elastic body model of suspension parts, sub-frame, and body have been incorporated into a multi-body model, and analysis of alignment characteristics has been carried out that takes elastic deformation into account. The prediction accuracy and the contribution of each part have also been verified.

This article reports on modeling techniques developed for practical application of these methods in vehicle development and software developed to assist in design through improved analysis and easier modeling.

2. Coupled Simulation of Multi-Body and Structure

2.1. Overview

Deformation and stress calculations for an elastic body utilize the finite element method, which segments the model geometry into small areas and couples together the load and the deformation for all adjacent small areas. However, the application of this finite element method just as it is for elastic bodies in a multi-body model introduces practical disadvantages. That is, the multi-body model calculates objects that move along a time history, regardless of whether

* Tochigi R&D Center

those objects are static or dynamic. Consequently, this model must calculate the deformation state of an elastic body at every step in the calculations. The amount of calculation becomes enormous, making practical turn-around impossible. Current multi-body simulation software therefore uses the modal synthesis method as a means of incorporating an elastic body into a multi-body model.

2.2. Modal Synthesis Method

The elastic deformation of members can generally be expressed by superposing the eigen modes of those members. In order to express local deformation, however, it is necessary to incorporate an extremely large number of eigen modes, including even high-frequency components. When the load input points are clearly defined, as in the case of suspension members, it is known that accurate expression, even down to local deformation, is possible by super positioning deformation modes for input to those points (in other words, the static correction mode) with a relatively small number of eigen modes(1). This method corresponds to the constrained mode method, one of the sub structuring methods used primarily for vibration analysis. Use of this method makes it possible to reduce the number of degrees of freedom significantly, from the several tens to hundreds of thousands of degrees of freedom found in an FEM model, to a number of degrees of freedom equal to just the number of modes employed in the model.

2.3. Mode Selection

Free oscillation caused by inertia does not occur in the static calculation of dynamic equilibrium used for analysis of suspension characteristics. It was expected, therefore, that the elastic deformation of members could be fully expressed by the superposition of static correction modes for all load input points. Two analyses were carried out in order to confirm this. First, an analysis was done of the knuckle and lower arm of a double-wishbone suspension modeled as an elastic body using only the static correction mode. This was compared with analysis using the normal mode from the lowest to the third order simultaneously to determine whether any difference appeared in the alignment variation. Figure 1 shows the change in the toe angle when lateral force is applied at the ground contact point. It was confirmed that there was no difference in either case, and the same was also true of other characteristics.

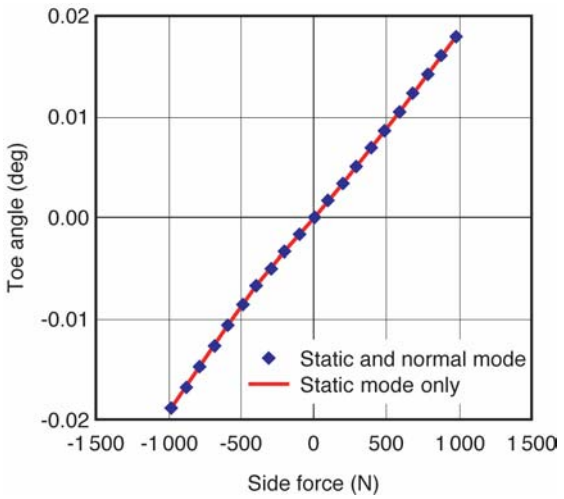


Fig. 1 Comparison of alignment

Next, an analysis was done using only a static correction mode with a four-wheel model that had a double-wishbone front and multi-link rear suspension. The body, sub-frame, and main suspension were treated as members of an elastic body. This was compared with a simultaneous analysis using eigen modes up to 100 Hz to determine whether there would be any differences in the displacement at the points where suspension members were attached to the body. Figure 2 shows the displacement at attachment points when lateral force is applied at ground contact points. It was confirmed that there was no difference in either case.

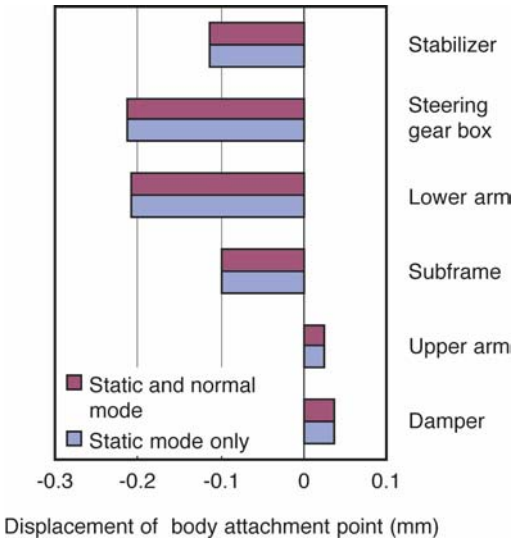


Fig. 2 Comparison of displacement

3. Verification of Prediction Accuracy

3.1. Comparison of Prediction With and Without an Elastic Body

Alignment characteristics were verified using a suspension that included arms functioning as elastic bodies. Figure 3 shows a comparison of the longitudinal force against toe angle when the arms are modeled as elastic bodies versus being modeled as rigid bodies. Likewise, Fig. 4 shows a comparison of the lateral force against toe angle.

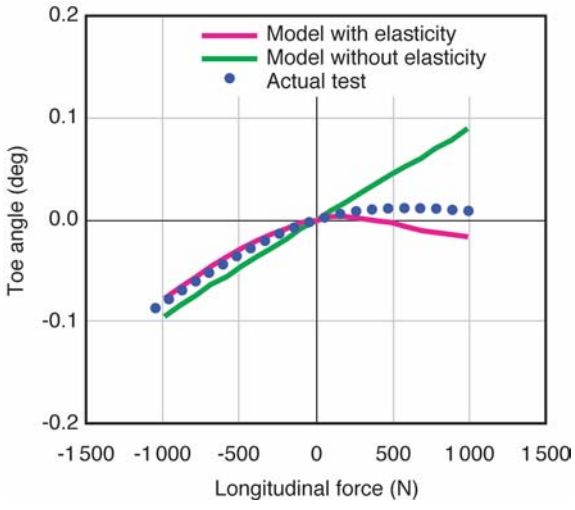


Fig. 3 Comparison of toe angle vs. longitudinal force

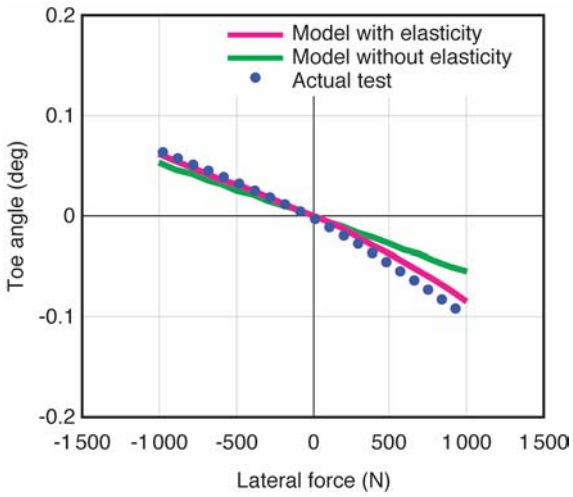


Fig. 4 Comparison of toe angle vs. lateral force

The model with arms as rigid bodies shows a straight-line rate of change. By comparison, the model that incorporates elastic bodies shows the characteristic varying with the direction of the longitudinal force, just as seen in the actual measurements. This is thought to result from the change in the balance between the bushing deflection and the variation in the elastic body caused by the difference in the spring stiffness when the bushings are pulled forward and backward.

3.2. Comparison of Differences in Elastic Body Rigidity

It is known that weight reduction measures for suspension parts, through change in thickness or shape, affect the alignment characteristics. Therefore the rigidity of the elastic bodies was varied and the changes in the characteristics were compared and verified. Modifications were made so that the change in rigidity would be significant in order to produce a distinct variation relative to the base. Comparison of alignment characteristics was performed with similar modifications also made to the model. Figure 5 shows the comparison of longitudinal force against toe angle. Figure 6 shows the comparison of lateral force against toe angle.

The results confirmed that the degree of effect on alignment characteristics, caused by different rigidity in elastic parts, was faithfully reproduced.

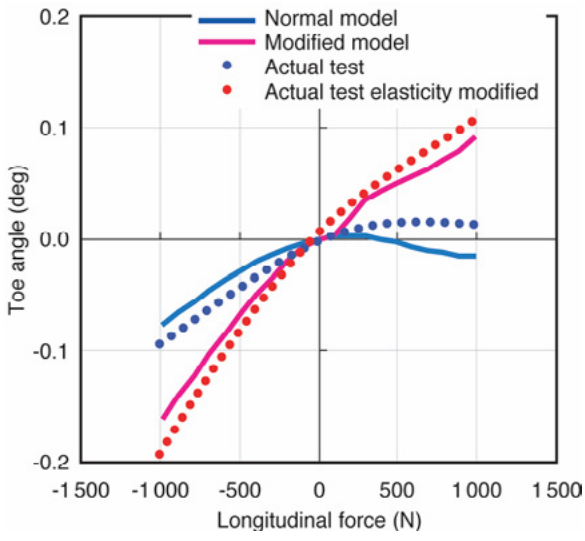


Fig. 5 Comparison of toe angle vs. longitudinal force

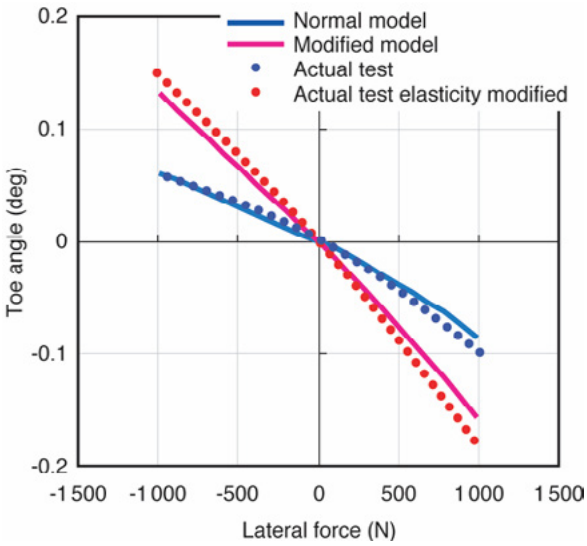


Fig. 6 Comparison of toe angle vs. lateral force

3.3. Verification of Prediction Accuracy for Lateral Stiffness at Tire Contact Point

The lateral stiffness at the tire contact point is considered affected by elastic deformation in the body and sub-frame. The accuracy of calculation of this stiffness was verified and the contribution made by the rigidity of the different parts was analyzed.

Lateral stiffness at the tire contact point is one index used in feeling tests that is considered affected by the vehicle cornering response. The measurement is made by attaching metal discs that can be treated as rigid bodies in place of the tires and measuring the lateral displacement that occurs when lateral force is applied at a location corresponding to the ground contact point. Therefore this only measures the vehicle characteristic and does not include the deformation of the tires.

Conceivable factors in displacement are the deflection of the suspension bushing and sub-frame mount bushing, elastic deformation of suspension members such as knuckles and arms, and local and overall elastic deformation of the sub-frame and body. The present model included all the suspension arms, the sub-frame, and the body as elastic bodies. Figure 7 shows a general view of the model.

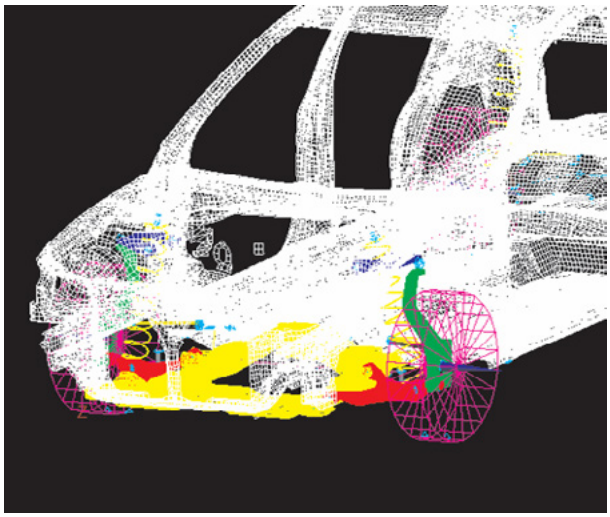


Fig. 7 Simulation model including elasticity of body, sub-frame and suspension

The verification confirmed that the results from the model incorporating the elastic body were much closer to the actual measurement than the model taken as a rigid body. Figure 8 shows the lateral displacement of the ground contact point in relation to the lateral force in the front suspension. The size of the contribution made by individual components could also be confirmed by adding elastic bodies, one by one, to a model that had contained no elastic bodies, then tracking the changes in displacement with each addition.

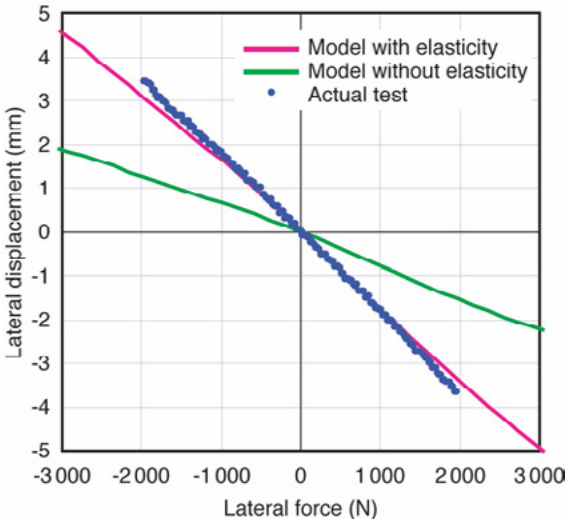


Fig. 8 Lateral compliance of front suspension

3.4. Modeling a Twist Beam Axle

When the left and right wheels stroke in alternate mode with a twist beam suspension, a large torsion deformation is caused in the beam components. The FEM model assumes a small and linear deformation, and in the case of a major deformation such as this, the small deformation is expanded linearly from its initial position. Therefore, as shown in Fig. 9, the resulting deformation mode differs radically from the actual deformation. Consequently, it is insufficient merely to model these components as elastic bodies. A method of modeling was therefore used that segments the FEM model of the twist beam axle into several parts, as shown in Fig. 10, which then rejoins them using multi-body simulation software. Figure 11 shows a general view of the model.

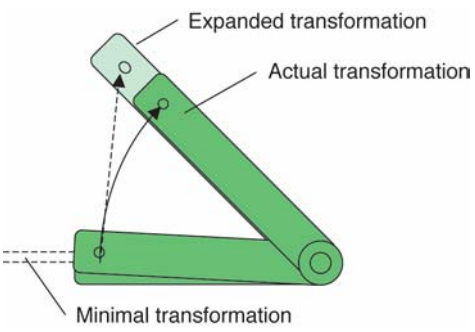


Fig. 9 Side view of twist beam axle

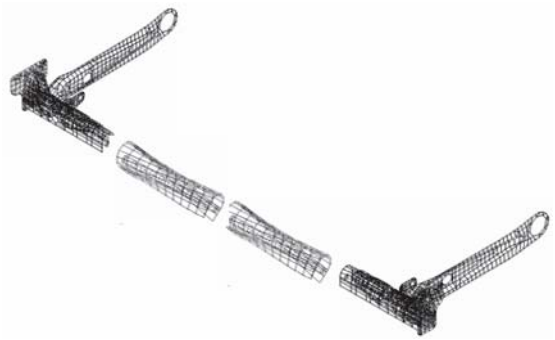


Fig. 10 Segmented FEM model of twist beam



Fig. 11 Suspension model with multi FEM segments

After calculating the static correction mode for the various segments of the FEM model, it was incorporated into the suspension model in the form of multiple separate elastic bodies. The elements on the segmented surface were then joined to each other using multi-body simulation software. This made it possible to simultaneously express the elastic deformation of components during major deformation, the independent movements of the segmented parts, and their rotational movement. It was confirmed that calculation accuracy was improved as a result. Figure 12 shows a comparison of the wheel center tracks that result with the suspension stroke in opposite phases laterally.

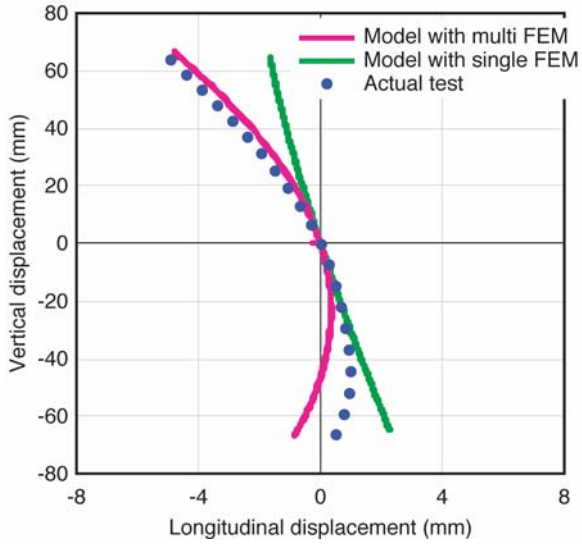


Fig. 12 Wheel center locus from side view

4. Design Assistance Software

4.1. Overview

The technique for analysis of a multi-body model that incorporates elastic bodies is extremely effective for chassis development. However, this requires the person performing the analysis to have skills in both multi-body simulation and structure analysis. Consequently, it is rather difficult for a designer without those skills to use. On the other hand, multi-body simulation of the suspension and FEM analysis of the suspension arm on its own are widely used techniques, and models using them are generated on an everyday basis. If it were possible to combine these and perform the calculations and post-processing simply and effectively, the result would be a practical analytical technique for the designer. Therefore software was developed that would automate the process of incorporating the FEM model into the multi-body model, and further carry out calculations and post-processing collectively. Figure 13 shows the overall flow of the processing. The processing flow has three major stages: (1) Pre-processing of the FEM model, (2) combination of the FEM calculations and the multi-body model, and (3) calculation and post-processing of the combined model. Figure 14 shows the software operation panel.

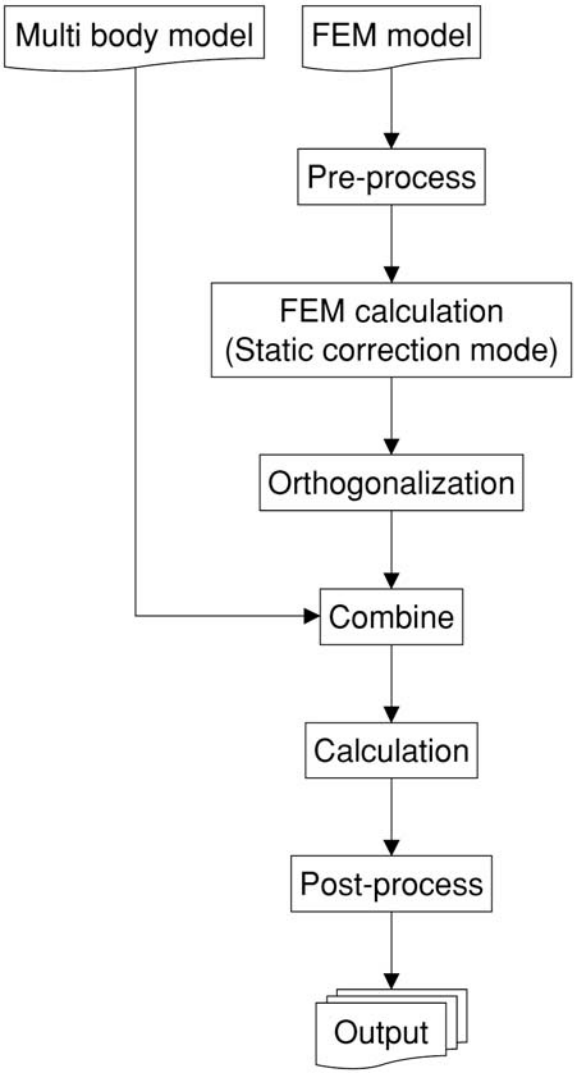


Fig. 13 Flow chart of automated process

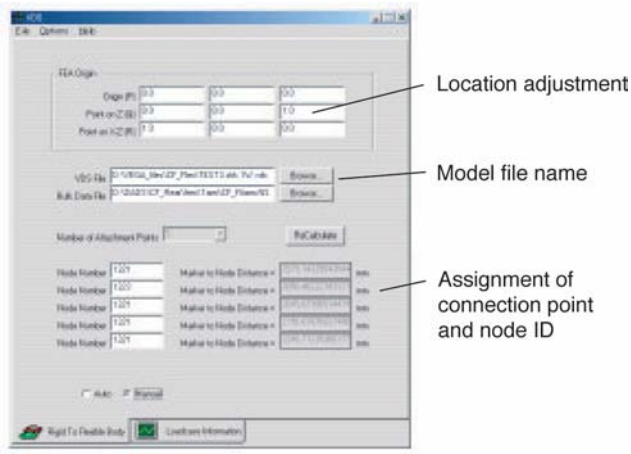


Fig. 14 Software operation panel

4.2. Coordinate Conversion and Mirror-Image Model Generation

When the multi-body model and the FEM model are combined, the reference axis systems of the original models may differ. In this case, there may be an issue if their attachment points do not match. Consequently, one or the other model must have its coordinates converted. The software converts the coordinates of the node positions of the FEM model to the coordinate system of the multi-body model. A four-wheel model will require symmetrical FEM models for the left and right pairs of wheels. Consequently, the FEM model for one side only is used to generate a mirror image FEM model for the other side.

4.3. Automatic Node ID Search and Boundary Condition Generation

When combining the multi-body model and the FEM model, the node ID information from the FEM model is required in order to define the attachment points (joints and bushings). In order to acquire these from an existing FEM model, it is ordinarily necessary to read them into FEM pre-processor and examine the node information. Some designers, however, are not familiar or comfortable with operations of FEM pre-processor. Therefore the software reads the node positions from the FEM model and compares them with the attachment point coordinate positions in the multi-body model. It automatically searches for the closest nodes, then informs the user and presents a list of them. Figure 15 shows an example of such a display. At this time, a setting is also simultaneously made for the boundary condition that is used to calculate the static correction mode from the FEM model, based on the node IDs determined here.

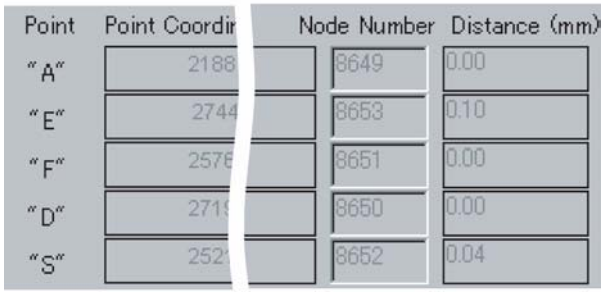


Fig. 15 Automatic search of node number connected to multi-body model

4.4. Adjustment of Attachment Point Coordinate Displacement

When the coordinate values for attachment points with the elastic bodies are to be changed during the process of design study, it is ordinarily necessary to change both the multi-body model and the FEM model. Therefore, as shown in Fig. 16, the node positions of the FEM model are automatically rewritten to match the node positions in the multi-body model by the software. As a result, it is also possible to generate models with different attachment points simply by changing the coordinates in the data input tool. This can be done without recreating the FEM model, if the range is small.

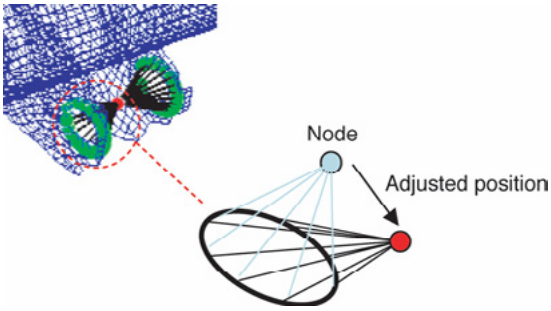


Fig. 16 Automatic adjustment of node's local position

4.5. Automatic Division of Elastic Body

When using twist beam FEM models, users specify the node IDs for the end points where segmenting begins. The software searches for adjacent nodes by following the segment surface from the end point, and takes those as the border for segmenting the model. In order to make it easier to recombine the segment surfaces afterward using the multi-body software, the nodes are organized into elements of several rigid bodies. Figure 17 shows the arrangement of the section surface.

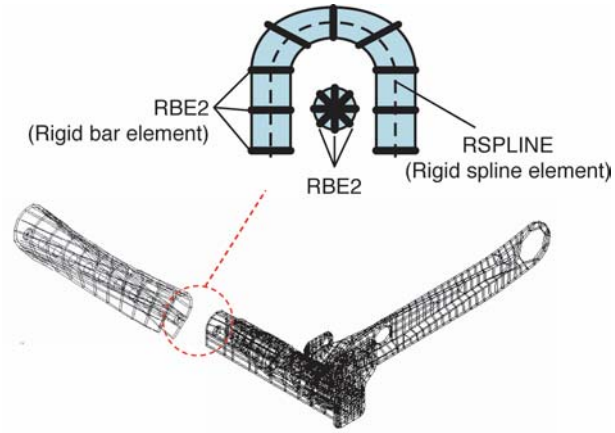


Fig. 17 Arrangement of elements at section

4.6. Automatic FEM Calculation and Model Combination

When the instruction is given to execute calculation at the stage when pre-processing has finished, operation is handed over to the FEM solver and the static correction mode is calculated. The file of calculation results is read into the multi-body software, the target rigid body components are replaced, and the combined multi-body and elastic body model is generated. Figure 18 shows an example of a combined model.

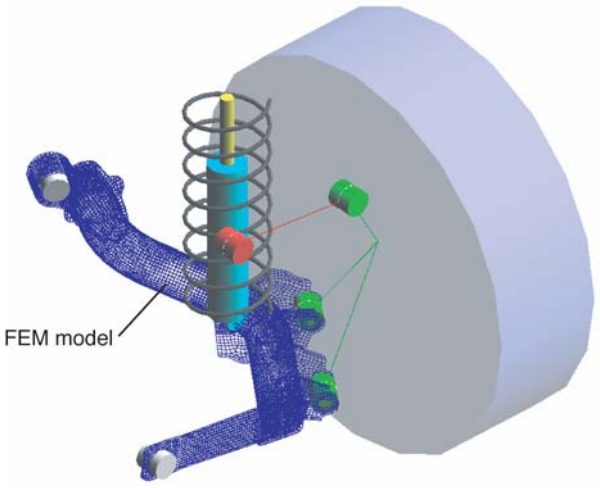


Fig. 18 Combined multi-body and FEM model

4.7. Combined Model Calculation and Post-Processing

The combined model is then handed over to the multi-body simulation solver for calculation of static time history behavior (quasi-static). After calculation, items that a designer wants to confirm can be extracted as necessary from the calculation results to generate a spreadsheet with a fixed format. This makes it easy to obtain the various kinds of tables and graphs needed for performance evaluation.

Figure 19 shows an example of the graph output.

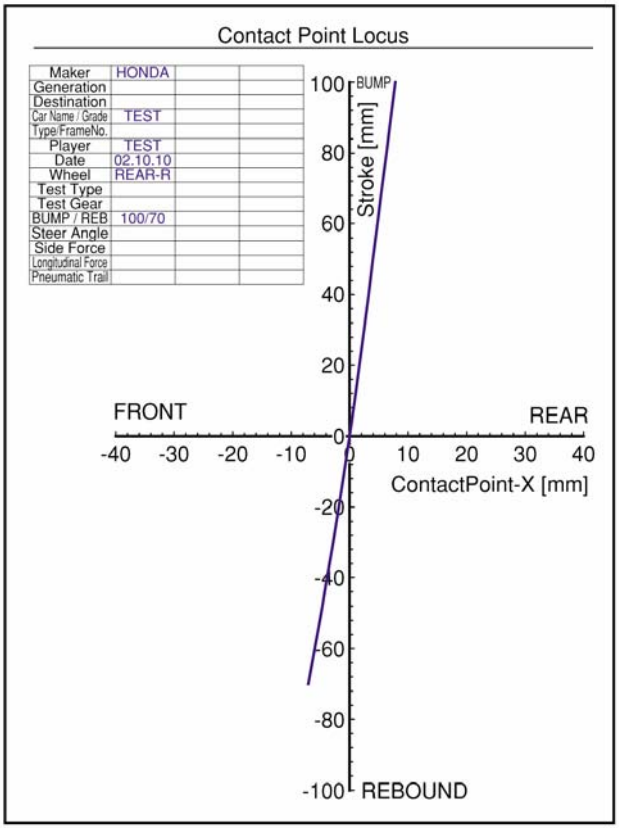


Fig. 19 Example of result output

5. Summary

It was found that incorporation of elastic bodies in the multi-body model to take elastic deformation into account significantly improves the accuracy of suspension and chassis analysis. By incorporating FEM models into the multi-body simulation software, it is possible to model characteristics contributed by lateral stiffness at tire contact point and other such rigidity of components such as the body, sub-frame, and suspension. The modeling extends to the non-linear spring characteristics of joint bushings. This makes it possible to perform calculations that simultaneously take account of the elastic deformation of the various individual elastic parts themselves, the movement of components as a whole caused by deflection of non-linear bushings, and their rotational movement. This indicates that more accurate results can be obtained by integrating multiple FEM models in a similar manner using FEM analysis software to perform calculations for a single large, linear FEM model.

A modeling technique was created that works by segmentation. It can also be used practically with conventional linear FEM models, without applying nonlinear FEM analysis techniques to the analysis of suspensions such as the twist beam type that involve significant elastic deformation. This necessitates complex, troublesome work to generate a model. However, this was made into a usable technique by developing a program that reads in the FEM models used for integration in advance, reads in and processes the attachment point information, and automatically generates a combined model.

Reference

(1) Craig, R. R., and Bampton, M. C. C.: Coupling of Substructures for Dynamic Analyses, AIAA Journal, Vol. 6, No. 7, p. 1313–1319 (1968)

■ Authors ■




Makoto TSUKAGOSHI Takuya SHUDO

Development of a Vehicle Dynamics Simulation System under a Running Mechanical Control Device

Ichiro TAKEMA* Hiroki YOKOYAMA*

ABSTRACT

A coupled simulation using concurrent execution of mechanical and control simulations was developed and applied to help predict vehicle behavior while under mechanical control. Also, a technique was developed for the automatic generation of real-time programs based on mechanical models applicable to HIL simulators, which require real-time executable calculations. This greatly eased accounting for the influence of vehicle body mechanisms in the behavior of suspensions and other systems. Thus, it is now possible to carry out “paper experimental tries” and HIL simulator tries of simulations of full vehicle behavior under the control of systems such as EPS or VSA. Formerly difficult predictions of vehicle behavior due to steering wheel torque or in non-linear regions have now become possible.

1. Introduction

During the initial stage of design of automotive suspensions, several modifications are performed to improve the steering stability and feeling of the vehicle. Many parameters are modified: stiffness of bushings, suspension mechanisms and structure, etc. Meanwhile, the functional range of vehicle mechanism control devices has been expanded with systems like electric power steering (EPS) and the vehicle stability assist (VSA) system. These contribute much to vehicle behavior.

No simulation technologies have yet been established, however, for predicting vehicle behavior while these mechanism control devices are functioning. This has restricted designers from considering the influence of the dynamic characteristics of the suspension during braking in development of related devices, for example, an ABS controller. A technique for coupled simulation of mechanisms and their controls using a simple mechanical model has been reported[(1)], but there have not been any examples of application to an automobile chassis.

In the present research, a technology enabling concurrent execution of simulations of mechanisms and controls including a hardware in the loop (HIL) simulator was developed in order to enable prediction of vehicle behavior while mechanism control devices are functioning. The results indicated that it allows consideration of the influences of the non-linear and dynamic characteristics of suspension and steering linkages on control systems.

2. Simulation Types

Two technologies were developed, for application in the appropriate methods or stages of development of the automobile control systems:

(1) Coupled simulation for mechanism controls; and
(2) Automatic generation of real-time executable programs for the HIL simulator.

Generally, when the control logic is already determined at the upper stages of development and a block diagram or other model can be made, this can be formulated and simulated off-line in a paper experimental try. Simulation (1) above is used when there is control-mechanism coupling. However, when the control logic is a blackbox, for example, or when the ECU hardware itself is to be investigated, tasks which usually occur in later stages of development, modeling must be done with an HIL simulator for the application to a

* Tochigi R&D Center

mechanism control.

Formerly, it was necessary to obtain many kinds of data in preliminary simulations and measurements in real systems in order to model mechanically coupled systems with an HIL simulator, but the tool in (2) above would enable direct incorporation of the influence of component mechanisms from design drawing information.

3. Coupled Simulation of Mechanism Control

3.1. Outline

The following describes an example of application to an EPS system as an outline of how a coupled simulation of a mechanism control is used. Figure 1 shows a schematic of the model. In the simulation software, DADS was used to model the mechanical portion (the vehicle) and MATLAB was used to model the control system. To model the EPS motor, MATLAB was used for the electrical circuitry, and DADS, for the rotor. DADS/Plant was used for transfer of the sensor signals, motor torque and other parameters in the models on both software bases, which were run concurrently.

Models of the steering torque and disturbances were created in MATLAB; noise signals, fail-safe signals and other components were also added to the latter as necessary.

3.2. Tire Model

The tire models were based on Magic Formula[(2)]. The tires exert a key influence on vehicle behavior simulations. The models and solvers were modified as necessary to allow coupled simulations.

3.3. Development of Fast Solver

A full-vehicle simulation generally includes large numbers of bushings and other components, which increase the calculation load. Therefore, in the fixed time step solver in DADS/Plant, of which a typical example is the Runge-Kutta method, it is necessary to make the sampling time, or calculation period, extremely short; this is impractical as it greatly lengthens the calculation time.

It was therefore made possible to use a solver with a variable time step for the coupled simulations. The resulting calculation times were considerably shorter than those in the fixed time step solvers, as shown in Table 1.

Table 1 Elapsed times for 5 second slalom simulation

		Fixed time step		Variable time step
Model	Number of bush	Sample time [sec]	Elapsed time [sec]	Elapsed time [sec]
A	5	0.0005	343.51	401.17
B	7	0.00025	604.06	326.22
C	30	0.00004	1962	488.54
D	63	2.00E-07	∞	662.42

3.4. Method for Creating Mechanical Model

Conventional methods for creating full vehicle mechanical models are very time-consuming; therefore, a tool was made for automatically converting the suspension model created during design to a vehicle model capable of immediate use in coupled simulations.

Figure 2 shows a screen image of the GUI. For EPS systems, the user can select between rack-assist and pinion-assist steering mechanisms. Some parameters such as the gear ratio and moment of inertia of the EPS motor are pre-determined and are added automatically. It is also possible to specify the initial vehicle speed and other run conditions for the simulation.

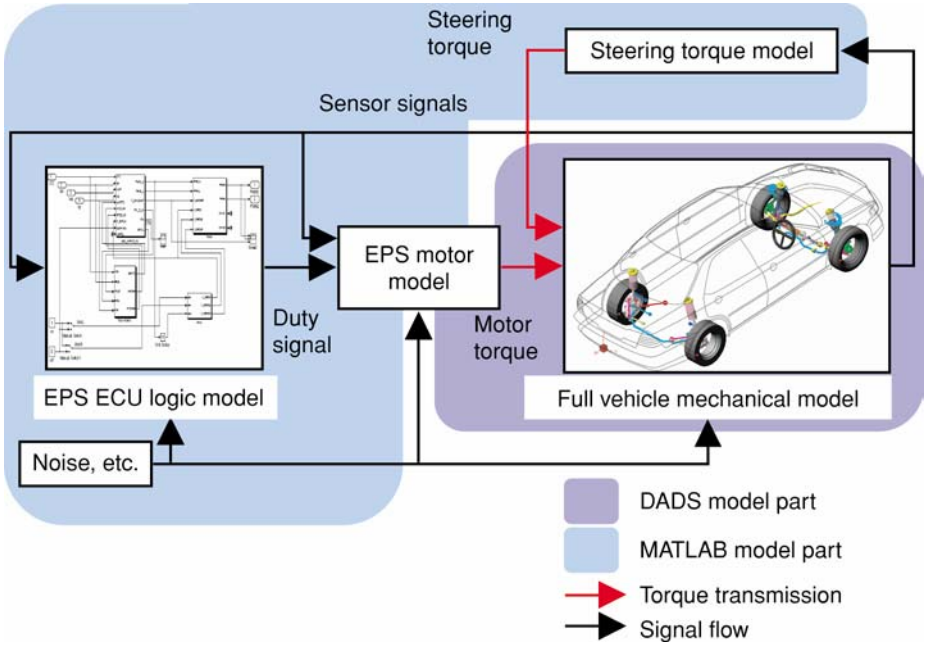


Fig. 1 System flow in coupled simulation

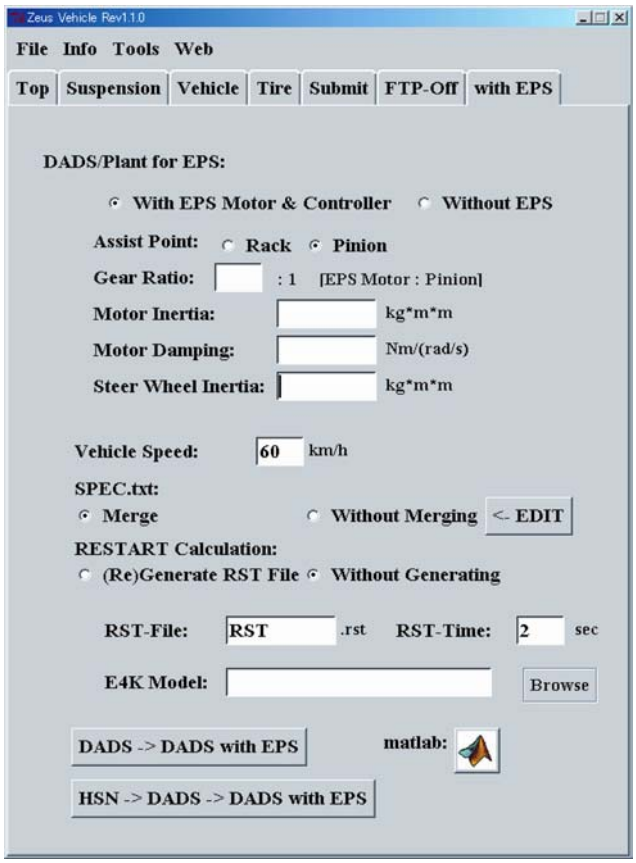


Fig. 2 Graphical user interface

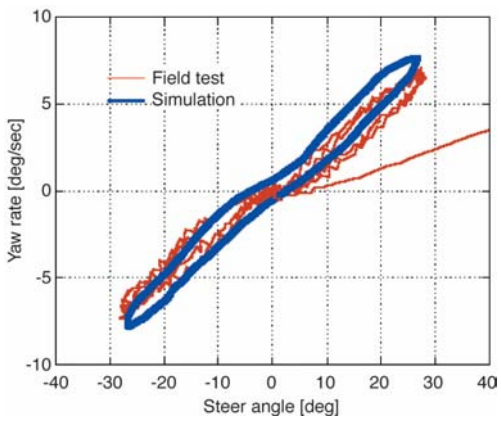


Fig. 3 Steer angle vs. yaw rate

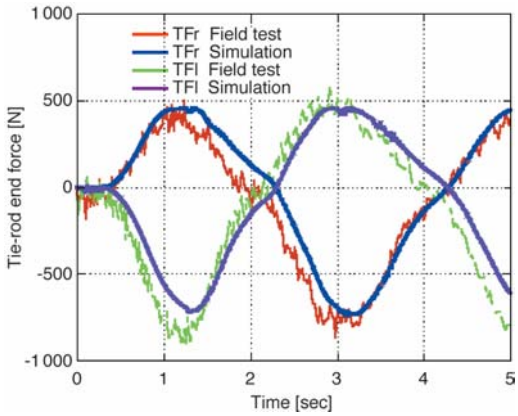


Fig. 4 Tie-rod end force

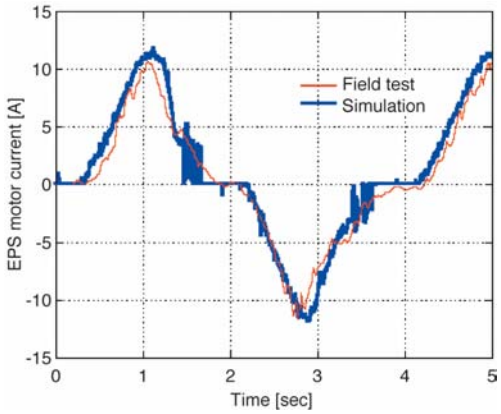


Fig. 5 EPS motor current under slalom

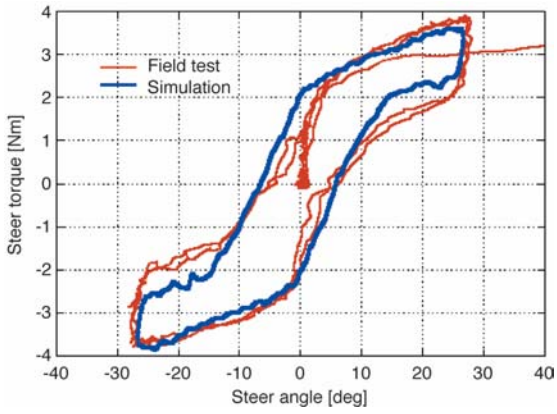


Fig. 6 Steer angle vs. steer torque

3.5. Calculation Results

This section shows some examples of comparison of the results of the coupled simulation of the mechanism control with the results in an actual car under similar conditions. The test conditions were a slalom task with a vehicle speed of 100 kph, a steering wheel angle of 30° and a steering wheel oscillation frequency of 0.25 Hz. The EPS was set at a standard mode of control.

The measured and calculated variations in yaw rate of the vehicle with steering angle are presented in Fig. 3 and a time series of the measured and calculated forces on the tie rod ends on both sides (TFl, TFr) of the vehicle are presented in Fig. 4. Both graphs of simulation results show good matches with the observed results. This method has enabled highly accurate prediction of dynamic vehicle characteristics in a full vehicle mechanical model.

Next, Fig. 5 shows the simulation and the actually observed values of the current supplied to the EPS motor during a slalom task under EPS control.

It is clear that accurate predictions were provided, even for simulations of a control system including feedback, by coupling the reaction forces from the road surface, as they are manifested in the steering gearbox, the EPS motor condition, and the ECU internal control logic.

Figure 6 shows the characteristics of the variation in steering torque with steering wheel angle during the same slalom task.

It can be verified that the observed hysteresis curves for each of the above characteristics were simulated quite well. The coupled simulations with mechanisms and control show that it has become possible to quite accurately predict not only the vehicle yaw rate but also the steering torque under EPS control.

4. Automatic Generation of Real-time Executable Programs

4.1. Outline

The overall construction of the HIL simulator used during development of a VSA is depicted in Fig. 7. The operation of the simulator is as follows. The VSA includes ABS and a traction control system (TCS)[3]. The HILS CPU in the figure performs the calculations of vehicle behavior and transmits the demand signals to the VSA ECU via an I/O board. Based on that information, the VSA ECU performs the calculations for the appropriate control actions for vehicle yawing behavior and the brake fluid pressure is fed back to the HILS CPU.

In order to perform a precise HIL simulation and to broaden the application of this method, it is essential to supply similar signals to the VSA ECU as in an actual vehicle, and to create a highly faithful model of the vehicle under conceivable driving condition.

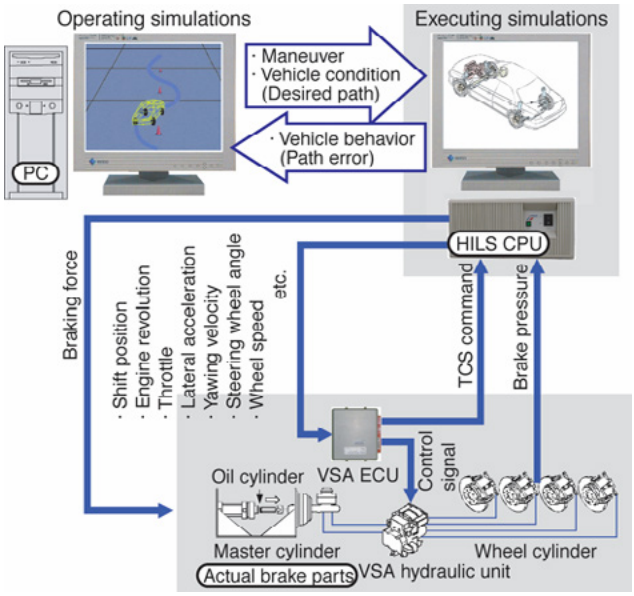


Fig. 7 Construction of HIL simulator for VSA[3]

4.2. Automatic Generation of Programs

A tool was developed for the generation of real-time executable programs capable of direct download into the HILS CPU from the mechanical model. The advantage of using an automatic tool is not only that non-linear and dynamic characteristics can be considered, but also that HIL simulation models are easily made with drawing information. This tool was used in the present research with the objective of generating a suspension linkage unit model as a MATLAB block and treating the variations in toe angle and in vertical load of tire as nonlinear functions of suspension stroke.

4.3. Model Structure

Figure 8 presents the structure of the HIL simulation model. It was based on a MATLAB model expressing the equations of motion of an automobile body with 6 degrees of freedom. In conventional models, suspension components were modeled by superposing with the toe angle map. This was replaced with the automatically generated real-time executable program shown in Section 4.2.

Also, in order to distribute the calculation load, the model was divided so as to run parallel calculations in the CPU for the left and right suspensions.

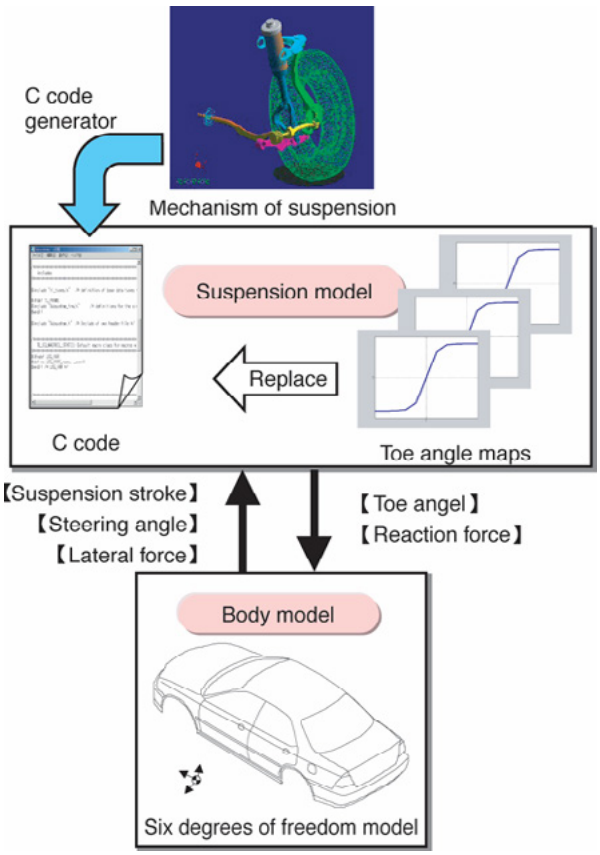


Fig. 8 Divided mechanical model

4.4. Hardware Structure

It is necessary to run the vehicle model in real time on the HILS CPU. The structure of the hardware in the HILS CPU used in this research is shown in Fig. 9.

A multi-board system with three Power PC 600 MHz boards (480 MFlops) was used as the processor board[4]. The automatic generated programs were installed on each of the boards. This structure enabled real-time calculations for this model, with a distributed calculation load.

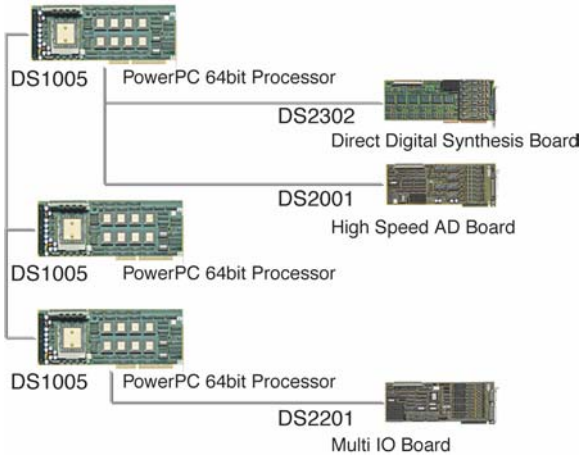


Fig. 9 Hardware layout in HILS CPU

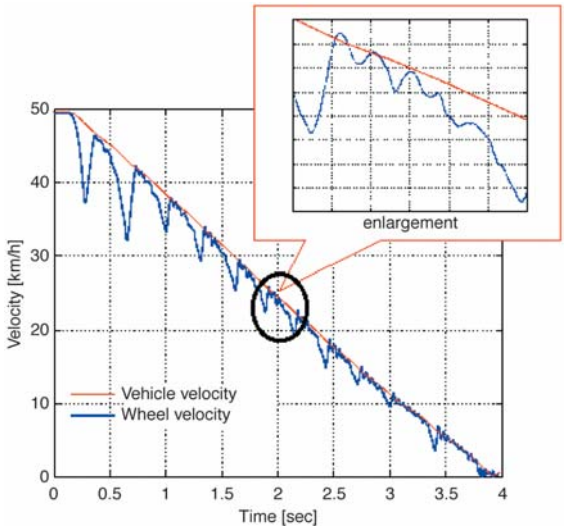


Fig. 11 Compliance vibration on mechanical HIL simulator

4.5. Results of HIL Simulator Execution

The vehicle model was set to drive in the steady state circular test for 30 m radius on a dry asphalt pavement on the conventional HIL simulator and the mechanical HIL simulator incorporating suspension linkage calculations; the results were compared with those from a vehicle test. The variation in the gains of yaw rate per steering wheel angle versus lateral acceleration, one characteristic of vehicle dynamics, is shown in Fig. 10. The red squares in the figure are the plot of results in the real vehicle, the black line is the results from the conventional simulator, and the blue line is the results with the present method.

The present model maintained good accuracy even in the lateral acceleration region above 0.5 G. Good results are shown here in automobile behavior where non-linear characteristics have a great influence, a problematic region for the conventional HIL model.

Next, a graph of the variation in wheel velocity during braking, as predicted by the HIL simulator, is shown in Fig. 11. The test conditions were entry at a speed of 50 kph on dry asphalt. ABS control was already activated at entry. The wheel velocity vibrations visible on an enlarged section of the trace in the figure appear to indicate vibrations in compliance of the tires in response to the longitudinal force; these are also seen in tests of real vehicles.

The results indicate that using the present model allows expression of the vibration characteristics of the suspension. The HIL simulator with the mechanical model can be used for considerations of dynamic characteristics.

The results of the simulation of excitation of the suspension linkage unit model, shown in Fig. 12, indicate the frequency response for longitudinal vibrations.

The resonant frequency around 15 Hz seen in the actual vehicle is reproduced here, confirming the validity of this automatically generated model for predicting dynamic characteristics.

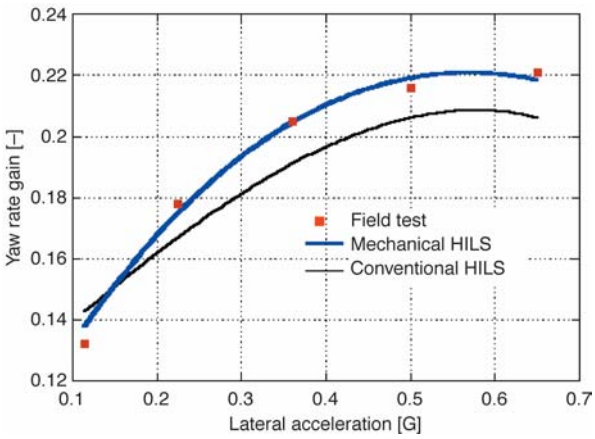


Fig. 10 Steady state circular test

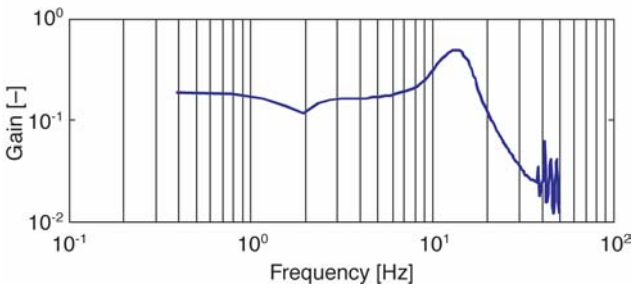


Fig. 12 Frequency response of suspension vibration on simulation

5. Summary

The following technologies were constructed and tools developed for making predictions of vehicle behavior while mechanism control devices are activated:

(1) Coupled simulation for mechanism controls

(2) Automatic generation of real-time executable programs for the HIL simulator.

It was possible to predict phenomena in the non-linear and dynamic effects of suspension and steering linkages and other components on the control system. Characteristics were also successfully predicted in relation to steering torque.

It is planned to extend this research with coupled simulation and HIL simulators to sophisticated vehicle control devices, such as steer-by-wire.

6. Acknowledgements

The authors extend their deep gratitude to Bill Prescott and Marcio Tokita of LMS International for their cooperation in this research.

References

(1) Hyon, S., Mita, T.: Simulation of Hopping Motion of One-legged Running Robot “Kenken” using DADS/Plant and SIMULINK, MATLAB & Partner Expo 2002

(2) Baker, E., Pacejka, Hans B., Lidner L.: A New Tire Model with an Application in Vehicle Studies., SAE Paper 890087

(3) Ohba, T., Takema, I., Minami, Y., Yokoyama, H.: Application of HIL Simulations for the Development of Vehicle Stability Assist System, SAE Paper 2002-01-0816

(4) Gehring J., Schutte, H.: A Hardware-in-the-loop Test Bench for Validation of Complex ECU Networks, SAE Paper 2002-01-0801

■ Authors ■



Ichiro TAKEMA



Hiroki YOKOYAMA

Development of a Lightweight CFRP Hood and Rear Spoiler

Yasuo YAMANE* Tomohiro SAKURABA*

ABSTRACT

A carbon fiber-reinforced plastic (CFRP) hood and rear spoiler were developed to achieve weight reduction in vehicle body parts. In addition to its low weight, CFRP's moldability shared by other polymeric materials allows a high degree of styling freedom. It was possible to integrate undercut areas with sections of varying thickness to achieve the required functional characteristics without an increase in weight. Utilizing CFRP instead of aluminum for the hood has enabled integral molding of aerodynamic air ducts, and bonding of the skin and frame with adhesives has increased the section modulus of the entire hood, making it approximately 30% lighter. Forming the rear spoiler from CFRP rather than sheet molding compounds (SMC) has enabled the undercut section, composed of numerous curved surfaces, to be formed as a monolithic structure without the necessity of joining separate parts. Thus, a reduction in weight of approximately 40% versus the '93 model has been achieved, despite the increase in size.

1. Introduction

Reducing vehicle body weight is an effective means for reducing automotive fuel consumption which is one of many ways to address global environmental issues. In applying lightweight materials to vehicle bodies, efforts are being made to increase the application rate of high tensile strength steel sheets. On the other hand, the adoption of all-aluminum bodies has achieved significant weight reductions for some small-scale production vehicles that emphasize either lower fuel consumption or for dynamic driving performance. Amidst these circumstances, there have also been numerous cases of weight reduction using plastic body panels. Reports of outer panels using reinforcing fibers include a hood made of a sheet molding compound (SMC)[(1)] which is a type of glass fiber reinforced plastic (GFRP), and large-sized GFRP outer panels for small-scale production vehicles[(2)]. Thermoplastic fenders[(3)] are reported as an example of outer panels using non-reinforced materials. Plastic materials thus far have had a small specific modulus, which has limited its scope of application compared to aluminum materials. Therefore, attention was given to the application of higher modulus carbon fiber reinforced plastics (CFRP) that are widely used in the aerospace or racing car fields in which weight reduction ranks as one of the most important elements.

However, there are few successful applications of CFRP materials to automotive parts in the high production volume vehicle arena. Additionally, there are uncertainties regarding the weight reduction effects, collision safety, durability and product performance of CFRP based applications. This paper describes the development of a lightweight CFRP hood and rear spoiler which are superior to aluminum parts for small-scale production mass sales vehicles.

2. Development Aims and Approach

Materials with a superior specific modulus are applied as efficient materials for weight reduction of automotive parts. Figure 1 shows the weight reduction effects with equivalent surface stiffness for typical automotive materials. Using a steel sheet as a basis, this figure shows that weight reduction effects of approximately 40% can be expected for SMC, approximately 50% for aluminum, and approximately 67% for CFRP. Note that the flexural modulus of the CFRP laminate used in this figure is the value for a quasi-isotropic

* Tochigi R&D Center

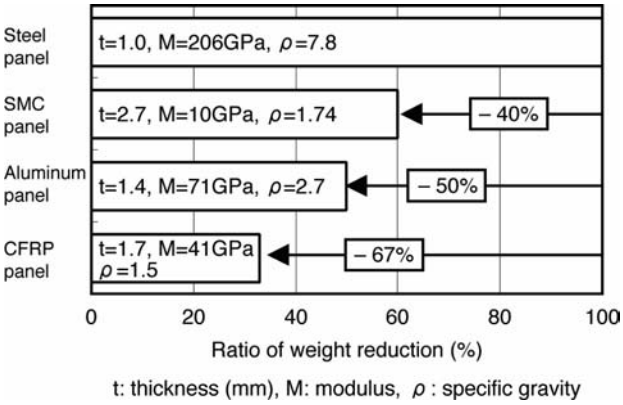


Fig. 1 Weight reducting effect with equivalent surface stiffness

laminate (in-plane isotropic of modulus)[4].

In addition, although CFRP are plastic materials with a high degree of molding freedom, they also exhibit brittle failure. Therefore, the following goals were set for this development.

1) Achieving weight reduction by integrated molding without adding elements for joining other parts which are a factor increasing weights even for complex shapes such as hoods with aerodynamic air ducts and rear spoilers with multiple undercut sections.
2) Ensuring collision safety equivalent to metal parts.
3) Ensuring durability and marketability equivalent to metal parts.

3. Material Properties

3.1. Material Specifications

The molding materials used were HTA-3K plain fabric cloth W3101/Q195 comprised of carbon fiber (CF) as a reinforcing fiber and epoxy resin, and a W3802/Q195 prepreg (an intermediate base material consisting of reinforcing fibers impregnated with resin in the semi-hardened state) with aramid fiber (AF)[5] which is resistant to shocks woven into the fabric. (Both materials were manufactured by TOHO TENAX Co., Ltd.)

The modulus of fiber direction (E11) of CFRP which is an anisotropic material exhibits the maximum value in the 0° direction and a value of approximately 10% in the 45° direction. Similarly, the shearing modulus (G12) exhibits the maximum value in the 45° direction and a value of approximately 10% in the 0° and 90° directions. Figure 2 shows an example of HTA-vf60% (volume fraction). Product development hypothesizes the load input from all directions, so a quasi-isotropic laminate is used as the basic structure, and a stack of reinforcing cloth materials are added in accordance with the required product functions.

3.2. Stacking Scheme and Material Properties

The hood used the stacking scheme described below to achieve both thinness for weight reduction and the required product functions.

The basic hood skin structure had a total of six layers, of which four layers were a quasi-isotropic laminate of CF cloth in order to ensure even surface stiffness for waxing and other work, and the center two layers were a 2-layer prepreg

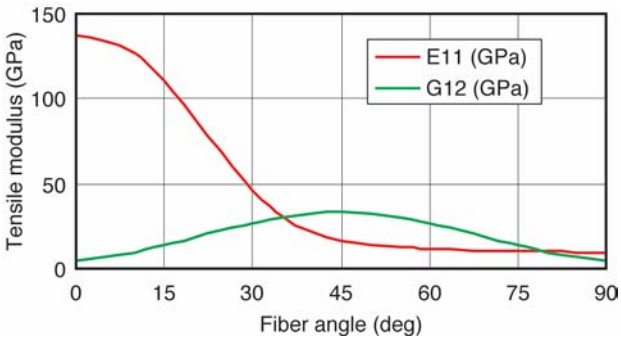


Fig. 2 Anisotropy of CFRP

laminate with AF woven in the ±45° direction. This stacking scheme was strong in the ±45° direction, but easily damaged by collision input from the front, so the AF layers prevented scattering in the event of collision. In addition, the hood frame had a total of four layers consisting of two CF cloth layers each in the 0° and 90° directions. This emphasized strength in the longitudinal direction to cope with light collision input, and the design shape ensured the optimum torsional rigidity when opening and closing the hood. In addition, an AF woven prepreg was also stacked for the same purpose as the skin.

The rear spoiler had a basic structure with a total 4-layer quasi-isotropic laminate, but 0° and 90° layers relative to the aerodynamic flexural direction were added to the center wing portion to increase the rigidity.

Table 1 shows the stacking scheme and basic properties of the hood and rear spoiler.

Table 1 Typical properties of several parts

		Hood skin	Hood frame	Rear spoiler
Stacking sequence		[±45/0,90/ ±45 (CF/AF)]S	[0,90/ ±45 (CF/AF)]S	[±45/0,90]S
0°, 90°	Flexural modulus (GPa)	30	26	45
	Flexural strength (MPa)	890	850	1 300
±45°	Flexural modulus (GPa)	41	14	45
	Flexural strength (MPa)	1 150	450	1 300
Fiber content (vol %)		50	50	50

3.3. Material Properties of Stacking Overlaps

In laminates using cloth-woven prepregs, the textile width is approximately 1,000 mm, so when molding parts exceeding that width the prepregs must be lapped to avoid a drop in the physical properties. However, using a long lap length increases the amount of materials used, which leads to an increase in the weight. Therefore, the optimum lap length value was obtained by performing tensile shearing tests using a 25 mm wide test piece with varying lap lengths to minimize the increased weight. Figure 3 shows the stack section, and Fig. 4 shows the test results. Based on these results, the lap length in the stack was set in the range of 10 mm to 15 mm.

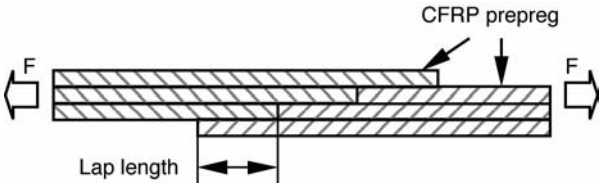


Fig. 3 Shearing testing

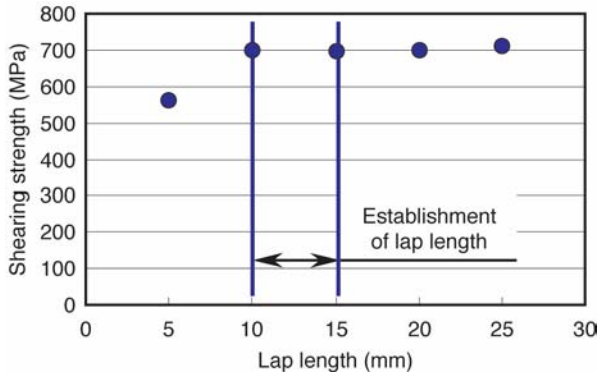


Fig. 4 Lap length vs shearing strength

3.4. Creep Properties of Metal Mounts

Composite laminate materials have a larger coefficient of thermal expansion than metal materials in the transverse direction (the direction perpendicular to the plate). Therefore, bolt loosening due to thermal creep is an issue when using steel bolts in the fastenings. Table 2 shows the coefficients of thermal expansion for metal materials and CFRP laminate.

Table 2 Coefficient of linear thermal expansion

Material		CLTE (°C⁻¹)
Steel		11.6 × 10E-6
Aluminum		21 × 10E-6
CFRP (vf 50%)	(vertical)	40 × 10E-6
	(horizontal)	0.1 × 10E-6

CFRP laminate has a coefficient of thermal expansion approximately twice that of aluminum in the transverse direction. Therefore, the thermal creep performance of CFRP laminate and the corresponding portion of a mass produced aluminum hood frame were compared through the following test. CFRP laminates molded to a thickness of 2.0, 2.9 and 3.7 mm were clasped between 90 × 25 × 2.0 mm stiffener plates which is the size that can be applied to parts in order to lower the surface pressure on the fastening, and clamped with M6 bolts at 7 N·m and 12 N·m which are the upper and lower limits of the prescribed torque. For comparison a 2.0 mm aluminum plate was clasped between 18 mm diameter washers for M6 and clamped in the same manner as the CFRP laminate. A hot-cold cycle load of –40°C and 80°C was then applied to both test pieces in this condition, and the residual axial force of the bolts was measured.

Figure 5 shows the CFRP test piece used in the test. In addition, the structure of a hood lock where a CFRP frame is

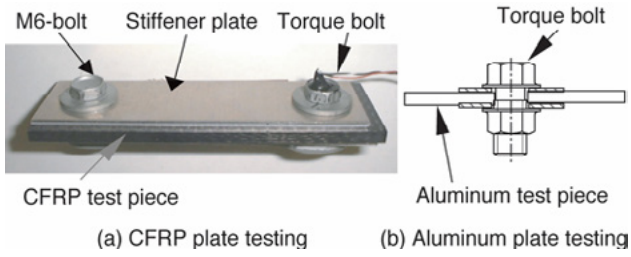


Fig. 5 Creep test piece

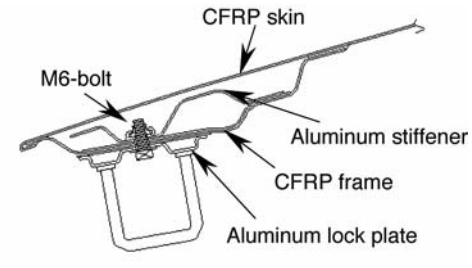


Fig. 6 Section of CFRP hood lock

clasped by an aluminum stiffener and locked by a bolt is shown in Fig. 6 as an example of a typical fastening.

Figure 7 shows the test results. Both the CFRP laminates and the aluminum plate finished the initial creep for the most part at the load for one cycle, and reached a steady creep range thereafter. In addition, the residual axial force increased as the CFRP laminates became thicker, and this is thought to be because the creep is absorbed by the surface layers of the laminate. These results showed that CFRP laminates which have the surface pressure lowered by a stiffener maintain a higher residual axial force than aluminum plates at the upper and lower limits of the clamping torque, and sufficient creep strength can be ensured with a plate thickness of 2 mm or more.

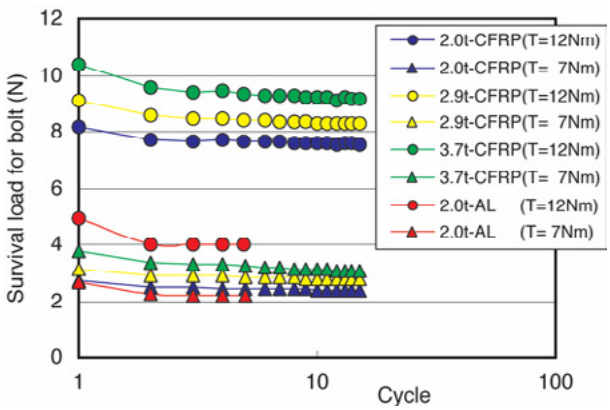


Fig. 7 Creep test results

4. Investigation of Manufacturing Methods

The hand lay-up (HLU) method which reduces die costs is an effective manufacturing method for creating parts for small-scale production vehicles[2]. The procedure for the autoclave (A/C) method using prepregs, which is a type of HLU method, is presented below.

The basic procedure consists of the following six processes. Figure 8 shows a part of these work processes.

(1) Prepreg cutting process in which the materials are cut to the prescribed specifications
(2) Hand lay-up process in which the prepregs are stretched and stacked over a die that has been treated for die release
(3) Bagging process for holding and transferring the materials between dies
(4) Autoclave process in which the prepregs are pressurized and hardened
(5) Part removal
(6) Trimming

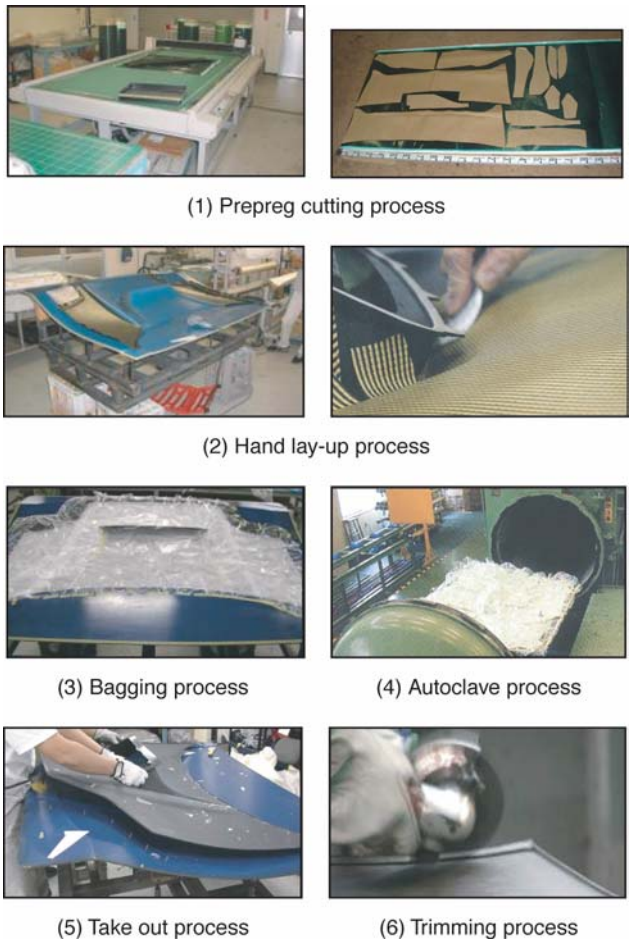


Fig. 8 A/C method

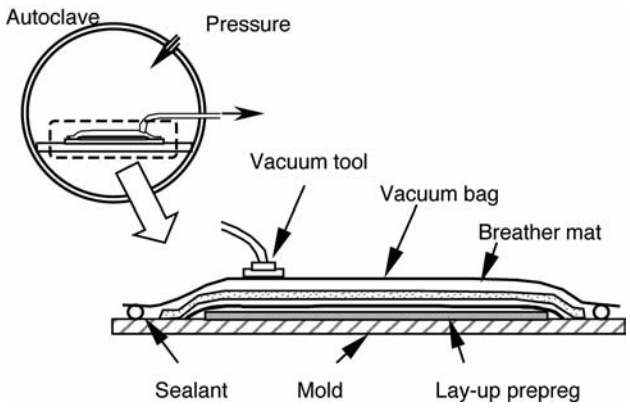


Fig. 9 Outline of A/C

Figure 9 shows an outline of the A/C process, and Fig. 10 shows an example of typical molding conditions. The A/C process generally stacks multiple thin prepregs to reach the prescribed thickness, hence some air becomes trapped between the layers. Therefore, all of the stacked prepregs are enclosed in heat resistant bag film, and the interior is depressurized using a vacuum pump to remove the air remaining air. Then, when the resin viscosity of the heated prepreg drops, the inside of the A/C is pressurized to further refine and disperse, or remove as much of the remaining air as possible. In addition, transfer performance can be improved by pressing the materials against the molding die using the A/C internal pressure.

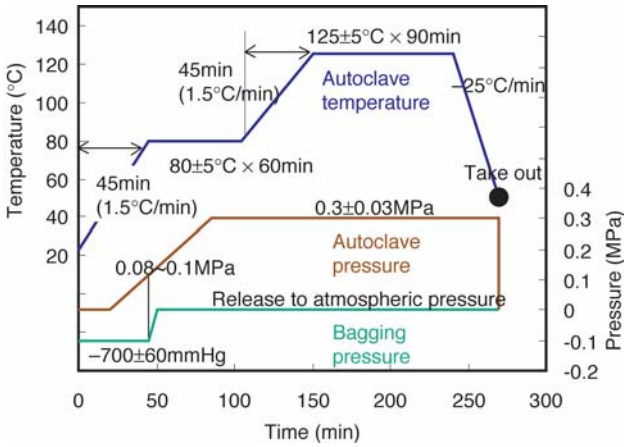


Fig. 10 Outline of cure cycle

5. Parts Structures

5.1. Hood

In addition to weight reduction, hoods require collision safety and marketability such as a rigid feeling when pressed and rigidity when opening and closing, etc.

Figure 11 shows the basic hood structure, and Fig. 12 shows an external view of the completed product. The basic thickness is 1.2 mm on the skin side, and 0.8 mm on the frame side. In addition, the thickness of the hinge and lock metal mount area is 2.2 mm for reinforcement purposes. The skin and frame flange were closely adhered to, to create a structure which raised the overall section modulus in order to improve the weight reduction efficiency compared to metal hoods. An air duct was also opened in the developed hood to generate front down force. When this type of hole is opened in conventional metal hoods using a press, plastic parts are generally added around the periphery of the hole as a garnish. However, dividing the molding die allowed an integrated structure that simultaneously achieved a beautiful, seamless finish and weight reduction.

In addition, to satisfy the requirements that the hood does not intrude into the cabin or split in the event of a collision, the hood must actively bend at the set locations. However, CFRP when compared to metals has an elastic characteristic, which means that it can undergo significant deformation and can accumulate a large amount of energy when subject to load input. Therefore, bend beads were located on the frame side in the same manner as metal hoods to create a structure that bends actively at the desired locations. In addition, bend beads cannot be located on the skin side for product

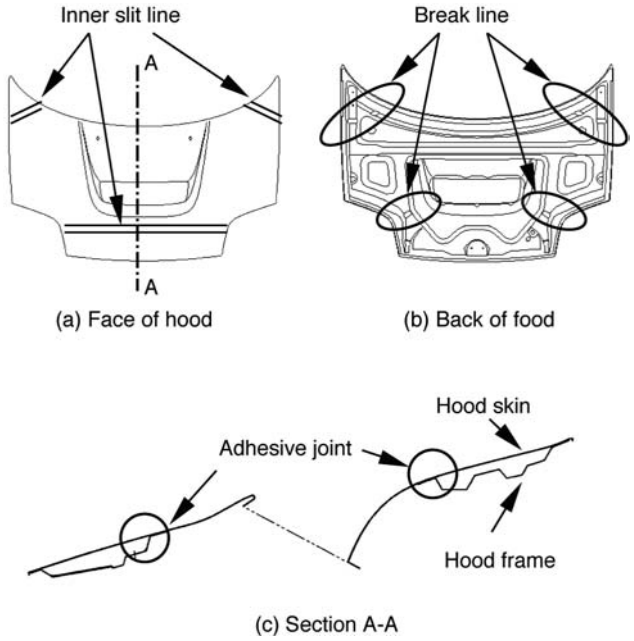


Fig. 11 Structure of CFRP hood



Fig. 12 External view of CFRP hood

appearance reasons, so slits were made in some of the surface layers near the frame bend beads to artificially reduce the skin strength in these locations and create an actively bending structure. AF which has strong anti-collision properties was also stacked in the inner layers of both the skin and frame to help prevent the hood from splitting in the event of a collision.

5.2. Rear Spoiler

In addition to improving the physical properties of the materials, eliminating the fastening bolts, flanges and adhesives also contributes greatly to reducing the structure weight. Rear spoilers are comprised of large numbers of minutely curved surfaces, so they are generally completed by creating individual parts which are then joined together. However, as the number of parts increases, the number of adhesive joints also increase, which in turn increases the weight. The developed rear spoiler used a FRP molding die which is lightweight and has excellent handing characteristics. This made the die easy to divide, and allowed a hollow integrated structure for the spoiler molded product that completely eliminated the unnecessary weight that was formerly required to join the individual parts.

The basic structure was produced by molding CFRP into the final shape based on the blow-molded structure that is employed for most spoilers currently on the market. This technology allowed designs that were formerly impossible with a structure that joins individual parts, which both improved the aerodynamic characteristics and facilitated cutting edge designs.

Figure 13 shows the basic section structure of the spoiler and the insert bolt locking conditions, and Fig. 14 shows the completed product. The basic plate thickness is 0.8 mm, and 1.0 mm in the wing areas. Performance with respect to pull-out load and rotational torque is guaranteed by positioning the bolts used to attach the spoiler to the vehicle body in the molding die, and then clasping the square bolt heads with the molding base material.

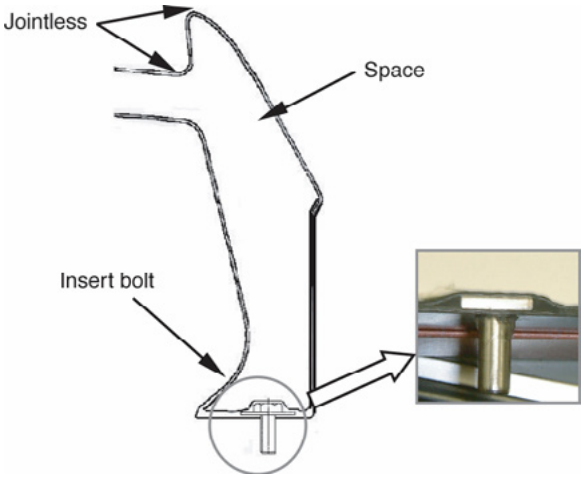


Fig. 13 Section of rear spoiler



Fig. 14 External view of CFRP rear spoiler

6. Parts Performance

The CFRP hood and rear spoiler experience almost no dimension change due to temperature, but the vehicle body side to which these parts are attached is made of aluminum which has a large coefficient of thermal expansion. Therefore, the following test was performed to confirm the effect of environmental temperature changes on the fit. The hood results are shown below as a typical example.

To simulate elevated temperature conditions an infrared lamp was set so that the surface temperature of the hood was around 80°C, and the amount of dimension change after four

or more hours was measured. Similar measurements were made at ambient temperature of –30°C. Points at a 100 mm pitch were also measured on the fender as a dimension change reference. Figure 15 shows the test conditions and measurement points.

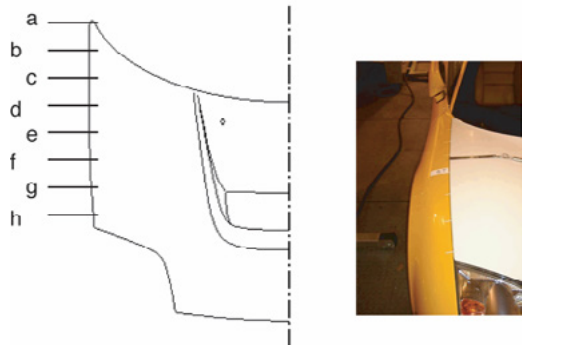


Fig. 15 Measurement points for dimension change

Figure 16 shows the results. The gap between the hood and fender reached a maximum of approximately 0.6 mm (point h) during the hot stage, and approximately 0.6 mm (point f) during the cold stage. This confirmed that dimension change was not a level that would be a problem in terms of product appearance.

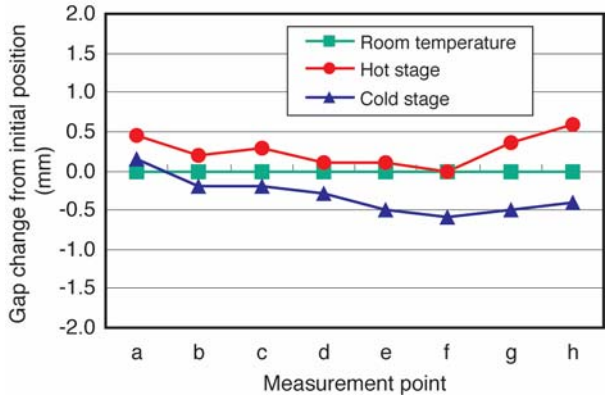


Fig. 16 Gap change in hot-cold cycle test of CFRP hood

7. Summary

Exterior parts were developed by effectively capitalizing on the anisotropy of CFRP materials and the degree of molding freedom of plastic as a means for reducing vehicle body weight. The hood product weight was 4.2 kg, which is a weight reduction of 30% compared to aluminum hoods, and the rear spoiler product weight could be kept to 2.3 kg, which is a weight reduction of 40% despite the increased size compared to the lightweight SMC spoiler for the ’93 model.

At the same time, the following occured through this development.

1) Regarding collision safety, bending initiation points were set using a bend bead shape on the frame side in the same manner as metal products. In addition, in locations where shape elements cannot be included for reasons of product appearance, bending start points were set without impairing the appearance by setting slits in the stacking constitution to artificially reduce the material strength.
2) Mechanical fastening using metal bolts can be guaranteed even for stacked materials which exhibit large thermal expansion in the plate thickness direction.

8. Afterword

Carbon fiber reinforced plastics are extremely effective for the weight reduction of automotive parts. The use of CFRP parts as standard parts for the ’02 model NSX type-R which, despite being a small-scale production vehicle, is a flagship car for Honda, and is thought to be a great leap forward for automotive weight reduction technology. How best to efficiently produce and use high priced carbon materials in mass production vehicles is a major issue, and it is the authors’ hope that carbon materials will become widely used throughout the world as lightweight materials in the future.

Acknowledgement

The authors wish to express their deep thanks to all related in-house and outside parties including TOHO TENAX Co., Ltd. and YACHIYO INDUSTRY Co., Ltd. for their immense cooperation with this development.

References

(1) Nomura, T., et al.: Present Status and Future Prospects of SMC Outer Panel for Vehicles, Journal of Society of Automotive Engineers of Japan, Vol. 43, No. 6, p. 32-38 (1989)

(2) Nishiyama, K., Ei, R., Kato, Y., Ishibashi, K.: Development of Small-scale Production Method for Large-size Exterior Plastic Parts, HONDA R&D Technical Review, Vol. 11, No. 1, p. 173-178 (April 1999)

(3) Takeuchi, A.: Development of ABS/PA6 Polymer Alloy for Body, HONDA R&D Technical Review, Vol. 12, No. 1, p. 183-188 (April 2000)

(4) Fukuda, H., et al.: Chapter 5 Inplate Problems of Flat Plates and Inplate Rigidity of Laminates, Introduction to Composite Material Dynamics, Tokyo, Kokon Shoin, 1989 first edition, p. 91-98

(5) Uemura, M., et al.: Chapter 1 Materials and Material Properties, FRP Structure Design Handbook, Tokyo, The Japan Reinforced Plastics Society, 1994 first edition, p. 1-12

■ Authors ■



Yasuo YAMANE



Tomohiro SAKURABA

High-Scratch Resistant Polypropylene for Instrument Panels

Bryan CERRA* Corey MCENHILL*

ABSTRACT

In an effort to reduce cost and foster an all-olefin material direction, a polypropylene material has been developed to perform without paint in applications traditionally requiring paint. An existing instrument panel polypropylene's scratch resistance has been enhanced by talc encapsulation, increased surface lubricity and reduced talc particle size. The additive loadings and types were balanced with physical property performance and material cost. Mold flow analysis and a sequential valve gate molding process were used to optimize the part appearance. The result is an impact-modified polypropylene with scratch characteristics equivalent to painted polypropylene with a minimal cost increase.

1. Introduction

Injection-molded polymers are the preferred construction for most interior parts. Instrument panels, however, have traditionally used skins or paints to cover their injection-molded retainers in order to meet quality expectations (scratch resistance, weld lines, etc.). In response to cost and weight reduction initiatives, the skin construction has given way to a painted polymer construction. The use of semi-crystalline polymers has made this construction expensive because special paint formulations are required to meet the instrument panel quality expectations. These circumstances have created an opportunity to reduce cost by eliminating paint. This opportunity has been successfully seized on small segment vehicles in the European and Japanese markets. However, seizing opportunities on full-size vehicles is more difficult due to the higher quality expectations.

Thus the goal was to develop a polypropylene that does not require paint to meet full-size vehicle quality expectations without increasing the polymer's cost.

Injection-molded instrument panels are generally one-piece designs, however, some models use multi-piece designs that provide an opportunity to remove paint selectively. Removing the paint from vertically oriented parts and not the horizontally oriented parts prevented the material from being subject to veiling glare requirements. Thus, the objectives became, in order of priority: scratch resistance, mold shrinkage, physical properties, molded-part appearance and cost.

2. Methodology

The primary concern with mold-in-color applications is scratch resistance. Paint prevents the base material from being scratched and increases the scratch resistance of the construction. To increase the scratch resistance of the substrate material to a level that does not require paint, two methods were considered; decreasing the size of the scratch and hiding the scratch[(1)]. Increasing the hardness and surface lubricity will decrease the size of the scratch. However, increasing the material's hardness was found to diminish the overall quality and increase the cost without a significant improvement in scratch resistance and was therefore abandoned. Encapsulating the talc, reducing the talc particle

* Honda R&D Americas, Inc.

size and optimizing the talc's adhesion within the polymer matrix helps to hide the scratch. The final strategy was to hide the scratch as mentioned above and decrease the scratch size by increased surface lubricity.

The mechanism of scratching a polymer was analyzed. This analysis determined how to characterize a material's scratch susceptibility, provided an approach to additive selection and identified appropriate scratch test equipment. The depth and color of the scratch were used for characterization and two pieces of test equipment were used; the Taber scratch machine (Fig. 1) and the Five-finger scratch machine (Fig. 2).

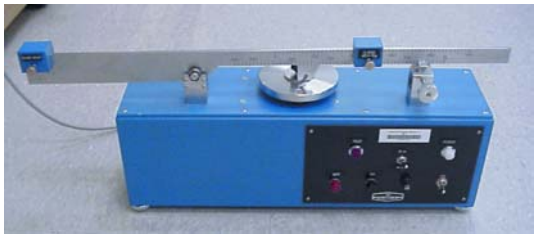


Fig. 1 Taber scratch machine

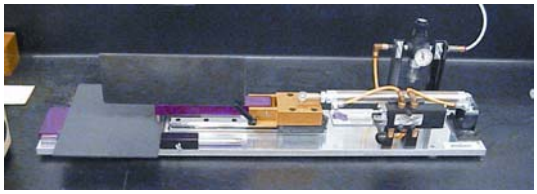


Fig. 2 Five-finger scratch machine

Exposed talc and titanium dioxide (TiO_2) are the primary contributors to the white appearance. Encapsulating the talc and increasing the interfacial bond strength between the talc and the polymer, minimize the white appearance. Optimizing the dispersion prevents significant exposure of the TiO_2 (Fig. 3).

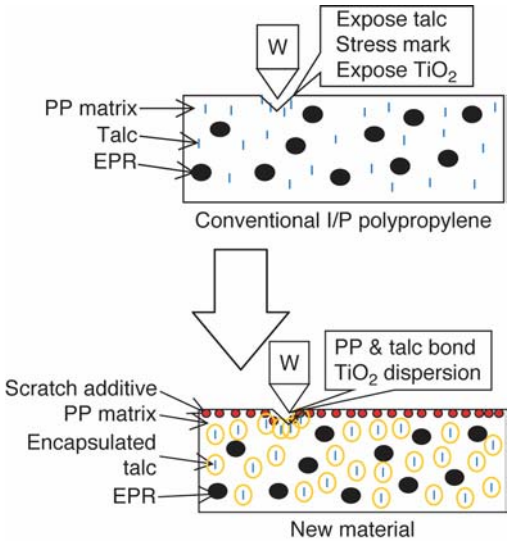


Fig. 3 Scratch mechanism

Optimizing the molding process and the gate configuration was intended to minimize appearance defects (weld lines, flow marks, etc.).

3. Results

The scratch was characterized by whitening[2]. That is, the depth of a scratch is intrinsic to the polymer family and not the grade. This ideology coincides with our conclusion to not increase the material's hardness.

To create the final formulation, several additives and additive combinations were considered. Additives A through E were evaluated as well as pigment-dispersing agents and talc. Additive A successfully increased the surface lubricity, however it also increased the cost, decreased the molded-part appearance and decreased the flexural modulus. Additive B strengthened the polypropylene's bond to the talc, which minimized the talc's contribution to a white appearance after being scratched. A loading range of 1.2 – 2.0% was optimum for maintaining the molded-part appearance and increasing the scratch resistance (Fig. 4).

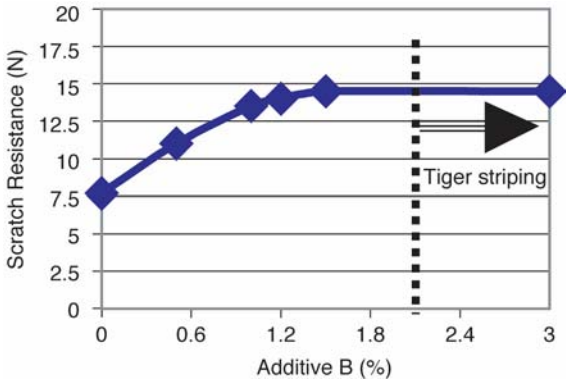


Fig. 4 Scratch resistance vs. additive B (with D)

Additive C aided surface lubricity but increased our haze percentage beyond the maximum value that meets the fogging target and was canceled. However, additive D increased the surface lubricity while having a lesser effect on the fogging level (Fig. 5).

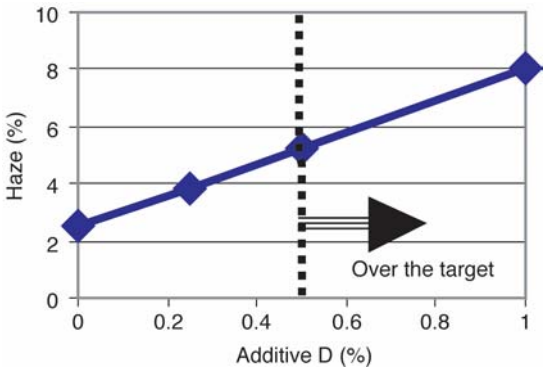


Fig. 5 Fogging vs. additive D

A loading range of 0.2 – 0.5% of additive D is sufficient to optimize scratch resistance and fogging performance (Fig. 6).

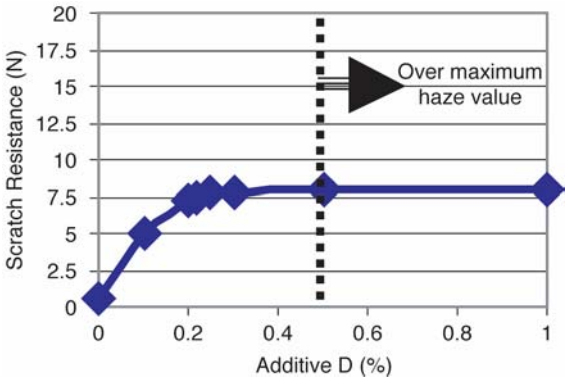


Fig. 6 Scratch resistance vs. additive D

Additive E increased the material's crystallinity and minimized the amount of whitening caused by stress. However, Additive E does affect the physical properties (Fig. 7).

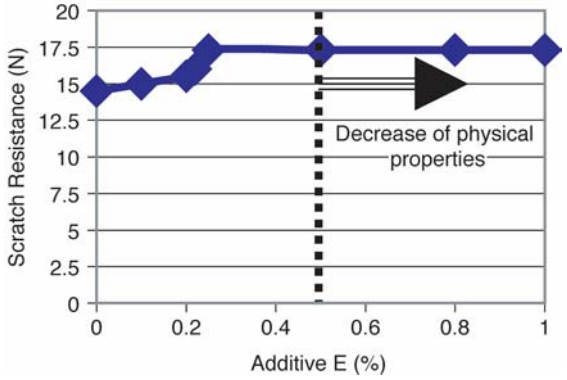


Fig. 7 Scratch resistance vs. additive E (with B & D)

A loading range of 0.2 – 0.5% of additive E is optimum for meeting the flexural modulus target while maximizing the scratch resistance (Fig. 8).

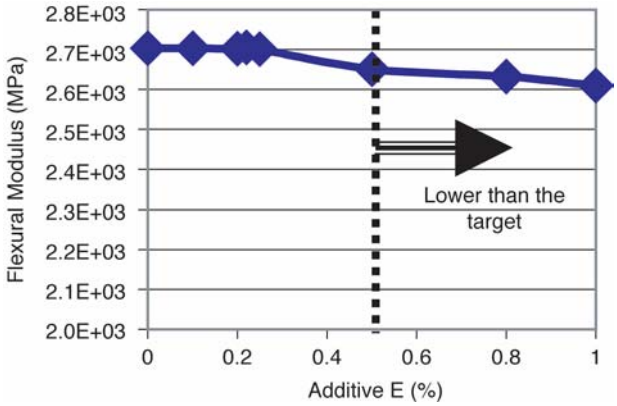


Fig. 8 Flexural modulus vs. additive E (with B & D)

Of the target colors, Fern (G59L) and not gray (NH361L), exhibited the most whitening when scratched. Light colors, such as Fern, contain more TiO_2 than dark colors and thus have a higher probability to whiten when scratched. The primary causes are poor dispersion of the TiO_2 and the talc particle size. Therefore, the magnesium stearate pigment-dispersing agent was replaced with a more effective high-density polyethylene pigment-dispersing agent. The monomer molecular weight was reduced by 96%. Additionally, the talc particle size was reduced from 7 mm to 2 mm. These changes improved the Fern's scratch resistance from 13N to 17N and did not adversely affect physical performance.

Table 1 summarizes the final formulation.

Table 1 New material formulation consideration

Constituent	Description	Benefit	Limitation
Additive A	Siloxane	Increases surface lubricity	Increased cost, reduced physical properties & poor appearance
Additive B	Grafted polyolefin	Talc bonding (+6N)	>2% loading yields tiger stripes
Additive C	Fatty acid amide	Increases surface lubricity	Increased cost and poor fogging
Additive D	Fatty acid amide	Increases surface lubricity (+2N)	Increased cost and >0.5% loading yields NG fogging values
Additive E	Petroleum resin	Maintain physical properties and reduces stress whitening (+2N)	>0.5% loading yields NG flexural modulus values
Dispersion Agent	Polyolefin	Improved dispersion of TiO_2 and additives (+1N)	None forseen
Talc	Reduced particle size	Minimizes the potential for talc exposure (+3N)	>70% reduction affects physical properties

The aforementioned formulation yields a Five-finger scratch performance improvement of 3N to 17N over conventional polypropylene as depicted in Figs. 9 and 10 respectively.

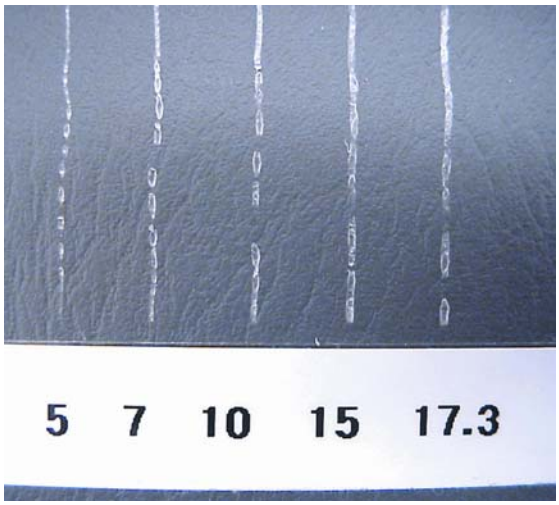


Fig. 9 Conventional TPO



Fig. 10 New material

While realizing the scratch resistance improvement, the target physical properties were maintained (Table 2).

Table 2 Key physical properties

Property	Units	Honda I/P target	New material
Izod Impact Strength (-30°C)	J/m	44	45
Tensile Strength	Mpa	23	23
Flexural Modulus	MPa	2780	2700
HDT (0.45MPa)	°C	131	131
Density		1.06	1.06
Scratch Resistance	g	200	**800**
Fogging	%	4.2	4.1

4. Part Performance

4.1. Molded-part Appearance

The molded-part appearance of the conventional polypropylene and the new scratch-resistant polypropylene were evaluated using a mass production Side Sill Garnish tool. An injection machine capable of sequential valve gating was selected to take advantage of the latest technology. A mold-flow analysis was used to optimize gate design and locations for the final tool. The straight black lines in Figs. 11 and 12 indicate weld line locations. The initial 10 × 1.5 mm fan gate design resulted in three weld lines (Fig. 11).

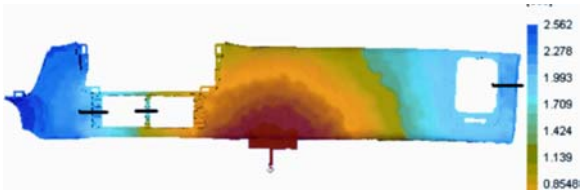


Fig. 11 One 10 × 1.5 mm fan gate

The final gate arrangement consisted of an 8 mm bore channel, one 10 × 1.5 fan gate and three 5 × 1.5 mm valve gates (Fig. 12).



Fig. 12 One 10 × 1.5 mm fan gate and three 5 × 1.5 valve gates

This arrangement resulted in two weld lines placed in the least observable regions. A melt temperature of 210 °C and mold temperature of 60 °C were found to be acceptable. Additionally, fill time, cavity pressure, and feed configuration were optimized to minimize the weld line's appearance and control their positions (Fig. 13).

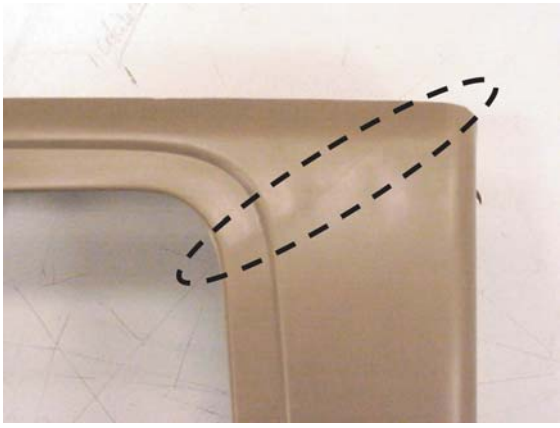


Fig. 13 Mass-production tool without grain

The mass production tool was not grained before development was scheduled to finish and the Side Sill Garnish grain was not deep enough to predict weld line appearance in an instrument panel grain (H-280C; 80 m). In order to make this prediction in time for mass production, a weld line was introduced into a plaque having the H-280C grain on one side and no grain on the other. The weld line on the non-grained plaque was matched to weld line on the non-grained injection-molded parts. The weld line on the flip side of the plaque with the H-280C grain was used to predict the appearance on grained parts. As predicted, the mass production part meets all the appearance requirements. (Fig. 14).

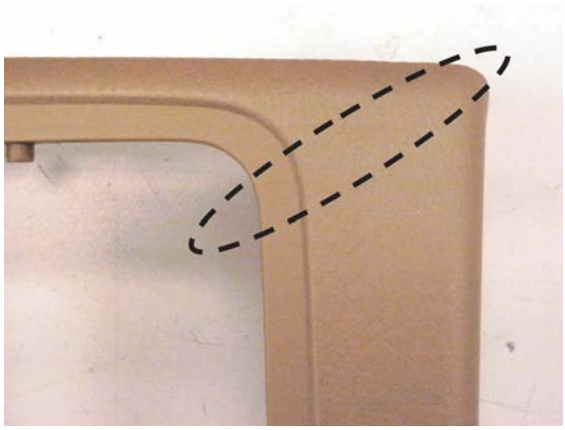


Fig. 14 Mass-production part with grain

The appearance of weld lines in the new material is no more noticeable than that of the conventional material. Therefore, the new material obeys the standard theory that deep, animal-like grains will make weld lines.

The tiger stripe appearance was removed by eliminating an additive that was incompatible with the polypropylene (Additive A), implementing sequential-valve gate molding and optimizing the mold temperature.

The new material can be painted using Honda's solvent or water-based paint systems at recommended bake conditions for low-gloss Honda colors[3].

4.2. Part Testing and Application

The physical properties of the new material matched those of materials that have met our cold-impact and thermal cycle requirements using similar designs. Once the formulation was stable enough, parts were molded and then evaluated for cold-impact and thermal cycle performance.

The parts molded in the mass production tool performed as expected in the instrument panel assembly; passing the cold-impact and thermal cycle requirements. A nominal wall thickness of 2.5 mm was sufficient for this material to meet the aforementioned standards. This material has been applied to the Honda Pilot's mid panel parts (Figs. 15, 16).



Fig. 15 DR Mid Panel



Fig. 16 AS Mid Panel

5. Conclusion

Through formulation optimization a high-scratch resistant polypropylene material for instrument panels has been developed.

(1) Impact-modified polypropylene's scratch resistance improved from 3N to 17N.
(2) The per/pound cost was not increased.
(3) The molding characteristics were not adversely affected.
(4) The physical property performance was not adversely affected.
(5) The part performance was not adversely affected.
(6) The part cost was reduced by 80% (S9VA AS/DR Mid Panels; Fig. 14 and Fig. 15).

The next generation of this material will be engineered to meet instrument panel veiling glare and visual feeling targets.

6. Acknowledgments

We appreciate the efforts of Color & Composite Technologies and Greenville Technologies.

7. References

(1) Sakumoto, S.: Advanced and improved Scratch Technologies for Molded-in-color Polypropylene Interior Parts, ITB Automotive Interiors 2002, March, 2002.

(2) Wolske, K., Anthony, K., Pollo, M., Tan, F., and Taylor, S.: Effect of Composition on the Scratch Resistance of Filled TPOs, SPE Automotive Global TPO Conference 2001, October, 2001.

(3) Kamei, S.: Innovative Thermoplastic Paint Process, SAE Paper 2001-01-0360, March, 2001.

■ Authors ■


Bryan CERRA


Corey MCENHILL

Development of Lead Free E-coating with Low Cost Anti-rust Pigments

Hiroyuki MORISHITA* Katsuyoshi KANEKO*

ABSTRACT

A new electrocoating has been developed as part of the ongoing efforts to move towards the use of lead-free cationic electrocoatings as an auto body primer. The new e-coat dispels concerns, such as increased cost and inferior rust protection due to the absence of lead, and will be able to be easily introduced to automotive production lines. Several technologies were necessary for this development: new corrosion inhibitors essential for rust protection; improvement of the performance of the base resin of the paint film; methods to control the viscosity of the deposited film, in order to prevent deterioration of the workability and the appearance of the paint; and optimization of pigment mixture to control costs.

1. Aims and Agenda of this Research

The demand to reduce the amount of environmentally harmful substances utilized in automotive manufacture is intensifying. This includes the inorganic lead compounds employed in the cationic E-coatings, which are conventionally used as body coats[(1)]. The aim of the research discussed in this paper was to create a lead-free E-coating, in order to further reduce the environmental impact for recycling of scrapped vehicles.

The lead component of existing coatings is added as an inorganic lead compound pigment. This pigment functions to prevent corrosion of the steel plate, and to act as a catalyst for the hardening reaction of the film during curing. If the amount of the lead component were simply reduced, both anti-corrosion performance and film hardness would decline.

Bismuth-based pigments are used in conventional lead-free E-coatings to replace the lead component, while ensuring that its functions are maintained. However, the higher price of this material increases the cost of the coat. This research project therefore adopted the following goals:

(1) Environmental friendliness: Zero lead component.
(2) Film performance: Identical anti-corrosion performance, physical performance, film smoothness, and durability to conventional coats.
(3) Workability: Able to be introduced to existing coating lines.
(4) Coating cost: Equivalent to or less than that of conventional coats.

2. Development of New Anti-corrosion Pigment

2.1. Functions of Conventional Anti-corrosion Pigments

The lead-based pigments utilized in existing cationic E-coats prevent corrosion by passivating the steel surface receiving the film, thus blocking the spread of rust, and by binding any corrosive agents entering the film (chloride ions, etc.) to prevent them from reaching the steel surface.

The mechanism of passivation by lead is as follows: the ionized lead component in the electro-coat solution is

* Tochigi R&D Center

precipitated onto the substrate surface during electrolysis, forming a metal oxide film. This film shifts the surface potential of the substrate to the noble range, thereby functioning to maintain passivity[(2)].

Bismuth-based pigments function in the same way as lead-based pigments, and are used as a replacement in conventional lead-free E-coatings. Measurements of corrosion currents on steel plates onto which lead and bismuth have been precipitated show that bismuth has a range of passive potentials virtually identical to that of lead[(2)]. Figure 1 shows the results of an evaluation of the anti-corrosion performance of films employing bismuth-based pigments in compound corrosion tests (CCT), and demonstrates that at least 1.5 wt% of bismuth must be added to achieve the same performance as a conventional coat. This is approximately the same as the amount of lead-based pigments added to E-coatings, but the higher cost of bismuth makes it economically unfeasible. The research project described here therefore developed a new and more economical pigment to replace bismuth-based pigments, and studied methods of reducing the amount of high-priced components utilized.

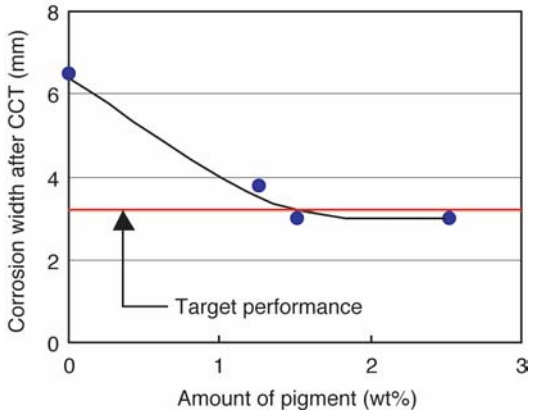


Fig. 1 Effect of concentration of bismuth pigment on anti-corrosion performance

2.2. Development of a New Anti-corrosion Pigment

Layered double hydroxides with layered crystal structures, such as graphite, display the ability to selectively absorb ions into their structure, a phenomenon known as intercalation. Research focused on a method of inhibiting rust by utilizing this function to prevent corrosion-promoting ions from reaching the substrate surface.

Having determined the viability of a substance capable of intercalating anions such as chloride ions as a corrosion inhibitor, considerations of chemical stability in the coating, ability to bind chloride ions, and suitability for electro-deposition led to the selection of a hydrotalcite-based pigment termed new pigment A. A model of a crystal structure displaying intercalation and an electron micrograph of new pigment A are shown in Fig. 2. The general formula for hydrotalcite is $[M^{2+}_{1-x}M^{3+}_{x}(OH)_2]^{x+}[A^{n-}_{x/n}\cdot mH_2O]^{x-}$. Hydrotalcite is composed of positively charged layers of divalent (M^{2+}) and trivalent (M^{3+}) metals. Between the layers there are anions (A^{n-}), which cancel the charge. These interlayer ions can be exchanged with other ions. New pigment A intercalates chloride ions by exchanging with the carbonic acid ions making up its interlayer anions.

Figure 3 shows the results of a comparison between the chloride ion absorbency of new pigment A and a conventional lead-based pigment. The new pigment was shown to possess a higher level of chloride absorbency than the conventional pigment.

Substances with a similar derivation to new pigment A are used as stabilizers in PVC resins and anti-oxidants in pharmaceuticals, and have not displayed any environmentally harmful effects.

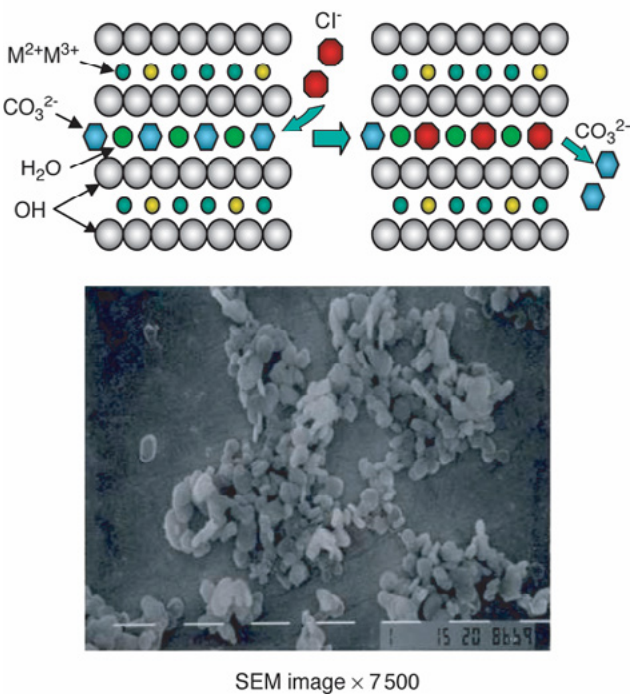


Fig. 2 Intercalation function (above) and SEM image of rust-inhibiting pigment 'A'

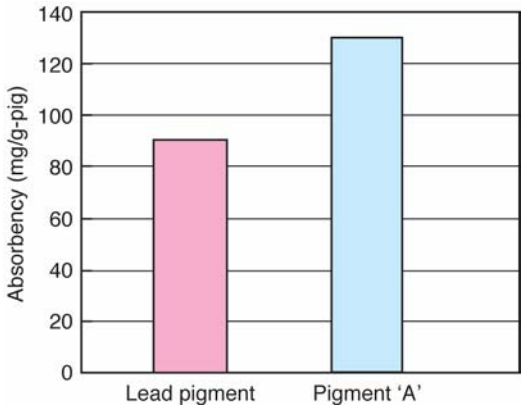


Fig. 3 Chloride absorbency of anti-corrosion pigments

The pH buffering performance of the new pigment in the acid domain (low pH domain) was studied in order to determine its effectiveness as a corrosion inhibitor. To study the pH buffering performance of various pigments, 2.0 wt% of each was added to 0.01 N solutions of hydrochloric acid, agitated, and left at 20 °C for 48 hours, after which the pH was measured. The results of these tests are shown in Fig. 4. New pigment A bound 3.3×10^{-3} mol/g of chloride ions, a figure close to the 4.0×10^{-3} mol/g predicted from studies of intercalation.

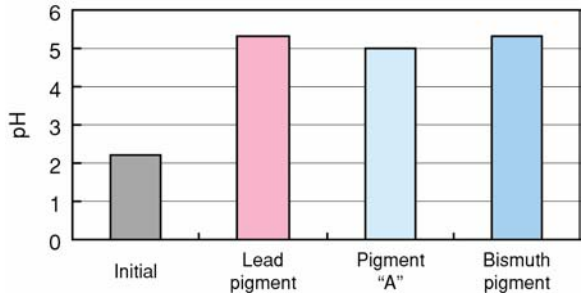


Fig. 4 pH buffering capacity of pigments

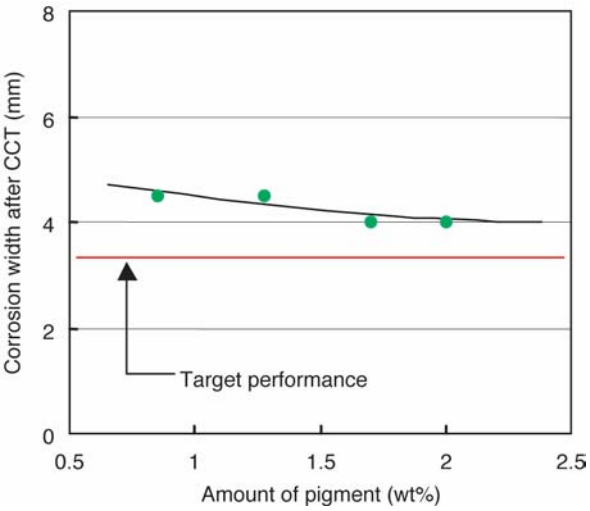


Fig. 5 Anti-corrosion performance of pigment 'A'

Prototype E-coats were formulated using new pigment A, and its corrosion inhibition performance was evaluated in compound corrosion tests. Cold-rolled steel (CRS) plates were utilized as the test substrates, and were E-coated after galvanization with zinc phosphate. A knife cut was made in the coat, and the width of the area of corrosion after CCT was measured. Figure 5 shows the results of these tests. The corrosion inhibition performance of new pigment A was inferior to that of conventional films employing lead-based pigments, and it was judged that increasing the amount of the pigment added to the coat would not enable it to reach target performance. A bismuth-based pigment was therefore mixed with new pigment A to supplement its corrosion inhibition performance. Study focused on optimizing the ratio of the pigments to achieve a balance of performance and cost.

The results of these studies led to the development of a mixture of 1.28 wt% new pigment A as the main ingredient and 0.43 wt% bismuth as a secondary ingredient. This ratio of pigments equaled the corrosion inhibition performance of lead-based pigments. New pigment A, in combination with improvements made to the base resin to be discussed below, enabled film performance to be maintained despite the reduction of the bismuth content to 0.29%, 80% less than used in conventional films employing bismuth-based pigments. Figure 6 shows the results of a test in which coated cold-rolled steel sheets were immersed in 5% salt water at 55 °C for 240 hours.

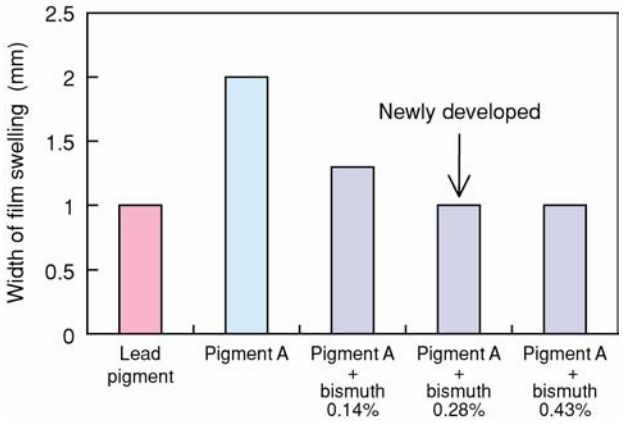


Fig. 6 Effect of ratio of pigment 'A' and bismuth pigment as demonstrated by hot salt water immersion test

3. Improvement of the Base Resin

Existing cationic E-coat films employ a bisphenol A-type epoxy resin as the base resin. The ends of the molecules of this resin are amino-denatured to render them water-soluble, and side chains with a flexible molecular structure are attached as a plasticizing component.

A cross-linking agent with an isocyanate reaction base is included as a component in the coating to enable the resin molecules to form cross-links in the baking process after electro-deposition of the film in the tank, ensuring that it becomes sufficiently hard (Fig. 7).

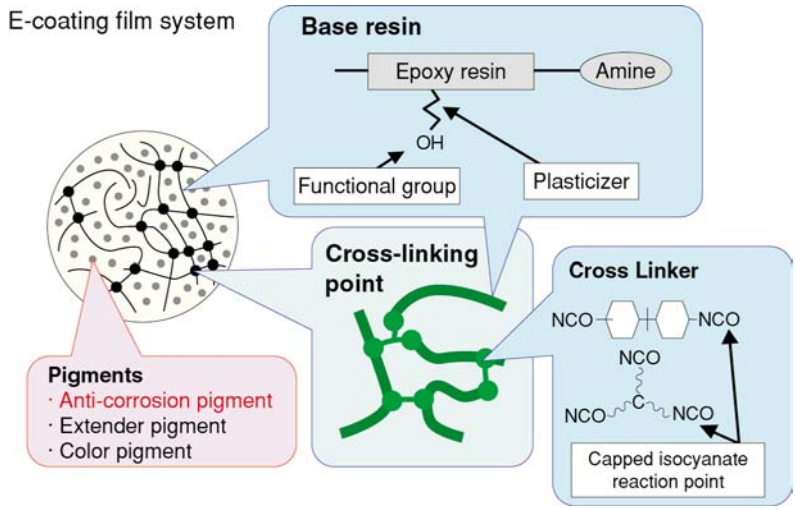


Fig. 7 E-coating film system consisting of pigments, epoxy-based resin and cross-linking resin

The research discussed here studied potential improvements to the resin from the dual perspectives of achieving improved blocking performance and reducing costs. However, no major changes were made to the epoxy resin backbone, with research focusing instead on adding multi-functional groups and adjusting the proportion of plasticizer to improve base resin performance. This would supplement the functioning of the corrosion-inhibiting pigment and the hardening catalyst, and enable lead-based pigments to be eliminated.

Various methods were predicted to enable improvement of the blocking performance of the film: Reducing the amount of isocyanate used in cross-linking, increasing the molecular weight of the base resin to increase the glass transition temperature (Tg), increasing the ratio of functional groups, and reducing the plasticizer content.

To increase the ratio of functional groups, the conventionally used single-function base resin was replaced with a resin with more than three functional groups. This increased the cross-linking reactivity of the resin, compensating for the loss of the lead component as a hardening catalyst. Figure 8 shows a conceptual diagram of the multi-function base resin.

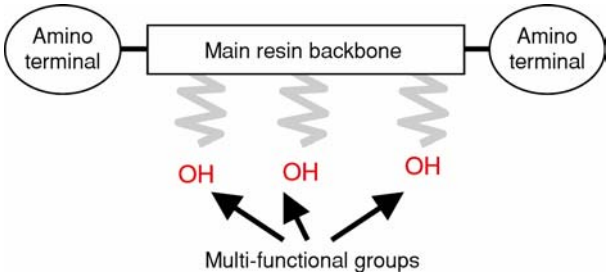


Fig. 8 Base resin with multi-functional groups

Tests were conducted to determine the effect of changes in plasticizer content on the performance of the coating. Ratios of 3-9% of plasticizers with flexible molecular side chains of varying lengths were added to the base resin and blocking performance and corrosion inhibition performance was studied.

Figure 9 shows the effect of the amount of plasticizer in the film on oxygen infiltration, as one measure of film performance. 9% plasticizer is added to the resins employed in conventional films; the reduction of this amount to 3% in the new film has enabled a 15% improvement in blocking performance.

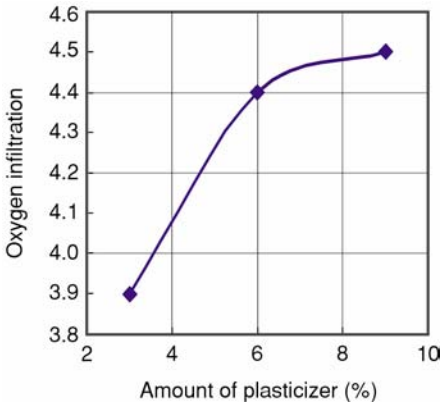


Fig. 9 Effect of plasticizer on barrier performance

Comparisons of the width of swelling in the film from a knife cut after immersion in 55 °C 5% hot salt water for 240 hours confirm that the reduction of the amount of plasticizer has increased the adhesiveness of the film (Fig. 10).

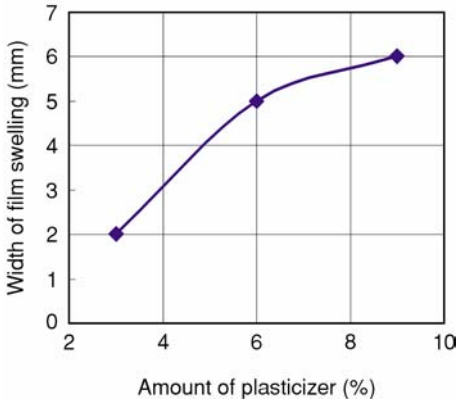


Fig. 10 Effect of plasticizer on adhesion performance in HSW test

4. Increasing Applicability of the Coat

Blemishes occurred in the finished coat when the new E-coat with a resin plasticizer content of 3% was used to coat an alloyed welded galvanized steel plate.

These blemishes are termed cratering, and show as pinhole imperfections in the film after baking and curing. Electrolysis during the coating process causes hydrogen gas bubbles to form on the surface of the substrate, and these gas bubbles enter the film. The application of high voltages causes electric discharges inside these bubbles, which in turn cause gelling of the surrounding resin. This gelling prevents the flow of heat across the surface when the film undergoes baking and curing, resulting in pinhole imperfections in the film. Figure 11 shows a schematic representation of the mechanism of cratering.

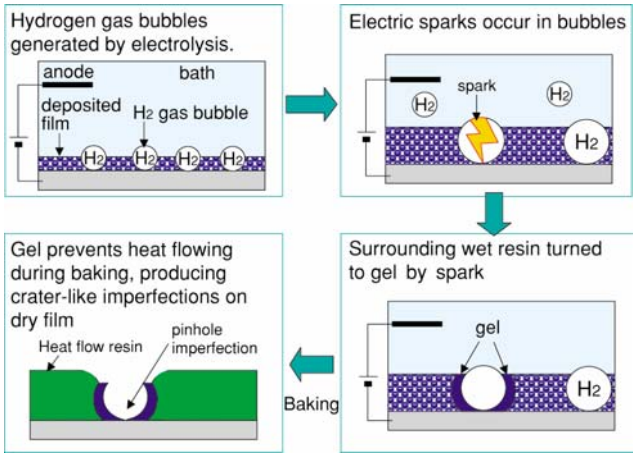


Fig. 11 Theory of occurrence of craters on GA substrate

The increased occurrence of cratering was believed to be due to the reduced plasticity of the base resin, which increased the viscosity of the precipitated resin, thus, reducing the ability of hydrogen gas to escape from the surface of the substrate. The plasticizer content of the base resin was therefore altered to adjust the viscosity of the precipitated resin in an attempt to promote the escape of hydrogen gas.

Increasing the plasticizer content to 4% enabled the achievement of a level of cratering performance equivalent to that displayed by conventional E-coats (Table 1). Anti-corrosion performance was also verified as being identical.

Table 1 Effect of plasticizer on GA cratering performance

	Conventional material	Newly developed material with 3% plasticizer	Newly developed material with 4% plasticizer
Critical voltage for occurrence of GA cratering	260 V	230 V	260 V

5. Film Performance

The newly developed E-coat was subjected to comprehensive film performance evaluations, including tests of physical characteristics focusing on smoothness, resistance to gravel chipping, resistance to impact, flexibility, and adhesiveness, and of chemical characteristics, such as chemical resistance, gasoline resistance, and suitability for use with a PCV plasticizer. The results of these tests demonstrated the performance of the newly developed coating to be equivalent to that of conventional coatings in all these areas.

To determine the suitability of the new coating to existing coating lines and facilities, additional tests included throwing power, applicability to the UF filters used in electro-coating facilities, resistance to contamination, ability to repel oil, suitability for the temperatures used over the specified period for oven baking, the amount of flux produced during baking, and reaction to buffing. Performance in these areas equaled that of conventional coatings, confirming that the new coating could be introduced to existing coating lines.

6. Cost

As a result of the employment of a low-cost anti-corrosion pigment and reduction in the cost of color pigments and other additives, the cost of the E-coating developed in this project is equivalent to or less than the cost of conventional E-coatings using lead-based additives.

7. Summary

Research to develop a lead-free E-coat employing a low-cost corrosion-inhibiting pigment produced the following results:

(1) Utilization of 1.28 wt% of a new corrosion-inhibiting pigment and 0.28 wt% of a bismuth-based pigment to replace lead-based pigments, in combination with improvement of the base resin, has enabled the achievement of anti-corrosion performance equaling that of lead-based pigments.

(2) Making the base resin multi-functional (more than three functional groups) has improved the blocking ability of the film. At the same time, utilizing a plasticizer content of 4% in the resin has improved GA cratering performance, enabling the achievement of a coating equivalent in quality to that of conventional films.

(3) The newly developed film has equivalent durability to conventional films, and can be introduced to existing coating lines.

(4) The cost of the new coating is equivalent to or less than that of conventional coatings.

8. Afterword

The current era is distinguished by a concern for the environment. The reduction in environmental pollutants, achieved in this research helps address this concern. At the same time, the new E-coat offers Honda's worldwide customers excellent rust-inhibition performance and superior vehicle exteriors, and is presently being introduced to the company's coating lines.

References

(1) Toryo sangyo to chikyu kankyo kenkyu kai: Current issues on lead and chrome in the coating industry and risk reduction, Japan Paint Manufacturers Association (1995)

(2) Hiraki, T. et al.: Lead-free electrocoat, Toryo no kenkyu, No. 132, p. 53-58 (1999)

(3) Fujitani, T. et al.: Studies on relationship between oxygen-permeability and anti-corrosiveness of coating films, Toryo no kenkyu, No. 122, p. 9-17 (1993)

(4) Publication of patent applications Tokkaihei 5-140487 "Electrocoating Composition"

■ Authors ■




Hiroyuki MORISHITA Katsuyoshi KANEKO

Expansion of the Use of Recycled Bumper Materials through the Modification of Properties

Satoshi HIRAWAKI* Kenji HIKITA* Tomoyuki UEMURA*

ABSTRACT

To expand the scope of parts incorporating recycled bumper materials, material property enhancement methods were developed to meet the requirements demanded in the individual parts. The parts targeted in the research were 1) Aerial under cover; 2) Side spacer; 3) Evaporator case; 4) Rear shelf; and 5) Floor carpet. The following methods were used to modify the properties of the material for the respective parts: 1) Melt flow was improved through the addition of low molecular weight additives; 2) Flexural strength was improved with additives to chemically bond filler and matrix resin; 3) Shrinkage performance was improved and flexural modulus was increased by the addition of filler and resin with high flexural modulus; 4) Flexural modulus was increased by the addition of filler; and 5) Tensile elongation was improved by the addition of an elastomer compatibilizer. In each case, these methods enabled the use of recycled materials at an equivalent cost to virgin materials.

1. Introduction

In 2001, the Home Appliance Recycling Law in Japan was introduced. In the one year since the introduction of this law, approximately 8.5 million electrical appliances have been collected.

With respect to automobiles, the market in Japan currently scraps approximately 5 million automobiles annually. The successful implementation of a recycling system is an important objective for automobile manufacturers.

Honda has developed a bumper recycling process and has collected old bumper parts that have either been repaired or replaced[(1)]. To date, these collected bumpers have been reprocessed as recycled bumper material (referred to as recycled material hereafter). This material has been used for splash shielding and sandwich injection molding for application in new vehicle bumpers[(2)]. The amount of bumper material collected by Honda is increasing every year, with 585 tons collected in the 1995 fiscal year and 1,186 tons collected in the 2001 fiscal year.

As the amount of bumper material collected continued to increase, research was conducted to expand the scope of parts in which newly recycled material can be used. This report describes this research activity.

2. Course of Development

The application of unmodified recycled materials to other parts raises a number of issues. Of particular note is the reduction in the surface quality of the products caused by paint film flakes included in recycled materials. For example, when unmodified recycled material is applied to exterior design parts such as the cowl top garnish, it gives off an undesirable finish due to the added flake component. Such testing of these exterior parts has led to the conclusion that untreated recycled material is not suitable.

Bumper materials contain 30% elastomer components,

* Tochigi R&D Center

which have a lower relative mold shrinkage. The difference in the shrinkage rate of virgin materials used for parts and of recycled materials creates a large gap when assembled to the vehicle.

Recent processing methodologies applied to recycled materials for reuse have been investigated. Also, targets have been set for recycled materials with equivalent costs for virgin materials for making new parts.

3. Perspectives on the Physical Properties of Recycled Materials and Approaches for Improvement

3.1. Processing of Collected Bumper Material

The recent methods employed for processing recycled bumpers and the results of the studies conducted are given below.

a) Removing paint film
Paint on recycled bumpers reduces impact resistance and also exhibits poor surface quality. To resolve these problems, a paint film removal process is applied. One method of this process is machine shearing exfoliation. The other is the method that uses solvent to swell up the paint film thereby reducing its adhesion to allow the film to be removed. The problem with these methods is the increased cost resulting from the cost depreciation of the specialized equipment used and the requirement for a process to dispose of the removed paint particles.

b) Fine particle processing
This process cools the collected bumper material to a temperature below that of the glass transition temperature and pulverizes it to a particle size less than 100 μm. Because this process is able to create fine particles of the paint film, it minimizes loss of impact resistance property. The problem with this process however is the increased cost resulting from the depreciation of the equipment used.

c) Blend mix processing
This is the granulation process that follows the pulverization and washing of the recycled bumper material. This process adopts a simplified treatment process and can be administered with already existing multipurpose equipment. Although the cost of this reprocessing is inexpensive, it does not assimilate processing to the paint film, which leaves the problem of reduced impact resistance and surface quality.

From the investigation into the different processes described above and from the perspective of enabling a sustainability, the blend mix processing was selected as the simplest process which can be employed at the lowest cost. This process was selected as a basis for research into its applicability to parts that do not require surface design finesse or impact resistance properties.

3.2. Techniques for Resolving Problems

Figure 1 provides a comparative illustration of the material properties of bumper material recycled through blend mix processing versus virgin bumper material. The radar chart indicates the percentage rate of material property retention for recycled material versus the virgin bumper material. As the figure shows, the recycled material exhibits a reduction in material properties.

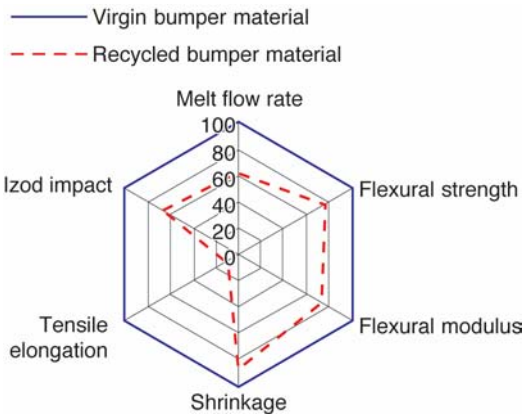


Fig. 1 Material properties of virgin bumper material and recycled bumper material

From the insights gained on these material properties, Table 1 lists the applicable parts selected for determining the applicability of modified material properties.

In the application of each part, as the recycled materials only exhibit reduced material properties, the compound material selected for each part is added to the recycled material to improve the overall physical properties of the materials.

The physical properties of the materials required for each part listed in Table 1 and the means for improving the materials are described below.

1) Aerial under cover
As this is a large part requiring thin structural formations, the melt flow of this material needs to be improved. Adding constituents with low molecular weight is an effective means of improving flow.

2) Side Spacer
To provide the side spacer with the necessary strength for supporting the bumper, the flexural strength of the constituent materials needs to be improved. To improve the flexural strength, filler and matrix resin surfaces have been chemically bonded and a filler with a large aspect ratio (in the longitudinal direction) has been added.

3) Evaporator case
To achieve dimensional accuracy in the current mold and to improve the flexural modulus required to maintain the shape of the part the shrinkage performance needed to be

Table 1 Applicable parts and requirements

● mark: Requirement

Applicable parts	Requirement					
	Melt flow rate	Flexural strength	Flexural modulus	Shrinkage	Tensile elongation	Izod impact
1) Aerial under cover	●					
2) Side spacer		●				
3) Evaporator case			●	●		
4) Rear shelf			●			
5) Floor carpet					●	

improved. To increase the flexural modulus and improve the shrinkage performance, homo-polypropylene (PP) without any elastomer constituency was added.

4) Rear shelf
To preserve the shape of the part required that the flexural modulus be increased. This was achieved by the addition of inorganic filler.

5) Floor carpet
To provide formation support when the part is molded, the tensile elongation needed improvement. This was achieved by the addition of an elastomer compatibilizer.

4. Improving Material Properties and Identifying Targeted Parts

This section describes the techniques applied to the parts targeted for this research.

4.1. Determining Applicability to the Aerial Under Cover

Figure 2 shows the positioning and shape of the aerial under cover. This part requires thin panel construction over the large part. Since recycled materials have low melt flow, this was targeted for improvement. The targeted value of the fluidity property was set according to the thickness of the panel, the size of the molding machine, and the number of mold gate points.

Since the fluidity of materials is dependent largely on molecular weight, the degree of fluidity could be improved by adding material with a low molecular weight. The material property has been improved by adding a 40% component of a high flow PP with a high degree of low molecular weight constituency.

Figure 3 illustrates the rate of Melt Flow Rate (MFR) achieved against the targeted MFR value of 100%. Adding the high flow PP has improved the MFR by 35% in comparison to untreated recycled material. This method successfully attained the targeted value required for material fluidity.

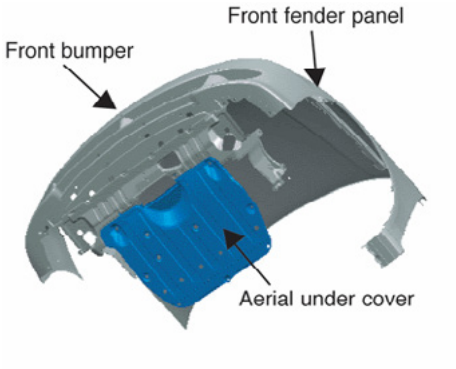


Fig. 2 Aerial under cover

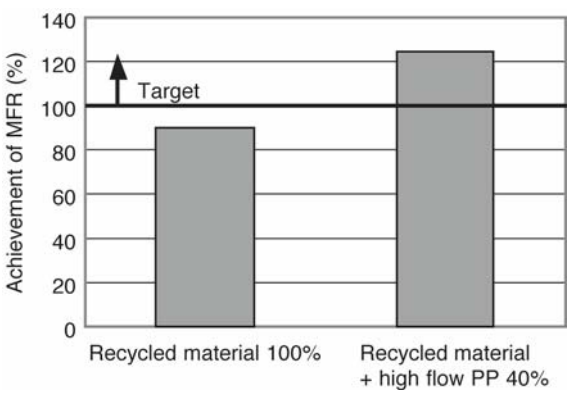


Fig. 3 MFR data

4.2. Determining Applicability for the Side Spacer

Figure 4 shows the positioning and the shape of the side spacer, which fixes the bumper. As a single bumper panel weighs approximately 4 kg, a sufficient amount of strength is required. The targeted strength value was determined according to the flexural load exerted on the part at elevated vehicle velocities.

To provide the required degree of strength, the part has been interfaced with chemically bonded filler and matrix resin. The selected process for chemical bonding was achieved by adding silane surface treated short glass fibers and PP modified with grafted functional groups to the recycled material.

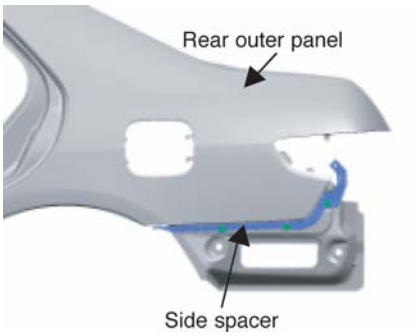


Fig. 4 Side spacer

Figure 5 shows photographs of scanning electron microscope (SEM) images of glass fiber and PP treated surfaces. These images have illustrated that for the material compound composed of surface treated glass + modified PP, the glass fiber surface is sufficiently wet to indicate that they have been successfully chemically bonded[3]. Figure 6 illustrates the rate of flexural strength achieved for the materials against the targeted value 100%. A 5% improvement over the targeted value for flexural strength has been achieved in material that has been treated by adding surface-treated glass fiber + modified PP. A 40% improvement in flexural strength was achieved over materials that have been supplemented with glass that has not been surface treated.

By employing this treatment method, the flexural strength was improved by 330% over untreated recycled materials. It has also been verified that this does not cause any problem when the vehicle is traveling.

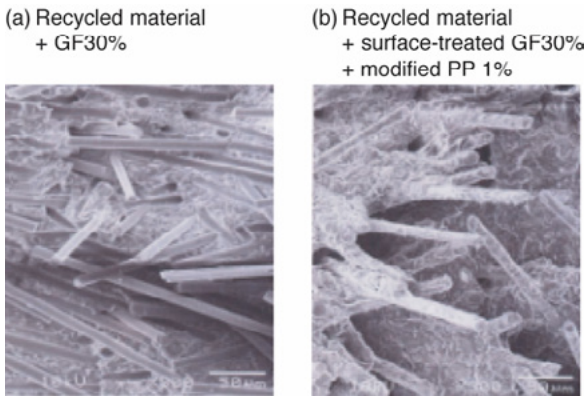


Fig. 5 SEM photographs of test pieces

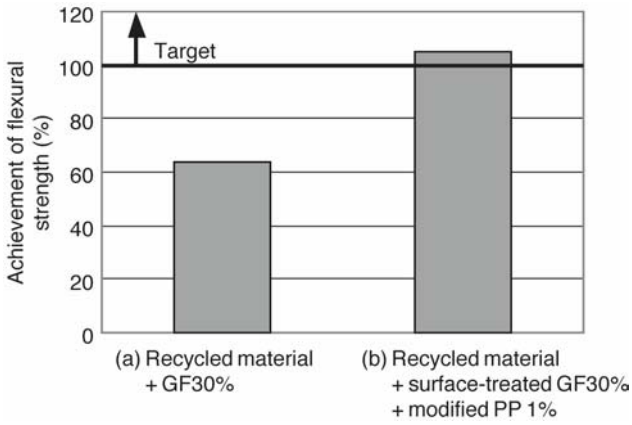


Fig. 6 Flexural strength data

4.3. Determining Applicability for the Evaporator Case

Figure 7 shows the evaporator case (referred to as the evapo case hereafter). This is used as the air conditioning cooling unit case and fits inside the instrument panel. To preserve the shape of the part required that the flexural modulus be increased. It was determined that the recycled material for this part be used with the existing mold for mass production. Therefore, the targeted value of the flexural modulus was set in accordance with the thickness of the part. The targeted value of the shrinkage performance was set to 14.5/1000, the shrinkage performance level of the current material.

Because recycled materials contain high elastomeric content, the mold shrinkage rate is less than that for other PP based materials and the flexural modulus is lower. This required that the shrinkage be increased and the flexural modulus improved. Adding homo PP was effective in improving the level of shrinkage performance. Talc has been applied to improve the flexural modulus.



Fig. 7 Evaporator case

Figure 8 shows the relationship, expressed by the dashed line, between the volume of recycled material with a shrinkage value of 14.5/1000 and applied volume of talc, and the level of flexural modulus achieved in relation to the volume of recycled material, expressed by the solid line. The volume of homo PP was calculated by subtracting the volume of recycled material and talc from 100. According to the dashed line in the figure, the volume of constituent content of the recycled material, which satisfies the required shrinkage performance, is less than 46%. Similarly, the solid line in the figure shows that the volume of constituent content of recycled material, which satisfies the required shrinkage performance, is less than 40%.

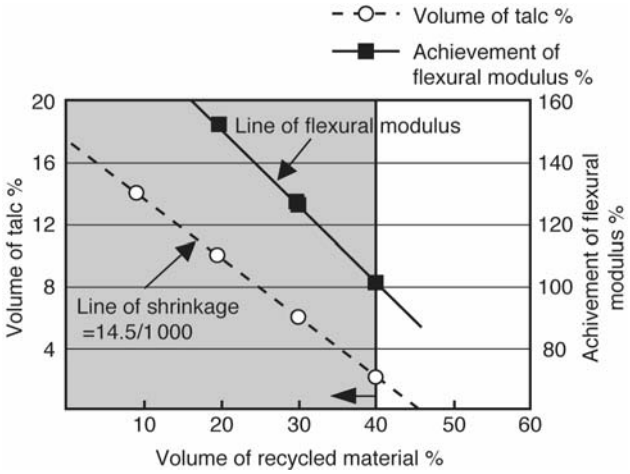


Fig. 8 Relationship between volume of recycled material and talc and flexural modulus data

To achieve the desired level of shrinkage performance and flexural modulus described above, the constituent content of the recycled material must be less than 40%. To improve the flexural modulus, the amount of recycled material used needs to be decreased. However, since it is desired to use a greater amount of recycled material, the volume of constituent recycled material used has been set to 40%.

From the above results, the composition of the part consists of 40 wt% recycled material, 2.5 wt% talc, and 57.5 wt% homo PP. Figure 9 shows the data for the physical properties of the flexural modulus of this composition. The physical modulus was improved by 48% in comparison to untreated materials. This method has successfully yielded the targeted value for flexural modulus and delivered a targeted value of 14.5/1000 for the shrinkage performance.

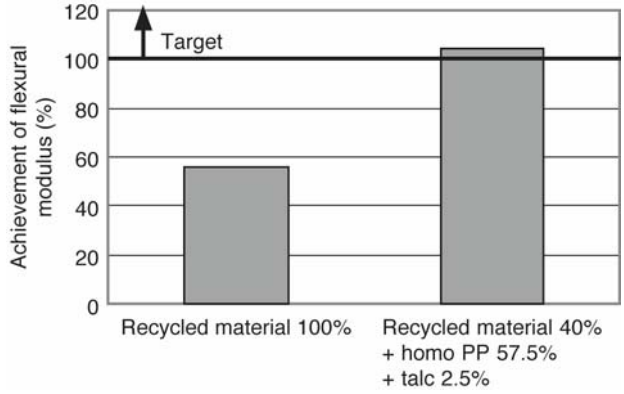


Fig. 9 Flexural modulus data

4.4. Determining Applicability for the Rear Shelf

The rear shelf part is used typically in hatchback type vehicles and separates the cabin area and the trunk space. The rear shelf is exposed to direct sunlight and must be able to support high loading. For these reasons, it is constructed of heat resistant resin base material containing core reinforcement material. Current resin materials are a blend of PP and wood powder and the targeted value for flexural modulus has been set according to this material.

As recycled materials contain approximately 30% elastomer components, it has a low flexural modulus in comparison to the current resin material. Talc has been added

to supplement the reduced flexural modulus and the material properties have been adjusted as required. Figure 10 show the flexural modulus data and the level of flexural modulus achieved against the targeted value of 100%. The same graph shows that the addition of recycled material reduces the flexural modulus by 20%. However, adding talc brings a 7% improvement over the targeted value to achieve acceptable rigidity. This method has successfully achieved the targeted value for flexural modulus.

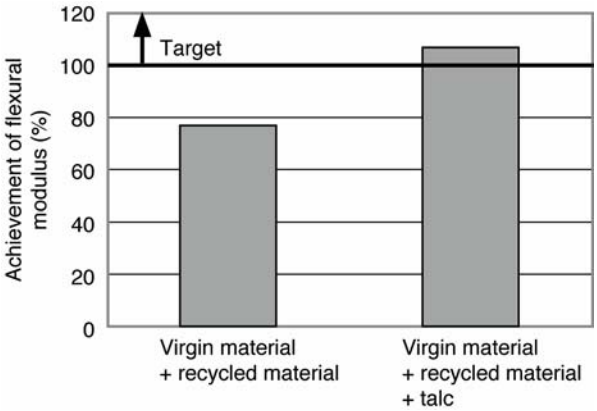


Fig. 10 Flexural modulus data

4.5. Determining Applicability for the Floor Carpet

To preserve the shape of the floor cover after it has been molded with the floor cover under surface, a low density polyethylene material is used for the underside of the floor carpet. Tensile elongation is required for the complex molding shape applied to the floor carpet underside material. A target value was set for the tensile elongation required in the floor carpet molding.

Recycled materials containing paint film flakes are low in tensile elongation properties. Recycled materials are also made of olefin type resin which is similar to polyethylene. However, in the simple blend process applied to such recycled materials, tensile elongation is not sufficient due to incompatibility of the immiscible component resins. To supplement this low tensile elongation, a compatibilizing agent made of olefin and styrene type elastomers is added to improve tensile elongation. Figure 11 shows the tensile elongation data associated with the floor carpet underside material. The tensile elongation was improved 18% above the targeted value. This process has satisfied the targeted value requirement for tensile elongation.

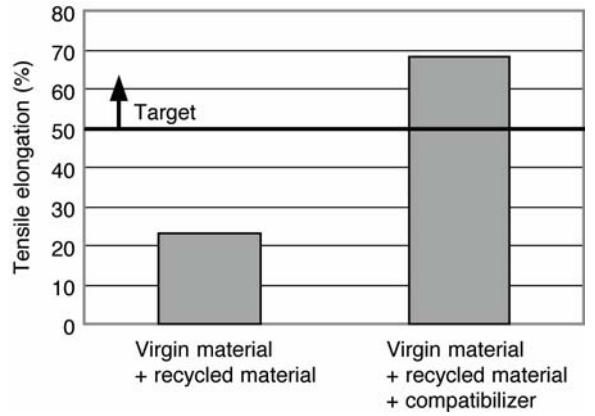


Fig. 11 Tensile elongation data

5. Summary

Methods for improving recycled materials have been developed to expand the applicability of parts and to increase the amount of recycled materials used in such parts. The various technologies that have been developed are described below.

1) Melt flow was improved to expand the applicability of materials to the aerial under cover. PP with high fluidity properties and low molecular weight has been added to constituents to improve the degree of fluidity by 130%.
2) Flexural strength was improved to expand the applicability of materials to the side spacer. Silane surface treated glass fibers and functional group grafted PP has been added to improve flexural strength by 330%.
3) Flexural modulus and shrinkage performance have been improved to expand the applicability of materials to the evaporator case. Homo PP and small amounts of talc have been added to improve the flexural modulus by 190% and control the part dimensions.
4) Flexural modulus has been improved to expand the applicability of materials to the rear shelf. Talc has been added to improve the flexural modulus by 30%.
5) Tensile elongation has been improved to expand the applicability of materials to the floor carpet. An elastomer type compatibilizing agent has been added to improve the flexural modulus by 90%.

The application of these material blending technologies has achieved the same level of cost as the initial targeted production cost employing virgin materials. The amount of recycled material used is now expected to increase 200 tons annually.

6. Acknowledgements

The authors would like to express their deepest gratitude to cooperating members from Sumitomo Mitsui Polyolefin Co., Ltd. and Honda Trading Corporation in addition to the large number of people who cooperated in the carrying out of the research activities described in this report.

References

(1) Inoue T.: Development of the Bumper Recycling Program, HONDA R&D Technical Review, Vol. 7, p. 170-178 (1995)

(2) Takeuchi, A et al: Improvement of Impact Resistance Property for Recycled Bumpers Applying Sandwich Injection Molding, Honda R&D Technical Review, Vol. 8, p. 186-193 (1996)

(3) Ide, F.: Function of Phase, Surface Modification of Polymer, Tokyo, Kindai Henshu, p. 229-243 (1987)

■ Authors ■


Satoshi HIRAWAKI


Kenji HIKITA


Tomoyuki UEMURA

Technical Papers Submitted to Out-of-company: July, 2002 to December, 2002

(English Papers only)

Date	Conference	Title	Author	Organization
2002.7.1	JSME/JSME International Journal	Modeling, control and experiment of a feedback active noise control system for free sound fields	Shuichi Adachi	Utsunomiya Univ.
			Hisashi Sano	Tochigi R&D Center
2002.7.3	ITS Asia-Pacific/5th Asia-Pacific ITS Forum (Seoul, Korea)	Introduction of Inter-vehicle communication system	Kazumitsu Kushida	Asaka R&D Center
			Masashi Satomura	Tochigi R&D Center
2002.7.8	38th AIAA/ASME/SAE/ASEE Joint Propulsion Conference & Exhibit/AIAA (Indianapolis, USA)	Flow Characteristics in a Transonic Ultra-Low-Aspect-Ratio Axial Turbine Vane	Naoki Kuno	Wako Research Center
			Toyotaka Sonoda	Wako Research Center
2002.7.9～11	Automotive & Transportation Technology Congress (Paris, France)	A Combined Experimental-Numerical Approach for Motorcycle Crank Noise: Modeling	Masahiko Sekita	Asaka R&D Center
			Hiroshi Tamura	Asaka R&D Center
			Bart Vandenplas	LMS International Engineering Services
			Wim Hendricx	LMS International Engineering Services
2002.7.15	ACTIVE 2002 (Southampton, UK)	Recent application of active noise and vibration control to automobiles	Hisashi Sano	Tochigi R&D Center
			Tsuyoshi Yamashita	Tochigi R&D Center
			Mitsuo Nakamura	Honda R&D Europe UK
2002.7.16～19	2002 International Technical Conference on Circuits/Systems, Computers and Communications (Phuket, Thailand)	Effects of comparison interval and order on subjective evaluation test of loudness	Junji Yoshida	Tochigi R&D Center
			Masao Kasuga	Tochigi R&D Center
			Hiroshi Hasegawa	Tochigi R&D Center
2002.7.22	The Japanese Section of the Combustion Institute (JSME)/Twenty-ninth InternationalSymposium on Combustion (Sapporo, Japan)	The Study on Establishment of Combustion Diagnosis Method and Application to Control Technology for Automotive Gasoline Engine	Yuichi Shimazaki	Tochigi R&D Center
	JSAE/JSAE INTERNATIONAL WORKSHOP (Yokohama, Japan)	Development of Honda CIVIC Hybrid Car	Teruo Wakashiro	Tochigi R&D Center
2002.7.23～25	JSAE Annual Congress (Yokohama, Japan)	Development of Metal Pushing V-Belt for Continuously Variable Transmission	Tooru Yagasaki	Tochigi R&D Center
			Shigeru Kanehara	Tochigi R&D Center
			Hideaki Aoyama	Tochigi R&D Center
			Toshihiro Saito	Tochigi R&D Center
		The Development of a New Lightweight, Compact and High Efficient CVT	Hisashi Kunii	Tochigi R&D Center
			Makoto Sumi	Tochigi R&D Center
2002.8.5	SICE/SICE Annual Conference 2002 (Osaka, Japan)	Control design of steering assistance system for driver characteristics	Yukihiro Fujiwara	Tochigi R&D Center
			Shuichi Adachi	Utsunomiya Univ.
		Estimation of road shape feature using H-inf filter	Yukihiro Fujiwara	Tochigi R&D Center
			Shuichi Adachi	Utsunomiya Univ.
			Tadahiro Fujihara	Utsunomiya Univ.
2002.8.12～16	NI Week 2002 Application Contest (Austin, USA)	Integrated Road Simulator Implemented at Low Cost	Shokichi Harashima	Asaka R&D Center
			Hiroshi Takahashi	Asaka R&D Center
2002.8.19～21	International Congress and Exposition on Noise Control Engineering (Dearborn, USA)	Development of Pass-by Noise Measurement System for Motorcycles	Tsuyoshi Mochizuki	Asaka R&D Center
			Kazuo Yamamoto	Asaka R&D Center
2002.9.4～6	AVL/14th International AVL Conference (Austria, Graz)	Development of a New Power Train for the Civic Hybrid	Masato Matsuki	Tochigi R&D Center
			Hideyuki Takahashi	Tochigi R&D Center
			Akira Fujimura	Tochigi R&D Center

Date	Conference	Title	Author	Organization
2002.9.9～13	JSAE/6th International Symposium on Advanced Vehicle Control (AVEC '02) (Hiroshima, Japan)	Effect of Longitudinal Acceleration Warning on Closed-loop Control Performance of Braking Assistance System	Hiroshi Mashita	Tochigi R&D Center
			Tomoyuki Fukumaru	Tochigi R&D Center
			Yoshimi Furukawa	Tochigi R&D Center
			Hideki Kaseyama	Tochigi R&D Center
		Enhanced Vehicle Stability and Steerability with VSA	Keiyu Kin	Tochigi R&D Center
			Hironobu Kiryu	Tochigi R&D Center
			Tohru Ikeda	Tochigi R&D Center
			Osamu Yano	PSG CO.,LTD.
		Vehicle Dynamics Evaluation by "Analytical Method of Equivalent Linear System using the Restoring Force Model of Power Function Type "	Kazuhito Misaji	Tochigi R&D Center
			Hiroyuki Tokunaga	Tochigi R&D Center
			Shigenori Takimoto	Tochigi R&D Center
			Yasuo Shimizu	Tochigi R&D Center
			Koichi Shibata	Nihon Univ.
		Improvement in Control Performance of Driver-Vehicle System with EPS using Cables to Connect the Steering Wheel and Gearbox	Katsuhiro Sakai	Tochigi R&D Center
			Atsuhiko Yoneda	Tochigi R&D Center
			Yasuo Shimizu	Tochigi R&D Center
		Suspension Characteristics Study using Genetic Algorithm	Hiroyuki Urabe	Tochigi R&D Center
			Yuji Sato	Tochigi R&D Center
			Takuya Shudo	Tochigi R&D Center
			Sadao Shibuya	Tochigi R&D Center
		The Analysis of the Influence of Front Lateral Bending Deformation on the Handling Characteristics	Masaki Nagahisa	Tochigi R&D Center
			Kaoru Kusaka	Tochigi R&D Center
			Tetsuji Nishimura	Tochigi R&D Center
		Steer Feel Evaluation Method Based on "Analytical Method of Equivalent Linear System using the Restoring Force Model of Power Function Type "	Hiroyuki Tokunaga	Tochigi R&D Center
			Kazuhito Misaji	Tochigi R&D Center
			Shigenori Takimoto	Tochigi R&D Center
			Yasuo Shimizu	Tochigi R&D Center
			Koichi Shibata	Nihon Univ.
		Vehicle Dynamics Controller Design based SRS and AHP	Shinya Nohtomi	Tochigi R&D Center
			Kazuyuki Okada	Tochigi R&D Center
			Shinichiro Horiuchi	Nihon Univ.
		Construction of the Rider Robot for Evaluating Two-Wheeled Vehicle	Shunichi Miyagishi	Nihon Univ.
			Ichiro Kageyama	Nihon Univ.
			Kouhei Takama	Nihon Univ.
			Masayuki Baba	Asaka R&D Center
			Hajime Uchiyama	Asaka R&D Center
2002.9.12	JSAE/SAE Joint Workshop on CFD Developments for Automotive Applications (Detroit, USA)	Predicting the thermal environment inside a car with CFD	Akihiro Fujita	Tochigi R&D Center
2002.9.16	ISMA (International Conference on Noise & Vibration Engineering)/ISMA2002 Conference (Belgium)	Optimal design of trim materials	Baldanzini N	Firenze Univ.
			Mantovani M	Rieter Automotive
			Kazuhito Misaji	Tochigi R&D Center
			Hiroko Tada	Tochigi R&D Center
			Tsuyoshi Yamashita	Tochigi R&D Center

Date	Conference	Title	Author	Organization
2002.9.16～17	International Motorcycle Conference: Safety-Environment-Future (Munich, Germany)	Advanced Brake Systems for Powered Two Wheelers: CBS, ABS and Future Directions	Tetsuo Tsuchida	Asaka R&D Center
			Yukimasa Nishimoto	Asaka R&D Center
			Michael Thiem	Honda R&D Europe
2002.9.18～20	International Research Council on the Biomechanics of Impact/International IRCOBI Conference (Munich, Germany)	Vehicle Impact Velocity Prediction from Pedestrian Throw Distance: Trade-Offs between Throw Formulae, Crash Simulators, and Detailed Multi-Body Modeling	K.Bhalla	University of Virginia
			P. Montazemi	University of Virginia
			J. Crandall	University of Virginia
			J. Yang	Chalmers University of
			X. Liu	Chalmers University of
			Yasuhiro Dokko	Tochigi R&D Center
			Yukou Takahashi	Tochigi R&D Center
			Yuji Kikuchi	Tochigi R&D Center
			D. Longhitano	Honda R&D Americas, Inc. Ohio Center
	Loughborough University/37th the United Kingdom Conference on Human Response to Vibration (UK)	Inter-Subject Variability of Vibration Characteristics of Human Seated in Car Seat	Mitsunori Kubo	Chiba Univ.
			Nobuharu Kuriki	Tochigi R&D Center
			Sachiko Yamada	Tochigi R&D Center
			Nobuaki Takata	Tochigi R&D Center
2002.9.20	Central Iron and Steel Research Institute/The Sino-Japan Workshop on Advanced Steels for Automobiles (Shanghai, China)	Automobile Material for Environment at Honda	Shinichi Sawai	Tochigi R&D Center
			Sukekuni Itoh	Tochigi R&D Center
			Yuichi Azuma	Tochigi R&D Center
2002.9.24～26	Global Powertrain Congress(Ann Arbor, USA)	An Approach to Controlling Auto-Ignition: Two-Stroke Gas Exchanging Method	Yoichi Ishibashi	Asaka R&D Center
			Kenji Nishida	Asaka R&D Center
2002.9.25	Pabst Science Publishers/Kongress der Duetschen Gesellschaft fur Psychologie (Psychological coference in Berlin) (Berlin, Germany)	Gruppenunterschiede bei kognitiven Landkarten eines Automobilcockpits (Group differences of cognitive maps of an automobile cockpit)	Miklos Kiss	Generation Research Program Ludwig-Maximilians-Univ.
			Marc Wittmann	Generation Research Program Ludwig-Maximilians-Univ.
			Martina Neidhart	Generation Research Program Ludwig-Maximilians-Univ.
			Ernest Poppel	Generation Research Program Ludwig-Maximilians-Univ.
			Peter Gugg	SCIENCIA GmbH
			Alexander Steffen	SCIENCIA GmbH
			Hiroyuki Kamiya	Tochigi R&D Center
		Positionseffekte eines Displays fur visual Zweitaufgaben im cockpit eines Fahrsimulators (Position effects of a display for secondary tasks in a cockpit of a driving simulator)	Marc Wittmann	Generation Research Program Ludwig-Maximilians-Univ.
			Miklos Kiss	Generation Research Program Ludwig-Maximilians-Univ.
			Martina Neidhart	Generation Research Program Ludwig-Maximilians-Univ.
			Ernest Poppel	Generation Research Program Ludwig-Maximilians-Univ.
			Peter Gugg	SCIENCIA GmbH
			Alexander Steffen	SCIENCIA GmbH
			Hiroyuki Kamiya	Tochigi R&D Center

Date	Conference	Title	Author	Organization
2002.10.1	JSAE/JSAE Review Vol.23 No.4	Development of the 2001 year model Civic	Chitoshi Yokota	Honda R&D Europe
			Yoshinori Nakamura	Tochigi R&D Center
			Shigeru Yada	Tochigi R&D Center
			Kouichi Funatsu	Tochigi R&D Center
			Fumio Kubo	Tochigi R&D Center
			Tsuyoshi Ohkubo	Tochigi R&D Center
			Tadashi Watanabe	Tochigi R&D Center
		Development of a new manual transmission	Keiji Nemoto	Tochigi R&D Center
			Toshiharu Kumagai	Tochigi R&D Center
			Yasushi Ohnuma	Tochigi R&D Center
		Development of chromium-free pretreatment system for aluminum bodies	Toshiya Nishino	Tochigi R&D Center
			Koichiro Izumi	Honda R&D Americas
2002.10.2	2002 IEEE/RSJ International Conference on Intelligent Robots and Systems (IROS2002)/IEEE/RSJ (Lausanne, Switzerland)	The intelligent ASIMO. System overview & integration.	Ryujin Watanabe	Wako Research Center
			Chiaki Aoyama	Wako Research Center
			Shinichi Matsunaga	Wako Research Center
			Nobuo Higaki	Wako Research Center
			Yoshiaki Sakagami	Wako Research Center
2002.10.7～8	VDI (Verein Deutscher Ingenieure)/CVT 2002 Congress (Munich, Germany)	Development of Metal Pushing V-Belt Stress Simulation for CVT	Toshihiro Saito	Tochigi R&D Center
2002.10.8	Aachen Colloquium/Aachen Colloquium "Automobile and Engine Technology (Aachen, Germany)	HONDA's Challenge in Addressing Environmental Concerns (Engine Technology)	Hiroo Shimada	Tochigi R&D Center
			Takanori Shiina	Tochigi R&D Center
			Takashi Moriya	Tochigi R&D Center
			Hiroki Katano	Tochigi R&D Center
2002.10.8～10	Natural Gas Vehicle Coalition, International Association for Natural Gas Vehicles, Inc./World NGV2002 8th International and 20th National Conference and Exhibition on Natural Gas Vehicles (Washington DC, USA)	Performance Evaluation of an Automobile Utilizing an Adsorbed Natural Gas Tank	Hiroshi Ogasa	Tochigi R&D Center
			Masaru Oku	Tochigi R&D Center
		Development of a 1.7 liter CNG Engine for the 2001 Honda Civic GX	Takushi Toda	Tochigi R&D Center
2002.10.19～23	The World Electric Vehicle Association (WEVA)/ The 19th International Battery, Hybrid and Fuel Cell Electric Vehicle Symposium (EVS-19) Pusan, South Korea)	Development of Inteligent Power Unit for HYBRID Car	Kazuhiko Aitaka	Tochigi R&D Center
		Development of Motor Assist System for Hybrid Four-door Sedan	Shuuji Kato	Tochigi R&D Center
			Atsushi Shibutani	Tochigi R&D Center
			Toshiaki Kaku	Tochigi R&D Center
		Strength Evaluation Method for Nd-Fe-B Rare Earth Sintered Magnet	Takaaki Nagi	Tochigi R&D Center
			Teruyoshi Kita	Tochigi R&D Center
2002.10.22	Covergence Transportation Electronics Association/Covergence2002 Conference Proceeding (Detroit, USA)	Development of the Motor Assist System for the Hybrid Automobile-the Civic Hybrid	Astushi Izumiura	Tochigi R&D Center
			Hirohisa Ogawa	Tochigi R&D Center
		Engine Control System for a Natural Gas Vehicle	Akira Murakami	Tochigi R&D Center
			Takushi Toda	Tochigi R&D Center
			Masato Matsuki	Tochigi R&D Center
2002.10.25	Human Factors and Ergonomics Society (HFES)/HFES Europe Chapter Annual Meeting 2002 (Dortmund, Germany)	Saccadic velocities reflect presaccadic task demand	Jan Churan	Generation Research Program Ludwig-Maximilians-Univ.
			Miklos Kiss	Generation Research Program Ludwig-Maximilians-Univ.
			Marc Wittmann	Generation Research Program Ludwig-Maximilians-Univ.
			Martina Neidhart	Generation Research Program Ludwig-Maximilians-Univ.
			Ernest Poppel	Generation Research Program Ludwig-Maximilians-Univ.
			Peter Gugg	SCIENCIA GmbH
			Hiroyuki Kamiya	Tochigi R&D Center

Date	Conference	Title	Author	Organization
2002.10.28～29	Hibbitt, Karlsson & Sorensen, Inc./2002 ABAQUS User's Conference (Newport, RI/USA)	Application of Metal Pushing V-belt Stress Simulation with Pulley Stiffness	Toshihiro Saito	Tochigi R&D Center
2002.10.29～31	JSAE・SAE-Int./SETC 2002 8th Small Engine Technology Conference (Kyoto, Japan)	Development of Pb-free Free-Cutting Steel Enabling Omission of Normalizing for Crankshafts	Atsushi Amataka	Asaka R&D Center
			Satoru Suwa	Asaka R&D Center
		Development of a Four-stroke Engine with Turbo Charger for Personal Watercraft	Takaharu Kurosaki	Asaka R&D Center
			Kazunori Okada	Asaka R&D Center
			Hitoshi Yokotani	Asaka R&D Center
		Development of a Titanium Material by Utilizing Off-Grade Titanium Sponge	Yuji Marui	Asaka R&D Center
			Toyotaka Kinoshita	Asaka R&D Center
			Kyo Takahashi	Asaka R&D Center
		A Combined Experimental and Numerical Approach for Motorcycle Crank Noise: Experimental Validation	Masahiko Sekita	Asaka R&D Center
			Hiroshi Tamura	Asaka R&D Center
			Bart Vandenplas	LMS International Engineering Services
			Wim Hendricx	LMS International Engineering Services
		Development of Silent Chain Drive System for Motorcycles	Haruomi Sugita	Asaka R&D Center
			Masahiko Sekita	Asaka R&D Center
			Tomohiro Fuse	Asaka R&D Center
		Development of Gear Train Behavioral Analysis Technologies Considering Non-linear Elements	Shingo Ueda	Asaka R&D Center
			Tatsuo Suzuki	Asaka R&D Center
			Mitsuyoshi Kamiya	Asaka R&D Center
			Tadashi Niino	Asaka R&D Center
		Development of the application of the automotive engine technology Outboard Motor	Masaki Tsunoda	Asakahigashi R&D Center
			Kentaro Furuya	Asakahigashi R&D Center
		Development of the application of the Hybrid System to Snow Thrower	Jitsumi Hanafusa	Asakahigashi R&D Center
			Tsutomu Wakitani	Asakahigashi R&D Center
			Takahiro Yamamoto	sakahigashi R&D Center
			Tsutomu Inui	Asakahigashi R&D Center
		Development of Exhaust Valve Seat Insert Material for High Performance Engines	Teruo Takahashi	NIPPON PISTON RING CO.,LTD.
			Arata Kakiuchi	NIPPON PISTON RING CO.,LTD.
			Kenichi Sato	NIPPON PISTON RING CO.,LTD.
			Katsuaki Sato	Tochigi R&D Center
			Katsuhiko Tominaga	Tochigi R&D Center
		New Indicated Mean Effective Pressure Measuring Method and Its Applications	Keiichi Nagashima	Tochigi R&D Center
			Kazuo Tsuchiya	Meiji Univ.
2002.12.1	John Wiley & Sons, Ltd/Handbook of Fuel Cell Technology Vol.3, Fuel Cell Technology and Applications	PEM Fuel Cell System for HONDA FCV	Shiro Matsuo	Tochigi R&D Center

Editor’s Postscript

This issue contains eight articles introducing technologies related to fuel cell vehicles. The actual work of writing these articles could not begin until around the same time as the deadline for the other articles in this issue, so the writing and editing schedule was very demanding. I want to express our gratitude to the authors who wrote their manuscripts for us in such a short time, the colleagues who gave their assistance, especially the members of the Manuscript Committee, and the Manuscript Office that kept the flow of manuscripts moving smoothly, as well as Kyoeido Printing Co., Ltd. Successful handling of such tight situations depends largely on the efforts of the various people involved, but neither can I play down the accumulated expertise and facilitating frameworks of the Manuscript Office and the Manuscript Committee. These are matters that fall out of view as soon the editing of an article is completed, but they are no less important than the quality of the article itself in efficiently bringing about the well-timed publication of research and development results. We view these as assets that we ourselves have built up over time, and we take great pride in them.

One other distinguishing feature of the present issue is that it contains more “Introduction of New Technologies” articles. Honda R&D Co., Ltd. has established different target areas for research and development at the Asaka, Asakahigashi, and Tochigi R&D Centers, as well as the Wako Research Center. The idea is that, by introducing their own specific research to each other, they will all gain a broader knowledge of their own company. Additionally, there is also the expectation that they will all be stimulated by research results and development technologies from different fields, thus producing a synergistic effect that will be typical of Honda. This is one of the objectives of the *Technical Review*, and the present issue achieves it in excellent form.

As the number of manuscripts submitted to us for publication grows larger, and the size of our research staff that contributes to our publication expands, the number of articles we carry in each issue is also tending to increase. The editing burden is going to become heavier, but we are committed to making this additional effort for the growth of the *Technical Review* and giving paper-writing activity a boost. We are hoping to receive even more of your understanding and support in the future.

(Tsuruga)

Honda R&D Technical Review English Version Vol.15 No.1
The following associates provided us with their cooperation and expertise:

Karen	Arneson	American Honda Motor Co., Inc.
Kevin	Aschenbach	Honda R&D Americas, Inc. Ohio Center
Bill	Bezilla	Honda R&D Americas, Inc. North Carolina Center
Jeff	Brown	Honda R&D Americas, Inc. Ohio Center
Dennis	Chung	Honda R&D Americas, Inc. Ohio Center
Mary	Christopherson	Honda North America Inc.
James	Davis	Honda Research Institute USA, Inc.
Jim	Dykeman	Honda R&D Americas, Inc. Ohio Center
Kikuo	Fujimura	Honda R&D Americas, Inc.
Charles	Gagliano	Honda R&D Americas, Inc. Ohio Center
Lee	Goldring	Honda North America Inc.
Ken	Keller	Honda R&D Americas, Inc. Ohio Center
Dan	Leibovitz	Honda R&D Americas, Inc. Ohio Center
Steve	Mathison	Honda R&D Americas, Inc. Los Angeles Center
Elie	Merheb	Honda R&D Americas, Inc. Ohio Center
Ashley	Nichols	Honda R&D Americas, Inc. Ohio Center
Chris	Nichols	Honda R&D Americas, Inc. Ohio Center
Bill	Post	Honda R&D Americas, Inc. Ohio Center
Hiroshi	Shinagawa	Honda R&D Americas, Inc. Ohio Center
Charles	Thomas	Honda R&D Americas, Inc. Ohio Center
Dan	Turk	Honda R&D Americas, Inc. Ohio Center
William	Willen	American Honda Motor Co., Inc.
Jun	Xin	Honda R&D Americas, Inc. Ohio Center

